IAEA TECDOC SERIES

IAEA-TECDOC-1829

IAEA-TECDOC-1829

Investigations of Materials under High Repetition and Intense Fusion Pulses

Report of a Coordinated Research Project 2011–2016

IAEA
International Atomic Energy Agency

INVESTIGATIONS OF MATERIALS UNDER HIGH REPETITION AND INTENSE FUSION PULSES

The following States are Members of the International Atomic Energy Agency:

AFGHANISTAN
ALBANIA
ALGERIA
ANGOLA
ANTIGUA AND BARBUDA
ARGENTINA
ARMENIA
AUSTRALIA
AUSTRIA
AZERBAIJAN
BAHAMAS
BAHRAIN
BANGLADESH
BARBADOS
BELARUS
BELGIUM
BELIZE
BENIN
BOLIVIA, PLURINATIONAL STATE OF
BOSNIA AND HERZEGOVINA
BOTSWANA
BRAZIL
BRUNEI DARUSSALAM
BULGARIA
BURKINA FASO
BURUNDI
CAMBODIA
CAMEROON
CANADA
CENTRAL AFRICAN REPUBLIC
CHAD
CHILE
CHINA
COLOMBIA
CONGO
COSTA RICA
CÔTE D'IVOIRE
CROATIA
CUBA
CYPRUS
CZECH REPUBLIC
DEMOCRATIC REPUBLIC OF THE CONGO
DENMARK
DJIBOUTI
DOMINICA
DOMINICAN REPUBLIC
ECUADOR
EGYPT
EL SALVADOR
ERITREA
ESTONIA
ETHIOPIA
FIJI
FINLAND
FRANCE
GABON
GEORGIA
GERMANY
GHANA
GREECE
GUATEMALA
GUYANA
HAITI
HOLY SEE
HONDURAS
HUNGARY
ICELAND
INDIA
INDONESIA
IRAN, ISLAMIC REPUBLIC OF
IRAQ
IRELAND
ISRAEL
ITALY
JAMAICA
JAPAN
JORDAN
KAZAKHSTAN
KENYA
KOREA, REPUBLIC OF
KUWAIT
KYRGYZSTAN
LAO PEOPLE'S DEMOCRATIC REPUBLIC
LATVIA
LEBANON
LESOTHO
LIBERIA
LIBYA
LIECHTENSTEIN
LITHUANIA
LUXEMBOURG
MADAGASCAR
MALAWI
MALAYSIA
MALI
MALTA
MARSHALL ISLANDS
MAURITANIA
MAURITIUS
MEXICO
MONACO
MONGOLIA
MONTENEGRO
MOROCCO
MOZAMBIQUE
MYANMAR
NAMIBIA
NEPAL
NETHERLANDS
NEW ZEALAND
NICARAGUA
NIGER
NIGERIA
NORWAY
OMAN
PAKISTAN
PALAU
PANAMA
PAPUA NEW GUINEA
PARAGUAY
PERU
PHILIPPINES
POLAND
PORTUGAL
QATAR
REPUBLIC OF MOLDOVA
ROMANIA
RUSSIAN FEDERATION
RWANDA
SAN MARINO
SAUDI ARABIA
SENEGAL
SERBIA
SEYCHELLES
SIERRA LEONE
SINGAPORE
SLOVAKIA
SLOVENIA
SOUTH AFRICA
SPAIN
SRI LANKA
SUDAN
SWAZILAND
SWEDEN
SWITZERLAND
SYRIAN ARAB REPUBLIC
TAJIKISTAN
THAILAND
THE FORMER YUGOSLAV REPUBLIC OF MACEDONIA
TOGO
TRINIDAD AND TOBAGO
TUNISIA
TURKEY
TURKMENISTAN
UGANDA
UKRAINE
UNITED ARAB EMIRATES
UNITED KINGDOM OF GREAT BRITAIN AND NORTHERN IRELAND
UNITED REPUBLIC OF TANZANIA
UNITED STATES OF AMERICA
URUGUAY
UZBEKISTAN
VANUATU
VENEZUELA, BOLIVARIAN REPUBLIC OF
VIET NAM
YEMEN
ZAMBIA
ZIMBABWE

The Agency's Statute was approved on 23 October 1956 by the Conference on the Statute of the IAEA held at United Nations Headquarters, New York; it entered into force on 29 July 1957. The Headquarters of the Agency are situated in Vienna. Its principal objective is "to accelerate and enlarge the contribution of atomic energy to peace, health and prosperity throughout the world''.

IAEA-TECDOC-1829

INVESTIGATIONS OF MATERIALS UNDER HIGH REPETITION AND INTENSE FUSION PULSES

REPORT OF A COORDINATED RESEARCH PROJECT 2011–2016

INTERNATIONAL ATOMIC ENERGY AGENCY
VIENNA, 2017

For further information on this publication, please contact:

Physics Section
International Atomic Energy Agency
Vienna International Centre
PO Box 100
1400 Vienna, Austria
Email: Official.Mail@iaea.org

Printed by the IAEA in Austria
December 2017

IAEA Library Cataloguing in Publication Data

Names: International Atomic Energy Agency.
Title: Investigations of materials under high repetition and intense fusion pulses / International Atomic Energy Agency.
Description: Vienna : International Atomic Energy Agency, 2017. | Series: IAEA TECDOC series, ISSN 1011–4289 ; no. 1829 | Includes bibliographical references.
Identifiers: IAEAL 17-01123 | ISBN 978–92–0–108217–6 (paperback : alk. paper)
Subjects: LCSH: Plasma (Ionized gases). | Plasma confinement. | Fusion reactors.

FOREWORD

This publication presents the research work accomplished within the framework of the coordinated research project (CRP) on investigations of materials under high repetition and intense fusion pulses, organized and conducted from 2011 to 2016, which promoted the use of small scale devices as test bed facilities among IAEA Member States to address issues of high relevance in large scale fusion devices. The focus was the field of plasma surface interaction relating to the performance of tungsten as a plasma facing material for next step fusion devices, such as the International Thermonuclear Experimental Reactor (ITER) and demonstration power plants. The CRP made use of the existing network of test bed devices, such as dense plasma foci, plasma accelerators and particle accelerators, electron beam facilities and nuclear fission reactors, in which it is possible to reproduce particles and heat load conditions expected in fusion reactors. The CRP helped improve the understanding of the underlying processes leading to material damage due to heat and neutron loads in fusion devices, while also contributing to the development of fusion technology.

Through its coordinated research activities, the IAEA has made it possible for States that are not yet members of the ITER project to contribute to ITER relevant scientific investigations, which have led to increased capabilities of diagnostics for plasma surface interaction. A total of 18 institutions participated from 15 Member States: Bulgaria, Chile, the Czech Republic, Estonia, Germany, India, the Islamic Republic of Iran, Italy, Kazakhstan, Malaysia, the Netherlands, Poland, the Russian Federation, Singapore and Ukraine. A remarkable impact has been the honing of the capabilities of young scientists in fusion relevant research in different Member States.

The IAEA wishes to express its appreciation to the members of the Technical Programme Committee and the authors of the reports. The IAEA is especially thankful to M. Barbarino for his contribution to drafting and review. The IAEA officers responsible for this publication were S.M. Gonzalez de Vicente and R. Kamendje of the Division of Physical and Chemical Sciences.

EDITORIAL NOTE

This publication has been prepared from the original material as submitted by the contributors and has not been edited by the editorial staff of the IAEA. The views expressed remain the responsibility of the contributors and do not necessarily represent the views of the IAEA or its Member States.

Neither the IAEA nor its Member States assume any responsibility for consequences which may arise from the use of this publication. This publication does not address questions of responsibility, legal or otherwise, for acts or omissions on the part of any person.

The use of particular designations of countries or territories does not imply any judgement by the publisher, the IAEA, as to the legal status of such countries or territories, of their authorities and institutions or of the delimitation of their boundaries.

The mention of names of specific companies or products (whether or not indicated as registered) does not imply any intention to infringe proprietary rights, nor should it be construed as an endorsement or recommendation on the part of the IAEA.

The authors are responsible for having obtained the necessary permission for the IAEA to reproduce, translate or use material from sources already protected by copyrights.

The IAEA has no responsibility for the persistence or accuracy of URLs for external or third party Internet web sites referred to in this publication and does not guarantee that any content on such web sites is, or will remain, accurate or appropriate.

CONTENTS

SUMMARY

1. INTRODUCTION

In the recent past, many advances have been made towards demonstrating the feasibility of controlled and sustained energy production from nuclear fusion. Milestone facilities based on magnetic and inertial confinement fusion are currently under construction or in operation aiming at demonstrating ignition and energy gain. In this context, both fusion approaches still present some basic issues which need to be urgently resolved. For instance, of critical importance is the characterization, qualification (testing) and development of advanced plasma facing materials that are able to withstand the extreme radiation and heat loads expected in fusion reactors based on magnetic and inertial confinement.

Fundamental understanding of PSI (also referred to as plasma wall interaction) processes in magnetic and inertial confinement fusion devices requires dedicated R&D activities in close connection with material characterization as well as with theory and modelling. There are many gaps in the field of PSI which must be addressed in order to develop the predictive capability in support of the plasma facing components design for the world's largest fusion experiment in Southern France, ITER, and for a fusion demonstration power plant (DEMO). Although a number of unresolved issues on plasma edge physics in magnetic confinement devices (e.g. scrape-off layer plasma widths, flows and turbulent transport) can only be addressed using tokamaks and stellarators, some other issues related to the impact of transient heat loads on materials, erosion and redeposition mechanisms, fuel retention, dust formation, as well as new material concepts can be explored using dedicated test bed devices. In fact, besides providing a good access to the plasma material interaction zone, allowing the specific diagnostics to be operational and an easy exchange of material samples, the reasons to explore the field of PSI using test bed facilities include the ability to:

— Provide ITER relevant particle and energy fluxes (high density and low energy semi-detached plasma);
— Reach ITER relevant fluence;
— Reproduce ITER relevant transient heat loads (edge localized modes, disruptions) not achievable in today's tokamaks but achievable in today's plasma accelerators;
— Make single parameters and single process parametric studies which are not possible in tokamaks;
— Provide well diagnosed test cases for benchmarking plasma wall interaction codes, as well as test beds for PSI diagnostics;
— Study combined effects of heat load and neutron damage on materials in dedicated facilities;
— Be robust in design and cost effective.

The purpose of the CRP on "Investigations of Materials under High Repetition and Intense Fusion Pulses" reported here was to plan and coordinate activities addressing relevant issues associated with the impact of intense transient heat and particle loads on plasma facing materials. Candidate plasma facing materials for next step fusion devices include tungsten (divertor and first wall), beryllium (first wall in ITER), and various types of ceramics and transparent materials as functional materials for insulation and diagnostics. The CRP has put particular attention in investigating different grades of tungsten as material to be used in the most loaded areas in ITER and currently as the primary choice in DEMO plasma facing material.

2. CRP OVERALL OBJECTIVE

The overall objective of this CRP has been to use the existing plasma accelerators network within the Member States to contribute to the knowledge and understanding of the performance and adequacy of candidate plasma facing materials for the next step fusion devices under extreme heat and particle load conditions.

A total of eighteen institutions from fifteen Member States participated in this CRP:

a) Bhabha Atomic Research Center (BARC), Mumbai, India;
b) Comisión Chilena de Energia Nuclear (CCHEN), Santiago, Chile;
c) Czech Technical University in Prague (CTU), Prague, Czech Republic;
d) FOM-Institute for Plasma Physics Rijnhuizen, Nieuwegein, Netherlands;
e) Forschungszentrum Jülich GmbH (FZJ), Jülich, Germany;
f) International Centre for Theoretical Physics (ICTP), Trieste, Italy;
g) Institute of Plasma Physics and Laser Microfusion (IPPLM), Warsaw, Poland;
h) International Centre for Dense Magnetized Plasmas (ICDMP), Warsaw, Poland;

i) Institute of Plasma Physics, National Science Center Kharkov Institute of Physics and Technology (NSC KIPT), Kharkov, Ukraine;
j) INTI International University, Putra Nilai, Malaysia;
k) Institute of Metallurgy and Material Sciences (IMET), Moscow, Russian Federation;
l) Ioffe Institute, St. Petersburg, Russian Federation;
m) Moscow Physical Society (MPS), Moscow, Russian Federation;
n) National Institute of Education, Nanyang Technological University (NIE/NTU), Singapore, Singapore;
o) National Nuclear Center of the Republic Kazakhstan (NNC RK), Kurchatov, Kazakhstan;
p) Plasma Physics Research Center of Islamic Azad University (PPRC), Tehran, Iran;
q) Sofia University St. Kliment Ohridski, Sofia, Bulgaria;
r) Tallinn University (TU), Tallinn, Estonia.

The set of heat and particle radiation sources employed consisted of fifteen dense plasma focus (DPF) devices working with deuterium, deuterium-tritium mixture and some other gases with energy in their banks between 200 J and 1 MJ, four particle accelerators (for both fast ions and electrons), two plasma accelerators and two plasma guns. The repetition rates of these devices are in the limits from 1 shot every 20 min to 10 Hz for DPF devices and up to 100 kHz for electron accelerator. The plasma temperatures in these devices range from few tens of eV (plasma guns) to 1 keV (DPF), whereas plasma densities range between 10^{20}–10^{25} m^{-3}. Available electron beams (JUDITH-1 and JUDITH-2) feature electrons with energies ranging between 30–150 keV while DPF devices typically have electron energies ranging between 30 keV and 1 MeV. Deuterons energies in DPF devices extend between 30 keV and few MeV. However, high-Z ions can be accelerated in these devices up to 100 MeV. The DC-60 cyclotron can accelerate ions in the range between 0.4 MeV/nucleon and 1.75 MeV/nucleon. DPF devices, plasma guns and plasma accelerators used can produce plasma streams with velocities higher than 10^5 m/s^1. Power densities (W/m^2, later referred to as power flux density) produced by plasma streams, fast electron and ion beams on the target surface range between 1 MW/m^2 and 10^{11} MW/m^2. These provide a similar heat load factor $F = q\sqrt{\tau}$ where q is the power flux density and τ the pulse duration, as in fusion devices. In addition, DPF devices provide the capability to activate samples with a neutron flux between -10^{20}–10^{21} $n \cdot m^{-2} \cdot s^{-1}$. The research reactor 6MW WWR-K (1.4×10^{18} $n \cdot m^{-2} \cdot s^{-1}$) was used for studying neutron induced damage. These facilities span a wide range of irradiation parameters which allows a meaningful contribution to the clarification of the damage mechanisms under powerful heat loads, the dynamics of erosion products and the adequacy of different tungsten grades material in fusion reactor environment.

3. SPECIFIC RESEARCH OBJECTIVES

The specific objectives of this CRP were as follows:

— Investigation of surface layers damage processes, fuel retention and dust issues in candidate plasma facing materials (different tungsten grades and coatings, beryllium, CFC, SiC) for next step fusion devices under high power and repetitive plasma impacts;
— Classification of main factors (pulse length and repetition rate, total fluence, fuel retention, etc.) affecting the performance and adequacy of candidate plasma facing materials for next step fusion devices. This will also include comparative studies of identical material samples on different devices;
— Establishment of a data base of erosion behaviour for selected materials (different tungsten grades and coatings, beryllium, CFC, SiC) under different heat and particle load conditions and different sample treatment scenarios;
— Validation of available codes against experimental results achieved in the framework of the CRP;
— Development and standardization of specific diagnostics relevant to the analysis of high power plasma impacts on selected material;
— Investigation of damage produced on tungsten sample by combined effects of neutron irradiation and thermal load in nuclear fission reactor.

4. EXPECTED RESEARCH OUTPUTS

The expected outputs of this CRP were as follows:

— Comprehensive review tabling the characteristics of the selected materials (different tungsten grades and coatings, beryllium, CFC, SiC) under well defined heat and particle load conditions;
— Database of the erosion rates of the selected materials (different tungsten grades and coatings, beryllium, CFC, SiC) under different heat and particle load conditions and different sample treatment scenarios;

— Scientific base for improved understanding of the mechanisms of plasma material interaction and surface modification, possibly leading to the development of more advanced plasma facing materials for fusion and other applications;
— Summary of the capabilities of the validated codes able to simulate the dynamics of plasma material interaction as well as the response of the materials to the heat and particle loads;
— Dissemination to the CRP participants of the designs and hardware of the standardized diagnostics relevant to the analysis of high power plasma impacts on the selected materials;
— Continuing and strengthening relationships between the scientists from the various institutions.

5. KEY INVESTIGATIONS PERFORMED

For the purpose of investigating the damage processes of the surface layers during transient heat loads, fuel retention and dust issues of the candidate plasma facing materials, the CRP activity focused on the PLANSEE double forged (PDF-W) tungsten samples (forged in two orthogonal directions aiming to obtain a dense and nearly isotropic grain structure). These samples were provided by the FZJ to all participating research teams. More than 100 samples of 12 mm × 12 mm × 5 mm were provided. All samples were expected to be identical, which was also demonstrated through microstructural and compositional investigations done by some of the participants. Round robin tests were performed using different plasma/nuclear facilities and particle accelerators. A total of 25 different devices were used for irradiation during this CRP which included plasma accelerators, dense plasma foci, a tokamak, a nuclear fission reactor, a cyclotron, and electron beam facilities. The list of key investigations and results are summarized in the Annex.

5.1. Irradiation with Plasma Accelerators

In plasma accelerator experiments at the NSC KIPT the main objective was to identify the erosion products emitted from the exposed PDF-W surfaces. This was accomplished by variating the impact heat load along with the detailed analysis of the particles ejection start time, their velocities and sudden changes of brightness of the particle traces. These data were recorded placing a charge coupled device in front of the target surface.

At Ioffe Institute, a plasma gun device and a spherical tokamak GLOBUS-M were employed to investigate the effects of high heat fluxes applied via hydrogen and helium plasma jets, as well as tokamak deuterium plasma. In addition to PDF-W, four other types of tungsten materials were also irradiated. These included single crystal tungsten, hot rolled tungsten, powder made V_MP tungsten, and JSC POLEMA (according to ITER specifications) tungsten.

5.2. Irradiation with Plasma Foci

A fleet of plasma focus devices, with storage energy ranging from hundreds of joules to one megajoule, was used for irradiation experiments.

The irradiation of PDF-W samples was performed at the CCHEN using the PF-400J. In addition, coarse grained tungsten (CGW) samples from the Institute of Nuclear Fusion, Polytechnic University of Madrid, Spain, were irradiated using PF-400J and PF-2kJ. The surface damage of the irradiated tungsten samples were investigated in terms of the morphological and structural modifications.

At the NTU, several experiments were conducted using the NX3 (10 kJ) and UNU-ICTP (3 kJ) devices to irradiate the PDF-W and commercial tungsten samples at different distances using different number of pulses. The main research objective was to perform irradiation experiments on PDF-W samples, without or reduced impurities, to investigate the changes in the structural, mechanical, morphological and compositional properties of the irradiated samples against the unexposed virgin sample.

The PF-12 device at TU was employed to investigate the interaction of pulsed deuterium plasma (0.1–1 keV) and fast ions (100 keV) streams with PDF-W samples. In addition, the dependence of the generation of cracks, droplets, holes, bubbles, grooves, and surface roughening on the irradiation conditions was analyzed. Additionally, single forged tungsten and tungsten doped with 1% lanthanum-oxide (all manufactured by PLANSEE) were irradiated to investigate the surface damage.

The collective work at four different plasma focus facilities, which included PF-1000U (ICDMP), PF-6 (IPPLM), PF-5M (IMET) and BORA (ICTP), dealt with the performance of the irradiation of PDF-W, of pure

tungsten and tungsten alloys, of carbon based composites (CFC and SiC), of titanium and its alloys, and of low activated stainless steel (Eurofer). The change in the morphology, structure, composition, mechanical properties, electrical conductivity and erosion properties was investigated. One of the main objectives was to determine the effects of hot plasma and fast ion stream, as well as shock wave produced by a fast ion stream in plasma focus devices on the surface, and bulk damages of the irradiated samples.

The PF-4kJ device at Sofia University was employed to irradiate samples of PDF-W, sintered tungsten sheets (0.2 mm thickness), casted molybdenum (18 mm × 18 mm × 5 mm) and stainless steel (20 mm × 20 mm × 1 mm) to study surface damages such as cracks, blisters and melting as well as changes in the chemical composition.

At INTI, experiments were carried out to investigate the surface damage of the PDF-W samples using the PF-3kJ device. The samples were exposed to hot plasma and fast deuteron ions at different distances from the anode top, and multiple numbers of shots were performed to study erosion and changes in the surface morphology, structure, and composition.

5.3. Irradiation with Electron Beam Facility

The electron beam facilities JUDITH-1 and JUDITH-2 at FZJ, were employed for multiple thermal shock loadings, up to 10^6 pulses, on PDF-W at different base temperatures. The material was investigated in its stress relieved and recrystallized state for a better understanding of the crack formation mechanisms when exposed to transient thermal loads, e.g., edge localized modes (ELMs). The influence of the ductile to brittle transition temperature (DBTT) and heat load parameters on the onset of cracking and crack evolution was investigated and quantified by metallographic means.

5.4. Irradiation with Nuclear Fission Reactor

Neutron irradiation of eight different types of tungsten materials, including PDF-W, was done by the NNC RK using the 6MW WWR-K nuclear fission reactor at the Institute of Nuclear Physics, Kazakhstan. The purpose was to perform basic characterizations of neutron irradiated PDF-W and to investigate combined neutron and high heat flux loading effects.

5.5. Irradiation with Particle Accelerator

Low energy alpha particles from the DC-60 accelerator at the Institute of Nuclear Physics, Kazakhstan (in collaboration with the NNC RK) were used to irradiate PDF-W samples to study erosion and changes in the structural, mechanical and compositional properties upon irradiation.

6. CRP ACHIEVEMENTS

6.1. Database of performance indicators of tungsten

With regard to the classification of the main factors affecting the performance and adequacy of the double forged tungsten as plasma facing material during transient events, the results of the investigations indicate that several parameters determine its performance and the most important are:

- Base temperature of the material;
- Heat flux factor;
- Thermo mechanical properties of the material;
- Pulse duration;
- Total number of pulses;
- Pulse frequency.

The base temperature relates to the tungsten transition from brittle to ductile state. The heat flux factor, which depends on the pulse duration and net energy delivered, determines the tungsten surface temperature increment during irradiation. It is also an indicator of whether cracking, melting and/or evaporation will occur. Thermomechanical properties and tungsten grain structure also influence the damage threshold and evolution (as a function of base temperature, heat flux factor, total number of pulses, and pulse frequency).

For example, the results of the low pulse number ELM-like thermal shock experiments performed with JUDITH-1 at FZJ are presented in Figure 1. Based on the analyzed surface modifications, the cracking threshold base temperature (related to the DBTT) was determined for the reference direction (longitudinal, grain elongated parallel to the loaded surface) ranging from 150°C to 200°C for the stress relieved material ranging from 200°C to 300°C for the recrystallized material.

Since the material is anisotropic, different cracking threshold base temperatures (> 500°C) were found in the orthogonal direction. The maximum roughness and surface elevation was observed just below the cracking threshold temperature. Crack formation in general followed the grain boundaries resulting in crack formation parallel to the loaded surface at a depth ranging from 200 µm to 600 µm for the reference direction, limiting the heat transfer capabilities of the material.

The pulse duration affects the deformation rate and the related stress level in the surface layer and, in case of melting, affects the melt motion. Furthermore, as showed in Fig. 1, an increasing number of pulses at moderate transient thermal loading conditions, delivered to tungsten via the electron beam facility JUDITH-2, increased the thermal fatigue damage. At elevated temperatures the damage induced in tungsten was related to the thermal fatigue only.

At lower temperatures, crack initiation was caused by fatigue, but crack propagation towards the bulk was brittle. However, the final crack depth and the material damage threshold (between 0.14 GW/m^2 and 0.27 GW/m^2) were independent of the damage mechanism.

The heat flux factor was an important parameter affecting the final crack depth. The same response was observed for thermal shock tests conducted for low pulse numbers and higher intensities as showed also in Fig. 2.

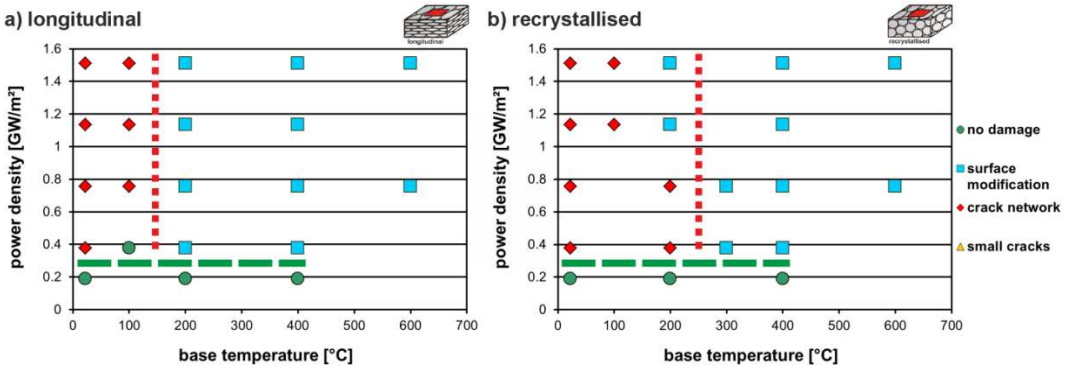

FIG. 1. (a) Damage mapping for the samples with longitudinal grain orientation; (b) damage mapping for the samples in the recrystallized state. The damage and cracking threshold are indicated by the green dashed and red dotted line, respectively.

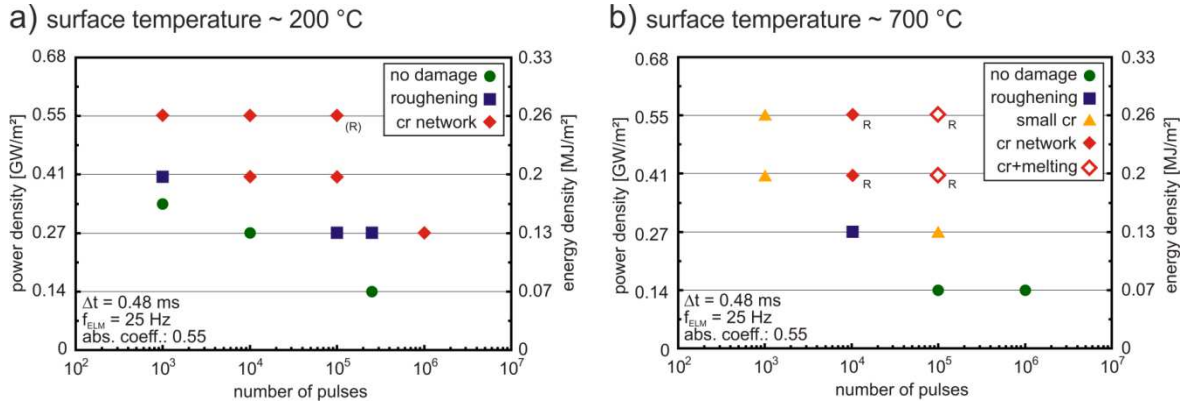

FIG. 2. (a) Surface condition of tungsten samples tested at a surface temperature of 200°C, here one sample showed recrystallization at the surface near a crack (R); (b) surface condition of tungsten samples tested at a surface temperature of 700°C, here samples that were cross-sectioned and showed recrystallization are indicated by 'R'.

In addition, the Annex provides a comprehensive review and database illustrating surface damage, structural and compositional changes of tungsten irradiated under well defined heat and particle load conditions in other plasma and particle accelerators employed.

6.2. Mechanisms of plasma material interaction

Based on the investigations performed on various types of plasma and particle accelerators, the mechanisms of plasma material interaction and surface modifications were identified.

6.3. Findings from plasma accelerators

Tungsten damage during transient events was mainly due to macroscopic erosion mechanisms related to cracking development and surface melting effects. The threshold energy load for the cracking development strongly decreased for a large number of repetitive plasma pulses. The tungsten melting led to melt motion and droplets splashing, as well as to the development of wavy structures on the irradiated surface due to Kelvin-Helmholtz instability. The erosion products, emitted in the form of droplets and solid dust from the exposed W surfaces, were distinguished by means of variation of the impacting heat load and by the analysis of the particles ejection start time, and particles velocities. In ELM-like regimes, droplets were emitted during the plasma exposure but contributed marginally to the overall mass loss, while dust generation and mass loss dominated at the end of the plasma pulse during melt resolidification and transition phase from ductile to brittle.

Several mechanisms of dust formation were identified for tungsten irradiated in plasma accelerators, which include the bifurcation of major cracks, development of fine cracks along the grains, resolidification of microbridges through the cracks and the material modification resulting in the formation of a nanostructured surface. It was found that the modification of tungsten upon irradiation with repetitive pulses led to the development of ordered subμm cellular structures, which might have contributed significantly to the nm-sized fraction of droplets and dust formation.

The study of macroscopic erosion of castellated targets showed that edge effects appeared to be the dominating mechanism of target erosion. It was found that the emission of droplets had threshold character and was cyclic in nature. New erosion mechanism, introduced by edge effects, was found to produce an order of magnitude increment in droplet size with some particles reaching submillimetre size.

6.3.1. Findings from plasma foci

It was found that cracking, surface melting, erosion and nanostructure formation were the dominating effects on irradiated tungsten. During the interaction of plasma and particles with materials in dense plasma focus devices it was observed that secondary plasma of several types was formed on the irradiated sample surface:

a) The relatively low temperature (<10 eV) secondary plasma generated by the interaction of cumulative plasma stream (generated by conical current sheath in pinch phase) with target material;
b) The relatively hot (>100 eV) secondary plasma generated by the interaction of stream of fast ions with target material;
c) The relatively low temperature (<10 eV) secondary plasma generated by the rarefaction wave (generated inside the target by the shock wave produced by fast ion stream).

It was found that for the target placed at a large distance from the anode, the beam of fast ions disintegrated and short circuited to the cathode of the DPF chamber after its penetration through the shock wave front into a residual atmosphere. In such a case, the power flux densities of both streams, hot plasma and fast deuterons, were estimated to be nearly the same.

6.3.2. Findings from Electron Beam Facility

During the load deposition process, the thermal expansion of the affected area was limited by the surrounding ‘cold’ material. Thereby, the induced compressive stresses would either exceed or not the yield strength of the material and lead in the positive case to plastic deformation, depending on the base temperature of the material (determining the mechanical properties of the material) and the stress amplitude (depending on temperature rise as a function of the absorbed power/energy density). With increasing number of pulses, plastic deformation, e.g. in form of dislocations, accumulates and results in thermal fatigue. At locations of highest stress and lowest

strength, e.g. grain boundaries, thermal fatigue, induced crack formation starts. Accordingly, roughening due to plastic deformation acts as a precursor for cracking.

6.4. Combined neutron and heat load damage

Tungsten samples encapsulated in hydrogen and helium at 700°C were exposed to thermal and fast neutron environment for 3255 hours in the 6MW WWR-K nuclear fission reactor at NNC RK. The flux of thermal and fast neutron was 7.3×10^{13} n · cm^{-2} · s and 6.8×10^{12} n · cm^{-2} · s, respectively. The fluence for thermal and fast neutrons was 8.6×10^{20} n/cm^2 and 8.0×10^{19} n/cm^2, respectively, leading to DPA in the order of 0.03. After a cool down post irradiation examinations of samples have started. Subsequently, the samples will be irradiated at the electron beam facility JUDITH-1 at FZJ. The successful characterization of these samples will contribute to the provision of design data for the use of tungsten as plasma facing material in fusion environments beyond ITER.

6.5. Validation of numerical codes

Experimental results obtained from plasma accelerators and e-beam facilities were used for the validation of PEGASUS and MEMOS codes (developed at Karlsruhe Institute of Technology, Germany). The PEGASUS code was upgraded to its new capabilities to quantitatively predict the cracking threshold of tungsten in ELM-like plasma exposures and its degradation in the course of repetitive pulses. The capability of the code to qualitatively describe the crack network evolution was also demonstrated. Results on melt layer erosion for flat targets and castellated structures were used for the validation of the MEMOS code, which was adopted for castellated geometries. This activity contributed to the development of the 3-D version of the MEMOS code for the modelling of melt layer erosion.

The Lee Code (initially developed by Lee Sing at University of Malaya, Malaysia) was modified to simulate the ion beam and fast plasma stream characteristics and parameters such as pulse length, fast ion beam fluence and flux, power flux and heat flux factors in plasma foci. The code was validated against published experimental results obtained with the PF-400J device at CCHEN.

6.6. Diagnostic developments

A series of diagnostics were developed at different laboratories to measure various physical quantities related to plasma surface interaction:

— 16 frame laser interferometer (1 ns time resolution) for measurement of plasma density and shock wave velocity near sample surface (ICDMP);
— Laser interferometers to measure the average density of the plasma jet and to record absolute values of the plasma jet pressure and power density (ICTP);
— 4 frame soft X ray pinhole camera (1 ns time resolution) for imaging of surface plasma (IPPLM);
— Absolutely calibrated magnetic probes for dynamics measurements of azimuthal and longitudinal magnetic fields in the pinch plasma (1 ns time resolution) (ICDMP);
— Fast photomultiplier tube and scintillator probes for neutron X ray diagnostics with improved sensitivity and time resolution of 0.3 ns with the ability to work in harsh environments (IPPLM, NIE/NTU);
— Neutron activation detectors based on different materials (e.g. Ag, In, Be, Y) (ICDMP, NIE/NTU);
— 4/5 pin diodes array for plasma temperature measurements in a soft X ray region (NIE/NTU);
— Spectroscopy diagnostic complex for measurement of temperature and dynamics of near surface plasmas (IPPLM, ICDMP);
— Fast two color pyrometer to measure the surface temperature of tungsten during and after irradiation (ICTP);
— Surface calorimetry methods and movable piezo detectors for the analysis of high power plasma impact on selected material surfaces (NSC KIPT);
— X ray portable diffractometer for in situ analysis of the irradiated sample surface (IMET);
— X ray microcomputer tomography system for the investigation of bulk damages in the irradiated samples (IMET).

7. IMPACT OF THE CRP

This CRP provided a unique possibility for experimental simulations of plasma surface interaction phenomena for materials under the extreme conditions expected in fusion reactors (such as ITER and DEMO) which cannot be studied in the present day tokamaks.

In particular, this CRP has promoted the use of small scale devices as test bed facilities to address issues of high relevance for large scale fusion devices. Activities therein have led to increased capabilities of diagnostics for plasma material interaction. In addition, it made it possible for countries not currently members of the ITER project to contribute to ITER relevant scientific investigations. It also provided opportunities for scientific cooperation among developed and developing countries. A remarkable impact has been made in honing the capabilities of young scientists in fusion relevant research in different member states.

The subject of materials under extreme conditions has applications in several research and industrial areas. The work performed within the framework of the CRP has relevance beyond its original scope (for example materials for aerospace applications, high temperature engineering, and novel plasma technologies).

REPORTS OF THE
COORDINATED RESEARCH PROJECT
PARTICIPANTS

IRRADIATION OF SAMPLES FOR FUSION PROSPECTIVE MATERIALS BY THE PLASMA FOCUS DEVICE OF SOFIA UNIVERSITY

S. ZAPRYANOV, A. BLAGOEV
Faculty of Physics, Sofia University,
Sofia, Bulgaria

Abstract

This paper presents the first results for irradiation of tungsten, molybdenum and stainless steel samples with the 4 kJ plasma focus (PF) device at the University of Sofia. The samples were placed 4 cm above the anode of the PF machine and were exposed to a considerable number of shots. The working gas was deuterium with the pressure adjusted in the range of 1–3.3 mbar. Thus, the plasma streams and the fast ion beam, which appear after the pinch phase, impinge the samples. The interaction of the pinch products with the targets causes substantial surface damage to the specimens. A mesh of partially melted cracks and recrystallized regions are revealed on this surface and various chemical compounds are also present.

S. Zapryanov and A. Blagoev, Phys. Scr. **T161** (2014) 014041

http://iopscience.iop.org/article/10.1088/0031-8949/2014/T161/014041

CHARACTERIZATION OF HIGH ENERGY DEUTERON PULSES PRODUCED BY DENSE MAGNETIZED PLASMAS

P. KUBES[*], M. PADUCH[**], D. KLIR[*], A. SHISHLOV[***], J. CIKHARDT[*], B. CIKHARDTOVA[*], K. REZAC[*], J. KRAVARIK[*]

[*] Czech Technical University,
Prague, Czech Republic

[**] Institute of Plasma Physics and Laser Microfusion,
Warsaw, Poland

[***] Institute of High Current Electronics,
Tomsk, Russian Federation

Abstract

Two external devices were employed (PF-1000, GIT-12) for the characterization of fast deuterons producing the fusion neutrons and for the more detailed description of the mechanisms of the acceleration of the fast particles using interferometric, X rays, neutron and corpuscular diagnostics. These devices recorded the evolution of the ordered dense structures. The generation of HXR and neutron radiation corresponds to the transformation of these structures, similarly as in fusion plasmas produced by the tokamaks and lasers. The generation of fast particles with energy of keV and MeV is based on the idea of reconnection of magnetic lines. In PF-1000, this reconnection can be realized with a filamentary structure. The plasma gun load in GIT-12 made possible to reach the high neutron yield of 10^{13} per shot, while the comprehensive neutron, corpuscular and X ray diagnostics show presence of the fast deuterons, protons and neutrons with energy up to 20–30 MeV.

1. INTRODUCTION

The investigations provided in the framework of the current CRP on "Investigations of Materials under High Repetition and Intense Fusion Pulses" were focused according to plan to:

a) Development of X ray, neutron and visualization diagnostics, and simulation methods for elaboration of signals. The new diagnostics were developed for spatial and energy distribution of fast deuterons and neutrons.
   (i) The temporal and spatial resolved MCP for soft X rays;
   (ii) The multipurpose detector for maximal deuteron energy (stack detector), spatial distribution of ion source (cathode ion pinhole) and beam profile;
   (iii) The cathode multi pinhole and anode pinhole for detection of ions, electrons and X rays;
   (iv) The absorption of ion emission using LiF target and spectroscopy of ions using the set-up of radiochromic films;
   (v) The simulations which adopted MCNP codes for scattering of neutrons and MC to test the influence of magnetic field on the fast ions traces.
b) Experiments with fusion plasma on the plasma focus and Z-pinch devices on the current level of 1–3 MA, see Fig. 1.
   (i) The plasma focus PF-1000 device located at IPPLM which operates at the current level of 1–2 MA and it produces, at the deuterium filling, a total neutron yield of 10^{10}–10^{11}, see Fig. 2.
      — The comprehensive interferometry, neutron and X ray diagnostics employed to obtain the detailed picture of the evolution of internal structures and their correlation with production of neutrons and X rays;
      — The presence of a self-generated axial component of the magnetic fields which was experimentally measured by magnetic probes;
      — At the compression of the puffing deuterium by the neon current sheath, the external neon resulted separated from the hot central region;
      — On the contrary, at the compression of the puffed central neon compressed by external deuterium, the similar value of fusion neutrons were registered due to possible penetration of the deuterium into the central radiating neon;
      — The internal structure of the dense column which was tested by the Al wire placed in the axis of the anode did not defend the typical evolution of the internal plasmoids and the production of neutrons.
   (ii) The facility GIT-12 located in Tomsk which was optimized for maximal neutron production.

— The registered ions and neutrons reached energy up to 20–30 MeV;
— The load configuration with the plasma gun and with the central gas puff made possible to reach the high neutron yield 3×10^{12} (highest in the world in Z-pinches for D–D fusion reaction during 2007–2014), see Fig. 3;
— These results were obtained at the conditions with the high implosion velocity;
— At this regime, the Z-pinch is a very efficient source of the intensive beams of deuterons, protons and neutrons in the energy above MeV.

c) Acquisition of the results obtained using the comprehensive diagnostics for the formulation of the intense pulses characteristics and mechanism of fast particles acceleration.
   (i) The observed characteristics of fast deuterons leads to the conclusion that the small sources of limited number of deuterons are connected with the filamentary structure of the current of 100 kA with diameter of 10–100 μm;
   (ii) The evolution of the organized dense structure can be combined with the fast deuterons characteristics to formulate the model of acceleration of fast electron and ions at the reconnection of magnetic lines in current filaments;
   (iii) Analog models for fast reconnection of magnetic lines as the mechanism of acceleration of fast electron and ions are also used for simulations in tokamak and laser produced plasmas.

d) Education of students in the frame of bachelor, diploma and doctoral works.
   (i) In the period of 2012–2015, four bachelors, three diplomas and four doctoral theses of students were produced.

e) Presentation of the results in journals and conferences.
   (i) During this period twenty-three papers were published in reviewed papers.

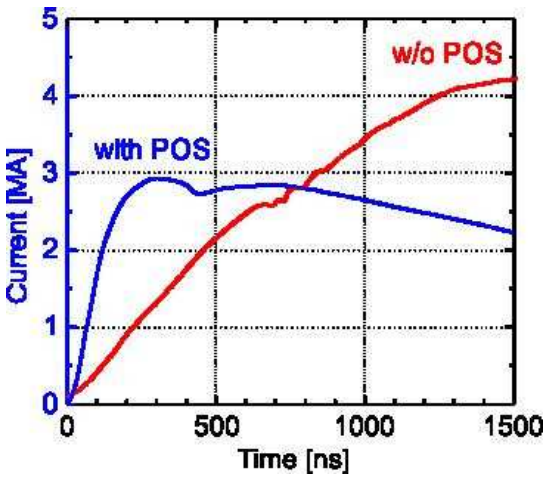

FIG. 1. Current with and without POS.

FIG. 2. Device with the DPF chamber and supplement parts with the current.

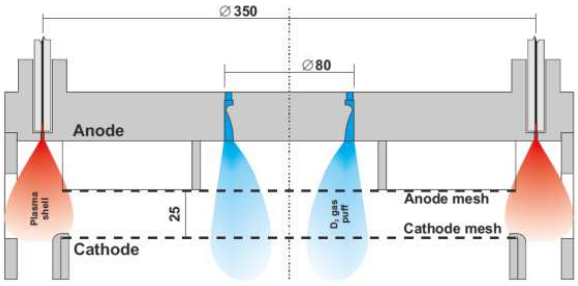

FIG. 3. Scheme of distribution of plasma gun (red) and gas puff (blue).

2. FAST IONS ACCELERATION MECHANISM

2.1. Equipment used in the experiments

Concerning the PF-1000, the existence of thermonuclear neutrons was discussed in [1–2]. The interferometric diagnostics shows existence of the dense organized toroidal and plasmoidal structures, transformation of which correlates with production of neutrons [3–7]. The experiments with magnetic probes confirmed the existence of the internal and external azimuthal component of the magnetic field. The existence and transformation of closed currents in organized dense structures were described in [8–9]. The influence of the external magnetic field on the plasma column and neutron production was published in [10–12]. This factor increases the stability of the pinch and decreases the fluctuation and the value of the neutron production in single shots. The production of neutrons and deuterons at the presence of the admixture of the elements with higher atomic number in the pinched plasma was described in [13]. Concerting the GIT-12, the main parameters are reported in Table 1.

TABLE 1. MAIN PARAMETERS OF THE GIT-12 DEVICE

Bank capacity	3.3 mF
Charging voltage	40 kV
Energy storage	2.6 MJ
Working gases	D2, C, H_2, He, N2
DPF chamber type	Z-pinch
Repetition rate	1 shot per 2 days
Lifetime of the DPF systems	~ 10^4 shots

2.2. Results obtained

At the compression of the deuterium injected from the gas puff by the neon plasma layer, the low energy of the soft X ray emission (in the level of shots with pure deuterium) was registered. At this load, the very effective compression exists in the axial region. The fast deuterons are accelerated to the mean axial energy of 50–100 keV with the total energy of a few kJ in one shot. The radial component has a lower mean energy of 20–30 keV. The production of fast deuterons strongly depends on the total mass of deuterons. At the neon linear mass of 50 μg/cm, the number of fast deuterons producing neutrons is one order higher at the linear deuterium mass of 7 μg/cm than for the higher linear mass of 15 μg/cm [14]. The filamentary structure of the pinched plasma column was also registered in the PF-1000. It shows the discrete structure of the current layer and it enables the fast reconnection as the possible acceleration mechanism of fast electrons and deuterons producing HXRs and neutrons [15]. At the compression of the neon injected from the gas puff by the deuterium plasma layer, the high neutron production is explored by the penetration of the deuterium into the neon plasma. This deuterium carries the current in form of filaments due to higher Spitzer conductivity. Consequently, the neutron production should be generated at the reconnection of filaments [16]. The return motion on the top of some lobules makes possible to form the scenario of the closed toroidal currents (which are reservoir of the magnetic energy confined in the pinch [17]) flowing out of the dense pinched column. It is generated in the external region of the necks at the breakdown, shortening the long discharge trace along the surface of the column.

Regarding the results obtained on the GIT-12, a substantial difference between neutron spectra in low yield (2×10^{11}) and high yield (3×10^{12}) shots were shown with the radial time of flight (TOF) signals measured at 10.13 m. In the shots with high neutron yield, the maximum neutron energies in the radial direction reached value 15.5 ± 0.5 MeV. The flux (>10 MeV) neutrons in the radial direction reached the value of $(3 \pm 1) \times 10^9$ n/sr. Most of the neutrons originated from $D(d,n)^3He$ reactions but a certain number of neutrons could be produced also by secondary $D(t,n)^4He$ reactions, deuteron break up, deuteron electrodisintegration, photonuclear and other endothermic reactions. The high yield regime was achieved mainly by a large number of deuterons with higher (MeV) energies. Due to the fact that fast neutrons were observed with the radial TOF detectors, the radial component of deuteron kinetic energy was significant. The Z-pinches can be a very efficient source of intensive beams of deuterons, protons and neutrons in the energy range of tens of MeV. This result was obtained at conditions with the small mass of the deuterium and the high implosion velocity. This finding is important for different physical, technical and biological applications [18–21].

During the presented research the bachelor, diploma and dissertation work of students Adam Pavlat, Vojtech Munzar, Jakub Cikhardt, Balzhima Cikhardtova, Ondrej Sila and Jiri Kortanek were realized. The results were published in twenty-three papers in reviewed journals.

ACKNOWLEDGEMENT

This work was supported in part by the Research Program under Grants MSMT No. LG 15013, GACR 1607036S, IAEA RC-16954, RC-16956, RC-17088, RC-17165, and SGS 13/194/OHK3/3T/13 as well by Polish Ministry of Science and Higher Education within the framework of the financial resources in the year 2015 allocated for the realization of the international cofinanced projects.

REFERENCES

[1] KLIR, D., KUBES, P., PADUCH, M., PISARCZYK, T., CHODUKOWSKI, T., SCHOLZ, M., KALINOWSKA, Z., ZIELINSKA, E., BIENKOWSKA B., HITSCHFEL J., KARPINSKI, L., KORTANEK, J., KRAVARIK, J., REZAC K., IVANOVA-STANIK, I., TOMASZEWSKI, K., Search for thermonuclear neutrons in a mega-ampere plasma focus, PPCF **54** (2012) 015001.

[2] KLIR, D., KUBES, P., PADUCH, M., PISARCZYK, T., CHODUKOWSKI, T., SCHOLZ, M., KALINOWSKA, Z., ZIELINSKA, E., BIENKOWSKA B., HITSCHFEL J., JEDNOROG, S., KARPINSKI, L., KORTANEK, J., KRAVARIK, J., REZAC K., IVANOVA-STANIK, I., TOMASZEWSKI, K., Response to Comment on Experimental evidence of thermonuclear neutrons in a modified plasma focus, Appl. Phys. Lett. **100** (2012) 016101.

[3] KUBES, P., KLIR, D., KRAVARIK, J., REZAC, K., PADUCH, M., PISARCZYK, T., SCHOLZ, M., CHODUKOWSKI, T., IVANOVA-STANIK, I., KARPINSKI, L., TOMASZEWSKI, K., ZIELINSKA, E., SADOWSKI, M. J., Energy transformation in column with plasma focus discharge with MA currents, IEEE Transactions on Plasma Science **40** (2012) 481.

[4] KUBES, P., KLIR, D., PADUCH, M., PISARCZYK, T., SCHOLZ, M., CHODUKOWSKI, T., KALINOWSKA, Z., REZAC, K., KRAVARIK, J., HITSCHFEL, J., KORTANEK, J., BIENKOWSKA, B., IVANOVA-STANIK, I., KARPINSKI, L., SADOWSKI, M. J., TOMASZEWSKI, K., ZIELINSKA, E., Characterization of the neutron production in the modified MA plasma focus, IEEE Transactions of Plasma Science **40** (2012) 1075.

[5] KUBES, P., KLIR, D., PADUCH, Z., REZAC, K.M., PISARCZYK, T., SCHOLZ, M., CHODUKOWSKI, T., KALINOWSKA, K., KRAVARIK, J., HITSCHFEL, J., KORTANEK, J., BIENKOWSKA, B., IVANOVA-STANIK, I., KARPINSKI, L., SADOWSKI, M. J., TOMASZEWSKI, K., Interferometry of the plasma focus equipped with forehead cathode, Nukleonika **57** (2002) 189.

[6] KORTANEK, J., KUBES, P., KRAVARIK, J., REZAC, K., KLIR, D., PADUCH, M., PISARCZYK, T., ZIELINSKA, E., CHODUKOWSKI, T., KALINOWSKA, Z., Current flow and energy balance during the evolution of instabilities in the plasma focus, Phys. Scr**. T161** (2014) 014044.

[7] CIKHARDTOVA, B., KUBES, P., CIKHARDT, J., PADUCH, M., ZIELINSKA, E., KRAVARIK, J., REZAC, K., KORTANEK, J., SILA, O., Temporal distribution of linear densities of the plasma column in a plasma focus discharge, Nukleonika **60** (2015) 315–318.

[8] KUBES, P., KRAUZ, V., MITROFANOV, K., PADUCH, M., SCHOLZ, M., PISARCZYK, T., CHODUKOWSKI, T., KALINOWSKA, Z., KARPINSKI, L., KLIR, D., KORTANEK, J., ZIELINSKA, E., KRAVARIK, J., REZAC, K., Correlation of magnetic probe and neutron signals with interferometry figures on the plasma focus discharge, Plasma Phys. Control. Fusion **54** (2012) 105023.

[9] KUBES, P., KLIR, D., KRAVARIK, J., REZAC, K., KORTANEK, J., KRAUZ, V., MITROFANOV, K., PADUCH, M., SCHOLZ, M., PISARCZYK, T., CHODUKOWSKI, T., KALINOWSKA, Z., KARPINSKI, L., ZIELINSKA, E., Scenario of pinch evolution in a plasma focus discharge, Plasma Phys. Control. Fusion **55** (2013) 035011.

[10] PADUCH, M., ZIELINSKA, E., KUBES, P., KLIR, D., KRAVARIK, J., REZAC, K., CIKHARDT, J., KORTANEK, J., SCHOLZ, M., KARPINSKI, L., Influence of the external magnetic field on the pinch evolution and neutron production in plasma focus discharge, Plasma Phys. Control. Fusion **55** (2013) 115013.

[11] CIKHARDT, J., BATOBOLOTOVA, B., KUBES, P., KRAVARIK, J., KLIR, D., REZAC, K., Influence of an external magnetic field on the dynamics of a modified plasma focus, Phys. Scr. **T161** (2014) 014042.

[12] KUBES, P., PADUCH, M., CIKHARDT, J., KLIR, D., KRAVARIK, J., REZAC, K., KORTANEK, J., CIKHARDTOVA, B., ZIELINSKA, E., Puffing deuterium compressed by a neon plasma sheath at the initial poloidal magnetic field in the plasma focus discharge, IEEE Transaction on Plasma Science **43** (2015) 2532–2538.
[13] KUBES, P., PADUCH, M., KLIR, D., KRAVARIK, J., REZAC, K. CIKHARDT, J., KORTANEK, J., KOWALSKA-STRZECIWILK, E., ZIELINSKA, E., SCHOLZ, M., KARPINSKI, L., Correlation of X ray emission with interferometry and neutron diagnostics at tungsten anode face and deuterium filling in plasma focus discharge, Plasma Phys. Control. Fusion **55** (2013) 115005.
[14] KUBES, P., PADUCH, M., CIKHARDT, J., KORTANEK, J., BATOBOLOTOVA, B., REZAC, K., KLIR, D., KRAVARIK, J., SURALA, W., ZIELINSKA, E., SCHOLZ, M., KARPINSKI, L., SADOWSKI, M. J., Neutron production from puffing deuterium in plasma focus device, Physics of Plasmas **21** (2014) 082706.
[15] KUBES, P., PADUCH, M., CIKHARDT, J., KORTANEK, J., CIKHARDTOVA, B., REZAC, K., KLIR, D., KRAVARIK, J., ZIELINSKA, E., Filamentary structure of plasma produced by compression of puffing deuterium or neon plasma sheath on plasma focus discharge, Physics of Plasmas **21** (2014) 122706.
[16] KUBES, P., PADUCH, M., CIKHARDT, J., CIKHARDTOVA, B., REZAC, K., KLIR, D., KRAVARIK, J., REZAC, K., KORTANEK, J., ZIELINSKA, E., Investigation of compression of puffing neon by deuterium current and plasma sheath in plasma focus discharge, Physics of Plasmas **22** (2015) 062705.
[17] KUBES, P., PADUCH, M., CIKHARDT, J., KLIR, D., KRAVARIK, J., REZAC, K., KORTANEK, J., CIKHARDTOVA, B., ZIELINSKA, E., Existence of a return direction for plasma escaping from a pinched column in a plasma focus discharge, Physics of Plasmas **22** (2015) 052705.
[18] KLIR, D., SHISHLOV, A.V., KUBES, P., REZAC, K., FURSOV, F.I., KOKSHENEV, V.A., KOVALCHUK, B.M., KRAVARIK, J., KURMAEV, N. E., LABETSKY, A.YU., RATAKHIN, N.A., Deuterium gas puff Z-pinch at currents of 2–3 MA, Physics of Plasma **19** (2012) 032706.
[19] KLIR, D., KUBES, P., REZAC, K., CIKHARDT, J., KRAVARIK, J., SILA, O., SHISHLOV, A.V., KOVALCHUK, B.M., RATAKHIN, N.A., KOKSHENEV, V.A., LABETSKY, A. YU., CHERDIZOV, R. K., FURSOV, F.I., KURMAEV, N.E., DUDKIN, G.N., NECHAEV, B.A., PADALKO, V.N., ORCIKOVA, H., TUREK, K., Efficient neutron production from a novel configuration of deuterium gas puff Z-pinch, Physical Review Letters **112** (2014) 095001.
[20] KLIR, D., SHISHLOV, A.V., KOKSHENEV, V.A., KUBES, P., LABETSKY, A.YU., REZAC, K., CHERDIZOV, R.K., CIKHARDT, J., CIKHARDTOVA, B., DUDKIN, G.N., FURSOV, F.I., GARAPATSKY, A.A., KOVALCHUK, B.M., KRAVARIK, J., KURMAEV, N.E., ORCIKOVA, H., RATAKHIN, N.A., SILA, O., TUREK, K., VARLACHEV, V.A., Efficient generation of fast neutrons by magnetized deuterons in an optimized deuterium gas puff Z-pinch, Plasma Phys. Control. Fusion **57** (2015) 044005.
[21] SILA, O., KLIR, D., REZAC, K., CIKHARDTOVA, B., CIKHARDT, J., MCNP calculations of neutron emission anisotropy caused by the GIT-12 hardware, Nukleonika **60** (2015) 323–326.

NON-LINEAR PROCESSES AT MESOSCALE PLASMA MATERIALS INTERACTIVE SYSTEMS

T. LAAS, Ü.UGASTE, R. MANKIN, A. REKKER, J. PRIIMETS, E. SOIKA, V. SHIROKOVA, K. LAAS, B. VÄLI, J. PAJU, A. AINSAAR
School of Natural Sciences and Health,
Tallinn University,
Tallinn, Estonia

Abstract

Processes of dense plasma beams, electrons and high energy ions interaction with construction materials of fusion devices are investigated. Experimental research on non-linear processes taking place in the interaction between (0.1–1 keV) deuterium plasma and fast ions (100 keV) streams with tungsten based materials are carried out using the dense magnetized plasma devices PF-12, PF-1000U and PF-6 as plasma sources generating 1 keV plasma and 100 keV ions. In the research, single forged tungsten, double forged tungsten and tungsten doped with 1% lanthanum-oxide are employed as material. In the experimental work, damages determined by scanning electron microscopy (SEM) images, measurements of microroughness, microhardness of cross-sections and conductivity are given for the investigated materials. To investigate the combined effect of plasma pulses with different plasma parameters, the double forged tungsten samples were irradiated by two different plasma devices. The work was performed in collaboration with the Institute of Metallurgy and Material Sciences, Moscow, Russian Federation, and the Institute of Plasma Physics and Laser Microfusion, Warsaw, Poland.

1. INTRODUCTION

The construction and development of a number of large fusion facilities — tokamaks, stellarators, and inertial confinement devices — is in visible progress. In this context, many basic problems investigated and solved are in common between the two main types of fusion energy approaches (magnetic and inertial confinement devices) as well in alternative fusion facilities. However, one of the main issue still not sufficiently investigated and connected to material sciences is how longstanding irradiation and heat loads generated in fusion devices (plasma, X ray and neutron flow) can affect the shield and the construction materials (mainly tungsten and tungsten alloys, ceramics). In fact, although tungsten has good resistance to the heat and plasma flow, its brittleness is considered a problem. Therefore, it is of utmost importance to investigate how the properties of different tungsten grades and alloys are influenced by plasma, heat and radiation flows. Recently, much research has been carried out to analyze the interaction of high temperature plasma with tungsten and tungsten alloys. It has been noted that different types of defects can occur in the surface of the material due to the interaction with plasma. For instance, waves, especially in the case of highly melted surfaces, also bubbles and holes due to the expansion of the deuterium that has diffused under the surface, or micro and macrocracks due to repeated thermal expansion and contraction. Also, structural changes of the materials have been found, for example, a change of the size of crystals and some phase changes in the case of multiphase materials. For this reason, when choosing the right construction materials for the ITER's divertor it is important to look at the thickness of the eroded layer of material in plasma irradiation, but also to have a high resistance to the cracks and stability of the mechanical properties.

Besides finding application in direct surface studies, the investigation and analysis of irradiated specimen's cross-sections is important to analyze and estimate the thickness of melted and solidified layer, structural and phase changes in the surface layer, generation of cracks in the materials interior, and so forth. As the analysis shows, these generated cracks are deeper in tungsten than, for example, in steels. This may be due to the higher brittleness of tungsten. Nevertheless, it is because of the big temperature gradient plasma irradiation that cracks in brittle materials cannot be avoided. For this reason, tungsten and alloys must both be investigated. The overall objective of this project is to carry out investigations by generating powerful radiation and heat loads in plasma accelerator devices to test their effect on the materials of interest for different type of fusion devices, to analyze the generated structural defects adding information to the fusion materials database, and finally, to elaborate a phenomenological theory to predict the construction materials defects characteristics, generated by plasma beams, irradiation and heat load. The following aims are of particular interest:

— Investigation of the high temperature plasma effect on various construction materials (different tungsten grades and its alloys, CFC and ceramic materials, multilayer composition materials), analysing the defects on the surface and the ones caused by the materials cross-sections [1–8].
— Investigation of interdiffusion in the construction materials surface layers due to heat flow and neutron flux, to find diffusion paths for different systems, perspective alloys at which non-desirable phases in diffusion zones would be excluded, and diffusion of plasma particles into melting material [9–12].

— Estimation of the effects of plasma waves (heat flow and big temperature gradient) and plasma shock waves as source of material defects, considering also the possible structural defects and phase changes due to repeated heating and cooling.
— Elaboration of a phenomenological theory to predict the type and number of defects generated due to interaction with plasma on the material surface and in its interior [1–8].
— Estimation by theoretical models [13–18] of the effects of stochastic processes on materials with a crystalline structure.

2. IRRADIATION EQUIPMENT AND ANALYTICAL

2.1. PF-12 irradiation experiments and plasma diagnostics

The investigation of high temperature dense plasma interaction with different plasma facing materials was performed with the dense plasma focus device PF-12, in Fig. 1. In recent years, the switch system of the dense plasma focus device PF-12 was rearranged to increase the reliability and durability of the discharge system. Because of these changes, a slight increase of signal rise time (from 1.7 μs up to 2.1 μs) occurred, while the maximum current increased about 1.2 times (220–245 kA in case of 20 kV capacitors voltage). The temporal resolution of a previously installed diagnostics system (time of flight type neutron and hard X ray detector) was increased to improve the estimations of the characteristics of the plasma ions impulses.

FIG. 1. The PF-12 vacuum chamber with measuring oscilloscopes.

In Fig. 2 the change in current recorded from the experiment and the corresponding neutron and hard X ray signals are shown. Calculations show the presence of 2.45 MeV neutrons which indicates the generation of fast ions. Newly installed neutron counter, assembled and calibrated at IPPLM, showed that, when deuterium was used as working gas, up to ~10^8 neutrons were produced per shot. However, it should be noted that the average neutron output is about ~10^6 per shot.

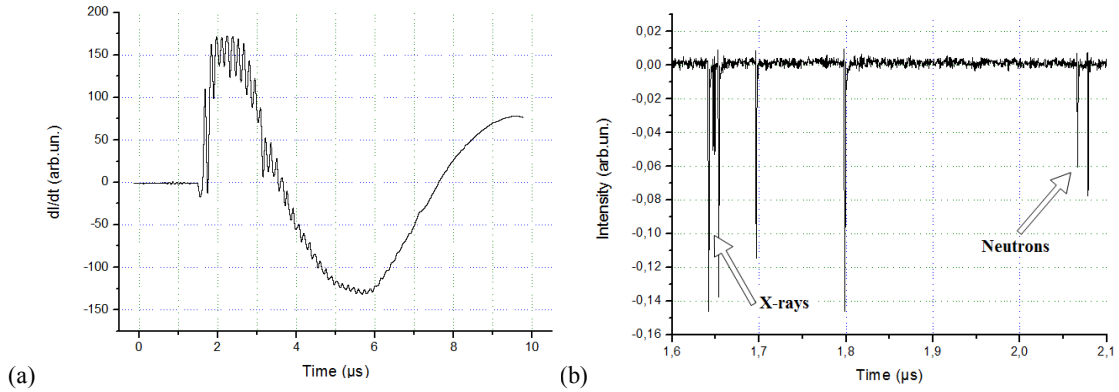

FIG. 2. (a) Change in current for PF-12; (b) signals from neutron and hard X rays TOF detector type.

The main parameters of the device are given in Table 1.

TABLE 1. MAIN PARAMETERS OF THE PF-12 DEVICE

Bank capacity	20 μF
Charging voltage	16–25 kV (maximum 35 kV, usual working voltage 20kV)
Energy storage	2.5–6.2 kJ (usual working energy storage 4 kJ)
Working gases	N_2, H_2, D_2, Ar, He or indoor air
DPF chamber type	The Mather configuration
Repetition rate	1 shot every 2–3 min
Maximum current before reconfiguration	160–250 kA (160 kA for 16 kV charging voltage, 205 kA for 20 kV charging voltage)
Maximum current after reconfiguration	190–280 kA (190 – 200 kA for 16 kV charging voltage, 220–240 kA for 20 kV charging voltage)
Current rise time before reconfiguration	1,7 μs
Current rise time after reconfiguration	2,1 μs
Life-time of the DPF systems	$\approx 10^4$ shots

For plasma diagnostics the following devices are used: Rogowski coil for current measurements, current variation and *U(t)* sensors, TOF type neutron and hard X ray detector with ultra-high temporal resolution UFNSP-1 (ACS Sp. Z.o.o, Poland), ultra-high speed iCCD camera Andor iStar DH312T, which are accompanied with two oscilloscopes LeCroy WaveSurfer 42Xs and LeCroy WaveSurfer 452. The works on this device were carried out mainly by the TU team. Several experimental sessions were carried out with CRP participants from IMET, IPPLM and ICDMP, who have also helped in the instalment of the neutron counter.

2.2. Preparation and analysis of the irradiated specimens

For the preparation of single forged tungsten (W) and tungsten doped with 1% lanthanum-oxide (WL10) samples, and for the analysis of irradiated samples the following equipment was used:

a) Grinder and polisher MetaServ 250, Buehler SimliMet 2;
b) Microhardness tester Wolpert Wilson WH-402MV;
c) Universal microscope Brunel SP400D with a computer camera;
d) Zeiss EVO MA-15 scanning electron microscopy with X ray spectrometer;
e) Perthometer Concept MFW 250 (MAHR) for 2-D microroughess measurements;
f) Bruker 3-D white light Optical Microscope Contour GT-K for 3-D microroughness measurements;
g) Sigma test 2.069 no 639/566 for conductivity measurements.

3. FUSION MATERIALS WITH PULSED HIGH TEMPERATURE DEUTERIUM PLASMA PULSES

3.1. Experimental set-up

During the experiments, three different samples were used:

a) Single forged tungsten (W) of 2 mm thickness;
b) Tungsten doped with 1% lanthanum-oxide La_2O_3 (WL10) of 4 mm thickness, manufactured in PLANSEE from tungsten powder (by isostatic pressing, sintering and rolling the plates);
c) Double forged tungsten (DFW) of 5 mm thickness, manufactured in PLANSEE and delivered in the framework of the current CRP.

Depending on the PF device parameters the power density may be up to ~ 10^{12} W/cm^2 while the duration of the plasma pulse can vary in the interval of 10^{-8}–10^{-6} s. However, the duration of secondary plasma with energies of some eV may be hundreds of microseconds. Part of the experiments were performed at PF-1000 (IPPLM), in which case the power flux density of deuterium plasma and fast ions was about 10^{12} W/cm^2; and at PF-12 (TU) in which case the power flux density of deuterium plasma varied from 5×10^6 W/cm^2 to 10^9 W/cm^2, while power flux density of fast ions varied in the range of 10^8–10^{10} W/cm^2. The variation of power density as well as pulse interval was modulated by changing the sample distance and the anode. In the experiments carried out with the PF-12 device, the initial pressure of deuterium in the plasma chamber before reconfiguration was 4.2 Torr and 9.0 Torr after reconfiguration. The capacitors were loaded up to 20 kV, the current rise time was 1.7 μs and about 2.1 μs after reconfiguration. During the experiments on PF-12, the samples distance from the anode was manipulated to vary the conditions of irradiation. The two different positions of the sample are shown in Fig. 3, denoted as zones A and B. In zone A (about 3.5 cm from the anode), the samples were affected at first by streams of hot plasma in the range of 0.1–1 keV, and afterwards by fast ion flows with the energy of about 100 keV. In zone B (about 6.5 cm from the anode) the plasma and fast deuterons reached the sample simultaneously. If the distance is greater than 6.5 cm, fast ions reach the sample first, while slow plasma reaches the sample about 60–100 ns after fast ions. In order to understand completely the physical processes and the cause of the damages during the irradiation, it should be noted, that after the interaction between initial plasma and material, some secondary tungsten plasma forms in front of the samples surface. The power flux density of plasma and fast ions with their interaction time are given in Table 2 with the descriptions of the samples and results. The surface changes (characterization of the defects) of the materials under the influence of plasma are displayed in Table 3. In the experiments carried out with PF-1000 device, the distance between the anode and the sample was about 7.5 cm, interaction time was 200 ns and the power flux density estimated by electron interferometric methods was ~ 10^{12} W/cm^2.

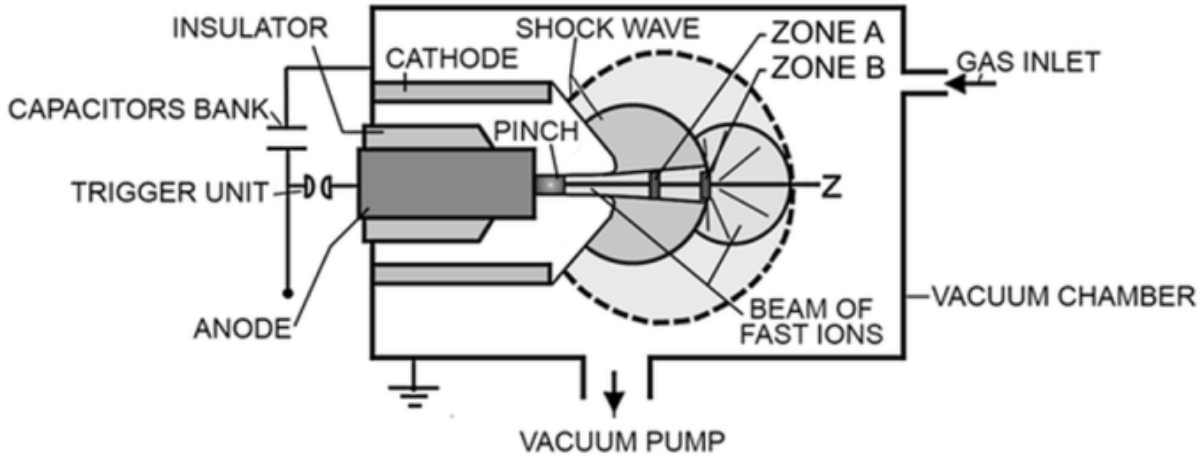

FIG. 3. The sample for plasma-ions irradiation is located on the holder at about 3.5–9.5 cm from the anode. The distance between the sample and anode determines the irradiation regime.

TABLE 2. IRRADIATION OF THE SAMPLES IRRADIATED AT PF-12 (TU)

Sample	(cm) from the anode	Pulses	Plasma flux density (MW/cm^2)	Plasma flow (μs)	Fast ions flux density (MW/cm^2)	Fast ions flow (μs)	Average micro-roughness (μm)	Macro-cells size (μm)	Micro-cells size (μm)	Micro-hardness (MPa)
1-W	3.50	2	500	0.05	5×10^4	0.01 – 0.02	3.28	–	4.0 ± 0.4	4912 ± 76
2-W	3.50	8	500	0.05	5×10^4	0.01 – 0.02	2.90	426 ± 20	6.0 ± 0.3	5419 ± 46
3-WL10	3.50	2	500	0.05	5×10^4	0.01 – 0.02	3.51	211 ± 94	5.0 ± 0.3	5147 ± 44
4-WL10	3.50	8	500	0.05	5×10^4	0.01 – 0.02	2.85	274 ± 18	5.0 ± 0.3	4792 ± 41
5-W	6.50	8	50	0.15 – 0.20	5×10^3	0.02 – 0.03	2.61	436 ± 166	18 ± 3	5300 ± 50
6-WL10	6.50	8	50	0.15 – 0.20	5×10^3	0.02 – 0.03	2.77	112 ± 19	13 ± 3	5090 ± 30
7-W	3.50	25	500	0.05	5×10^4	0.01 – 0.02	–	639 ± 62	27 ± 3	–
8-W	3.50	100	500	0.05	5×10^4	0.01 – 0.02	7.10	545 ± 50	91 ± 3	4660 ± 60
9-W	6.50	100	50	0.10 – 0.15	5×10^3	0.02 – 0.03	–	550 ± 110	10 ± 3	–
10-WL10	3.50	25	500	0.05	5×10^4	0.01 – 0.02	–	339 ± 39	–	–
11-WL10	3.50	100	500	0.05	5×10^4	0.01 – 0.02	7.60	347 ± 57	76 ± 11	–
12-WL10	6.50	100	50	0.10 – 0.15	5×10^3	0.02 – 0.03	–	100 ± 23	–	4500 ± 60

TABLE 3. ESTIMATED DAMAGES OF THE SAMPLES IRRADIATED AT PF-12 (TU)

Sample	Defects
1-W	Cracks (72%), crests (26%)
2-W	Cracks (56%), crests (42%)
3-WL10	Cracks (14%), crests (80%), holes (6%)
4-WL10	Sputters and crests (93%), cracks (4%), holes (2%)
5-W	Droplets (80%), crests (20%)
6-WL10	Droplets (42%), cracks (5%), bubbles (53%)
7-W	Mesh of micro and macrocracks
8-W	Molten surface, cracks
9-W	Macrocracks, traces of Cu
10-WL10	Partially molten surface, cracks
11-WL10	Grooves, molten surface
12-WL10	Crates, blisters, grooves, cracks

3.2. Comparative analysis of the irradiated tungsten and tungsten doped with LA_2O_3 samples

3.2.1. Analysis of the irradiated surfaces by scanning electron microscopy

For pure tungsten, one of the main properties inhibiting its extensive use as a high temperature material is the brittleness and low recrystallization temperature which leads to deterioration of the mechanical properties of the sample. Therefore, it is of interest to investigate the change of physical properties and defects on the surface as well as in the volume of tungsten. In many cases different dispersed oxides (La_2O_3, Y_2O_3, and TiO) are used to improve the mechanical properties of different metals and their alloys, allowing changes in ductile to brittle transition temperature (DBTT), recrystallization temperature and brittleness. For comparative analysis on the performance of pure tungsten (W) and tungsten doped with 1% La_2O_3 (WL10), the samples were irradiated under the same conditions by PF-12 [1]. Then, the irradiation conditions as well as numerical results of W and WL10 samples are shown in Table 2. However, experiments and analysis of the samples irradiated with either two or eight plasma pulses were carried out before the start o the current CRP. Therefore, the data is shown here only for completeness. The surfaces of the irradiated specimens were investigated by using scanning electron microscopy and optical microscopy. Most significant damages were found by analyzing the SEM images so that the damage factor was computed, see Table 3. The damage factor is defined as ratio between the damages area and the total area under observation. Some photos by optical microscopy are shown in Fig. 4, and as can be seen, the surface damages of irradiated materials depend on the power flux density. The SEM images of the irradiated samples are given in Fig. 5, and their analysis reveals that high temperature plasma with fast ion stream caused the melting of the surface layer of the material, thus creating some wave-like structures (roughness without high frequency terms) which are of the same wavelength and amplitude for both materials W and WL10 (irradiated under the same conditions). In general, wave-like structures on tungsten are also caused by the influence of plasma on the thin melted layer of tungsten. In the analysis, the value of microroughness does not vary very much, see Table 2. Besides, SEM images indicate a mesh of cracks, which has appeared on the surface of the material. This is caused by crystallization of the melted layer in the process of fast cooling. The same defects appear on different samples of WL10 at all power flux densities. Pulses of powerful plasma beams on a surface of tungsten cause the occurrence of a mesh of microcracks. The increase of density of apparent microcracks on the surface of WL10 is slower than in case of W samples, when the overall number of pulses on the samples is increased. The changes in WL10 may be slower due to lanthanum-oxide incorporation in the sample.

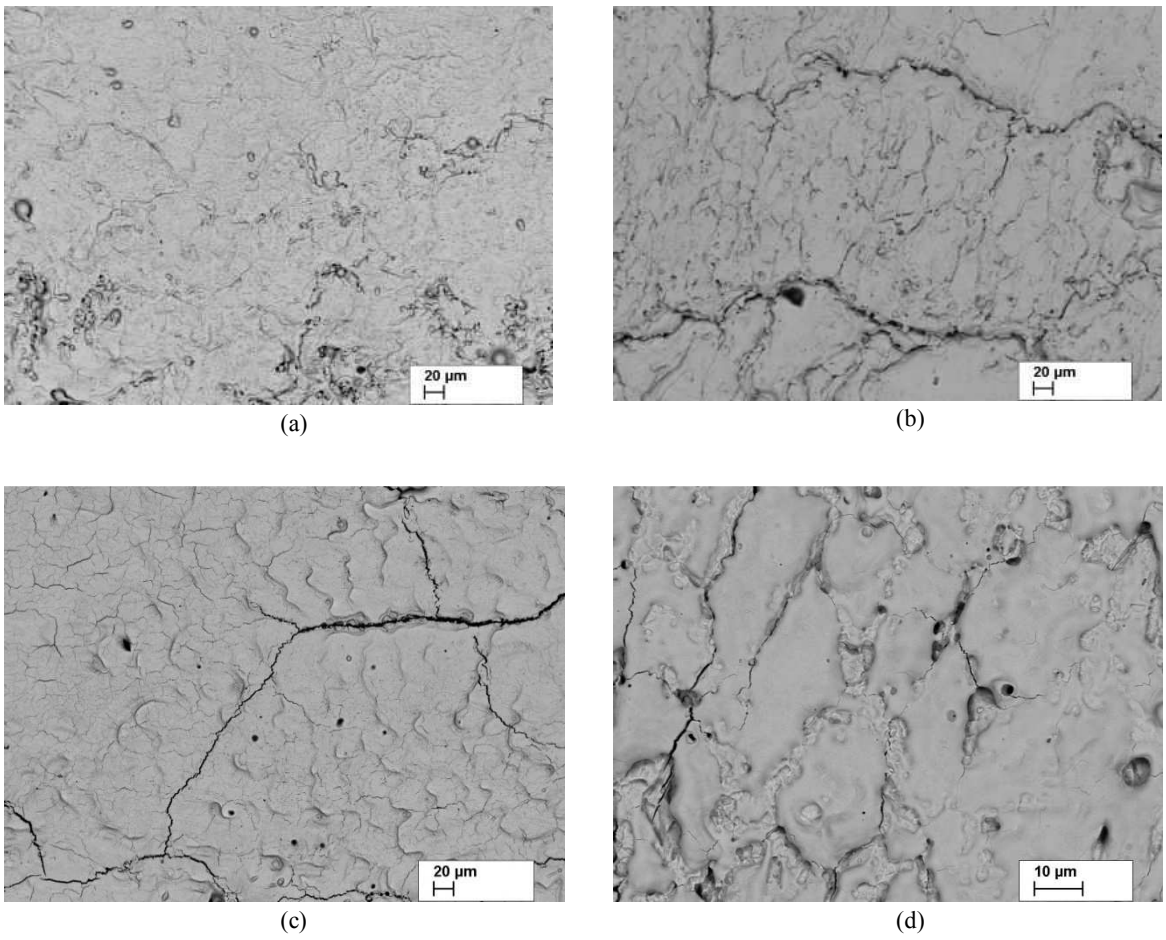

FIG. 4. (a) 5-W, 8 pulses, PF-12, distance from the anode 6.5 cm (zone B); (b) 6-WL10, 8 pulses, PF-12, distance from the anode 6.5 cm (zone B); (c) 2-W, 8 pulses, distance from the anode 3.5 cm (zone A); (d) 4-WL10, 8 pulses, distance from the anode 3.5 cm (zone B).

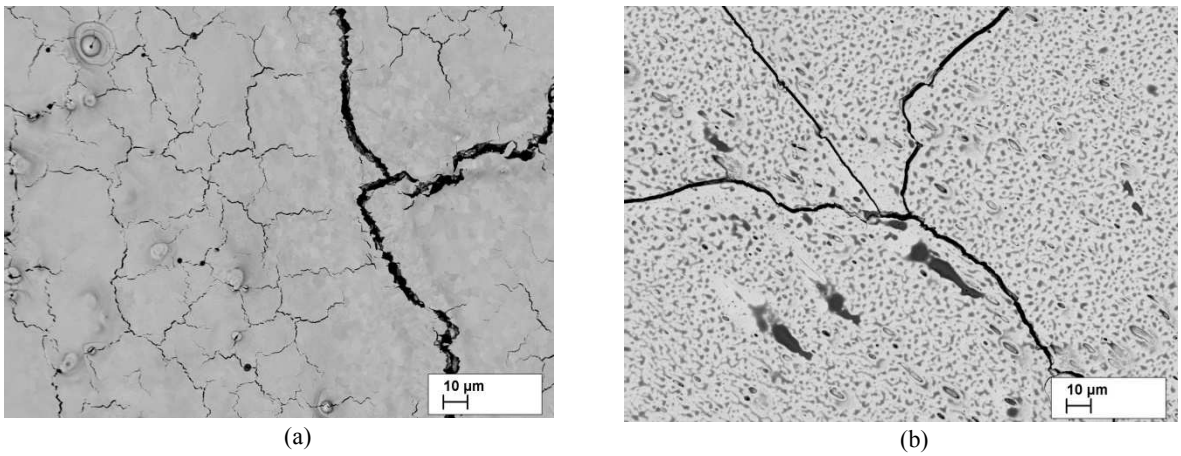

FIG. 5. (a) 7-W samples irradiated with 25 shots of deuterium plasma and fast deuterons in distance from the anode 3.5 cm (zone A), power flux density about 5×10^8 W/cm^2; (b) 10-WL10 samples irradiated with 25 shots of deuterium plasma and fast deuterons in distance from the anode 3.5 cm (zone A), power flux density about 5×10^8 W/cm^2.

However, comparing the defects on W and WL10, the different types of defects is dominant. While pure tungsten mainly has cracks as dominating damages, the WL10 samples have droplets, sputter craters and

bubbles. Increasing the number of deuterium plasma pulses on W and WL10 samples reveals the different performance of materials in a better way. The SEM images of W and WL10 samples under 25 and 100 plasma pulses are shown in Figs 5 and 6. The analysis of the surfaces irradiated with 2, 8, 25 and 100 deuterium plasma pulses shows that the increase of the number of pulses on the surface leads to development of different kind of defects on the samples. There are strong melting traces and major cracks in W samples due to repeated melting and resolidification of the surface layer. Also, mesh of microcracks is generated along the borders of grains. Increasing the number of pulses has led to diminishing the microcrack mesh due to the development of molten resolidified tungsten layer (in case of pure W). WL10 has a different kind of characteristic surface defects: although the surface has melted and recrystallized, also sputters and droplets can be seen, as showed in Figs 6(b) and (d). In case of small number of pulses (2, 8 and 25) almost no microcracks occur. However, the generation of mesh of microcracks can be seen on sample irradiated with 100 plasma pulses (Fig. 6(b)), where increasing the number of shots (up to 25 or 100 shots) has led to generation of grooves on the sample. When comparing the results considering WL10 and W samples that have been irradiated with smaller number of pulses, such performance was not observed.

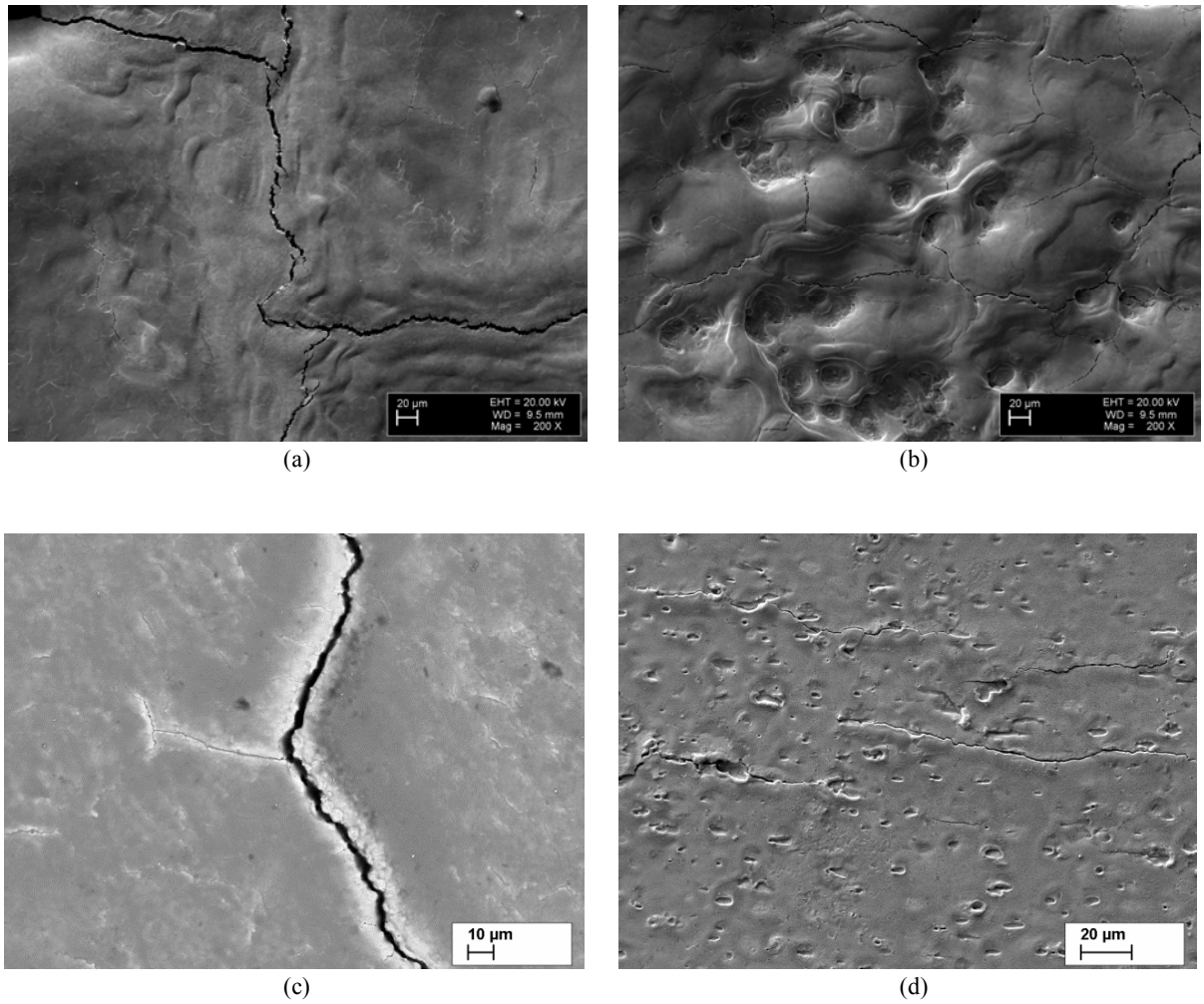

FIG. 6. (a) 8-W samples irradiated with 100 shots of deuterium plasma and fast deuterons in distance from the anode 3.5 cm (zone A), power flux density about 5×10^8 W/cm^2; (b) 11-WL10 samples irradiated with 100 shots of deuterium plasma and fast deuterons in distance from the anode 3.5 cm (zone A), power flux density about 5×10^8 W/cm^2; (c) 9-W samples irradiated with 100 shots of deuterium plasma and fast deuterons in distance from the anode 6.5 cm (zone B), power flux density about 5×10^7 W/cm^2; (d) 12-WL10 samples irradiated with 100 shots of deuterium plasma and fast deuterons in distance from the anode 6.5 cm (zone B), power flux density about 5×10^7 W/cm^2.

3.2.2. *Microroughness of irradiated W and WL10 samples*

2-D measurements of microroughness were conducted on W and WL10 samples, which had previously been irradiated with small number (2 and 8) deuterium plasma pulses. Some examples of the microroughness profiles of the irradiated sample surfaces are shown in Fig. 7. The microroughness parameters are given in Table 2. Regardless of the damage factor, which is given in Table 3 (surface density of damages computed up to about 10 μm), the microroughness shows a difference of damages in 10–100 μm or more in length and in μm or tens of μm in height. The microroughness and the damage factor (or SEM images) indicate damages of different scales. A comparison of the numerical values of microroughness shows that in general the microroughness of WL10 is almost the same as of W. In general, samples of W and WL10 irradiated under the same conditions display, almost in all cases, the same microroughness. Differences are only observed in samples subjected to multiple shot irradiations at bigger distances from the anode (5-W, 6-WL10, 9-W, and 12-WL10). In this case the material is affected not only by direct short plasma pulses, but also by longer (up to 1 ms) contact with secondary tungsten plasma. As the melting temperature of lanthanum-oxide is lower, repeated irradiation may lead to differentiation of the W and lanthanum-oxide phases, which are characterized by different structures (droplets and sputters) on the material surface, possibly adding to surface microroughness. But considering the profile of the irradiated samples it can be seen that in WL10 the length of bumps and pits in the profile are greater than in pure tungsten. This relates to the fact that in tungsten the main type of defects are cracks and crevices, while different types of bigger formations (bubbles, sputters) will appear on the surface of WL10. As bigger defects play a greater role in the development of defects in the following shots, it could be concluded that the profile of microroughness may predict which kind macroscopic defects may appear on material.

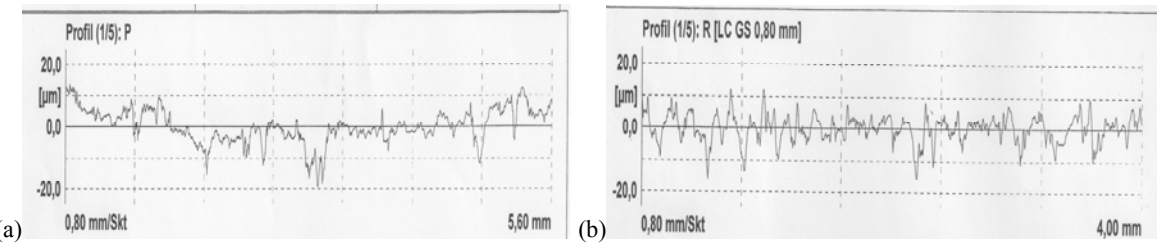

(a) (b)

FIG. 7. (a) 3-WL10 microroughness profiles of samples irradiated at PF-12 (2 shots, distance from the anode 3.5 cm; (b) 1-W microroughness profiles of samples irradiated at PF-12 (2 shots, distance from the anode 3.5 cm.

On the samples of W and WL10, irradiated with 25 or 100 pulses, the microroughness was analyzed by 3-D method using special optical microscopy (Bruker 3D white light Optical Microscope Contour GT-K). In this case the average microroughness should be used solely for estimation of roughness as a comparative indicator for different samples. Microroughness of the samples irradiated with 100 shots at distance 3.5 cm from the anode (power flux density about 5×10^8 W/cm^2) are as follows: 7.6 μm for 8-W and 7.1 μm for 11-WL10, which do not differ from each other very much. However, maximum microroughness (difference between highest peak and lowest crevice) differ greatly: 53 μm for W and 92 μm for WL10. In Fig. 8, 3-D microroughness images of irradiated samples show that in case of pure W large surface regions have been migrated.

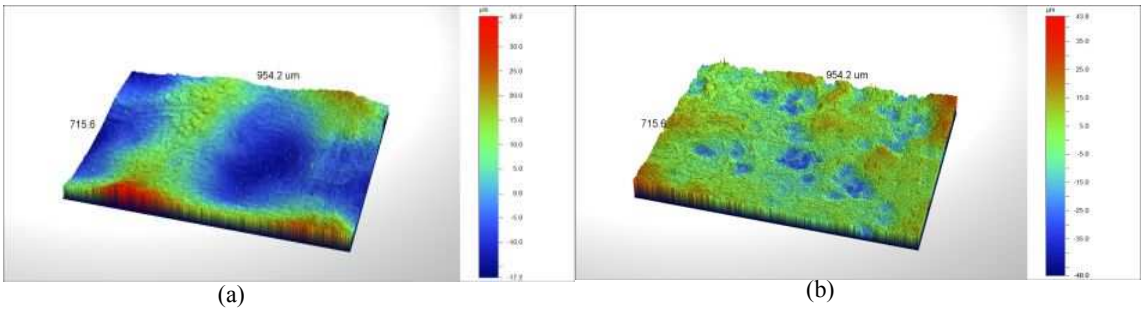

(a) (b)

FIG. 8. (a) 8-W microroughness; (b) 11- WL10 microroughness. Both samples are irradiated with 100 plasma shots. The distance from the anode is 3.5 cm (zone A), and the power flux density is about 5×10^8 W/cm^2.

After that the surface has solidified, no big cracks or crevices have been detected by optical microscopy. In case of WL10, regions of migrated material are smaller (50–100 mm**)** and it is in correlation with material migration in smaller scales, see Figs 7(b) and 5(b).

3.2.3. Study of bulk defects of irradiated W and WL10 samples

Hardness through the cross-section of the materials was measured to study the defects in the bulk, and the analysis of SEM images was carried out for W and WL10. In Fig. 9, measurements of the irradiated samples show that for both materials there exists a layer with decreased the hardness value. Comparison with our previous studies shows that while the average hardness of the irradiated samples does not change significantly, the depth of the layer with decreased hardness increases. In specimens that were irradiated with eight plasma shots, the depth of decreased hardness layer was either ~ 200 μm (WL10) or absent (W). In the case of tungsten, the depth of the layer with decreased hardness increases with the number of shots until reaches about 200–250 μm, in accordance with the depth of the damaged layer found by SEM images of cross-sections, see Fig. 10. In the case of WL10, the initial layer with lower hardness (the measurements of non-irradiated specimens showed the existence of a layer with lower hardness next to the first hard layer) develops wider until it reaches about 500 μm, after that the hardness of this layer will increase and the depth of the first layer with lower hardness reaches 250 μm, as in the case of W. The increase of hardness is in accordance with the images of cross-sections (Figs 10(b) and (c)) which show a decrease of bigger cracks in the damaged layer of WL10. The depth of damaged layer can be explained by mechanical shock of fast ions, which penetrate deep into the material.

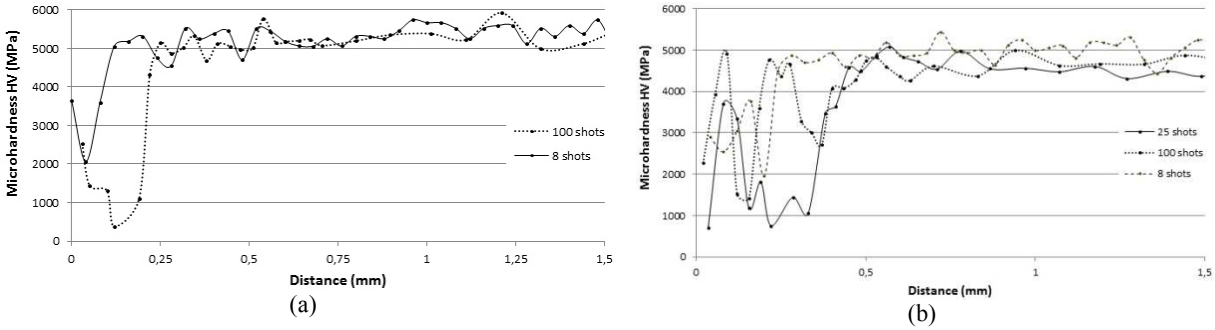

FIG. 9. (a) W change of the microhardness of the irradiated sample surface with an increase in the number of plasma shots; (b) WL10 change of the microhardness of the irradiated sample surface with an increase in the number of plasma shots. All the samples are irradiated at zone A (power flux density of plasma stream 5 × 10^8 W/cm^2.

Analysis of cross-sections of irradiated samples (Fig. 10) reveals that the depth of the cracked layer for both materials (W and WL10) does not significantly depend on the number of pulses and the power flux density, being about 150–200 μm. However, it should be noted that with an increase of the number of shots, the width of cracks in WL10 decreases significantly. This may be due to the greater ductility of WL10 given to disperse oxide particles.

3.3. Analysis of double forged tungsten irradiated with pulsed deuterium pulses

In the framework of the current CRP, DFW was irradiated with number of deuterium plasma ($E_i \approx 0.1–1$ keV) and fast deuterons ($E_i \approx 100$ keV) pulses in different regimes. Two series of plasma pulses irradiations were carried out to investigate the performance of damaged specimens under mild plasma irradiation. First, when surface of irradiated samples were damaged significantly. Secondarily, when the influence of plasma leads the surface of tungsten to melting (little higher than melting point). The testing was organized in cooperation with IMET, IPPLM and NSC KIPT research teams. Some samples were irradiated first at PF-1000 or PF-6 at IPPLM, analyzed and irradiated later with PF-12 at TU.

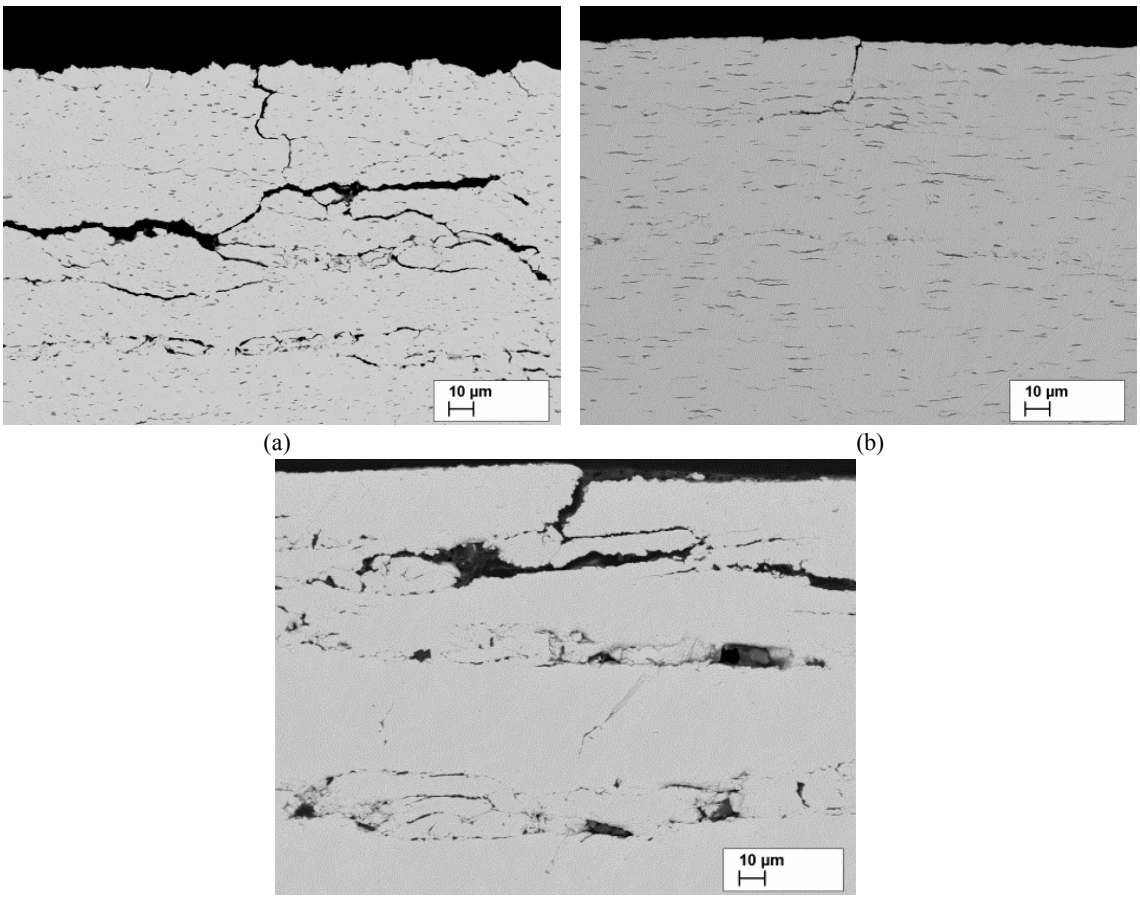

(a) (b)

(c)

FIG. 10. (a) 10-WL10, 25 pulses, cross-sections of the irradiated materials by SEM; (b) 11-WL10, cross-sections of the irradiated materials by SEM; (c) 8-W, 100 pulses, cross-sections of the irradiated materials by SEM. All samples are irradiated at zone A with power flux density of plasma 5 × 10^8 W/cm^2.

3.3.1. Analysis of irradiated surfaces by scanning electron microscopy

The data about irradiation conditions as well as some results for the irradiated double forged tungsten samples are given in Table 4 and Table 5. The samples with suffixes '-a' are irradiated with one series of plasma pulses, while the samples with suffixes '-b' are irradiated with two series of plasma pulses in different conditions. Irradiated surfaces were investigated by scanning electron microscopy. Although, numerous images were obtained during the study, only a number of images are presented. DFW samples irradiated at different PF-devices are shown in Figs 11 and 12. The results of measurements of microroughness and cell sizes are given in Table 4. Here, the macrocell is defined as the area bordered by so called macrocracks (with width up to 2 µm) and a microcell is the area bordered with microcracks (with width 10–50 nm). It was observed that all samples have practically identical damage features: wave-like structures, microcracks and macrocracks formation, or pores. However, the density of different kind of damages (ratio between the total area of a specific kind of defects and the total area of investigated surface) depends strongly on the plasma and ions flows power flux densities, determined by SEM images. It can be seen that high heat loads result in droplets formation (and possible ejection) from the tungsten surface with the simultaneous movement of the molten layer, see Figs 11(d) and 12(c). Then, a closer exploration of SEM images shows that the droplets are located next to grooves or holes, and therefore these should have been emanated from the same grooves or cracks; see Figs 11(d) and 12(c). In Table 4 some of the results are shown. To begin with, the sizes of cells measured from SEM images are presented.

TABLE 4. DOUBLE FORGED TUNGSTEN (DFW) SAMPLES IRRADIATION CONDITIONS

Sample	Device	(cm) from the anode	Pulses	Plasma flux density (MW/cm^2)	Plasma flow (μs)	Fast ions flux density (MW/cm^2)	Fast ions flow (μs)	Average micro-roughness (μm)	Macro-cells size (μm)	Micro-cells size (μm)
85-DFW-a	PF-12	6.5	25	50	0.15 – 0.2	5×10^3	0.03	1.1/28.9	500 ± 91	23 ± 4
86-DFW-a	PF-12	3.5	25	500	0.05	5×10^4	0.01–0.02	1.9/16.2	365 ± 25	150 ± 50
87-DFW-a	PF-12	3.5	100	500	0.05	5×10^4	0.01–0.02	5.4/119.1	378 ± 41	103 ± 16
88-DFW-a	PF-12	6.5	100	50	0.15 – 0.2	5×10^3	0.03	5.1/120.2	189 ± 10	27 ± 1.5
1-DFW-a	PF-6	–	50	500	0.05	5×10^4	0.01–0.02	2.2/19.0	297 ± 17	–
2-DFW-a	PF-1000	–	2	10^3–10^4	0.1	10^5 – 10^6	0.05	1.9/21.7	1300	–
3-DFW-a	PF-1000	–	4	10^3–10^4	0.1	10^5–10^6	0.05	1.5/11.9	1100	–
4-DFW-a	PF-6	–	10	500	0.05	5×10^4	0.01–0.02	0.9/13.2	276 ± 31	–
87-DFW-b	PF-12 + QSPA-50Kh	–	100+10	0.36	250	–	–	2.5/38.7	329 ± 19	42 ± 4
88-DFW-b	PF-12 + QSPA-50Kh	–	100+10	0.36	250	–	–	9.6/105	215 ± 44	25 ± 5
1-DFW-b	PF-6 + PF-12	–	50+ 50	500	0.05	5×10^4	0.02	2.6/19.6	282 ± 23	20 ± 2
2-DFW-b	PF-1000 + PF-12	–	2+50	10^3–10^4	0.1	10^5–10^6	0.05	1.9/52.8	204 ± 14	9 ± 2
3-DFW-b	PF-1000 + PF-12	4+50	10^3–10^4	–	0.1	10^5–10^6	0.05	1.5/25.9	127 ± 7	70 ± 5
4-DFW-b	PF-6 + PF-12	10+50	500	–	0.05	5×10^4	0.02	1.4/12.9	168 ± 13	46 ± 6

Cells size is defined as the average cell diameters. Also, the average microroughness of each sample is indicated. This has been measured along crossed lines over the investigated surface. Sum of maximum peaks height and valleys depth is also shown. It should be noted that the average roughness of a polished sample before irradiation was 0.33 μm and maximum is 5.2 μm. Plasma-materials interaction studies show that higher heat flux $f = q\tau^{1/2}$, leads to higher values of microroughness on irradiated surfaces. Therefore, the sample 87-DFW-a should have greater microroughness values than 88-DFW-a. However, the difference between the values of microroughness for samples 87-DFW-a and 88-DFW-a is negligible (about 5–6%), and the density of cracks is bigger in the case of 88-DFW-a.

TABLE 5. DOUBLE FORGED TUNGSTEN (DFW) SAMPLES ESTIMATED DAMAGES

Sample	Defects
85-DFW-a	Cracks (25%), boiling bubbles (75%), weak Cu traces
86-DFW-a	Cracks
87-DFW-a	Cracks, pores
88-DFW-a	Bubbles, cracks, craters, holes. Cu traces (but not in bubbles region)
1-DFW-a	W wave traces, grooves, macrocracks, strong Cu traces
2-DFW-a	W wave traces, droplets, macrocracks
3-DFW-a	Strong wave traces, erosion traces, droplets, macrocracks, weak Cu traces
4-DFW-a	Molten surface, droplets, bubbles, craters, cracks, weak Cu traces
87-DFW-b	Grooves, macrocracks, holes
88-DFW-b	Holes, craters, grooves, macrocracks
1-DFW-b	Cracks, molten layer. Strong Cu traces, which have partly covered microcracks
2-DFW-b	Mesh of macro and microcracks, bubbles, droplets.
3-DFW-b	Cracks, droplets, strong erosion traces, Cu traces.
4-DFW-b	Cracks, strong Cu traces

In Fig. 11(c), the examination of SEM images with higher magnification reveals that there exists a mesh of microcracks, with almost no visible separating lines between the cells. This allows suggesting that secondary tungsten plasma has covered the microcracks. The same phenomenon is valid for cells mesh development on sample irradiated by PF-1000. For samples that have either been irradiated with small number of shots, for instance 2-DFW-a and 3-DFW-a, or with powerful ion beams, as 86-DFW-a and 87-DFW-a (in which case there is a cracks covering effect of secondary plasma), the micro-cells size is more than 25 μm (44–55 μm). The size of microcells diminishes with either increasing the number of shots or by irradiating the samples 87-DFW-b and 88-DFW-b with QSPA Kh-50. On the other hand, when mesh of microcracks was developed during plasma pulses at PF-12, followed by irradiation of the sample with QSPA Kh-50 (with much smaller values of power flux density), no significant change of micro or macrocells size occurred. For comparison, when tungsten is produced by usual rolling and single forging technology, the mesh of microcracks already occurs on the samples after 8 shots of plasma. Irradiation of samples, which have been previously irradiated with high deuterium plasma pulses with higher power flux densities, later on with 50 pulses of quite low deuterium plasma pulses (q = 8–10 MW/cm^2) leads to the generation of bubbles and development of cracks mesh (Fig. 13). It should be noted that irradiation of polished pure single forged tungsten with 50 deuterium plasma pulses under the same conditions leads only to rather mild generation of melting traces. Therefore, the influence of first rather shocking plasma pulses changes the surface of DFW in such a way that irradiation of the same surface with low plasma flux densities (low heat flux factor) may lead to significant amplifying of damages. Furthermore, while the impact of fast deuteron flux leads to implantation of deuterium atoms into the materials, the influence of plasma pulses with low power flux densities leads to the evaporation of the implanted deuterium, which changes the tungsten surface significantly.

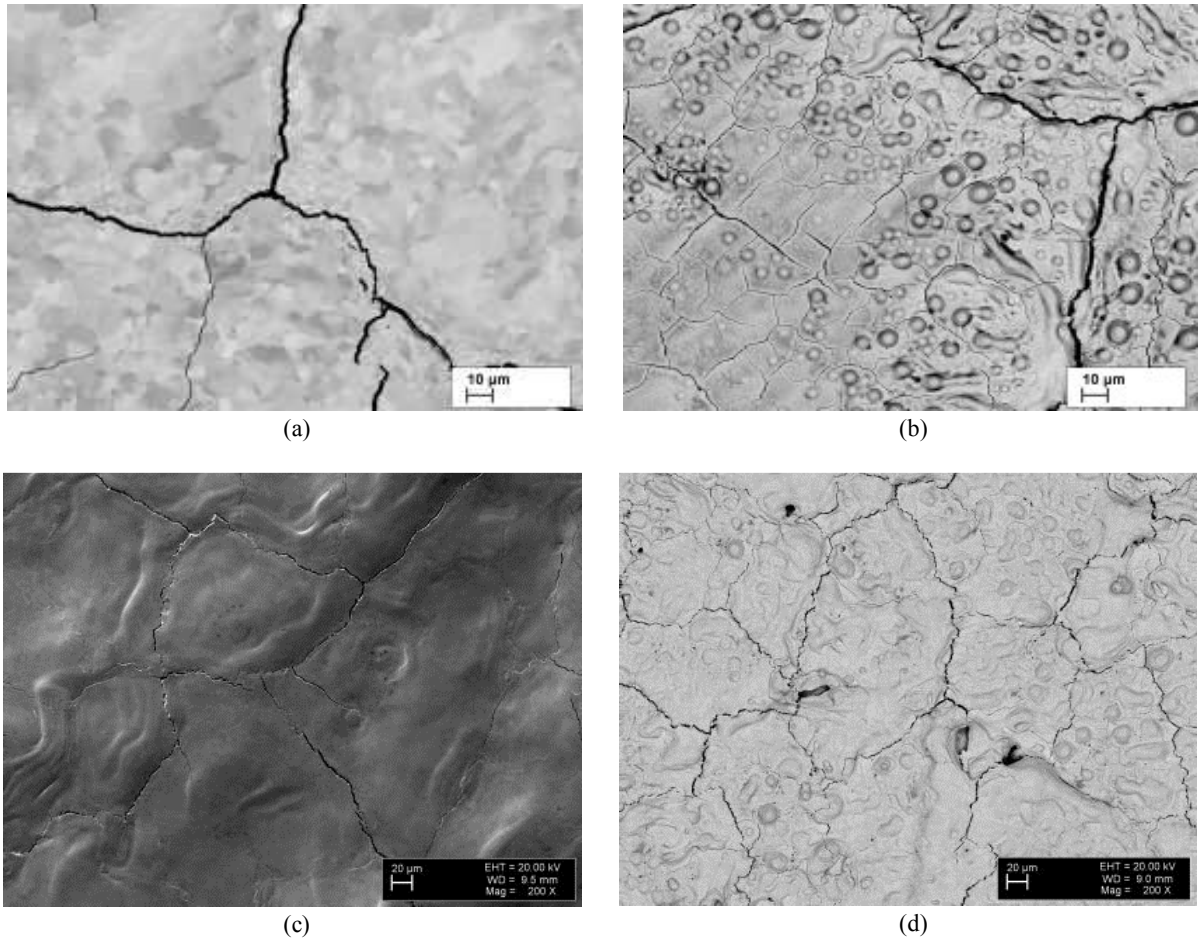

FIG. 11. (a) 86-DFW-a, 25 pulses, q=500 MW/cm^2; (b) *85-DFW-a, 25 pulses, q*=50 MW/cm^2; (c) *87-DFW-a, 100 pulses, q*=500 MW/cm^2; (d) *88-DFW-a, 100 pulses, q*=50 MW/cm^2. *DFW samples irradiated with deuterium plasma and fast deuterons pulses in PF-12.*

Experiments carried out with QSPA Kh-50 have shown that the generation of molten layer leads also to the emission of droplets, and therefore to the appearance of tungsten dust. Thus, as density of cracks on 88-DFW-a is greater than on 87-DFW-a, also, the characteristic defects on the samples are different (presence of droplets, groves and craters on 88-DFW-a). This leads to the generation of more groves, holes and macrocracks on 88-DFW-b, see Fig. 13(b), which may be the main reason for the increase of the average microroughness of a sample (88-DFW-b in Table 4).

In Fig. 13(a), the sample 87-DFW-b has more pronounced defects on the bigger scale, but the surface between bigger holes and craters is in general smoother (lack of small holes and groves). This may be the reason for smaller microroughness of the sample 87-DFW-b, in fact the density and character of defects on 87-DFW-b is different in comparison with 88-DFW-b. After irradiation of both samples (87-DFW-b and 88-DFW-b) by QSPA Kh-50 with hydrogen plasma flows and lower power flux densities, an increase of apparent melting traces occurs, see Figs 13(a) and (b).

On the other hand, when comparing the samples in microscale, the damages of both samples are quite similar. However, the mesh of microcracks has developed more on the sample which was more damaged previously (88-DFW-a). In Fig. 14, 3- D microroughness of double forged tungsten samples after irradiation at PF-12 and after irradiation at PF-12 and QSPA Kh50.

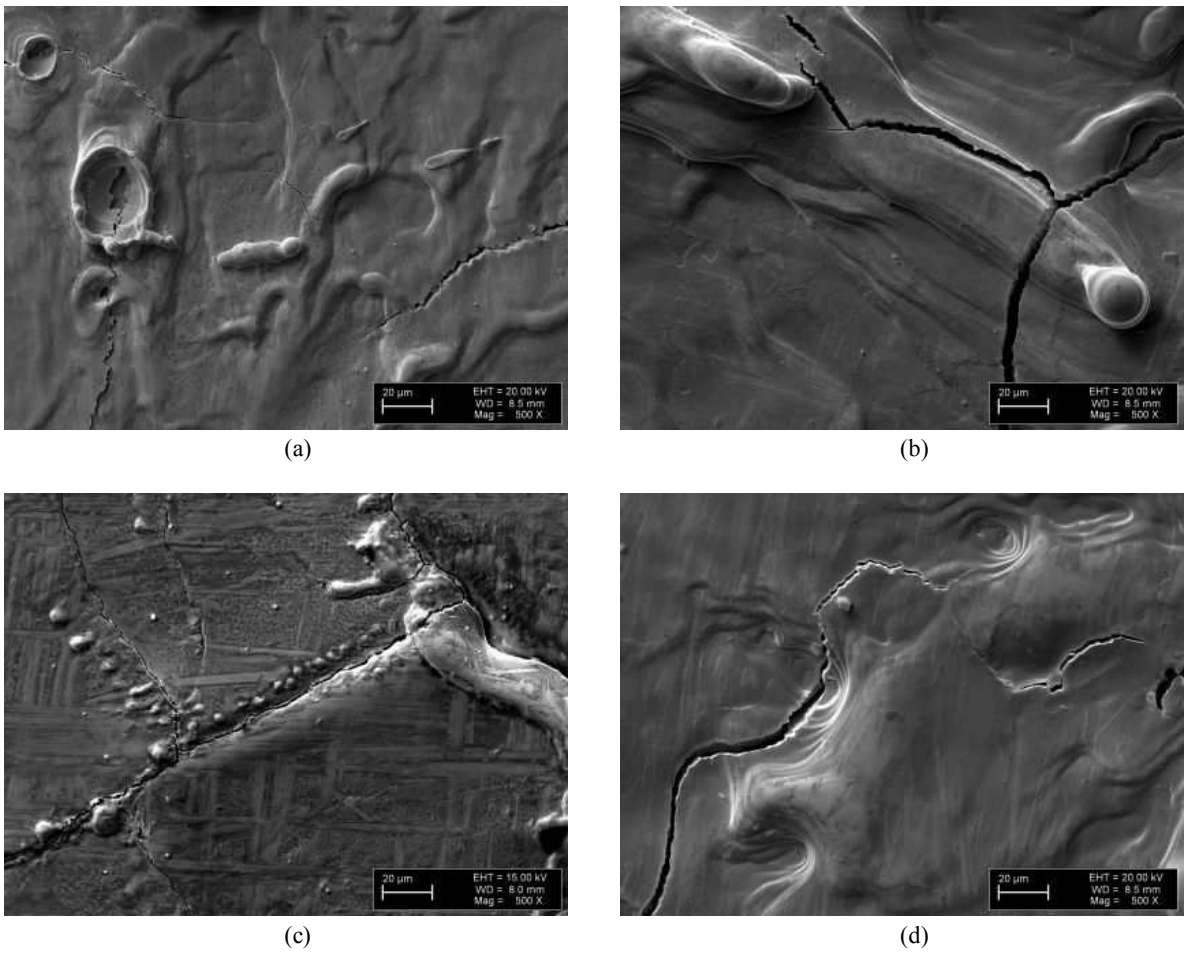

FIG. 12. (a) 4-DFW-a, PF-6, 10 pulses, q=500 MW/cm^2; (b) *2-DFW-a, PF-1000, 2 pulses, q*=10^3 MW/cm^2; (c) *1-DFW-a, PF-6, 50 pulses, q*=500 MW/cm^2; (d) *3-DFW-a, PF-1000, 4 pulses, q*=10^3 MW/cm^2. *DFW samples irradiated with deuterium plasma and fast deuterons pulses at IPPLM.*

Conclusively, the initial cracks mainly will propagate and the material will deteriorate, so that all cracks will widen and new defects will be generated upon the older ones. On the other hand, on the sample which initially had a rather damaged surface, the additional irradiation of the sample by QSPA Kh-50 has diminished the prominence of droplets and caverns on the surface, leading in general to a smoother surface (number of holes per investigated area decreases, while the average area of the holes increases).

Nevertheless, the average microroughness as well as the maximum microroughness diminished with irradiation of samples by secondary series of plasma streams. Thus it can be concluded that even if the surface of the irradiated surface has modified in such a way that it has different droplets and bubbles, as probable sources of tungsten dust, the influence of much lower plasma flux densities can lead to reduction of such sources.

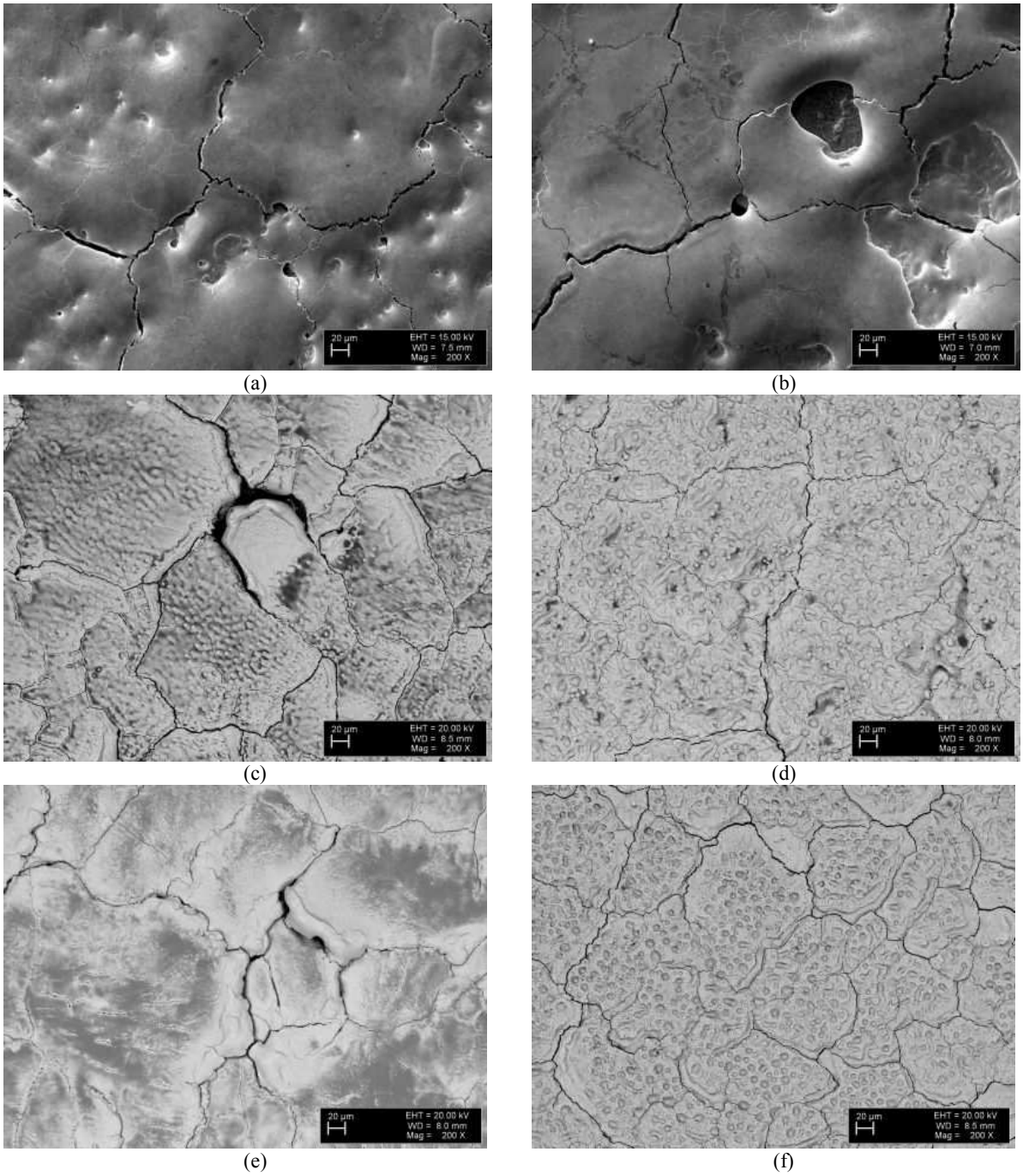

FIG. 13. (a) 87-DFW-b; (b) 88-DFW-b; (c) 4-DFW-b; (d) 2-DFW-b; (e) 1-DFW-b; (f) 3-DFW-b. Double forged samples after irradiation with second series of plasma pulses (see Table 4 for conditions).

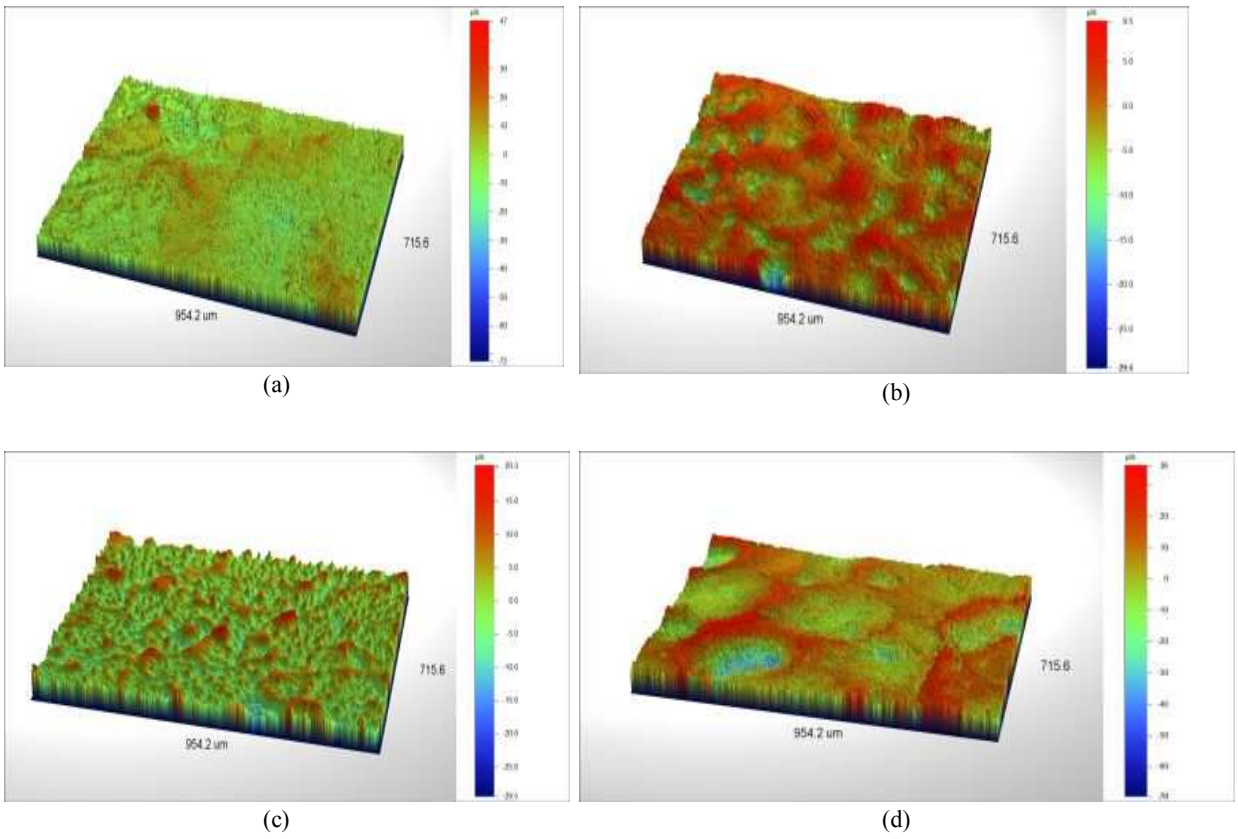

(a) (b)

(c) (d)

FIG. 14. (a) 87-DFW-a irradiated with 100 pulses at PF-12 at zone A with 100 pulses; (b) 88-DFW-a irradiated with 100 pulses at PF-12 at PF-12 with 100 pulses; (c) 87-DFW-b irradiated first at PF-12 and then at QSPA Kh50 with 10 hydrogen pulses; (d) 88-DFW-b irradiated first at PF-12 and then at QSPA Kh50 with 10 hydrogen pulses. 3-D microroughness of double forged tungsten samples after irradiation at PF-12 and after irradiation at PF-12 and QSPA Kh50.

3.3.2. Study of bulk defects of irradiated double forged tungsten samples

In order to estimate the depth of the damaged layer, a non-destructive method of measurement of electrical conductivity was used on DFW samples. It is known, that conductivity of solid material depends on the concentration of defects point, microcracks, and other occurring bulk defects. The results of the analysis can be seen in Fig. 15. Initially, the conductivity of the material was 18 MS/m which did not depend on depth. The results indicate that the depth of damaged layer is generally in correlation with the power flux density values of plasma and fast ions. On the other hand, the dependence on the number of pulses is rather weak. Cooperative experiments with the IPPLM research team have shown that powerful ion beams generate shock waves penetrating into material and also through thin materials. This phenomenon was also theoretically shown by Latyshev from IMET. Computations by Latyshev et al. have shown that the pressure of the shock wave can reach 20 GPa in the bulk, and it can go as deep as 500–800 μm inside the bulk, depending on the initial power flux density of fast ions on the surface of the sample. When comparing the results of conductivity for samples that have been irradiated with the same device and under the same conditions, varying only the number of pulses, the results indicate that the average influence of fast ions during each pulse does not vary greatly, and the cumulative effect of pulses is weak. Nevertheless, powerful ion beams penetrating into the material can generate damages in the bulk; even in cases when the surface damages are inessential (see samples 87-DFW-a, 88-DFW-a, 1-DFW-a, and 4-DFW-a in Figs 11 and 12).

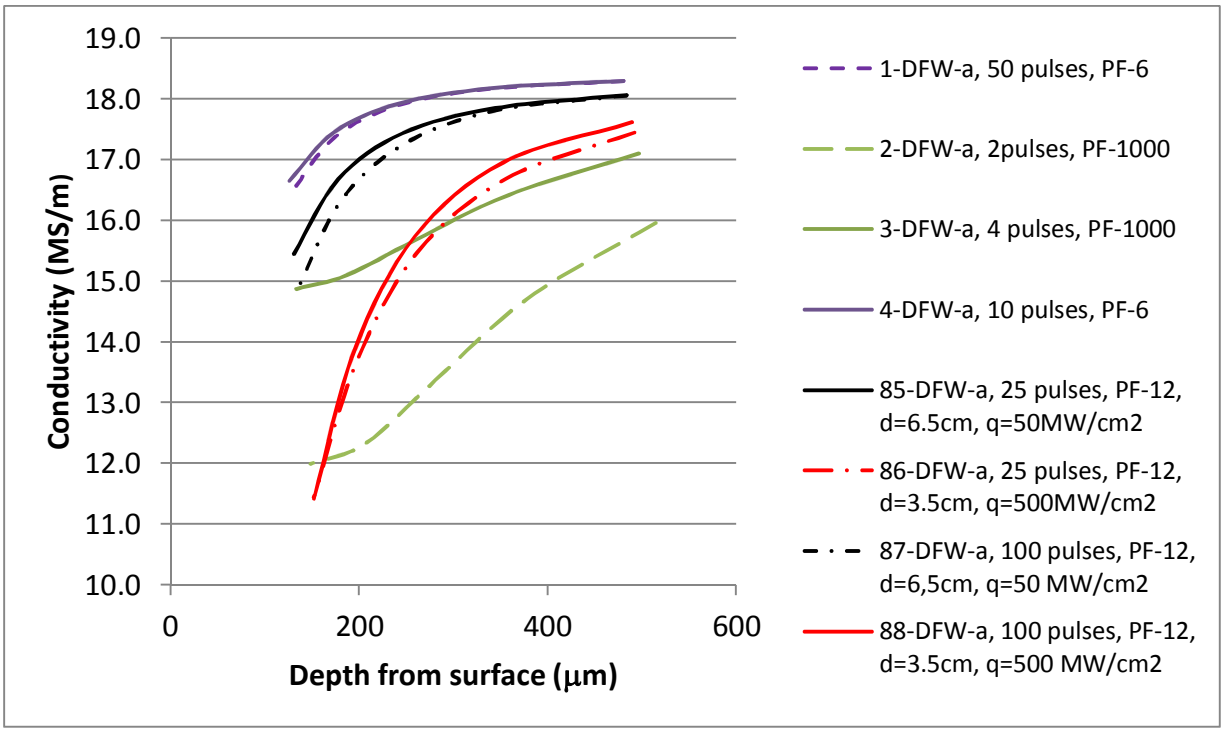

FIG. 15. Dependence of conductivity of double forged tungsten samples on the depth from the surface.

4. INVESTIGATION OF A STOCHASTIC OSCILLATOR MODEL

In recent years, increasing attention has been paid to the constructive role of noise in nature and engineering, since the impact of noise is not restricted to destructive and thermodynamics effects but can have unexpected ordered outcomes. The examples include stochastic resonance, noise enhanced stability, noise induced multistability and phase transition. More realistic models of physical systems require a system which is driven by white noise (e.g. heat) and colored noise simultaneously (e.g. mechanical shock wave or powerful ions flux). It can be shown that the effect of colored noise in the oscillator frequency may lead to various resonant phenomena: for example, it may cause energetic instability which manifests itself in an unlimited increase of the second order moments of the output with time. There are various applications of oscillators with varying frequency. The change of the oscillator frequency in nanomechanical resonators has often been thought of as a result of random attachment and detachment of ions, atoms, molecules (or nanoparticles) to and from a resonator. Therefore, such systems are in interest in field of plasma-materials interaction where the mass of oscillators can be varied due to interaction of plasma particles, ions or dust.

As a model for an oscillatory system strongly coupled with a noisy environment, we consider the stochastically perturbed harmonic oscillator with a random mass m

$$m\big(1+\mathrm{Z}(t)\big)\ddot{\mathrm{X}}+2\gamma\mathrm{X}+\omega^2\dot{\mathrm{X}}=\xi(t) \qquad (1)$$

where $\mathrm{X}(t)$ is the oscillator displacement, γ is a damping parameter, the driving force $\xi(t)$ is Gaussian white noise with a zero mean and with the δ-correlated correlation function and the constant ω is the eigenfrequency of the oscillator. The random force $\xi(t)$ describes the thermal fluctuations with an intensity D. Fluctuations of the mass m are expressed by a Markovian trichotomous noise $\mathrm{Z}(t)$, which is equal to a, 0 and $-a$, with $a > 0$. The jumps follow in time the pattern of a Poisson process.

In the basis of a harmonic oscillator with a fluctuating mass subjected to an additive white noise, we have proved the existence of energetic instability generated by multiplicative trichotomous noise. Our main result is that for a harmonic oscillator, colored fluctuations of the mass can cause noise correlation time induced transitions from energetic stability to instability, as well as in the opposite direction.

Furthermore, the transition is found to be reentrant, e. g. if the damping coefficient is lower than a certain threshold value, then the energetic instability appears above a critical value of the noise correlation time, but disappears again through a reentrant transition to the energetically stable state at a higher value of the noise correlation time. Oscillators with varying mass are important in many systems, e. g. in nanomechanical resonators with randomly attaching and detaching atoms, ions, molecules or nanoparticles. For this reason, we believe that the results of this work may be used for the analysis of plasma-materials interaction and to find the plasma heat and influence time parameters for energetically stable oscillator systems.

Inspired by previous paragraph, one of the interesting noise induced phenomena evoked by stochastic fluctuations is related to the anomalous diffusion with the mean square displacement of particles $\langle r^2(t)\rangle \sim t^{\alpha}(\alpha \neq 1)$, which can be found for different systems including viscoelastic media. Namely, anomalous diffusion may appear near the melting point of material which is one the interest of our work. One kind of system, where anomalous diffusion appears is in the behavior of Brownian motion in quiescent fluids which is modelled via generalized Langevin equation. Although the behavior of Brownian motion in quiescent fluids has been investigated in detail, our understanding of thermally induced particle dynamics in flows, impurities in plasma flows or dust particles penetration into semiliquid material, is still unknown. Especially in shear flows, little is known about the dynamics of Brownian particles and about hydrodynamic interaction effects in spite of their fundamental relevance and importance in microfluidic applications. Of particular interest are small mesoscopic systems such as colloidal particles, nanoparticles in solutions, all of which are dominated by fluctuations.

In order to model the movement of Brownian particles in the viscoelastic fluid, we consider a Brownian particle of the unit mass (m = 1) suspended at the position r = (X, Y, Z) in a viscoelastic flow field with parallel streamlines in the x direction

$$\vec{\mathbf{v}}(\vec{\mathbf{r}},t) = \rho \mathrm{Y}\ \cos(\Omega t)\,\vec{\mathbf{e}_{\mathbf{x}}} \tag{2}$$

with $\vec{\mathbf{e}_{\mathbf{x}}}$ denoting the unit vector in the x direction, ρ the shear rate, and Ω the shear frequency. The particle is trapped by a harmonic potential with its minimum $\vec{\mathbf{r}_{\mathbf{0}}} = 0$

$$U(\vec{\mathbf{r}}) = \frac{\omega^2}{2} r^2 \tag{3}$$

where ω is the trap frequency. As a model for such a system with memory, strongly coupled with a noisy environment, we consider a generalized Langevin equation (GLE) with a fluctuating harmonic confinement potential $U(\vec{\mathbf{r}})$

$$\ddot{\vec{\mathbf{r}}} + \gamma \int_0^t \eta(t - t')\left[\dot{\vec{\mathbf{r}}}(t') - \vec{\mathbf{v}}(\vec{\mathbf{r}}(t'), t')\right]\mathrm{d}t' + \vec{\nabla} U(\vec{\mathbf{r}}) = \vec{\xi}(t) \tag{4}$$

where $\dot{\vec{\mathbf{r}}} \equiv \mathrm{d}\vec{\mathbf{r}}/\mathrm{d}t$, γ is the damping coefficient, and $\vec{\xi}(t)$ is an external 3-D random force representing the action of non-thermal fluctuations, and $\eta(t)$ is the dissipative memory kernel characterizing the viscoelastic properties of the medium (dense plasma or material, e.g. tungsten, near the melting point). Fractional Gaussian noise with correlation function is given by

$$\langle \xi_i(t)\, \xi_j(t')\rangle = (D\delta_{ij})/(\Gamma(1 - \delta)\lceil t - t' \rceil^{\delta}) \tag{5}$$

where D characterizes the noise intensity, and $\Gamma(y)$ is the gamma function. The memory exponent δ can be taken as $0 < \delta < 1$, and it is determined by the viscoelastic properties of the medium. The dissipative kernel $\eta(t)$ is modelled by a power law memory

$$\eta(t) = 1/(\Gamma(1 - \alpha)\, t^{\alpha}) \tag{6}$$

Moreover, by taking the time limit $\alpha \to 1$, the memory kernel $\eta(t)$ possesses all properties of the δ-function. As a result, the memory kernel corresponds to Stokes friction in the GLE. In other words, we have studied, in the long time regime, the dynamics of a Brownian particle due to oscillatory external noise (e.g. Rayleigh instabilities in plasma or in liquid) as an oscillatory viscoelastic shear flow. Starting from a generalized Langevin equation with a power law type memory driven by an internal noise and a multiplicative noise, we have been able to derive

exact analytical expressions of the second order moments and cross-correlation functions of the fluctuating displacement for the Brownian particle in the shear plane.

Firstly, on the basis of a GLE with a power law memory kernel we have analyzed the behavior of the velocity correlation functions and the angular momentum of a 'free' underdamped Brownian particle embedded in a viscoelastic oscillatory shear flow if $U = 0$. Its interaction with fluctuations of environmental parameters is modelled by an external additive fractional Gaussian noise with an exponent δ. As our main result we have established, in the long time regime, a cage effect induced trapped (confined) regime of the velocity process of the Brownian particle, which is characterized with a bounded variability of the particle's mean angular momentum. Such a trapped regime is possible if the memory exponent $\alpha < 1/2$ and if the exponent δ characterizing the external noise fulfils the inequality $2\alpha < \delta < 1$. In the case of an internal noise the corresponding velocity process in the shear flow directions is always subdiffusive, i.e., unbounded.

Secondly, we have found the following main results for the case, when $U \neq 0$. We have established that in the investigated model, the interplay of the multiplicative noise, the shear flow, and memory effects can generate a rich variety of non-equilibrium cooperation phenomena:

a) Existence of critical memory exponents $\alpha_{cr1} = 1/2$ and $\alpha_{cr2} = 2/3$ for oscillatory and time independent shear flows, respectively, which mark dynamical transitions from the confined dynamics of a Brownian particle to the subdiffusive regime;
b) Resonance-like dependence of the anisotropy of the particle position distribution on the memory exponent α;
c) Crossover between two different asymptotic power law regimes in time τ for the cross-correlation functions, e.g. $\tau^{-2\alpha}$ and $\tau^{1-2\alpha}$ for $\langle X(t)Y(t+\tau)\rangle_{as}$;
d) Multiresonance of the second moment of the particle displacement in the shear flow direction $\langle X^2\rangle$ and the cross-correlation $\langle XY\rangle$ between the orthogonal directions in the shear plane versus the frequency Ω of the shear flow, up to three peaks for $\langle X^2\rangle$ and up to two peaks for $\langle XY\rangle$;
e) Existence of a memory dependent critical intensity of the fluctuations of the trapping potential well, above which an energetic instability occurs;
f) Resonance of the mean angular momentum $\langle L_z\rangle$ of Brownian particles versus the frequency Ω.

The last phenomenon is relatively strong at intermediate values of the memory exponent α. This contrasts with the case of Stokes friction ($\alpha = 1$) in the shear flow, where such an effect is absent (the amplitude of $\langle L_z\rangle$ is a decreasing function on Ω). Thus it seems that the appearance of a resonant peak of $\langle L_z\rangle$ vs Ω can provide an experimentally convenient criterion enabling estimation of the importance of the viscoelastic properties of the shear flow. We believe that the results of this paper not only supply material for theoretical investigations of fractional dynamics in stochastic systems, but also suggest some possibilities for interpreting experimental data, e.g. for particles trapped by optical tweezers in dusty plasmas, where issues of memory and multiplicative noise can be crucial. For an oscillatory shear flow, possible experiments are in the field of dusty plasmas and trapped colloidal dispersions.

ACKNOWLEDGEMENT

This research has been supported by the grant CR IAEA 16931 "Non-linear processes at mesoscale plasma-materials interactive research", Estonia grant number ETF9005 "Dynamical properties of systems described by a generalized Langevin equation with a multiplicative noise", by the ministry of Education and Research of Estonia under Grant No. SF0130010s12 "Stochastic processes in nano and mesosystems: Theory and applications in material sciences and biochemistry", and by the European Union through the European Regional Development Fund (Estonian Center of Excellence "Mesosystems-Theory and Applications", TK114).

REFERENCES

[1] SHIROKOVA, V., LAAS T., VÄLI, B., PRIIMETS, J., AINSAAR, A., DEMINA, E.V., PIMENOV, V.N., MASLYAEV, V.N., GRIBKOV, V.A., DUBROVSKY, A.V., SCHOLZ, M., "Sensitivity of tungsten and tungsten doped with La_2O_3 to deuterium plasma processing", 8th International Conference of DAAAM Baltic, Industrial Engineering (Proc. Int. Conf. Tallinn, Estonia, 2012), TAUNO, O. (Ed.), Tallinn University of Technology (2012).
[2] SHIROKOVA, V., VÄLI B., LAAS, T., DEMINA, E.V., PRUSAKOVA, M.D., "Modification of the ODS tungsten surface layer after dense plasma shots", 11th Kudowa Summer School Towards Fusion Energy (Proc. Int. Conf. Kudowa, 2012), Institute of Plasma Physics and Laser Microfusion (Ed.), Warsaw, Poland (2012).

[3] SHIROKOVA, V., LAAS, T., PRIIMETS, J., DEMINA, E.V., PRUSAKOVA M.D., SCHOLZ, M., Estimation of tungsten and ODS tungsten damages after dense plasma exposure in PF-12 and PF-1000. Problems of Atomic Science and Technology **6** (2012) 232–234.
[4] SHIROKOVA, V., LAAS, T., AINSAAR, A., PRIIMETS, J., UGASTE, Ü., DEMINA, E.V., PIMENOV, N.V., MASLYAEV, S.A., DUBROVSKY, A.V., GRIBKOV, V.A., SCHOLZ, M., MIKLI, V., Comparison of damages in tungsten and tungsten doped with lanthanum-oxide exposed to dense deuterium plasma shots, J. Nucl. Mater. **135** 1–3 (2013) 181–188.
[5] DEMINA, E.V., GRIBKOV, V.A., PIMENOV, V.N., MASLYAEV, S.A., PRUSAKOVA, M.D., SHIROKOVA, V., LAAS, T., UGASTE, YU., Effect of irradiation with pulsed fluxes of high temperature deuterium plasma and fast ions on the structure of the surface layer of W-1% La_2O_3 alloy, Inorg. Mater.: Appl. Res. **5** 3, (2014) 211–218.
[6] SHIROKOVA, V., LAAS, T., AINSAAR, A., PRIIMETS, J., UGASTE, Ü., GRIBKOV, V.A., MASLYAEV, S.A., DEMINA, E.V., DUBROVSKY, A.V, PIMENOV, V.N., PRUSAKOVA, M.D., MIKLI, V., Armor materials' behavior under repetitive dense plasma shots, Phys. Scr. **T161** (2014) 014045.
[7] GRIBKOV, V.A., PADUCH, M., ZIELINSKA, E., LAAS, T., SHIROKOVA, V., VÄLI, B., PAJU, J., PIMENOV, V.N., DEMINA, E.V., LATYSHEV, S.V., NIEMELA, J., CRESPO, M.L., CICUTTIN, A., TALAB, A.A., POKATILOV, A., PARKER, M., Parallel investigation of double forged pure tungsten samples irradiated in three DPF devices, J. Nucl. Mater. **463** (2015) 341–346.
[8] VÄLI, B., LAAS, T., PAJU, J., SHIROKOVA, V., PADUCH, M., GRIBKOV, V.A., DEMINA, E.V., PIMENOV, V.N., MAKHLAJ, V.A., ANTONOV, M., The experimental and theoretical investigations of damage development and distribution in double forged tungsten under plasma irradiation initiated extreme heat loads. Nukleonika, **61** 2 (2016) 169–177.
[9] PRIIMETS, J., UGASTE, Ü., Relations between diffusion paths and interdiffusion coefficients in the ternary system Fe–Co–Ni. Defect and diffusion forum **326** (2012) 209–214.
[10] UGASTE, Ü., PRIIMETS, J., Calculating of diffusion profiles in ternary systems using effective interdiffusion coefficients of components. Defect and Diffusion Forum **333** (2013) 73–82.
[11] PRIIMETS, J., UGASTE, Ü., Diffusion paths in single phase ternary metal systems. Philosophical Magazine, **93** 16 (2013) 2026–2032.
[12] UGASTE, Ü., KODENTSOV, A.A., VAN LOO, F.J.J., Concentration dependence of interdiffusion coefficients in Cu–Fe–Ni system, The Physics of Metals and Metallography **114** 1 (2013) 54–62.
[13] SOIKA, E., MANKIN, R., PRIIMETS, J., Generalized Langevin equation with multiplicative trichotomous noise, Proceedings of the Estonian Academy of Sciences **61** 2 (2012) 113–127.
[14] SAUGA, A., MANKIN, R., AINSAAR, A., "Resonant behavior of a fractional oscillator with fluctuating mass", Applications of Mathematics in Technical and Natural Science 4th International Conference for Promoting the Application of Mathematics in Technical and Natural Science (Proc. Int. Conf. Varna, Bulgaria 2015), AIP Conference Proceedings (2012).
[15] SOIKA, E., MANKIN, R., LUMI, N., "Parametric resonance of a harmonic oscillator with fluctuating mass", Applications of Mathematics in Technical and Natural Science 4th International for Promoting the Application of Mathematics in Technical and Natural Science (Proc. Int. Conf. Varna, Bulgaria 2015), AIP Conference Proceedings (2012).
[16] MANKIN, R., LAAS, K, LUMI, N., Memory effects for a trapped Brownian particle in viscoelastic shear flows, Physical Review E **88** (2013) 042142.
[17] MANKIN, R., LAAS, K., LUMI, N., REKKER, A., Cage effect for the velocity correlation functions of a Brownian particle in viscoelastic shear flows, Physical Review E **90** (2014) 042127.
[18] LAAS, K., MANKIN, R., "Resonance of Brownian vortices in viscoelastic shear flows", Applications of Mathematics in Technical and Natural Science 7th International Conference for Promoting the Application of Mathematics in Technical and Natural Science (Proc. Int. Conf. Albena, Bulgaria 2015), AIP Conference Proceedings (2015).

INVESTIGATION OF MATERIALS UNDER HIGH REPETITION AND INTENSE FUSION PULSES

M. WIRTZ, J. LINKE, T. LOEWENHOFF, G. PINTSUK
Forschungszentrum Jülich GmbH,
EURATOM Association,
Jülich, Germany

Abstract

The increasing importance of tungsten and tungsten alloys for future nuclear fusion facilities and reactors requires an increasing understanding of the materials behavior under operational loading conditions. Among others, this comprises the thermal shock and thermal fatigue resistance of the material before and after recrystallization. This study in particular aims for the qualification of deformed tungsten forged in two orthogonal directions intending to obtain a dense and nearly isotropic grain structure. The material is investigated in its stress relieved and recrystallized state and acts as a reference material for a better understanding of the cracking process when exposed to transient thermal loads, e.g. edge localized modes. This is addressed by multiple thermal shock loadings up to 10^6 in the electron beam facility JUDITH-1 and -2 at different base temperatures. Hereby the influence of the ductile to brittle transition temperature on the onset of crack formation is verified and the latter qualified and quantified by metallographic means.

1. INTRODUCTION

Tungsten is being considered as the plasma facing material of the next step fusion devices such as the divertor for ITER [1]. The main advantages of W are its high melting point and thermal conductivity, the low thermal expansion and tritium retention [2], and the high resistance against sputtering and erosion. Different W grades produced by powder metallurgy, casting, plasma spraying, and chemical vapor deposition are industrially available [3]. Since these materials have different thermomechanical properties, their performance at the expected heat flux conditions could be significantly different. For fusion application, the most essential properties are thermal conductivity, ductility, structural stability at elevated temperature, and stability of properties under neutron irradiation and activation [4].

On the other hand, the main drawback of tungsten is its brittleness. Different methods have been tried to improve the toughness of tungsten [5–8], which also requires a balance of strength and ductility. For instance, dopants such as potassium are used to increase the recrystallization temperature of the tungsten [8]. Improvement in the fabrication technique is an alternative way. In the present study, the tungsten was double forged. The operational window of the ITER divertor [9] is limited by the rather high ductile to brittle transition temperature (DBBT) and low recrystallization temperature of tungsten. The degradation of materials that are loaded with up to 10^6 transient events and heated, at the same time, with a stationary heat load (SHL) to create accurate thermal operational conditions was investigated.

2. MATERIAL PRODUCTION AND PROPERTIES

The material used for the thermal shock test under edge localized modes (ELMs) relevant conditions was double forged pure tungsten (purity 99.97 wt%) supplied by Plansee AG, Austria. Additionally to forging the rod in radial direction, the tungsten was also forged axially into a flat disc shaped geometry. The reason for this was the idea to obtain an isotropic material, without a preferential grain orientation. A schematic illustration of the manufacturing process and a picture of the tungsten blank as received are shown in Fig. 1. A closer investigation of the microstructure of the tungsten blank showed that the grain orientation is not isotropic. The grains are elongated in radial direction and numerical processing is giving an average aspect ratio A equal to 0.4 (A = 1 corresponds to a completely symmetrical shape). This elongated grain structure disappears after the recrystallization process of selected parts of the tungsten blank. After a heat treatment of 1600°C for 1 h the grain structure was much more homogenous. However the recrystallization reduces the mechanical strength of the material by about a factor of two due to a much lower defect density and a weak cohesion between single grains.

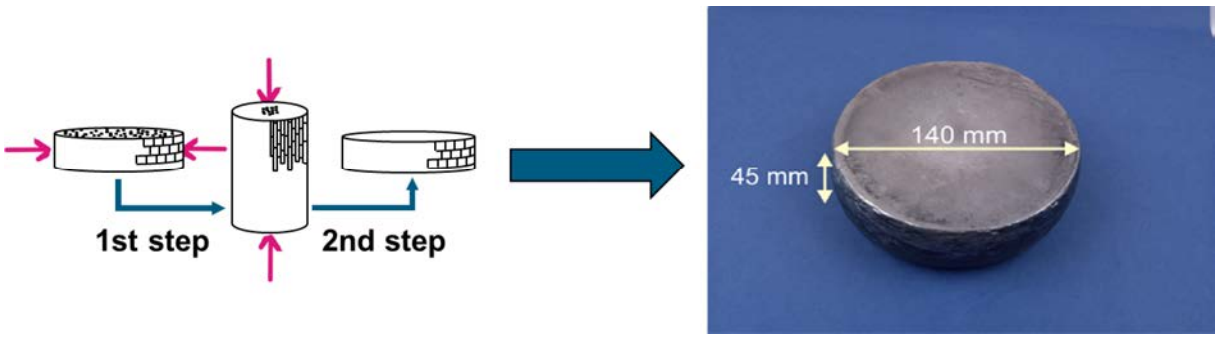

FIG. 1. Schematic illustration of the manufacturing process (left) and of the tungsten blank as received (right).

3. LOW PULSE NUMBER THERMAL SHOCK TESTS

Both the investigated tungsten grades, before and after recrystallization, were exposed to 100 ELM like thermal shock events in the electron beam facility JUDITH-1 with a pulse duration of 1 ms and a repetition frequency of 0.5 Hz. The samples (12 mm³ × 12 mm³ × 5 mm³) were cut with grains parallel to the loaded surface (longitudinal). Some of them were recrystallized subsequently and all of them were polished to a mirror finish in order to obtain an undamaged reference state. ELM like thermal shock tests were performed at an absorbed power density between 0.19 GW/m² and 1.51 GW/m², and base temperatures between RT and 600°C. The results of these tests are shown in Figs 2(a) (longitudinal) and (b) (recrystallized). These damage mappings enable us to define two threshold values for both tungsten grades. First, the damage threshold (green dashed line): for loading conditions below this threshold the induced thermal stresses are not high enough to induce any visible damages such as surface modifications or cracks. Second, the cracking threshold (red dotted line): above this threshold the material provides sufficient ductility to deal with the occurring stresses by plastic deformation. The damage threshold for the longitudinal and recrystallized samples is located in the same region between 0.19 GW/m² and 0.38 GW/m². In contrast to that, the cracking threshold for the recrystallized material is much higher (200–300°C) than for the material with longitudinal grain orientation. The difference can be traced back to the significantly reduced mechanical strength and weak cohesion between grains of the recrystallized material. This explanation is supported by analysis of the cross-sections which were prepared for the cracked samples to characterize the crack propagation into the material. The recrystallized samples show a much higher loss of complete grains during the preparation compared to the material as received due to the reduced cohesion between grains after recrystallization.

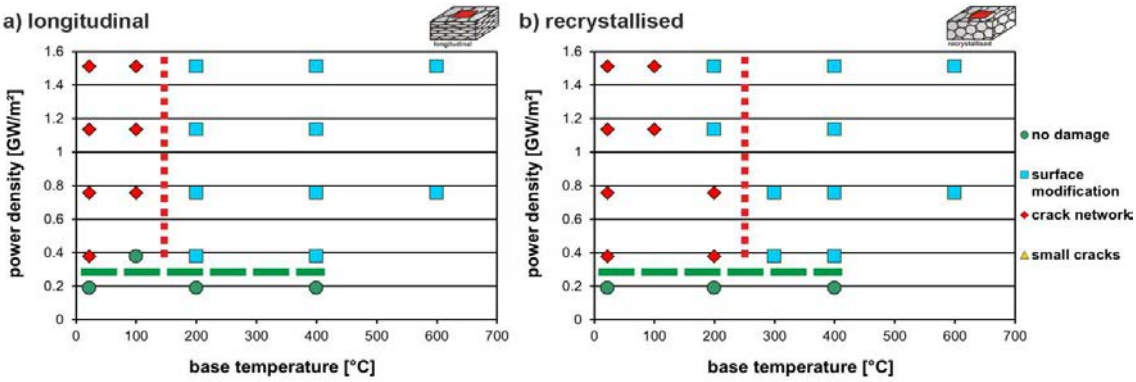

FIG. 2. (a) Damage mappings for the samples with longitudinal grain orientation; (b) damage mappings for the samples in the recrystallized state. The damage and cracking threshold are indicated by a green dashed and red dotted line, respectively.

The representative cross-sections of a longitudinal and recrystallized sample were exposed to 1.51 GW/m² at RT, and are shown in Fig. 3. The thermal shock cracks propagate perpendicular to the loaded surface into the material. They stop at a certain depth and start propagating parallel to the loaded surface. This kind of crack propagation was observed for both tungsten grades loaded in the range below the respective cracking threshold.

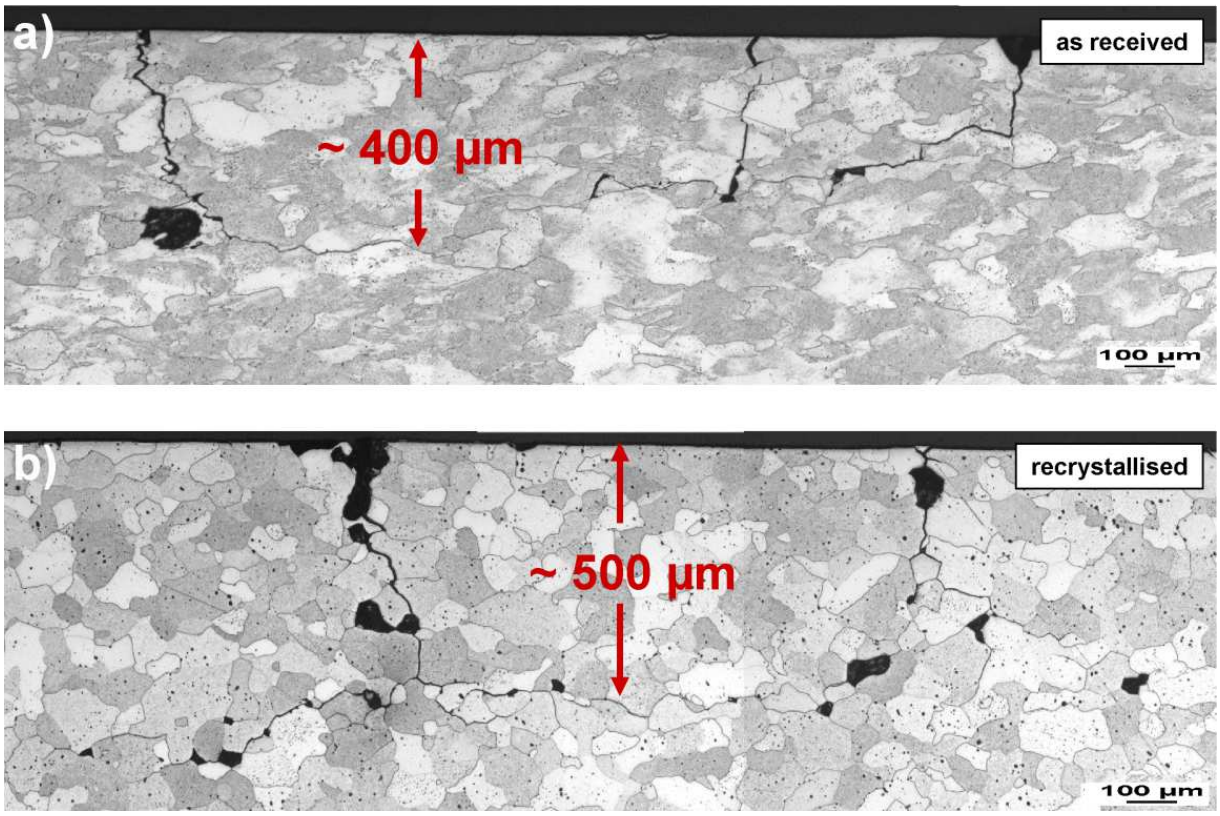

FIG. 3. (a) LM images of representative cross-section of the longitudinal material exposed to 1.51 GW/m² at RT; (b) LM images of representative cross-section of the recrystallized material exposed to 1.51 GW/m² at RT.

Furthermore, the crack propagation depends on the microstructure. For the longitudinal grain orientation, cracks parallel to the loaded surface propagate predominantly intergranular into the material, while cracks perpendicular to the loaded surface show also transgranular crack propagation. Due to the reduced cohesion between single grains, cracks propagate for the recrystallized material predominantly intergranular. The cracking parallel to the loaded surface is a severe problem. These parallel cracks act as a thermal barrier and will, with increasing pulse number, lead to an overheating of the material surface. In the worst case the material will melt and/or whole surface parts will be eroded and contaminate the plasma. First thermal shock experiments with 1000 pulses have shown that the induced surface modifications such as crack formation and surface roughness due to plastic deformations is not stable. Surface roughness and crack width increase for higher pulse numbers. This behavior exacerbates the risk of component failure due to fatigue effects, erosion, and melting.

4. HIGH PULSE NUMBER THERMAL SHOCK TESTS

The electron beam facility JUDITH-2 was employed for high pulse number thermal shock tests. Experiments were designed to apply transient events with a power density of 0.14–0.55 GW/m² for 0.5 ms, followed by a sample scanning phase that produced a homogeneous SHL of 0, 5 MW/m² or 10 MW/m². This pattern repeats with 25 Hz, applying 104 ELM-like pulses in 400 s. Thermal shock experiments were done with pulse numbers between 103 and 106. While the beam path of the SHL is designed to obtain a homogeneous loading of the full test specimen, the transient event is applied locally and homogeneous conditions are achieved within a circular area of $r \approx 1–2$ mm. The test components consisted of tungsten tiles of 12 mm × 12 mm × 5 mm, cut from the material described in Section 2 with longitudinal and recrystallized grain structure, brazed to an actively cooled copper heat sink. After exposure to the heat loads, the tungsten tiles were examined by light microscope, SEM and laser profilometry as well as by metallographic investigation of the cross-section of the specimens. The damage was categorized according to the type of observed degradation (as for low pulse number experiments). In Fig. 4, the graphs show the results of different experiments. Roughened samples show a change in reflectivity visible at optical inspection and on light microscope images. Cracks appear with increasing pulse number (‘small cracks’) and connect to a ‘crack network’. Small cracks were only observed at elevated temperatures of ~ 700°C. After further pulses, melting of crack edges took place for the most severely loaded samples.

In contrast to the low pulse number thermal shock tests described in Section 3, performed at higher power densities and lower pulse numbers, the results showed a slow evolution of degradation. This development suggested that cracks originate from thermal fatigue. A first directly observable effect of this fatigue is roughening. In general a more pronounced roughening was found for higher base temperatures and pulse numbers. It also appears earlier for higher temperatures, i.e. at 0.27 GW/m² for 104 pulses there was no damage at surface temperature of 200°C, but roughening was observed at surface temperature of 700°C. The roughening process continued after crack formation, leading to highly deformed surfaces. Protruding parts were characterized by deteriorating thermal contact, overheated and partially melted forming droplets on the surface.

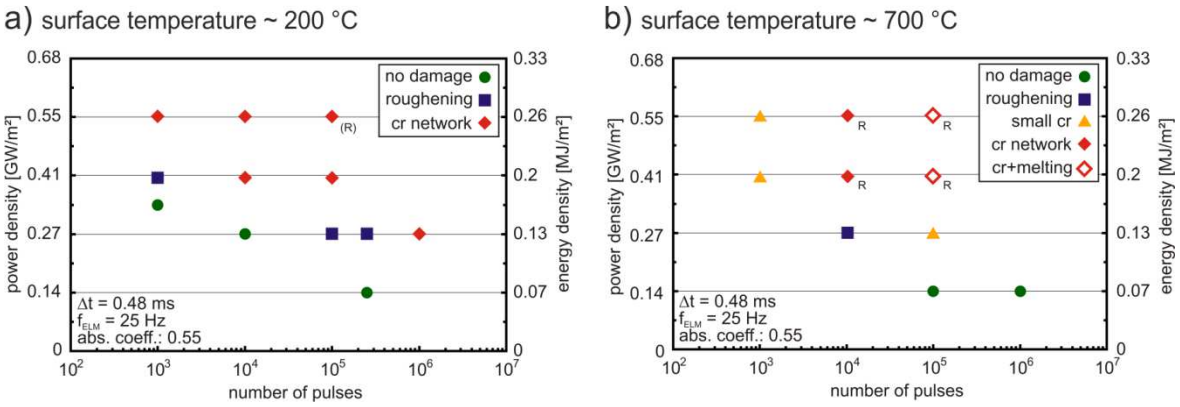

FIG. 4. (a) Surface condition of tungsten samples tested at a surface temperature of 200°C (no SHL), here one sample showed recrystallization at the surface near a crack indicated by (R); (b) Surface condition of tungsten samples tested at a surface temperature of 700°C (10 MW/m² SHL), here samples that were cross-sectioned and showed recrystallization are indicated by 'R'.

In case of surface temperature of 200°C, cracks typically appeared more sudden than at elevated temperatures, because the material appears to be still fully or partially in a brittle state. Hence a small cracks phase may exist but was not observed. Low pulse number experiments with the same material showed that 150–200°C is a critical temperature, above which the material behaved more ductile. Brittleness also explained the evolution of crack depth which did not increase from 104 to 105 pulses at surface temperature of 200°C, but did so for the exact same loading conditions (0.41 GW/m² and 0.55 GW/m²) at surface temperature of 700°C. Additionally the crack depth at surface temperature of 700°C was significantly lower at 104 pulses. This suggests a slow development as it was expected for fatigue cracks in a more ductile regime.

5. SUMMARY AND CONCLUSION

A new double forged tungsten grade was investigated in its stress relieved and recrystallized state. The material was found to be anisotropic with a grain elongation in radial direction and a remaining porosity in the center of the disc shaped tungsten blocks. After annealing, it was found a huge grain growth on the outside, coupled with a limited or no grain growth in the center which is influenced by the remaining porosity. Furthermore, a reduction of anisotropy was observed.

In low pulse number thermal shock tests applying ELM-like loading conditions in the electron beam facility JUDITH-1, the cracking threshold base temperature, which is related to the DBTT, was determined for the reference direction to 150 – 200°C for the stress relieved material, and to 200–300°C for the annealed material. Since the material is anisotropic different, i.e. higher cracking threshold base temperatures (> 500°C) were found in the orthogonal direction. Relating these results to the yet reduced number of comparable investigations and taking the orientation dependence into account, the material behaves similar to other pure tungsten grades. Increasing the ductility is expected to improve the performance of tungsten by addition of alloying elements or by decreasing the grain size in combination with a minimum amount of manufacturing induced stresses. The maximum roughness/surface elevation is observed at temperatures closely below the cracking threshold temperature. Crack formation in general follows the grain boundaries resulting in crack formation parallel to the loaded surface in a depth of 200–600 µm for the reference direction limiting the heat transfer capabilities of the material.

The high pulse number experiments performed in JUDITH-2 showed that thermal shocks of the intensity of mitigated ITER ELMs induced fatigue damage in tungsten at elevated temperatures. At lower temperatures crack initiation was caused by fatigue, but crack propagation was brittle due to the increasing material brittleness with decreasing temperature (also the distance from the surface might play a role here). However, the final crack depth and the material damage threshold (between 0.14–0.27 GW/m²) were independent on the damage mechanism. The load intensity was the important factor for the final crack depth. This intensity dependence is in agreement with thermal shock tests at low pulse numbers, but higher intensities (100 pulses, up to 1.3 GW/m²), where the same behavior was found.

REFERENCES

[1] LINKE, J., Plasma facing materials and components for future fusion devices development, characterization and performance under fusion specific loading conditions, Phys. Scr. **T123** (2006) 45–53.

[2] KIRK, A., LISGO, S., NARDON, E., EICH, T., HERRMANN, A., KALLENBACH, A., LOARTE, A., J. Nucl. Mater. **390** (2009) 727–732.

[3] WITTLICH, K., HIRAI, T., COMPAN, J., KLIMOV, N., LINKE, J., LOARTE, A., MEROLA, M., PINTSUK, G., PODKOVYROV, V., SINGHEISER, L., ZHITLUKHIN, A., Damage strucutre in divertor armor materials exposed to multiple ITER relevant ELM loads, Fusion Eng. Des. **84** 7–11 (2009) 1982–1986.

[4] ZHITLUKHIN, A., KILMOV, N., LANDMAN, I., LINKE, J., LOARTE, A., MEROLA, M., PODKOVYROV, V., FEDERICI, G., BAZYLEV, B., PESTCHANYI, S., SAFRONOV, V., HIRAI, T., MAYNASHEV, V., LEVASHOV, V., MUZICHENKO, A., Effects of ELMs on ITER divertor armour materials, J. Nucl. Mater. **363** (2007) 301–307.

[5] UEDA, Y., TODA, M., NISHIKAWA, M., KONDO, K., TANAKA, K.A., Effects of repetitive ELM-like heat pulses on tungsten surface morphology, Fusion Eng. Des. **82** 15–24 (2007) 1904–1910.

[6] UMSTADTER, K.R., DOERNER, R., TYNAN, G., Effect of bulk temperature on erosion of tungsten plasma-facing components subject to simultaneous deuterium plasma and heat pulses, Phys. Scr. **T138** (2009) 014047.

[7] PINTSUK, G., UYTDENHOUWEN, I., "Thermomechanical and thermal shock characterization of potassium doped tungsten", (Proc. 7th Plansee Seminar) **1** 2009 RM8/1-10.

[8] UYTDENHOUWEN, I., DECRETON, M., HIRAI, T., LINKE, J., PINTSUK, G., VAN OOST, G., Influence of recrystallization on thermal shock resistance of various tungsten grades, J. Nucl. Mater. **363** (2007) 1099–1103.

[9] HIRAI, T., PINTSUK, G., LINKE, J., BATILLIOT, M., Cracking failure study of ITER-reference tungsten grade under single pulse thermal shock loads at elevated temperatures, J. Nucl. Mater. **390** (2009) 751–754.

IMPLEMENTATION OF THE DENSE PLASMA FOCUS DEVICE BORA

V.A. GRIBKOV[*12], J. NIEMELA[*], C. TUNIZ[*], A. CICUTTIN[*], M.L. CRESPO[*], C. ZANOLLI[*], E.V. DEMINA[*], S.V. LATYSHEV[*], V.N. PIMENOV[*], M.D. PRUSAKOVA[*], M. CHERNYSHOVA[2], A.A. TALAB[3], G.G. GIANNINI[4], F. LONGO[4], M.R. ARUCA[5], K. TOMASZEWSKI[6]

Abstract

Upgrading of the dense plasma focus device Bora and its diagnostic complex to fit all the demands of radiation material sciences and some spin-off applications has been fulfilled. Samples of materials counted as perspective ones for use in the first wall and construction elements in nuclear fusion reactors with magnetic and inertial plasma confinement (W, Mo, Ti, Al, low activated ferritic steel Eurofer and some alloys) were irradiated in the device in the frame of the IAEA CRP round robin tests. The device Bora generates powerful streams of hot dense ($T \sim 1$ keV, $n \leq 10^{19}$ cm^{-3}) deuterium plasma ($v \leq 3 \times 10^7$ cm/s) and fast deuterons ($E \sim 0.1$–1.0 MeV) of power flux densities up to 10^{10}–10^{12} W/cm^2 correspondingly. The damage factor, $F = P \times \tau^{0.5}$, ensures an opportunity to simulate radiation loads (predictable for both reactors types) by the plasma and ion streams, which have same nature and namely those parameters as expected in the fusion reactor modules. Before and after irradiation we provided investigations of our samples by means of a number of analytical techniques. Among them we used optical and scanning electron microscopy to understand character and parameters of damageability of the surface layers of the samples. Atomic force microscopy was applied to measure roughness of the surface after irradiation. These characteristics are quite important for understanding the mechanisms and values of dust production in fusion reactor that may relate to tritium retention and emergency situations in fusion reactor facilities. We also applied two new techniques. For surface examinations we elaborated the portable X ray diffractometer that combines X ray single photon detection with high spectroscopic and angular resolutions. For bulk damageability investigations we applied an X ray microscopic computerized tomography system. We have also provided numerical simulation of the fast ion beam action. The paper contains also results on the laboratory activity in some spin-off applications of the device in nuclear medicine, dynamic quality control and for training of young researchers.

1. INTRODUCTION

Radiation material science plays an important role in a contemporary nuclear fusion program as the radiation and heat resistance of materials is a key issue for the future fusion reactors (FR) based on Magnetic Plasma Confinement (MPC) like ITER [1] or Inertial Plasma Confinement (IPC) as NIF [2]. In this direction, one of the areas of experiments is testing of the materials perspective for use in chambers of modern FRs [3, 4]. The fusion relevant materials include two classes: first wall (plasma facing) components and construction elements. Both categories must be tested under direct irradiation by hot plasma, fast ion and electron beams as well as by neutron and X ray radiations, since inside a FR the construction modules may in principle be subjected to the straight irradiation if a certain first wall element will be lost during exploitation of a facility.

Heat loading produced upon the FR chamber components by hot plasma (its temperature near the first wall is about 1 keV) and fast ions (generated due to charge exchange process in tokamaks with neutral beam heating of plasma and because of the acceleration processes in chambers with IPC) are counted as the most dangerous factor of risk. Maximal heat loads expected in FRs with MPC have power flux densities P of about 10^4 W/cm^2 with pulse duration in the range of 0.1–10 ms. These events occur at the development of the edge localized modes (ELMs), the vertical displacements of plasma (VD) and at the disruption instability (DI). In the reactors based on IPC, these figures may reach values up to $P = 10^8$ W/cm^2. However in this second case the pulse duration is much shorter (0.1–10 μs). We have provided these tests with a dense plasma focus (DPF) device that can not only ensure the fulfilment of the values of the heat loads power much higher compared with the above mentioned ones, but it is able to produce them namely with the same load carriers (hot plasma and fast ions) having the same parameters expected on the plasma facing components of the contemporary mainstream fusion devices (like ITER and NIF) [5].

[*] International Centre for Theoretical Physics, Trieste, Italy.
[1] Institute of Metallurgy and Material Science, Moscow, Russian Federation.
[2] Institute of Plasma Physics and Laser Microfusion, Warsaw, Poland.
[3] Atomic Energy Authority, NRC, Plasma Physics and Nuclear Fusion Department, Egypt.
[4] Department of Physics, University of Trieste, Trieste, Italy.
[5] Institute of Nuclear Science, Havana, Cuba.
[6] ACS Ltd., Warsaw, Poland.

2. IRRADIATION EQUIPMENT EMPLOYED AND ANALYTICAL METHODS

2.1. Equipment employed in the irradiation experiments

2.1.1. The Bora device

In Fig. 1, the device developed by ICTP [6] during the fulfilment of the current CRP in cooperation with the MPS, All Russia Research Institute of Automatics, A. I. Alikhanov Institute of Experimental and Theoretical Physics (ITEP), ACS Ltd. and IPPLM. The general characteristics of the device are presented in Table 1. The experiments were carried out by the ICTP team from MLab in close collaboration with colleagues from several other institutes including participants of the CRP: MPS, IPPLM, ICDMP, and IMET.

TABLE 1. MAIN PARAMETERS OF THE DEVICE

Bank capacity	25 μF
Bank inductance	10 nH
Charging voltage	12–20 kV
Energy storage	1.8–5 kJ
Working gases	D_2, N, H_2, Ar
Duration of the ¼ part of the discharge period	1.5 μs
Maximal amplitude of a discharge current	360 kA
DPF chamber type	The Mather configuration
Maximal neutron yield per shot in full solid angle (for 2.45 MeV neutrons)	10^8
Maximal hard X ray yield per shot in full solid angle (for photons with energy > 80 keV)	1 J (~ 10^{14} photons)
Repetition rate (a limit set by safety measures)	1 shot per 20 s
Lifetime of the DPF elements and systems	~ 10^4–10^6 shots

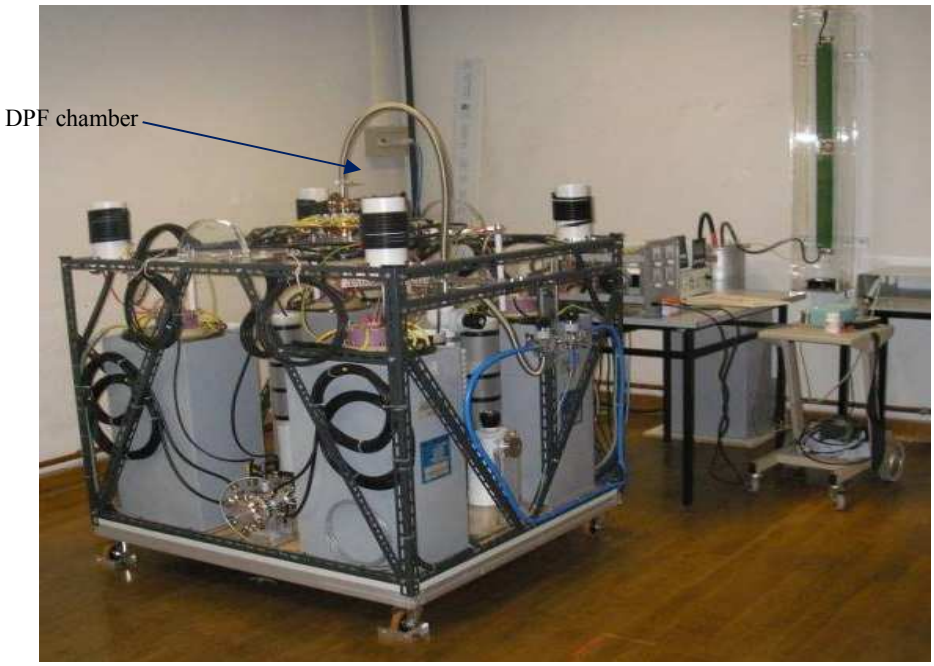

FIG. 1. The Bora device with the DPF chamber and supplement parts.

2.1.2. The Bora device metrology

During previous period and the current CRP activity we have furnished the device with the following diagnostic:

a) An absolutely calibrated Rogowski coil for the total current measurements (manufactured and calibrated by IPPLM);
b) four magnetic probes for the capacitor and switches synchronization monitoring;
c) A fast photomultiplier tube with a plastic scintillator (PMT+S) for neutron and hard X ray time resolved measurements;
d) An absolutely calibrated silver activation neutron counter for neutron yield measurements;
e) An X ray detector, Röntgen gamma dosimeter (Dresden, Germany), for absolute measurements of the X ray yield of the device in the range from 3 keV to 3 MeV photon energy.

During the experiments, a Faraday cage was employed to preserve the equipment from a very harsh environment produced during the operation of the Bora facility. The ICTP has equipped the diagnostic complex with a UPS device for the independent feeding of the firing generator, the oscilloscope LeCroy (1 GHz) and the photomultiplier tube with their power supplies. The whole assembly of the devices is presented in Figs 2 and 3.

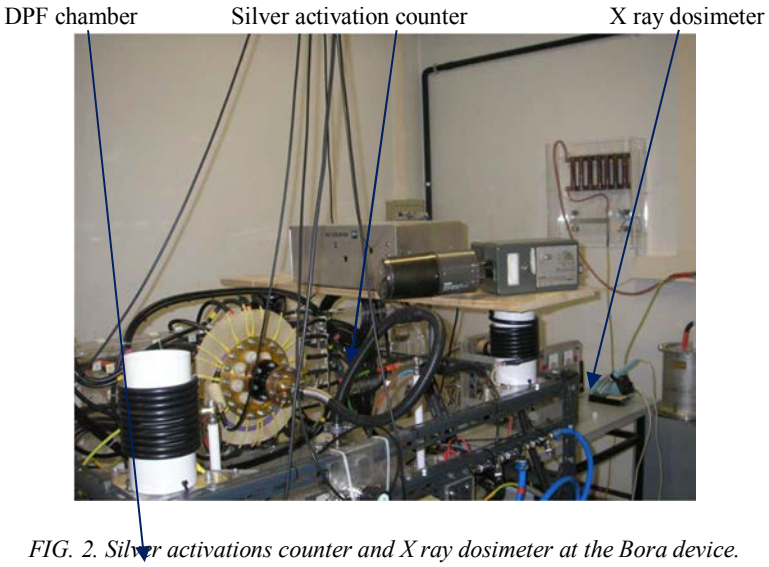

FIG. 2. Silver activations counter and X ray dosimeter at the Bora device.

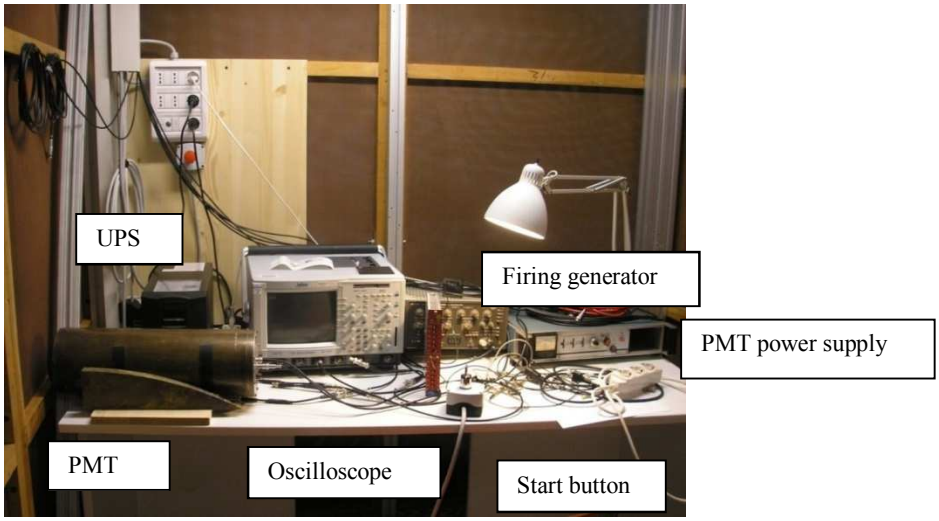

FIG. 3. Interior of the Faraday cage with control and registration units; note the UPS block (on the left-hand side of the picture) feeding all the equipment inside the cage during a DPF shot when the mains are disconnected.

The last step gave us an opportunity to eliminate inside the Faraday cage all electrical noises and to see the oscilloscope traces of the hard X ray and neutron pulses without any interfaces. Examples of the traces of current variation taken at the output cables of four capacitors showing good synchronization of all channels are presented in Fig. 4. The oscilloscope trace obtained by means of PMT+S during the DPF shot with the neutron yield on the level of about 5×10^7 neutrons is shown in Fig. 5.

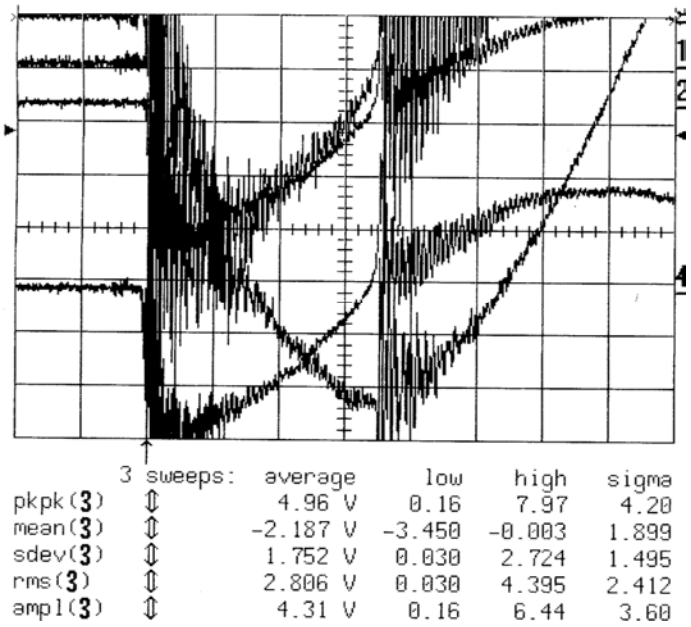

FIG. 4. Oscilloscope traces of current variation taken by magnetic probes positioned at the output cables of four capacitors of the main DPF bank.

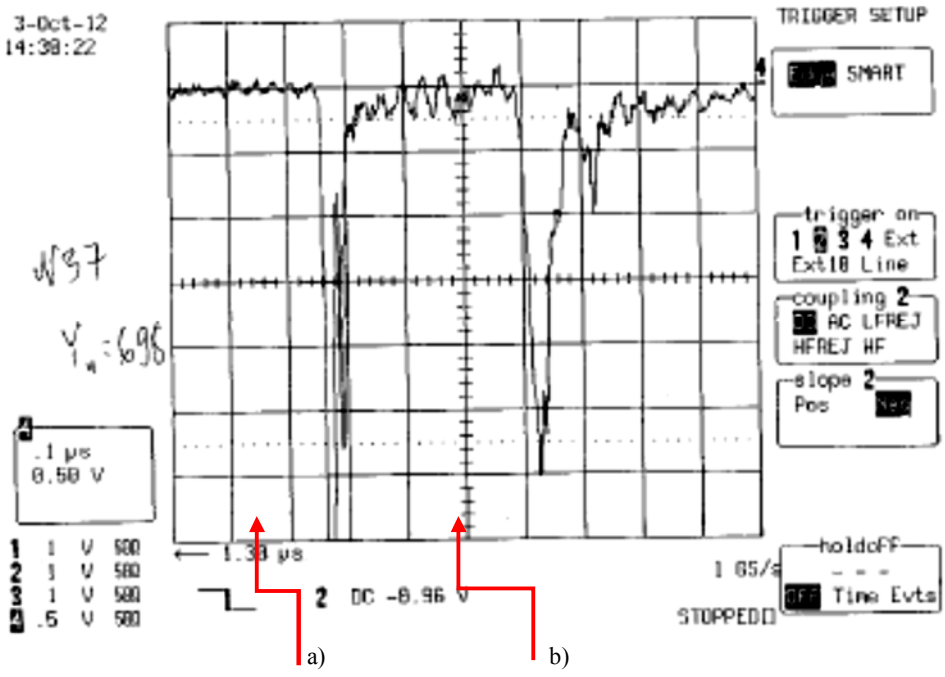

FIG. 5. (a) Oscilloscope trace of hard X ray; (b) neutron pulses generated by DPF Bora device.

We have elaborated and manufactured a number of additional parts to our DPF chambers optimized for hard X ray production (for spin-off application of our project devoted to the dynamic quality control) and for experiments on radiation material sciences. Some of them are presented in Fig. 6. These elements may allow us

now to irradiate samples placing them in various distances from the anode of the chamber. It gives an opportunity to irradiate specimens with or without melting of their surfaces. We made an outlet hole in the wall separating our DPF room from the control and registration room with a Faraday cage. This orifice gave us an opportunity to increase a time of flight (TOF) base of neutrons until about 10 m for use Bora device in spin-off applications in nuclear medicine. In this aperture we have installed a collimator made of Teflon with an inverse cone to prevent capturing signals of parasitic neutrons reflected from its walls that can reach our PMT+S probe, see Fig. 7.

FIG. 6. Several elements of the additional part of the chamber prepared for experiments in the field of radiation material science and for a number of spin-off applications.

FIG. 7. An outlet hole in the wall with the Teflon inverse cone for TOF neutron experiments.

2.2. Equipment used in the analysis of the irradiated specimens

For the instrumental analysis of the irradiated specimens we have used equipment as follows:

a) Optical microscopes NU-2E and Neopot-32 with computerized image processing as well as three optical microscopes of the MLab ICTP (one connected to a PC) that gave us information on the damageability of the samples, see Fig. 8;

b) Scanning multi-microscope VMM-2000;
c) Focused beam microscope VEGA/SBU with a system of X ray energy dispersion microanalysis (Oxford Instruments);
d) High precision X ray diffractometer (Rigaku Ultima IV, III Thin-film).
e) Optical emission spectrometer based on a glow discharge (Leco GDS-850A);
f) Universal test instrumentation MicroTester 5848 and Electropuls E3000 (Instron);
g) Unit for measuring of nanohardness (NanoTest, Micromaterials Ltd).

FIG. 8. Three optical microscopes used in experiments on radiation material science at ICTP.

Additionally we used weighing of samples before and after irradiation, profilometry, elastic recoil detection analysis (ERDA), X ray microprobe (i.e. elemental), structural and diffraction analysis. Furthermore, we have applied a portable X ray diffractometer that combines X ray single photon detection with high spectroscopic and angular resolutions (see Fig. 9) for surface investigations. The electromechanical system allows moving the X ray source and the detector independently each other. The mechanic angular resolution of each stage is better than 7×10^{-5} rad, and the use of high precision contact switches (~ 1 μm) allows the determination of the home position of the stages with excellent accuracy and repeatability.

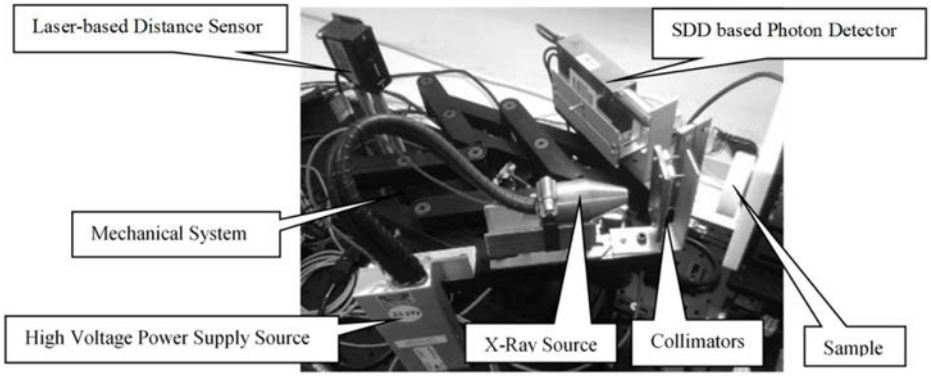

FIG. 9. X ray portable diffractometer mounted on an optical table for calibration and characterization of specimens after irradiation by X ray luminescence.

All main components, for instance X ray source, silicon drift detector (SDD), photon detector, motors, and laser distance measurement system are controlled from a PC. Besides, we applied X ray microscopic computerized tomography (micro CT) system where X rays were produced by a Hamamatsu microfocus source (150 kV, 500 μA, 5 μm focal spot size) for investigations of bulk damageability produced during our tests, see Fig. 10. The X ray microfocus source is positioned on the right-hand side of the picture beyond its border. The detector was a Hamamatsu CMOS flat panel coupled to a fiber optic plate under the Gadolinium oxysulfide GOS (Gd_2O_2S) scintillator. The reconstruction of 3-D data was run with Cobra 7.4 (Exxim Computing Corp.) and DIGIX CT software while VG Studio Max 2.1 (Volume graphics) and Amira 5.3 (Visage Imaging) were used for segmentation and rendering.

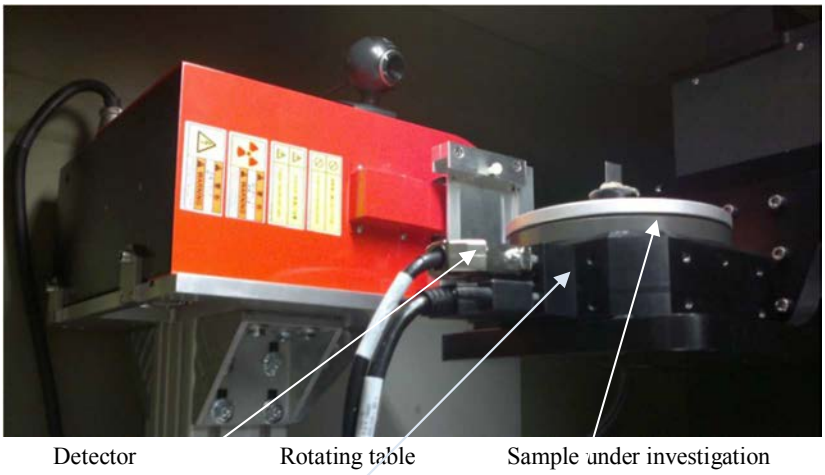

FIG. 10. The X ray microtomography device (X ray microfocus source is on the right-hand side out of the picture field).

3. IRRADIATIVE EXPERIMENTS WITH THE BORA DEVICE

3.1. Irradiation of specimens of the double forged tungsten and some other materials

Plasma streams and fast ion beams acting upon materials in the contemporary and future FR chambers are counted as the most dangerous heat carriers producing the highest damageability of their elements. Electron, X ray and neutron streams are rated as less hazardous because of the difference in their penetration depths and absorption laws compared to ions. It is known [7–14] that irradiation of materials by powerful streams of fast ions and hot plasma within different accelerators including the dense plasma focus (DPF) device results in changes of phase and structure states as well as in properties of surface layer (SL). Main features of a DPF device differ from other irradiation facilities used for simulation of the heat loads like pulsed plasma guns, injectors, plasma accelerators, fast ion and electron accelerators and laser beams [15]. DPF generates hot plasma jets (plasma temperature is in the range from several hundred eV until several keV) with velocities $v = (2–5) \times 10^7$ cm/s produced simultaneously with streams of fast ions (energy of fast deuterons are in the range from 50 keV up to several MeV). Because the powerful phase of the DPF discharge is very short and lasts usually about 10^{-8}–10^{-6} s, this device is able to irradiate targets with power flux densities of the above mentioned types of radiation on the level up to $P = 10^{10}$ W/cm^2 for hot plasma, and $P = 10^{12}$ W/cm^2 for fast ions. Energy of fast ions, obtained due to acceleration in a quasi-stationary electrostatic field induced within the DPF, is in the range $E_d \sim$ 0.1–1.0 MeV for deuterons and may reach an order of about $E_z \sim 100$ MeV for high Z ions.

Continuous (in time) beams of electrons and laser light used for heat simulation [2] in the present day materials tests have specific features. The absorption mechanisms of these beams in the solid state [16] are very different (if not opposite) from those intrinsic in ions. Zones of absorption of these beams are dissimilar to those where ions are absorbed (in particular for laser beams). Energy of individual heat carriers in these simulators (usually $E_e \sim 100$ keV, and $E_{hv} \sim 1$ eV) are tremendously differed from those observed in FRs ($E_e \sim 10$ MeV in a runaway regimes of tokamaks, and $E_{hv} \sim 10$ keV in both types of FRs). Damage features quite often are very dissimilar to those obtained during irradiation by hydrogen isotopes ions in FRs. For example blisters, a very typical defect observed in FRs may have various natures: boiling of the target material itself, evaporation of light components of a material (e.g. of Mn in stainless steels) or obtained by forced injection of hydrogen isotopes (deuterium and tritium) into material. The last one is of particular significance in connection with the problem of tritium retention in tokamaks but cannot be simulated with electron and laser beams. Thus the laser and electron beams

simulating heat loads presented in FRs are not able to reflect a number of specific features, but a DPF allows modeling them.

A DPF produces namely the same heat carriers and with the same parameters that observed near the first wall in tokamaks except the pulse duration. The latter is much shorter compared with ELMs, VD and DI events in FR with magnetic plasma confinement MPC, being however exactly the same as in FR based on IPC. However the rise time of e.g. ELMs events is less than 1 μs [17]. So a DPF with its pulse durations is able to simulate the most destructive part of this plasma instability. Besides, the very high power flux density of streams in DPF gave an opportunity to use a so called integral damage factor [18]

$$F = P \times \tau^{0.5} \tag{1}$$

Impact of the working gas plasma and fast ions produced at the cathode part of a DPF chamber may take place with and without SL melting at the power flux densities of $P > 10^8$ W/cm^2 and $P < 10^7$ W/cm^2 correspondingly. Also we are able to accomplish the impact of plasma and fast ion streams in the ablation mode (i.e. by conversion and sublimation of solid matter of a target into plasma missing the melting and boiling phases) at $P \geq 10^{11}$ W/cm^2. It attains by variation of a distance from samples to the DPF anode and by dissimilarity of charging voltages of the DPF bank of the capacitor. In these three dissimilar cases the structure and properties of the specimens under irradiation will be different.

In this set of experiments we placed our targets usually at a distance of 3.5 cm from the anode lid. It means that we have irradiated our samples at the position that is very close to the upper part of the pinch. Our materials, besides the double forged tungsten, were aluminum and molybdenum foils, as well as a titanium alloy. Working gas of the device was deuterium.

3.1.1. Experimental results

In Fig. 11, two optical microscopy (OM) images of a part of the tungsten sample DF60 are presented for the cases before and after irradiation. The conditions of the Bora device operation were initial deuterium pressure p_0 = 2.75 Torr, charging voltage U_0 = 12 kV, and seven irradiation shots. A very well developed crack net, in Fig. 11(b), appears with the characteristic size of a cell (~ 100 μm). The same results have been obtained by using scanning electron microscopy (SEM); see Figs 11(c)–(d). This net has a subnet with the characteristic size about a few tens μm that is not so clearly pronounced.

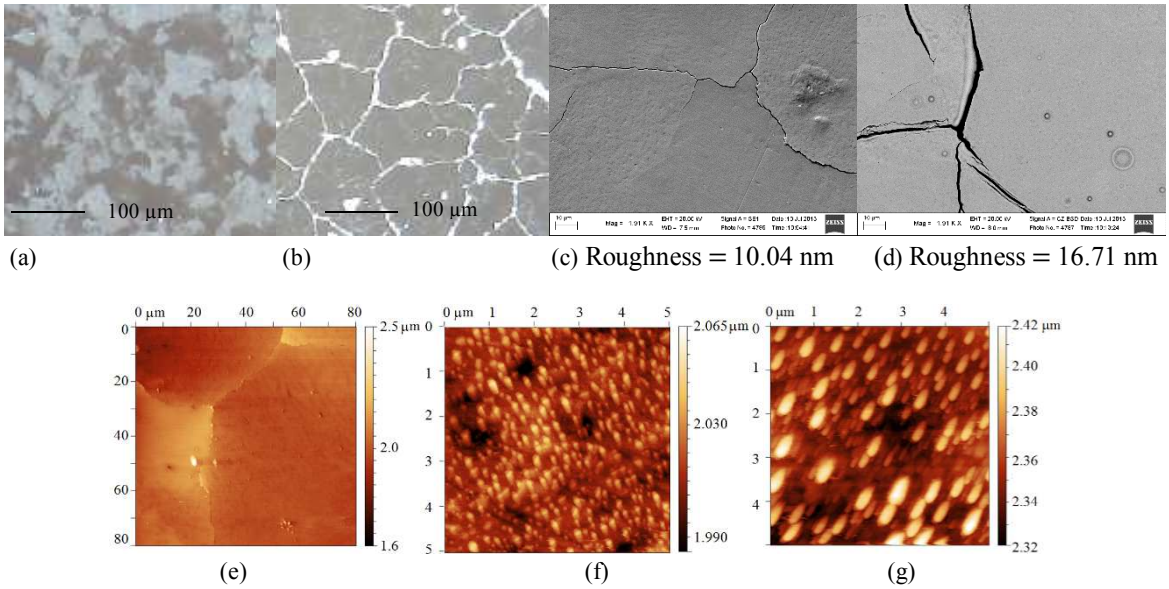

FIG. 11. (a) Optical microscopic images of the surface of the DF60 specimen of W before irradiation by seven pulses of hot plasma and fast deuterons; (b) optical microscopic images of the surface of the DF60 specimen of W after irradiation by 7 pulses of hot plasma and fast deuterons; (c) SEM images of the DF10 sample after four shots; (d) SEM images of the DF11 sample after eight shots; (e) image of the DF9 sample after four shots obtained by means AFM; (f) different magnification image of the DF9 sample after 4 shots obtained by means AFM; (g) DF11 after eight shots.

In order to see it better, we have provided the AFM visualization of tungsten samples with the parallel measurements of its roughness appeared on the surface after irradiation. Two pictures of the specimen DF9 (4 shots) made with different magnifications are presented in Figs 11(e) and (f), whereas Figure 11(g) represents the AFM image of the DF11 specimen subjected to eight shots of Bora. One may see that besides crack cells of the size of a few tens μm, there is a dense sub subnet of a needled pile with an individual peaks of the lateral size of about 100 nm as well as a number of open pores of the size of a half of a μm. In the other experiment, with the sample of tungsten DF11 that has been irradiated by eight pulses, the number of 'needles' was decreased by 3 times whereas their size increased by the same ratio. Roughness of the surface also increased from the value 10.04 nm up to 16.71 nm. It is quite clear that such a modification of the surface of tungsten grades may have a very poor consequence for FRs: this needled pile will be easily subjected to brittle destruction with production of a dust. In Fig. 12, the X ray micro CT images processed by the above mentioned techniques [19] are presented. Streams of fast ions and hot plasma struck all the samples from the left hand side. In Fig. 12(a), one can see the surface damages of the Al specimen, in particular the surface looking shaggy from the irradiation side.

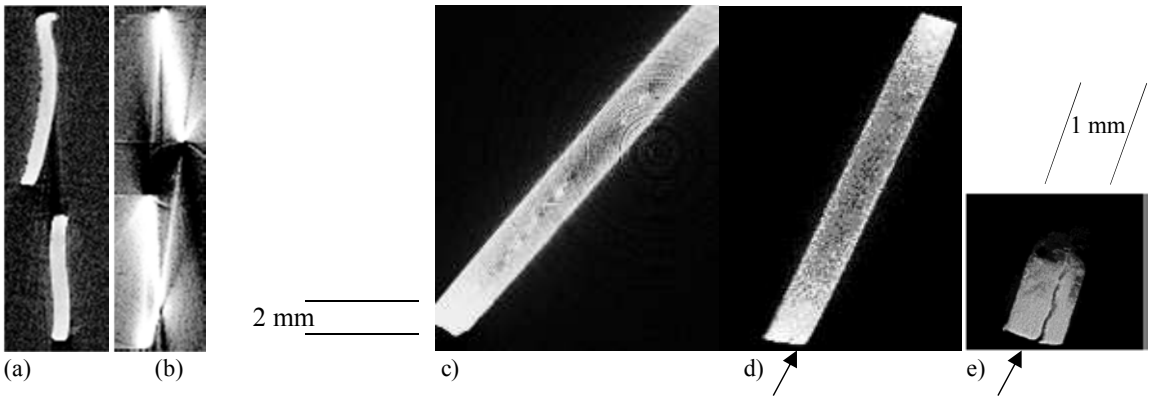

FIG. 12. (a) X ray micro CT images of two cross-sections of the Al foil sample (10 mm × 10 mm × 0.5 mm) before (below) and after (above) irradiation; (b) two cross-sections of a sample of a Mo foil (10 mm × 10 mm × 0.1 mm) taken before (above) and after (below) irradiation; (c) two cross-sections of the Ti alloy foil (13 mm × 13 mm × 1 mm) before irradiation; (d) 2 cross-sections of the Ti alloy foil (13 mm × 13 mm × 1 mm) after irradiation; e) magnification of the bottom part of the Ti alloy foil after irradiation.

This is a result of the melting and evaporation processes taking place during the irradiation of the Al sample surface by the powerful streams of hot plasma and fast ions. In Fig. 12(b), an internal spot of the longitudinal size of 2 mm is seen in the below part of the Mo foil. Sucessive images of the sample taken at its movement inside the microCT device along the foil has shown that the lateral dimension of this spot is the same, i.e. about 2 mm. Its size coinside with the diameter of our beam of fast deuterons at a distance of 3.5 cm from the anode of the DPF. So this defect (material with the lower density compared with the surrounding substance) is very likely produced in the internal part of the foil as a results of an action of a shock wave (SW). This SW is generated by the powerful beam of fast ions, and it is followed by an appearance of the unloading (rarefaction) wave. We provided a numerical modeling of the process of generation of the shock wave by the beam of fast deuterons and its penetration through the foil. We used an upgraded quasi-two-dimensional hydrodynamic model, developed previously for calculation of the parameters of secondary plasma, generated due to interaction of intense ion and plasma streams with solid targets placed in DPF [20]. In this case, the equations of a cold solid state has been added to the model according to the books [16, 21]. Pulse shape of the ion beam power flux density was taken as a sine function: $q(t) = q_0 \sin(\pi t/\tau)$. The mean free path of deuterons having energy E_d = 100 keV in molybdenum was d = 1 μm [16]. Results of numerical simulations are presented in Table 2.

TABLE 2. RESULTS OF NUMERICAL SIMULATION OF SHOCK WAVE AND UNLOADING (RAREFACTION) WAVE IN THE Mo SAMPLE

q_0 (W/cm^2)	T (ns)	T (Ev)	Z	L (μm)	P_{SW} (Gpa)	P_A (Gpa)	P_{UW} (Gpa)
10^{11}	10	20	6	2	30	30	-20

In Table 2, T and Z are the plasma temperature and the average charge of ions at the moment of the maximal intensity of the ion beam, respectively; L is the thickness of the evaporated layer of molybdenum to the end of the ion beam action; P_{SW} is the amplitude of the shock wave at the end of the action of the ion beam; P_{UW} is the maximal negative pressure in the unloading wave; P_A is the ablation pressure in plasma calculated by the formula:

$$P_A = \sqrt{\frac{q_0 \rho_0 d}{\tau}} \tag{2}$$

where ρ_0 is a specific weight of molybdenum. In Fig. 13 one may see the pressure distribution inside the foil at different moments of time counted from the moment of the beginning of the ion beam action.

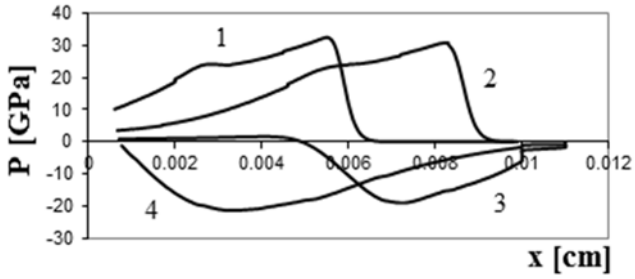

FIG. 13. Pressure distribution within the target at different moments of time indicated by progressive numbers 1 to 4, with '1' corresponding to 10 ns after the start of the ion beam action, '2' corresponding to 15 ns shock wave compression, 3 and 4 corresponding to 25 ns and 35 ns unloading wave propagating inside the sample after a SW pressure relief.

The tensile stress is about 20 GPa and is gradually increased with the penetration of the unloading wave to the irradiated surface of the target, qualitatively in agreement with the description of the unloading wave of the not strong SW having the triangular shape [21]. Its maximal value is reached in the region 20–30 μm away from the irradiated surface. Our maximal value of the power flux density of the beam of fast deuterons can be an order of magnitude higher compared with the value (10^{11} W/cm^2) used in the modeling. Short time strength σ_B of Mo depends on its initial structure and the preprocessing. It can be within the limits 0.5–1.0 GPa [22]. Treatment of samples by penetration radiation may only decrease the above value [23] and this explains the effect observed.

Comparing Figs 12(c), (d) and (e) one may see the results of the irradiation action of the powerful fast ion stream ($q \sim 10^{12}$ W/cm^2) upon the target made of the above mentioned titanium alloy foil manufactured with the use of a rolling procedure. The formidable enhancement of the initial internal structure defects produced during the preparation (rolling) of the foil and an appearance of a crack at its butt are observed in the sample after its irradiation in the Bora device. It results again from the SW action produced and penetrated the sample after the action of the stream of fast ions generating high volumetric energy density within it. For elemental and structure analysis of the irradiated specimens of titanium alloy and tungsten grade we used the X ray portable diffractometer. Results are presented in Figs 14 and 15, also Tables 3, 4, 5 and 6.

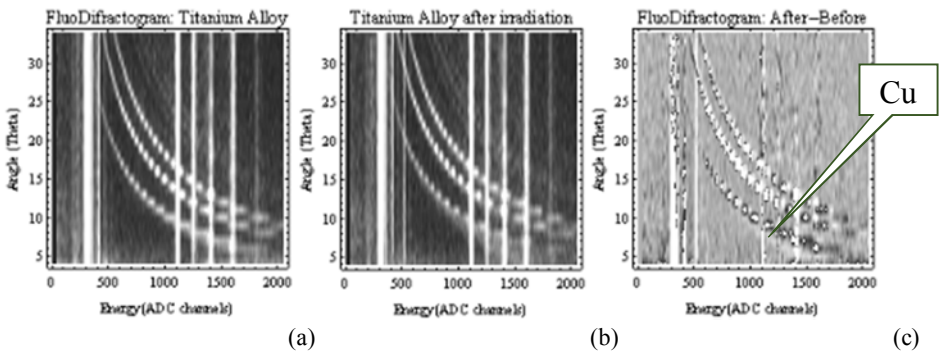

FIG. 14. (a) X ray energy and diffraction angle analysis of the Ti alloy before irradiation; (b) after irradiation; (c) subtraction of (a) from (b).

TABLE 3. X RAY FLUORESCENT LINES OBSERVED IN THE Ti ALLOY SAMPLE

Element candidate	Our XRF lines (keV)	Element candidate XRF lines (keV)	Difference (keV)	Relative intensities	Notes
Ar	2.907	2.957	-0.05	Weak	–
Ti	4.572	4.510	0.062	Strong	–
V	4.997	4.952	0.045	Strong	–
Cr	5.468	5.415	0.053	Medium	–
Cr($K_{\beta 1}$)	6.081	5.946	0.135	Medium	–
Mn($K_{\alpha 1,2}$)	6.081	5.898	0.183	Weak	–
Fe	6.458	6.403	0.055	Medium weak	–
Fe($K_{\beta 1}$)	7.086	7.058	0.028	Weak	–
Ni	7.511	7.478	0.033	Weak	–
Cu($K_{\alpha 1}$)	8.08	8.05	0.03	Very weak	After irradiation only
Ni($K_{\beta 1}$)	8.328	8.264	0.064	Weak	–
Cu ($K_{\beta 1}$)	8.96	8.90	0.06	Very weak	After irradiation only
Mo	17.473	17.479	-0.006	Strong	–
Mo($K_{\beta 1}$)	19.641	19.608	0.033	Medium	–
Ag	22.155	22.162	-0.007	Medium	Anode material
Sn	25.219	25.271	-0.052	Medium	–

TABLE 4. THE INTERPLANAR DISTANCES OBSERVED BEFORE AND AFTER IRRADIATION OF Ti APPLOY

Inter-planar distances *d* (Å) before irradiation	Relative intensities	After irradiation (Angstrom)	Differences (Angstrom)
1.27	Strong	1.25	-0.02
1.55	Strong	1.52	-0.03
2.16	Strong	2.15	-0.01
0.84	Very weak	0.83	-0.01
0.90	Very weak	0.90	0.00
0.98	Very weak	0.97	-0.01

In Figs 14 and 15 the vertical lines correspond to X ray fluorescent photons (XRF) while the curved lines correspond to photons that are subjected to Bragg reflections. Each curved line corresponds to the interplanar distance of the reflective planes in the crystalline structure. It is clear the appearance of new lines belonging to Cu (evaporated from the DPF chamber walls by the irradiations and deposited on the surface of the specimen) and small negative changes in the values of the Bragg angles of X ray diffraction from the sample's lattice.

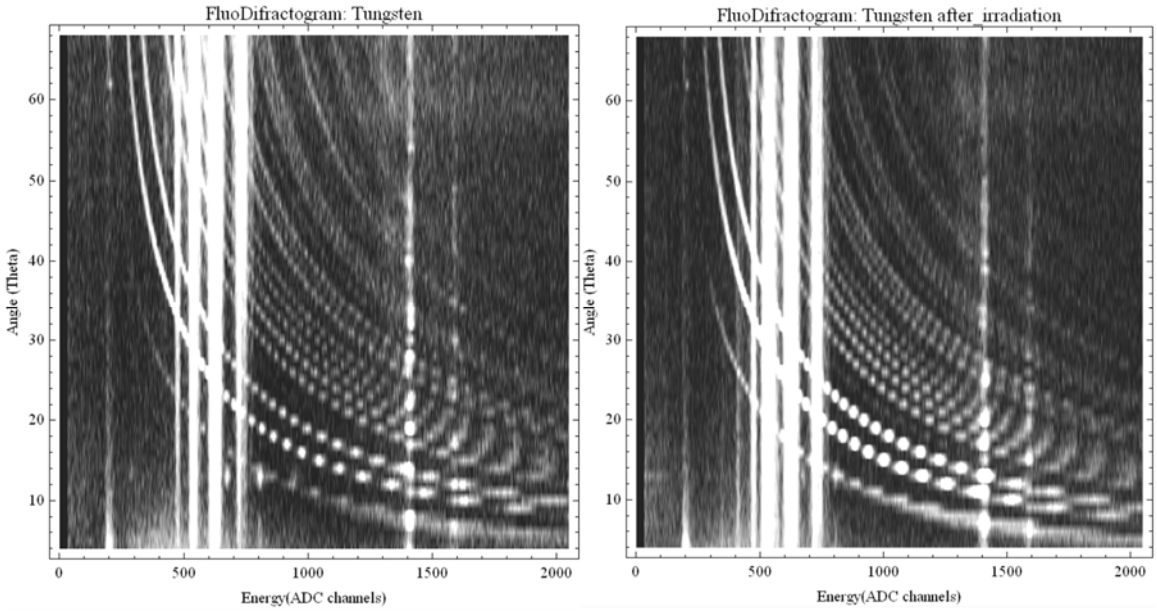

FIG. 15. (a) X ray energy and diffraction angle analysis of W sample before irradiation; (b) after irradiation.

Results on the irradiated tungsten grade differ. In particular, besides new lines belonging to iron and nickel (they enter into composition of our DPF chamber) the changes in the interplanar distances after irradiation of the sample have mainly positive values, as it is seen from Table 6. The observed dissimilar changes in the lattice parameters of the irradiated Ti and W specimens demand more detailed investigations. However at this stage it is possible to suppose that an increase in these parameters in tungsten very likely results from implantation of deuterons inside the specimen. On the contrary a certain decrease of them in titanium happens because of its good tendency at absorbing various impurities that escape from the sample during the very powerful heat loads applied to it at the irradiation.

TABLE 5. X RAY FLUORESCENT LINES OBSERVED BEFORE AND AFTER IRRADIATION IN THE W SPECIMEN

Element candidate	Our XRF lines (keV)	Element candidate XRF lines (keV)	Relative intensities	Notes
S ($K_{\beta 1}$)	3.14	2.464	Strong	
Fe	6.45	6.404	Weak	Only after irradiation
Ni	7.45 (7.49)	7.478	Strong	Only after irradiation
W ($L_{\alpha 1}$)	8.50	8.397	Very strong	
W ($L_{\beta 1}$)	9.85	9.672	Very strong	
W ($L_{\gamma 1}$)	11.34	11.286	Very strong	
Ag	22.20	22.162	Weak	Anode material
Ag	25.00	24.94	Weak	Anode material

TABLE 6. THE INTERPLANAR DISTANCES OBSERVED BEFORE AND AFTER IRRADIATION OF W GRADES

Inter-planar distances *d* (Å) before irradiation	Relative intensities	After irradiation (Å)	Differences (Å)
2.12	W	2.19	+0.07
1.51	S	1.55	+0.04
1.23	S	1.25	+0.02
0.97	W	0.97	0
0.88	W	0.90	+0.02
0.81	W	0.82	+0.01
0.77	W	0.78	+0.01
0.73	W	0.73	0
0.66	W	0.66	0
0.60	W	0.61	+0.01
–	VVW	0.57	–
0.53	VW	0.53	0
0.50	VW	0.50	0
0.44	VW	0.44	0
0.38	VVW	0.38	0

3.2. Irradiation of specimens of 10Cr12Mn14Ni4AlMo austenitic steel

Implantation of ions of various elements is one of the modern methods of modification of SL [7–14] aiming at improving its properties. The main aim of the present portion of the work was the investigation of the SL modification for samples of the austenitic steel 10Cr12Mn14Ni4AlMo irradiated by powerful streams of fast nitrogen ions (peak energy ~ 100 keV) and of hot nitrogen plasma (about several hundred eV temperature) within the above mentioned values of their power flux densities. We studied damage characteristics and we examined perspectives of the use of such irradiation by nitrogen streams generated in DPF devices for improvement of the mechanical properties of these materials.

Unlike to the case of powerful laser beams, the above two radiation types of a DPF produce simultaneously a volumetric action upon the surface layers of materials. These facets can be ensured in a DPF device all together providing synergetic effects. It means that the DPF device can produce unprecedented changes of structure, phase composition and some other characteristics of the specimens under irradiation.

All these experiments were carried out in cooperation with our collaborators IMET, IPPLM, ICDMP, and MPS in the frame of current CRP. They were provided with identical specimens to make comparison of results obtained by different teams.

3.2.1. Experimental results

In the present set of experiments, nitrogen was used as a working gas for a DPF chamber filling (instead of deuterium as it was done in our previous tests of materials candidates for fusion reactors [8, 12]).

Energies of the bank of Bora device were varied from 2 kJ up to 5 kJ depending on the applied charging voltage. Main part of the irradiations was provided with the energy of about 3 kJ. An additional part of the DPF chamber was specially installed for placing in it our samples for irradiation. In Fig. 16, a DPF chamber of the Bora device designed for experiments in the field of radiation material science.

(a) (b) (c)

FIG. 16. (a) The anode part made as a tube to prevent sputtering of its material by electron bombardment; (b) the cathode part with a sample of stainless steel mounted inside it; (c) the material chamber ready assembled.

In these experiments, samples were placed in front of the anodes with distances from 3.5 cm to 11.5 cm to realize two regimes of irradiation, with melting of SL and without it. Numbers of irradiating pulses produced in each set of experiments were fifty. This experiment was devoted to radiation tests of materials used either as a plasma facing component (in the chambers used in the reactors based on inertial plasma confinement) or as a construction element. The latter case is related to the emergency situation in fusion reactors based on magnetic plasma confinement when an element constituting the first wall component could be reduced occasionally making the construction component naked. In Fig. 17, the optical microscopic photo of the is sample placed in a close vicinity to the anode (3.5 cm) for radiation tests of the material under a high power flux density of both types of radiation producing strong melting of a sample. In this regime we had the power flux density of hot plasma about 10^9-10^{10} W/cm^2 whereas this figure for the stream of fast ions was circa $10^{11}-10^{12}$ W/cm^2. In this picture one may clearly see pores, craters and ridges produced during and after melting of SL of the specimen. Sizes of these damage features are observed in the range from 10 μm to more than 100 μm.

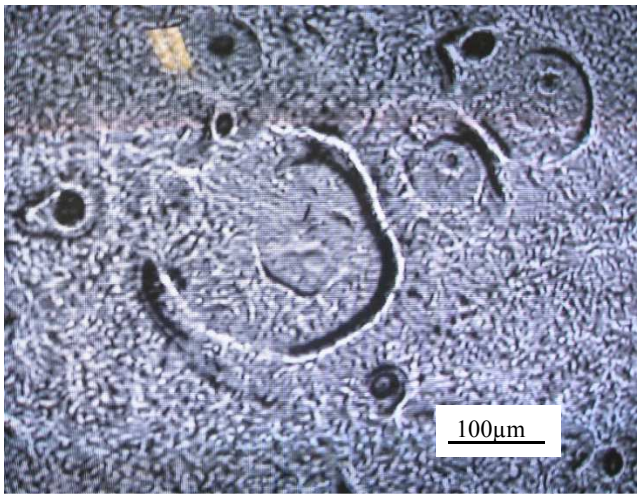

FIG. 17. Optical microscopic picture of the surface layer (SL) of the sample of stainless steel irradiated by hot plasma and streams of fast nitrogen ions at high power flux density.

In Fig. 18, a macroscopic photo and typical images of optical microscopy and SEM of the surface layer of austenitic steel 10Cr12Mn14Ni4AlMo irradiated in Bora facility (3 kJ) are presented. The sample inside the device was placed at a distance of 5 cm from the anode (10^8 W/cm^2 for hot plasma stream and 10^{10} W/cm^2 for fast ion beam). In this case the irradiation was produced when placing the specimen in the intermediate zone, i.e. in the region where we had only slight melting of the SL. As one may see, damage in these cases is characterized by pores, bubbles, droplets and cracks. Optical microscopy shows the size of these defects of about several tens of μm. SEM pictures reveal additionally the lower sizes of the pores, droplets and bubbles on the level of ~ 1 μm. X ray diffraction method of analysis has shown that during irradiation the 'a' parameter of the gamma phase was noticeably increased due to an implantation of nitrogen atoms into the lattice of austenitic steel (see Table 7). Similar results were previously obtained by us for the 0.3Cr10Mn33WV austenitic steel irradiated within DPF in the same conditions [24].

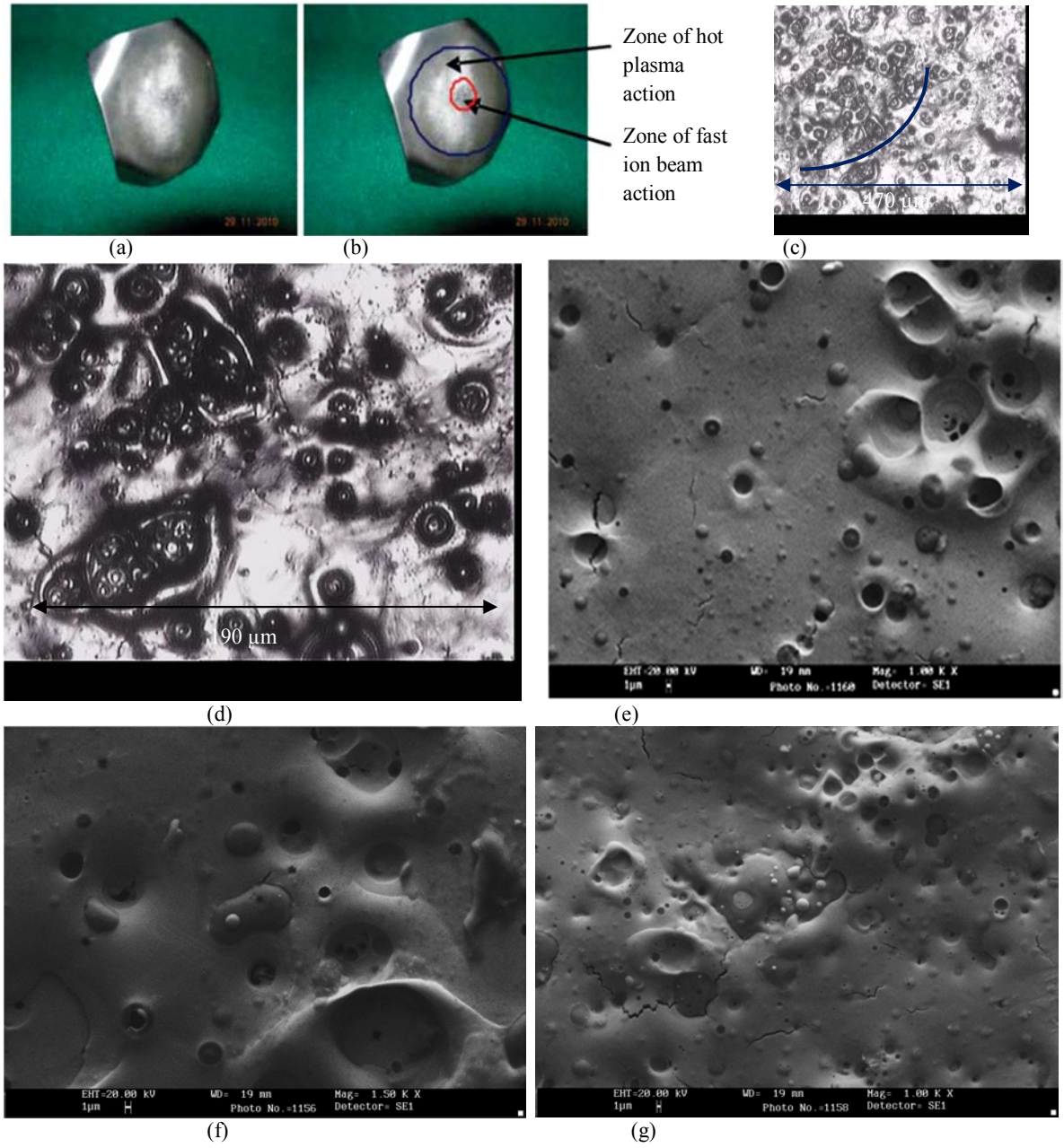

FIG. 18. (a) Macroscopic photo of the austenitic steel sample irradiated in the Bora device; (b) regions irradiated by plasma only; (c) optical microscopy of the region near the border of two action zones; (d) higher magnification of the beam of fast ions action zone; (e, f, g) electron microscopy of the regions.

TABLE 7. PARAMETERS OF THE FCC LATTICE OF AUSTENITIC STEEL IRRADIATED BY NITROGEN IONS AND PLASMA

No. of a sample	State	a (Å)	V (Å^3)
1	Before irradiation	3.6012	46.70
2	After irradiation by fast ions and plasma of nitrogen	3.6234	47.57

An increase of nitrogen concentration in the solid solution, which is an effective stabilizer of gamma phase, compensates a certain loss of manganese. Ferritic and martensitic phases inside the SL were not observed. After high temperature irradiation with subsequent fast cooling, this matrix solution has a structure of the perfect gamma phase. A small amount of martensitic phases (ε and α martensite) presented in virgin samples of the

austenitic steel as a result of manufacturing deformation was turned by a diffusionless change into austenite during rapid heating at the irradiation by the first pulse of plasma. Table 8 presents the nitride phases created in the SL of this steel due to chemical activity of nitrogen atoms in relation to the components of the steel. Thus the X ray phase analysis has shown that different nitrogen atoms under investigation implanted into the SL of the steel behave themselves in the lattice of the gamma austenite by a dissimilar manner. In particular, one part of them occupies places within the interstitial sites of the lattice that results in the increase of the lattice parameter observed, see Table 7. Whereas the other part of them is employed for the formation of fixed nitride phases. The above mentioned features usually favor an increase of hardness of the material. We intend to prove measurements of microhardness of the irradiated specimens in our subsequent works.

TABLE 8. TYPE AND QUANTITY OF NITRIDE PHASES IN SL OF THE ABOVE STEEL AFTER IRRADIATION

No. of a specimen	Nitride phase	Lattice type	Quantity (%)
1	$FeN_{0,0880}$	fcc	8.5
2	$FeN_{0,0939}$	bcc	< 2
3	Fe_4N	B1	< 2
4	Fe_3N	hexagonal	< 2
5	Fe_2N	orthorhombic	< 2

4. SPIN-OFF APPLICATIONS

4.1. Dynamic quality control

4.1.1. The Bora device characterization

Temporal resolution of our PMT+S probe is about 5−7 ns that was proved by measurements of cosmic radiation pulse. This figure is comparable with the duration of pulses of hard X rays and neutrons of Bora set-up. For better characterization of these values we measured temporal characteristics of ionizing radiations (neutrons and hard X rays) by means of a very fast probe UFNSP-1 in cooperation with IPPLM and ACS Ltd., see Figs 19(a) and (b). This probe is based on the microchannel plate plus PMT+S having time resolution higher than 0.3 ns. These traces obtained by two PMTs placed at different distances (1.627 m, 1.951 m for Fig. 19a and 1.417 m, 1.741 m for Fig. 19b) show both X ray and neutron pulses with their time separation due to different velocities of X ray photons (3×10^{10} cm/s) and 2.5 MeV neutrons (2×10^{9} cm/s). One may see how individual flashes produced in a plastic scintillator of the BC-408 type, and by recoil protons and photoelectrons are merged at increased intensity. It appears that the duration of the hard X ray pulse generated by the Bora device is about 4 ns at the full width of the pulse half maximum (FWHM) whereas for the neutron pulse the FWHM is about 8 ns. We have provided measurements of absolute hard X ray and neutron yields with both values being about the same as it was expected. The overall neutron yield was on the level of $(5-10) \times 10^{7}$ neutrons/pulse, which is also about the same as it was known from the scaling law.

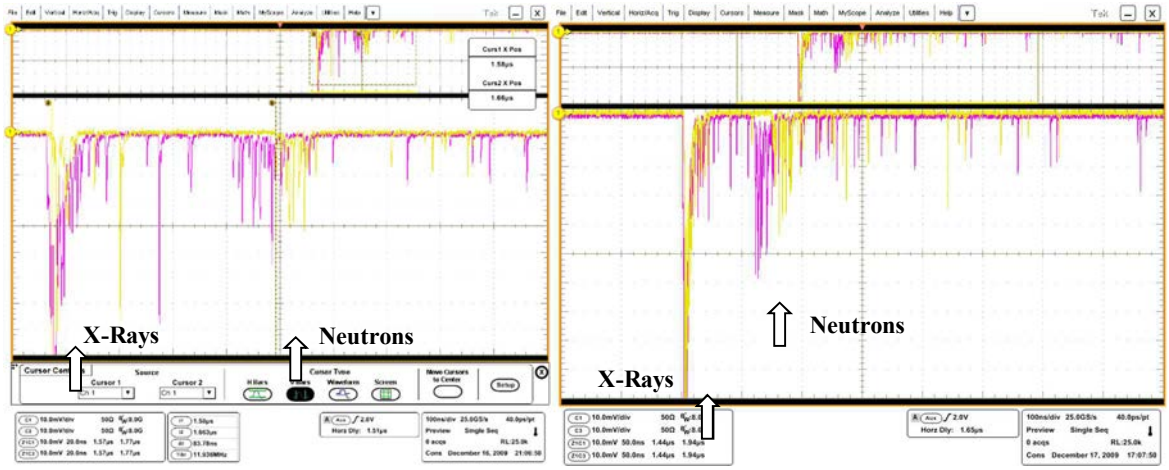

FIG. 19. Oscilloscope traces taken by two PMTs placed at different distances from the DPF chamber.

4.1.2. Results of the experiments on the dynamic quality control

We have proposed to use nanosecond X ray flashes generated by a DPF device to provide quality control of machines and mechanisms during their operation [25]. The idea is that if a construction detail has a defect not seen in a static position it may manifest itself in dynamics (e.g. a crack in a turbine blade may be opened during its rotation because of a centrifugal force). We have provided experiments with the Bora device in the field of the dynamic quality control. By this technique using just a single flash of the DPF's hard X ray radiation we can take an X ray picture of machines during their operation as if it was done in a static position. It is possible because of a very short X ray pulse generated by a DPF (about 4 ns as it is seen from the above Fig. 19). During such an interval of time a car wheel is turned on about 1 μm at the car speed of about 100 km/h. We take two pictures of a fan in its static position (seven shots with the same position of its wing) and in its dynamic (rotating) state (just a single shot) (see Fig. 20). Normal rotation speed of the fan was 1000 RPM. We used for the output window of the DPF chamber a stainless foil that cut the X ray spectrum of the DPF device at the photon energy of about 60 keV.

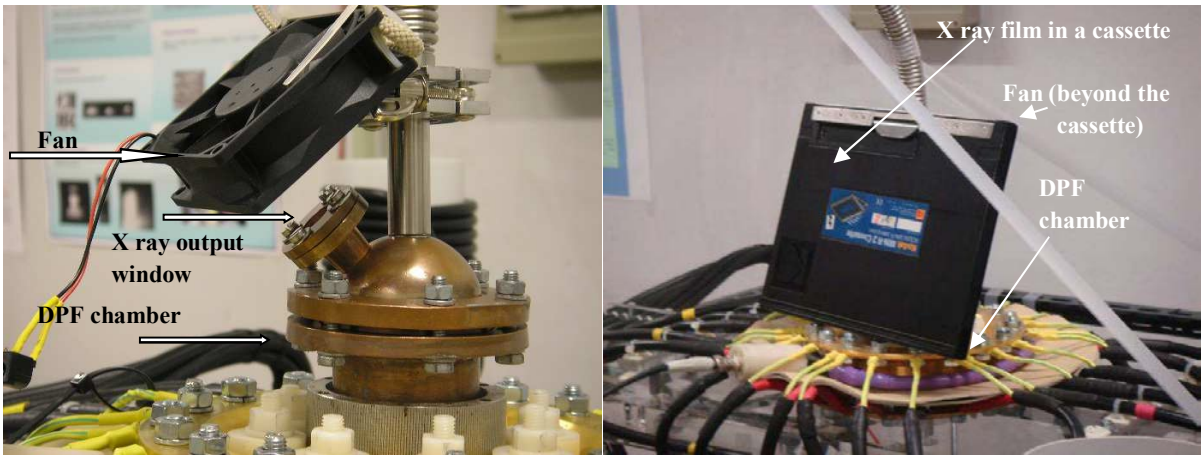

FIG. 20. Experiment on dynamic quality control.

The results are shown on the next page in Fig. 21. It is clear that there are no differences in the X ray images obtained in static and in dynamic states. The pictures show that just a single shot of a DPF is enough to obtain a clear X ray photo of the blade. Fig. 21(b) (static position) is evidently saturated (overexposed). The fan blades were rather thin and made of plastic. Its thickness is gradually decreased to the edges. It is clear that for improved quality of the fan blade visualization in both cases it would be better to use softer spectrum of hard X rays, starting from X ray photon energies of about 5–10 keV (i.e. a thinner foil on the output window).

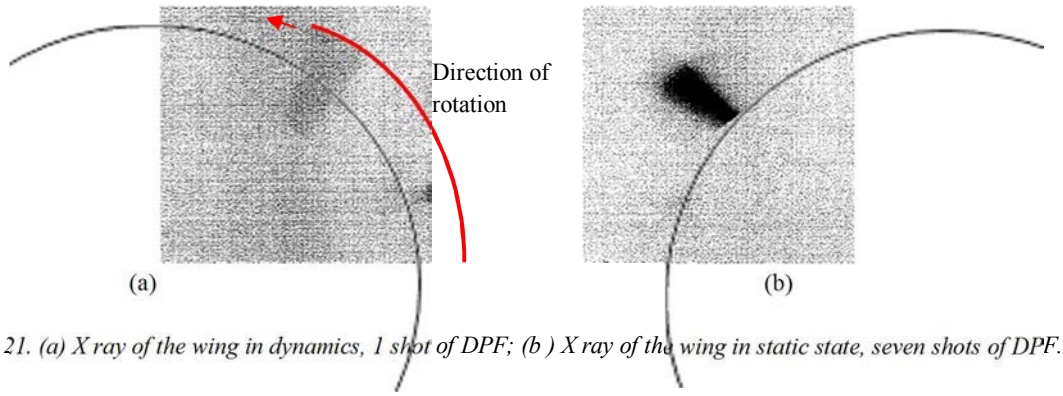

FIG. 21. (a) X ray of the wing in dynamics, 1 shot of DPF; (b) X ray of the wing in static state, seven shots of DPF.

4.2. Plasma focus source for neutron capture therapy

4.2.1. Introduction

Radiation therapy is one of the methods used in cancer treatment. It is common to combine radiation therapy with surgery, chemotherapy, hormone therapy, and immunotherapy or with a mixture of these. Neutron irradiation is a part of radiation therapy, which is used in the treatment of patients in general and specifically in the cure of brain tumors [26, 27]. This method is not yet widely used in medical practice. In this therapy, some new techniques are under way such as combined neutron X ray cure, neutron capture therapy (NCT) thermal and epithermal neutrons, plus fast neutron treatments and a powerful short pulse neutron irradiation therapy [27]. These techniques are investigated side by side with some problems inherent to the approaches having a long history: classical boron neutron capture therapy (BNCT) with thermal neutrons and therapy by fast neutrons. A vast majority of researchers working in the field of neutron therapy are now of the opinion that the best neutron energy spectrum fitted to the NCT treatment of brain tumors has to be peaked at around 10−50 keV (the so called epithermal neutrons). In this case the cross-section of the reaction of neutrons on boron nuclei will be an order of magnitude higher compared with others presented in living tissues, and the penetration depth of them will be a few cm, which is necessary to reach these tumors without craniotomy. Moreover, during this path length, energy of these neutrons will be decreased, and the corresponding cross-section will be much higher to the end of the capture length. Thus intermediate tissues will obtain lower dose. The characteristics of the radiation fields in this case of 'classical NCT' by epithermal neutrons are neutron intensity on the tumor surface 10^9 n · cm^{-2} · s^{-1}, time of irradiation 40–60 min and dose 60–70 Gy. It means that the overall neutron fluence is at the level of ~ 10^{12} n/cm^2 and the dose rate is equal to ~ 1 Gy/min. Isotopes, nuclear fission reactors, cyclotrons and other types of accelerators are currently being used as neutron and X ray sources for the above purposes. In spite of their successful application, some important parameters are desirable to be much better (neutron biological selectivity and efficiency, dose depth distribution, stability, cost, dimensions, ecological compatibility, possibility of multi-field, multibeam and rotational irradiation). Several important problems in neutron therapy have to be resolved before the treatment of a patient. These issues relate to dosage for intermediate layers of the organism, and to neutron scattering, penetration within tissues, and combined irradiation modes, while the deeply located tumor is under irradiation. Most of these issues are resolved in the course of the proper quality assurance procedures for patient dosimetry implemented at neutron therapy [28]. However, some of these problems may be committed by implementation of innovative neutron sources having specific characteristics. Therapeutic efficacy of neutron irradiation versus dose rate or dose power (in the case of very short and intensive pulses) as well as pulse frequency is virtually not studied. In accordance with some theoretical concepts and recent experimental observations in radiation biology [29–31], short-pulse powerful radiation action upon tumor may be especially effective. It is so because within the pulse time, which is short compared to the duration of physical, chemical (in particular with free radicals) and biochemical reactions, any reparation and recovery processes might have not enough time to take place, and various effects of cumulative influence and synergism would be possible. The main feature that differentiates the so called pulsed radiation chemistry in its perfect sense from continuous and long pulse or short pulse low dose irradiation is a criterion that can be formulated in the following two principles performed simultaneously [31]:

— Microvolumes of the activity of primary (neutrons, X ray photons) or secondary (nuclear reaction products, protons, α particles, solvated electrons, free radicals) particles must be overlapped within the tissue (e.g. overlapping of spurs and blobs);
— This overlapping must be fulfilled during the time interval short compared with the duration of chemical biochemical reactions (transformations) induced by the irradiation (e.g. duration of chemical reaction with free radicals that takes time interval of more than 1 μs).

One of the devices able to generate fusion neutrons (of 2.5 MeV and 14 MeV energies) and X rays (with 0.1 keV and 600 keV photons) during very short (1–100 ns) and powerful pulses is the dense plasma focus (DPF) [32]. The interval of the bank energy E_b feeding these devices ranges from 1 J to 1 MJ. It is an ecologically clean ('push-button' type and working at a somewhat low voltage, 10–25 kV), compact, relatively cheap device able at the same time to ensure dose power up to 10^8–10^9 Gy/min in neutrons and 10^9–10^{10} Gy/min in X rays [32–36]. Our analysis [37] has shown that a DPF presents the following opportunities for its application in radiation therapy of cancer patients:

— DPF devices of medium size (5–10 kJ, 1–2 m^2 footprint) can ensure the necessary dose of neutron irradiation in about 3 h working time with a moderator (epithermal neutrons) if it is operated with a repetition rate of 100 cps with D_2 or with 1 cps with D–T mixture as a working gases.
— Devices of this scale with water cooled electrodes and anode orifices have been tested successfully up to 16 cps and during a quarter of a million of shots without wearout replacements [34].
— One of the innovative future possibilities to increase the intensity of the neutron beam and simultaneously to localize its action in the wanted place (besides a collimation) is connected with using several DPFs all at once irradiating the tumor from different sides. It seems possible with medium-sized devices with $E_b \sim 5$ kJ and neutron yield $Y_n \sim 10^{11}$ of 14 MeV neutrons per pulse of 10 ns width or a few times bigger (30 kJ and 10^{12} neutrons per pulse).
— The large DPF of energy several hundreds of kJ (occupying a volume of ~ 20–30 m^3) operating with the D–T mixture at 1 cps will be able to make this job in a few minutes.

In the work [38], we found that there is almost no difference in the consequences of neutron irradiation of dissimilar bio-test objects by a DPF or a neutron generator of classic type or a fission reactor operating below the above mentioned dose power (6×10^9 Gy/min). It is already an important result that opens up an opportunity to use for neutron therapy this 20 kV compact and cheap device instead of the less ecologically friendly, expensive and cumbersome fission reactors, isotopes and MeV accelerators. However, one can expect here some synergetic effects with DPF if it will be used either with just fast/epithermal neutrons of the ns pulse duration producing high concentration of their secondary products (α particles, Li nuclei and free radicals) in cells or at the combined application of fast epithermal neutrons and hard X rays for a suppression of malignant cells at the dose power exceeding 10^9 Gy/min. Possible reasons for these expected effects are:

— A simultaneous break of both spirals of DNA (double strand rapture) and diffusion of rubbles during the ns period of time produced by a high intensity neutron flux and/or a high concentration of secondary products of nuclear reactions on boron and of free radicals.
— A threshold-like behavior of radiation damage of malignant cells within a neutron field having a high concentration.

The last opportunity that might increase the selectivity and efficacy of the neutron therapy must be explained here in more details. Indeed, at the present time, chemicals used for an increase of boron capture by malignant tissues of the intracranial tumors for the subsequent BNCT provide an increase of boron concentration in cancerous cells by about ≤ 5 times higher compared with the living cells (e.g. blood) due to different penetrability of their blood–brain barriers and because of some other reasons [39], which is not enough. The optimal figure should be about 20. In that case the difference in damageability of live and malignant cells would not be the same as it is at present time when both types of cells are destroyed during the neutron irradiation (low selectivity). Unfortunately, the factor 20 is unattainable at the moment in experiments (there are no proper chemicals). However, if we wish to ensure the above mentioned overlapping of microvolumes of activity of secondary particles at the irradiation in the case of the action of present day chemicals in the malignant cells only – but not in the living tissues (due to the above mentioned five times boron concentration difference) – then we might have the expected synergetic effect. It could be managed in analogy with our previous experiments where such an effect was observed in the case of X ray photon irradiation of enzymes and photoresists [30–32, 37, 39]. Both the above opportunities open the way for a low dose (and probably a single pulse) therapy of cancer. However, to start experimental works, we need to clarify several important questions that can be modelled by numerical calculations. In this work we focus on the development of a detailed simulation of the interaction of short pulse radiation from a DPF with a moderator to estimate the output spectrum and pulse duration for this dynamic case. The simulation was carried out by means of the Geant4 toolkit in two main steps:

— Modeling of the pulsed neutron source device (DPF) itself.
— Study of the interaction of fast monoenergetic neutrons with different moderators specific for BNCT.

4.2.2. Geant4 simulation of the plasma focus device

Geant4 [41, 42] is a multi-tasking Monte Carlo toolkit for the simulation of the passage of particles through matter. It is one of the first main high energy physics (HEP) software tools to use the methods of object oriented programming (in C++). It is developed and maintained by the Geant4 Collaboration. Its application areas include high energy and nuclear physics, medical physics, dosimetry, accelerator developments and space physics experiments. As Geant4 is a toolkit, it contains several different methods for describing material properties, handling complex geometries, taking care of particle interactions and tracking inside matter, taking into account detector response and visualizing particle interactions inside detector geometries. Because of its general purpose nature, Geant4 was used in this study for analyzing interactions of neutrons generated by the plasma focus devices with external matter to estimate how their spectra and time profile are modified by the interaction with the device structure. In the current simulation the 9.4.p02 version of the toolkit was used. In this work, in order to take into account properly the neutron interactions down to thermal energies, the QGSP BERT HP physics list was used, as recommended by the Geant4 Collaboration. QGSP BERT HP uses the processes contained in the QGSP physics list. QGSP is the basic physics list applying the quark gluon string model for high energy interactions of protons, neutrons, pions and kaons and nuclei. The high energy interaction creates an exited nucleus, which is passed to the pre-compound model modeling the nuclear de-excitation. It uses also the Geant4 Bertini cascade for primary protons, neutrons, pions, kaons below ~ 10 GeV. The Bertini model yields good agreement with the experimental data at low energy. In addition QGSP BERT uses the data driven high precision neutron package (NeutronHP) to transport neutrons below 20 MeV down to thermal energies. The geometry and the material description of the plasma focus devices were easily implemented in Geant4 using simple solids (tubes, spheres mainly) and defining properly the characteristics of the moderator material Fluental^{TM} as described in the following. The principle configuration of the DPF device is presented in Fig. 22.

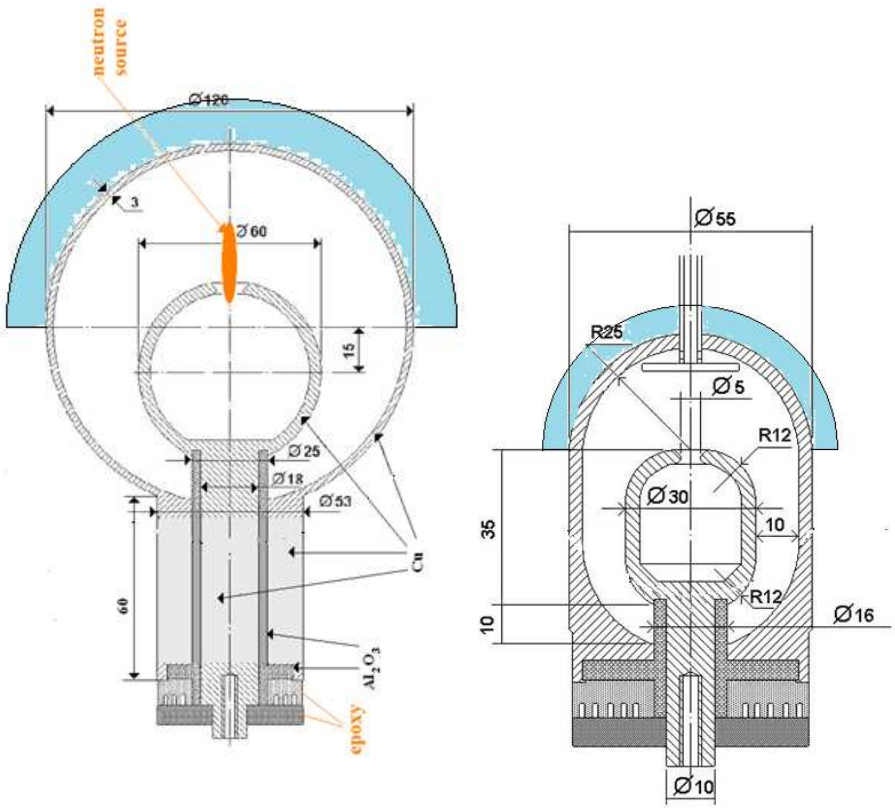

FIG. 22. Principle scheme of DPF with the Fluental^{TM} layer on the top of the chamber.

Materials used in the DPF are: Cu, Al_2O_3, and Epoxy. As a moderator in our numerical experiments we used mainly Fluental^{TM} that contains: AlF_3 69%, Al 30%, LiF 1%. This choice was made because it was expected that the deceleration of neutrons in this material will be fulfilled much faster compared with water or paraffin due to multiple peaks in cross-sections of nuclei of its components. Thus we hoped to preserve short pulse duration of our neutron radiation during the process of neutrons slowing down. Two different DPF configurations were simulated, see Figs 22(a) and (b). They differ mainly for the external dimensions, and both may be used for

generation of quasi-monochromatic spectra of neutrons peaked at 2.45 MeV or 14 MeV depending on the working gas (deuterium or D–T mixture). FWHM of the spectral distribution of neutrons is about 3–5% of the maximal energy of them for both cases.

Use of the Geant4 toolkit allowed simulating both configurations (see Figs 23 and 24) without changing the rest of the Monte Carlo Software. In both simulations the X ray spectrum generated by the DPF was properly taken into account.

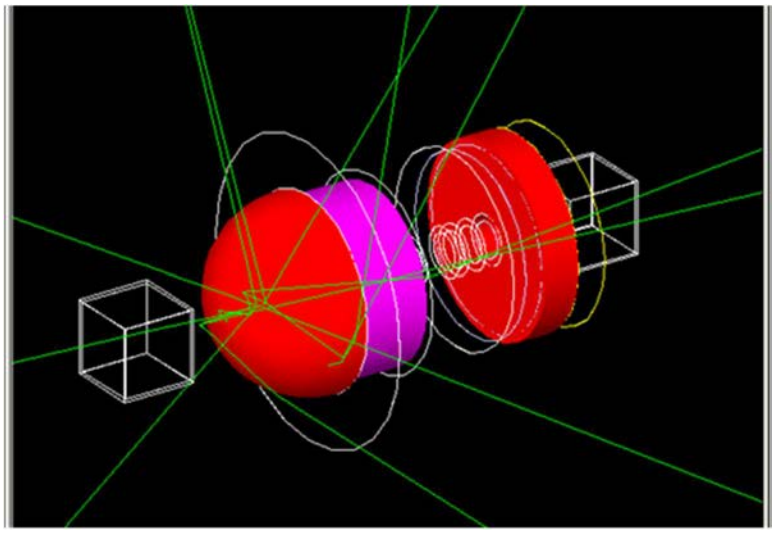

FIG. 23. Geant4 Monte Carlo visualization of the small chamber of the Bora device. The two white boxes are the control volumes where the neutron and X ray spectrum are evaluated. The Fluental™ moderator hemisphere is not shown (only its bottom surface is shown in white).

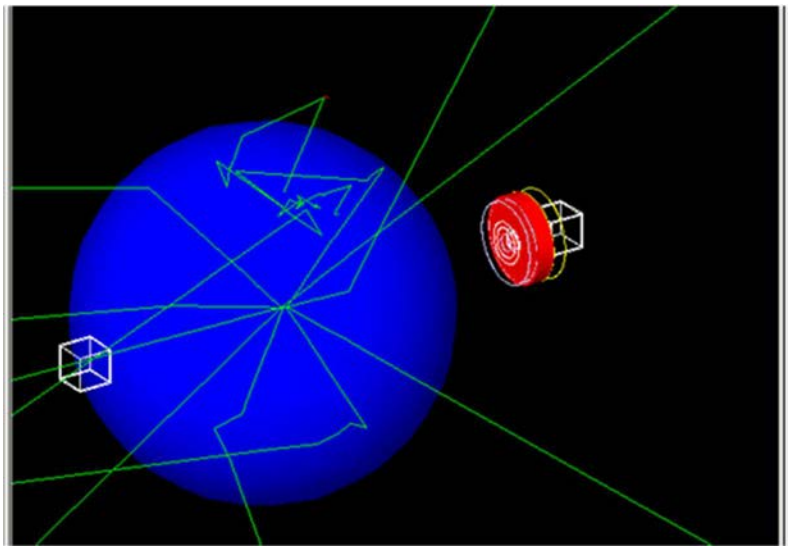

FIG. 24. Geant4 Monte Carlo visualization of the large chamber of the Bora device. The two white boxes are the control volumes where the neutron and X ray spectrum are evaluated. The Fluental™ moderator hemi-sphere is shown in blue.

4.2.3. Moderator thickness studies

The evaluation of the Fluental™ moderator size was done by means of the simulation previously described. A pulse of quasi-monochromatic neutrons (with an energy spread FWHM of 3–5%) was generated at the centre of the DPF device, where the plasma column was placed. The neutrons then propagated through the device and their energy spectra and time profile were measured in the control boxes described above. The size of the moderator is critical to generate quasi-thermal isotropic neutrons (suitable for BNCT applications) as well as for

changing the time profile of the neutron spectra. The latter parameter is the most crucial one, since to use the expected synergetic effect of the neutron pulse generated by the DPF in a combination with the X ray pulse, not too affected by the moderator, we need the neutron pulse duration to remain well shorter than 1 μs. Fig. 25 shows the results of the application of a 5 cm Fluental™ moderator on the small chamber of the Bora device, while Fig. 26 shows the effect of a 15 cm Fluental™ moderator on the same device. Both the outgoing neutron spectrum and its time profile are shown. It is clearly seen that with the 15 cm layer the amount of quasi-thermal neutrons is greatly increased. Our simulations have also shown that similar moderation could be done with a tungsten moderator. Comparisons with experimental data are then foreseen to validate the present results.

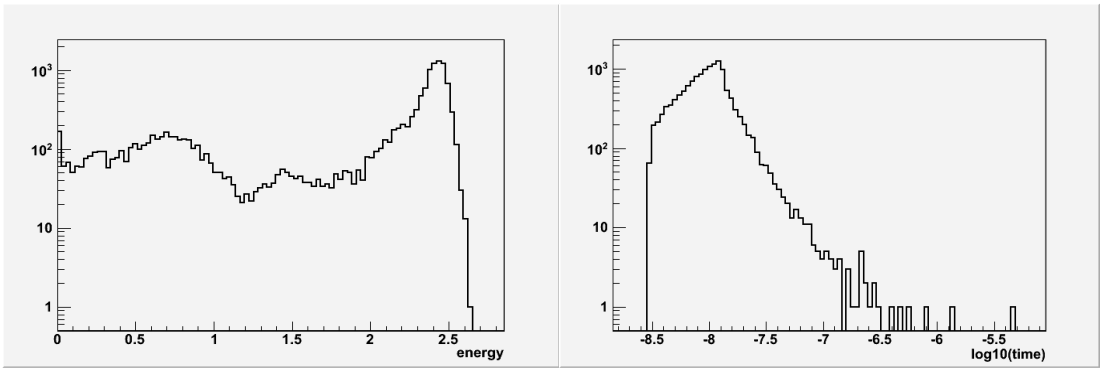

(a) (b)

FIG. 25. (a) Neutron energy spectrum obtained by simulating a monochromatic 10 ns neutron pulse of 2.45 MeV in the small chamber of the Bora device with the 5 cm Fluental™ moderator; (b) time profile obtained as above.

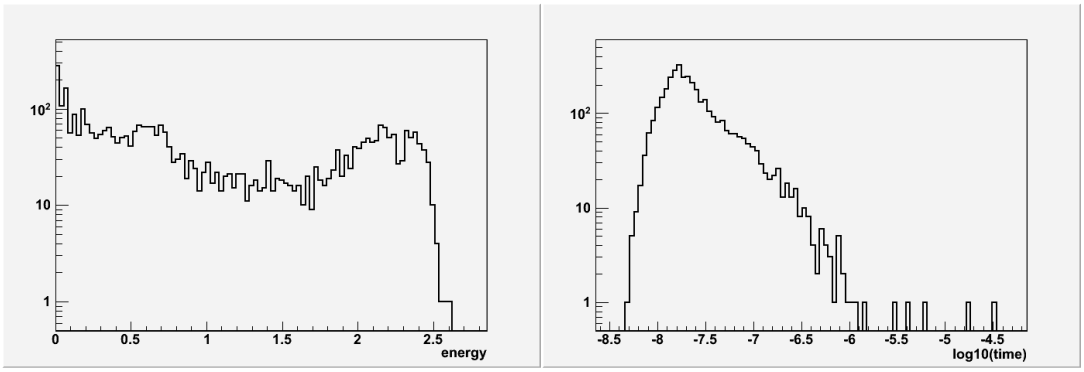

(a) (b)

FIG. 26. (a) Neutron energy spectrum obtained by simulating a 10 ns monochromatic pulse of 2.45 MeV neutrons in the Bora device with 15 cm Fluental™ moderator; (b) time profile obtained as above.

In Fig. 27, similar results are presented for the large chamber of the Bora device, this time using 15 cm tungsten moderator, starting from a 14.5 MeV quasi-monochromatic neutron pulse of the same pulse shape (10 ns). Here the larger energy and size of the device cause a significant change in the outgoing spectra and time profile. For better seeing imagery these effects are presented in log and linear scales. The most important results of this set of calculations can be summarized as follows:

— Thicknesses 5 cm and 15 cm of both moderators used (Fluental™ and tungsten) convert almost monochromatic initial spectra of fast neutrons generated by DPF with pure deuterium and deuterium–tritium mixture as working gases into spectra with well developed epithermal tails (yet having an appreciable number of fast neutrons).
— Use of both types of moderators makes neutron pulse duration longer, however in both cases their full FWHM remain noticeably shorter than the duration of chemical reactions with free radicals (~ 10^{-6} seconds or more).

As it was mentioned above, the resulting spectra have in our cases a considerable component of fast neutrons. However there is a number of works published in literature that is devoted to this point. Some of the authors count a combination of fast and epithermal neutrons as a good tool to improve treatment of brain tumors. For

example in Ref. [43], it is given a set of reasons for combining fast neutron therapy, which to date has not been useful for treating patients with brain tumors, with BNCT. Fast neutrons lose energy as they penetrate tissue, and those that are thermalized can be captured by ^{10}B. The authors present the rationale for using this approach to obtain a boost, the underlying physics, and supporting in vitro and in vivo data. Since there currently is an active clinical fast neutron therapy program at the University of Washington, this approach could be implemented for a variety of tumors, if the appropriate boron compound(s) were available. Although the dose contribution from the ^{10}B capture reaction would be small, the authors suggest that the steep nature of the fast neutron radiation response curve would result in a significant therapeutic gain.

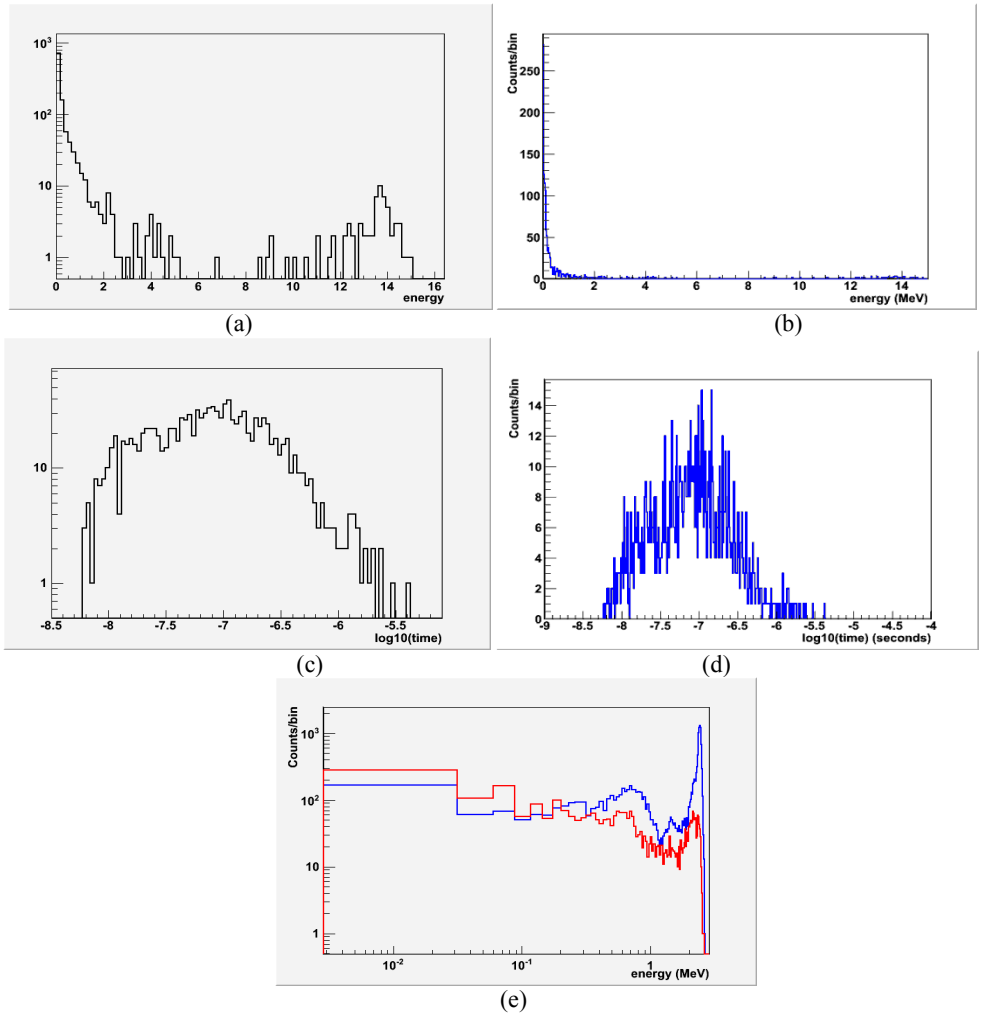

FIG. 27. (a) Neutron energy spectrum in logarithmic scale; (b) neutron energy spectrum in linear scale; (c) time profile in logarithmic scale obtained by simulating a monochromatic 10 ns neutron pulse of 14.5 MeV energy in the large chamber of the Bora device with 15 cm tungsten moderator; (d) time profile in semilogarithmic scale; (e) comparison of two energy spectra are presented in log-log scale for 5 cm (blue) and 15 cm (red) tungsten moderator thicknesses.

4.2.4. Preliminary cell interaction study

The following study was aimed to perform with Geant4 to simulate the interactions at cellular level. For this purpose we simulated a cluster of cells, in which we introduced enriched ^{10}B materials (suitable for BNCT applications). The cell cluster is shown in Fig. 28. Each cell is simulated as a sphere of ~ 10 µm size filled with water-based material. A slightly different material is used for the cell membrane. Both materials are taken from Geant4 examples. The outgoing neutron and X ray spectrum obtained by the previous Geant4 simulation of the DPF, taken from the already defined control volumes, was then used to get the dose deposited in each cell of the cluster. The results are still uncertain since the available physics processes in the simulation were not tested at the cellular level.

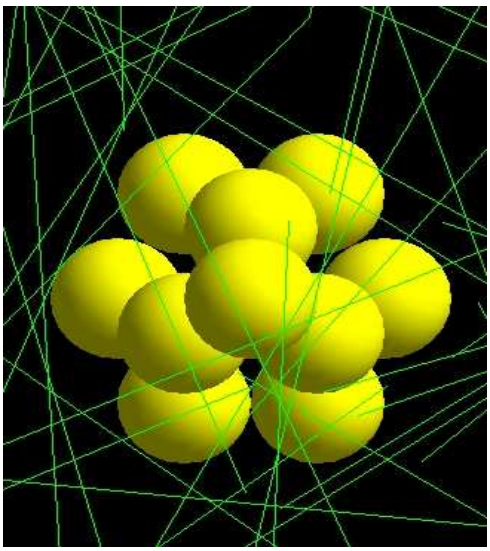

FIG. 28. Simulation of the neutron irradiation of a cell cluster with Geant4.

4.2.5. Initial experimental results

In Fig. 29, it is provided the initial experimental investigations of changes in time behavior and spectrum of neutrons that pass through a tungsten moderator. Two tungsten plates having thicknesses of 40 mm and 44 mm were installed near the small DPF chamber filled with pure deuterium (modeling a situation close to Figs 25 and 26).

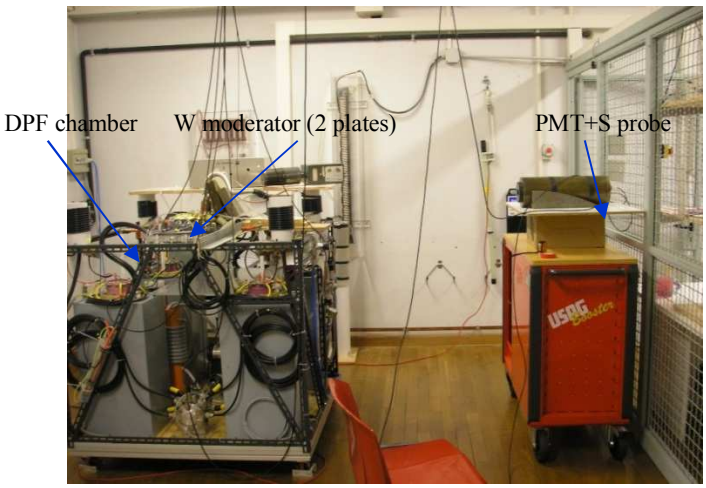

FIG. 29. Configuration of the experiment on measurement of modifications in neutron pulse duration and spectrum after passing the neutron radiation through the tungsten moderator.

The PMT+S probe were placed at different distances from the assembly of DPF+W moderator in order to measure an increase in neutron pulse duration produced when the PMT+S probe is placed in close vicinity to the DPF+moderator. At the same time, a long distance between the source, the moderator and the PMT+S probe (large TOF base) will give information on the spectrum modification. First, the PMT+S probe was placed at a distance of 1.94 m from the DPF+moderator assemblage. In this case the oscilloscope trace of the neutron pulse obtained is shown in Fig. 30.

FIG. 30. Oscilloscope trace of the neutron pulse obtained at the distance 1.94 m from the moderator.

From this figure one may see that in a close vicinity to the moderator the neutron pulse change its duration in a very small degree, and its FWHM appeared to be equal to 24.5 ns. It means that the tungsten moderator has increased the pulse duration by about 2.5 times only. Yet the pulse obtained a relatively long tail (about 200 ns) as a result of the neutron spectrum moderation. But still we can establish that its duration is preserved on the level that is much shorter compared with the duration of chemical reactions with free radicals (> 1 μs). Then, the PMT+S fast probe was moved from the source to the longer distances. In Fig. 31 the oscilloscope trace (50 ns per division) is presented for the case when a TOF base l_{TOF} is equal to 4.64 m, X ray and neutron pulses are registered without moderator.

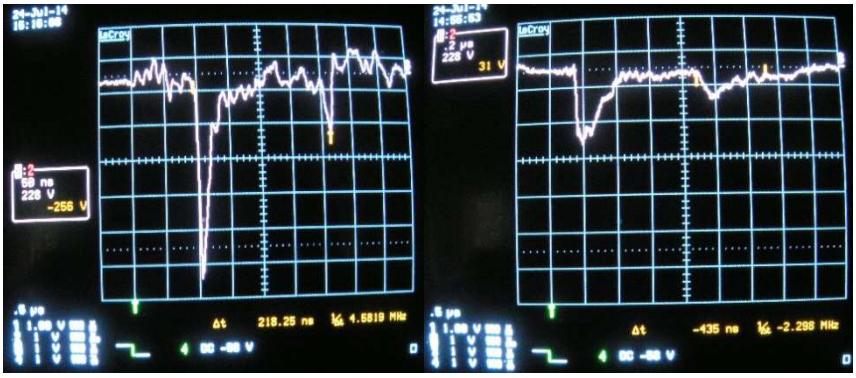

FIG. 31. Oscilloscope trace of hard X ray and neutron pulses in different conditions for the distance from the source to the PMT+S probe equal to 4.64 m.

Calculations via:

$$E_n\,(\mathrm{MeV}) = [72.24 \times l_{\mathrm{TOF}}\,(\mathrm{m})/t_{\mathrm{TOF}}\,(\mathrm{ns})]^2 \qquad (3)$$

taking into consideration that usually a neutron pulse peak inside the DPF chamber of Bora device appears at $\Delta t \approx 8$ ns later in comparison with the peak of hard X ray pulse, show that the energy of neutrons in its peak is about 2.5 MeV. It is expected for the neutrons irradiated in a side on direction to Z axis of the DPF chamber. At this situation the neutron pulse duration is about 13 ns (FWHM). The same calculations for Fig. 31(b) (200 ns per division) when the PMT+S probe was preserved in the same distance from the source but the trace was registered with the above mentioned moderator (84 mm of tungsten) gave $t_{\mathrm{TOF}} \approx 800$ ns. Calculations using Eq. (3) have shown that neutron energy in the pulse peak is equal to $E_n = 180$ keV. It means that we have obtained a noticeable moderation of neutrons energy. The total pulse duration (at the level 0.1 of its amplitude) increased up to 435 ns (~ 200 ns FWHM). Besides, at this situation the tail of the neutron pulse was extended until the 1.4 μs. Therefore, the energy of the appreciable amount of neutrons at the end of this tail are decreased until the value E_n < 50 keV (range of the epithermal neutrons). However taking into consideration the original neutrons pulse

duration these figures do not give a pure spectrum of neutrons. Rather they combine temporal and spectral characteristics of the neutron radiation.

Then, the PMT+S probe was moved to the TOF base equal to 8.89 m and the oscilloscope traces obtained are shown in Fig. 32. At this distance in a majority of shots the hard X ray pulse was very weak or even absent due to strong absorption and scattering in tungsten. So synchronization by means of the signal of a current derivative was made. Again, in Fig. 32(a), it is shown a neutron signal obtained without moderator. One may see that the pulse duration was increased until the value of about 16 ns (FWHM). The analogous oscilloscope trace obtained with the two plates of tungsten at this distance is shown in Fig. 32(b).

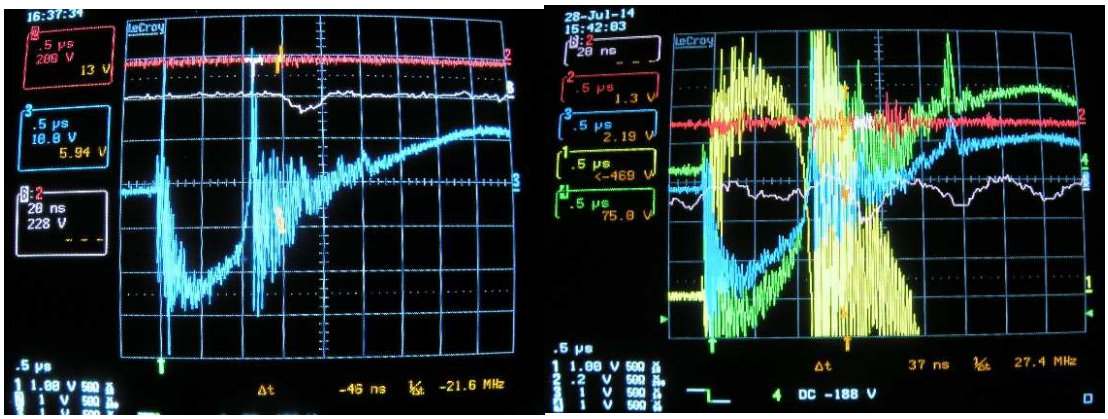

FIG. 32. Oscilloscope traces obtained for distance 8.89 m from the source to the PMT+S probe.

In Fig. 32, from the red line trace it is possible to determine the TOF of neutrons along this base and to calculate corresponding values of energy. It appears to be equal to:

- 750 ns and 730 keV for the beginning of the pulse;
- 937 ns and 470 keV for the beginning of its peak;
- 1387 ns and 210 keV for the end of its peak;
- 1681 ns and 140 keV for the tail of the pulse.

It means that the visible part of the neutron pulse here has duration of about 1 µs. In yellow, a part of the pulse (100 ns) is represented with better time resolution. One may see that the pulse has an oscillatory character. It should be mentioned here that relatively poor sensitivity of our probe does not give us an opportunity to see a presence of epithermal neutrons (10−50 keV) at this last TOF base.

4.2.6. Future works

The previous successful experiments with a low dose (about 4 orders of magnitude smaller) activation and inactivation of enzymes by medium energy X rays of a very high intensity [30, 31, 33] has shown that to obtain this synergetic effect we must ensure an overlapping of microvolumes occupied by secondary products of radiation action (free radicals, solvated electrons, products of nuclear reactions) during time interval short compared with time of chemical reactions (or in our case with time of destruction of malignant cells) with these particles. The estimations for the BNCT products (α particles and Li nuclei occupying microvolumes of a diameter equal to about 20 µm) produced by irradiation with epithermal neutrons in living tissue have shown that to achieve these conditions we have to have minimum a neutron flux of about 10^{12} n/cm^2 (~10^{10} Gy/min) [38].

This can be achieved with already existing devices such as the PF-1000U facility of IPPLM, see Fig. 33. However for such purpose this device has to be modified in the following manner:

— It must work with D–T mixture instead of pure deuterium; in this case its neutron yield of about 10^{12} neutrons per pulse in full solid angle will be changed into 10^{14} neutrons per pulse.
— Its charging polarity must be changed, instead of applying positive polarity of its charger to the anode we have to apply the negative polarity to the cathode leaving the anode grounded.

In this case (see Fig. 34) a bio test object (a human phantom) can be moved to the close vicinity of the source of neutrons separated from it only by the anode lid and a layer of a moderator. Thus, as one may see, such experimental works in radiation biology on the level, which is estimated to be perfect for synergetic effects, is attainable in principle with the contemporary DPF devices.

(a) (b)

FIG. 33. (a) Side view of the PF-1000 chamber facility; (b) collector with lid of the anode (back view of the chamber).

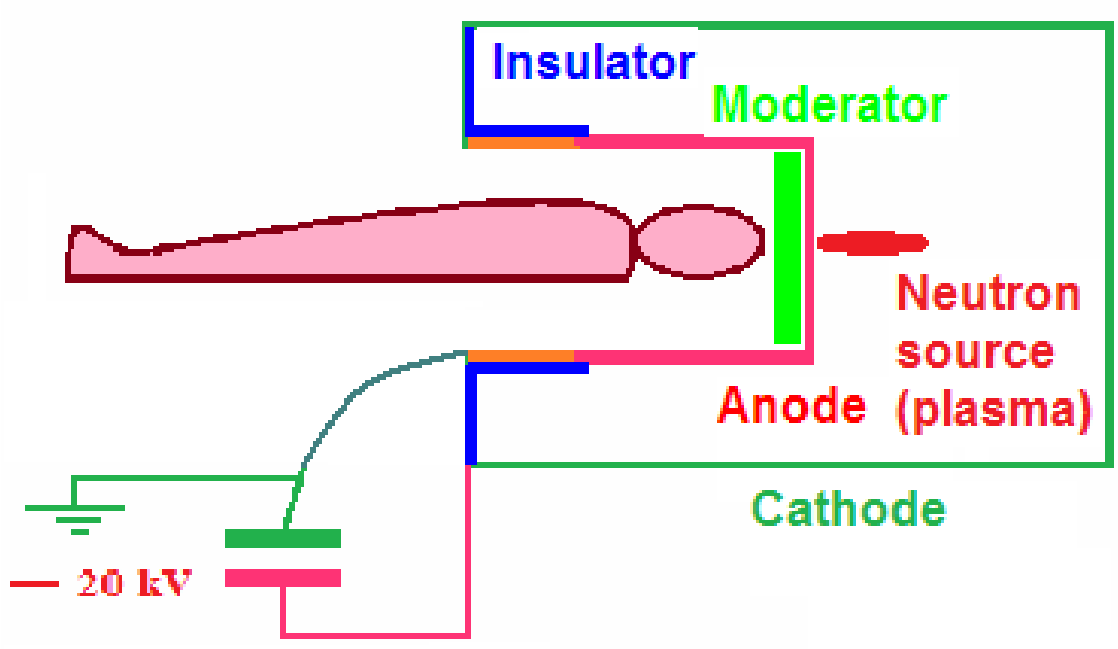

FIG. 34. Scheme of irradiation by neutrons of a human phantom in PF-1000U facility (side view of the DPF chamber).

Besides the future numerical modelling, works are planned in the following directions:

— Development of a biological model to quantify the interaction of the pulsed neutron beam with a cellular cluster;
— Validation of the simulation results obtained;

- Experimental tests in melanoma cells to prove the impact of short neutron pulse, with and without boron;
- The quantification of DNA damage lead by synergetic effect using the proper neutron flux density and short pulses;
- Combine the use of short neutron pulse with carbon nanotubes as boron agent for BNCT.
- Combine metallic nanoparticles delivered by antibodies selectively into malignant cells with irradiation by ns powerful X ray pulses in a manner proposed by the authors of Ref. [44] for laser irradiation (extending the expected opportunities into deeply positioned tumours).

5. PROVIDING A WORKSHOP FOR YOUNG SCIENTISTS

In the period from 8 to 12 October 2012, we have held a school named "International School and Training Course on Dense Magnetized Plasma as a Source of Ionizing Radiations, their Diagnostics and Applications." The purpose of the school was building capacity in the field of DMP and ionizing radiation generation and diagnostics, among young scientists from developing countries. This purpose has been achieved by means of several tutorial lectures on current status, performance and limitations of contemporary DMP devices as well as by means of experimentation at the Plasma Focus Laboratory at the ICTP Multidisciplinary Laboratory (MLAB). Particular attention has been devoted to mechanisms of generation and characteristics of various types of ionizing radiation (neutrons, beams of high energy electrons and ions, soft and hard X rays, plasma streams) emitted by the DMP devices. Passive and active diagnostic techniques used for characterization of their parameters including development of new instrumentation and methodologies were considered. A number of applications of these devices in science, industry and for biomedicine have been examined. The school included practical experiences DPF devices and a number of diagnostics to measure various parameters of plasma and ionizing radiations generated by the devices. Furthermore, the school included laboratory activity in experimentation with a DPF Bora device, based on modern technology, which is in operation at the ICTP MLAB. Plans were to use the device for experimental sessions devoted to characterization of different types of radiation generated by the facility, as well as for demonstration of selected applications of these radiation pulses in various fields. This must help to provide cost effective solutions in the field of the DMP instrumentation to meet the needs for research and training in developing countries. The school has also provided basic concepts and techniques necessary to work on leading edge technologies in support of radiation material sciences, radiation biology and nuclear medicine. Some of the topics covered were as follows:

- Plasma parameters defined by spectrometry and laser techniques;
- Status and advances in passive and active techniques for plasma diagnostics;
- Methods of investigation, characterization and metrology of different types of ionizing radiation (dose, dose power, power flux density, spectrum, spatial and angle distribution) and their role in plasma diagnostics;
- Modelling at DMP devices of different phenomena taking place in the mainstream fusion facilities;
- Various applications of DMP devices, those that are already implemented, in process of development and perspective ones;
- Atomic data and modelling tools for the analysis of the experimental results.

6. CONCLUSIONS

a) We have upgraded the Plasma Focus laboratory at the ICTP MLAB, supplying it with additional diagnostics, periphery devices and contemporary analytical instrumentation. In particular, we have put into operation a portable X ray diffractometer that combines X ray single photon detection with high spectroscopic and angular resolutions for a surface investigation of irradiated samples. Besides, we implemented another new device, the X ray micro CT system where X rays were produced by a Hamamatsu microfocus source (150 kV, 500 μA, 5 μm focal spot size) for investigations of bulk damageability produced during our radiation material tests.
b) We have provided with our own and obtained by a collaboration of various unique diagnostic techniques a precise characterization of Bora device, making measurements of its neutron and hard X ray radiations with 0.3 ns time resolution and high exactness of their absolute values.
c) We have irradiated by means of hot plasma and fast ion streams generated in Bora device the specimens of materials that are counted as perspective ones for use in FR based on MPC and IPC. Among them we used double forged W, Eurofer steel, Mo, Al and Ti alloy.

d) We have analyzed these materials after irradiation with a number of instruments. We have found different types of surface and bulk damage features depending on the power flux density and the number of shots. Among them we discovered by micro CT a bulk damage defect produced by shock wave acting with a subsequent rarefaction wave. We verified this phenomenon with a computer modeling.
e) We have investigated mass loss in the materials, structure changes and modification of the lattice parameters. The last one appeared to be opposite in its sign for tungsten and titanium alloy.
f) We have shown that irradiation of the specimens of austenitic stainless steel 10Cr12Mn14Ni4AlMo by nitrogen hot plasma (<1 keV) and fast ion (>100 keV) streams at the DPF device allowed modification of their surface layers by means of two mechanisms simultaneously by implantation of nitrogen ions into materials and by additional doping by some elements.
g) We have also found that in certain DPF operational regimes realized (at power flux densities of about 10^7–10^8 W/cm^2) nitrogen ions implanted into alloys on the basis of iron had different behaviour. In the lattice of gamma austenite, one part of them occupies places within the interstitial sites of the lattice (that resulted in the increase of the lattice parameter observed), whereas the other took part in the formation of nitride phases.
h) We have provided experimental and theoretical works in a number of spin-off applications. In particular, in the field of dynamic quality control we have obtained a single shot X ray picture of rotating fan blade. In the area of nuclear medicine we have demonstrated a possibility to use reasonable thickness of different moderators to obtain spectra of neutrons generated by a DPF device with well developed epithermal part without tremendous loss of the output neutron flux. Besides, we have shown an oopportunity to preserve neutron output pulse duration within the limits less than 1 μs that allows expecting a realization of synergetic effects in a malignant tumor treatment with short powerful neutron pulses.
i) We have held a school named “International School and Training Course on Dense Magnetized Plasma as a Source of Ionizing Radiations, their Diagnostics and Applications”, and more than 30 young scientists from developing countries participated in this event. They were trained in theory of magnetized plasma production and diagnostics, in practical assembling of portable DMP devices and their implementation in radiation material science, neutron spectroscopy and nuclear medicine, as well as in handling of computational codes used for simulation of plasma processes.

ACKNOWLEDGEMENT

This research has been partially supported by the IAEA in the frame of an Agreement and of the Contracts on the CRP “Investigations of Materials under High Repetition and Intense Fusion Pulses” Nos. RC-16931, RC-16932, RC-16954, RC-16955, RC-16956, RC-16960, and by the IAEA CRP Contract No. 17167 as well.

REFERENCES

[1] ITER, http://www.iter.org/
[2] NIF, https://lasers.llnl.gov/
[3] ZEMAN, A., INOZEMTSEV, V., KAMENDJE, R., BEATTY, R.L., IAEA coordinated research activities on materials for advanced reactor systems, J. Nucl. Mater. **442** 1–3 (2013) S77–S83.
[4] LINKE, J., LOEWENHOFF, T., MASSAUT, V., PINTSUK, G., RITZ, G., RÖDIG, M., SCHMIDT, A., THOMSER, C., UYTDENHOUWEN, I., VASECHKO, V., WIRTZ, M., Performance of different tungsten grades under transient thermal loads, Nucl. Fusion **51** (2011) 073017.
[5] GRIBKOV, V.A., “Current and Perspective Applications of Dense Plasma Focus Devices”, Plasma and Fusion Science 17th IAEA Technical Meeting on Research Using Small Fusion Devices (Proc. Int. Conf. Lisbon 2007), AIP Conference Proceedings, New York (2008).
[6] http://mlab.ictp.it/uploads/C1/cK/C1cKba2XDKJNeoN26x5GmA/Dense-Plasma-Focus-BoraICTP.pdf
[7] DEMINA, E.V., et al., Structure modifications and nitride phases creation within a surface layer of Fe-based alloys at pulsed irradiation by nitrogen plasma and fast ions, Rare Metals **28** (2009) 853–859.
[8] GRIBKOV, V.A., et al., Interaction of high temperature deuterium plasma streams and fast ion beams with condensed materials in dense plasma focus device, J Phys D: Appl. Phys. **36** (2003) 1817–1825.
[9] RADJKUMAR, K.M., KUMAR, D., GEORGE, P.J., Semiconductor applications of plasma immersion ion implantation technology, Bull. Mater. Sci. **25** 6 (2002) 549–551.
[10] LI, Z.G., et al., Preparation of nanocomposite thin films by ion beam and plasma based sputtering processes, Surf. Coat. Technol. 173/174 (2003) 1140.
[11] PELLETIER J., ANDERS, A., Plasma-based ion implantation and deposition: A review of physics, technology, and applications, IEEE Trans. Plasma Sci. **33** 6 (2005) 1.
[12] PIMENOV, V.N., et al., Influence of powerful pulses of hydrogen plasma upon materials in PF-1000 device, Nukleonika **47** 4 (2002) 155.
[13] POGREBNIAK, A. D., TIURIN, YU.N., Modification of material properties and coating deposition using plasma jets, Physics–Uspekhi **48** 5 (2005) 487–514.

[14] ZHANG, T., et al,. Pure high dose metal ion implantation using the plasma immersion technique, Rev. Sci. Instrum. **70** 11 (1999) 4359.
[15] GRIBKOV, V.A., Physical processes taking place in dense plasma focus devices at the interaction of hot plasma and fast ion streams with materials under test, Plasma Phys. Control. Fusion **57** (2015) 065010.
[16] GRIGORIEV, I.S., MEILIKHOV, E.Z., RADZIG, A.A. (Eds.), Handbook of Physical Quantities, Taylor & Francis, Bosa Roca, United States (1996).
[17] SNIPES, J.A., "Plasma Operation in ITER", ITER–IAEA–ICTP Advanced Workshop on Fusion and Plasma Physics, Trieste, Italy 2011.
[18] FUJITSUKA, M., et al., Thermal shock experiments for carbon materials by electron beams, J. Nucl. Mater. **179** (1991) 189–192.
[19] TUNIZ, C., et al., The ICTP-Elettra X-ray laboratory for cultural heritage and archaelogy, Nucl. Instr. Meth. Res. **A711** (2013) 106–111.
[20] LATYSHEV, S.A., et al., International Symposium on Plasma Focus, Nilai, INTI International University, Malaysia 2013.
[21] ZEL'DOVICH, YA.B., RAIZER, YU.P., Physics of Shock Waves and High-Temperature Hydrodynamic Phenomena, Academic Press, New York (1967).
[22] BUKHANOVSKIJ, V.V., Strength Problems **4** (2000) 75–85.
[23] MAKSIMKIN, O.P., et al., Problems of Atomic Science and Technology (2001) 69–71.
[24] DEMINA, E.V., et al., Structure modifications and nitride phases creation within a surface layer of Fe-based alloys at pulsed irradiation by nitrogen plasma and fast ions, Rare Metals, Spec. Issue 28 (2009) 853.
[25] GRIBKOV, V.A., "Russian Dense Plasma Focus Installations for Various Applications", IAEA TCM on Res. Using Small Fusion Devices, Cairo, Book of Abstracts, D-1 (1997).
[26] TSYB, A. F., et al., Neutrons in the Treatment of Cancer (Obninsk, Kaluga region: BIST) (2003)
[27] BARTH, R.F., SOLOWAY, A.H., Boron neutron capture therapy of brain tumors—current status and future prospects, J. Neurooncol. **33** (1997) 3.
[28] MUNCK AF ROSENSCHEOLD, P.M., et al., Quality assurance of patient dosimetry in boron neutron capture therapy, Acta Oncol. **43** 4 (2004) 404.
[29] HALL, E. J., The dose-rate factor in radiation biology, Int. J. Radiat. Biol. **59** 3 (1991) 595.
[30] ORLOVA, M.A., et al., Enzyme activation and inactivation induced by low doses of irradiation, Applied Biochemistry and Biotechnology **88** (2000) 243.
[31] GRIBKOV, V.A., "Pulsed radio-biology: possibilities and perspectives", Proceedings of the First Workshop on Biological Physics 2000, (Proc. Int. Conf. Bangkok, 2000) World Scientific, Singapore (2001).
[32] BERNARD, A., et al., Scientific status of plasma focus research, J. Moscow Phys. Soc. **8** (1998) 93.
[33] GRIBKOV, V.A., ORLOVA, M.A., On various possibilities in pulsed radiation biochemistry and chemistry, Radiat. Environ. Biophys. **43** (2004) 303.
[34] LEE, S., et al., High rep rate high performance plasma focus as a powerful radiation source, IEEE Trans. Plasma Sci. **26** (1998) 1119.
[35] VERMA, R., et al., Realization of enhancement in time averaged neutron yield by using repetitive miniature plasma focus device as pulsed neutron source, J. Phys. D: Appl. Phys. **42** (2009) 235203
[36] BURES, B.L., KRISHNAN, M., JAMES, C.A., Plasma focus electronic neutron generator, IEEE Trans. Plasma Sci. **40** (2012) 1082.
[37] RAMOS ARUCA, M., et al., "Pulsed neutron source for boron neutron capture therapy–initial simulation results", Proc. 13th Int. Congress on Neutron Capture Therapy, Florence, Italy, 2008.
[38] GRIBKOV, V.A., et al., The development of methods and apparatus for cancerous growth diagnostics and therapy on the base of neutron and X ray radiation pulse generator, Issues of Atomic Science and Technology, Nuclear Instrument-Building, All-Russian Federation Research Institute of Automatics (2010) 178.
[39] LU, D.R., MEHTA, S.C., CHEN, W., Selective boron drug delivery to brain tumors for boron neutron capture therapy, Adv. Drug Deliv. Rev. **26** (1997) 231.
[40] GRIBKOV, V.A., DUBROVSKY, A.V., ORLOVA, M.A., SCHOLZ, M., Opportunities afforded by new generation of pulsed radiation sources in flash radiation physics and chemistry, Res. J. Chem. Environ. **9** (2005) 11.
[41] AGOSTINELLI, S., et al., Geant4—a simulation toolkit, Nucl. Instr. and Meth. A **506** (2003) 250.
[42] ALLISON, J., et al., Geant4 developments and applications, IEEE Trans. Nucl. Sci. **53** (2006) 270.
[43] BUCHHOLZ, T.A., et al., Boron neutron capture enhanced fast neutron radiotherapy for malignant gliomas and other tumors, J. Neurooncol. **33** (1997) 171.
[44] DICKERSON, E.B., et al., Gold nanorod assisted near-infrared plasmonic photothermal therapy (PPTT) of squamous cell carcinoma in mice, Cancer Lett. **269** (2008) 57.

INVESTIGATION OF CHANGES IN STRUCTURE OF TUNGSTEN

M.K. SKAKOV[*], I.L. TAZHIBAYEVA[*], V.V. BAKLANOV[*], Y.T. KOYANBAYEV[*], S.B. KISLITSYN[**], A.Z. MINIYAZOV[*]

[*] RSE National Nuclear Center,
Kurchatov

[**] Institute of Nuclear Physics,
Almaty

Kazakhstan

Abstract

This paper presents the results of post-irradiation study of the structure and property changes of the tungsten surface irradiated by neutrons at the WWR-K reactor and by low energy alpha particles at the DC-60 accelerator. Furthermore, a detail comparison with non-irradiated samples is given.

1. INTRODUCTION

To date, the parameters of the hydrogen isotopes interaction with tungsten and the obtained parameters (such as diffusion, permeability and solubility coefficients) have differed over several orders of magnitude for various studies [1]. In addition, these parameters were obtained for normal conditions, while the real conditions of the fusion facilities, i.e. simultaneous impacts of high heat and neutron loads are a major factor in the reliability of results of such experimental studies. Preliminary analysis of the published papers showed that there is a considerable number of effects of plasma flows on physical and mechanical properties of tungsten [2–7]. At the same time, there is almost no experimental data on the effects of neutron irradiation on the parameters of the hydrogen isotopes interaction with tungsten and on the changes in its physical and mechanical properties. Therefore, obtaining new experimental data on the parameters of the hydrogen isotopes interaction with neutron irradiated tungsten is an extremely important task to predict its behavior in fusion reactors.

2. IRRADIATION EQUIPMENT AND ANALYTICAL METHODS

2.1. Equipment used in the irradiation experiments

2.1.1. Nuclear fission reactor WWR-K and irradiation parameters

Irradiation of various tungsten samples was carried out in a side channel (10–2) of WWR-K reactor at NNC RK (Fig. 1). The main parameters are given in Table 1.

FIG. 1. Nuclear fission reactor WWR-K.

TABLE 1. MAIN PARAMETERS OF THE DEVICE

Type	Pool type reactor on thermal neutrons
Power	6 MW
Neutron flux	1×10^{14} n · cm^{-2} · s)
Fuel enrichment	36% ^{235}U
Coolant, moderator and reflector	Desalted water

Irradiation device includes the external case (ampoule), where two capsules with tungsten samples were located. Ampoule was filled with air of atmosphere pressure. Ampoule with capsules was not sealed and communicated with atmosphere through the tube (diameter of 6 mm, thickness of 1 mm, and length of 5000 mm). Capsules were sealed and filled with various gases. Top capsule was filled with hydrogen (pressure of 30 kPa under temperature of 20°C). Bottom capsule was filled with argon (or helium) (gas pressure of 30 kPa under temperature of 20°C). During irradiation the ampoule device with two capsules was placed in the case of peripheral water channel of WWR-K reactor. Ampoule was washed with water of 40°C-temperature during irradiation. All the ampoule and capsule materials were made of stainless steel $Cr^{18}Ni^{10}Ti$. Test samples, fluence and flux density of irradiation are described in Table 2 and 3.

Temperature measurements were carried out in three points of ampoule device: middle 724.63°C, top 715.36°C and bottom 717.29°C. The latter temperature was a little higher than the calculated one (600°C). Nine campaigns were carried out at the reactor WWR-K, and irradiation time was 3255 hours.

TABLE 2. DESCRIPTION OF TEST SAMPLES

Sample	Material description	№
A45 A46	W-UHP (ultra-high-purity tungsten, single forged)	2
B40 B41	WVMW (potassium doped tungsten; K-content < 40 ppm, single forged)	2
C29 C30	WTa1 (1 wt% Ta content, single forged)	2
D37 D38	WTa5 (5 wt% Ta content, single forged)	2
E39 E40	Pure W, single forged	2
VL-39 VL-43	MIM W T_HIP + 50 °C (metal injection molded pure W 50 °C higher sintering temperature).	2
VL-16 VL-22	MIM W (metal injection molded with isotropic grains)	2
DF	Double forged pure. Less anisotropic than single forged W. DF 101-118 polished to a mirror finish. DF 121-124 unpolished.	22

TABLE 3. GAINED FLUENCE AND FLUX DENSITY OF IRRADIATION

Type of neutron flux	Fluence, n/cm^2	Density, $p/cm^2 \cdot s$
Thermal	8.59×10^{20}	7.3×10^{13}
Fast	7.96×10^{19}	6.8×10^{12}

2.1.2. DC-60 cyclotron and the parameters of the experiment

The samples were irradiated up to the doses of 10^{17} p/cm^2 and 10^{18} p/cm^2 by the ions $^4He^{+2}$ in low energy channel of DC-60 cyclotron, branch of NNC RK. The irradiation conditions are given in Table 4.

TABLE 4. CONDITIONS FOR IRRADIATION OF TUNGSTEN SAMPLES

Samples	Irradiation conditions	Irradiation parameters			
		Channel	Particles	Particle energy	Irradiation fluence
2 tungsten samples in frame	Sample size 2 cm × 0.5 cm $T_{irrad} < 150^o$	Low energies	$^4He^{+2}$	45 keV	1.5×10^{18} cm^{-2}

In accordance with the calculations by SRIM software, the path of alpha particle of 45 keV was ~ 100 nm, straggling ~ 80 nm, i.e. helium in the irradiated samples accumulated in the near surface layer.

FIG. 2. Cyclotron based complex DC-60.

The irradiation of pure tungsten was carried out by double charged helium ions at DC-60 cyclotron in low-power channel of WFE source. Two samples of 20 mm × 2 mm × 1 mm were irradiated during the experiments. During irradiation, temperature did not exceed 150^{o}C, while the total power per ion was 45 keV, and path was lower than 20 nm.

2.2. Equipment used in the analysis of the irradiated specimens

2.2.1. Investigation of neutron irradiated tungsten

Samples of tungsten have been examined to obtain data on the degree of change in the structure and physicomechanical properties of the material as a result of reactor irradiation. Firstly, gamma spectrometric measurements to determine the isotopic composition and activity of the radioactive emitters in the samples of tungsten were carried out using a spectrometric complex 'InSpector' with a scintillation detector. Mass and density of the samples were measured on an analytical scales and data on the density was obtained by hydrostatic weighing. Investigation of tungsten surface was performed via optical microscopes and scanning electron microscopy. Microhardness testing is performed on the unit for measuring of microhardness PMT-3 according to

the scheme Vickers with a load on the indenter 150 g. For the instrumental analysis of the irradiated specimens we have used equipment as follows:

a) Optical microscopes BX41M, Olympus and Metam LV-41, Lomo with computerized image processing;
b) Scanning Electron Microscope JSM-6390, Jeol;
c) Unit for measuring of micro-hardness PMT-3;
d) Analytical scales AG-204, REGWAG;
e) Spectrometric complex "InSpector" with a scintillation detector, Canberra.

2.2.2. Investigation of tungsten irradiated by low energy alpha particles

The structure of the samples surface has been studied by optical metallography, scanning electron microscopy and atomic force microscopy, as well as the elemental composition was determined using a scanning electron microscope, which was equipped with energy dispersive X ray analyzer. For the instrumental analysis of the irradiated specimens have used equipment as follows:

a) Optical microscope;
b) Atomic force microscopy;
c) Scanning Electron Microscope TM 3030, HITACHI;
d) Energy dispersive X ray analyzer, BRUCKER;
e) Unit for measuring of micro-hardness PMT-3.

3. INVESTIGATION OF IRRADIATED SAMPLES

3.1. Post irradiation study of the structure and property changes of the tungsten surface

Information about the investigated samples after irradiation are presented in Table 5 and 6. Comparative analysis was conducted to study the morphology of tungsten samples in initial state and after irradiation, the changes in the structure of the samples and the structural changes of the surface of tungsten occurred as a result of reactor irradiation in the atmosphere of hydrogen and helium, see Fig. 3.

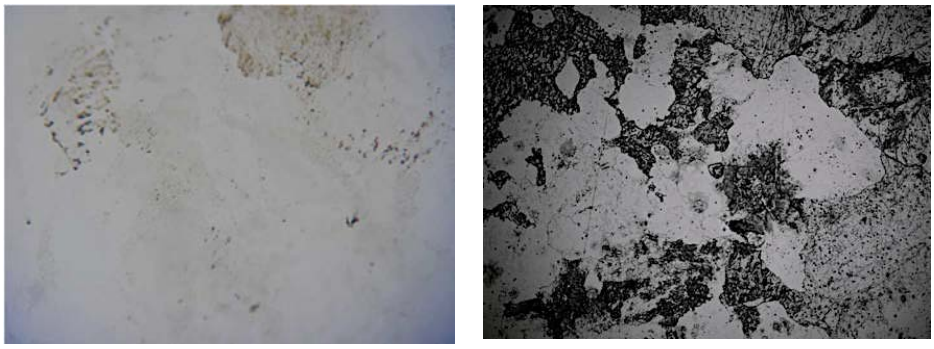

(a) (b)

FIG. 3. (a) Optical image of the sample A45 non irradiated; (b) SEM image of the sample A45 H irradiated.

TABLE 5. SAMPLES WERE IRRADIATED IN A HYDROGEN ATMOSPHERE

№	Objects	Activity (Bq)	Isotopes-emitters	Weight (g)		Density (g/cm^3)
				m_{irrad}	Δ (g)	
1	A45	2.0E+05	^{182}Ta	13.4972	+0.0209	19.04
2	B40	4.1E+05	^{60}Co, ^{182}Ta	12.7104	+0.0040	19.00
3	E39	4.2E+05	^{60}Co, ^{182}Ta	13.4054	+0.0013	19.01
4	VL16	3.8E+05	^{60}Co, ^{182}Ta	12.8008	+0.0007	18.64
5	VL39	2.3E+05	^{60}Co, ^{182}Ta	12.6810	-0.0011	18.74

TABLE 6. SAMPLES WERE IRRADIATED IN A HELIUM ATMOSPHERE

№	Objects	Activity (Bq)	Isotopes-emitters	Weight (g)	Density (g/cm^3)
1	B41	6.9E+05	^{60}Co, ^{182}Ta	12.9298	18.85
2	E40	2.3E+05	^{60}Co, ^{182}Ta	13.0891	18.99
3	VL22	5.0E+05	^{60}Co, ^{182}Ta	12.7401	18.62
4	VL43	4.2E+05	^{60}Co, ^{182}Ta	12.5762	18.75

SEM images of the surface of the tungsten sample A45 are presented in Fig. 4. It can be seen that the initial state of the sample surface A45 is a fine grained structure without cracks or other defects, see Fig. 4(a). Then, after irradiation there is a change in the surface topography, which can be found with a partial etching of the surface after neutron irradiation, and the surface is characterized by fine grained structure, with clearly defined boundaries, see Fig. 4(b).

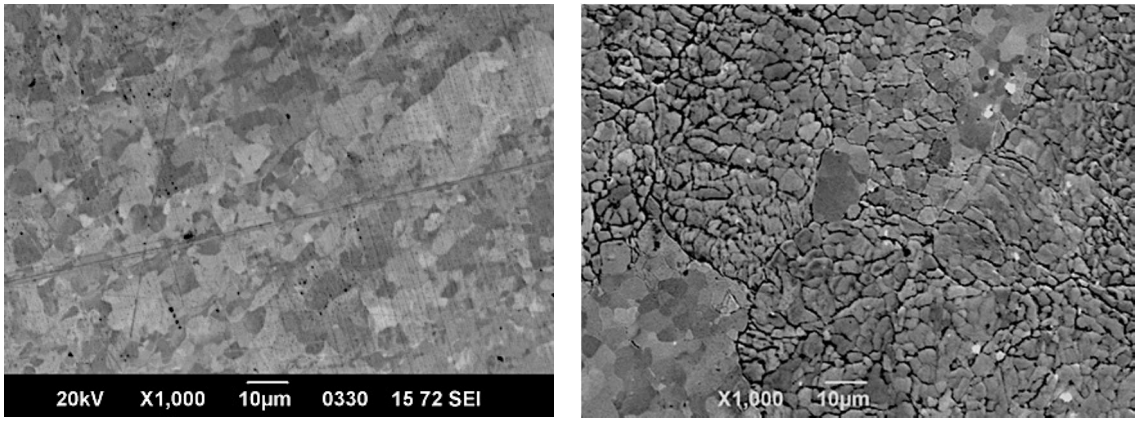

(a) (b)

FIG. 4. (a) SEM-images of the samples A45 non irradiated; (b) SEM-images of the samples A45 H irradiated.

The structure of the surface tungsten samples of series B are shown in Figs 5 and 6. The initial state has uniformly distributed inclusions on the sample surface.

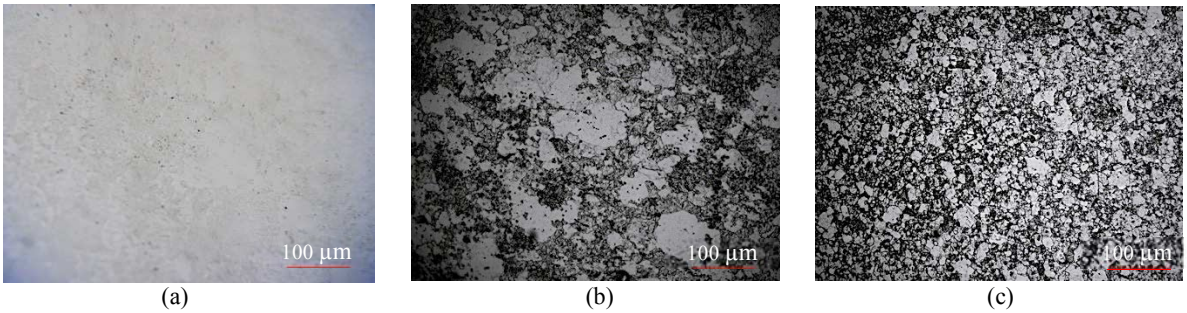

(a) (b) (c)

FIG. 5. (a) Optical images of the sample B40 non-irradiated; (b) optical images of the sample B40 H irradiated; (c) optical images of the sample B41 He irradiated.

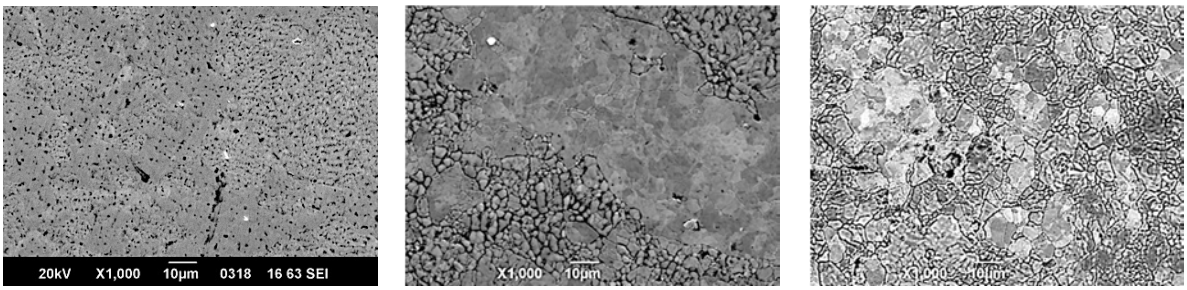

(a) (b) (c)

FIG. 6. (a) SEM images of the sample B40 non-irradiated; (b) SEM images of the sample B40 H irradiated; (c) SEM images of the sample B41 He irradiated.

The surface structure of the sample B40, irradiated in hydrogen atmosphere has non-uniform etching. Here, the nature of changes in the structure of the sample surface B41 irradiated in the atmosphere of helium differs from that of the sample irradiated in hydrogen atmosphere. The surface has uniform erosion as a result of irradiation and this is confirmed by the results of SEM in Fig. 6. Furthermore, the SEM images show uneven erosion of the surface after irradiation as in Figs 6(b)–(c).

Electron microscopic image of the surface structure of samples of series 'E' are presented in Fig. 7. The original structure of the sample E39 has a uniform distribution of inclusions. After the test, samples are in the erosion surface and traces of etching are also found on the surface, see Fig. 8.

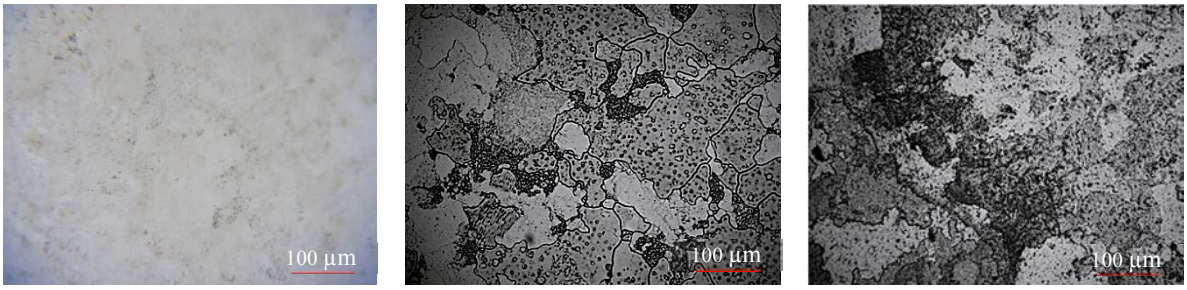

(a) (b) (c)

FIG. 7. (a) Optical images of the sample E39; (b) optical images of the sample E39 H irradiated; (c) optical images of the sample E40 He irradiated.

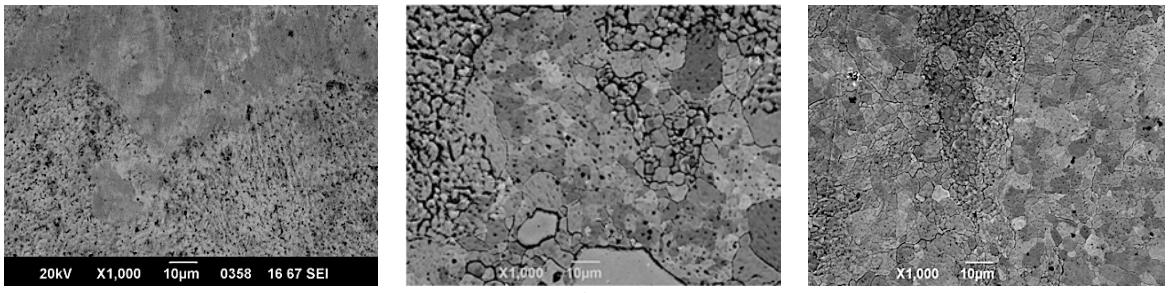

(a) (b) (c)

FIG. 8. (a) SEM images of the sample E39 non-irradiated; (b) SEM images of the sample E39 H irradiated; (c) SEM images of the sample E40 He irradiated.

The study of surface structure of samples of tungsten series 'VL' indicates a strong erosion of the surfaces of samples irradiated in the atmosphere of hydrogen and helium, see Figs 9 and 10. In the samples VL16 and VL39 irradiated in hydrogen atmosphere is discovered that erosion is cross-boundary in nature, see Figs 9(b)–(e). In samples VL22 and VL43 irradiated in a helium atmosphere is observed uniform erosion at the grain boundaries

and in the body of the grain. On the SEM images in Fig. 10, it is clearly showed the relief surface, as a result of erosion of the surface during irradiation, with no defects form cracks. The measurements summarized in Table 7 reveal an increase in the microhardness of tungsten after irradiation. In particular, the microhardness of the initial samples was measured at 200 g, while before the irradiation it was measured at 150 g.

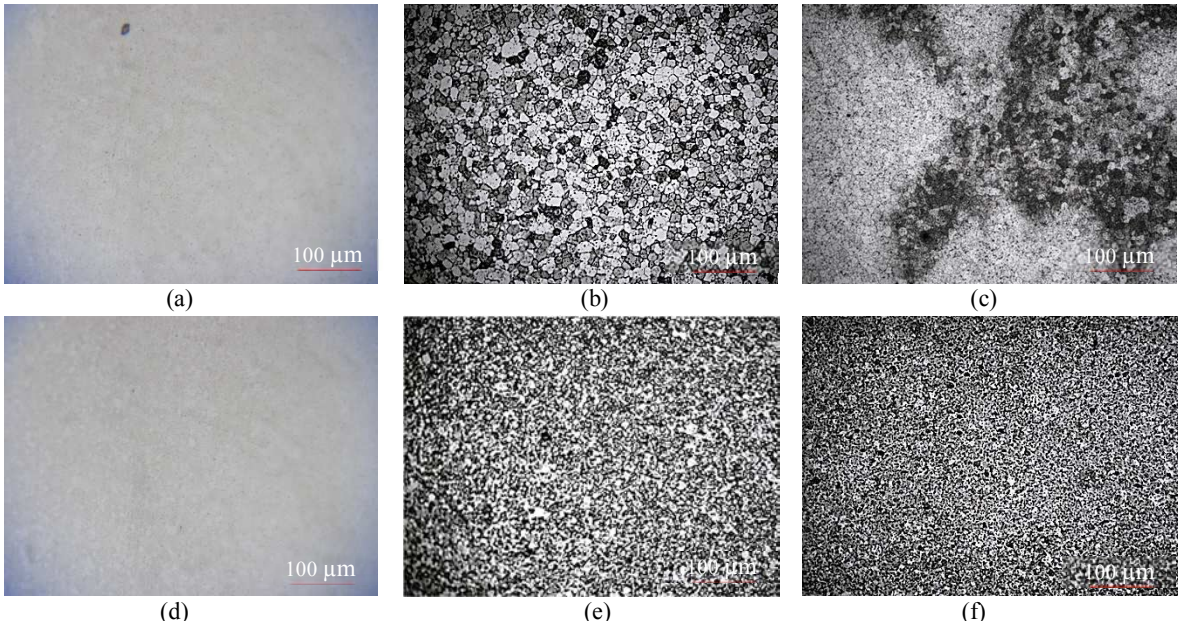

FIG. 9. (a) Optical images of the samples VL16 non-irradiated; (b) optical images of the samples VL16 H irradiated; (c) optical images of the samples VL22 He irradiated; (d) optical images of the samples VL39 non-irradiated; (e) optical images of the samples VL39 H irradiated; (f) optical images of the samples VL43 He irradiated.

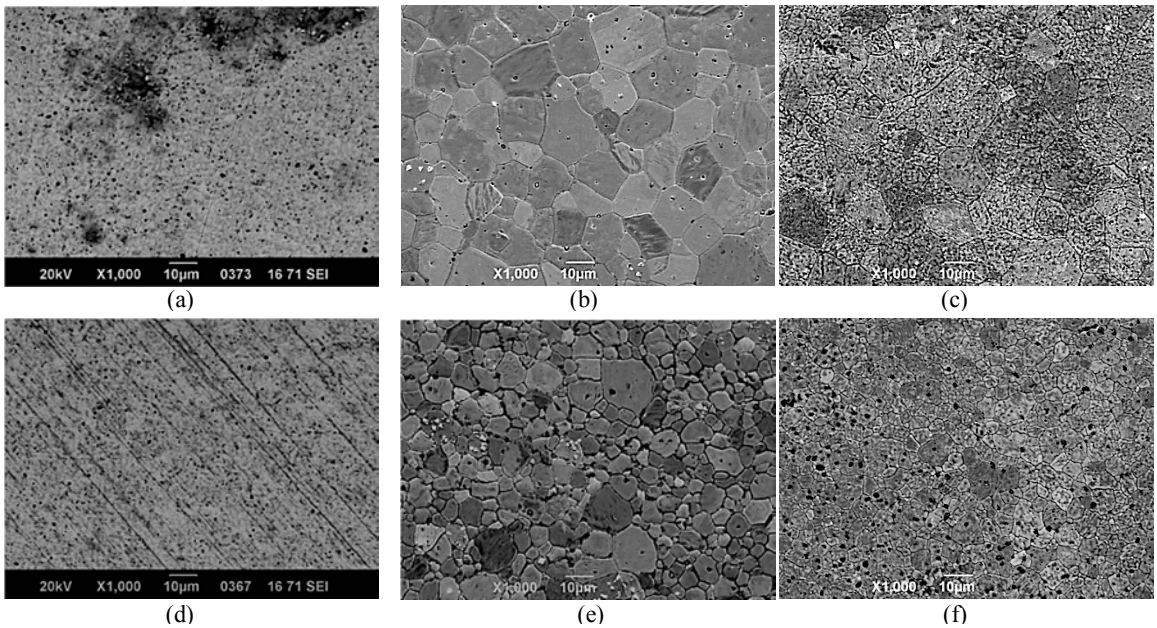

FIG. 10. (a) SEM images of the samples VL16 non-irradiated; (b) SEM images of the samples VL16 H irradiated; (c) SEM images of the samples VL22 He irradiated; (d) SEM images of the samples VL39 non-irradiated; (e) SEM images of the samples VL39 H irradiated; (f) SEM images of the samples VL43 He irradiated.

To summarize, from the study of tungsten samples irradiated in the WWR-K reactor in an atmosphere of hydrogen and helium we can conclude that:

- According to the obtained data there is erosion of the surface of samples;
- In tungsten irradiated in hydrogen atmosphere prevails erosion along grain boundaries;
- In the samples irradiated in the atmosphere of helium is observed uniform erosion at the grain boundaries and in the body of the grain;
- On the surface of samples irradiated in a helium atmosphere evident relief, as a result of etching of the surface during irradiation;
- Weight data showed a slight increase (in the sample VL39 the observed decrease in the mass of material);
- The change in the density of the samples is not detected;
- An increase in microhardness is shown as a result of comparison of values of microhardness of the samples before and after irradiation.

3.2. Post-irradiation study

In order to study the structural changes in the surface irradiated by low energy alpha particles we selected extra pure tungsten, DF-W grade (made in Germany), which is one of the most promising materials for armor of the tokamaks divertor plates. Tungsten samples were prepared in the form of strips of 20 mm × 2 mm × 1 mm. In Fig. 11, the surface images obtained by optical and scanning electron microscopy are shown.

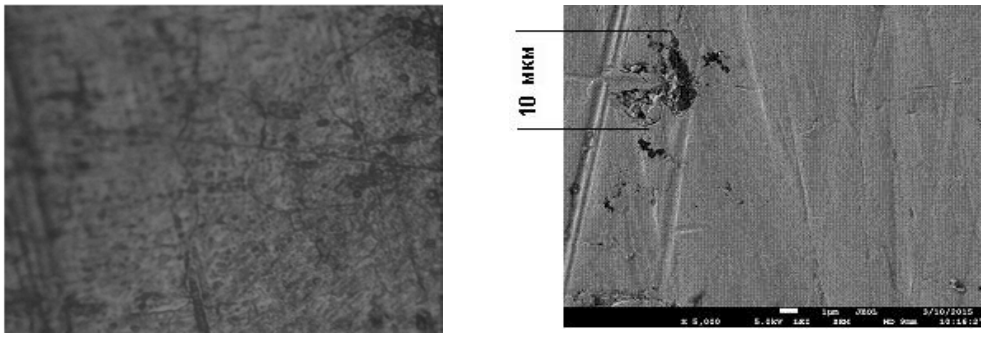

(a) (b)

FIG. 11. (a) Optical microscope (×200) image of the surface of tungsten samples; (b) scanning electron microscope (×5000) image of the surface of tungsten samples.

These images indicate that the samples had high surface undulation as bands and cavities, which were most likely the grains chipped during the surface preparation. The data obtained by optical and scanning electron microscopy were confirmed by the results of atomic force microscopy of the tungsten samples. In Fig. 12, 3-D images of the surface and surface profilogram are presented.

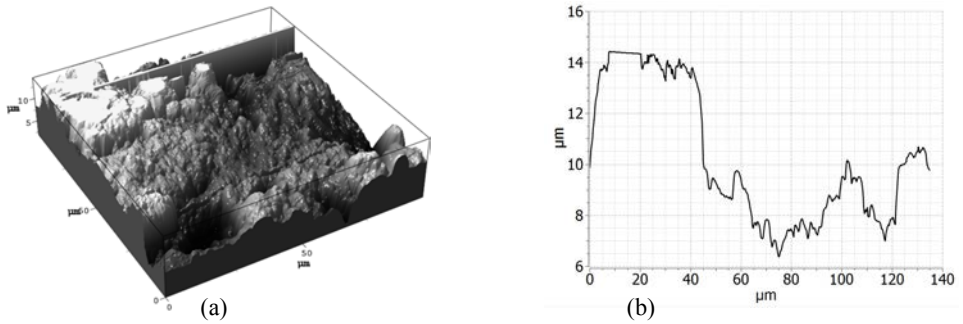

(a) (b)

FIG. 12. (a) 3-D image of the surface of non-irradiated tungsten sample; (b) surface profilogram of the surface of non-irradiated tungsten sample.

The elemental composition of tungsten samples was determined by using EDAX. Results of the analysis (X ray spectrum) are given in Fig. 13. Analysis of the obtained spectrum showed that DF-W grade samples are practically pure tungsten. Pre-radiation studies included measurement of tungsten samples hardness. Vickers microhardness was measured by the microhardness tester PMT-3, and indentation load was of 1.92 N (200 g), since the smaller load of 140 g did not leave the imprint on the surface.

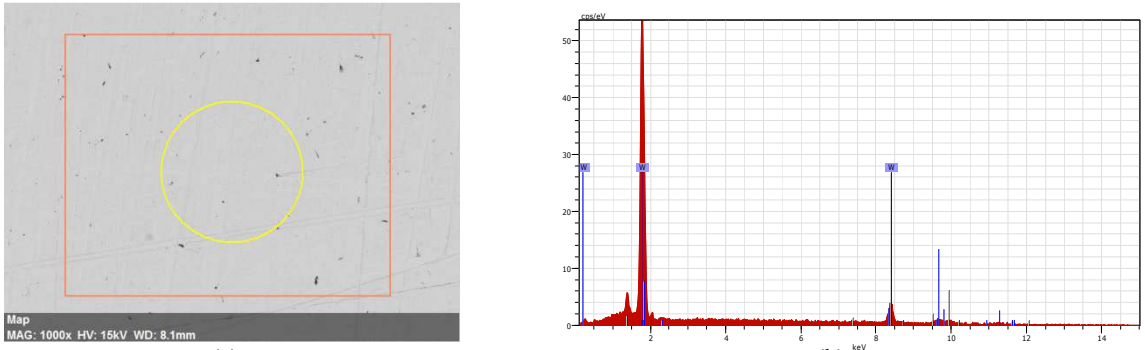

(a) (b)

FIG. 13. (a) Determination of elemental composition of the tungsten samples using EDAX (area under study inside the yellow circle); (b) X ray spectrum of the non-irradiated tungsten sample.

Attempts to measure nanohardness using a scanning nanohardness tester 'NanoScan-COMPACT' were not successful because of the high degree of surface roughness. The measured microhardness was 1500 MPa. Since the surface of the samples had a high degree of roughness, they were subjected to further mechanical grinding and polishing. After additional preparation the surface roughness decreased significantly but measurement of the surface nanohardness was still not possible. In order to identify the effects of irradiation on the tungsten samples the surface structure and microhardness of the samples were measured using the same methods as before irradiation.

Studies of the elemental composition of the near surface layers of tungsten showed that the elemental composition of the samples has not changed (taking into account that helium is not determined by EDAX technique). In Fig. 14, the X ray spectrum shows that samples after irradiation were DF-W-grade pure tungsten.

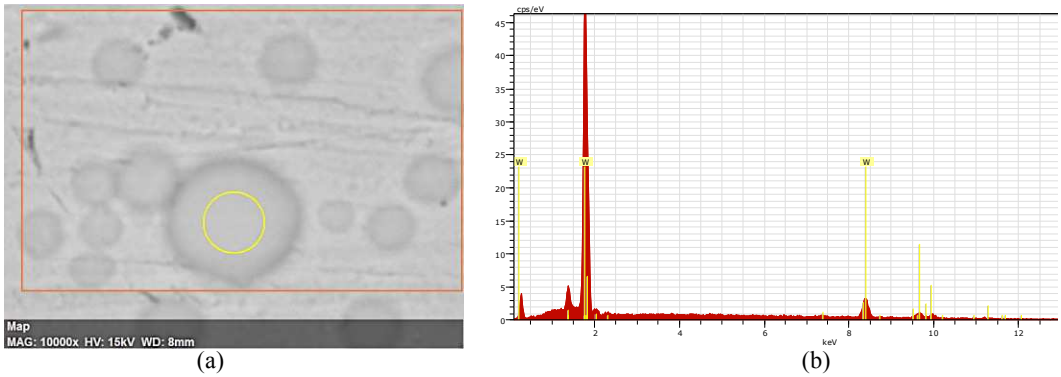

(a) (b)

FIG. 14. (a) Study of the elemental composition of near surface layers of tungsten (area under study in yellow); (b) X ray spectrum of irradiated tungsten sample.

The OM, SEM and AFM methods used to study surface of the tungsten samples irradiated with alpha particles revealed significant changes in the surface structure. In Fig. 15, a picture of the surface structure obtained by OM technique. Even with this relatively small magnification we can see light spherical spots on the irradiated surface, which can be interpreted as a display of helium porosity. On the next page in Fig. 16, surface electron micrographs of high magnification allow estimating the size and density of the spots on the surface is illustrated.

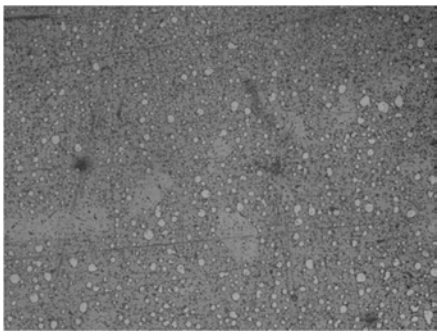

FIG. 15. Surface structure of tungsten irradiated by alpha particles (×200).

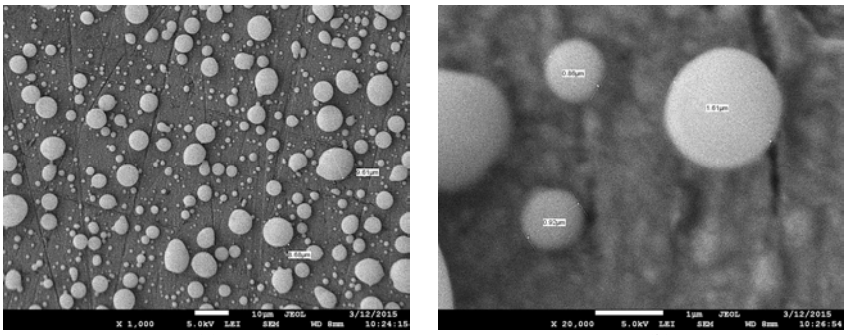

(a) (b)

FIG. 16. (a) Image (×1000) of irradiated tungsten samples; (b) image (×20 000) of irradiated tungsten samples.

The dimensions of the spherical formations at the surface are ranging from tens of nanometers up to several μm, see Fig. 16(b). The density of the spherical formations on the surface is several hundred per square millimeter. Studies of the surface structure by AFM technique demonstrated that the surface had pores with a diameter of up to 10 μm, which depth can reach up to 100 nm. In Fig. 17, the scanning area is 80 × 80 μm^2. The measured values of micro hardness $N\mu$ = 570 MPa showed that irradiation with low energy alpha particles resulted in the surface softening. The analysis of the obtained experimental results allows proposing the following model of helium accumulation and release under irradiation of tungsten with low energy alpha particles. Irradiation leads to high concentrations of helium and irradiation generated vacancies in the straggling area. The high density of helium and vacancies stimulates an intensive formation of the bubbles filled with helium in this area. Since straggling area is located near the surface, then the pores migrate to the surface due to excess gas pressure in them (blistering occurs) and gas filled bubbles are released (flaking of surface). Flaking of the surface in turn results in decrease of strength properties, in particular, decrease in hardness.

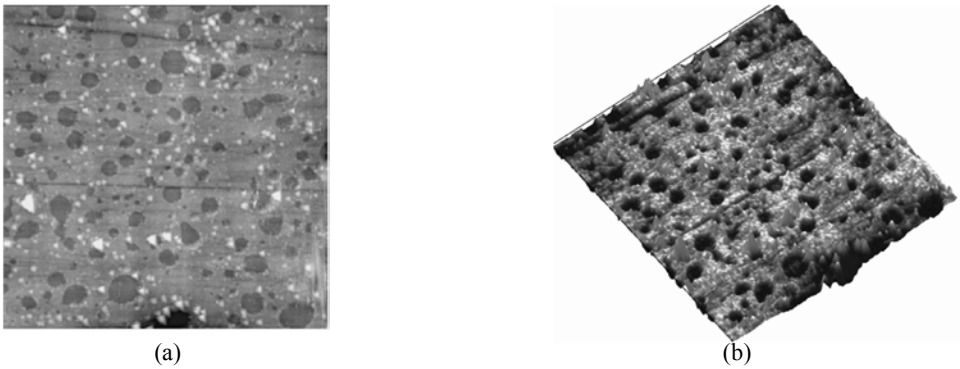

(a) (b)

FIG. 17. (a) 2-D scanned image of irradiated tungsten surface; (b) 3-D scanned image of irradiated tungsten surface.

The experimental results on the effects of tungsten irradiation with low-energy alpha particles are in full consistency with the results on irradiation of steel $^{12}Cr^{18}Ni^{10}Ti$ with alpha particles [8]. The formation of helium bubbles, blistering and flaking were also observed during the experiments on irradiation of the steel samples with alpha particles of 40 keV up to a fluence of 1×10^{18} cm^{-2} at the same temperature of $< 150^{o}C$.

As a result of the post-irradiation study of the structure and property changes of the tungsten surface irradiated by low energy alpha particles at the DC-60 accelerator:

- It was experimentally determined that irradiation with low energy alpha particles results in formation of helium-filled bubbles in the straggling area, i.e. in the alpha particles deceleration area (for alpha particles with energy of 45 keV straggling area is located in the near-surface layers of tungsten);
- It was shown that helium filled bubbles move to the surface, causing blistering and flaking of the surface, which was a result of the opening of the gas filled pores at the surface.
- Flaking of the surface leads to softening of the near surface layer of tungsten, which results in a significant decrease in microhardness.

ACKNOWLEDGEMENT

This research has been performed in the framework of the research program “Investigation of changes in structure and properties of tungsten irradiated by neutrons, alpha particles and heavy ions within the temperature range up to $600^{o}C$ to predict its behavior in thermonuclear fusion reactors.”, No. 17398, IAEA.

REFERENCES

[1] GUSEVA, M.I., et al., Erosion of tungsten in the experiments to simulate the operation of the divertor of the ITER reactor, Problems of Atomic Science and Technology, Series Fusion **3–4** (2002) 20–30.
[2] CAUSEY, R.A., Hydrogen isotope retention and recycling in fusion reactor plasma-facing components,” J. Nucl. Mater **300** (2002) 91–117.
[3] ALIMOV, V.H., The accumulation of deuterium in tungsten, carbide and mixed tungsten-carbon films. Problems of atomic science and technology, Series Fusion **2** (2001) 44–50.
[4] FEDERICI G., et al., Plasma-material interactions in current tokamaks and their implications for next step fusion reactors, Nucl. Fusion **41** (2001) 1967.
[5] BENAMATI G., SERRA, E., WU, C.H., Hydrogen and deuterium transport and inventory parameters through W and W-alloys for fusion reactor applications, J. Nucl. Mater. **283–287** (2000) 1033.
[6] GARCÍA-ROSALES, C., et al., Re-emission and thermal desorption of deuterium from plasma sprayed tungsten coatings for application in ASDEX-upgrade, J. Nucl. Mater. **233–237** (1996) 803.
[7] ZAKAHROV, A.P., SHARAPOV, V. M., EVKO, É. I., Hydrogen permeability of polycrystalline and monocrystalline molybdenum and tungsten, Mater. Sci. **9** (1975) 149.
[8] KISLITSYN, S.B., et al., Blistering and $\alpha \rightarrow \gamma$ transformations during annealing steel $^{12}Cr^{18}Ni^{10}Ti$ irradiated by low-energy alpha particles, Issues of Atomic Science and Technology, Series Physics of Radiation Damages and Radiation Material Science **2** (2013) 17.

INVESTIGATION OF INTENSE FUSION PULSES

S.H. SAW[*1], S. LEE[*12]

Abstract

The Lee model code was extended to include computation of ion beam fluence (ions/m^2), ion beam flux (ions·m^{-2}·s^{-1}), ion beam energy fluence (J/m^2), energy flux (W/m^2) and damage factors. The extended Lee model code was then used to compute the ion beam and to simulate the ion beam flux, average plasma parameters, and radiation yields for various gases and plasma focus facilities producing many papers published and presented at conferences. Numerical experiments were systematically carried out using available measured current signal from the plasma focus facilities working on irradiation experiments and the reference data tabulated. The plasma focus facilities studied are: PF1000, NX3, BARC PF, PF6, BORA, INTI PF, NX2T, PF12, University of Sofia PF, PF5M, PF-400J and FMPF3. Validation of our computations is reported in regards to fast ion beam (FIB) and fast plasma stream (FPS) properties particularly damage factor, power flow density and FPS energy for the case of PF-400J. Our computed values agree with those reportedly measured by Soto et al. Irradiation of tungsten target using INTI PF was also carried out.

1. EXTENSION OF THE LEE MODEL CODE

1.1. Formulation of the production of ion fluence and ion flux

1.1.1. Deuterium: the ion beam fluence equation

A detailed description of the model [1] is available on the internet [2]. Neutron yield Y_n using a phenomenological beam target neutron generating mechanism was incorporated. A beam of fast deuteron ions is produced by diode action [3] in a thin layer close to the anode, with plasma disruptions generating the necessary high voltages. The beam interacts with the hot dense plasma of the focus pinch column to produce the fusion neutrons. The beam target yield $Y_{b\text{-}t}$ [4,5] was deduced as $Y_n = Y_{b\text{-}t}$:

$$Y_{b\text{-}t} = C_n n_i I_{pinch}^2 z_p^2 \ln(b/r_p)\sigma/U^{1/2} \quad (1)$$

Here n_i is the pinch ion density, I_{pinch} is the current through the pinch, r_p and z_p are the final pinch radius and length, respectively, b is the cathode radius, σ is the cross-section of D–D fusion reaction n- branch, and U is the disruption caused diode voltage. Data fitting gave $U=3V_{max}$ where V_{max} is the maximum voltage induced by the radially collapsing current sheet, and $C_n = 8.54 \times 10^8$ (all quantities in SI units) is a constant which was calibrated at an experimental point of 0.5 MA from a graphical presentation of all available measured Y_n data. The plasma focus Y_n computed from this model is found to agree well with experiments over all ranges of energy. The agreement is good enough to allow experimental measurements and numerical experimental results to be combined into a Global Scaling Law (neutrons) with a range from subkilojoule to tens of MJ. With the proven success of this model which assumes a deuteron beam interacting with the pinch plasma we extend the model to extract information about the deuteron beam. We note that for a beam passing through a plasma target, by definition, cross-section = reaction rate/(beam ion number flux × number of target particles). By rewriting Eq. (1) using this definition, we obtain:

$$Y_{b\text{-}t} = (n_b v_b) n_i (\pi r_p^2 z_p)\tau\sigma = (J_b\tau)\sigma n_i(\pi r_p^2 z_p) \quad (2)$$

Here $Y_{b\text{-}t}/\tau$ is the D–D fusion reaction rate, $J_b = n_b v_b$ is the beam ion flux with units of (number of ions · m^{-2} · s^{-1}), n_b is number of beam ions per unit plasma volume traversed, v_b is the beam ion speed, and the number of plasma target particles is $n_i(\pi r_p^2 z_p)$ with n_i being the target plasma ion density, and τ is the beam target interaction time assumed to be the confinement time of the plasma column. We also denote $J_b\tau$ as the beam ion fluence with units of (number of ions/m^2). This is the ion fluence that is generated by the inductive plasma diode action [6]. From Eqs (1) and (2) we may write the ion fluence as:

$$J_b\tau = C_n I_{pinch}^2 z_p \ln(b/r_p)/(\pi r_p^2 U^{1/2}) \text{ (ions/m}^2\text{)} \quad (3)$$

[*] Centre for Plasma Research, INTI International University, Nilai, Malaysia.
[1] Institute for Plasma Focus Studies, Chadstone, Australia.
[2] Department of Physics, University of Malaya, Kuala Lumpur, Malaysia.

As the ion beam traverses the pinch along the axial direction, there is attenuation of the beam due to interaction with the hot dense plasma. However the proportion of ions that undergoes interactions is small and most of the ions pass through and exit the pinch. We assume that Eq. (3) gives the number of ions/m^2 exiting the pinch for each PF shot.

1.1.2. Various gases: the ion beam flux and fluence equations

We now proceed to estimate the flux of the ion beam for various gases [7]. We write the ion beam flux as: $J_b = n_b v_b$, where n_b is the number of beam ions N_b divided by volume of plasma traversed by the beam, and v_b is the effective speed of the beam ions. All quantities are expressed in SI units, except where otherwise stated. Note that $n_b v_b$ has units of ions $\cdot$ m^{-2} $\cdot$ s^{-1}. We then proceed to derive n_b from the kinetic energy of the beam ions (BKE) and pinch inductive energy (PIE) considerations. The BKE is contributed from the total number of beam ions N_b where each beam ion has a mass Mm_p and speed v_b and is represented by BKE = $(1/2)N_b M m_p v_b^2$. The mass of the proton m_p is 1.673×10^{-27} kg and M is the mass number of ion e.g. neon ion has mass number M = 20. This BKE is imparted by a fraction f_e of the PIE represented by PIE = $(1/2)L_p I_{pinch}^2$ where $L_p = (\mu/2\pi)\ln(b/r_p)z_p$ is the inductance of the focus pinch, $\mu = 4\pi \times 10^{-7}$ Hm^{-1}, b is the outer electrode of the plasma focus carrying the return current, r_p is the pinch radius carrying the current through the plasma, z_p is the length of the pinch and I_{pinch} is the pinch current value taken at start of pinch. Then $(1/2)N_b M m_p v_b^2 = f_e\,(1/2)(\mu/2\pi)\ln(b/r_p)z_p I_{pinch}^2$. This gives:

$$n_b = N_b/(\pi r_p^2 z_p) = \mu/(2\pi^2 m_p)(f_e/M)\ln(b/r_p)/r_p^2(I_{pinch}^2/v_b^2) \quad (4)$$

Next, we proceed to derive v_b from the accelerating voltage provided by the diode voltage U to an ion. Each ion with effective charge Z_{eff} is given kinetic energy of $(1/2)M m_p v_b^2$ by diode voltage U. Thus, $(1/2)M m_p v_b^2 = Z_{eff}\, eU$ where e is the electronic (or unit) charge 1.6×10^{-19} C. Hence

$$v_b = (2e/m_p)^{1/2}(Z_{eff}/M)^{1/2}U^{1/2} \quad (5)$$

Now, we take Eq. (4) and combine with Eq. (5). And noting that $\mu/[2.83\pi^2(e m_p)^{1/2}] = 2.75 \times 10^{15}$, we have the flux equation as follows:

$$J_b = 2.75 \times 10^{15} f_e/(MZ_{eff})^{1/2}\ln(b/r_p)/r_p^2(I_{pinch}^2/U^{1/2}) \text{ (ions} \cdot \text{m}^{-2} \cdot \text{s}^{-1}) \quad (6)$$

Then, the fluence is the flux multiplied by pulse duration τ, thus

$$\text{Fluence (ions/m}^2) = 2.75 \times 10^{15}\, \tau f_e/(MZ_{eff})^{1/2}\ln(b/r_p)/r_p^2(I_{pinch}^2/U^{1/2}) \quad (7)$$

We now compare Eq. (7) for fluence per shot with the equation for fluence derived for deuterons by Lee and Saw. In that paper, the pulse duration is taken as the pinch duration and hence is taken as proportional to anode radius which also has a proportional relationship to pinch length z_p. We may take pinch duration as 10 ns per mm pinch radius and pinch length is about 1 cm per mm pinch radius. Hence pinch duration is 1 μs per m pinch length giving $\tau = 10^{-6} z_p$, which gives a fluence of

$$\text{Fluence (ions/m}^2) = 2.75 \times 10^9\, \pi z_p f_e/(MZ_{eff})^{1/2}\ln(b/r_p)/(\pi r_p^2)(I_{pinch}^2/U^{1/2}) \quad (8)$$

Then for deuteron M = 2 and $Z_{eff} = 1$, take $f_e = 0.14$ (i.e. 14% of PIE is converted into BKE), we have:

$$J_b\tau = 8.5 \times 10^8\, I_{pinch}^2 z_p \ln(b/r_p)/(\pi r_p^2)U^{1/2} \text{ (ions/m}^2) \quad (9)$$

Equation (9) is exactly the same as Eq. (6) of the paper by Lee and Saw used to determine the deuteron ion beam fluence and flux. In other words starting from first principles we have derived exactly the same equation as Lee and Saw did using empirical formula derived with quantities all with proportional constants finally calibrated at a 0.5 MJ point of neutron yield. In this present derivation from first principles, we only need one additional condition $f_e = 0.14$ (the fraction of energy converted from PIE into BKE) and the approximate scaling $\tau = 10^{-6} z_p$. This additional condition of $f_e = 0.14$ is equivalent to ion beam energy of 3–6% E_0 for cases when the PIE holds 20–40% of E_0 as observed for Type 1 or low inductance plasma focus device [8]. We also conclude that the flux in Eq. (6) derived here is the more basic equation to use as it does not have to make any assumptions about the ion beam pulse duration. According to Eqs (6) and (7) the flux and fluence are dependent on $(MZ_{eff})^{-1/2}$, if all other pinch properties remain equal. From this simple dependence one would expect the flux and fluence to reduce as we progress from H_2 to D_2, He to Kr and Xe. However, the pinch properties (primarily the pinch

radius) change drastically for different gases at different regimes of operation due to thermodynamic and radiative effects. The change in r_p and the associated consequential changes in pinch dynamics and other properties, as computed from the code we use in this paper, have profound effects on modifying this simple dependence. Hence, we summarize the assumptions:

— Ion beam flux J_b is $n_b v_b$ with units of ions $\cdot$ m^{-2} $\cdot$ s^{-1};
— Ion beam is produced by diode mechanism;
— The beam is produced uniformly across the whole cross-section of the pinch;
— The beam speed is characterized by an average value v_b;
— The BKE is a fraction f_e of the PIE, taken as 0.14 in the first instance, to be adjusted as numerical experiments indicate;
— The beam ion energy is derived from the diode voltage U;
— The diode voltage is $U = 3V_{max}$ taken from data fitting in extensive earlier numerical experiments, where V_{max} is the maximum induced voltage of the pre pinch radial phase.

However for cases exhibiting strong radiative collapse, the strong radiative collapse generates an additional induced voltage Vmax*. This voltage is very large and from extensive numerical experiments appears to be a reasonable estimate of the beam ion energy from the point of view of the various energy distributions including the ion beam energy relative to the fast plasma stream energy. Hence the feedback from our extensive examinations of the data suggests that we take, in such cases, $U = V$max*.

The value of the ion flux is deduced in each situation for specific machine using specific gas by computing the values of Z_{eff}, r_p, I_{pinch} and U by configuring the Lee Model code with the parameters of the specific machine and specific gas [7]. The code and the procedure are discussed in more detail in a later section.

Once the flux is determined, the following quantities are also computed:

a) Energy flux or power density flow (W/m^2) is computed from $J_b \times Z_{eff}U$ converting from eV to J;
b) Power flow (W) is computed from energy flux × pinch cross-section;
c) Current density (A/m^2) is computed from J_b × ion charge eZ_{eff};
d) Current (A) is computed from current density × pinch cross section;
e) Ions per sec (ions s^{-1}) is computed from J_b × pinch cross-section;
f) Fluence (ions/m^2) is computed from $J_b \times \tau$
g) Energy fluence (J/m^2) is computed from $J_b \times \tau \times Z_{eff}U$;
h) Number of ions in beam (ions) is computed from fluence times the pinch cross-section;
i) Energy in beam (J) is computed from the number of ions in beam times $Z_{eff}U$;
j) Damage factor (W $\cdot$ m^{-2} $\cdot$ s$^{0.5}$) is computed from $J_b \times Z_{eff}U \times \tau^{1/2}$;
k) Energy of fast plasma stream (J).

Experimentally it is found that as the focus pinch starts to break up a fast shock wave exits the plasma focus pinch in the axial direction preceding the ion beams which rapidly catches up and overtakes it. Associated with this fast post-pinch axial shock wave is a FPS [9]. We estimate the energy of the FPS by computing the work done by the magnetic piston through the whole radial phase from which is subtracted twice the ion beam energy (the second count being for the oppositely directed relativistic electron beam which we assume to have the same energy as the ion beam) and from which is further subtracted the radiation yield of the plasma pinch.

1.2. Numerical experiments of plasma focus devices

Each of twelve machines was fitted using parameters (bank, tube and operation) supplied with a measured current trace. Where necessary the fitting of the code output current waveform to the measured current waveform also entailed adjustments [1, 2, 10] to the values of static inductance L_0 and stray resistance r_0. Examples of the detailed fitting of several machines had already been given in each of the progress reports. The results of the fitting are a set of model parameters f_m, f_c for the axial phase and f_{mr} and f_{cr} for the radial phase. Once fitted, the dynamics in terms of axial, radial speeds and trajectories are found as the plasma axial phase and radial phase, and the pinch plasma properties such as temperatures and densities and neutron yields (in D). Also computed are the properties (number, energy fluence and flux, power flow and damage factors, ion energy and current) of the FIB and the energies and properties of the FPS. The most important of the computed properties of the IAEA CRP plasma focus machines are listed in Table 1. The results of these and other numerical experiments carried out within the framework and duration of this IAEA CRP are listed in references [6, 7, 10–27]. Some validation

of our computations in regards to FIB and FPS properties in relation to the damage testing is presented in [16]. In particular our computed values of damage factor, power flow density and FPS energy [16] for the case of PF-400J agree with those reportedly measured by Soto et al. in [28].

TABLE 1. THE PARAMETERS OF THE IAEA CRP PLASMA FOCUS MACHINES

Parameters	units	PF1000	NX3	BARC	PF6	Bora	INTI	NX2T	PF12	Sofia	PF5M	PF400J	FMPF3
E_0	kJ	486	14.5	11.5	6.2	3.5	3.4	3.0	2.6	2.6	2.0	0.4	0.2
C_0	mF	1332	100	40.0	28.0	24.4	30.0	29.0	20.0	20.0	16.0	1.0	2.4
L_0	nH	33.0	50.0	65.0	21.0	54.0	110	20.0	80.0	80.0	33.0	40.0	34.0
r_0	mΩ	6.3	2.3	5.0	2.9	6.0	12.0	2.7	6.0	6.5	6.0	10.0	11.0
B	cm	16.0	5.2	6.1	5.1	2.5	3.2	3.8	2.7	3.1	2.6	1.6	1.5
A	cm	11.6	2.6	3.0	3.0	1.5	1.0	1.6	0.9	1.0	1.5	0.6	0.6
b/a	–	1.4	2.0	2.0	1.7	1.7	3.4	2.5	3.0	3.1	1.7	2.7	2.5
z_0	cm	60.0	16.0	7.7	4.0	6.0	16.0	4.5	7.2	14.5	5.0	1.7	1.7
V_0	kV	27.0	17.0	24.0	21.0	17.0	15.0	14.5	16.0	16.0	16.0	28.0	13.0
P_0	Torr	3.5	11.0	3.0	4.0	7.6	3.5	15.2	3.5	4.0	2.0	6.6	3.4
t_{rise}	µs	10.4	3.51	2.53	1.20	1.80	2.85	1.20	1.99	1.99	1.14	0.31	0.45
I_{peak}	kA	1846	564	482	584	305	180	402	187	198	258	129	96
I_{pinch}	kA	862	347	279	314	196	122	233	128	127	165	84	63
T_{pinch}	10^6K	1.1	1.6	1.6	1.3	1.0	7.2	1.7	5.4	6.2	7.4	6.5	1.4
$n_{i\ pinch}$	10^{23} m^{-3}	3.9	13.8	6.6	7.2	21.7	3.5	22.5	5.6	3.9	2.1	4.2	9.8
r_{min}	cm	2.23	0.40	0.46	0.54	0.23	0.13	0.23	0.12	0.14	0.22	0.09	0.1
z_{max}	cm	18.8	4.0	5.0	5.1	2.6	1.4	2.2	1.4	1.5	2.3	0.8	1.1
t_{pinch}	ns	255	46	52	60	33	7.6	33	8.3	8.7	12	5.1	11
V_{max}	kV	126	84	81.8	79.2	43.2	75.5	54.6	73.3	69.0	97.3	53.4	18.5
Y_n	10^8 n	1157	27.6	13.1	15.4	1.87	0.11	3.52	0.19	0.13	0.34	0.013	0.001
Fluence	10^{20} m^{-2}	5.75	8.29	4.79	4.31	7.77	2.14	10.7	2.73	2.37	1.41	1.68	2.98
Flux	10^{27} m^{-2}·s^{-1}	2.3	18.1	9.3	7.2	23.6	28.1	32.7	32.8	27.3	11.6	33.0	27.2
U	keV	126	84	82	79	43.2	74.1	54.6	73.3	66.3	97.3	53.4	18.5
En Fluence	10^7 J/m^2	1.16	1.12	0.63	0.55	0.54	0.25	0.94	0.32	0.25	0.22	0.14	0.09
En Flux	10^{13} W/m^2	4.56	24.5	12.1	9.18	16.4	33.4	28.6	38.6	29.0	18.1	28.3	8.08
P Flow	10^{10} W	7.14	1.23	0.79	0.85	0.26	0.18	0.48	0.19	0.18	0.28	0.07	0.02
Ions	10^{15}	899	41.5	31.3	40.0	12.5	1.15	18.1	1.33	1.45	2.21	0.39	0.77
En Bm	J	18201	561	410	508	86.4	13.6	159	15.6	15.4	34.4	3.3	2.3
I_{ion}	kA	564	145	97	107	60.7	24.1	88.6	25.6	26.7	29.0	12.2	11.2
DamFac	10^{10} W·m^{-2}·s$^{0.5}$	2.30	5.24	2.76	2.24	2.97	2.91	5.17	3.52	2.70	1.99	2.02	0.84
v_{ion}	cm/µs	347	284	279	275	203	266	228	265	252	305	226	133
FPS En	J	27214	1509	571	572	172	269	289	124	290	143	21.3	12.4
FPS En	% E_0	5.6	10.4	5.0	9.3	4.9	8.0	9.5	4.8	11.3	7.0	5.4	6.1
FPS sp	cm/µs	18.2	24.2	32.8	25.8	29.4	47.4	23.5	52.1	43.0	48.5	35.6	35.2
SF	kA/cm·Torr$^{-0.5}$	85.5	65.4	92.8	97.4	73.7	102	66.6	111	99.1	121	83.5	86.8
peak v_a	cm/µs	10.8	7.7	6.6	8.2	6.5	9.5	7.0	9.4	9.9	11.8	8.9	7.0
peak v_s	cm/µs	17.3	17.8	18.0	17.9	13.8	36.1	14.4	31.3	33.6	37.9	35.1	16.5
peak v_p	cm/µs	13.2	12.3	12.0	11.9	9.2	24.9	10.0	21.3	23.3	25.7	23.5	11.0
EINP	J	63616	2631	1391	1588	344	296	606	155	321	212	28.0	16.9
f_m	–	0.14	0.10	0.18	0.20	0.20	0.08	0.11	0.10	0.08	0.15	0.08	0.15
f_c	–	0.70	0.70	0.61	0.70	0.70	0.70	0.70	0.70	0.70	0.70	0.70	0.70
f_{mr}	–	0.35	0.25	0.43	0.50	0.55	0.16	0.38	0.26	0.16	0.20	0.11	0.55
f_{cr}	–	0.70	0.70	0.64	0.70	0.69	0.70	0.70	0.70	0.70	0.70	0.70	0.70

2. IRRADIATION OF PLANSEE DOUBLE FORGED TUNGSTEN SAMPLES

2.1. Background

Samples provided by the IAEA under this project were irradiated in the INTI PF. The irradiated samples were characterized to assess damage. The results of four 12 mm × 12 mm × 5 mm tungsten target samples that have been exposed by INTI PF operating at the intense focus regime (fast focus mode) are presented in the following sections.

2.2. Experimental set-up

INTI PF is a low energy 3 kJ plasma focus device [29]. It has a 16 cm length 0.95 cm radius copper anode, surrounded by six 16 cm length copper bars arranged to form a concentric cathode of radius 3.2 cm. Pyrex tube is used as an insulator between cathode base plate and anode bar. It uses a single capacitor rated at 30 μF, 15 kV, 30 nH. The static inductance of the discharge system is 110 nH. Its stainless steel vacuum chamber is evacuated by means of a 12 m^3/h rotary vacuum pump to a base pressure of 10^{-3} mbar. Then working gas is released into chamber at selected working pressure. For all four tungsten target samples, we fired INTI PF at 12kV and 2.5 Torr D. For sample TS1 we did not use a shutter. For the other three samples we used two shutters each with a 3 mm aperture as shown in Fig. 1. Experimental set-up for each tungsten target is presented in Table 2. All signals were recorded by 3034C 300 MHz oscilloscope. For tungsten TS1, Channel 1, 2, 3, and 4 of oscilloscope record d*I*/d*t*, X ray 1, X ray 2 and voltage signals respectively. For the other three samples Channel 1, 2, 3 and 4 record d*I*/d*t*, PMT scintillator, X ray and voltage. We positioned PMT tube 2.6 ± 0.01 m away from the tip of anode in a side on geometry and its applied voltage was -1600 V. INTI plasma focus sample holder is shown in Fig. 2 on the following page.

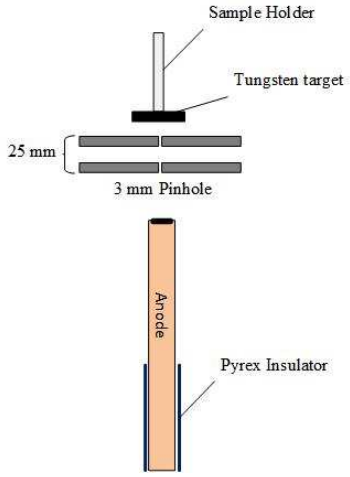

FIG. 1. Experimental set-up, adjustable sample holder and shutter for INTI PF.

TABLE 2. TUNGSTEN TARGET SAMPLES: EXPERIMENTAL SET-UP

Target Sample (TS)	V (kV)	Deuterium gas pressure (Torr)	Shutter	Target distance from Anode (mm)	Target distance from upper shutter (mm)	Number of shots	Target weight Before firing (±0.0001 g)	Target weight after firing (±0.0001 g)	δm (g)
1	12	2.5	No	40	–	1	13.6562	13.6559	-0.0003
2	12	2.5	Yes	40	2	5	13.6457	13.6457	0
3	12	2.5	Yes	80	15	10	13.4730	13.4731	+0.0001
4	12	2.5	Yes	60	5	10	13.6595	13.6597	+0.0002

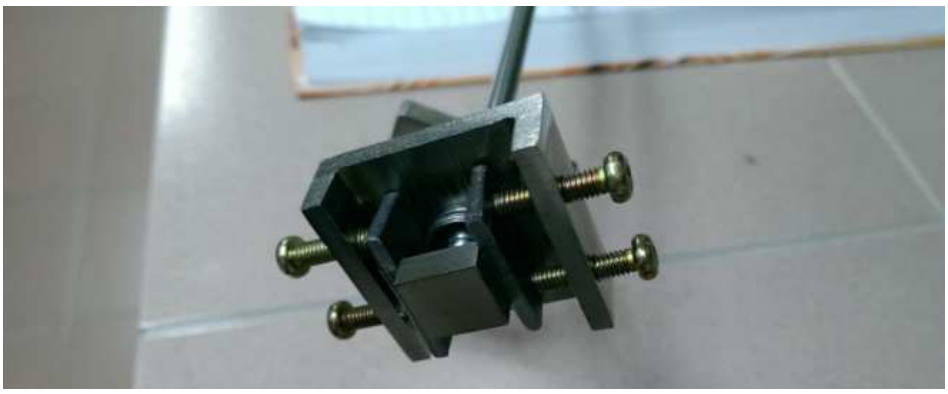

FIG. 2. INTI plasma focus adjustable sample holder.

The double aperture is 3 mm diameter while the small central spot (TS4 sample at 6 cm) is < 2 mm diameter (ion beam). The tungsten target samples are shown in Figs 3 and 4.

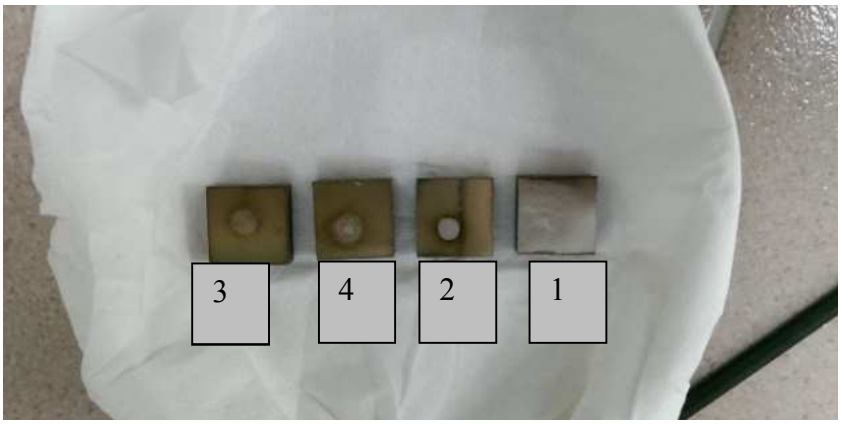

FIG. 3. Tungsten target samples TS1, TS2, TS4 and TS3 (right to left) after plasma focus irradiation.

Outer spot is ~4 mm diameter (FPS), and pinch x-section has diameter of 2.4 mm (computed)

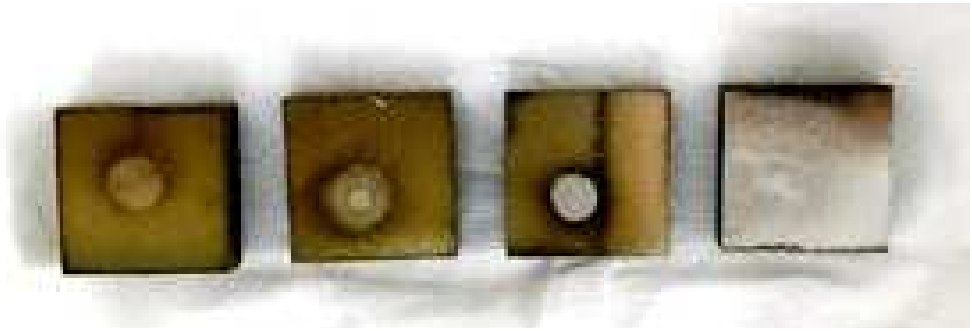

FIG. 4. Enlarged image of Fig 3.

Tungsten target sample TS1 was exposed with 12 kV, 2.5 Torr D with single shot without shutter. Magnified recorded signals for this shot are shown in Fig. 5. Model parameters of the shot are obtained by fitting computed current waveform to measured current waveform. The fitting based on Lee model code shows that these shots produce 3×10^6 neutrons. For each tungsten target sample a measured current waveform was selected for fitting

by the Lee model code. The resulting properties of the FIB and FPS are shown in Table 3. Lee model code fitted parameters and operational parameters of a shot for target sample TS1 are also given.

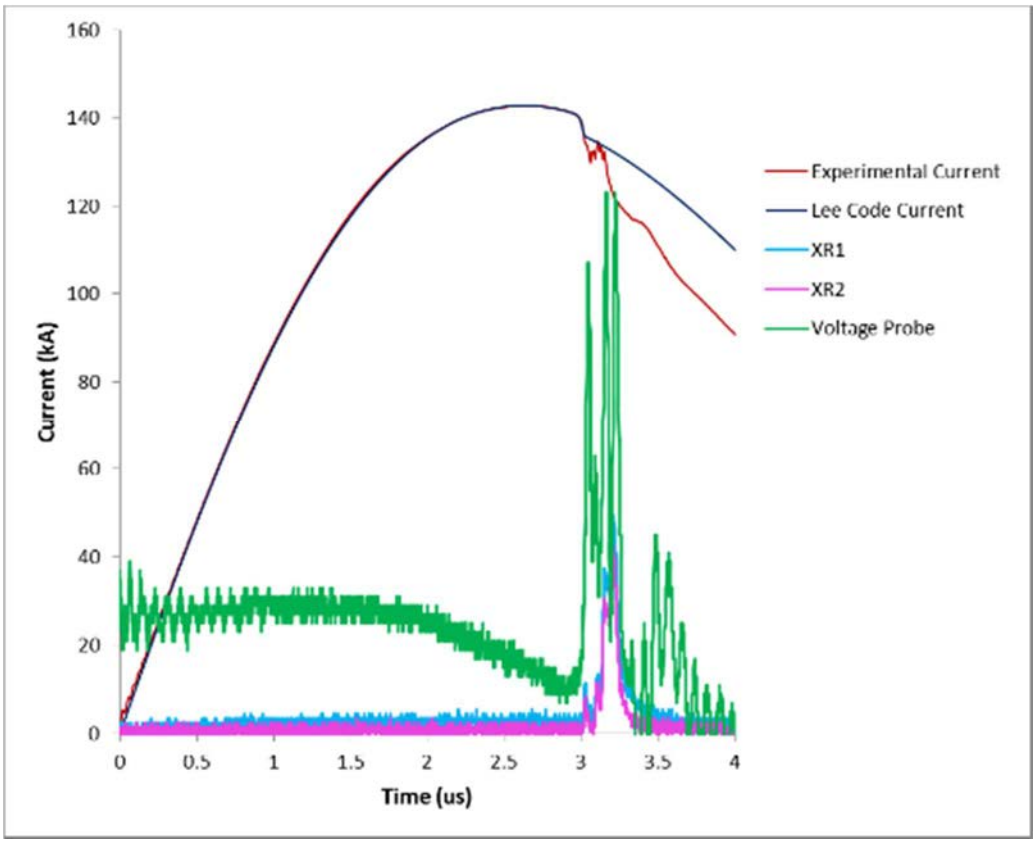

FIG. 5. INTI PF measured signals at 12 kV, 2.5 Torr Deuterium fitted by Lee model code (shot 295, sample TS1).

TABLE 3. MODEL AND OPERATIONAL PARAMETERS OF SHOT FOR SAMPLE TS1

massf	currf	massfr	Currfr	Fitted Model Parameters	
0.093	0.7	0.15	0.7		
V_0	P_0	MW	A	At-1 mol-2	Operational Parameters
12	2.5	4	1	2	

For tungsten sample TS2 we used shutter to reduce the shock wave effects on the surface. Each shutter has a central 3 mm aperture. The distance between apertures was 25 mm as shown in Fig. 1. The best recorded signal among five shots for this sample is presented in Fig. 6.

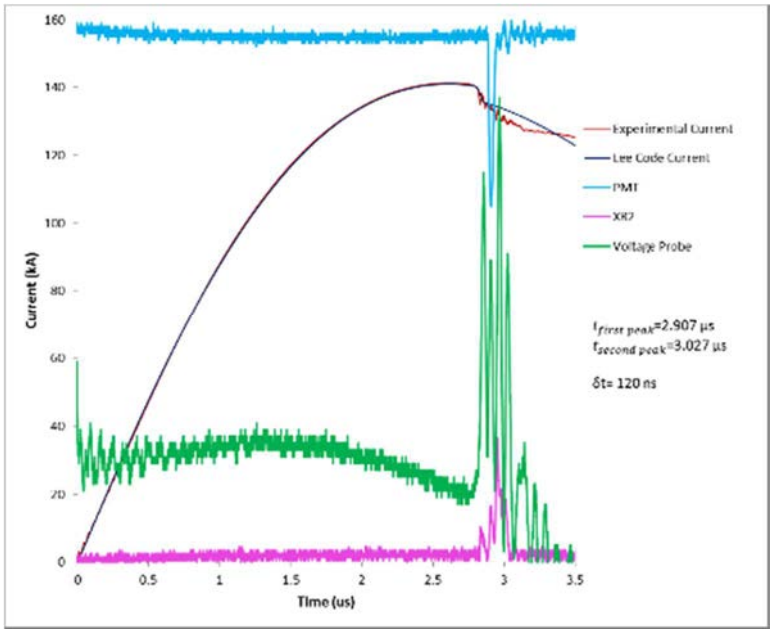

FIG. 6. INTI PF measured signals at 12 kV, 2.5 Torr Deuterium fitted by Lee model code (shot 300, sample TS2).

TABLE 4. FIB AND FPS DATA SIMULATED BY LEE CODE FOR SELECTED SHOTS

Parameter	Sample 1	Sample 2	Sample 3	Sample 4
b (cm)	3.2	3.2	3.2	3.2
a (cm)	0.95	0.95	0.95	0.95
c	3.4	3.4	3.4	3.4
z_0 (cm)	16	16	16	16
P (Torr)	2.5	2.5	2.5	2.5
V_0 (kV)	12	12	12	12
I_{peak} (kA)	143	141	140	141
I_{pinch} (kA)	96	96	95	96
v_a (cm/µs)	8.3	9.0	9.3	8.8
v_s (cm/µs)	34.5	34.5	34.4	34.6
v_p (cm/µs)	23.9	23.8	23.7	23.8
I/a (kA/cm)	150	148	148	149
SF (kA · cm^{-1} · $Torr^{-0.5}$)	95	94	93	94
FIB ion energy (keV)	56	56	56	56
FIB beam energy (J)	7.6	7.6	7.6	7.6
FIB energy flux (W/m^2)	1.8E14	1.8E14	1.8E14	1.8E14
FIB damage ftr ($W \cdot m^{-2} \cdot s^{0.5}$)	1.6E10	1.6E10	1.6E10	1.6E10
PS energy (J)	173	165	162	167
PS speed at pinch exit (cm/µs)	44	44	44	44
Plasma Footprint radius at exit (mm)	1.3	1.3	1.3	1.3
J_b flux ions ($m^{-2} \cdot s^{-1}$)	2.0E28	2.0E28	2.0E28	2.0E28
Fluence ions (m^{-2})	1.6E20	1.6E20	1.6E20	1.6E20
EINP	9	8	8	8
EINP1 work expended on pinch (J)	188	180	177	182
Ion Current (kA)	17.0	16.9	16.9	17.0
Current Density (A/m^2)	3.2E9	3.2E9	3.2E9	3.2E9
Number of ions per shot	8.5E14	8.4E14	8.4E14	8.4E14

Tungsten samples TS3 and TS4 were positioned at 8 cm and 6 cm away from the tip of anode, respectively. Ten shots were fired at each sample. Figs 7 and 8 show the best recorded signals of these samples.

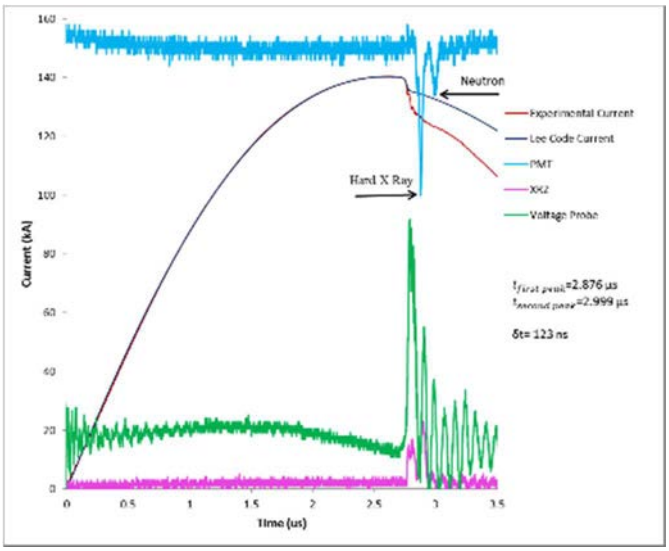

FIG. 7. INTI PF recorded signals at 12kV, 2.5 Torr Deuterium fitted by Lee model code (shot 310, sample TS3).

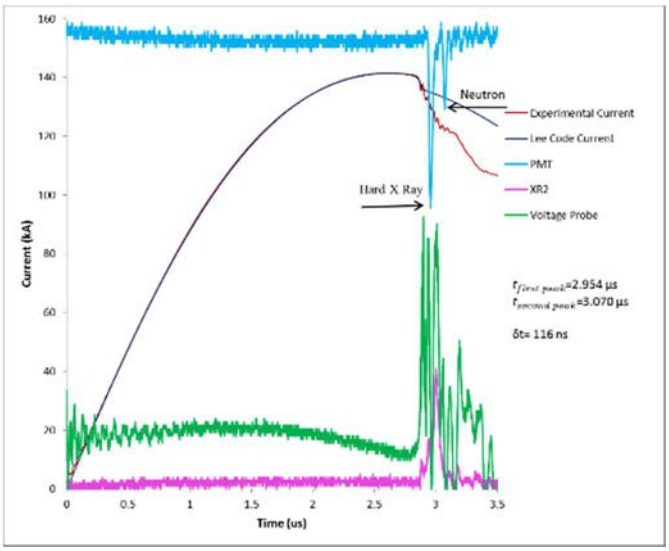

FIG. 8. INTI PF measured signals at 12 kV, 2.5 Torr Deuterium fitted by Lee model code (shot 312, sample TS4).

2.3. Results and discussion

We fired INTI PF 1, 5, 10 and 10 shots for tungsten target samples TS1 to TS4, respectively. Sample TS1 was exposed without shutter, however the others were exposed using shutter. All samples were analyzed by means of scanning electron microscopy (SEM) and energy dispersive spectroscopy (EDS) spectrum.

In Fig. 9, SEM image for sample TS1 shows cracks and also melting phenomena on the exposed surface. Damage area for sample 1 is much bigger than other samples, because there was no shutter to limit the damage area. EDS results shows there are around 92% tungsten and 8% carbon, iron and oxygen on bombarded surface.

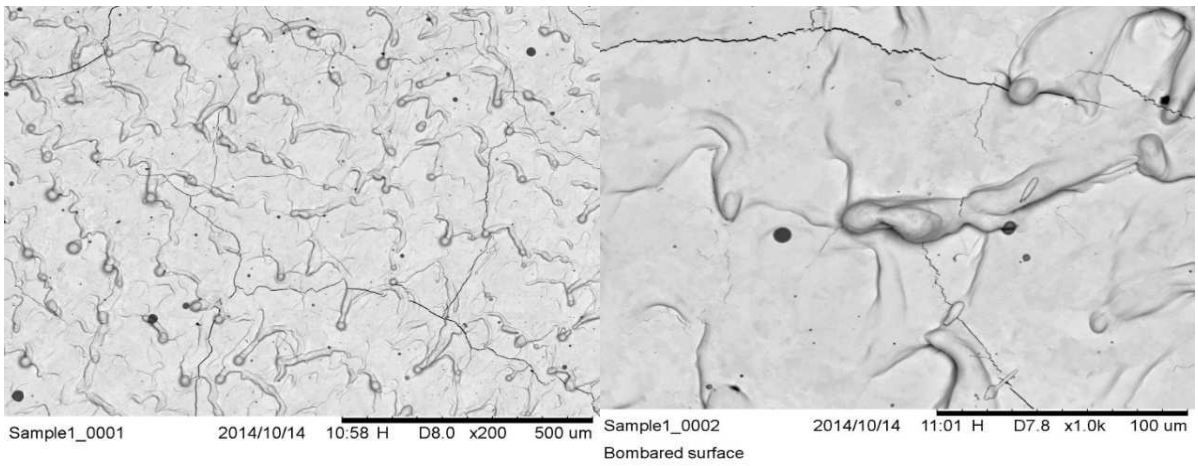

FIG. 9. SEM image of tungsten target sample 1. Single shot without shutter at 12 kV, 2.5 Torr D.

For sample TS2, as mentioned in Table 1, tungsten target sample 2, the distance between anode and target was 40 mm as sample 1. However, there was a steel shutter as shown in Fig. 1. SEM image after five shots shows that high energy ions generated by pinch, have sputtered shutter material which was detected on target surface.

All dark material on target surface is iron and carbon as shown in Fig. 10. EDS analyzes shows more than 72% iron on dark area. Because of high energy ions, there are a lot of holes and cracks on the surface. Holes dimensions are about 1–5 μm and almost all holes are accompanied by melting effects.

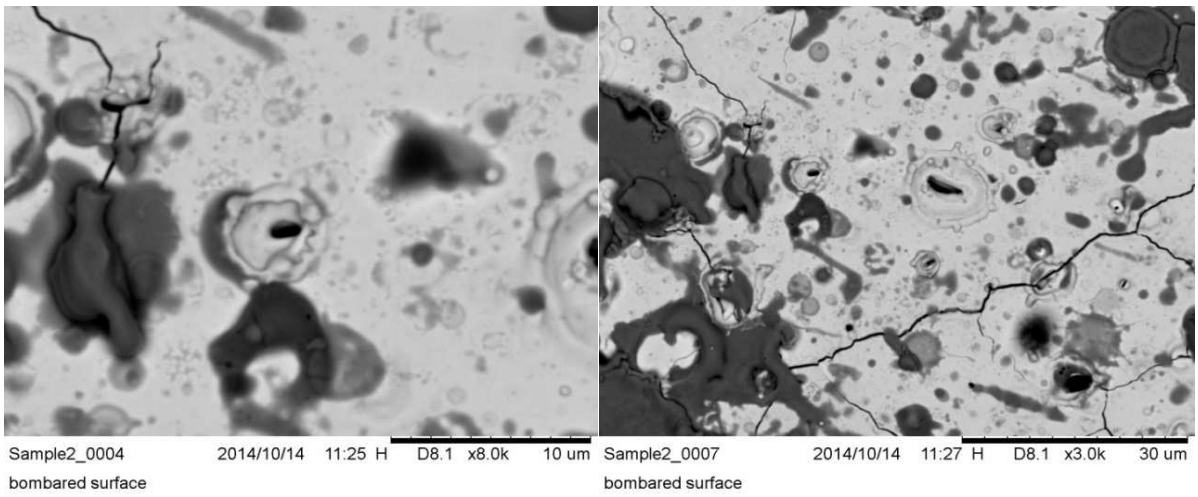

FIG. 10. SEM image of tungsten target sample 2 with 1.49 μm hole and cracks. Five shots at 12 kV, 2.5 Torr D.

For sample TS3, the distance between tungsten target and anode was 80 mm. Exposure was ten shots. SEM results show less damage on surface when compared with other samples. There are no significant holes or cracks on its surface. Similar to TS2, dark areas are found to be composed of iron while the dimensions of dark area are less than those for TS2. It is clear that target surface damage when placed near to anode tip is more than when the target is placed further away from the anode tip. EDS results show that more than 95% of dark areas consist of iron and carbon.

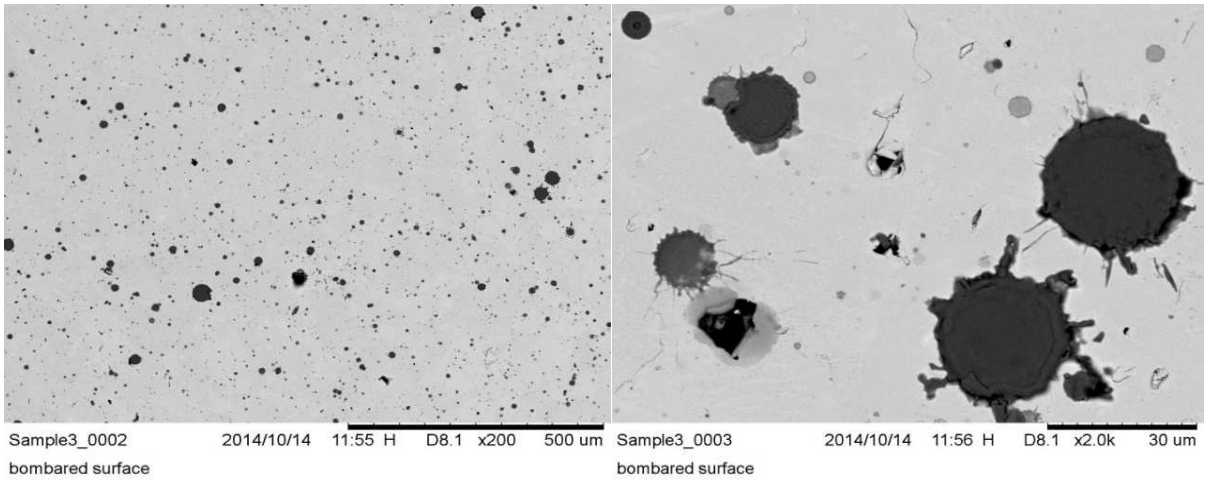

FIG. 11. SEM image of tungsten target sample 3 placed at 8 cm. Holes and cracks are much less than other samples. Ten shots at 12 kV, 2.5 Torr D.

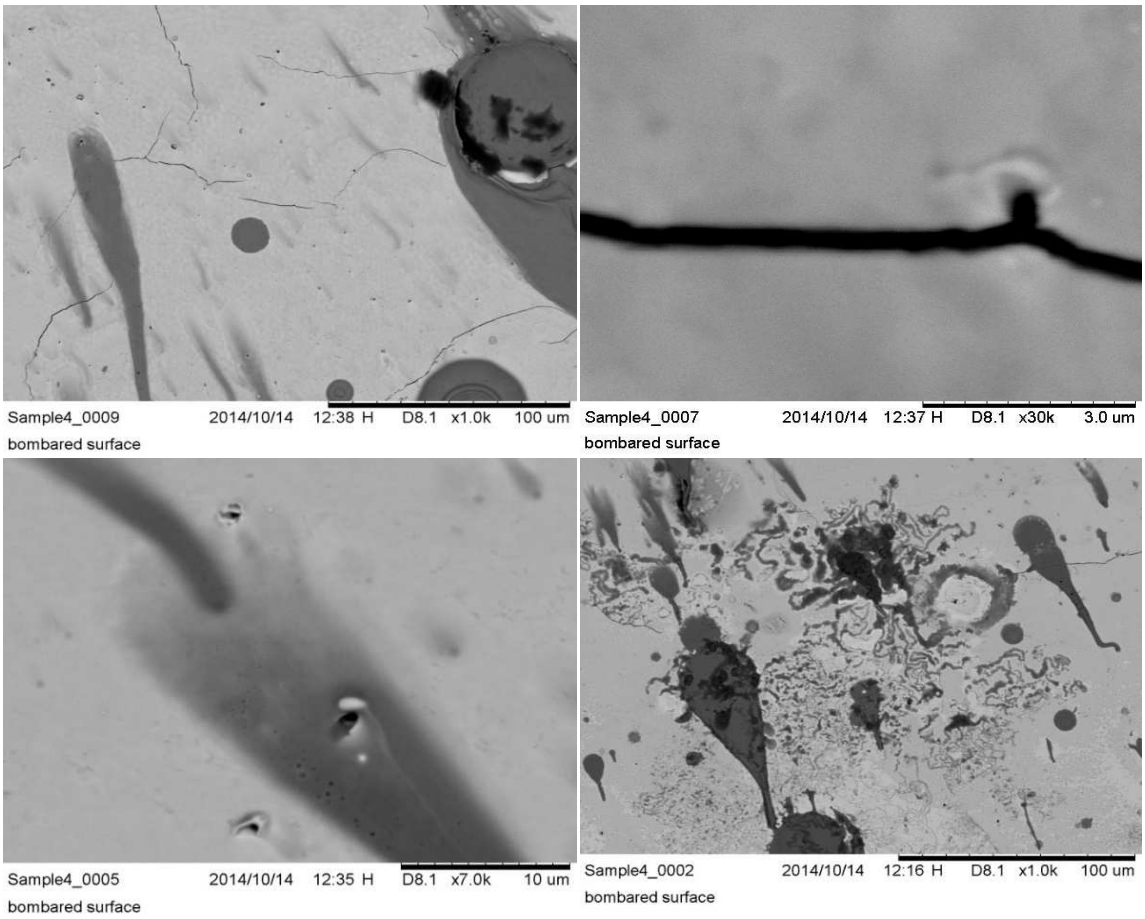

FIG. 12. SEM image of tungsten target sample 4 placed at 6 cm from anode tip. Exposure is ten shots at 12 kV, 2.5 Torr D.

For sample TS4, we positioned tungsten target sample 60 mm away from the tip of anode. We fired INTI PF ten shots at 12 kV, 2.5 Torr D. As shown in Fig. 2, there are two different damage areas on the surface. The central spot of TS4 (with diameter of just under 2 mm) which we tentatively assign to the FIB. The outer circular region of TS4 (with diameter of 4 mm) which we assign to the FPS. SEM results show that there are cracks and also holes at central area while there are no cracks and holes in the outer exposed area. The bigger distance between TS4 and anode in comparison with that of TS2 appears to have greatly reduced the damage on the surface of TS4

in comparison with that of TS2. The width of cracks and also dimensions of holes in TS4 are smaller than those in TS2. SEM results show the width of cracks for TS3 is around 300 nm and for holes are about from 500 nm to 1.5 μm as shown in Fig. 12. SEM images of tungsten target sample 4 shows melted area on its surface.

2.4. Summary

Four 12 mm × 12 mm × 5 mm tungsten target samples were exposed by INTI PF device at different distances from anode at the same operational parameters of PF at 12 kV, 2.5 Torr D. The current waveforms are fitted by the Lee model code yielding the plasma focus parameters. Fitting results show yield of 3×10^6 neutrons and 8.5×10^{14} ions per shot. Analysis shows the extent of damage on tungsten surface. Cracks up to 300 nm and from 500 nm to 5 μm holes together with signs of melting are found on the tungsten surfaces depending on their distances from the anode tip.

The code reveals that in these experiments (12 kV, 2.5 Torr D) INTI PF operates in fast focus mode producing 10^{14} ions (averaging 56 keV per ion) at pinch exit, capable of damage factor of 1.6×10^{10} $W \cdot m^{-2} \cdot s^{0.5}$ on a target at pinch exit. As a target is placed further and further away from the pinch exit, the ion beam is attenuated by collisions with plasma and gas along the path of the beam. There is also divergence of the beam. Thus by placing the targets at varying distances away from the pinch exit the damage and patterns of damage are varied. This is seen in the results presented in this paper.

These results indicate that near the pinch exit, the FIB has a footprint of just under 2 mm (not limited by the double aperture), while the FPS has a footprint of more than 4 mm being limited by the double aperture.

2.5. Conclusion

In the framework of INTI IU participation in this CRP, the Lee model code was extended to include computation of ion beam fluences and ion beam flux (respectively in units of ions/m^2 and ions $\cdot m^{-2} \cdot s^{-1}$), and ion beam energy fluence and energy flux (respectively in units of J/m^2 and W/m^2) and damage factors.

The extended Lee model code was then used to compute ion beam and used to simulate ion beam flux, average plasma parameters and radiation yields for various gases and plasma focus facilities, resulting in many papers published and presented at conferences. Numerical experiments were systematically carried out using available measured current signal from the plasma focus facilities used in irradiation experiments and the reference data tabulated. The participating plasma focus facilities studied are: PF1000, NX3, BARC PF, PF6, BORA, INTI PF, NX2T, PF12, University of Sofia PF, PF5M, PF-400J and FMPF3. Validation of our computations is reported in regards to FIB and FPS properties particularly damage factor, power flow density and FPS energy for the case of PF-400J. Our computed values agree with those reportedly measured by Soto et al. [28]. Irradiation of tungsten target using INTI PF was also carried out.

REFERENCES

[1] LEE, S., Plasma focus radiative model: review of the Lee model code, J. Fusion Energ. **33** (2014) 319.
[2] LEE, S., Radiative Dense Plasma Focus Computation Package (2007), http://www.plasmafocus.net, http://www.intimal.edu.my/school/fas/UFLF/
[3] GRIBKOV, V.A., et al., Plasma dynamics in the PF-1000 device under full-scale energy storage: II. Fast electron and ion characteristics versus neutron emission parametersn and gun optimization perspectives, J. Phys. D: Appl. Phys. **40** (2007) 3592–3607.
[4] LEE, S., SAW, S.H., Pinch current limitation effect in plasma focus, Appl. Phys. Lett. **92** (2008) 021503.
[5] LEE, S., SAW, S.H., Neutron scaling laws from numerical experiments, J Fusion Energ. **27** (2008) 292.
[6] LEE, S., SAW, S.H., Plasma focus ion beam fluence and flux scaling with stored energy, Phys. Plasmas **19** (2012) 112703.
[7] LEE, S., SAW, S.H., Plasma focus ion beam fluence and flux for various gases, Phys. Plasmas **20** (2013) 062702.
[8] LEE, S., SAW, S.H., ABDOU, A. E., TORREBLANCA, H., Characterizing plasma focus devices–Role of the static inductance–Instability phase fitted by anomalous resistances, J Fusion Energ. **30** (2011) 277.
[9] PIMENOV, V.N., et al., "Innovative powerful pulsed technique, based on a plasma accelerator, for simulation of radiation damage and testing of materials for nuclear systems", AT/P5-04, paper presented at International Topical Meeting on Nuclear Research Applications and Utilization of Accelerators, Vienna, Austria, 2009.
[10] SAW, S.H., LEE, S., "Plasma focus numerical experiments and BORA", ICTP 2370_6, paper presented at School and Training Course on Dense Magnetized Plasma as a Source of Ionizing Radiations, their Diagnostics and Applications, International Centre for Theoretical Physics, Trieste, Italy, 2012.
[11] SAW, S. H., Plasma focus ion beam-scaling laws, Int. J. Mod. Phys. Conf. Ser. **32** (2014) 1460317.
[12] SAW, S.H., LEE, S., Multi-scaling of the dense plasma focus, J. Phys. Conf. Ser. **591** (2015) 012022.

[13] AKEL, M., SALO, S. A., SAW, S. H., LEE, S., Characterization of oxygen ion beams emitted from plasma focus, Vacuum **110** (2014) 54.
[14] LEE, S., SAW, S.H., The slow focus mode in plasma focus for fast plasma stream nano-materials fabrication: selection of energy of bombarding particles by pressure control, Journal of Science, Engineering and Technology **10** (2014) 17.
[15] SAW, S.H., LEE, S., The plasma focus scaled for neutrons, soft X-rays, fast ion beams and fast plasma streams, Journal of Science, Engineering and Tech **10** (2014) 42.
[16] AKEL, M., et al., Deuterium plasma focus as a tool for testing materials of plasma facing walls in thermonuclear fusion reactors, J. Fus. Energ. **35** (2016) 694.
[17] SAW, S.H., Centre for Plasma Research, INTI International University, Nilai, Malaysia, unpublished data.
[18] SAW, S.H., LEE, S., "Numerical experiments universal plasma focus laboratory - The Lee model code", ICTP 2370_6, paper presented at School and Training Course on Dense Magnetized Plasma as a Source of Ionizing Radiations, their Diagnostics and Applications, International Centre for Theoretical Physics, Trieste, Italy, 2012.
[19] LEE, S., SAW, S.H., "Scaling laws for ion beam number (and energy) fluence and flux, paper presented at School and Training Course on Dense Magnetized Plasma as a Source of Ionizing Radiations, their Diagnostics and Applications, International Centre for Theoretical Physics, Trieste, Italy, 2012.
[20] SAW, S.H., LEE, S., "Scaling Trends for Deuteron Beam Properties at Plasma Focus Pinch Exit", paper presented at International Symposium on Plasma Focus in series SPFE2013 INTI International University, Nilai, Malaysia, 2013.
[21] LEE, S., SAW, S.H., "Scaling of ion beams from plasma focus in various gases, paper presented at International Symposium on Plasma Focus in series SPFE2013 INTI International University, Nilai Malaysia, 2013.
[22] SAW, S.H., "Plasma focus ion beam scaling Llaws, paper presented at International Conference on Plasma Science and Applications, Singapore, 2013.
[23] SAW, S.H., LEE, S., "A plasma focus regime to improve nano-materials deposition - The slow focus mode", paper presented at Conference on Plasma Focus, Malaysia, 2014.
[24] LEE, S., SAW, S.H., "The slow focus mode in plasma focus for fast plasma stream nano-materials fabrication: selection of energy of bombarding particles by pressure control", paper presente at International Conference on Plasma Science and Applications, Kathmandu, Nepal, 2014.
[25] SAW, S.H., LEE, S., "The plasma focus scaled for neutrons, soft X rays, fast ion beams and fast plasma streams", paper presented at International Conference on Plasma Science and Applications, Kathmandu, Nepal, 2014.
[26] SAW, S.H., LEE, S., "Radiative cooling and collapse in the plasma focus", paper presented at 22nd IAEA Technical Meeting on Research Using Small Fusion Devices, Prague, Czech Republic, 2015.
[27] SAW, S.H., DAMEDIH, V., LEE, S., "60 kJ dual plasma focus – Concept, design and installation", paper presented at Conference on Plasma Focus, Malaysia, 2015.
[28] SOTO, L., et al., Characterization of the axial plasma shock in a table top plasma focus after the pinch and its possible application to testing materials for fusion reactors, Phys. Plasmas **21** (2014) 122703.
[29] LEE, S., et al., A simple facility for the teaching of plasma dynamics and plasma nuclear fusion, Amer. J. Phys. **56** (1988) 62.

EXPERIMENTAL INVESTIGATIONS OF DAMAGE CHARACTERISTICS PRODUCED BY HOT PLASMA AND FAST ION BEAMS

V.A. GRIBKOV[*1], M. PADUCH[*], E. ZIELIŃSKA[*], M. SCHOLZ[*], L. KARPIŃSKI[*], K. TOMASZEWSKI[*], B. BIENKOWSKA[*], M. CHERNYSHOVA[*], V.M. PIMENOV[1], E.V. DEMINA[1], M.J. SADOWSKI[2], E. SKLADNIK-SADOWSKA[2], R. KWIATKOWSKI[2], A.V. DUBROVSKY[3], T. LAAS[4], V. SHIROKOVA[4], I. GARKUSHA[5], V. MAKHLAI[5], M. LADYGINA[5], V.I. KRAUZ[6], V.N. MITROFANOV[7], A. TALAB[8]

Abstract

We have elaborated, manufacture and put into operation an upgraded version of the PF-1000 facility (PF-1000U) supplying it by a gas puff system, and we have continued the development of diagnostics capabilities of the PF-1000 laboratory. In particular we have developed absolutely calibrated miniature magnetic probes able to work in hot plasma and near the centre of the device's anode, 16-frames laser interferometry, 4-frame X ray pinhole camera. Physical processes taking place during the irradiation of targets in the PF-1000U facility chamber were under research. Measurements of structures of a plasma sheath and a current flowing through the pinch as well as two components (longitudinal and azimuthal) of magnetic field generated in close vicinity to the plasma column have been investigated by the above tools. We applied for the aims of examination of secondary plasma, which is produced near the target surface by powerful streams of hot plasma and fast ions after the pinch phase, a 1 ns, 4-frame self-luminescence and a laser interferometric 16-frames techniques, as well as spectroscopic method. Using the PF-1000U facility we have carried out experiments on parallel and sequential irradiation of a number of mock-ups, perspective in the mainstream technology for fusion energy reactors of both types with magnetic and inertial plasma confinement. Among them there are tungsten grades, samples of carbon based composites and some other materials, intended for use as the first wall and constructive elements in fusion reactor chambers. We irradiated materials supplied by the IAEA and by our partners, as well as our own specimens. Our irradiation conditions were provided by namely the same heat carriers (hot plasma and fast ions) having the same parameters as expected on the first wall of the nuclear fusion reactors. Taking part in the round robin tests of these materials we have collaborated with our CRP partners. Besides the PF-1000U device, we used for irradiation of identical specimens the facilities of our collaborators, some other dense plasma focus devices and plasma accelerators such as QSPA, PF-6 device, PF-5M, Bora, and PF-12 in parallel and sequential experiments. We have executed analytical investigation of tungsten based and other specimens irradiated during the period of the current project. We used optical and scanning electron microscopy, X ray elemental and structural analysis, weighing of samples before and after irradiation.

1. INTRODUCTION

Throughout the duration of the CRP, our experimental efforts at the PF-1000U facility on plasma accelerator of the dense plasma focus (DPF) type [1] were concentrated in five fields [2-14], with attention to:

- Upgrading the PF-1000 facility and developing its diagnostic complex;
- Investigations of physical processes taking place in the device itself;
- Examination of physical events induced by powerful hot plasma and fast ion streams at the irradiation of targets in a DPF chamber;
- Providing the irradiation sessions of perspective materials for use in the first wall and constructive elements of nuclear fusion reactors (NFR);
- Analytical investigation of the irradiated mock-ups.

During the whole period of the current CRP activity, the ICDMP facility has hosted in the PF-1000U laboratory the researchers from more than ten laboratories of the DMP community (see our list of mutual publications). We present here the most important results obtained at the ICDMP laboratory mainly in the frame of the tasks formulated from 2011 to 2015 on these investigations.
The device PF-1000U (Fig. 1) was operated at the bank energy in the interval between 170kJ and 600 kJ with a discharge current in the range between 1 and 2 MA.

[*] Institute of Plasma Physics and Laser Microfusion, Warsaw, Poland.
[1] Institute of Metallurgy and Material Science, Moscow, Russian Federation.
[2] National Centre for Nuclear Research, Otwock/Swierk, Poland.
[3] Moscow Physical Society, Moscow, Russian Federation.
[4] School of Natural Sciences and Health, Tallinn University, Tallinn, Estonia.
[5] Institute of Plasma Physics, NSC KIPT, Kharkov, Ukraine.
[6] National Research Centre Kurchatov Institute, Moscow, Russian Federation.
[7] Troitsk Institute for Innovation and Fusion Research, Troitsk, Moscow, Russian Federation.
[8] Atomic Energy Authority, NRC, Plasma Physics and Nuclear Fusion Department, Egypt.

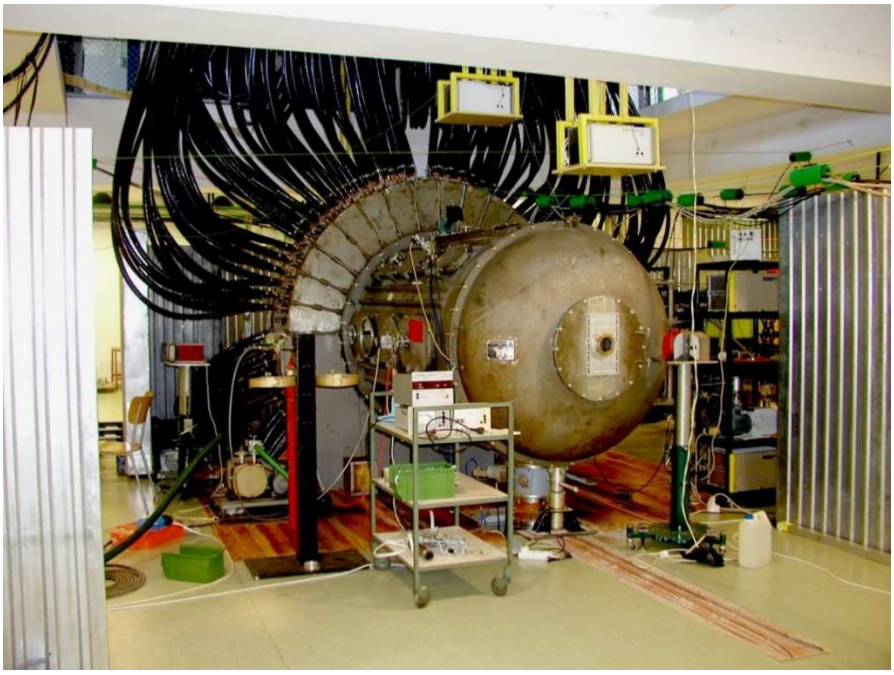

FIG. 1. The discharge chamber of the PF-1000U facility with a collector connecting the chamber by means of cables with the capacitor bank (located in the other floors of the building) and some parts of the diagnostic complex.

Among the irradiated specimens we had tungsten (samples of double forged tungsten supplied to participants of the current CRP by the IAEA and FZJ) and its alloys, carbon based composites, low activated stainless steels and some other mock-ups provided to us by IMET and TU, as well as our own materials.

As it was shown in the experiments [10–14] the irradiation of solid state targets by pulsed streams of fast ions (FI) and high temperature plasma (HTP), in the devices of the plasma accelerator type, makes possible to perform a powerful action upon their surface layer (SL) and in the bulk of a material. This impact produces changes in target composition, structure, and properties. Realization of maximum values of the streams of the radiation types specified above allows performing tests of materials, which can be used in controlled nuclear fusion reactors of both types with magnetic plasma confinement (MPC) and inertial plasma confinement (IPC).

The use of an accelerator device of the DPF type for these problems ensures generation of directed streams of fast ions of the energy $E_i \sim 0.1–1.0$ MeV (for deuterons) and of hot deuterium plasma with its temperature $T_{pl} \sim 0.1–1.0$ keV having extremely high power flux densities Q (up to $Q_{FI} \sim 10^{16}$ and $Q_{HTP} \sim 10^{14}$ W/m^2 respectively). These parameters allow using devices of the DPF type with a relatively low power supply (between 5–500 kJ) in comparison with the full scale prototypes of reactors of the above types for modelling the conditions on the first wall of the latter. Moreover, it can be fulfilled in this case exactly by the same radiation types and with parameters identical (or even higher) to those realized on the first wall of the contemporary and future fusion facilities.

At the same time, using the optimum choice of the irradiation mode, it is possible to get a modified SL of a target with improved mechanical and corrosion properties, as well as with higher radiation stability of the irradiated material. It was shown in [10-14] that by using a DPF device, it is possible to modify not only an external SL of the processed product, but also an internal one, which is not easily accessible. In particular, it has been demonstrated by the example of the irradiation of hexahedral hollow tubes, made of low activated austenitic steel and placed along the axis of the DPF chamber in front of the anode, that it is possible to create a strengthened modified SL both along the external and internal surfaces of a rather extended tube cavity. The relevant changes of the structural phase state of the alloy and topology of the irradiated surface alongside with the possibility of ion-plasma doping of the surface layers open new prospects for a gain of better mechanical and physicochemical properties of materials.

The experiments were performed at the location of samples under tests near the axis of a working chamber of the DPF device in front of the anode. The methodology of the experiments, which were performed on the DPF device PF-1000U, and the irradiation modes are presented in the next chapter.

2. IRRADIATION EQUIPMENT AND ANALYTICAL METHODS

2.1. The PF-1000U device and its metrology

Our PF-1000 facility was upgraded during the reporting period (PF-1000U). We have made a special gas puffing system [2, 9] that gives us an opportunity to inject gas in the central part of the anode. The main experimental chamber was filled up with the pure deuterium under the pressure between 1 and 3 Torr. The gas puff system was triggered between 1 and 2 ms before the initiation of the discharge. The gas valve injected about 1 cm^3 of pure deuterium (grade 99.7%, containing < 5000 ppm of the deuterium hydride, < 200 ppm of the hydrogen, and < 2 ppm in total of hydrocarbons). Since the mechanical valve was open for at least several milliseconds, a gas inflow occurred practically during the whole plasma discharge. The plasma discharges were supplied from a large 1.32 mF condenser bank charged up to the initial voltage between 16 and 30 kV, which corresponded to the bank energy between 0.17 and 0.60 MJ. The maximum discharge current in this set of experiments amounted to 2 MA. However the main part of the experiments were performed at the charging voltage within the range between 16kV and 23 kV with stored energy between 0.17 and 0.35 MJ and currents on the level of 1.5 MA.

The facility is equipped with a contemporary diagnostic complex containing six silver neutron activation counters, beryllium, indium and germanium activation detectors, six fast hard X ray/neutron probes based on photomultiplier tubes plus scintillators (PMT+S probes) for tracing the temporal behavior of hard X ray/neutron radiations, Cherenkov detectors for examination of fast electrons, 4-frame 1 ns self-luminescence recorder (visible range, time interval between frames of 20 ns), Rogowski coil and four magnetic probes placed at 90° to each other at the collector part near the main DPF anode's insulator, etc. New diagnostics that we have implemented during the four years period of CRP were:

a) Optical emission spectroscopic technique (temporal resolution of 50 ns);
b) Pin diode array (four pin diodes covered with Be foils of 7 μm and 10 μm thickness for estimation of plasma temperature using soft X ray emission, temporal resolution of 1 ns);
c) 4-frame vacuum ultraviolet soft X ray (VUV-SXR) pinhole camera for visualizing both primary and secondary plasmas (time resolution of 1 ns)
d) 16-frame laser interferometric technique (second harmonic of Nd-glass laser, exposure time is 1 ns, intervals between frames from 10 to 20 ns).

All these methods have high spectral, spatial and angle resolution. Another new diagnostic technique was intended for providing experiments with use absolutely calibrated magnetic probes to measure dynamics of current and magnetic fields (both azimuth and axial ones) throughout the rundown and implosion phases of plasma current sheath (PCS) at the PF-1000U facility [8]. Here we describe the results of the experiments obtained by these probes in combination with a 1 ns 16-frame laser interferometry to investigate in parallel the dynamics and evolution of plasma and current density in this PCS [3]. These measurements were also supported by neutron detectors:

- Silver activation detectors for the total neutron yield measurements in six directions that were absolutely calibrated in situ by AmBe source;
- Beryllium activation detector;
- Indium activation method;
- Time resolved measurements provided by PMT+S technique giving information on the neutron time of flight (TOF) characteristics.

A miniature magnetic probe located near the system axis on the anode lid is subjected to intense radiation and particle fluxes and, therefore, is destroyed during one shot. Before each subsequent discharge, it is necessary to replace the destroyed probe with a new one.

FIG. 2. Geometry of the electrodes at the PF-1000 facility and arrangement of the magnetic probes.

For this purpose, a vacuum lock was created to introduce the probe in the axial region of the system without violating vacuum conditions in the discharge chamber of the facility. This is necessary for the initial discharge parameters (the gas pressure, the concentrations of admixtures in the working gas, etc.) to remain them unchanged, because the PF discharge is very sensitive to these conditions. The probes were introduced from the collector side through the vacuum lock along the axis of the hollow anode.

The system design allowed one to place the sensitive element of the probe near the system axis, namely, near the anode surface at radii of 1.2 and 4 cm and at a distance between 0.5 and 1.5 cm from the surface of the end flange of the central electrode (anode). The arrangement of the probes in the discharge chamber is shown in Fig. 2. It should be noted that, in these experiments, the anode was at a high voltage. In this case, high voltage breakdown may occur between the anode and the probe, which can lead not only to the probe destruction, but also to a damage of the recording system. To prevent high voltage breakdowns onto the probe, a special measurement scheme was used, in which the entire 'probe oscilloscope' measurement channel was under the anode potential.

The question naturally arises concerning the characteristic scale length and relaxation time of the induced plasma perturbation. The papers devoted to studying the problem of supersonic flow around bodies of different shapes by magnetized plasma in high-current discharges are few in number. In our experiments, we used two probe modifications with a plane case (0.5×3 mm^2) and a cylindrical case (with a diameter between 2.0 and 2.5 mm).

The perturbations introduced by the probes were studied using laser interferometry. Figs 3 and 4 show interferograms obtained in discharges with a plane probe (shot No. 9120) and a cylindrical probe (shot No. 9127) correspondingly for the same initial conditions (D_2, P_0 = 1.8 Torr, U_0 = 24 kV and W_0 = 380 kJ). Fig. 3(a) relates to the time, at which the PCS passes the probe.

The magnetic probe diagnostics of plasma is a contact method, which assumes the plasma impact on the probe and vice versa. In other words, we are dealing with the plasma perturbation introduced by the probe. In this case, the problem of flow of magnetized plasma around a probe is of primary importance. The accuracy and time resolution of magnetic probe measurements depend on whether the magnetic field has enough time to diffuse from the plasma into the probe body. The situation is especially complicated in the case of supersonic flow around the probe by plasma with a frozen-in magnetic field, accompanied by the formation of a shock wave.

After passing the plane probe, the PCS perturbation occupies a narrow region (~ 1 mm) width along the radius, Fig. 3(b), and 40 ns later the perturbation completely vanishes, see Fig. 3(c).

The plasma perturbation introduced by a cylindrical probe is wider (~ 4 mm) which is about 1.6 of the probe size, see Fig. 4. Although the PCS perturbation in this case is larger than that introduced by the plane probe, it rapidly decays as the PCS propagates toward the system axis.

An even larger PCS perturbation is observed in experiments performed with a cylindrical probe at a higher gas pressure value (P_0 = 2.4 Torr, Fig. 5). The size of the perturbed region behind the PCS just after it has passed the probe is ~ 6 mm, Fig. 5(a), which is about 2.5 of the initial probe size. After 30 ns, the size of the perturbed region behind the PCS decreases to ~ 2.5 mm, see Fig. 5(b) and, after another 40 ns, the perturbation practically vanishes, see Figure 5(c). In this case, an unperturbed pinch is observed on the axis; see Figure 5(d).

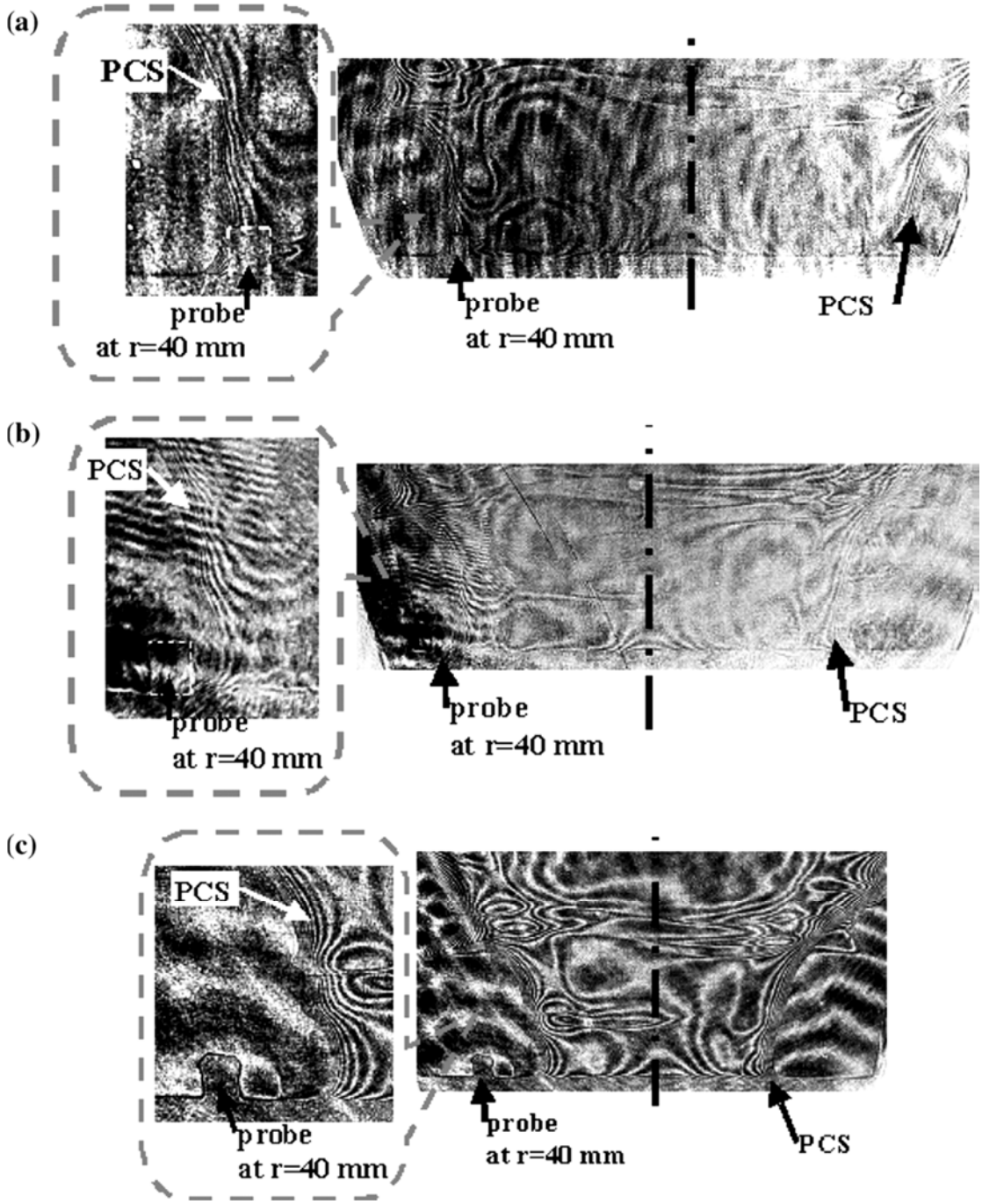

FIG. 3. (a) 5824 ns; (b) 5844 ns; (c) 5884 ns. PCS interferograms recorded near the system axis in the shot No. 9120 (D_2, P_0 = 1.8 Torr, U_0 = 24 kV and W_0 = 384 kJ) with plane probe at different instants from the beginning of the discharge. The neutron yield is $Y_n \sim 1.3 \times 10^{11}$ neutrons/shot.

It should be noted that the radial probe size with account of the projection onto the observation direction is ~ 3.5–4 mm, which is somewhat larger than the initial probe size. This can be related to the residual PCS plasma and the plasma formed on the probe surface under the action of radiation in the final stage of plasma compression. This plasma can shield the probe and make an appreciable impact on the accuracy of the measurement of the magnetic fields. The degree of this influence strongly depends on the probe shape.

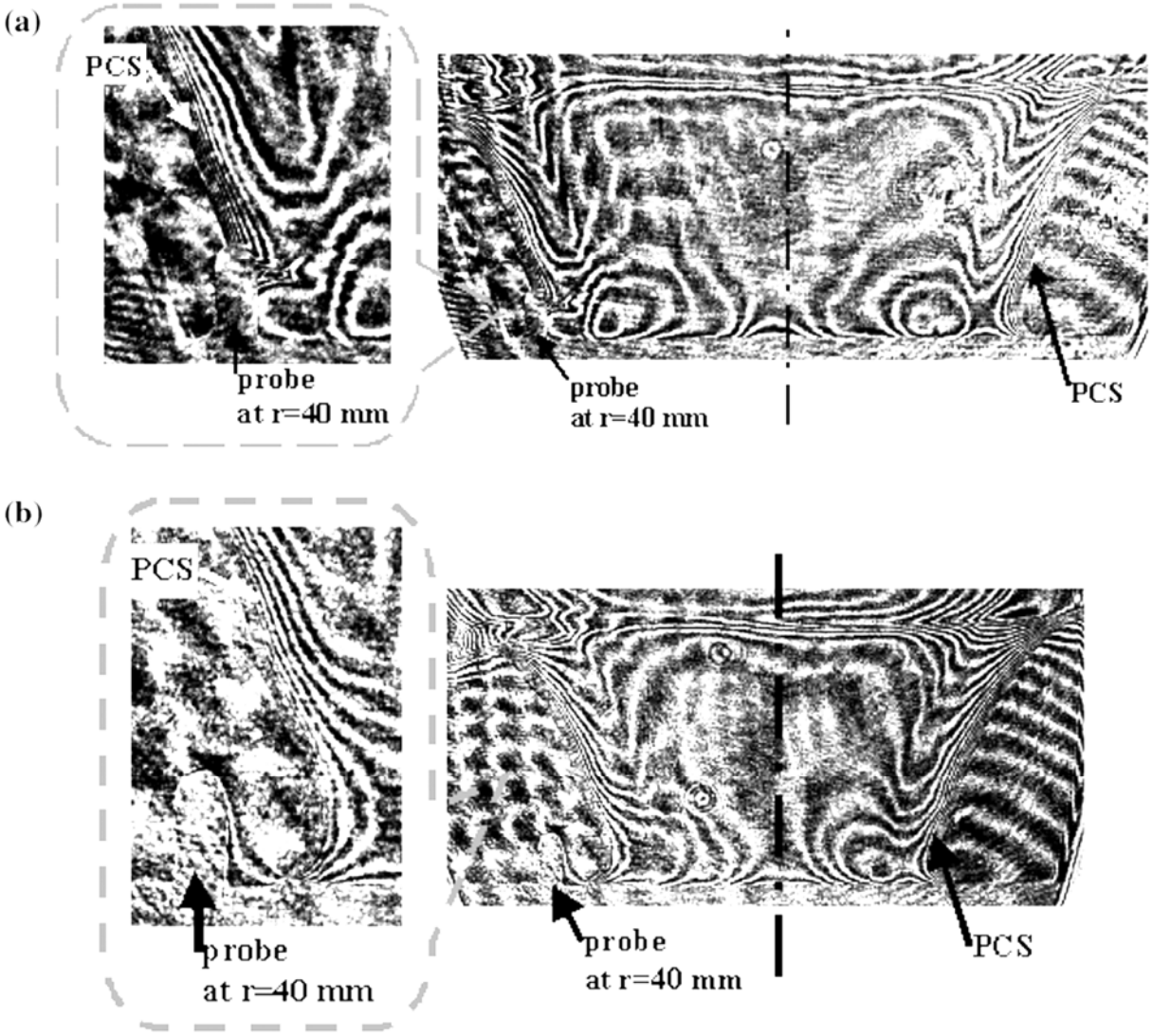

FIG. 4. (a) 5793 ns; (b) 5913 ns. PCS interferograms recorded near the system axis in the shot No. 9127 (D_2, P_0 = 1.8 Torr, U_0 = 24 kV and W_0 = 384 kJ) with cylindrical probe at different instants from the beginning of the discharge. The neutron yield is $Y_n \sim 1.7 \times 10^{11}$ neutrons/shot.

The influence of the plasma flow with a frozen-in magnetic field on the probe signal for probes of different shapes was numerically modelled [15]. As it follows from these calculations magnetic field perturbations introduced by a plane probe are about 7%. It was found that the measurement error of probes with a plane screen is less than that of probes with a conventional cylindrical screen. For a cylindrical probe having a diameter equal to 1 mm, this error is already 25%. This result was confirmed experimentally on the Angara-5-1 facility.

The following important conclusions can be drawn from these results:

— In the case of a plane probe, the PCS perturbation is much smaller than in the case of a cylindrical probe (it is necessary to take into account the quantitative measurements);
— In spite of a relatively large plasma perturbation introduced by a cylindrical probe, it rapidly relaxes as the PCS propagates toward the axis, so no perturbation introduced by the probe is observed near the axis;
— The probe parameters do not render an essential influence on its time characteristics;
— It allows using the probes of the cylindrical shape, for example, the magneto-optical probes [3], for studies of the PCS structure.

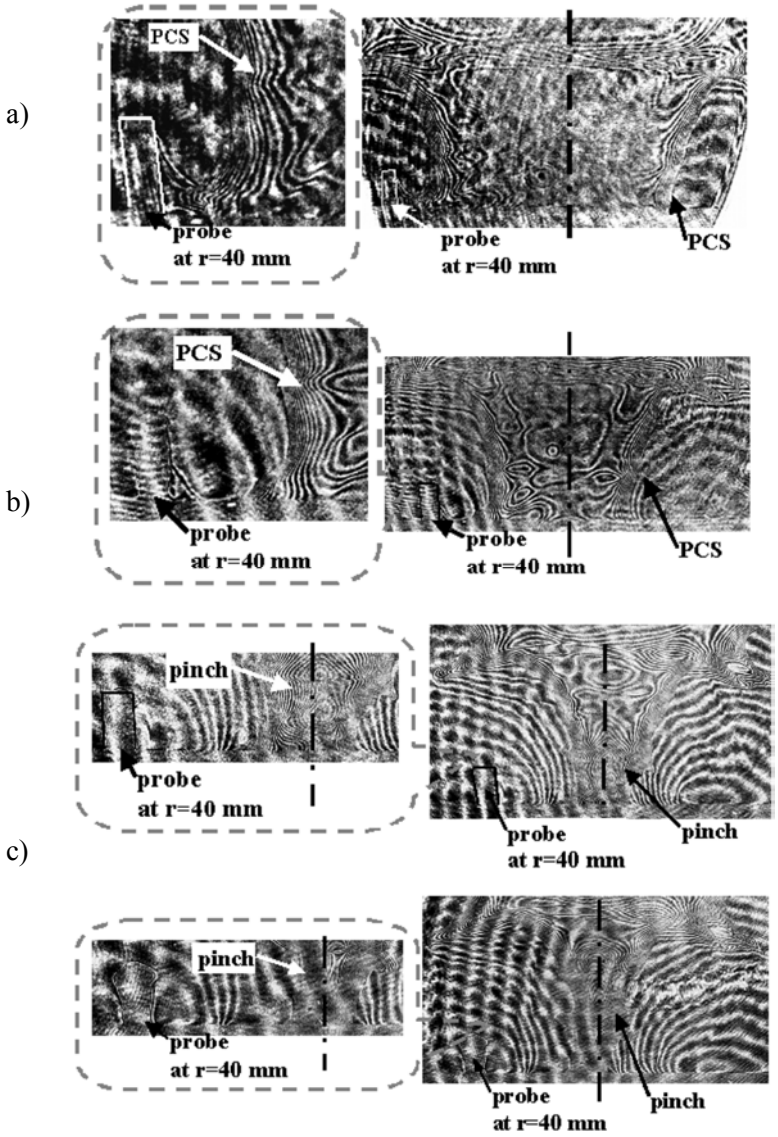

FIG. 5. (a) 6479 ns; (b) 6509 ns; (c) 6549 ns; (d) 6569 ns. PCS interferograms recorded near the system axis in the shot No. 9131 (D_2, P_0 = 2.4 Torr, U_0 = 24 kV and W_0 = 384 kJ) with cylindrical probe at different instants from the beginning of the discharge. The neutron yield is $Y_n \sim 8.7 \times 10^{10}$ neutrons/shot.

The dynamics of the azimuthal magnetic field during PCS radial compression was investigated in four experimental sessions with different initial conditions [8]. Taking into account that the number of shots was limited by the number of available probes, the first experiments were performed in a well reproducible mode with deuterium at an initial pressure of P_0 = 3 Torr and a discharge voltage of U_0 = 27 kV. In these experiments, the stored energy was about 485 kJ. Before each shot with the magnetic probe, a series of conditioning discharges were performed until the neutron yield became higher than 10^{10} neutrons/shot. Since the probes were destroyed in each shot, the working gas in the chamber was usually refreshed before the next experiment. In Fig. 6, the typical oscilloscope traces obtained by the above magnetic probes during the discharge. By means of the above probes we have investigated the distributions of the current density and plasma structure over the PCS thickness obtained for three typical discharges [3]. Analysis of these distributions allows us to draw the following conclusions. First of all, the PCS in the final stage of plasma compression is rather compact. At low gas pressures, the FWHM of the magnetic piston is as small as 0.5 cm and its full width is about 1 cm. Apparently these are the upper estimates, because the average propagation velocity of the PCS from the probe to the axis used in our estimates can be higher than the PCS velocity near the probe.

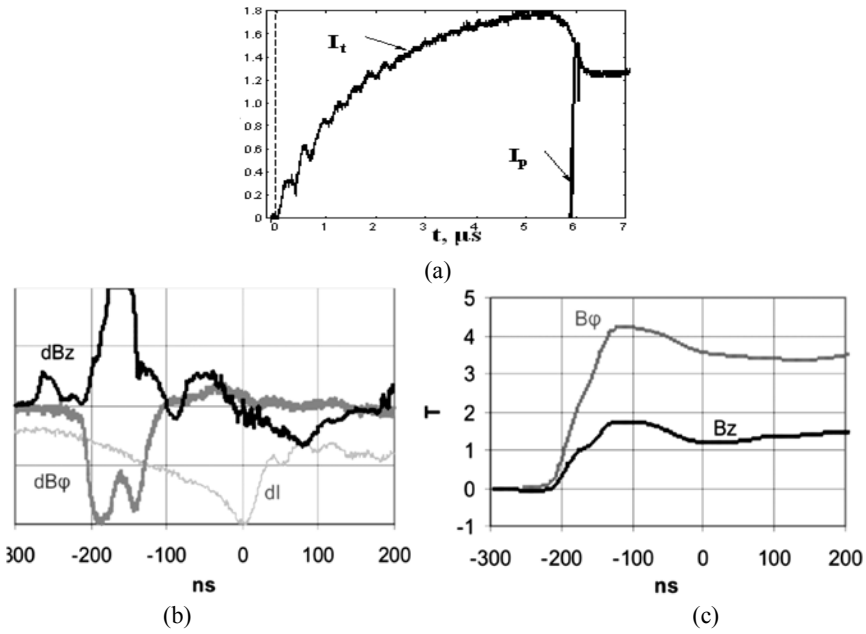

FIG. 6. (a) External current I_t and current flowing through the pinch I_p measured by the Rogowski coil and by the magnetic probe installed at R = 4 cm correspondingly (D_2, P_0 = 2 Torr, U_0 = 23 kV, W_0 = 352 kJ, and $Y_n = 1.0\times10^{11}$ neutron/shot); (b) temporal evolution of the current derivative dI/dt (thin grey), the signal of the azimuth dB_ϕ (thick grey) and axial dB_z (black) components of the magnetic field registered at 4 cm distance from the center of the anode; (c) temporal evolution of the azimuth B_ϕ (grey) and axial B_z (black) components of the magnetic field.

As the pressure increases, the width of the magnetic piston increases by nearly a factor of 2, while the total current is preserved. This event naturally leads to a decrease in the linear current density in the PCS. However, this insignificantly affects the neutron yield. Finally, if we assume that the thickness of the shock front is determined by the front duration of the light signal, whereas the subsequent glow is caused by the plasma surrounding the probe, then we find that the width of the shock front also increases from several millimetres at a low pressure to ~ 1 cm at higher pressures. An important consequence of these estimates is that the most part of the current flows in the magnetic piston. Thus, it can be stated that a compact high quality PCS forms in the standard operating mode of the PF-1000U facility in the final stage of plasma compression, and that the dynamics and structure of the PCS are well described by the snow-plough model. In this case, the gas snow-ploughing efficiency is fairly high and, accordingly, the leakage currents are low. It should be noted that, in all of the above mentioned discharges, the current measured by the probe coincided with the total discharge current, and the neutron yield was high.

The above considerations clearly demonstrate the problem of the efficiency of discharge current transportation toward the axis. Fig. 7 shows the measured neutron yield as a function of the current measured by a probe installed at a radial distance of 40 mm from the axis. It is seen that the known neutron scaling agrees well with the data obtained using the magnetic probe. At the same time, the neutron yield is practically independent on the total discharge current. Obviously, the high neutron yields in Fig. 7 correspond to the high efficiency of current compression onto the axis. It should be noted that, in some discharges, the neutron yield is very low in spite of the high value of the total discharge current. This fact is related to secondary shunting breakdowns, due to which only a lower fraction of the total current contributes to the pinch formation. The measurements performed with the help of multicomponent probes have demonstrated a presence of the B_z field in both stages of the PCS radial compressing and of the pinch confinement itself [8]. In the implosion stage, the axial component of the magnetic field runs up to ~ 10% of the azimuth component. This axial magnetic field improves plasma confinement and influences the shapes of trajectories of fast deuterium ions (helping to fill the pinch plasma column by them). Because of these features the axial component of the pinch magnetic field produces an important positive influence upon the mechanism of neutron generation in DPF. On the other hand, it is necessary to take into account that the presence of the too high axial magnetic field component in front of the PCS can hinder the pinching process (thus decreasing density of a plasma target pinch) and so it can prevent the achievement of the maximum plasma and current densities.

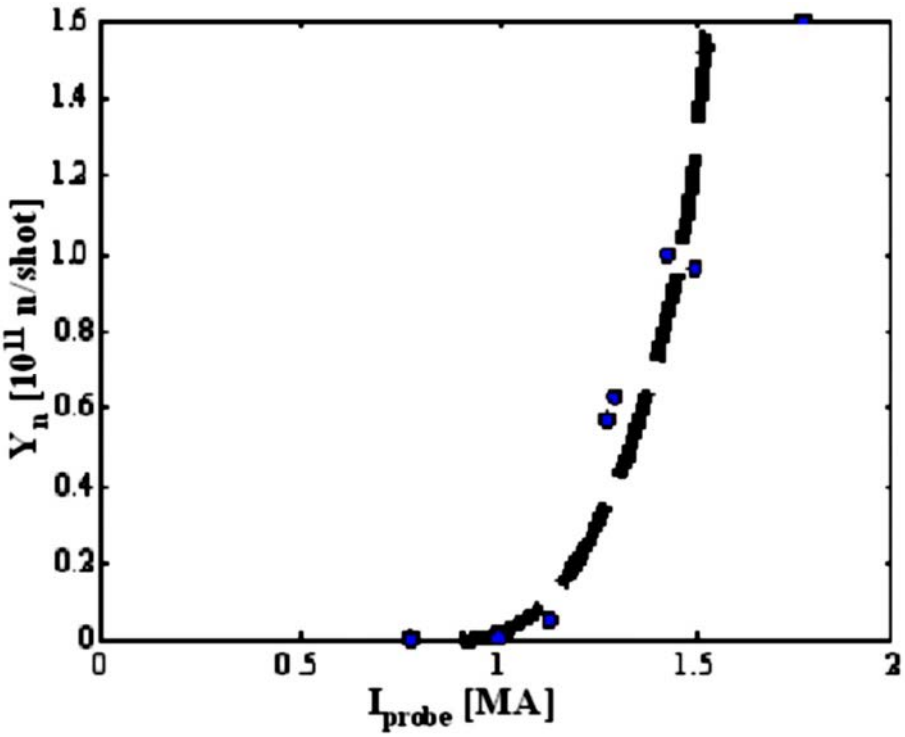

FIG. 7. Neutron yield Y_n as a function of the maximum current recorded by the magnetic probe at a radius of 4 cm.

2.2. Irradiation conditions and diagnostics

During the experiments, the device was operated at the bank energy in the interval between 170 and 600 kJ with a discharge current in the range between 1.2 and 2.0 MA. Our experimental efforts at the PF-1000U facility were concentrated mainly in the irradiation sessions where our main materials were tungsten with its alloys; carbon based composites, and some other materials e.g. low activated stainless steels and titanium alloys. To prevent metal spraying upon the sample of the above materials in the maximal degree we have elaborated a special holder for the specimens shown in Figs 8 and 9. We supplied the same samples of materials to our colleagues. So these specimens, e.g. W, SiC and CFC materials have been irradiated in the dissimilar conditions at a number of different dense magnetized plasma devices in the laboratories of IMET (PF-5M), NSC IPP, Ukraine (QSPA), IPPLM (PF-6), PF-12 (TU) and ICTP (Bora). At the ICDMP operating with the PF-1000U facility we used a 16-frame laser interferometry (pulse duration and synchronization precision of 1 ns, time delays between frames of 10 ns or 20 ns) for observation of the interaction process.

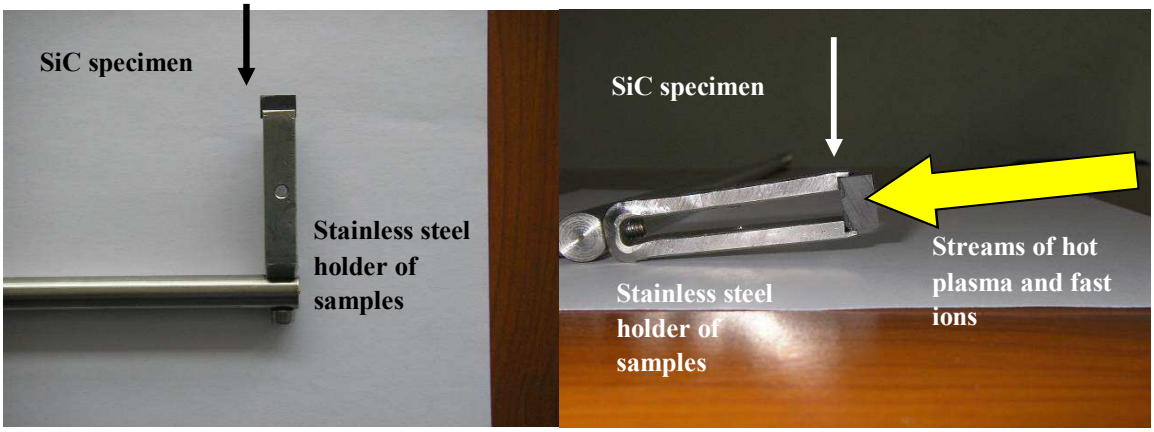

(a) (b)

FIG. 8. (a) Side view construction of a stainless steel holder with a specimen of SiC in two projections; (b) top view with a certain magnification.

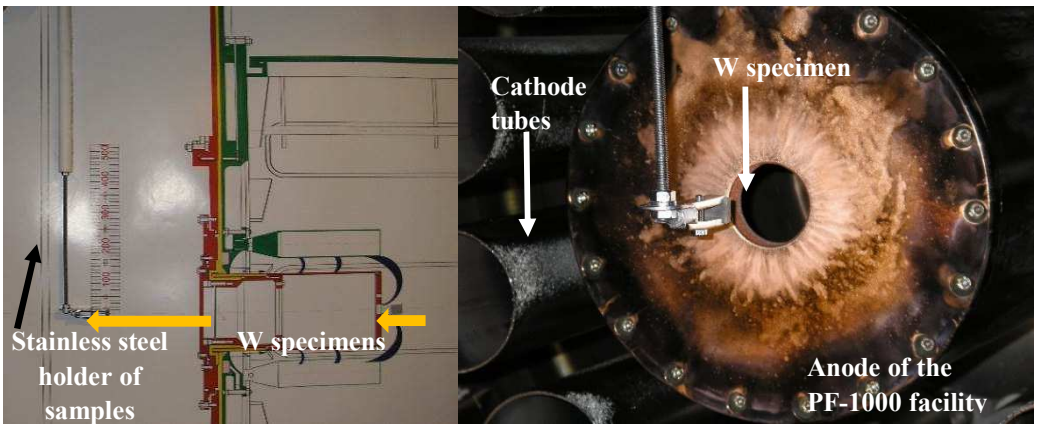

FIG. 9. (a) Schematic of the positioning inside the chamber of the construction of a stainless steel holder with a specimen of W and Teflon attachment rod; (b) real arrangement in front of the PF-1000U anode.

SiC samples are shown in Fig. 10. During these sessions we have also provided some spectroscopic measurements to obtain information on ionization states and main parameters of our secondary plasma produced by HTP and FI streams at the surface of our specimens under irradiation. Examples of the spectra obtained at different time moments near the surface of the Ta target are presented in Fig. 11. We used in these tests the W samples manufactured for all participants of the current CRP by FZJ. Besides, we used tungsten specimens supplied to us by IMET, IEPA, TU, NCBJ, and by Politechnika Warszawska. Distance between the anode plate (with a central hole to prevent creation of debris from it) and the sample were between 7 and 15 cm. We placed our specimens exactly at the Z-axis of the device.

The subsequent examination of the targets placed at the close distance from the anode and subjected to the action of the powerful ion beam has shown the contour trace of the beam also called the 'autograph' of the fast ion stream as it is named in the technique of high current beams.

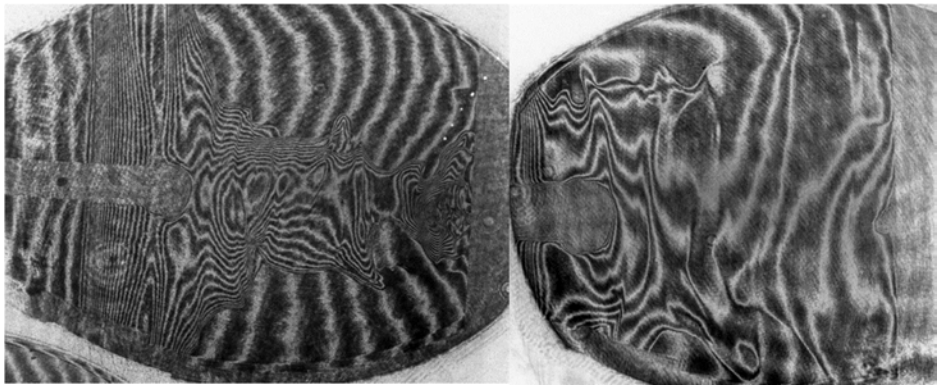

FIG. 10. Typical laser interferometric pictures taken during the process of interaction of HPS and FIB with the carbon based target at the PF-1000U device. The time interval from left to right is circa 200 ns (same spatial scale).

The diameter of the spot, recording the most powerful component of the fast ion beam on the tungsten plate, located at the distance of 10 cm from the anode, was about 12 mm (Fig. 12). This size gives the angle of the beam divergence of about 7°, which is close to the angle recorded in the self-luminescence pictures (Fig. 13) from the luminosity of plasma that irradiates during passing of the beam through it [14]. We have irradiated the tungsten specimens so that each sample has been subjected to a number of pulses with total neutron yield produced (during this set of shots via PF-1000U) equal to 10^{11} (usually between 2 and 5 shots). Because plasma target was about the same, the number of neutrons had a correlation with the number of the irradiating fast ions. This fact ensured us the same fluence and about the same average power flux densities for both hot plasma streams and fast ion beams for each sample under irradiation.

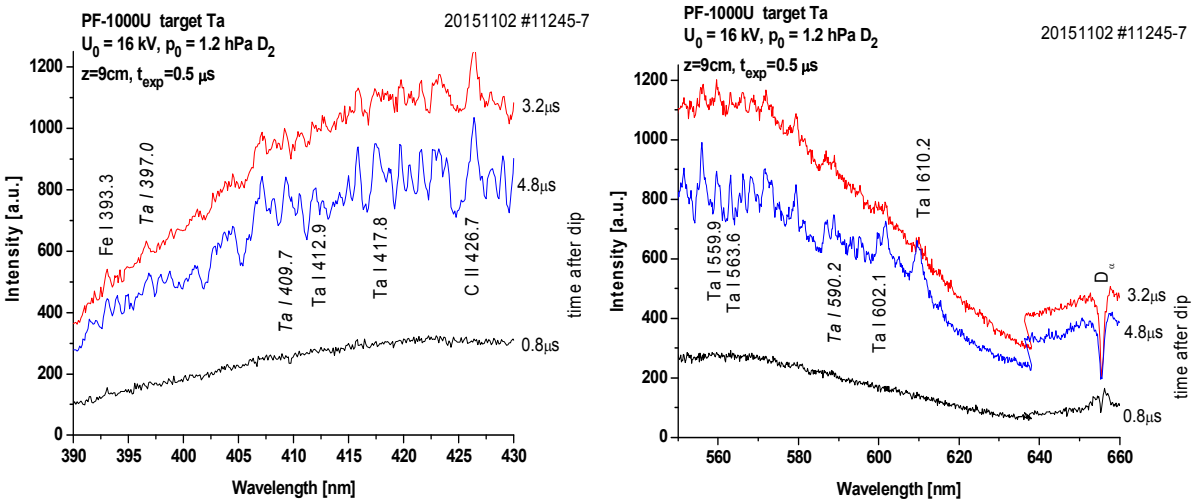

FIG. 11. Evolution in time of spectra obtained for secondary plasma produced by HPS and FIB at the surface of a target made of Ta.

Using DP foci of our partners we have repeated these sessions of irradiation of tungsten specimens (i.e. in the frame of the round robin tests) in some other conditions (smaller energy of the device and dissimilar distances from the anode, different working gases, and various diagnostics).

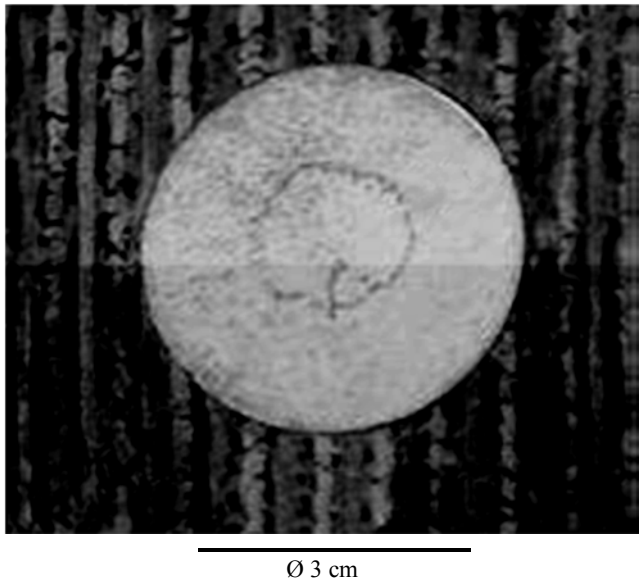

FIG. 12. The 'autograph' of the powerful ion beam on the tungsten target (a disc in the center of the rectangular specimen made of carbon based composite) placed at the distance of 10 cm from the anode end.

FZJ supplied through the IAEA the same samples of W. So these specimens of tungsten material have been irradiated in parallel and sequential sessions in the dissimilar conditions at a number of different DPF devices and plasma accelerators in the laboratories of IMET, RF (PF-5M), IPPLM (PF-6), TU (PF-12), ICTP (Bora) and other institutions. We compared the results obtained.

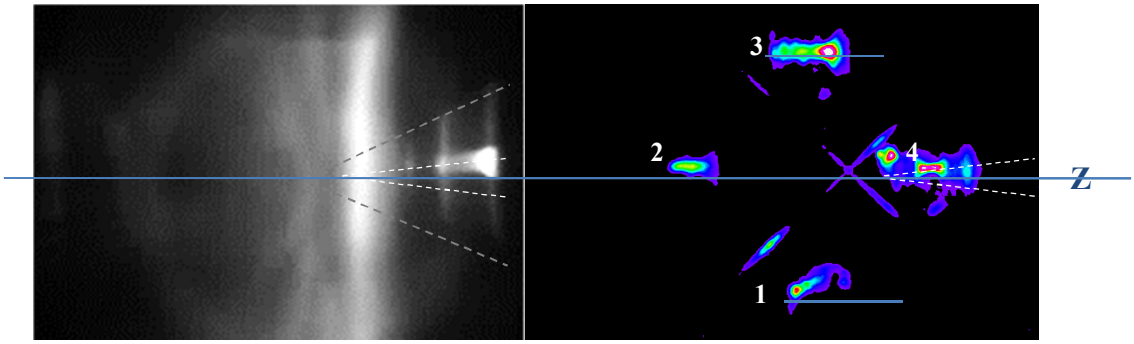

FIG. 13. (a) Self-luminescence single frame with time exposure of 1 ns of two components of the fast ion stream with the angles of divergence 6° and 22°; (b) soft X ray four frames (1, 2, 3, 4) with time exposure of 1 ns and time intervals between frames of 20 ns (range for the fast ion beam transportation and its interaction with a flat target). On the right hand side, the surface is shown by a vertical line.

2.3. Equipment used in the analysis of the irradiated specimens

For the instrumental analysis of the irradiated specimens we have used equipment available at our partners at the IMET RAS and TU as follows:

- Optical microscopes NU-2E and Neopot-32 with computerized image processing;
- Scanning electron multimicroscope VMM-2000;
- Focused beam microscope VEGA/SBU with a system of X ray energy dispersion microanalysis, Oxford Instruments;
- High precision X ray diffractometer, Rigaku Ultima IV (III Thin-film);
- Optical emission spectrometer based on a glow discharge Leco GDS-850A;
- Universal test instrumentation MicroTester 5848 and Electropuls E3000, Instron;
- Unit for measuring of nanohardness NanoTest, Micro-Materials Ltd.

3. INVESTIGATION OF THE PHYSICAL PROCESSES

3.1. INTRODUCTION

During the implosion phase of the DPF discharge and at the current abruption event this device generates powerful streams of plasma [1, 16], relativistic electrons and fast ions [17], neutrons and hard X rays. The streams of high temperature plasma ($T_{pl} \sim 0.1–1.0$ keV) have a pulse duration $\tau \sim 100$ ns and power flux density on the target surface $Q \approx 10^{13}–10^{14}$ W/m^2. High energy electron and ion beams ($E_D \sim 0.1–1.0$ MeV for deuterons) have a pulse duration in the range $\tau \sim 10–50$ ns, and their power flux density on an impediment plate may reach values up to $Q \approx 10^{17}$ W/m^2.

New unexpected effects were discovered recently in the DPF experiments, in which solid state targets that were placed in front of the anode of the PF-1000U facility (bank energy 400 kJ) have been irradiated with plasma/ion streams [14]. In particular, spectroscopic studies have shown that the secondary plasma (SP) produced near the target surface can exist during a time interval of $\tau \sim 100$ μs (after the current abruption) that is much longer compared with the duration of irradiation pulses and with fly-off time of SP, see Fig. 14(a). During this time period the SP temperature T_e gradually decreases down to 2 eV in parallel with its density N [14]. Furthermore, the process of transportation of the stream of fast ions inside the tubes made of different materials, i.e. stainless steel (SS) and copper (Cu), and placed along Z-axis of the chamber in front of the anode, see Fig. 14(b), as well as their damage have anomalous and dissimilar character [14] that depends on the tube's material, see Figs 14(c)–(d).

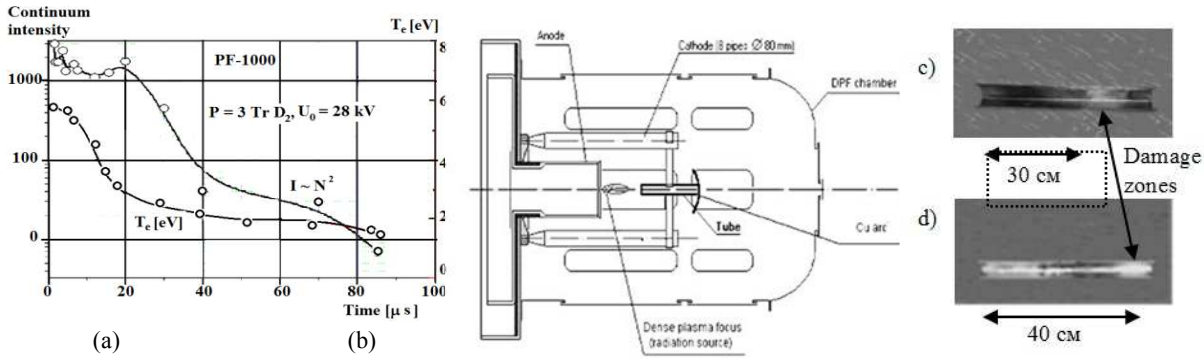

FIG.14. (a)Time behavior of the secondary plasma temperature and density; (b) geometry of irradiation of tubes made of stainless steel and copper; (c) results of the irradiation for SS case; (d) results of the irradiation for Cu case.

3.2. Plasma implosion and cumulative stream/shock wave formation

In Fig. 15(a) one may see the schematic of the implosion phase of the DPF discharge produced by an azimuthal magnetic field of the main discharge current with a compression of a longitudinal component of a seed magnetic field (magnetic field of Earth and residual fields of construction materials of a DPF chamber). Because a compression ratio is about 100 by radius (10^4 by area) the corresponding value of the longitudinal component reaches about 10% of the azimuth field magnitude, see section 2 of this paper and Refs [8, 16]. Figs 15(b)–(c) demonstrate a process of generation of a cumulative plasma stream (jet) created at the conical compression of plasma and a production of a shock wave (SW) in the residual gas above the pinch. This is supported by the experimental results in Fig. 16.

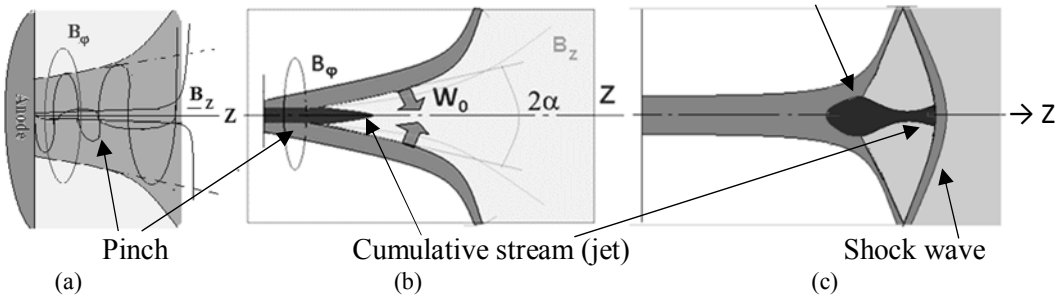

FIG. 15. (a) Generation of a cumulative stream (jet) at a cone plasma compression with the cone angle 2α; (b) trace (pest) of the stream; (c) production of a shock wave by the jet.

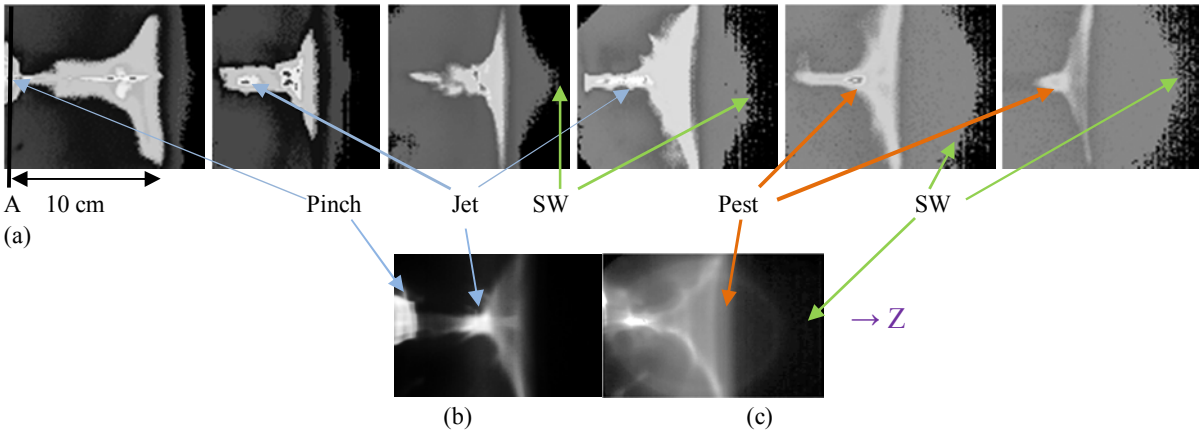

FIG. 16. (a) Development in time of accumulation process with a formation of a jet; (b) the trace of the accumulation jet; (c) hemispherical shock wave along Z-axis of the chamber. Frame pictures of a self-luminescence of plasma in visual range, time exposure of each frame is 1 ns, and time interval between frames in (a) is about 50 ns.

The jet speed W_{jet} produced in such a configuration is [18]:

$$W_{jet} = W_0/tg\ (\alpha/2) \tag{1}$$

3.3. Irradiation of a solid target by a hot fast plasma stream

Let a flat solid target not very far from the top of the pinch (in PF-1000U this distance is 9–15 cm), and let us irradiate it first with a hot plasma stream (jet + SW) having a speed about $v \sim 3 \times 10^7$ cm/s and consisting of deuterons of energy ~ 1 keV, see Fig. 17(a). This primary plasma (PP) will be collected in front of the plate (if its size is large compared with the plasma stream diameter) and then it will start to heat the target. Upon heating the target, secondary plasma (SP) will appear near the surface and it starts to propagate in the direction opposite to the primary plasma (PP) stream movement, see Fig. 18(b).

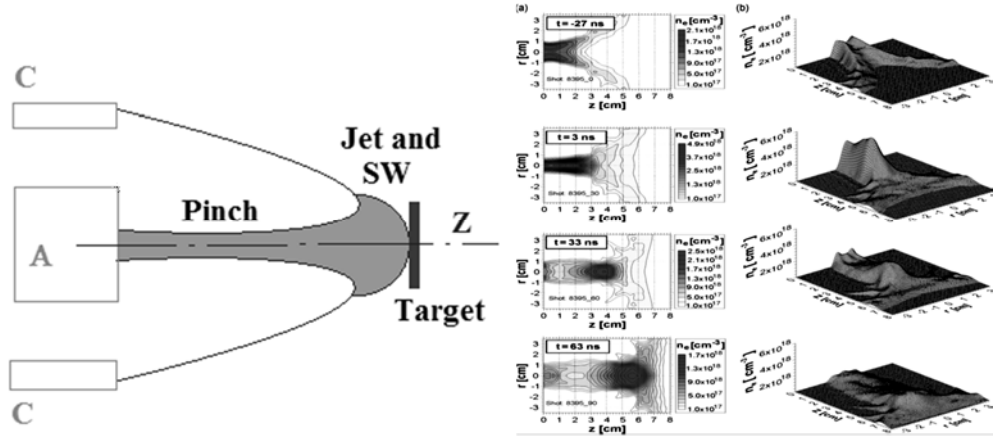

(a) (b)

FIG. 17. (a) Schematic of irradiation of a flat solid target (a plate) placed at the cathode part of a DPF chamber; (b) processing of the interferometric pictures of a jet and SW formations.

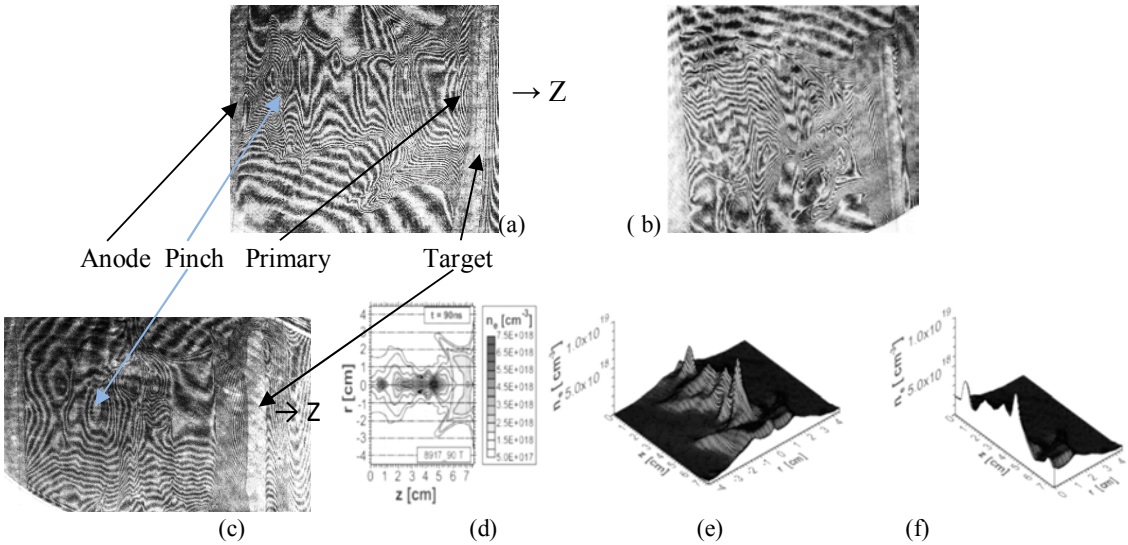

(c) (d) (e) (f)

FIG. 18. (a) Primary plasma colliding and accumulated in front of the target surface; (b) secondary plasma propagating in the opposite direction to the movement of the primary plasma stream; (c) secondary plasma; (d) lines of constant density; (e) interferometric image processing showing the 3-D electron density distribution; (f) 3-D electron density distribution. Laser frame interferometry: τ = 1 ns, PF-1000, shot No. 8917.

In these interferometric pictures the upper limit of measurable electron density is implied by the lateral size of a plasma cloud. In our cases the value is $\leq 5 \times 10^{18}$ cm^{-3} at the position of the SP propagating from the surface of the target and it is about 10^{19} cm^{-3} at the position of the SP plum from the anode produced by a self-focused relativistic electron beam. The total energy content of the irradiating stream may be estimated as the entire mass of particles in the pinch m_p plus the mass of the particles captured by the SW m_{SW} taken from the laser interferometric pictures processing in Fig. 17(b) [14] all moving with the above velocity:

$$E_{pl} \leq [(m_p+m_{SW})\, v^2 / 2 \approx 10^4 \text{ (J) (efficiency } \eta \approx 2.5\%) \quad (2)$$

The maximal power flux density on the target surface is about $Q_{pl} \approx 10^{14}$ W/m^2 (pulse duration $\tau \approx 100$ ns, irradiated area S of a few cm^2) whereas a penetration depth of the plasma deuterons (of a 1 keV energy) into the target surface layer is about a few nm [19]. In Fig. 18 the interferograms and their procession are presented for the moments of time when a SP is produced and starts moving in the direction opposite to the primary plasma stream. The value of the propagation velocity of the edge of the SP cloud in the direction of the anode is about 3×10^6 cm/s. It means that its temperature T_{SP} is about 10 eV [20]. Our numerical simulations support these figures [21].

3.4. Plasma diode, electron and ion beams dynamics, transport and interaction with a solid target

After the above described processes the kinetic stage of the DPF development starts [17]. It consists of the so-called 'current abruption' phenomenon, plasma diode formation, acceleration of electrons and ions, transportation and self-focusing of the electron beam inside the pinched plasma to the anode, propagation with a certain divergence of the ion beam within plasma and outside the pinch along Z-axis from the anode. This phase supersedes the previous plasma development having the chiefly hydrodynamic character. Physical processes taking place during the period of the DPF kinetic dynamics was investigated experimentally [17] and explained on the base of the electron magnetic hydro-dynamics theory [22]. The electrodes diameters of a virtual plasma diode are of the order of the pinch diameter, and the anode–cathode separation value is based on a parapotential model [23], which permits a generation of the electron beam and ion beam I_b of the order of the previous collisional current I_c:

$$I_b \approx 8500\, \beta\gamma\, r/d \approx I_c \text{ (A)} \quad (3)$$

where β and γ are relativistic factors, r/d is the so called aspect ratio, i.e. the ratio of the radius of the diode $r \approx r_{pinch}$ to the distance (gap) d between the virtual plasma anode and the plasma cathode, and I_b and I_c are in Ampere. To be in a conformity with Eq. (3) and assuming that the current of fast electrons (for $E_e \sim 100$ keV, $\beta = 0.62$, $\gamma = 1.28$) is of the order of the pinch current, we shall have for the anode–cathode gap d of our virtual diode (where $r \approx 0.45$ cm is the pinch diameter) $d \approx 0.15$ mm. It results in a generation within this gap a vortex electric field $E \approx 10^7$ V·cm^{-1}. At the same time, by these estimates the validity of the demands on the magnetization of the electrons and subsequent free streaming of the ions within this diode is established based on comparisons of the diode gap and the Larmor radii for electrons and deuterons:

$$r_{Be} (\geq 3.37(W_\perp)^{1/2}/B_\varphi = 5 \times 10^{-3} \text{ cm}) < d < r_{Bd} (\geq 204\, (W_\perp)^{1/2}/B_\varphi = 3 \times 10^{-2} \text{ cm}) \quad (4)$$

Thus all the above mentioned estimates open the opportunities for the validity of the Gyrating particle model [16, 17]. This picture is supported by our experimental results obtained by means of visualization of the processes with the frame self-luminescence and with the laser interferometric images of the plasma diode formation, see Figs 19(a)–(b), after which an acceleration of electrons in it by the vortex electric field takes place. Then we have a self-focusing of the electron beam inside the pinch during its propagation right up to the anode (Fig. 19(c) laser 5-frame shadowgraph). Interaction of fast electrons with the anode surface results in a production of hard X rays (HXRs), in a creation of two hemispherical SWs – within the pinch plasma and inside the anode's material as well as in a vaporization of the anode matter. Propagations of the electron and ion beams inside the pinched hot dense plasma are ruled by a law of the super Alfven currents transportation. It means that they can exist only with self-induced back currents. It is only possible in the ionized plasma of high density. Alfven-Lawson limit is [23]:

$$I_A = (mc^3/e)\, \gamma\beta_z \text{ (CGS)} = (4\pi mc/\mu_0 e)\, \gamma\beta_z \text{ (SI)} \quad (5)$$

It gives for our electrons $I_{Ae} \approx 5$ kA and for ions $I_{Ad} \approx 600$ kA. Both restrictive currents are much less than the discharge current ($I_c \geq 2$ MA). Then upon the magnetization of the electrons, the beam of fast ions comes into play.

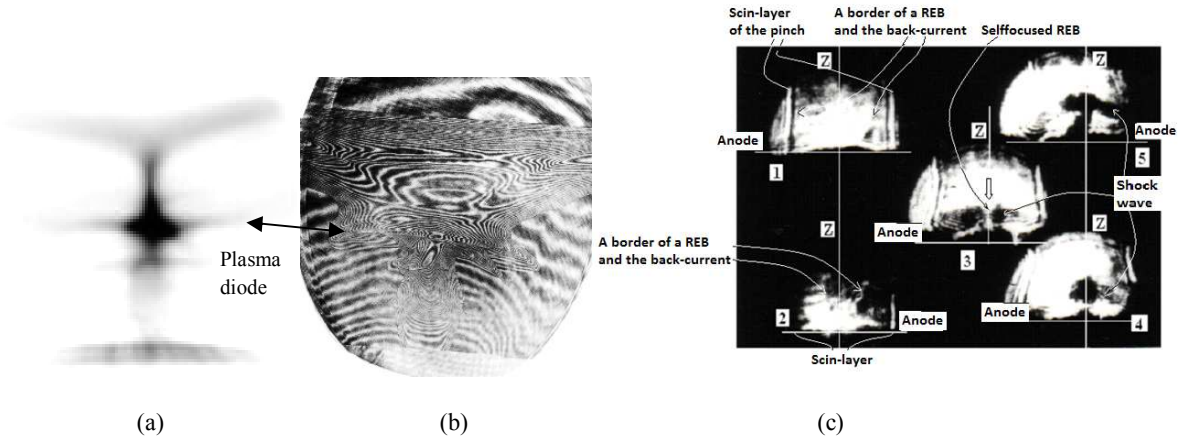

FIG. 19. (a) 1 ns self-luminescence of the pinch during development of MHD instability and the plasma-diode (shown by the arrow) formation on the plasma column; (b) interferometric pictures; (c) 5-frame laser shadow images of the beam of electrons propagating and self-focusing inside the pinch (time interval 20 ns).

In Fig. 20, two components of the fast ion beam can be distinguished (seen as two cones). The first part of these accelerated ions that are magnetized in the combined B_φ/B_Z magnetic field escapes the pinch within the cone of the angle of about 25–30°, see Fig. 20(a). However the main part of the beam of fast ions is propagated in a relatively narrow cone near the singularity line of the B_φ component (Z-axis of the pinch) with a small divergence of about 5°. So it irradiates a target in a small spot with a high intensity, see Fig. 20(b). Our powerful part of the beam has at this distance namely this diameter (see also Fig. 12).

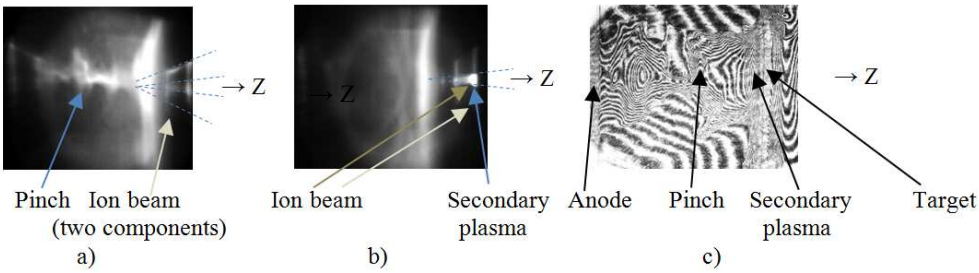

FIG. 20. (a) 2-frame photos of plasma in its self-luminescence produced by the action of the ion beam; (b) same ad (a); (c) interferometric picture of interaction of the beam of fast ions with a solid target, i.e. production of the SP cloud.

The propagation speed of this type of a SP appears to be about 2×10^7 cm/s, see Figs 20(b)–(c). So the temperature T_{SP} is a few hundred eV [20]. In Fig. 21, interferometric images of target plasma (SiC specimen material) taken at 4 consecutive time moments (temporal resolution of 1 ns). We are able to monitor the whole irradiation process including the production of the unloading (rarefaction) wave. It appears after SP blow-off and removal of the pressure of hot plasma from the target surface as a non-transparent cloud for the laser light. Its front moves with a speed of 2×10^6 cm/s that evidences the temperature of a few eV [20]. Numerical modelling supports this picture [21].

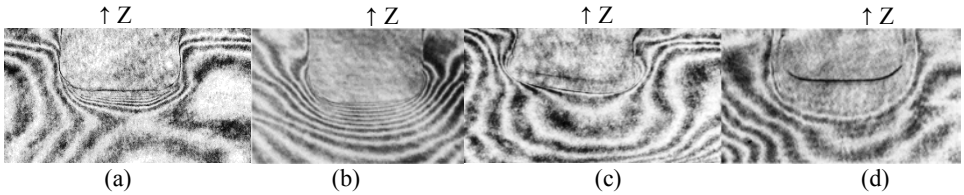

FIG. 21. (a) Beginning of the secondary plasma formation; (b) developed secondary plasma cloud; (c) beginning of the formation of the non-transparent unloading wave; (d) developed unloading wave.

3.5. Dependence of the physical processes dynamics on the target size and its distance from the anode

Fast electrons and ions are charged particles and interact with each other. They also represent currents and must be organized in closed circuits. Moreover their currents are the super Alfven currents, and for their propagations they must have an opportunity to induce back currents. It means that when the ion beam pierces through the front of the SW the ions find themselves in a neutral gas having density value about the same as the density of the ions in the beam. The mean free path of the 100 keV ions in the neutral deuterium atmosphere of pressure ~ 1 mbar is approximately 1 m. Both factors mean that the ion beam has no possibility of ionizing the working gas in the chamber above the SW and to provide the back current in it. That is why the ions rush to the cathode of the chamber along the magnetic field lines immediately after the penetration of the shock wave front, see Fig. 22(a).

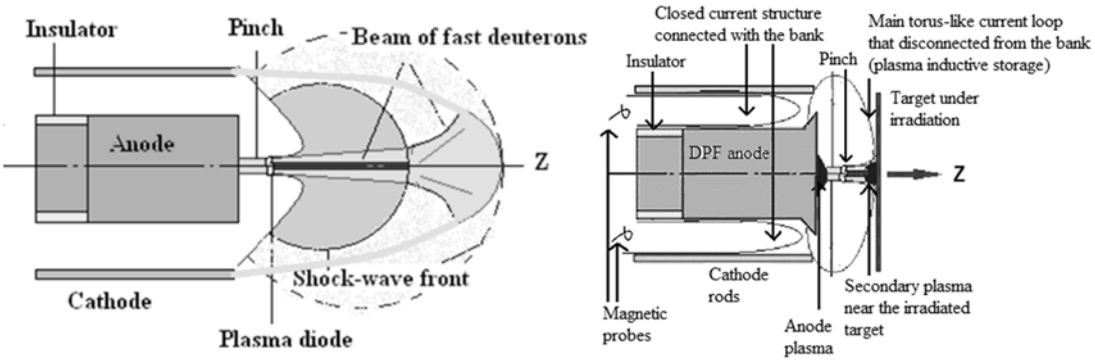

FIG. 22. (a) Scheme of dynamics of plasma streams and of fast deuterons beams; (b) Picture showing current loops configurations that are self-organized inside the DPF after secondary breakdown between ends of cathode rods and edge of the anode.

However if a DPF chamber has a big flat target in front of the anode and the sharp edge of the anode lid then there is another opportunity. In this case at the moment of the current abruption and generation of a very high electric field across the pinch a breakdown may occur in vacuum space between the edge of the anode and the ends of the rods of the cathode due to field cold emission. In this case a closed torus-like plasma configuration may be created in the space between the anode's lid and the target's plate, see Fig. 22(b). The last event is supported by an interferometric picture taken 10 μs after the moment of the current abruption and by oscilloscope traces of d*I*/d*t*, taken by four magnetic probes placed at the angles 0°, 90°, 180° and 270° around a collector of the PF-1000U facility. One may see the long lasting 'post-pinch' in the middle of the anode (Fig. 23).

FIG. 23. Interferometric picture taken at the 10th μs after the current abruption phenomenon (dip) at the PF-1000 facility.

It was also clearly seen that during the first oscillating period of the dI/dt their shapes coincide in all four magnetic probes whereas later they have different behavior (even opposite in phase), see Fig. 24. We found that the existence (confinement) time of the above mentioned torus-like loop with the post-pinch in the center is determined by damping of the plasma inductive storage system:

$$\Delta t \sim L/R \tag{6}$$

where $L \sim 10^{-7}$ H is the inductance of the torus-like structure whereas $R \approx 10^{-3}$ Ω is the resistance of the pinch column having a mean temperature of about 10 eV. According to Eq. (6), Δt for the PF-6 device is about 30 μs, whereas $\Delta t \sim 100$ μs for the facility PF-1000U. These data found their full support in the interferometric and spectroscopic measurements provided in the DPF devices PF-1000U (ICDMP), PF-6 (IPPLM) and PF-5M (IMET), see Figs 14(a) and 24. As it was seen before, the beam of fast ions has a small divergence (circa a few degrees). Its irradiation area is a few mm^2. So it produces a value of power flux density on the target surface up to 10^{16}–10^{17} W/m^2 at the penetration depth of 100 keV deuterons into the solid matter of about a few hundred nm and up to 1 μm [19]. Because of these parameters, a shock wave can be generated inside a solid target and come out from a rear side of a thin target into residual gas. This may also be seen in Fig. 23.

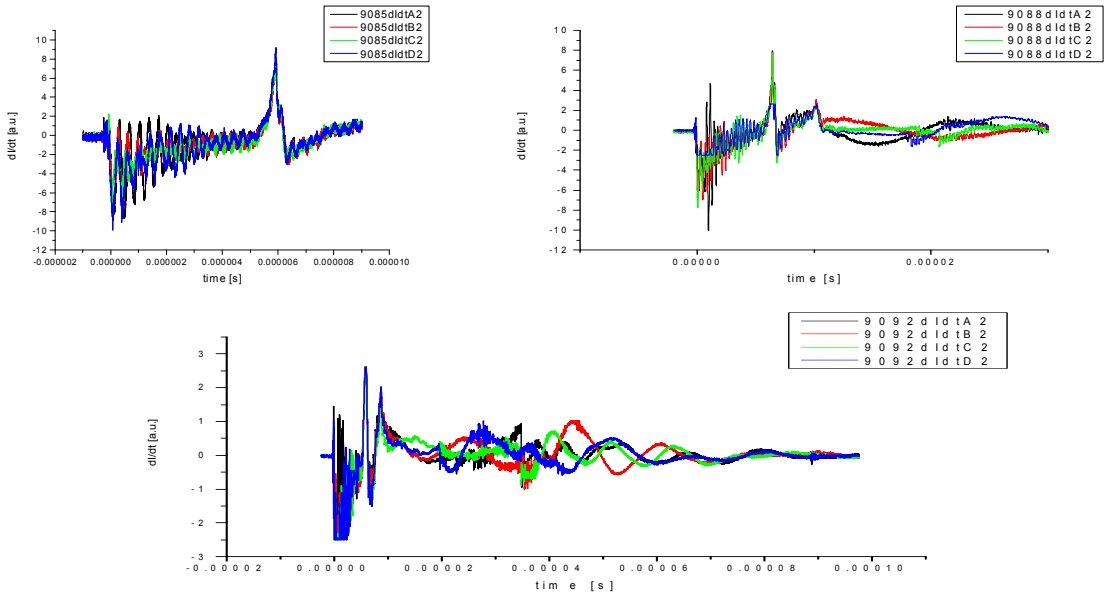

FIG. 24. Oscilloscope traces of dI/dt, taken by four magnetic probes placed near collector of PF-1000 at the angles 0°, 90°, 180° and 270° around a collector in dissimilar time scales. It is clearly seen that during first period their shapes are coincided whereas later they have different behaviour (been even opposite in phase).

3.6. Transport of the beam of fast ions inside tubes and final stages of a discharge

Inside a tube made of conducting material (e.g. stainless steel or copper) and placed along the Z-axis of a DPF chamber from the anode or the cathode side one may transport beams of relativistic electrons or fast ions for a long distance. Both effects are fulfilled for these super Alfven currents of relativistic electron and fast ion beams due to induction of a back current of electrons inside the conductive material of these tubes. These back currents of electrons in the tubes compensate intrinsic magnetic fields of the beams. It is clear that because the back currents in conducting materials are dissipative, the transport distance depends on the resistance of the material. Estimates for our geometry and materials have shown that at the overall resistance of approximately $R \approx 10^{-2}$ Ω of our part of the stainless steel tube having length $L \approx 40$ cm the total energy dissipation of our back current is:

$$E \approx I^2 Rt \approx 4 \times 10^{12} \times 10^{-2} \times (40/3 \times 10^8) \approx 5 \times 10^3 \text{ (J)} \tag{7}$$

where 3×10^8 cm/s is the velocity of our fast deuterons having energy about 100 keV. This value is a formidable part of the whole energy of our beam of fast ions (10–20 kJ). That is why at a distance of approximately 40 cm from the 'hot' end of the tube this beam of fast ions is fallen out to the walls inside it; see Fig. 14(c). Because

conductivity of copper is about 60 times higher than that of the stainless steel, the beam of fast deuterons propagates farther, hence to the end of this copper tube, see Fig. 14(d).

The final remark refers to the behavior of the discharge plasma during the subsequent oscillations of the discharge current in the DPF device and its possible effect on the conditions of the irradiation of the target. The complete oscilloscope trace of the derivative of the discharge current in a small scale PF-5M device is shown in Fig. 25(a). Separate parts of this trace, the middle in Fig. 25(b), and the final stages of the discharge in Fig. 25(c), are shown as well.

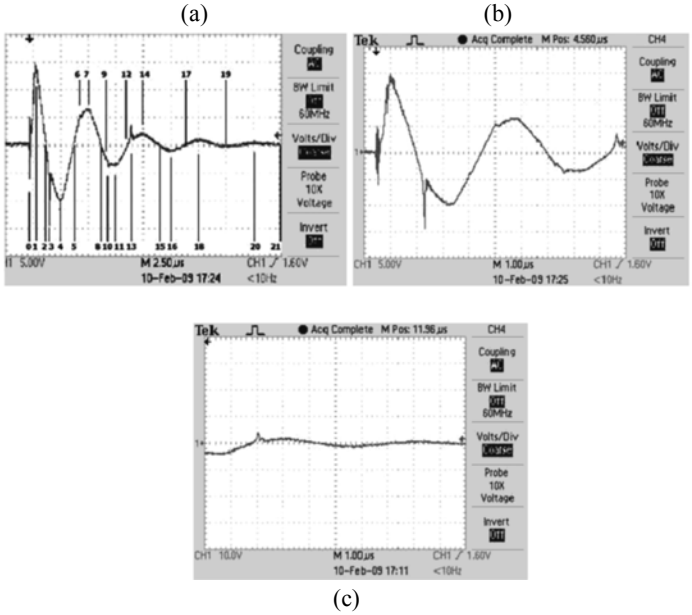

FIG. 25. (a) Complete oscilloscope traces of the derivative of the discharge current in the PF-5M device; (b) middle stages of the discharge; (c) final stages of the discharge.

Five periods of the decaying discharge seen in the traces, especially the oscilloscope trace in Fig. 25(c) obtained for the fourth period with the high enhancement, have about identical durations being very close to 5 μs. This means that the inductance of the channel where the current passes the plasma and plasma size are approximately identical in all these periods. In its turn, this leads to the fact that after the powerful HTP and fast ion irradiation in the first half period of the discharge, the targets located close to the anode are subjected to the smoothing action of the low temperature plasma, which exists near the DPF anode during the following half periods up to the complete decay of the discharge current. This effect is not important for the targets, which are located at the relatively distant regions from the anode. At the same time, it is necessary to remember that, at a significant distance of the target position from the DPF anode, the action of the high current fast ion stream decreases sharply due to strong scattering of the ion beam at the external border of the region, where its compensation by the reverse current is impossible. All these facts mean that there is a certain intermediate zone inside the DPF chambers where the action of the fast ion stream is very strong, and where subsequent oscillations of current do not produce a smoothing effect.

4. RESULTS OF IRRADIATIONS

The detailed characterization of materials damageability that were irradiated in the PF-1000U facility and in the devices of our partners are presented in the reports of IMET, ICTP, NCBJ and TU groups. We shall describe here only some features of these modifications of a surface layer and a bulk of the irradiated specimens. After irradiations of various specimens produced in different number of pulses of the PF-1000U facility we have provided the analytical investigation of specimens.

First information about damageability of the samples of tungsten, carbon based composites and other materials was obtained from the comparison of mass losses of samples irradiated with different numbers of discharges, for example Table 1 experiments were provided in cooperation with NCBJ at the low power flux density of FI and HTP streams ($\leq 10^9$ W/cm^2 for both). These experiments were provided at a low charging voltage of the bank.

Besides, specimens of tungsten were placed at a distance from the anode (≈30 cm) where power flux densities of hot plasma and fast ions streams were about the same. It turned out that the W sample lost about 0.5 mg per one discharge. Such an estimate is very rough and a more accurate analysis (e.g. with an EDS method) is needed, because some impurities were deposited upon the investigated targets.

TABLE 1. ANALYSIS OF MASS OF THE THREE INVESTIGATED W SAMPLES

	W sample after 1 discharge	W sample after 3 discharges	W sample after 5 discharges
Initial mass [g]	8.2804	8.6732	8.4694
Loss of mass [mg]	0.40	2.50	2.00
Loss of mass per one discharge [mg]	0.40	0.83	0.40

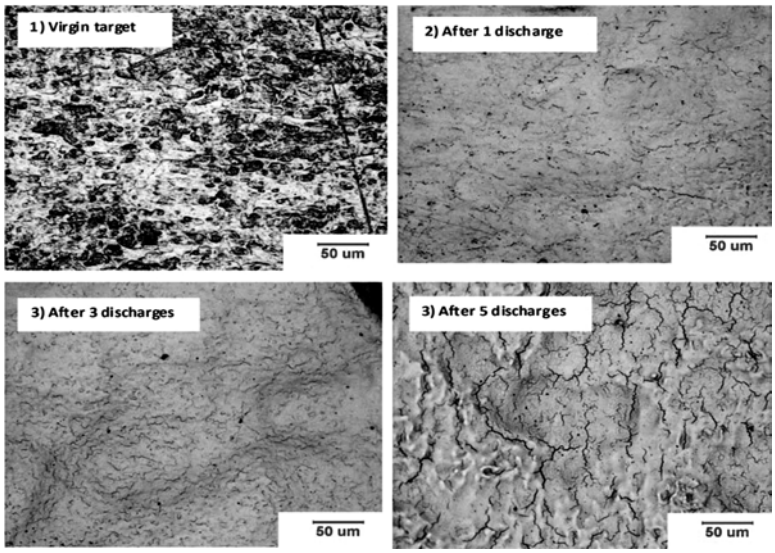

FIG. 26. Pictures showing the changes on the surfaces of the samples after different numbers of discharges.

The changes of the surfaces after their irradiation with intense and high density plasma and fast ion streams generated by the PF-1000U facility were studied with the use of an optical microscope. In Fig. 26 we compare microscope images of a pristine sample (i.e. before irradiation) with images of samples subjected to different number of discharges. Some results of parallel investigation by scanning electron microscopy and optical microscopy of identical W samples irradiated in PF-1000 facility as well as in Estonian PF-12 device and Bora set-up are shown in Fig. 27. It was observed that the samples have practically identical damage features, wave-like structures, micro and macrocracks formation, and pores. Also, the examination has shown that high heat loads result in droplets formation (and possibly in droplets ejection) from the tungsten surface with the simultaneous movement of the melted layer, see Fig. 27(a). Closer exploration of SEM images shows that droplets are located next to grooves or holes. Therefore it is very likely that the droplets have emanated from the aforementioned grooves.

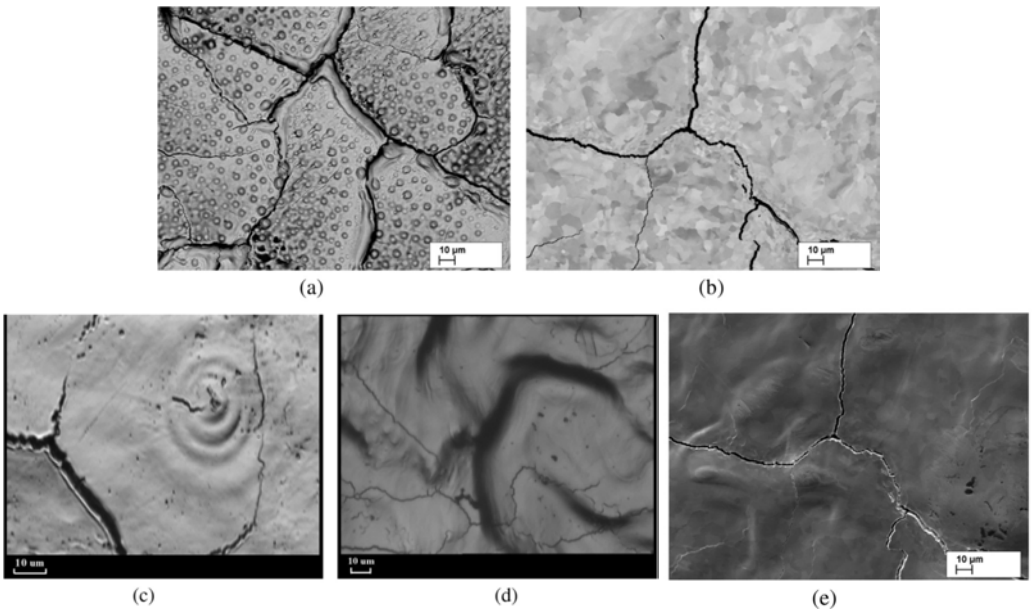

FIG. 27. (a) PF-12, 25 shots, P = 10^9Wcm^{-2}; (b) PF-12, 25 shots, 10^{11}Wcm^{-2}; (c) Bora, 4 pulses, 10^{11}Wcm^{-2}; (d) PF-1000, 4 pulses, 10^{12} Wcm^{-2}; (e) PF-12, 25 pulses, $5{\cdot}10^8$Wcm^{-2}, by SE (secondary electrons).

Though, such behavior is not yet confirmed by actual observation of materials surfaces while irradiating it with plasma/ions impulses using very fast CCD cameras. Influence of deuterium plasma and fast ions generates cracks and mesh of microcracks due to fast rise of temperature and thermal stresses appeared due to temperature gradient during repeated heating-cooling cycles on the surface layer. Depth of damaged layer was measured by change of electrical micro-conductivity, which depends on structure of material and its defects [24]. The thickness of the damaged (and possibly melted and resolidified) layer is about 350–500 μm, which is illustrated by the graphs of the electrical conductivity of W versus depth from the surface layer at different irradiation conditions (see Fig. 28). The electrical conductivity was measured using the measuring standard derived from [24]. Thus Fig. 28 shows the appearance of the structural changes in the material as the electrical conductivity decreases (pores, microcracks, the lack of adhesion and shearing processes at the grain boundaries). The observed depth of the micro-conductivity changes is much larger compared with the projective mean free path of fast deuterons in solid matter [19]. So it is rather reasonably to propose that these imperfections were appeared during irradiation because of an action of a shock wave generated in the bulk of the solid material by a powerful stream of fast deuterons. We found a relatively high concentration of deuterium in a very thin surface layer of irradiated targets. Presence of deuterium of rather high concentration in the nanolayers under investigation supports the fact that after pulsed implantation into the bulk of the material it does not eliminated completely from it by evaporation or by the diffusion way.

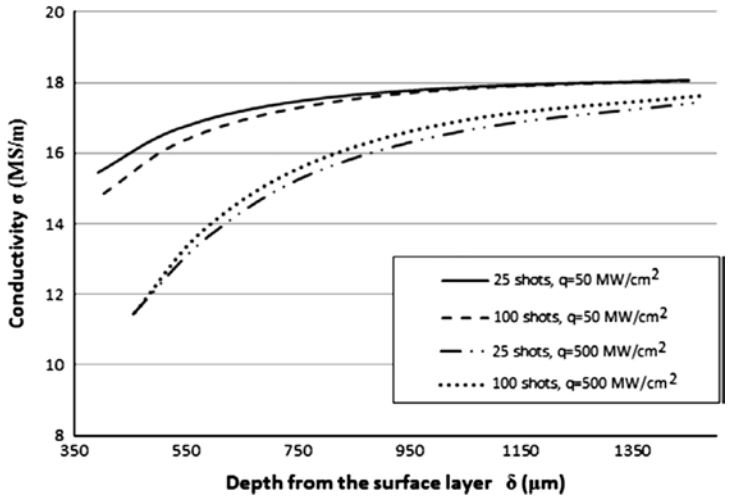

FIG. 28. Value of electrical conductivity of a W sample versus the depth of material.

Optical microscopy and SEM have shown that the degree of the damageability was increased with the number of pulses. At the highest power flux densities of streams of HTP and FI obtained by placing the specimens at the distances of ≈ 10 cm from the anode and at high charging voltages of the bank of the PF-1000U facility an average mass loss of W samples in all cases appeared to be an order of magnitude higher compared with the low powerful operation of about 0.008 ± 0.002 g/shot. We found that the losses of mass in each shot of the DPF devices are approximately proportional to the discharge current in the power 2 (in the range of the current 0.16–1.6 MA):

$$\Delta m/\mathrm{N} \sim \mathrm{I}_{\mathrm{disch}}{}^{2} \tag{8}$$

provided that all other conditions (distances, charging voltages, neutron yield) are preserved. Specimens irradiated in the QSPA device after influence upon them by HTP and FIB in the PF-1000U device have less pronounced damageability than in a pure DPF action. It means that plasma pulses obtained in QSPA provide a smoothing effect on the target.

5. CONCLUSIONS

- A compact high quality PCS is formed in the standard operating mode of the PF-1000U facility in the final stage of plasma compression, and the dynamics and structure of the PCS are well described by the snow plough model.
- In this case, the gas snow ploughing efficiency is fairly high and, accordingly, the leakage currents are low.
- In the implosion stage, the axial component of the magnetic field comprises ~ 10% of the azimuth component.
- PF-1000U facility generates penetrating radiations with neutral and charged particles with high efficiency (up to 10%).
- Characteristics of neutral particles (photons and neutrons) depend on mechanisms of their production only; their propagation in space is independent of each other.
- Charged particles are represented by quasi-neutral pinch plasma, directed plasma streams and beams of fast electrons and ions.
- Quasi-neutral plasma cumulative streams propagate in space of the DPF chamber as broadening jets that produce in an ambient atmosphere of the working gas a shock wave (SW). Its power flux density may be up to 10^{10} W/cm^2.
- A beam of relativistic electrons has a super Alfvenic current value, which induces a back current and self-focuses inside the pinch plasma.
- Its action upon the anode surface produces SW within the pinch plasma and in the anode material and generates hard X rays of a specific space pattern, while its power flux density may reach on the anode's surface a value of about 10^{13} W/cm^2.
- A beam of fast ions outside the pinch at the rear side of the SW propagates as a narrow stream with small divergence and induces behind the SW a following back current of electrons.
- Its power flux density may be about 10^{12} W/cm^2, and it may generate a SW in the target's material if the target is not very far from the anode. If the target is placed at a large distance from the anode this beam of fast ions, after its penetration through the SW front into a residual atmosphere, is disintegrated and short circuited to the cathode of the DPF chamber. In this case power flux densities of both hot plasma stream and fast ion beam on the target's surface become equal all along the surface, and their values are < 10^9 W/cm^2.
- With large flat targets placed close to the top of the pinch and with sharp edges of the anode lid and the cathode's rods it is possible to create a long lasting toroidal plasma structure within a DPF chamber.
- Inside the tubes made of conducting materials and positioned along the Z-axis of a DPF chamber above or below the anode's face both super Alfven beams of fast electrons and ions may be transported for a long distance, limited by the damping of the back-current induced in these tubes, i.e. by the conductivity of their materials.
- Samples after irradiation in different DPF devices have practically identical damage features: wave-like structures, micro and macrocracks formation, pores, droplets, and blisters (the last ones are appeared at a very high power flux densities).
- The high heat loads result in droplets formation (and possibly in droplets ejection) from the tungsten surface with the simultaneous movement of the melted layer.
- Depth of damaged layer measured by change of electrical conductivity is about 350–500 μm that is much higher compared with the projective mean free path of fast deuterons in solid matter. So it is rather reasonably to propose that these imperfections were appeared during irradiation because of an action of a shock wave generated in the bulk of the solid material by a powerful stream of fast deuterons.

— Presence of deuterium in the nanolayers under investigation supports the fact that after pulsed implantation into the bulk of the material it does not eliminated completely from it by evaporation or by the diffusion way.
— The degree of the damageability was increased with the number of pulses.
— At the highest power flux densities of streams of HTP and FI an average mass loss of W samples in all cases appeared to be an order of magnitude higher compared with the low powerful operation of about 0.008 ± 0.002 g/shot. The losses of mass in each shot of the DPF devices are approximately proportional to the discharge current in the power 2 (in the range of the current 0.16–1.6 MA): $\Delta m/N \sim I_{disch}^2$.
— Specimens irradiated by long-pulse plasma fluxes in the QSPA device after an influence upon them by HTP and FI streams in the PF-1000U have less pronounced damageability than in a pure DPF action. It means that plasma pulses obtained in QSPA provides a smoothing effect on the target.

ACKNOWLEDGEMENT

This research has been supported by the program "Research in Frame of the International Center for Dense Magnetized Plasmas", by the Contract No. ME09087 "Research of Plasma of Fast Z-Pinches", by the grant "Research Center of Laser Plasma" of the Ministry of Education, Youth and Sport of the Czech Republic and by the GACR grants No. 202-08-H057 "Modern Trends in Plasma Physics", by grant CRP IAEA 14817 "Research of D–D fusion reactions at the CTU in Prague", by grant CTU SGS 10-2660-OHK3-3T-13, and by the IAEA CRP grant numbers RC-16931, RC-16932, RC-16954, RC-16955, RC-16956, RC-16960, and by the IAEA CRP Contract No. 17167 as well.

REFERENCES

[1] BERNARD, A., et al., Scientific status of plasma focus research, J. Moscow Phys. Soc. **8** (1998) 93.
[2] SCHOLZ, M., et al., "Status of Plasma-Focus research in Poland", PLASMA-2013 (Proc. Int. Conf. Warsaw, Poland, 2013).
[3] KRAUZ, V., et al., Experimental study of the structure of the plasma-current sheath on the PF-1000 facility, Plasma Phys. Control. Fusion **54** (2012) 025010.
[4] KLIR, D., et al., Search for thermonuclear neutrons in a mega-ampere plasma focus, Plasma Phys. Control. Fusion **54** (2012) 015001.
[5] KUBES, P., et al., Characterization of the neutron production in the modified MA plasma focus, IEEE Trans. Plasma Sci. **PS-40** (2012) 1075.
[6] SADOWSKI, M.J., SCHOLZ, M., Important issues in high-current plasma experiments of the Z-pinch type, Nukleonika **57** (2012) 11.
[7] KUBES, P., et al., Interferometry of the plasma focus equipped with forehead cathode, Nukleonika, **57** (2012) 189.
[8] KRAUZ, V.I., et al., Experimental evidence of existence of the axial magnetic field in a plasma focus, EPL **98** (2012) 45001.
[9] SCHOLZ, M., et al., Progress in MJ plasma focus research at IPPLM, Nukleonika **57** (2012) 183.
[10] CICUTTIN, A., et al., Experimental results on the irradiation of nuclear fusion relevant materials at the dense plasma focus 'Bora' device, Nucl. Fusion **55** (2015) 063037.
[11] JAKUBOWSKA, K., et al., Optical emission spectroscopy of plasma streams in PF-1000 experiments, Nukleonika, **56** (2011) 125.
[12] DEMINA, E.V., et al., Changes in the structure and nitride phase formation in the surface layer of Fe-based alloys under the pulsed action of nitrogen ions and nitrogen plasma, Inorganic Materials: Applied Research **2** (3) (2011) 230.
[13] GRIBKOV, V.A., et al., Irradiation of austenitic steel 10Cr12Mn14Ni4AlMo and titanium alloy Ti-Al-V by pulsed streams of fast nitrogen ions and plasma in a dense plasma focus, Nukleonika **57** (2012) 291.
[14] GRIBKOV, V.A., Physical processes taking place in dense plasma focus devices at the interaction of hot plasma and fast ion streams with materials under test, Plasma Phys. Control. Fusion **57** (2015) 065010.
[15] GLAZYRIN, I.V., et al., Problems of Atomic Science and Engineering, Ser. Thermonuclear Fusion **2** (2009) 67.
[16] GRIBKOV, V.A., et al., Plasma dynamics in PF-1000 device under full-scale energy storage: I. Pinch dynamics, shock-wave diffraction, and inertial electrode, J. Phys. D: Appl. Phys. **40** (2007) 1977.
[17] GRIBKOV, V.A., et al., Plasma dynamics in the PF-1000 device under the full-scale energy storage: II. Fast electrons and ions characteristics versus neutron emission parameters and gun optimization perspectives, J. Phys. D: Appl. Phys. **40** (2007) 3592.
[18] COURANT, R., FRIEDRICHS, K.O., Supersonic Flow and Shock Waves, Applied Mathematical Sciences Volume 21, Springer-Verlag, New York (1999).
[19] GRIGORIEV I.S., MEILIKHOV E.Z., RADZIG A.A., Handbook of Physical Quantities, CRC Press LLC, Boca Raton, Florida (1997).
[20] ZEL'DOVICH, YA.B., RAIZER, YU.P. Physics of Shock Waves and High-Temperature Hydrodynamic Phenomena, Dover Books on Physics, New York (2002).
[21] LATYSHEV, S.A., GRIBKOV, V.A., MASLYAEV, S.A., PIMENOV, V.N., "Numerical simulation of the thermal effects in plasma focus experiment", paper presented at International Symposium on Plasma Focus in series SPFE 2013, Nilai, Malaysia, 2013.

[22] KINGSEP, A.S., CHUKBAR K.V., YAN'KOV, V.V., Electron magnetic hydrodynamics, Problems of Plasma Theory **16** (1987) 209.
[23] MANKOWSKI, J., KRISTIANSEN, M., A review of short pulse generator technology, IEEE Trans. Plasma Sci. **PS-28** (2000) 102.
[24] POKATILOV, A., et al., Inhomogeneity correction in calibration of electrical conductivity standards, Measurement **46** (2013) 1535.

APPLICATION OF THE PF-6 DEVICE FOR RADIATION MATERIAL SCIENCES

V.A. GRIBKOV[*1], S. JEDNOROG[*], M. CHERNYSHOVA[*], E. KOWALSKA-STRZECIWILK[*], M. KUBKOWSKA[*], R. MIKLASZEWSKI[*], M. PADUCH[*], T. PISARCZYK[*], E. ZIELINSKA[*], R. PROKOPOVICZ[*], E.V. DEMINA[1], V.N. PIMENOV[1], S.A. MASLYAEV[1], K. DROZDOWICZ[2], D. DWORAK[2], M. VILEMOVA[3], J. MATEJICEK, K. TOMASZEWSKI[4], S. UL'YANENKO[5], M. ORLOVA[6], T. LAAS[7], V. SHIROKOVA[7], E. SKLADNIK-SADOWSKA[8], K. PYTEL[8], A. ZAWADKA[8]

Abstract

We developed new diagnostics and operational capabilities for the PF-6 laboratory (IPPLM). In particular, we have put into operation a new powerful charger that ensured an opportunity to work with the device at a repetition rate up to 1 Hz. We introduced a newly designed and constructed DPF chamber with large spherical electrodes that allows to reach with this device neutron yield with the deuterium as a working gas the value of 2×10^9 neutrons/pulse (2.5 MeV neutrons). We also implemented two sealed chambers filled with the D–T mixture as a working gas. It gave us an opportunity to work with 14 MeV neutrons for some spin-off applications. As a continuation of diagnostics techniques development we implemented a new neutron detector based on radioyttrium for determination of the emission rate of the 14 MeV neutrons at the operation of the PF-6 device with sealed chambers working with a D–T mixture. By means of this PF-6 device we have provided experiments on irradiation of tungsten based specimens and a number of other materials that can be used for the first wall and construction elements of fusion reactors. The specimens were supplied by FZJ, IMET, and TU. The same samples were irradiated in the frame of the round robin test experiments in parallel and in sequential sessions with the Bora device (ICTP,), at the PF-1000U facility (ICDMP), PF-12 machine (TU), at the plasma accelerator QSPA Kh-50 facility, and at the PF-5M device (IMET). We compared the results of these irradiation experiments provided with dissimilar devices and in different irradiation conditions. Investigation of physical processes taking place in the PF-6 facility during the irradiation experiments was executed side by side with analogous researches made in cooperation with our colleagues at their laboratories with the above mentioned devices. We have provided analytical investigations of the damage character of the specimens of tungsten, carbon-based composites, ceramics and some other materials being irradiated during the CRP activity. Optical microscopy, scanning electron microscopy, atomic emission spectroscopy, images in secondary electrons and in characteristic X ray luminescence of different elements (i.e. the X ray elemental analysis) present results for a number of materials including low-activated ferritic and austenitic stainless steels, β-alloy of Ti, as well as W (candidate material for divertor in ITER) and its alloy. As the spin-off applications we used X ray and neutron flashes to provide experiments on unveiling of hidden objects (in particular, on a disclosure of the concealed fissile materials), on nuclear medicine, on radiation biology (radioenzymology), and on the dynamic quality control as well.

1. INTRODUCTION

Maximal power of heat loads expected such as edge localized modes (ELMs), vertical displacements (VD) and disruption instabilities (DI) in nuclear fusion reactors (FR) with magnetic plasma confinement (MPC) are about 10^4 W/cm^2 [1, 2, 3]; whereas in reactors with inertial plasma confinement (IPC) the values of power of these stresses may reach 10^8 W/cm^2 [4, 5]. Time duration of the events heating the first wall and construction elements in the chambers is 10^{-5}–10^{-2} s for FR with MPC whereas for FR with IPC this value corresponds to 10^{-7}–10^{-6} s. In the contemporary and future fusion devices the following sorts of radiation are provided the above mentioned influences upon the plasma facing materials:

— Soft and hard X rays;
— Fusion neutrons (of about 2.5 MeV and 14 MeV energy) and alpha particles;
— High temperature plasma (HTP) streams ($T_{pl} \approx 0.1$–1.0 keV, $v_{pl} \geq 10^7$ cm/s);
— Beams of fast ions (FI) of hydrogen isotopes, which produced in both types of FR due to plasma acceleration processes, nuclear fusion reactions and (in particular for the FR with MPC) by neutral beam heating of plasma (0.1 MeV for JET and 1..0 MeV for ITER).

[*] Institute of Plasma Physics and Laser Microfusion, Warsaw, Poland.
[1] Institute of Metallurgy and Material Science, Moscow, Russian Federation.
[2] Institute of Nuclear Physics, Polish Academy of Sciences, Krakow, Poland.
[3] Institute of Plasma Physics, Prague, Czech Republic.
[4] The ACS Limited, Warsaw, Poland.
[5] Medical Radiological Research Center, Obninsk, Kaluga, Russian Federation.
[6] M.V. Lomonosov Moscow State University, Moscow, Russian Federation.
[7] School of Natural Sciences and Health, Tallinn University, Tallinn, Estonia.
[8] National Centre for Nuclear Research, Otwock/Swierk, Poland.

Among these irradiations the most hazardous are ions (belonging both to plasma and fast ion streams) because of their short projective pass length in solid matter and specificity of absorption mechanism. All others are counted as less dangerous.

It is well known that dense plasma focus (DPF) devices [6] are able to generate very powerful streams of hot deuterium ($T_{pl} \approx 0.1–1.0$ keV) or deuterium/tritium plasma and fast ions ($E_i \approx 0.1–1.0$ MeV, for deuterons). The PF-6 device (5.6 kJ) [7] operational at the IPPLM, Warsaw, Poland, is our main instrument employed for tests of perspective materials that are intended for use in future FR like ITER [1], NIF [4] and Z-machine [8]. The maximal amplitude of a discharge current in the PF-6 device reaches very high values of up to 0.76 MA, i.e. setting a record for the apparats of its respective class. This set-up generates very powerful pulsed directed streams of hot ($T_{pl} \sim 0.1–1.0$ keV) dense ($n_{pl} \sim 10^{15}–10^{19}$ cm^{-3}) plasma and fast ions ($E_i \sim 0.1–1.0$ MeV for deuterons) along Z-axis of its chamber from the anode. Power flux density of the streams on the target surface may reach 10^{10} W/cm^2 and 10^{12} W/cm^2 for plasma and fast deuterons respectively (they can be decreased by increasing a distance between the device's anode and a target). Besides, the PF-6 device produces very short ($\tau \sim$ 10 ns) bright pulses of fast electrons ($E_e \sim 0.1–1.0$ MeV), soft and hard X rays ($E_{hv} \sim 10^{-1}–10^3$ keV) and fusion neutrons ($E_n \approx 2.5$ MeV or 14 MeV) [6, 7]. A so-called 'integral damage factor' [9] side by side with the above mentioned parameters of the plasma/ion streams of the PF-6 device ensure a capability to use this device having much lower energy storage compared with the basic nuclear fusion reactors like NIF and ITER for materials tests.

According to our knowledge any accurate measurements (in the ns range) of a rise time of events like ELMs in reactors with MPC are absent up to the moment [2, 10]. One may say only that it is noticeably shorter than 1 μs. In reactors with IPC the first action of hot plasma and streams of fast ions (counted as the most dangerous factors in materials damage) upon the chamber wall has a duration $10^{-8}–10^{-7}$ s. Thus our devices are very well fitted for simulation of irradiation processes taking place in chambers with IPC and can be quite fruitful for modelling of the initial (and the most powerful) period of plasma/ion streams action upon the chamber walls in NFR with MPC. Besides, with a special anode's geometry of a DPF chamber an extraordinary regime of operation can extend duration of a heat load inside a DPF chamber up to 30 μs in the PF-6 device (and up to 100 μs in the PF-1000 facility correspondingly) [10].

It is very important to mention here that modelling of the heat loads in our DPF is produced just by streams of the same nature (plasma and fast ions) having parameters as expected on the first wall in the future FR modules (plasma temperature ~ 1 keV, fast ion energies ~ 0.1–1.0 MeV). So in comparison with the devices where electron and laser beams are used for verification nature tests (where dissipation laws and even absorption zones are quite different) our DPF facilities simulate the real events in the most adequate way. One important example is connected with the generation of blisters, a very common damage defects arising at irradiation material tests. In principle, blisters may be produced by boiling up of light fractions of materials or materials themselves. Another type of them is generated by injection (forced implantation) of hydrogen isotopes into the bulk of a specimen. It is clear that the second type that is the most dangerous one and connected with the very important tritium retention problem can be simulated only in plasma accelerators and DPF machines. In addition, our PF-6 device has a large number of unique contemporary diagnostic techniques that allow providing investigations of irradiation processes of tested samples with 1 ns temporal and high spatial, angular and spectral resolution. During the irradiation experiments, we monitored a large number of parameters including temporal and spatial evolution of primary (a DPF pinch and accumulation stream) plasma density and temperature, power flux densities of fast ion and relativistic electron beams on targets under irradiation, soft and hard X ray and neutron radiations, angular, temporal and spatial distributions of these radiations types. We also measured the same characteristics for secondary plasma, produced by these penetrating radiations at the surface of a solid state target under test. By means of this PF-6 device we have carried out experiments on irradiation of materials that can be used as the first wall and construction elements in future nuclear fusion reactors. Among them we irradiated different grades of tungsten (in particular, the samples of double forged tungsten) and its alloys, carbon based composites, various types of low activated stainless steels (e.g. Eurofer), titanium alloys and some other materials counted as perspective ones for their use in FR.

Equal samples have been irradiated in the frame of the round robin test experiments in parallel and in sequential sessions with the Bora set-up (ICTP), at the PF-1000U facility (ICDMP), PF-12 machine (TU), at the plasma accelerator QSPA Kh-50 facility, and at the PF-5M device (IMET). Subsequent analysis of the irradiated specimens provided with contemporary analytical methods has yielded information on the changes that occurred in the irradiated materials elemental and molecular contents, structure and properties that were produced during the experiments.

2. DIAGNOSTICS AND OPERATIONAL CAPABILITIES OF THE PF-6 LABORATORY

2.1. Equipment used in the irradiation experiments

2.1.1. PF-6 device and its parameters

Our main instrument — the PF-6 device — depending on the initial charging voltage is able to ensure in principal the characteristics, presented in the Table 1.

TABLE 1. MAIN PARAMETERS OF THE PF-6 DEVICE

Bank capacity	28 μF
Charging voltage	12–20 kV
Energy storage	2.0–5.6 kJ
Discharge current	350–760 kA
¼ of the discharge period	0.9–1.2 μs
Working gases	D_2, D–T mixture (50%–50%) N, H_2, Ar, Xe, He, CH_4
DPF chamber type	DF6 or DF9, Mather configuration
Repetition rate	Up to 1 Hz
Life time of the DPF systems	~ 10^6 (10^4 for an anode) shots

However when using the PF6 chamber (the VNIIA nomenclature) in the PF-6 device the maximal parameters distinguished in the device are as follows: bank charging voltage of 16 kV, bank energy of 3.6 kJ, and maximal current amplitude of 500 kA. A typical oscilloscope trace of the $\partial I/\partial t$ is presented in Fig. 1.

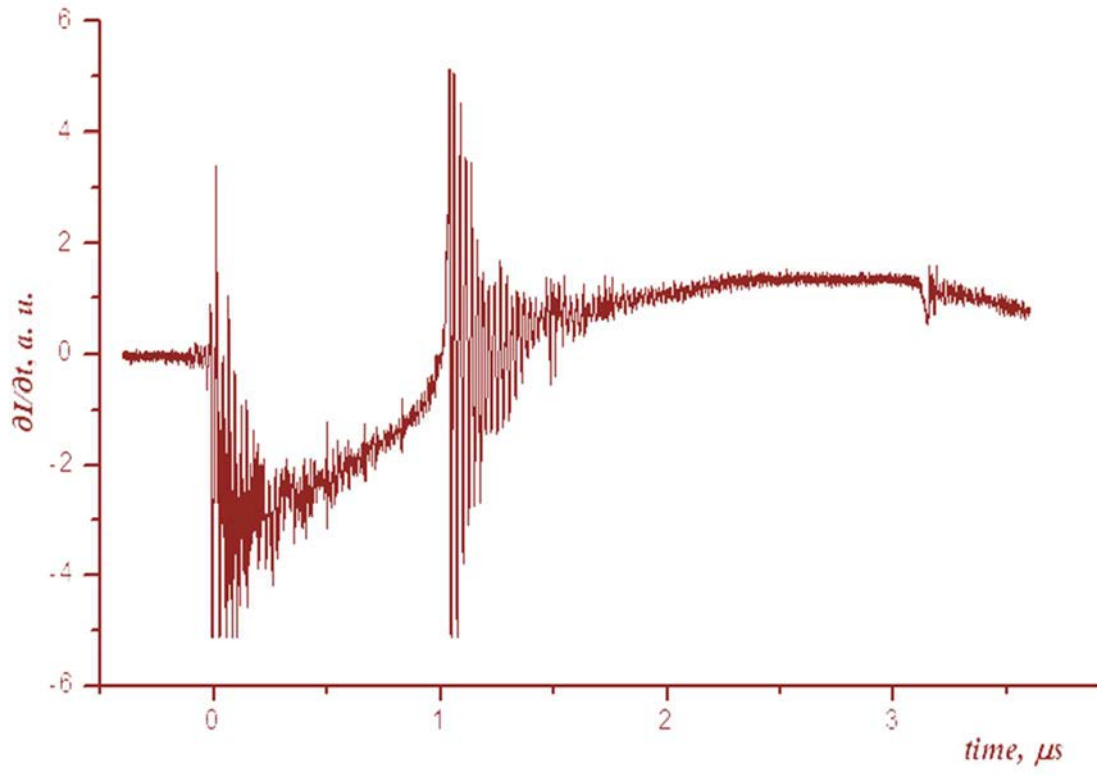

FIG. 1. An oscilloscope trace of the current derivative $\partial I/\partial t$ taken during the experimental session of the year 2013 at the PF-6 device with the PF-6 chamber.

In a process of the CRP fulfilment we have put into operation a new powerful charger that ensured an opportunity to work with the device at a repetition rate up to 1 Hz. This new charger consumes a charging current from the mains on the level of about 25 A. The equipment is presented in Fig. 2.

FIG. 2. A new charger of the PF-6 device able to ensure operation of the facility with a repetition rate up to 1 Hz.

2.1.2. A new spherical dismountable DPF chamber

We have manufactured and successfully tested new big spherical chamber of our own design counted for use at the full charging voltage of our PF-6 capacitor bank, i.e. at 20 kV (before we might use this bank up to 16 kV only). Figs 3(a)–(b) show PF-6 device with the chamber, as well as the above mentioned chamber separately with a magnification. One may see that in contrast to the PF9 chamber (manufactured by VNIIA) this chamber is demountable. It gives an opportunity to open it for maintenance, change of anode's inserts, etc. We are planning to manufacture a special coupling arrangement and place it between the upper and lower hemispherical parts of the cathode that will have windows. It will allow us to use laser interferometry, spectroscopy and other diagnostics to observe processes of interaction of super high energy streams (SES) with different targets inside the chamber. We have produced with this chamber a number of conditioning shots. After that we increased charging voltage of the bank up to the magnitude 20 kV. In this regime we have made about 20 working shots, and the chamber has entered into the proper regime of operation very soon. The working gas used was pure deuterium. We have monitored the total neutron yield (Y_{nTOTAL}) using two silver activation counters. In the best (last) shots the Y_{nTOTAL} magnitude was in the range of (2.0–2.5) × 10^9 neutrons per pulse.

(a) (b)

FIG. 3. (a) The PF-6 device with a new spherical chamber; (b) dismountable chamber shown with a magnification.

Besides we applied two fast scintillator probes with photomultipliers and plastic scintillators having resolution time equal to 1.3 ns (ACS Limited, Poland). The distances between the newly mounted DPF chamber and the probes were about 1 m. Both probes were positioned perpendicular to the Z-axis of the chamber. A typical oscilloscope trace is presented in Fig. 4. One may see that the duration of the hard X ray pulse (the first one) is about 10 ns whereas the duration of the neutron pulse (the second one) appeared to be about 15 ns. The time separation between the pulses was equal to 50 ns as it was expected because of the distance between the source and the detector as well as the neutron energy (~2.45 MeV).

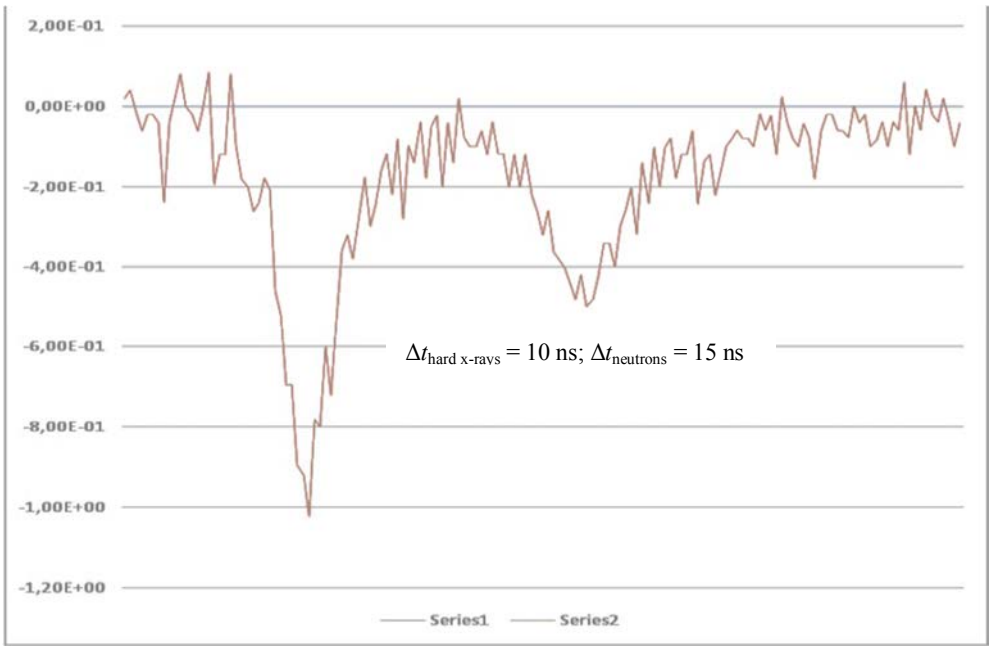

FIG. 4. Oscilloscope trace taken with the operation of the new spherical DPF chamber at a 1 m distance from the source.

To increase an average neutron yield per shot at the operation of DPF with pure deuterium it is necessary to maintain the optimum pressure inside the DPF chamber by purging the deuterium through the chamber continuously at an optimal flow rate. The most sensitive element is the anode of the discharge chamber, which has a life time of about 10^3–10^4 shots depending on its construction. With a proper design the chamber can be changed in a few minutes. All other elements can survive during about 10^6–10^7 shots.

2.2. Equipment used in spin-off applications

2.2.1. D–T chambers for use of the 14 MeV neutrons in DPF spin-off applications

DPF devices of small sizes (having a 1 m^2 footprint) as our PF-6 set-up can produce very short ($\tau \sim 10$ ns) and bright flashes of neutrons (up to 10^{20} n · s^{-1}· ster.) and hard X ray pulses of a few J at once. Such a DPF device is a neutron source that is able to generate pulses of almost monochromatic ($\Delta E_n/E_n \approx 3$–5%) neutrons of the energy of $E_n = 14.0$ MeV if operating with D–T mixture (50%–50%) as a working gas. This D–T DPF device is usually supplied with a sealed discharge chamber and a build-in generator, able to release a mixture of deuterium and tritium to the chamber's volume at the heating of a special gas generator. It is commercially available from the VNIIA. We have implemented two chambers manufactured by VNIIA with such generators, in particular one is similar to the PF-6 chamber and another one is analogous to the PF-9, see Fig. 5.

Neutron yield that is time averaged over 30–200 shots of the medium sized DPF devices (~1 m^2 footprint, ~5 kJ bank) was $\geq 10^{11}$ neutrons per shot. Variation of the neutron yield from shot to shot was about 2 times. Typical oscilloscope trace of hard X ray (first) and 14 MeV neutron (second) pulses registered at our PF-6 device with the second of the above mentioned chamber is presented in Fig. 5. We found that the pulse durations were in the ranges 25–32 ns for hard X rays and 30–40 ns for neutrons. These features provide an opportunity to use the time of flight (TOF) technique with relatively short flight bases (a few metres) in various potential applications.

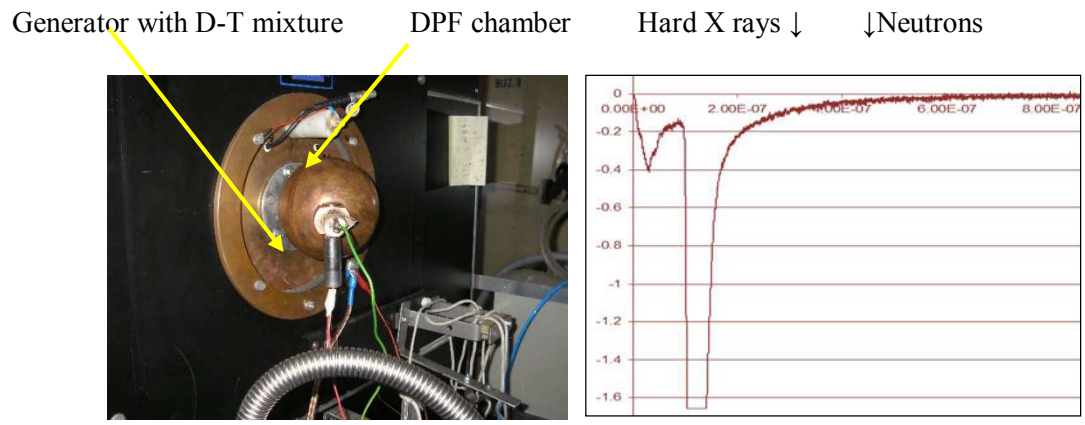

FIG. 5. An oscilloscope trace of hard X ray (first, $E_{hv} > 80$ keV) and neutron (second, $E_n \approx 14$ MeV, saturated) pulses obtained at 6 m distance from the source with the chamber filled with a D–T mixture as a working gas.

2.2.2. Emission rate for the 14 MeV neutron generators

The neutron emission rate (Y_n) is one of the most important parameters defining the emissivity of contemporary neutron sources including DPF devices. It could be determined in different ways but the activation technique still is very important [12]. The aim of this our experiments was to assess the reaction rate *R* and Y_n for the neutron generator (NG) installed in the National Centre of Nuclear Research in Swierk, and later on for the DPF chambers with a mixture of deuterium and tritium as a working gas used at IPPLM, correspondingly. To this aim the nuclear properties of the radioyttrium were carefully studied. They showed that yttrium nuclide could be effectively used as a neutron monitor. In these experiments the yttrium sample was irradiated for a predefined time. Finally, the activity of the yttrium sample was measured by means of a γ-spectrometry method. Yttrium has only one stable isotope: ^{89}Y. Neutrons interact with yttrium target causing inelastic scattering. As a result, the following nuclear reaction occurs [13]:

$$n + {}^{89}\mathrm{Y} \rightarrow {}^{89m}\mathrm{Y}\ (T_{1/2} = 15.663\ \mathrm{s}) + n' + \gamma\ (E_\gamma = 908.96\ \mathrm{keV};\ I_\gamma = 99.16\%) \qquad (1)$$

where E_γ is the γ-quanta energy, and I_γ is probability of particular γ-quanta emission. An isotope of yttrium produced in this reaction has a relatively short half-life, and returns to the ground state with the intensive emission of the monoenergetic γ radiation. The yttrium sample used for measurements had diameter of 80 mm and thickness of 5 mm. The optimization of the geometry of the sample for its optimal activation and high detection efficiency was the subject of our earlier work [14]. Fig. 6 shows the cross-section for the considered nuclear reaction as given by the TENDL-2013 nuclear data library.

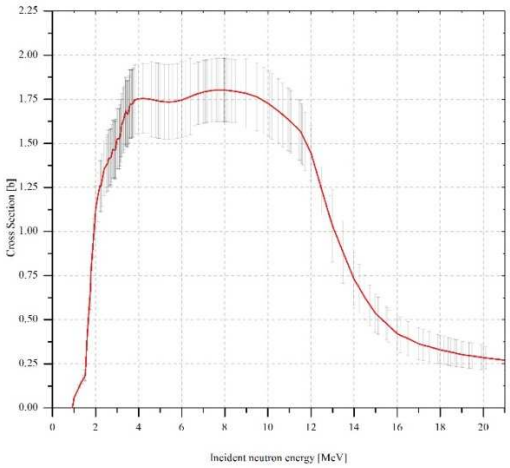

FIG. 6. The cross-section for activation of ^{89}Y (TENDL-2013 nuclear data library) [15].

The $n + {}^{89}Y$ reaction is a threshold reaction and occurs when neutron energy exceeds ~ 919 keV [15]. The cross-section assumes its maximum value (i.e. 1.8 barns) for the neutron energy 7.80 MeV. The cross-section for 14.14 MeV neutrons is approximately half of the maximum value (0.7 barn) and lies on the descending part of the curve. The reaction does not occur for slowed down and scattered neutrons with energy below the threshold.

A 14 MeV NG SODERN Model: GENIE 16 (Fig. 7) was used as a source of neutrons for determination of the neutron production rate using yttrium sample.

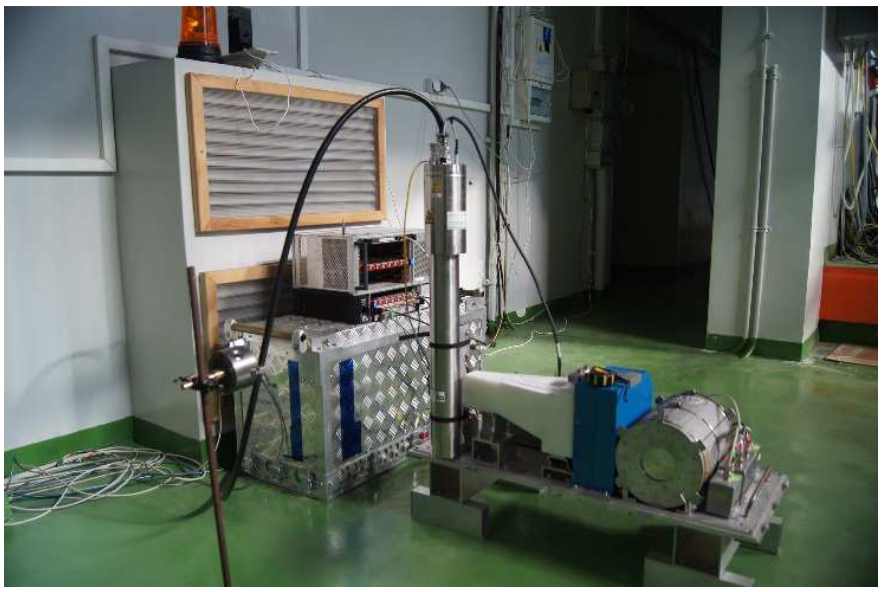

FIG. 7. The 14 MeV neutron generator.

The maximum neutron yield of the generator is 2×10^8 n/s. During the NG life cycle the Y_n decreases. The neutron energy spectrum is strongly dependent on NG's directions regarding unit axis but also on environment and neighborhood. This is due to the neutron interactions with walls, floor and other massive elements that are close to the NG. The NG used in this experiment was permanently fixed to the floor. The configuration of shields and other massive objects was preserved. Therefore it is expected that the neutron spectrum in the particular location does not change in time. In Table 2 the current of the deuterium ions on the target and the neutron emission rate for some of the electrical settings of the NG used in this experiment.

TABLE 2. BASIC PARAMETERS OF THE 14 MEV NEUTRON GENERATOR

Acceleration voltage [kV]	Current of the deuterium ions on the target [μA]	Neutron emission in 4π [n/s]
75	30	0.39×10^8
90	20	0.51×10^8
85	35	0.70×10^8
90	35	0.88×10^8
90	40	$1.0 \quad 10^8$

The main operating parameters of the NG were the acceleration voltage 90 kV and the current of the deuterium ions on the target 40 μA. The total spent working time for the NG in this experiment was less than 500 hours. The yttrium sample was fixed 30 cm from the center of the neutron source along the direction perpendicular to the main axis of the NG. The sample was put into a thin nylon foil attached to the arm of the metal stand. It was assumed that the saturation time of yttrium is $t_s \approx 6\ T_{1/2}$ and the irradiation time was taken as twice the saturation time and equal to $t_i = 200$ s. The sample was activated, and then manually transferred to the measuring stand. The samples cooling time ranged from 12 to 14 s. The n-type HPGe detector with relative efficiency of 30% and resolution 1.80 keV (for the 1332 keV peak of ^{60}Co) supplied by Canberra was used for the determination of the radioactivity induced in the yttrium sample by neutrons from the NG. The measurement was performed using the Inspector 2000 Multichannel Analyzer and analyzed with the use of the Genie PC software. The detector was supplied with its numerical characteristic (pre calibration). LabSOCS® software (Laboratory Sourceless Object

Calibration Software) allows mathematical energy efficiency calibration without the use of calibration sources for practically unlimited measurement geometries as well as sample geometry.

The efficiency of registration is understood as the efficiency determined for the absolute full energy peak efficiency (AFEPE). The standard deviation of the mathematical energy efficiency calibration is 3.0–7.1% [16, 17]. The energy efficiency calibration was based on the numerical characteristic of the HPGe detector. Fig. 8 shows the energy efficiency calibration curve for the considered geometry of the yttrium sample. After activation of the sample and its cooling the γ-spectrum was recorded for 100 s. The resulting spectrum is shown in Fig. 9. The yttrium radioactivity was determined by means of γ-spectrometry method. Activation of each sample was determined for the moment when activation was completed. It is expressed by:

$$A = \lambda N_p/[I_\gamma \, eff \, (e^{-\lambda t_s} - e^{-\lambda(t_c + t_m)})] \tag{2}$$

where: λ is the decay constant of ^{89m}Y [s^{-1}], N_p is the number of counts (unitless), eff (E_γ) is the AFEPE (unitless) for γ-quanta with energy E_γ = 909 keV, I_γ is the emission intensity (unitless), t_c is the cooling time (s), and t_m is the measurement time (s). Let A be the yttrium radioactivity (Bq), A_{rel} the atomic mass of the target nucleus (g/mol), m the mass of irradiated sample (g), f_i the abundance of particular nuclide in the sample (unitless), N_{Av} the Avogadro constant (mol^{-1}), t_{irr} the irradiation time (s). Then the reaction rate R is given by:

$$R = AA_{rel}/[mf_iN_{Av}(1 - e^{-\lambda t_m})] \tag{3}$$

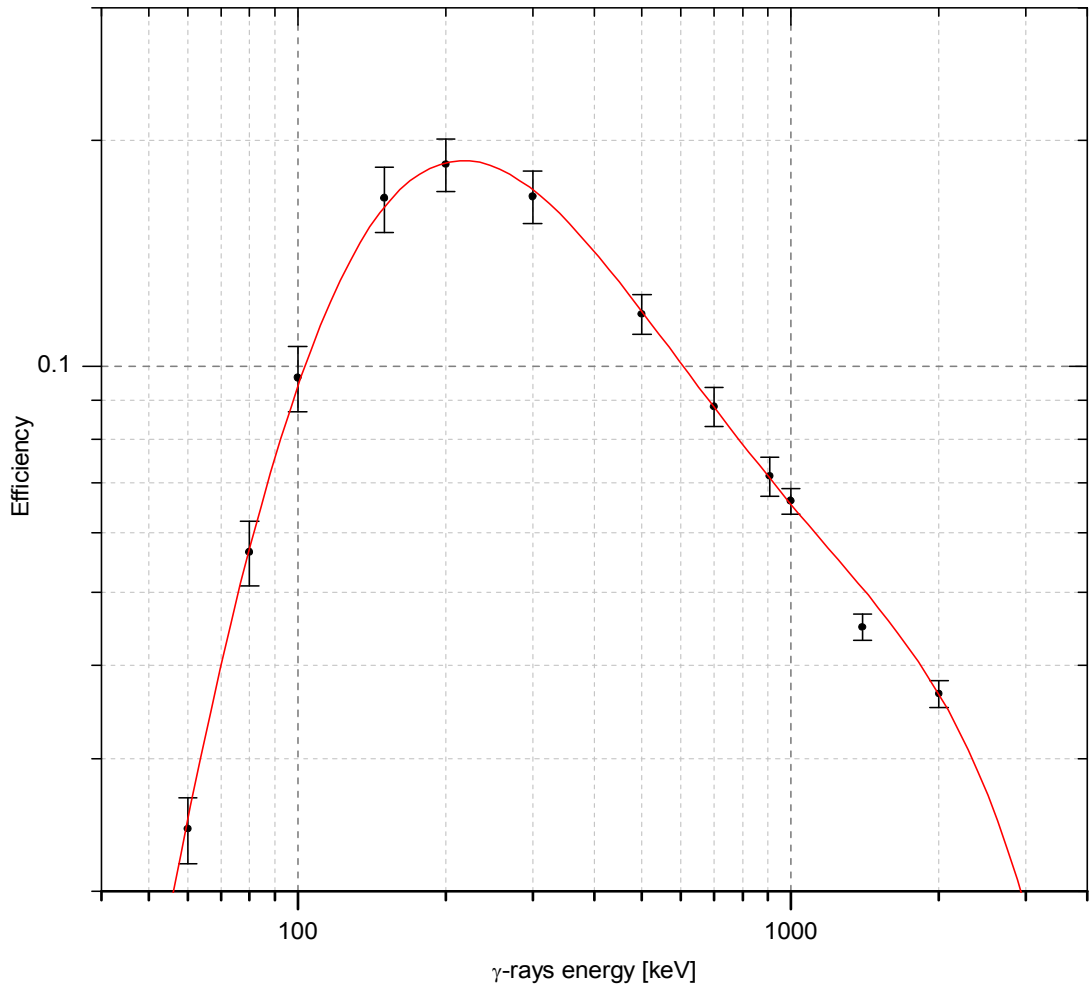

FIG. 8. Energy efficiency calibration curve for the considered geometry of the yttrium sample.

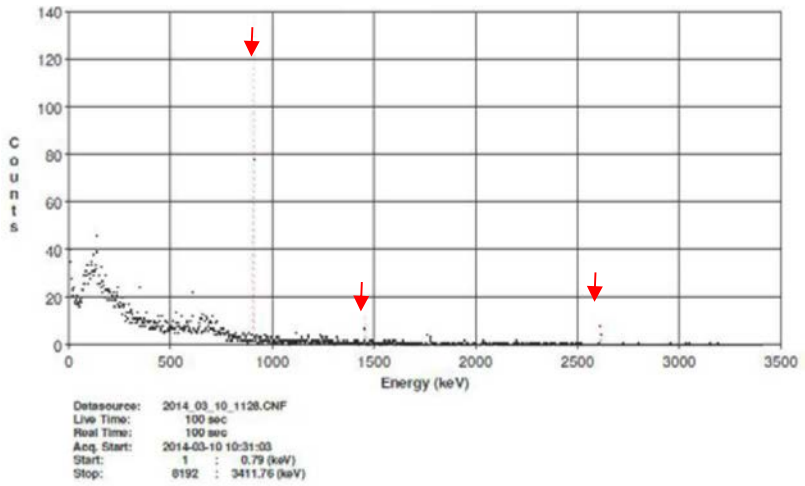

FIG. 9. The spectrum measured for the yttrium sample. The consecutive peaks 909 keV (^{89m}Y), 1460 keV (^{40}K) and 2614 keV (^{208}Tl) are labeled with red arrows.

The neutron emission rate Y_n is expressed by:

$$Y_n = (R4\pi d^2)/\sigma(E_n) \quad (4)$$

where d is the distance of the sample from the detector (cm), $\sigma(E_n)$ is the value of the cross-section for 14.14 MeV neutrons (cm^2). The values of the parameters used in calculation of the neutron emission rate with the use of the yttrium activation are shown in Table 3.

TABLE 3. PARAMETERS USED IN THE CALCULATION OF THE NEUTRON EMISSION RATE

Parameter	Value	Relative error (%)
A (Bq)	5010	5.77
A_{rel} (g·mol^{-1})	88.91	–
σ (cm^2)	7.20×10^{-25}	8.60
m (g)	114.74	0.01
f_i	1	–
N_A (mol^{-1})	6.022×10^{23}	4.48×10^{-6}
λ (s^{-1})	0.0443	0.03
t_i (s)	200	–
d (cm)	30	3.33

2.2.3. Results

The value of AFEPE for the E_γ = 909 keV of γ-quanta used for the radioactivity calculation was 2.15 ± 5%. The spectra from the activated samples were measured using the γ-spectrometer and then the radioactivity of each sample was determined. The average activity of yttrium was A = 5.01 ± 0.29 kBq (value calculated on the basis of four measurements obtained from Genie 2000). The calculated reaction rate was $R = 6.45 \times 10^{-21}$ ± 5.77% reactions s^{-1} and the neutron emission rate was found to be $Y_n = 1.04 \times 10^8$ ± 10.88% n/s. This technique is intended for use in future with our DPF chambers filled with D–T mixture as a working gas.

3. INVESTIGATION OF PHYSICAL PROCESSES

3.1. Equipment used in the irradiation experiments

Side by side with our main facility PF-6 employed for tests of perspective materials, together with our colleagues we used in these experiments PF-1000U (maximal energy of its capacitor bank is 1.2 MJ, IPPLM) and Bora (ICTP) facilities for comparative testing samples intended for use in future fusion reactors (FR) like ITER [1]

and NIF [4]. All these DPF devices in these irradiation experiments explored pure deuterium as a working gas. Their maximal discharge currents may reach very high values from 0.30 (Bora) and up to 2.0 MA (PF-1000U). Moreover, these devices have a large number of unique contemporary diagnostics helping to provide investigations of irradiation processes of tested samples with a high temporal, spatial, angular and spectral resolution. During irradiation experiments, we monitored a large number of parameters including temporal and spatial evolution of primary (DPF pinch and accumulation streams) plasma density, power flux densities of fast ion and relativistic electron beams on targets under irradiation, soft and hard X ray and neutron radiations, angular and spatial distribution of these radiations types. We also investigated the same characteristics for secondary plasma, produced by these penetration radiations at the surface of a solid state target under test. Our devices generate very powerful pulses of hot dense ($T_{pl} \sim 1$ keV, $n_{pl} \sim 10^{15}$–10^{19} cm^{-3}) deuterium plasma (HP) jets (velocity $v_{pl} \sim (2–4) \times 10^7$ cm/s, pulse duration $\tau_{pl} \sim 50–500$ ns) of maximal power flux densities on the target's surface $P_{HP} \sim 10^9$ W/cm^2 and fast ion (deuteron) streams (FI) (with deuterons energy $E_d \sim 0.05–1.0$ MeV and pulse durations $\tau_d \sim 20–100$ ns) with maximal power flux densities $P_{FIS} \sim 10^{12}$ W/cm^2 respectively.

During the PF-6 device operation we monitored the following parameters: current derivative by magnetic probes, full discharge current by Rogowski coil, neutron and hard X ray pulses by 2 photomultiplier tubes with scintillators with the time resolution of this last technique of ≈ 1.3 ns (see Fig. 10 for an oscilloscope trace taken at the PF-6 device during the irradiation process), plasma dynamics by 1 ns 4-frame self-luminescence and 16-frame laser interferometry visualization, absolute neutron yield using Ag, In, Y and Be activation counters. Besides we measure the absolute hard X ray and neutron yield using the Röntgen-gamma dosimeter RFT (Germany) and 2 silver activation counters correspondingly. Current was up to 300 kA with rise times of 1.0 μs and 1.5 μs in two devices in these experiments (PF-6 and Bora correspondingly) and about 2 MA with the rise-time of 4 μs at the PF-1000U facility. Pulse durations of the deuterium plasma and fast deuterons streams in these devices were ≈ 100–500 ns and 20–100 ns respectively; whereas FWHM of neutron and hard X ray pulses for PF-6 device in the irradiation regimes were 8–12 ns and 18–23 ns respectively (see Fig. 10).

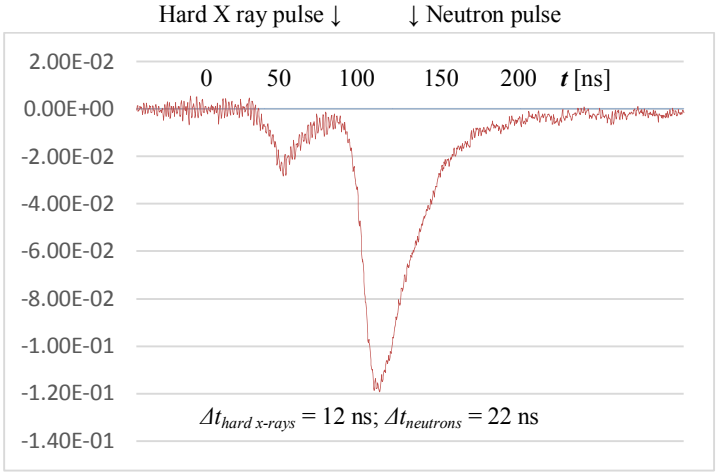

FIG. 10. Hard X ray (left) and neutron (right) pulses are shown by arrows for the PF-6 device.

3.2. Results obtained

In the experiments devoted to radiation tests of materials maximal neutron yield was about 2×10^8 neutrons/pulse for the PF-6 facility and about 7×10^7 neutrons/pulse for the Bora device whereas the overall hard X ray flux may reach 1 J in the full solid angle for both small machines. In the case of PF-1000U device the maximal neutron yield was about 10^{11} neutrons per pulse.

It is important to note that because of our diagnostic complex we can investigate the samples not only after their irradiation by various analytical methods. In fact we are able to monitor the irradiation process itself with high temporal, spatial and spectral resolution by laser interferometry (Fig. 11) or by registering self-luminescence of plasma in a visible range of spectrum (i.e. by streak camera with a slit scan of implosion process as in Fig. 12 and with spectroscopic investigations of ionizing states of ions in target plasma as in Fig. 13). From Fig. 12 one may measure a velocity of the implosion of the plasma/current sheath near the axis (≈2×10^7 cm/s).

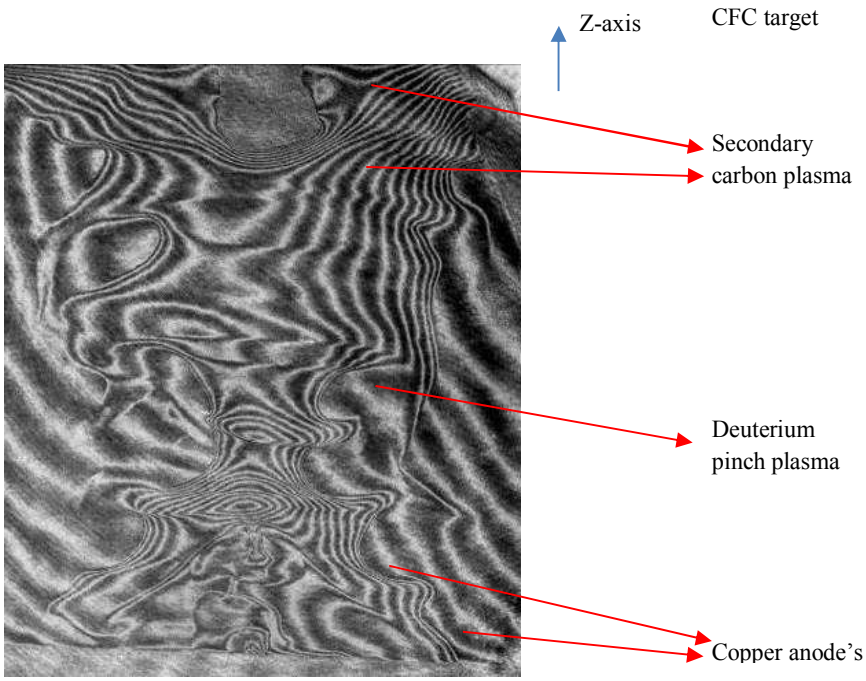

FIG. 11. Interferometric picture of a deuterium plasma pinch and secondary carbon plasma produced on a CFC sample surface.

From the interferograms one may measure a speed of the outer boundary of the spreading secondary plasma. After irradiation of a target by a powerful ion streams its value reaches a value $\geq 10^7$ cm/s. It means that the temperature of the secondary plasma at the moment of its heating is about 100 eV [18].

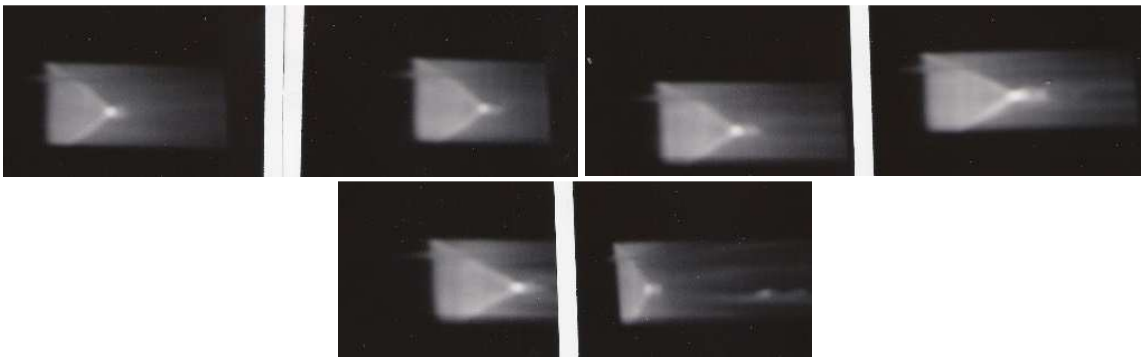

FIG.12. Streak camera slit scans of the pinching processes in six consecutive shots of PF-6 device occurring with different implosion velocities (the same sweep speed).

From Fig. 13 one may see that in the first period of time after the Current Abruption (CA) phenomenon [19] our spectrometer registers mainly deuterium plasma lines (Dα, Dβ). This is our 'primary' plasma generated in the pinch and colliding with the target. Then at the moments near the second microsecond after the moment of CA a cloud of secondary plasma is generated near the target (in this case a sample of SiC). One may see here mainly lines of the target material (C and Si). The degree of ionization (e.g. an observation of CIV lines) confirms the high value of secondary plasma temperature that was deduced earlier from the velocity of its expansion. In the later stages the spectrometer registers a mixture of both substances.

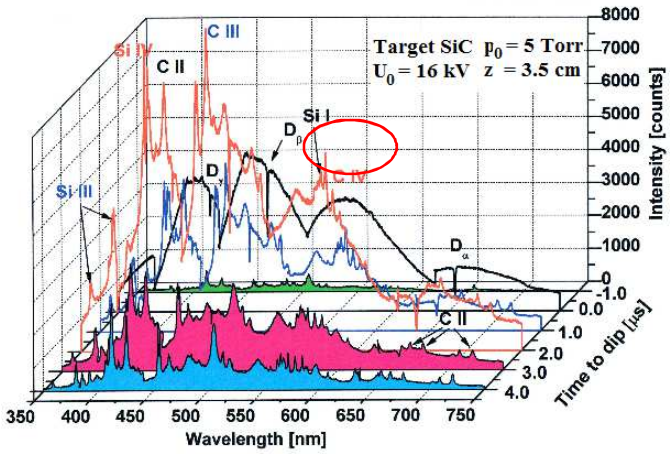

FIG. 13. Spectra obtained at different moments of the discharge with a SiC target.

4. IRRADIATION EXPERIMENTS

4.1. Materials

The same samples were irradiated in the frame of the round robin test experiments in parallel and sequentially — besides the PF-6 device — at the PF-1000U facility (ICDMP), at the PF-12 machine (TU), at the plasma accelerator QSPA Kh-50 facility (IPP, Kharkov, Ukraine) and at the PF-5M device (IMET). We compared the results of these irradiation experiments produced with dissimilar devices and in different irradiation conditions. Our samples were the double forged W (supplied by the IAEA and FZJ [20]) and the tungsten alloy (W 1% La_2O_3), different types of ceramics (Al_2O_3) and carbon-based materials (CFC and SiC), Ti and Ti alloy ($Ti^{18}V^{5}Mo^{3}Fe$(Sn, La)), Al, low activated ferritic steel (Eurofer) and some others that are counted as the perspective ones for FRs.

4.2. Conditions of irradiation

In Fig. 14(a) one may see a top view of the discharge chamber of the PF-6 device without the upper lid and a side view of the upper part of this chamber with a holder where a SiC specimen is vised. One may see that the anode has a central hole whereas the holder grasps a target below its upper part facing to the irradiating streams. These measures gave us an opportunity to minimize redeposition of unauthorized materials upon the target surface.

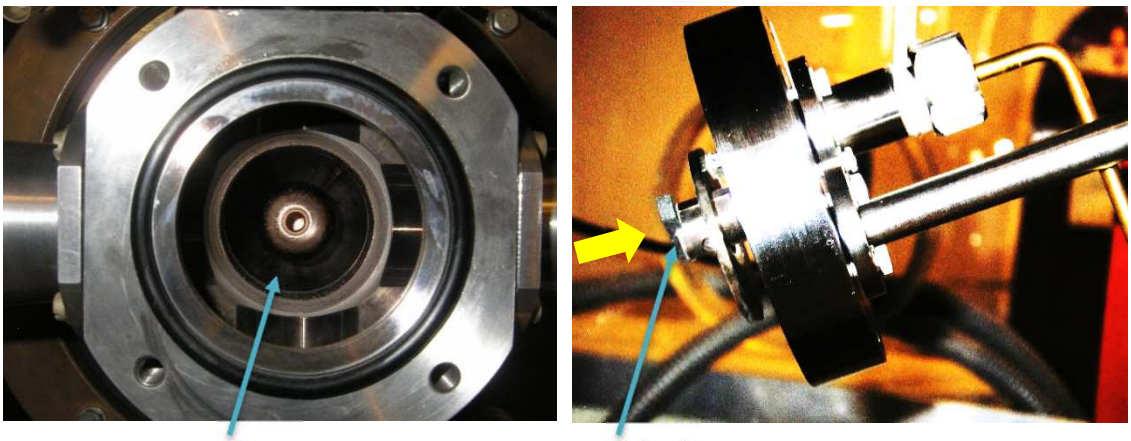

Anode
(a)

SiC sample in a holder at the cathode part of the PF-6 chamber
(b)

FIG. 14. (a) Discharge chamber of PF-6 device with hollow anode; (b) radiations material part with a sample.

The majority of radiation tests with the above mentioned materials was conducted with the PF-6, Bora and PF-1000U facilities at the energy levels of 2 kJ (for the first two devices) and 240 kJ (PF-1000) correspondingly. We placed our specimens in the cathode part of the PF-1000U chamber on its axis at the distances from the anode 7 and 11.5. In the PF-6 and Bora devices this distance was usually 3.4 cm. It ensured the same (maximal) power flux density as in the PF-1000U facility yet on a smaller area. Penetration depth of the 1 keV ions belonging to a hot plasma stream is equal to few nanometers whereas the value for the 100 keV fast deuterons is ≤ 1 μm [21]. Thus, taking into consideration power flux densities for hot plasma and fast ion streams, these devices may produce ablation of the material under pulsed irradiation (i.e. its sublimation and conversion into hot plasma without melting) during the radiation action period. Later, after the pulses end, the target material will be melted due to a presence of expanding secondary plasma and recrystallized. So we may certify that our DPF device in general and PF-6 set-up in particular are very well fitted by all parameters for their use in irradiation tests.

A so-called integral damage factor [9] ensures an opportunity to simulate radiation loads (predictable for both reactors types) by the plasma/ion streams generated in DPF. It is so because the values of the power flux densities of hot plasma and fast ions q are much higher compared with those expected at the first wall of FRs of both types. It compensates the short pulse duration of these streams generated in a DPF associated with e.g. ELMs events periods. However here we must note that this integral damage factor must be used with a caution and in a very specific range of irradiation conditions.

5. INVESTIGATION OF DAMAGE FOR TUNGSTEN AND OTHER SPECIMENS

5.1. Methods

Before and after irradiation we provided investigations of our samples by means of a number of analytical techniques. Among them we used digital optical microscope (OM) and scanning electron microscopy (SEM) to understand character and parameters of damageability of the surface layers of the samples. Atomic force microscopy (AFM) was applied to measure roughness of the surface after irradiation. These characteristics are quite important for understanding of mechanisms and values of dust production in FR that may relate to tritium retention and emergency situations in FR facilities. Subsequent analysis of the irradiated specimens yielded also information on the changes that occurred in the irradiated materials' elemental and molecular contents, structure and properties produced during the experiment.

5.2. Results

After producing the above mentioned irradiations with a different number of pulses, we carried out an analytical investigation of our specimens. Fig. 15 depicts SEM images of the surface of the above mentioned ferritic steel (Eurofer) virgin, after one shot and after five shots of the PF-6 device. A wave-like structure of the surface with initial traces of the microcracks nucleation is observed, see Fig. 15(b), after one shot of the PF-6 device (by HTP and FI streams). A strongly developed wave-like structure of the surface of the same material melted with a fracturing pattern, see Fig. 15(c) becomes apparent after five shots of the same device produced under similar conditions as in the case of Fig. 15(b).

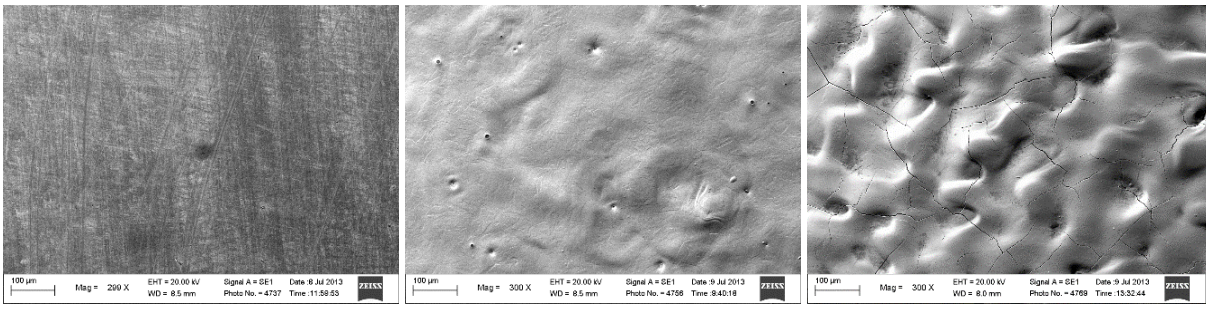

(a) (b) (c)

FIG. 15. (a) SEM images of the stainless steel (Eurofer) virgin material; (b) after 1 shot of the device PF-6; (c) after 5 shots.

In the zones of the maximal power flux densities the damage of the ferritic steel surface acquires a new feature (see Fig. 16, PF-6, eight shots, zone of the FIS action). The material in this case is melted during irradiation. In

addition to the same types of damageability as depicted in Figs 15(b)–(c) (wave-like surface and microcracks) one may observe a number of blisters, see Fig. 16(b), with broken covers Figs 16(c)–(d). In this case, the diameters od the blisters typically range from 100 μm down to less than about 10 μm.

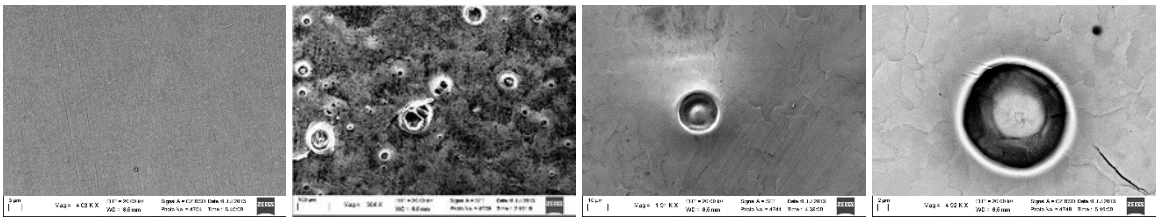

(a) (b) (c) (d)

FIG. 16. (a) SEM images of the ferritic steel sample virgin surface; (b) SEM images of the ferritic steel sample after its irradiation in the zone of maximal power flux density of the FI stream pulse; (c) SEM images after irradiation (different magnifications); (d)) SEM images after irradiation (different magnifications).

Similar blisters but of smaller sizes (lower than 1.00.1 μm) were observed (Fig. 17) in our experiments with the austenitic steel $^{25}Cr^{12}Mn^{20}W$, see its chemical composition in Table 4.

TABLE 4. CHEMICAL COMPOSITION OF THE AUSTENITIC STAINLESS STEEL

Steel	Elements, mass %								
	C	Cr	Mn	Si	W	V	Sc	P	S
$^{25}Cr^{12}Mn^{20}W$	0.26	12.9	19.3	0.13	2.0	0.15	0.1	0.04	0.008

In these experiments a hexahedral tube was placed in the cathode part of the DPF chamber along its Z-axis. The distance between the hot end of the tube and the anode was the same as in the previously described case (for the flat target). However, now the hot plasma jet and the powerful stream of fast ions stroke the internal and external tube surfaces tangentially. We investigated surface layers (SL) and metallographic sections of our samples by SEM (using the microanalyzer EVO 40) and by atomic emission spectroscopy (AES) (using a glow discharge spectrometer SA-2000, "LECO" company). The blisters appeared in the hot part of the tube facing the anode of the chamber. In this case the blisters are not opened; see Fig. 17(a). We observed a remarkably higher concentration of deuterium in the internal part of the tube compared with its content in the external nanolayer; see Fig. 17(b).

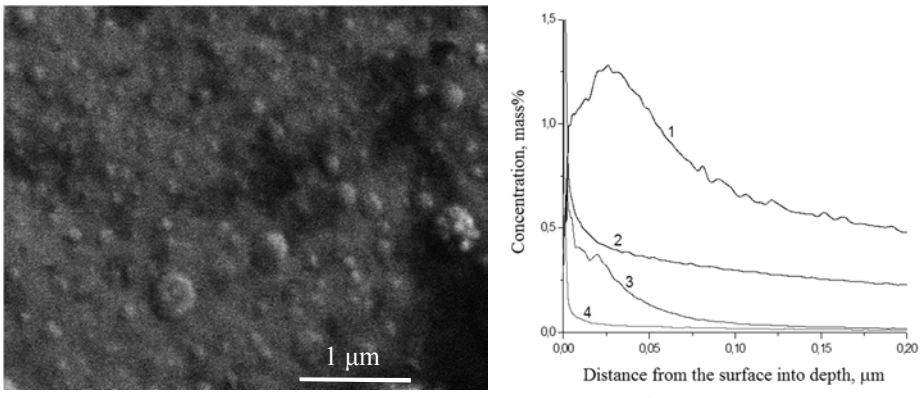

(a) (b)

FIG. 17. (a) C concentration distribution of deuterium and oxygen in the material's depth; (b) '1' refers to deuterium on the internal surface, '2' deuterium on the external surface, '3' oxygen on the internal surface, and '4' oxygen on the external surface of the tube.

Presence of deuterium in the nanolayers under investigation supports the fact that after pulsed penetrating the specimen, deuterium was never fully eliminated from it by evaporation or diffusion. On the contrary, deuterium was preserved inside the crystal lattice. Interestingly, chemical interaction of implanted deuterium with interstitial atoms of the specimen's impurities is very unlikely under circumstances due to a low level of bond energy between the deuterons and these elements.

As a matter of fact, deuterons may have been partially diluted inside the lattice or captured by trapping centers. In the first case, atoms of deuterium left the SL very fast via a diffusion process through an irradiated surface into the chamber volume or into the bulk of the material. The trapping process of atoms was very likely accompanied by creation of vacancy complexes (binding energy of hydrogen with vacancy in iron is 0.5 eV, with the vacancy cluster 0.7–0.8 eV). On the other hand, deuterium was trapped by means of interactions of deuterons with lattice defects of the type of atoms of impurities, pores, oxycarbonitride particles presenting in the material, etc. E.g., the binding energy of the hydrogen atom with the interstitial atoms of carbon and oxygen is within the limits 0.05–0.08 eV [22]. It is highly probable that binding energy of a deuterium atom is within the same spectrum.

At the same time according to theoretical calculations [23] the binding energy of hydrogen atom with impurity interstitial atoms (He, C, N, O) is noticeably higher but nevertheless it does not exceed 0.2 eV. This figure is several times less compared with the binding energy of hydrogen atom with vacancies or vacancy clusters in iron. Subsequent sequential pulsed actions of the energy streams upon the material resulted again in explosion-like melting, partial evaporation and boiling of the liquid phase of the SL. Deuterium atoms (implanted in previous shots) present in the specimens together with extrinsic oxygen and carbon contributed to yielded gas inclusions bubbles [24] inside the melted volume. Some of them escaped through the free surface whereas others implanted mainly into the nanolayers and deeper parts of the irradiated tube.

Fig. 18 presents optical microscopic pictures of the surfaces of tungsten samples manufactured in the Russian Federation and in Germany [20] after their irradiation at the PF-1000U facility.

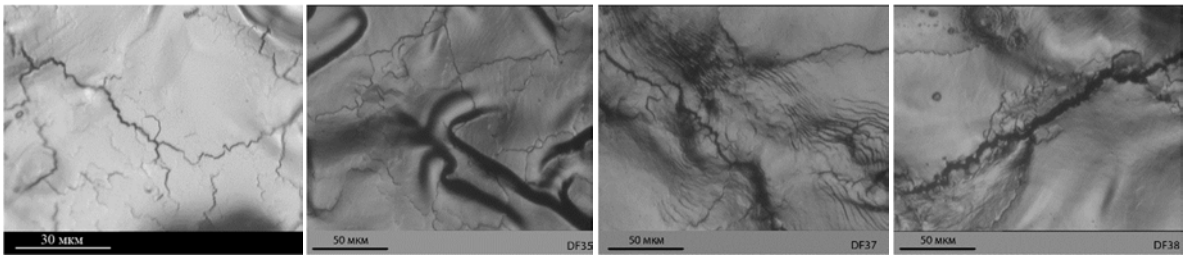

(a) (b) (c) (d)

FIG. 18. (a) Optical microscopic pictures after their irradiation at the PF-1000U facility by two sequential pulses obtained for the surfaces of tungsten samples manufactured in the Russian Federation; (b) optical microscopic pictures after their irradiation at the PF-1000U facility by two sequential pulses obtained for the surfaces of tungsten samples manufactured in Germany, sample DF35; (c) optical microscopic pictures after their irradiation at the PF-1000U facility by four sequential pulses obtained for the surfaces of tungsten samples manufactured in Germany, sample DF37 manufactured in Germany; (d) optical microscopic pictures after their irradiation at the PF-1000U facility by eight sequential pulses obtained for the surfaces of tungsten samples manufactured in Germany sample DF38 manufactured in Germany.

In general the damage character in the comparable specimens is about the same, see Figs 18(a)–(b). It is a wave-like surface and an intergranular fracture. However, in FZJ samples there is a microcracks net developing along the grain body (the transcrystalline damage).

The degree of the damageability was increased with the number of pulses, see Figs 18(c)–(d). Nevertheless, the nature of microstructure defects remained the same: a wave-like structure, intergranular and transcrystalline cracks.

Results of the precise weighing of the samples after their irradiation are presented in a Table 5. As depicted in this table, the average mass loss in both cases (FZJ and IMET samples) is quite high, about 0.008 ± 0.002 g/shot.

TABLE 5. MASS CHANGE AFTER IRRADIATION OF W SAMPLES

No. of a sample	Mass before irradiation	Mass after irradiation	Number of irradiation pulses	Mass change
DF35 (FZJ)	–	–	2	–
DF36 (FZJ)	–	–	2	–
DF37 (FZJ)	–	–	4	–
DF38 (FZJ)	13.0453	12.9564	8	-0.0889
DF39 (FZJ)	12.8765	12.8329	8	-0.0436
DF40 (FZJ)	–	–	4	–
No. 1 (IMET)	28.6880	28.6280	8	-0.060

However, in parallel with erosion process the total mass of the sample was increased due to the redeposition of different elements of the DPF chamber material upon the surface as it was found after irradiation (see Fig. 19, elemental analysis of the sample DF9). The same processes (redeposition of materials and absorption of hydrogen isotopes) take place in fusion reactors. Thus the figures depicted in the Table 5 present both processes of mass loss and mass increase, and one has to consider them as the relative physical data, not the absolute ones.

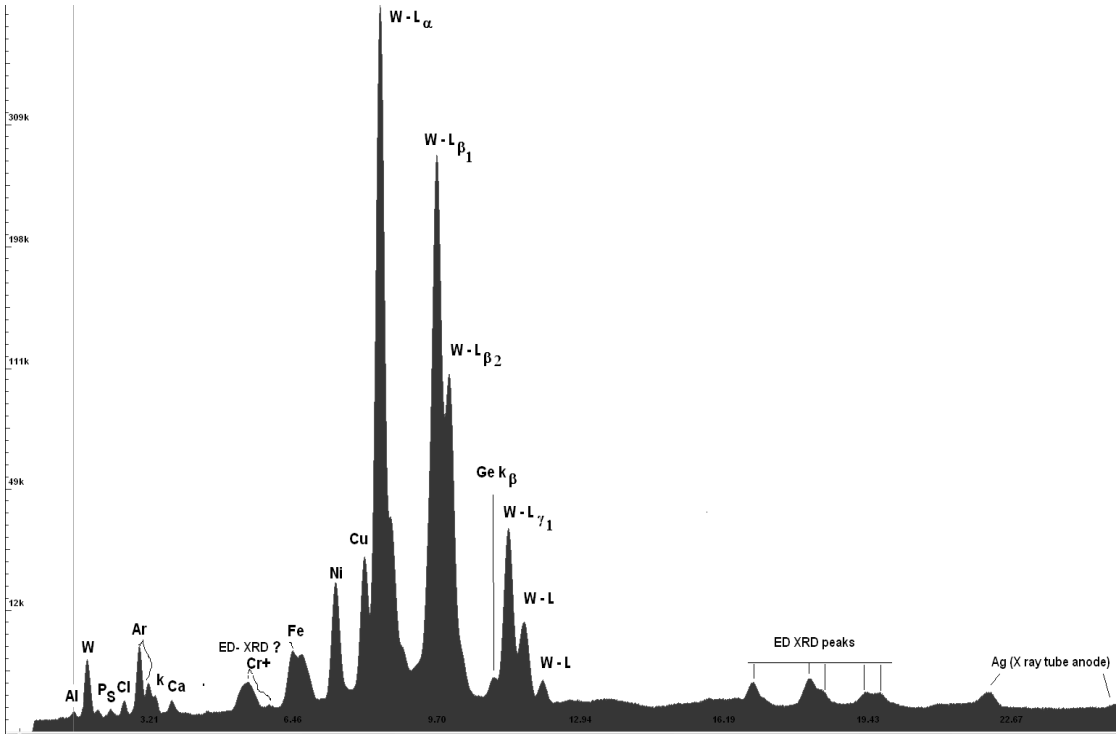

FIG. 19. Elemental analysis of the sample of tungsten DF9 after its irradiation by 8 pulses.

We also conducted a comparative study of the samples of the tungsten alloy of the following type: W 1% La_2O_3. Interest in this material is connected with its easier machinability (in comparison with pure tungsten). Fig. 20 depicts images of this surface layer (SL) irradiated by eight shots at the same distance as above for the double forged tungsten in the PF-1000U facility. These pictures were obtained after its analysis by SEM, in secondary electrons and in some characteristic lines.

Microstructure of the SL contains cracks and porosity. In proximity to cracks, the material tends to peel. Pictures of the same part of the sample scanned in the characteristic line radiation for elements La, O, and C show their higher concentrations in lighter zones.

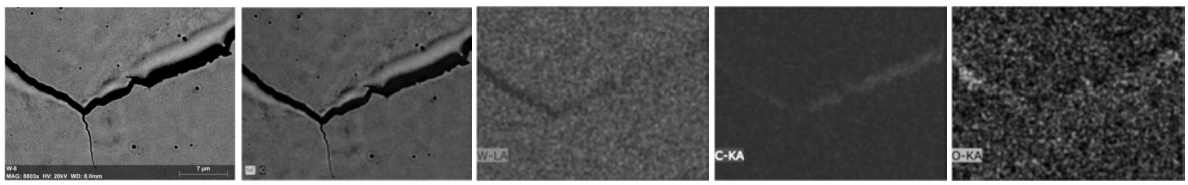

(a) (b) (c) (d) (e)

FIG. 20. (a) SEM images of the W–1% La_2O_3 target after its irradiation in the PF-1000 facility; (b) images in secondary electrons; (c) characteristic line radiations of La; (d) line radiations of C; (e) line radiations of O.

Fig. 21 depicts the SEM and X ray elemental analysis investigations of the β-alloy Ti-, V-, Cr-, bbc lattice, in the area 8 of the sample No. 4 after its irradiation in the PF-6 device by 5 pulses.

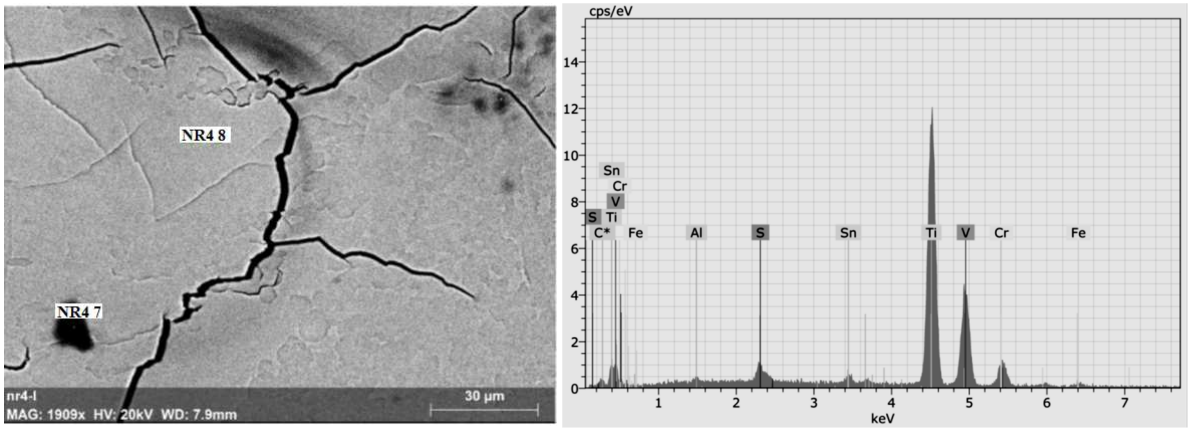

(a) (b)

FIG. 21. (a) SEM elemental analysis investigations of the Ti-alloy sample No. 4 (area 8) after its irradiation in the PF-6 device; (b) X ray elemental analysis.

Elemental content of the SL of the sample in this zone 8 is presented in Table 6. Our β-alloy of titanium is a complex doped high-strength alloy. It contains V, Cr, Fe, Sn, Al. Although virgin material did not contain the elements Mg, Si, S, and O, they were found after irradiation (see Tables 6 and 7).

TABLE 6. ELEMENTAL CONTENT OF THE SL OF THE SAMPLE IN ZONE 8 OF SAMPLE NO. 4

Element	Atomic number	Series	Norm. concentration (wt. %)	Norm. concentration (at. %)
C	6	K-series	0.00	0.00
Al	13	K-series	0.33	0.60
S	16	K-series	1.80	2.75
Ti	22	K-series	70.81	72.36
V	23	K-series	17.35	16.66
Cr	24	K-series	5.61	5.28
Fe	26	K-series	1.43	1.25
Sn	50	L-series	2.67	1.10

However these materials existed in the construction and functional elements of the working chamber of PF-6 device: oxygen and sulfur were the impurity components of corrosion resistant steel $Cr_{16}N_{10}T$ that was used for the working chamber of the facility. Diagnostic windows, insulator and special target holder (placed inside the DPF chamber) contained S, Mg and Si. Presence of these elements in the SL of the titanium alloy shows that during irradiation experiments the above mentioned materials were evaporated by powerful streams of deuterium plasma and fast deuterons. These materials precipitated upon the surface of the specimen target after each pulsed discharge.

TABLE 7. ELEMENTAL CONTENT OF THE TI ALLOY (SAMPLE NO. 4, ZONE 7) AFTER ITS IRRADIATION IN THE DEVICE PF-6

Element	Atomic number	Series	Norm. concentration (wt. %)	Norm. concentration (at. %)
C	6	K-series	0.00	0.00
O	8	K-series	29.36	53.00
Mg	12	K-series	5.03	5.98
Al	13	K-series	0.26	0.28
Si	14	K-series	5.07	5.21
S	16	K-series	1.00	0.90
Ti	22	K-series	43.13	26.01
V	23	K-series	10.62	6.02
Cr	24	K-series	3.33	1.85
Fe	26	K-series	0.78	0.40
Sn	50	L-series	1.41	0.34

The X ray elemental analysis investigation enabled us to identify a black spot in the lower left corner of SEM image. Table 7 and Fig. 22 have shown a very strong increase of oxygen in this area.

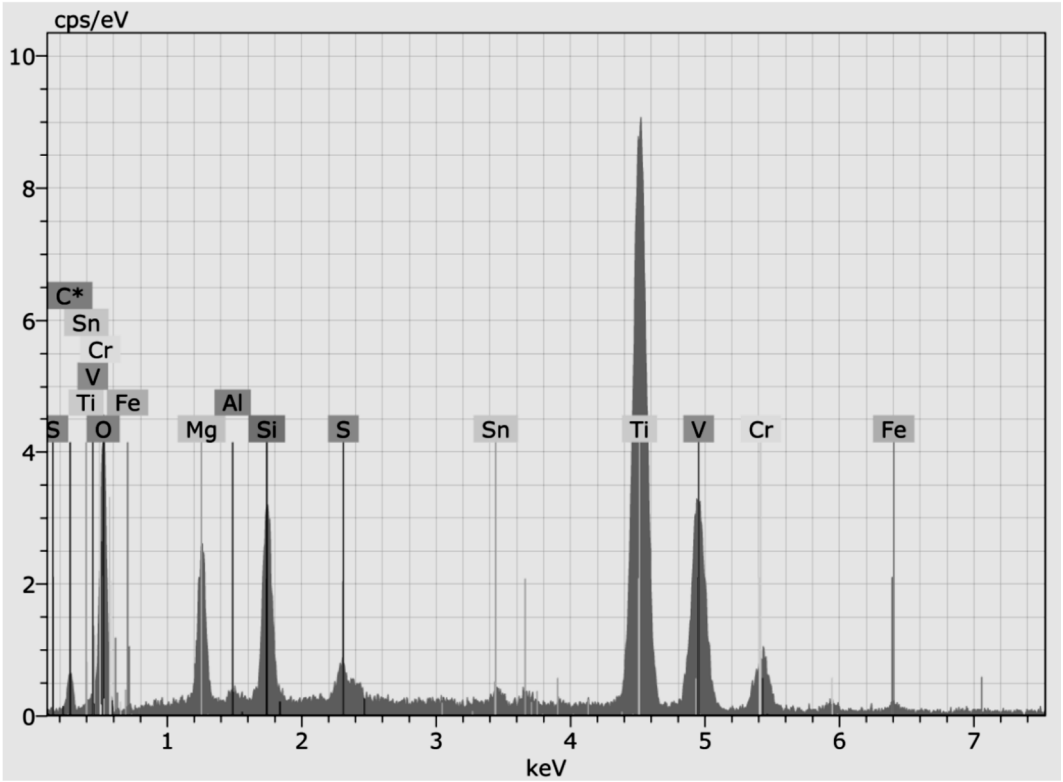

FIG. 22. X ray elemental analysis of the NR4 sample of Ti alloy in the area 7 (black spot).

5.3. Discussion

Results of irradiation were investigated by optical microscopy, SEM, AES, by images in secondary electrons and in characteristic X ray luminescence of different elements, and by X ray elemental analysis. The data were obtained for a number of materials including low-activated ferritic and austenitic stainless steels, β-alloy of Ti, as well as the double forged W (candidate material for divertor in ITER) and for tungsten alloy.

On one hand, deposition of S observed all over the samples (see zone 8 in Fig. 21 and Table 6) was realized mainly by ion-atomic mechanism. On the other hand, Mg, Si and O present only as separate inclusions viewed as

dark spots (see Region 7 in Fig. 21 and Table 7). It indicates that these materials were very likely evaporated by a cluster mechanism and captured by the surface of our specimen as separate particles (droplets) (with dimensions from one to tens of μm). Taking into account a very high concentration of oxygen in these particles (see Table 7) we may assume that these droplets represent the complicated oxides. Besides, oxygen was a part of a virgin titanium alloy (as an impurity element because there is a high affinity between titanium and oxygen [25, 26]). It may happen that fields of temperature gradients and microstresses created in SLs of titanium alloys at an action of pulses of energy help to an increase of a mobility of interstitial impurity atoms. It results in their transfer to sinks that represented by a vacancy cloud containing Ti and precipitated Mg and Si.

We found that with an increase of the power flux density of hot plasma and fast ion streams irradiating the surface, its morphology changes from a weak wave-like structure of the surface to the strongly developed one for the same material. After ablation this surface was melted by a secondary plasma cloud with the appearance of the fracturing pattern, first along the borders of grains and then with the intergranular net of microcracks. At the highest values of power flux densities multiple blisters appeared.

In case of tungsten samples at the irradiation produced normally to its surface, blisters look opened without covers and have sizes of 10–100 μm. In the case of austenitic stainless steel samples at their oblique irradiation, blisters look as closed bubbles of the sizes smaller than 1.0–0.1 μm. Besides, in this last case cracks are produced because of microstresses during solidification of melt.

Presence of deuterium within the surface nanolayers of irradiated ferritic steel was analyzed. It is shown that after this pulsed implantation of deuterium into the bulk of a sample it did not go out from it by diffusion or evaporation processes. Very likely, this capture of deuterons results from their interaction with lattice defects of the types of impurity atoms, pores and oxycarbonitride particles presenting in the material.

Analysis of the mass changes due to target irradiation was done for W specimens. In spite of the fact that the mass losses are quite high (about 8 mg per shot) these our results are a combination of two processes e.g. erosion of targets material and redeposition of the DPF chamber materials evaporated during operation of a device.

6. SPIN-OFF APPLICATIONS OF THE PF-6 DEVICE

6.1. Comparison of biophysical and radiological responses of bio test objects to pulsed and continuous X and neutron irradiations

6.1.1. Introduction

As the spin-off applications we have provided a set of experiments devoted to the investigation of biophysical and radiological responses of bio test objects to the pulsed and continuous X ray and neutron irradiations. We made these works in cooperation with our colleagues from the M.V. Lomonosov Moscow State University, Moscow, and the Medical Radiological Research Centre, Russ. Ac. Med. Sci., Obninsk, Kaluga region.

In the up to date data, circa 70% of oncological patients have a need in radiation therapy (side by side with surgery and chemical therapeutic methods) [27, 28]. X rays and neutron radiation fluxes here have their own special niches in cancer treatment (together with different ionizing particle beams as protons, muons, etc.), i.e. these fluxes are used for irradiation of different type tumors positioned at various depths. In particular, neutron therapy is prescribed for about 30% of oncological patients [29]. This therapy is made in over 20 countries in the world. Under correct patient choice the therapy allows at least 20% enhancement of direct and long term treatment results [30, 31]. Recently the development of new methods of neutron therapy is under way such as combined neutron capture plus X ray and neutron capture plus fast neutron therapy. Together with oncology a series of new applications of neutrons in various fields of clinical practice is developed. One of the most perspective lines in use of neutron radiation is a so called boron neutron capture synovectomy, i.e. non-surgery treatment of arthritis.

Isotopes, nuclear fission reactors, cyclotrons, X ray tubes, and other type accelerators are currently used as neutron and X ray sources for therapeutic purposes. Although they allow large success, some important parameters are desirable to be much better (neutron biological efficiency and selectivity, dose depth distribution, stability, availability, cost, dimensions, ecological compatibility, possibility of multifield, multibeam and rotational irradiation). Some problems are badly studied here. These issues relate to dosage for the intermediate layers of organism while deeply located tumor is under irradiation, to neutron scattering and penetration within organism, combined irradiation modes, etc. Therapeutic efficiency of neutron radiation versus dose rate (or dose

power in particular while short pulse irradiation) and pulse frequency is virtually not studied. In accordance with some theoretical concepts namely the short pulse radiation influence upon tumor (of the shock-like nature) may be especially effective because within such a pulse duration the reparation and recovery processes have no time enough to take place, and various effects of cumulative influence and synergism are possible [27, 32].

Among fundamental problems of radiation biology a new presently born discipline radioenzymology occupies important place. It is a comprehensive approach to study molecular mechanisms of ferment injury under effect of radicals produced while tissue's interrogation by different type ionizing radiation. Radioenzymology is at the same time one of the most sensitive methods to determine conformational changes of molecules. For instance, radioenzymology allows determination of molecular structure and conformational state and also individual amino acid residue effect upon catalysis process while comparable study of ferment mutant forms. Short powerful neutron and X rays pulses are necessary for various radiobiological tasks. Among them, for example, the determination of contribution of fast cell metabolism processes (damaged DNA reparation, oxygen effect, etc.) into formation of final cell and organism damages by radiation, effect of different type radiations, their spectral composition and pulse duration upon radiation injury of cells being at various stages of mitosis.

This work is devoted to comparative study of biophysical and radiological responses of bio test objects to pulsed and continuous X and neutron irradiations.

6.1.2. Apparatus

We used ^{60}Co, medical X ray tubes and nuclear fission reactor BR-10 as continuous sources of X rays and fast neutrons plus gamma rays respectively. Alternatively as pulsed sources of neutrons and X/gamma rays we applied pulsed reactor BARS-6 and DPF devices PF-5M and PF-6. Among various radiation types a DPF device produces:

- Soft (E_{hv} ~ 0.1–10 keV) and hard (E_{hv} ~ 10–1000 keV) X rays;
- Fusion neutrons (E_n ~ 2.45 and 14 MeV) due to a number of collective effects taking place inside the plasma because of its turbulence [19].

This type of sources is more ecologically acceptable compared with isotopic ones, classical high voltage accelerators and reactor facilities since they use relatively low voltage (10–25 kV) chargers for the capacitor banks, which operate from the mains 230 V, 6 A, 50–60 Hz. Furthermore, they become ionizing radiation sources only under electric power application (on demand, i.e. they are push button devices). In the off state they are completely safe, and in contrast to isotopes and fission reactors they do not require special containers for storage, so they are accident free compared with nuclear fission reactors (there is no criticality parameter in these devices). In addition these generators have low cost (a few orders of magnitude lower than classic generators with the same neutron yield), are compact and low weight (from 20 to 200 kg), have a small sized irradiation chamber (a few cm), and a record brightness of emitted ionizing radiations [7]. With respect to a number of parameters they are more convenient in clinical applications and open therein a series of new opportunities. They may be used in computer tomographic facility for diagnostics with rotating source around the patient, rather than the patient rotating around a beam. The radiation chamber of a miniature generator may be inserted inside a patient‘s body, which in some events provides large advantages (for instance, for panoramic photography in stomatology). Portable generators, which can be powered from domestic mains or accumulators, may be indispensable in ambulance, sport medicine and field surgery. On the other hand, the development of a system consisting of a few powerful generators around the patient should allow strongly optimize dose field geometry during the therapy. However because they ensure unprecedented dose powers of X ray and neutron radiations (due to nanosecond pulse durations) these devices must be examined with various bio test objects for their safety in comparison with classical sources. On the other side their extreme high brightness may result in synergetic effects and open perspectives for a low dose high power neutron therapy of cancer.

X ray and gamma spectra of all the above mentioned sources used in our experiments ranged (and varied) in the limits from a few keV to several MeV, with peaks at about 8.979 keV (DPF), 150 keV (DPF), and 1.3 MeV (^{60}Co). Neutron energy ranged from thermal to 16 MeV with peaks positioned at 2.5 (2.7) MeV (PF-6), 1.44 MeV (fission reactors) and 14 (16) MeV (PF-6). The dose rates (for continuous sources) and dose powers (for DPF sources) were varied from 10^{-3} to 10^{9} Gy/min for neutron radiation and 10^{0}–10^{11} Gy/min for X rays depending on the devices and on radiosensitivity of biological objects. Irradiations were produced by X rays, gamma rays and neutrons separately, and in combinations. The mixed gamma–neutron character of radiation

from the sources based on nuclear fission reactors (the value of $D_\gamma / D_{n+\gamma}$ was varied from 5 to 50%) has been also taken into account.

6.1.3. Materials

As biological test objects of different contents and complexity we used enzymes of various types (angiotensin converting enzyme, different plant peroxidases), serum, seminal fluid, yeasts, human lymphocytes, mice bone marrow (splenetic colony forming units), mice of line Black and F1 (CBA´C57B1). These materials were obtained from companies of Russian Federation and foreign countries (for instance, Biozyme, U.K., Enzymol International Inc., U.S.A.).

If necessary, all materials were purified using original technique developed at MSU. Their activity is checked prior to experiment (for ACE, for example, by stoichiometric titration with specific competitive inhibitor Lisinopril). Concentration was determined by spectrophotometry. Thermal stability of peroxidases was studied at incubation of an enzyme (under needed concentration) at 50°C and 80°C in the corresponding buffer (for instance, in phosphate–borate one). Operational stability (inactivation during reaction) was calculated on the base of total curve of increased chemiluminescence obtained under optimum conditions (luminometer Wallac 1251-002). Preparation homogeneity was tested by electrophoresis method in poly-acryl-amide gel in presence of potassium dodecylsulphate. In each case albumen content was determined by spectrophotometric method.

Ferment activity prior to and after irradiation was measured using spectrophotometer (Hitachi) within the wavelength range $\Delta\lambda$ = 300÷750 nm according to up to date techniques, for instance, for the horseradish peroxidase in relation to ABTS, KI, o-phenylendiamine, guayacol, phenol-antipinine probe.

6.1.4. Methodology

Special measures on the following lines were taken during the experiments:

- Cross correlation of the whole number of diagnostic and dosimetry devices, based on different principles and used on various installations in differing conditions;
- Comprehensive (as wide as possible) use of various detectors set in each experiment;
- Measurement of as many parameters as possible in each experiment (dose, pulse duration, spectrum);
- Support of experimental dosimetry by numerical mathematical modeling of interaction process, special attention therein was paid to difference between stationary (continuous irradiation) and non-stationary (pulsed) modes;
- In a course of the experiments same objects was irradiated in different conditions;
- Everywhere effects of the non-linear, triggering and hysteresis type were taken into account in dependence on changing of the parameters.

6.1.5. Results and discussions

The ultimate objective of the work is an elaboration of methods and equipment for diagnostics and therapy of malignant tumors based on pulsed generators of neutron and X ray radiations. To realize the above aims the following scope of work was provided using the technical approach to obtain expected results described below:

- Elaboration and manufacturing of neutron and X ray DPF based generators with neutron energy of 2.5 MeV and 14.0 MeV, X ray photon energy of 10–600 keV, duration of neutron and X ray pulses of 10–25 ns, neutron yield per pulse of 10^8–10^{11} neutrons in full solid angle, repetition rate of neutron pulses of 0.01–1 cps, X ray yield up to 10 J/pulse;
- Development of schemes and methods of irradiation of bio object by the above mentioned types of radiation, generated by stationary and newly elaborated pulsed DPF based sources;
- Working out of control measuring and dosimetry equipment, able to operate in pulsed and stationary streams of ionizing radiation;
- Gaining of new fundamental data about physicochemical and biological influence of powerful flashes of X ray and neutron radiations on bio objects.

— Investigation of relative biological effectiveness (RBE) of the influence of X ray and neutron radiations upon bio objects in dependence on parameters of their pulses.

At the new devices of the type DPF the record characteristics by dose power P were achieved. Maximal values of P for X ray radiation were of the order of 10^{10}–10^{11} Gy/min whereas for neutrons these values were about the same as at pulsed fission reactor BARS, around 10^{8}–10^{9} Gy/min for the device PF-6. The DPF based generators of both types of radiations are small (volume about 1 m^3), cheap and more convenient for their implementation in clinics for diagnostics and therapy in comparison with sources commonly used at present time (fission nuclear reactors, isotope sources, high voltage accelerators and X ray tubes).

We present here some results on usage of these sources together with classical ones in our irradiation tests. Somatic and testicular forms of angiotensin converting enzyme (ACE) as well as some complicated compositions containing dissimilar concentrations of ACE (blood serum and seminal fluid) at variations of conditions of an enzyme existence and on parameters of powerful pulsed and stationary sources of irradiation were investigated. Besides short pulsed powerful irradiation influence on different types of peroxidases were examined. These experiments have shown appearance of deviations in catalytic activity (both activation and inactivation) at super low doses of X ray radiation (by 4–5 orders of magnitude lower compared with the case of the isotopes sources) but at a very high dose power (by 9 orders of magnitude higher than in the case of irradiations by isotopes). It was found that for this phenomenon it is important a presence of the K_α-line of copper 8.98 keV in the radiation spectrum as well as the parameter product of dose and dose power (or an integral damage factor, see above), in particular within the range of its values 10^{-1}–10^{1} Gy^2/s (Fig. 23). In these experiments especially the dose region nearby $\approx 10^{-4}$–10^{-5} Gy was marked. One may see that quite 'chaotic' oscillations seen in the upper picture Fig. 23(a) are collected in the narrow 'corridor' in the lower picture Fig. 23(b). It should be noted here that the same general effect of relative independence of materials damageability on the product of *D* and P was observed at the interaction of nanosecond powerful pulses of fast ions generated by DPF with various types of steel and other solid state materials [33]. It means that an extrapolation of results obtained with the short strong pulses may be provided for a longer interaction time observed at a lower power. It was declared that such action may be performed using the so called integral damage factor (IDF) [9]:

$$F = \mathrm{P}\tau^{1/2} \tag{5}$$

where P is power flux density of the irradiation beams and τ is their pulse duration. The method (being very attractive in principle) demands, however, careful investigation of the validity of the above factor for a wide range of parameters and for different materials.

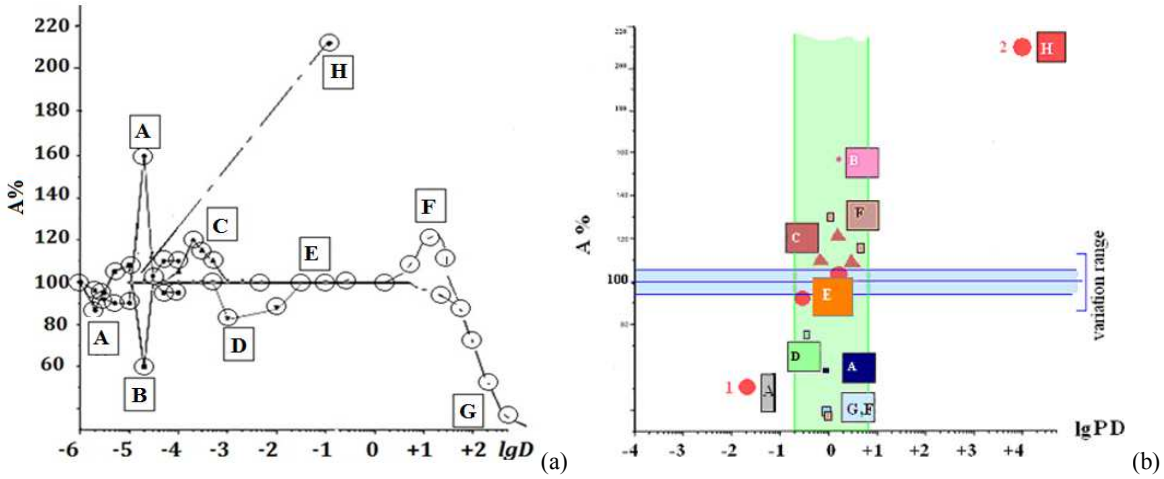

FIG. 23. (a) Dependence of activity of enzymes on the dose; (b) dependence on the product of dose and dose power at their irradiation by dissimilar sources of X rays. 'A', 'B' PF-0.2, Cu filter; 'C' PF-2, Cu filter; 'D' X ray tube, U = 50 kV; 'E' isotope β-source Sr-Y with Al filter: 40 keV < E_{hv} < 150 keV; 'F', 'G' γ-source ^{137}Cs: E^{hv} max = 662 keV; 'H' PF-6, d = 3 cm, Cu filter, P = 1010 Gy/min.

Two exceptions from this basic accumulation law namely points 1 ('A') and 2 ('H') in Fig. 23(b) were obtained. They are related correspondingly: the first one to the shortest pulse duration ($\tau < 2$ ns), and the second one to the highest product $PD = D^2/\tau = P^2\tau = F^2$ ever achieved before in all radiation devices. Presence of the above effects at so small doses in the conditions of a very high intensity of pulsed radiation (at ns pulses) indicates the existence of peculiar (punctured) dots in the dose curves, which may pose a hazard for biological objects functioning. Add-on neutron irradiation (at its dose powers $\leq 10^8$ Gy/min) in the conditions of combined X ray/neutron and gamma/neutron fields did not show sound effects in catalytic activity changes of ACE and peroxidases, yet it was reflected in a certain amplification of them.

In this study the cytogenetic action of neutron fission spectrum, generated by two nuclear fission reactors BARS-6, BR-10 and of fusion 14 MeV neutrons from PF-6 were studied with one of the most widespread in the world test-system – chromosomal aberrations in human lymphocytes. Results obtained with reactors versus ^{60}Co-source are shown in Fig. 24.

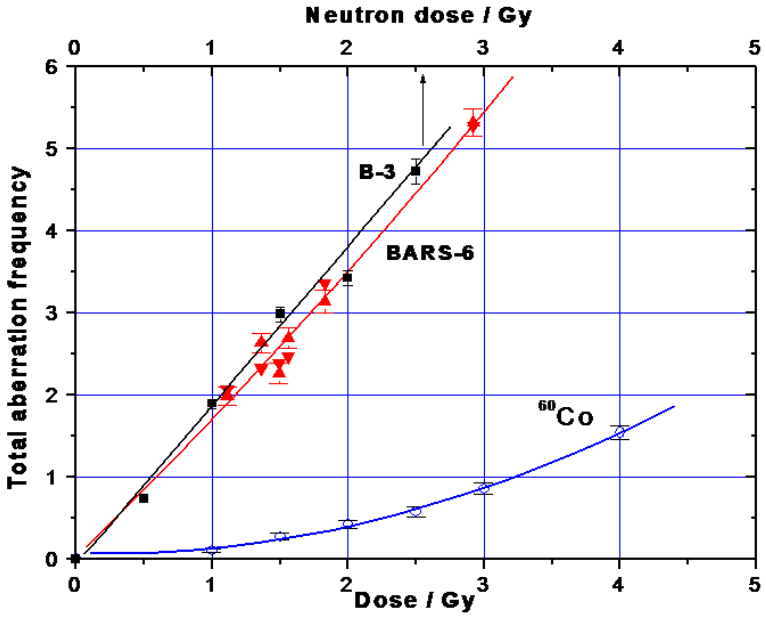

FIG. 24. Dose dependences of the total chromosomal aberration yield in human lymphocytes irradiated with the reactor BARS-6 (pulsed mode); B-3 effect from the reactor BR-10 (continuous neutron radiation action) and the effect of irradiation by the standard isotope source ^{60}Co of γ-radiation.

Five plastic tubes with blood samples were placed in a cylinder plastic container near the DPF chamber. Diameter (inner) of the container was 55 mm, diameter of each tube was 10 mm, and wall thickness was 1 mm. Since in these experiments DPF produced only one pulse every 10 minutes, to prevent damage reparation between pulses container was filled with melting ice. Neutron kerma was calculated using two types of detectors, the fission ^{237}Np detector and the activation silver detector SIVN 61. X rays doses were measured with a 27012 clinical dosimeter (Dresden). The blood samples were received 16 pulses in total. The maximum 14 MeV neutron tissue kerma was 0.8 Gy, whereas for X rays it was 0.5 Gy. Dose curves for the total chromosome aberration yields and for dicentrics yields in human lymphocytes irradiated with unfiltered mixed X rays and neutron pulsed radiation from dense plasma focus source are presented in Figs 25(a) and (b) correspondingly. For comparison some cytogenetic results obtained at continuous irradiation regime by the 14 MeV neutron generator known from literature are also shown here.

Experimental data presented in Fig. 25 were fitted to linear regression provided that one excludes from the analysis a data point marked with an arrow. As it follows from the data comparison the DPF neutron source data are closer to the data of Pohl-Ruling et al. [34] if dosimetry is based on the activation silver detector. If dosimetry is based on ^{237}Np fission detector, the experimental data are closer to those of Lloyd et al. [35]. Nevertheless, in both cases the experimental data for the DPF are within the published data for 14 MeV neutrons.

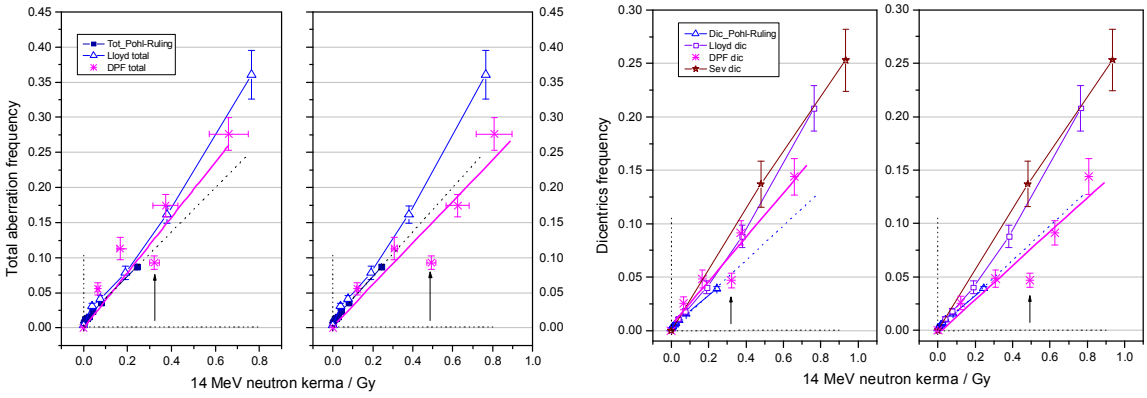

FIG. 25. (a) Dose curves of the total chromosomal aberration yield in human lymphocytes irradiated with 14 MeV neutron, neutron kerma was calculated using ^{237}Np fission detector (left panel) and using SIVN 61 silver detector (right panel), linear regression equation are $Y_{tot} = (0.041\pm0.009)+(0.36\pm0.022)K$ and $Y_{tot} = (0.021\pm0.01)+(0.28\pm0.028)K$, respectively. DPF – dense plasma focus; (b) dose curves of the dicentric chromosome yield in human lymphocytes irradiated with 14 MeV neutrons, neutron kerma was calculated using ^{237}Np fission detector (left panel) and using SIVN 61 silver detector(right panel), linear regression equation are $Y_{dic} = (0.012\pm0.006)+(0.21\pm0.026)K$ and $Y_{dic} = (0.005\pm0.01)+(0.15\pm0.026)K$, respectively.

At least two conclusions may be inferred from the Fig. 25. First, the major contribution to the cytogenetic effect of DPF neutron generator radiation is made by neutrons. Second, pulsed neutron radiation of very short, nanoseconds, duration is as effective as it is at continuous mode of neutron radiation, at least, within the mutual experimental uncertainties at its relatively high values ($<10^8$ Gy/min) for 14 MeV neutrons. It gives hope of applicability of DPF for the potential methods of neutron therapy instead nuclear reactors.

6.2. A single shot neutron pulsed technique for a disclosure of fissile materials

6.2.1. Introduction

Among promising approaches to the problem of interrogation of hidden objects containing fissile materials, the methods, which use neutrons, are of a pertinent interest at present time. In principle these methods can exploit a number of sources with long-pulse or continuous neutron radiation such as isotopes and classical neutron generators (direct type accelerators generating $\leq 10^8$ neutrons per pulse having duration ~ 10 μs) or low power sources like the Van de Graaff accelerator irradiating $\leq 10^3$ neutrons during a pulse of duration of 2 ns [36-42]. These methods ensure the necessary solutions in some cases; yet the techniques proposed on their base meet some awkward problems. Among them the most important one is rather low signal to noise ratio (SNR) at the detection part of an interrogation system. To reach a high value of SNR in those techniques it is necessary to integrate over many pulses with the above neutron sources ($>10^6$ pulses, for generators) or to ensure a long operation time (>half an hour, for isotope sources). These facts lead to high activation and to a long period of an interrogation of objects.

The aim of this work is to verify advantages of nanosecond impulse neutron investigation system (NINIS) [43, 44], a technique based on an interaction of just a single powerful nanosecond pulse of neutrons generated by a DPF device [45] with matter for a disclosure of hidden materials. This method was developed for an interrogation of objects, in particular of fast-moving objects containing explosives. Now we should like to analyze an opportunity to apply this technique for interrogation of items containing fissile materials. One preliminary result on this point with a single oscilloscope trace was presented in our work [46]. In this paper we describe all results obtained during the whole experimental session. We present their analysis and comparison with computational simulations provided specifically for our experimental conditions. Sensitivity and restriction of the method will also be discussed.

As it was mentioned above, DPF devices of small sizes (having a 1 m^2 footprint) [7, 46] can produce very short (τ ~ 10 ns) and bright flashes of neutrons (up to 10^{20} n · s^{-1}· ster.) and hard X rays of a few J at once. Such a DPF

device is a neutron source that is able to generate pulses of almost monochromatic ($\Delta E_n/E_n \approx 3–5\%$) neutrons of the energy of $E_n = 2.45$ MeV and/or $E_n = 14.0$ MeV. Neutron flux that is time averaged over 30–200 shots of the medium sized DPF devices (~1 m^2 footprint, ~5 kJ bank) is 10^8–10^9 neutrons at operation with pure deuterium as a working gas and 10^{10}–10^{11} neutrons when a deuterium tritium (DT) mixture is used. Variation of the neutron yield from shot to shot is about 2 times. These features provide an opportunity to use time of flight technique with relatively short flight base (a few metres) at the potential NINIS application. Important elements of the NINIS are also detectors with nanosecond and subnanosecond time resolution ($\Delta\tau$ = 1.3–0.276 ns in our case) and perfect screening.

6.2.2. NINIS: a single shot technique for disclosure of hidden objects

In the NINIS technique we use elastic and inelastic scattering of our almost monoenergetic neutrons produced in D–D or D–T nuclear fusion reactions upon nuclei of unknown elements (Fig. 26).

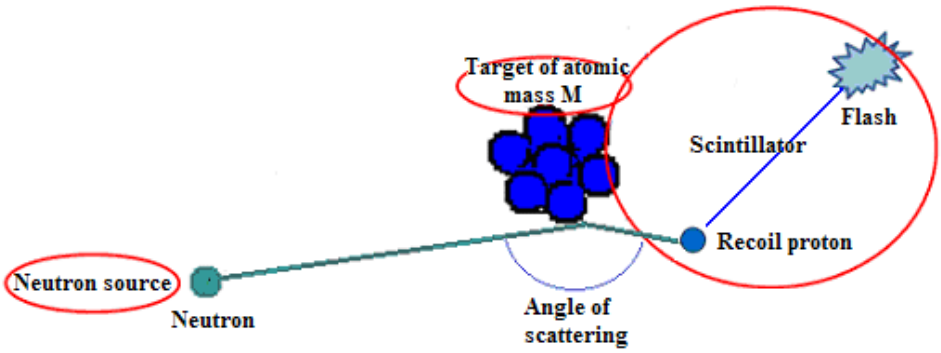

FIG. 26. Scheme of the process used in the NINIS technique.

After a collision the elastically scattered neutron will change its energy E_n (and speed v) depending:

a) On mass of the nucleus scatterer;
b) On angle of scattering.

Kinematics of the elastic scattering of neutrons in dependence of these parameters can easily be calculated. It is represented in Fig. 27 [36–42].

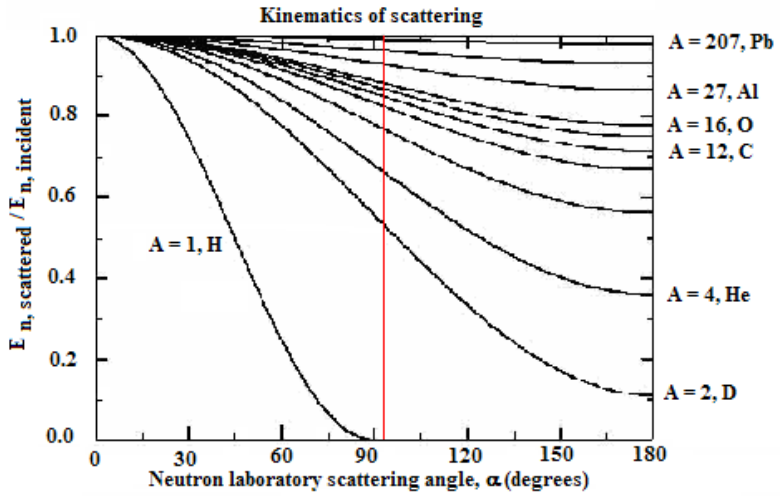

FIG. 27. Dependence of energy loss of a neutron on nuclei masses A and angles of elastic scattering α.

However, contrary to many techniques where individual flashes are collected during many irradiation shots (so photomultiplier with plastic scintillator are working in the regimes of counting of pulses with terms of loads) we are working with our detectors in their current measuring mode when an amplitude of a current produced by merged pulses are measured during a nanosecond time interval. It means that inside the scintillator neutrons will produce a distribution of brightness of flashes depending on impact parameters, i.e. on energies of recoil protons appeared inside the scintillator block after impacts by neutrons. But individual flashes with their dissimilar amplitudes start to merge when intensity of the registered neutrons is increased (see Fig. 28). But for each group of ~ 10 monoenergetic neutrons a linear dependence is proved for the averaged (merged) nanosecond signal (i.e. for the total integral under the pulse trail) versus the number of neutrons. This dependence will be violated due to saturation effects in the photon detector, MCP and regular photomultiplier (PMT). Besides, they also suffer from saturation problems and secondary pulses (after pulses) when exposed to short, intense light flashes as well. But if one can use a high-current PMT (like the SNFTTM type with linear current up to 7–10 A) the saturation effect may appear when micro-spheres of the action of recoil protons start to overlap each other resulting in change in excitation mechanism. However, for a scintillator block with a diameter ϕ = 10 cm and a length l = 10 cm it will be at its registration of about 10^{15} neutrons per this block. This value is much higher than the total neutron yield of our device and very far from those amplitudes of the scattered neutron pulses registered in our experiments. Thus the technique based on NINIS is operational within the limits of number of neutrons N registered in a single pulse of several nanoseconds duration with the above mentioned scintillation block and high current PMT: $10^2 < N < 10^{14}$. For light elements of the first part of the periodic table of elements the energy change in a scattering act (i.e. lower speed v of scattered neutrons) will result in a later time of arrival of the scattered neutrons to a detector, in our case it is a photomultiplier with plastic scintillator (PMT+S), compared with the arrival time of direct neutrons coming to the detector from the source without scattering [36–48]. Taking into consideration these time lags, amplitudes of pulses and corresponding cross section of scattering it is possible to reconstruct an elemental content of the material under interrogation from an oscilloscope trace [36, 43, 45].

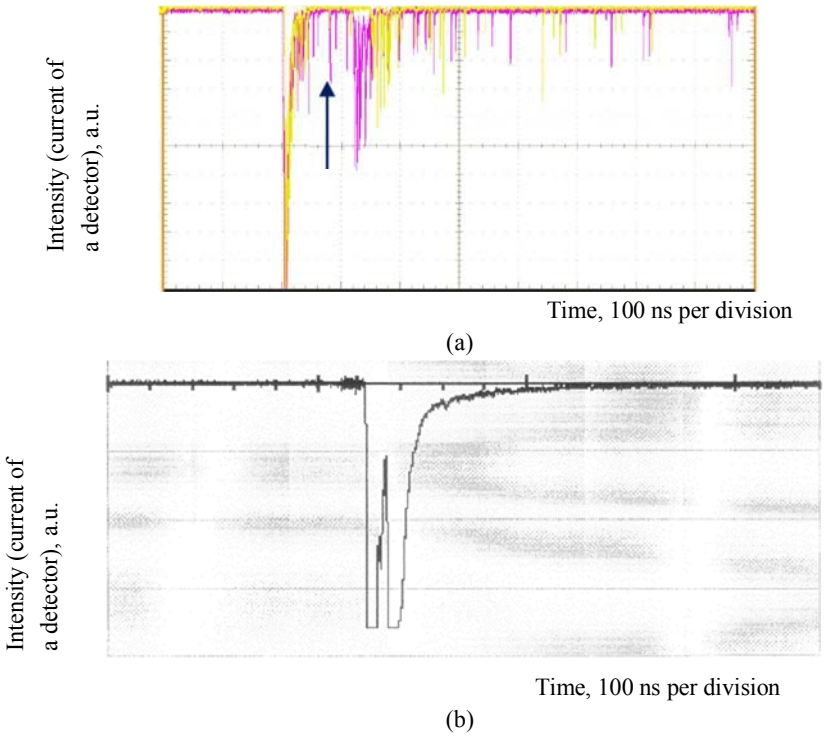

FIG. 28. (a) Oscilloscope traces of pulses of X rays and neutrons generated by DPF and registered by a detector with scintillator having 0.275 ns resolution: sequences of individual flashes produced inside a scintillator by each hard X ray photon (i.e. by photoelectron) and 14 MeV neutron (i.e. by recoil proton) during the time interval when the radiation has low intensity; their merged parts and correspondingly, which were registered during the period of their high intensity; red and yellow traces refers to two detectors placed at slightly different distances from the source (6 and 7 m accordingly); the same for the distance of about 5 m but for temporal resolution of PMT+S of about 3 ns; both traces were obtained in a relatively good environment without many scatterers; (b) an oscilloscope trace obtained by PMT+S with 1.3 ns time resolution for high-intensity hard X ray (first) and neutron (second) flashes; both signals are the merged sequences of individual flashes and they are even saturated because of their very high intensities.

However, as one may see from Fig. 27 this difference between energy of direct neutrons coming from the source to the detector and elastically scattered by the nuclei becomes negligible for heavy nuclei comprising fissile materials (for elements with A ≥ 232 for isotopes of Th, U, of the end part of the periodic table of elements). Fortunately neutrons produced due to inelastic scattering by nuclei of fissile materials have a wide energy spectrum extended from about 0.5 MeV to about 5 MeV with a plateau around 1.5 MeV (a so called Watt fission spectrum). To understand whether it would be possible to distinguish them from elastically scattered neutrons we have provided numerical modeling of the situation, including in particular calculation of our real experimental conditions.

6.2.3. MCNP modeling

We undertook attempts to simulate scattering of 2.45 MeV and 14 MeV neutrons by various objects using MCNP [49, 50] and FLUKA [51] codes. We applied standard MCNP5 (version 5 of the MCNP). These our computational works were aimed first at elaboration of the theoretical basis for the fissile materials detection concept and to verify expected experimental results in this study. The first part of simulations applies a FLUKA code [51] to investigate detailed interaction of neutrons with E_n = 2.45 MeV with localized objects. The fuel assembly MR-6/80, whose fuel section includes 80% of enriched uranium, was used as a target.

Figs 29(a)–(b) demonstrate the geometry and give an example of energy distributions of neutrons (in units scattered neutrons per cm^2 per incident neutrons per unit length of the fuel element) escaping the target at a certain angle (i.e. for a certain detector) after irradiation. The calculations were provided in the idealized geometry, Fig. 29(a), with neutrons presented as a parallel beam falling onto the target through an aperture of a diameter ϕ = 7 cm. Solid line in red color in Fig. 29(b) shows results for original fuel elements MR. Green dashed line presents results obtained for pure aluminum, i.e. at the substitution of uranium fuel layers by aluminum layers to show clearly an effect of the aluminum background. Boundary energy is the energy of the irradiating neutron beam, above which every neutron originates only from fission of uranium in the fuel layer. Due to this feature fission neutrons are seen especially clear. It was found that the number of fission neutrons shown by red color in Fig. 29(b) may amount to a few percent of the low energy scattered neutrons demonstrated here by green color.

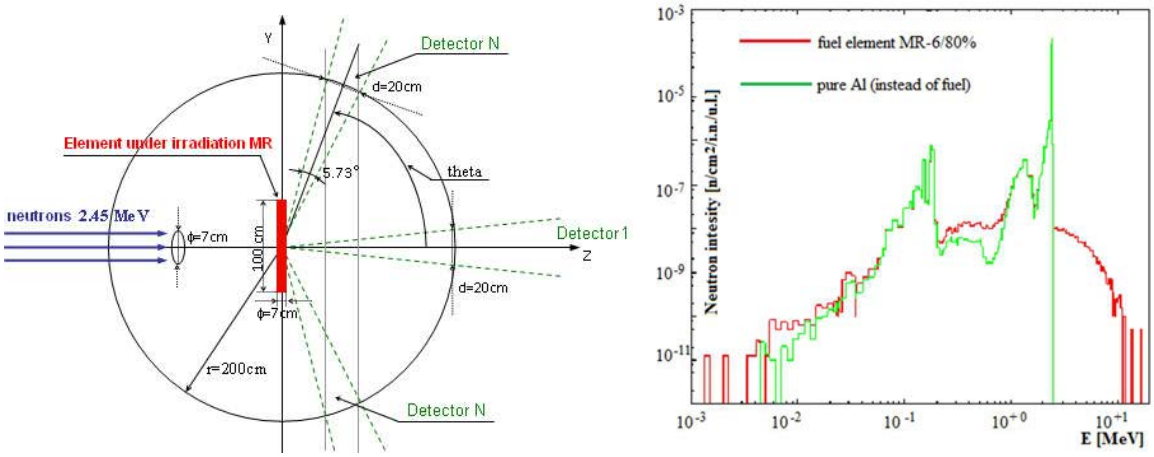

a) b)

FIG. 29. (a) Scheme of irradiation; (b) number of neutrons produced due to fission processes in the fuel element MR-6/80% and registered at 2 m from it (red color) and neutrons scattered on the aluminum layers substituted instead of the fuel rods (green color).

In principle these group of outrunning neutrons having spectrum extended to higher energies can easily be distinguished from the almost monochromatic primary neutrons and lower energy neutrons elastically scattered by the fuel element materials (so losing their energy). This group of fission neutrons will be seen as a precursor at the front of the pulse of scattered neutrons (pulse overshoot).

However, we have found that at the distance *r* of 2 m from the target we can expect no more than (2–3) × 10^{-9} fission origin neutrons (with energy E_0 above 2.45 MeV the used beam energy) per one cm^2 and per one beam neutron hitting the MR-6/80 target. But our DPF device (PF-6) can produce neutron yield in full solid angle on

the level of $\leq 10^9$ neutrons per pulse only. It is so for neutrons with $E_0 \approx 2.45$ MeV, i.e. for the PF-6 operating with pure deuterium as a working gas. Thus it is easy to calculate that:

- At a distance to the target from the point neutron source of about 10 cm;
- At the irradiation of the whole MR fuel element;
- At a distance of the scintillator from the target equal to 2 m.

The number of high energy (i.e. fission) neutrons coming to the scintillator having the area $S = 80$ cm^2 in the geometry will be $\sim 10^{-2}$ neutrons only that is not high enough to be detected. Thus this method could be applied with the DPF neutron yield $\geq 10^{11}$ for neutrons with $E_0 \approx 2.45$ MeV per pulse with a width of a few nanoseconds and with a distance between the fuel element and the detector not more than 1 m.

Consequently, we have decided to use 14 MeV neutrons from DPF operating with DT mixture as a working gas. In this arrangement the total neutron yield of PF-6 in a single shot is two orders of magnitude higher for this device ($\sim 10^{11}$ n/pulse). However in this case spectrum of fission neutrons will have energies less compared with the almost monoenergetic spectrum of primary neutrons peaked near the energy $E_0 = 14$ MeV. So the main idea is just opposite to the previous one concerning neutrons with 2.45 MeV energy: in this very case we have to distinguish elastically scattered neutrons (having about the same energy as the incident one and slightly lower) from fission neutrons having energy much lower compared with the neutrons of energy $E_0 = 14$ MeV. As a consequence the next step in our simulation works was done in the geometry more close to our real experiments produced with the PF-6 device (yet still idealized). Namely we put the DPF chamber as a point source in the distance of 10 cm to the center of the fuel element EK-10 (including 10% enriched uranium, what is also more realistic) and we use a distance from the fuel element to the detector $r = 6$ m. The EK-10 fuel assembly was modeled as 16 cylindrical fuel pipes. Each pipe is 50 cm high and has an external diameter equal to 10 mm (7 mm of fuel +2 × 1.5 mm of aluminum wall). The pipes are parallel to each other and they form a sort of a ring bundle. Looking at the bundle cross sections (horizontal plane) the centers of these 16 pipes are on the ring with diameter 6 cm, and go around, thus the pipes are almost close to each other. In this way we can say that the external diameter of this ring of the pipes (whole assembly) is equal to 7 cm, and its internal diameter is equal to 5 cm. In this modeling the source is very simple. It is the monoenergetic ($E_0 = 14$ MeV), point, instant, and fully isotropic source. For this reason one cannot observe in the spectra a peak at the energy $E_1 = 2.45$ MeV originated from the D–D reaction taking place inside the DPF chamber and seen in the real oscilloscope traces (see below). With this geometry we provided numerical modeling by use the FLUKA code again.

Fuel composition is mixed UO_2 and Mg (73.33 g of U-238, 8.05 g of U-235, 13.03 g of Mg). An individual fuel element is a cylinder: 50 cm high and 7 mm in diameter, enclosed in an aluminum envelope. Fuel density is 5.4762 g/cm^3. Total amount of U-238 was 1173.28 g, whereas total amount of U-235 was 128.8 g (see Table 8).

TABLE 8. COMPOSITION OF THE FUEL ELEMENT EK-10

Element	Atomic number	Atomic weight (u)	Proportion by number (%)	Proportion by weight (g/cm^3)
U-235	92	235.044	2.19	0.4184
U-238	92	238.051	19.71	3.8113
O	8	15.999	43.80	0.5693
Mg	12	24.305	34.30	0.6772

Figs 30 and 31 show results of these calculations for the 14 MeV neutrons scattered by fissile materials of the EK-10 fuel assembly, that means the energy spectra recalculated into the shape of the oscilloscope trace expected at a distance equal to 6 m. Because a 1 m distance takes about 20 ns for TOF of 14 MeV neutrons the second pulse (with the 10 ns rise time) in the case of a 6 m TOF will be situated at the moment [(75–85)-30] × 6 = 270–330 ns to the moment of the neutron production inside the DPF chamber, or about 200 ns in relation to the start of the pulse of elastically scattered neutrons, or delayed for about 300 ns compared to the start of the hard X ray pulse at the oscilloscope trace (20 ns TOF of a 6 m distance by X rays). For the same idealized scheme but for all elements of EK-10 and for a 6 m distance we provided MCNP calculations and obtained a spectrum presented in Fig. 31. Then we used our real geometry with all objects filled our experimental hall having concrete walls, floor and ceiling.

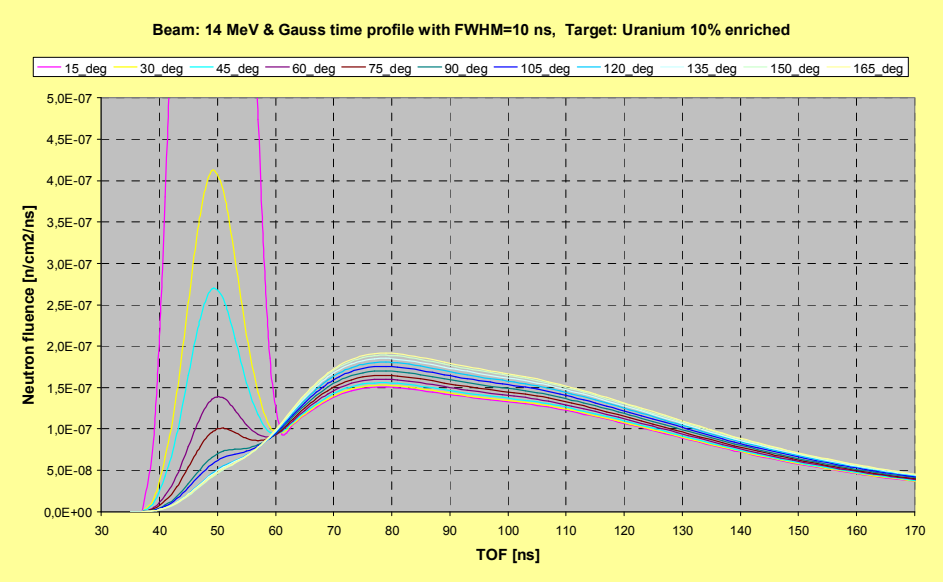

FIG. 30. The expected oscilloscope trace of 14 MeV neutrons elastically and inelastically scattered by fissile materials of the EK-10 and registered by a PMT with plastic scintillator at 1 m.

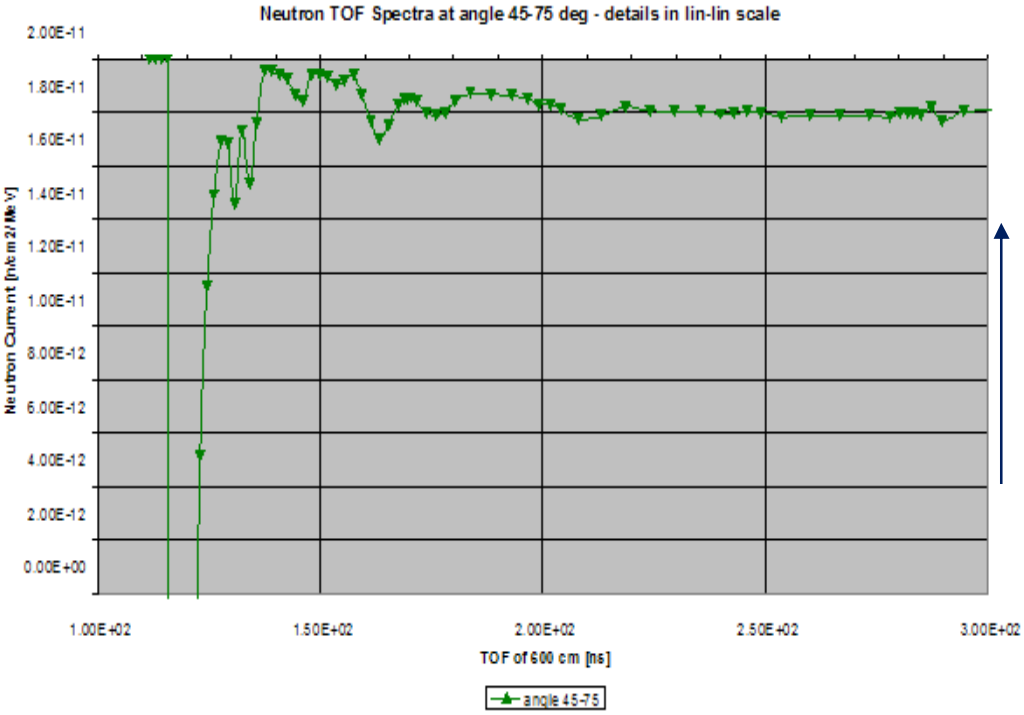

FIG. 31. MCNP calculations for all elements of the EK-10 fuel element made for a distance 6 m; note the main (elastic scattering) and several additional peaks; the peak of fission neutrons shown by an arrow is the same as in Figure 30 but for distance 6 times longer.

We made MCNP simulation for geometries of installation specific positioning of the DPF chamber PF9 and the fuel element FK-10 (Fig. 32), paraffin screen and different objects scattering neutrons during our experiments (Figs 33 and 34). Our previous experiments have shown that in clean conditions our neutron pulse has a bell-like shape with rise time equal to its pulse decay time (~10 ns each). However, from Figs 33 and 34 one may see that in this experimental conditions, which are very far from ideal, we can expect a long tail of our scattered neutrons resulted from elastic scattering by numerous concrete objects that we have in our experimental hall.

(a) (b)

FIG. 32. (a) Positioning of the DPF chamber PF9 of the device PF-6 and the fuel element FK-10; (b) enlargement. Diameters of the PF9 chamber of the PF-6 device and of the fuel assembly are 120 mm and 70 mm correspondingly.

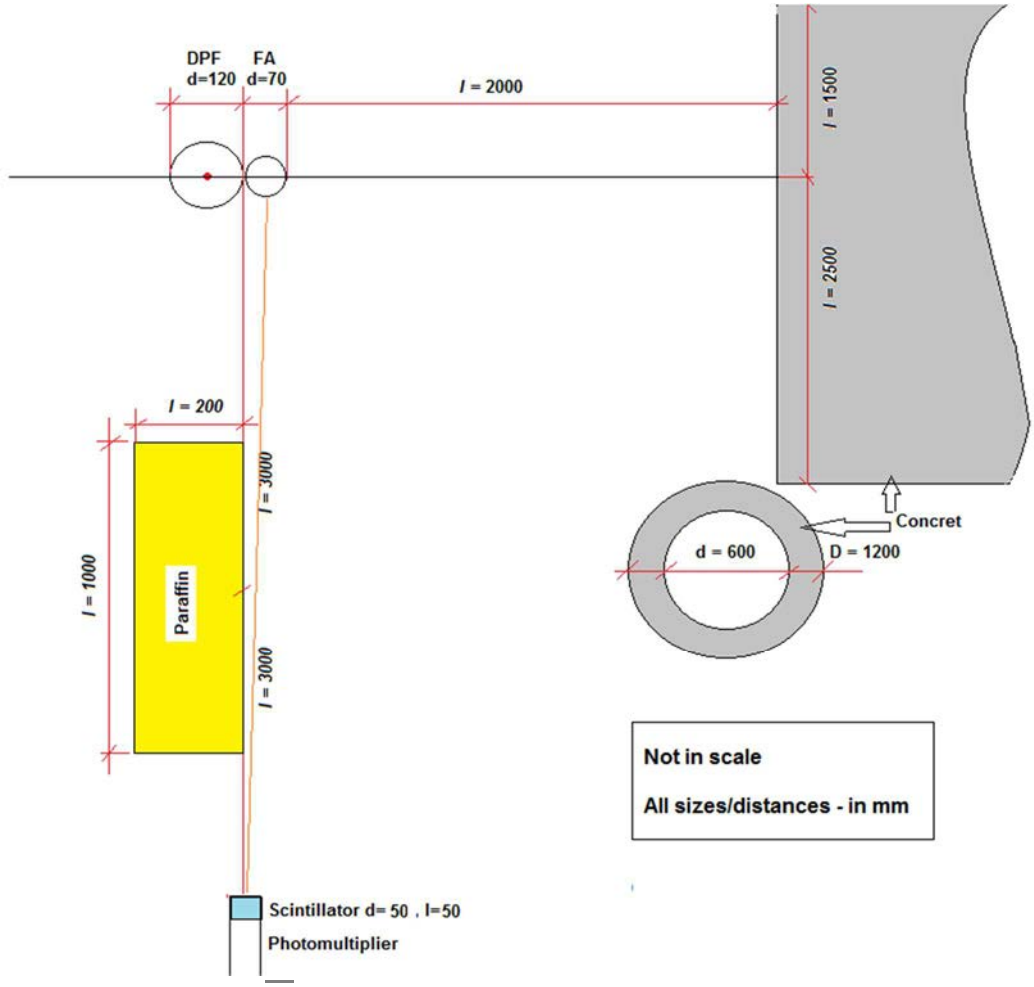

FIG. 33. Schematic of the top view of the experiment with sizes/distances in mm.

During different shots of DPF we put our 1000 × 200 mm^2 paraffin screen along the direct neutron beam (as in Fig. 34) and perpendicular sometimes adding a block of several paraffin plates (Fig. 35). Our calculations have shown that in this geometry we have a very asymmetric pulse of scattered neutrons indeed with a very long decay time (extended until 800 ns). In Fig. 36 we present our calculations by MCNP code for a comparison of 'All' (the overall neutrons elastically and inelastically scattered by the fuel element) and 'Fuel Flagged' (i.e. neutrons in particular produced by fission reactions in the fuel element) neutrons, counted by the same

scintillator. The same trace related to fuel flagged neutrons only and flipped vertically is presented in Fig. 37. One may see a specific peak observed at about 180 220 ns after the beginning of the neutron pulse or about 300–340 ns in relation to the start of neutron generation inside the DPF chamber, same as in Fig. 31 and analogous to that in Fig. 30 for a distance of 1 m). This peak corresponds to the energy of neutrons in the range 1.6–2.1 MeV that are in the middle of the spectrum of neutrons generated in uranium by external 14 MeV neutrons.

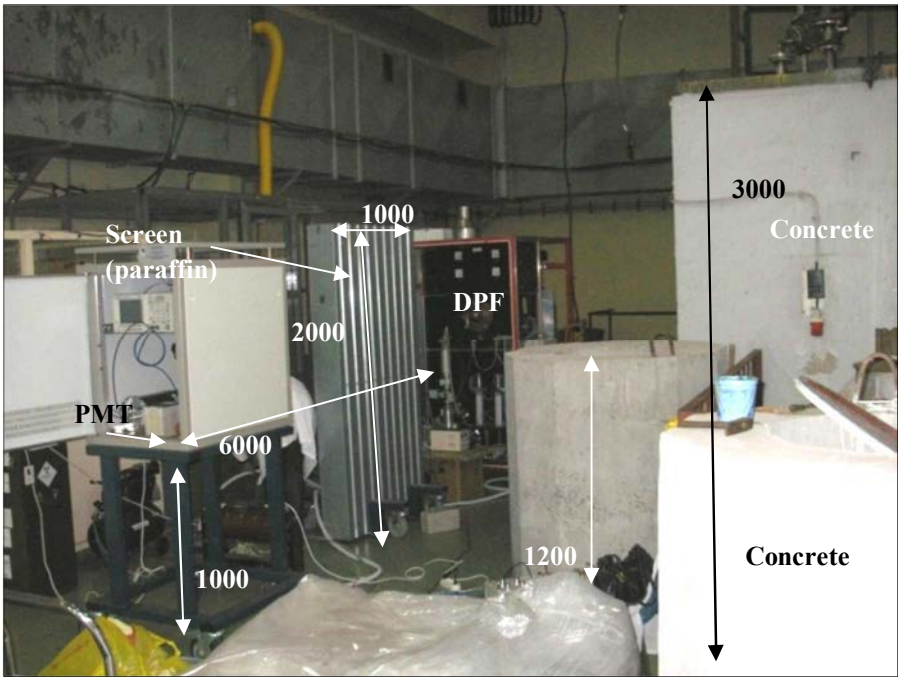

FIG. 34. Side view of the experiment with sizes/distances in mm.

A view from the PMT Faraday cage to the fuel element along the axis of PMT+S with environment is shown in Fig. 35.

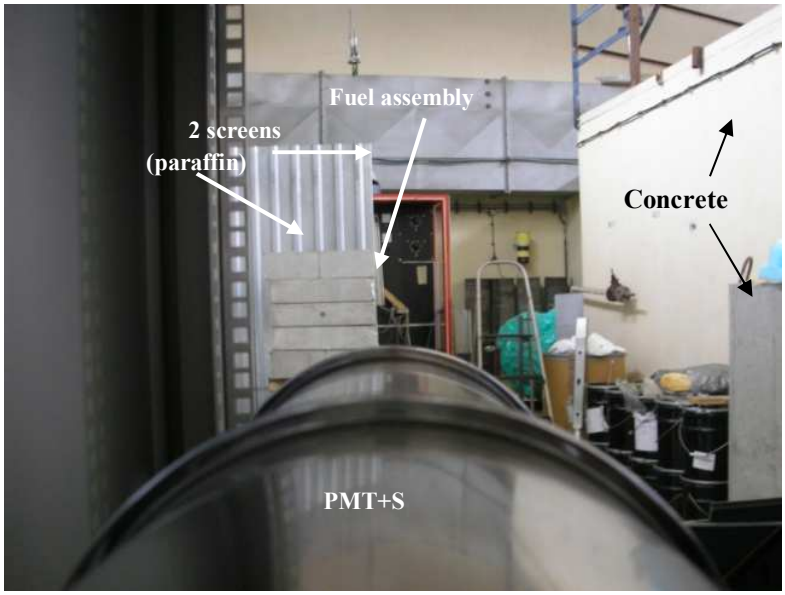

FIG. 35. View from the PMT Faraday cage.

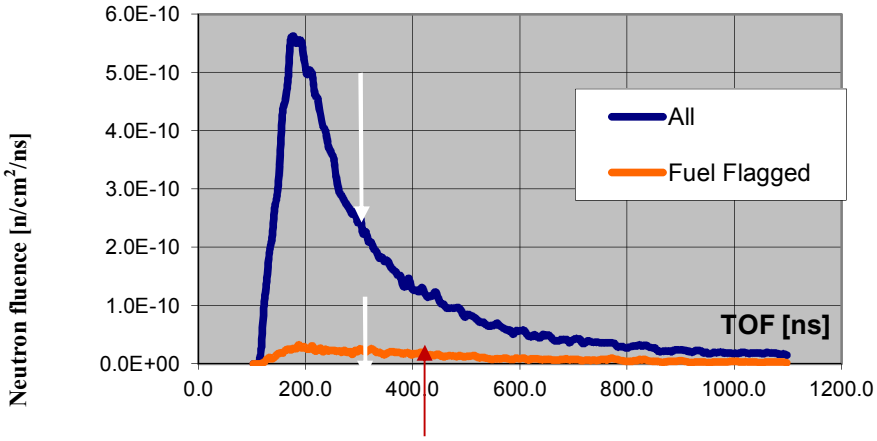

FIG. 36. The oscilloscope trace expected at 6 m from the EK-10 bundle (14 MeV PF source shielded by the paraffin block). Comparison of 'All' and 'Fuel Flagged' neutrons counted by the same scintillator at a 6 m distance.

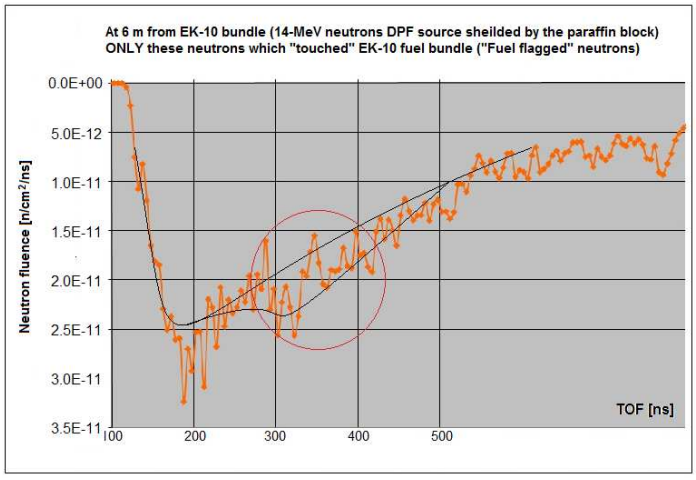

FIG. 37. The same trace as in Fig. 36 but related to fuel flagged neutrons only and flipped vertically; note an additional peak shown by an arrow.

6.2.4. Experimental technique

As a source of neutrons and X rays we used the PF-6 device (Fig. 32) working with deuterium tritium mixture as a working gas. This transportable device (IPPLM) had in these experiments the following parameters: bank energy of 5.6 kJ, amplitude of the discharge current of 760 kA, neutron yield per shot $\geq 10^{11}$ for a D–T mixture. A chamber used for the device PF9, see Fig. 32(b), was elaborated at the VNIIA [52]. Detection of hard X rays and neutrons (both directly coming from the source and scattered by the object under interrogation and by surrounding items as well) was provided by PMT+S detectors and chevron microchannel plates + scintillator with time resolution 2.0 ns and 0.3 ns correspondingly. They were positioned inside a movable Faraday cage stands shown in Fig. 38. Making a choice in favor of one of these techniques we have to find a compromise. From one side if we should like to have a temporal resolution of about 0.3 ns we cannot use a scintillator thickness more than 1 cm because TOF of 14 MeV neutrons for 1 cm is about this figure. But in this case we lose sensitivity in a very high degree. From the other side a 10 cm scintillator ensures the 2 ns time resolution, which is enough for our case with appropriate collection of neutrons number in the scintillator. Thus we used a 1 cm scintillator with chevron microchannel plates for characterization of the neutron source itself whereas for our scattering experiments we used two sizes of scintillators with 5 cm or 10 cm (for their diameter and length correspondingly). General view of the experimental hall used for the study of fission fuel element interrogation is shown in Fig. 39.

FIG. 38. Movable stand Faraday cage with detectors of two types described.

FIG. 39. General view of the experimental hall

6.2.5. Results and discussions

We used 14 MeV neutrons in experiments devoted to irradiation of fissile materials (Fuel assembly EK-10). We have provided our experiments in the geometry as it is presented in Fig. 33. Our preliminary estimations and examination of the above Figs 30, 31, 36 and 37 and some others gave us the following positions of peaks expected in our TOF oscilloscope traces:

a) Main neutron energy peak from the DPF source originating from D–T nuclear reactions according to our previous measurements is 14.0 MeV;
b) $^{8}O_{16}$: 12.5 MeV; 11.0 MeV; 8.0–5.0 MeV; 2.5 MeV;
c) $^{13}Al_{27}$: 5.5 MeV; 4.0 MeV; 2.7 MeV;
d) $^{12}Mg_{24}$: 12.5 MeV; 5.5 MeV; 4.0 MeV; 2.3 MeV; 2.0 MeV; 1.8 MeV; 1.6 MeV;
e) Neutron energy peaks from the DPF source originating from D–D nuclear reactions (having more than 2 orders of magnitude lower amplitude compared with the main 14 MeV peak) according to our previous measurements: 2.5 MeV or 2.7 MeV;
f) $^{92}U_{238}$ and $^{92}U_{235}$ (fission neutrons): 3.5 MeV, 1.6–2.1 MeV, 0.5 MeV with a weak peak at energy in the range 1.6–2.1 MeV.

One may see that some of the above mentioned peaks are overlap. Taking into consideration that the hard X ray peak is generated inside the DPF chamber several ns earlier compared with the maximum of the main pulse of 14 MeV neutrons, TOF of hard X ray of 6 m is 20 ns, we estimate positions of the most important pulses in the TOF oscilloscope traces recalculated from the above energies to time of flight for PMT+S detector placed at the distance 6 m in this case from the beginning of the registered start of the hard X rays:

- HXR start (and very often the top of the pulse), 0 ns;
- 14 MeV (direct) neutrons (top); 100 ns;
- 2.5 MeV D–D neutrons, 255 ns;
- 1.6–2.1 MeV, 280–322 ns with a peak at about 300 ns (fission neutrons).

We found that the rise time of the neutron peak on the levels 0.1–0.9 of its amplitude in these our experiments is the same as it was measured for this device (15 ns) in good premises without different concrete scatterers. Yet the tail of the neutron pulse appeared to be very long here (as it was predicted by MCNP calculations of Figs 36 and 37). It reflects scattering of neutrons by many concrete blocks filling the experimental hall. Fortunately as one may see in Fig. 40 taken without fuel element (the reference pulse) this tail is very smooth. Below we have presented several oscilloscope traces obtained during the time interval of the availability of the fuel element. We provided 13 shots without fuel element to fit sensitivity and trigger level of the oscilloscope and to fit geometry (partially). Then we provided 10 shots with fuel element. Among them we have registered 9 shots in one or two channels of the oscilloscope (working with dissimilar sensitivity). Throughout this period we changed positions and orientation of our shield(s), used different pressures of working gas and moved our PMT+S trying to find the highest signal at the lowest noise levels. Neutron yield measured in these experiments by activation of copper and by silver activation counter was within the range 4×10^{10}–2×10^{11} of 14 MeV neutrons per shot.

Analysis of the peaks appeared in the oscilloscope traces of Fig. 41 through Fig. 47 has shown that they are coincided with the above estimations for scattering (elastic and inelastic) on nuclei of elements contained in the fuel element as well as with our modeling simulations presented in Figs 30 (with corrections for distance), 31, 36 and 37.

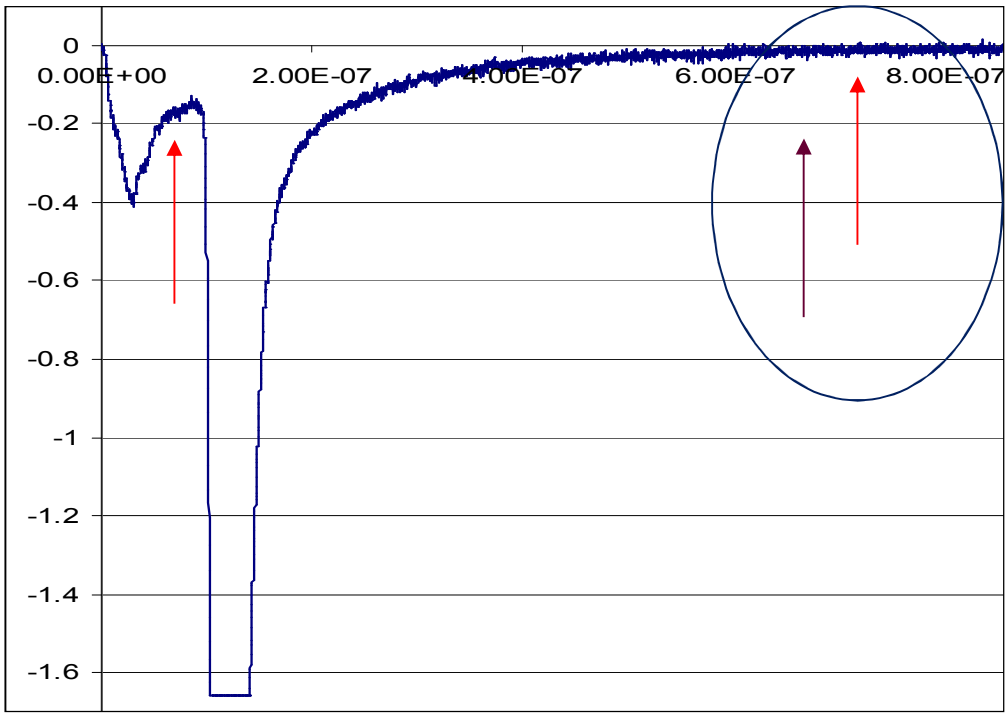

FIG. 40. Oscilloscope trace of hard X ray (first) and neutron (second) pulses taken at 6 m distance from the PF-6 chamber filled with D–T mixture without paraffin shielding and without fuel element (reference pulse).

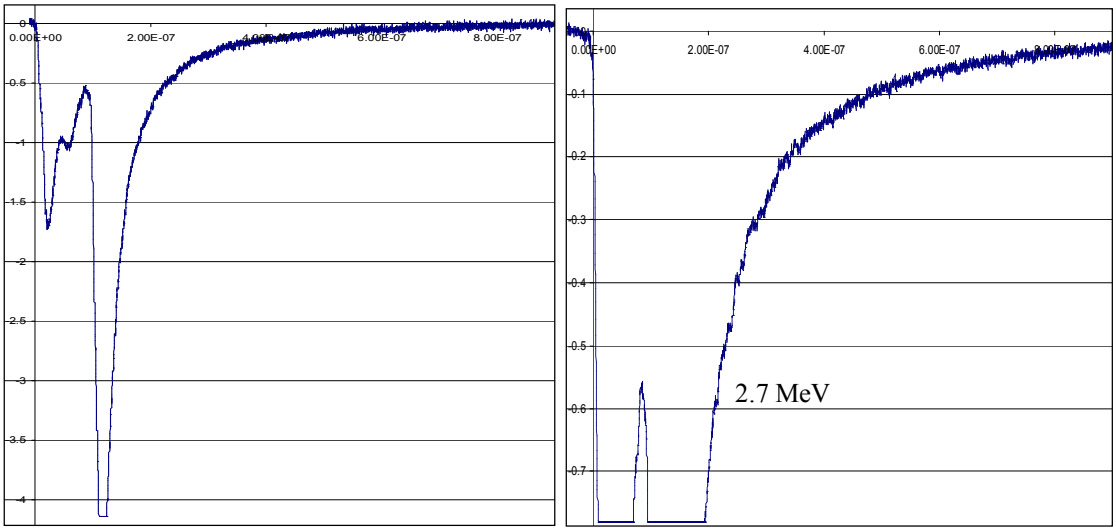

FIG. 41. Oscilloscope traces taken from DPF with fuel element near it (as in Fig. 32) with two dissimilar sensitivities of channels in the same shot of DPF; the main paraffin screen is placed perpendicular to the direct neutron beam as it is in Fig. 35; one may see the expected peak at 300 ns better pronounced at the right trace with higher sensitivity of the oscilloscope channel plus several additional peaks including those inside the oval that correspond to different materials contained by the fuel element; note in the right trace a small peak with a position related to neutrons with energy 2.7 MeV; if it is connected with elastically scattered D–D neutrons by fuel element its area must be lower than the area of scattered 14 MeV neutron pulse by more than 200 times: this demand is met.

We have to mention here that one may see several additional peaks on the oscilloscope's traces of these figures having nothing with our object under interrogation. They result from several weak abruptions of current after the main one in the DPF (correspondingly see them also in the tail of the X ray pulses). However we know where we have to expect the peaks of our interest in the oscilloscope traces beforehand, and we have found them namely in these time positions. Fortunately in this case we have no overlapping of these peaks with peaks from other small abruptions as it was also proved by the comparative amplitude analysis. A very similar result was obtained in the next 2 shots made in the same conditions, Fig. 42. The oscilloscope trace was taken only with the higher sensitivity compared to that in the Fig. 41. Because of higher noise the above peaks are perceptible with more difficulties.

Then we have reoriented our main paraffin screen installing it along the neutron beam as it is seen in Fig. 34. We suppressed direct beam in a higher degree, and our expected pulses became more profound (Fig. 43).

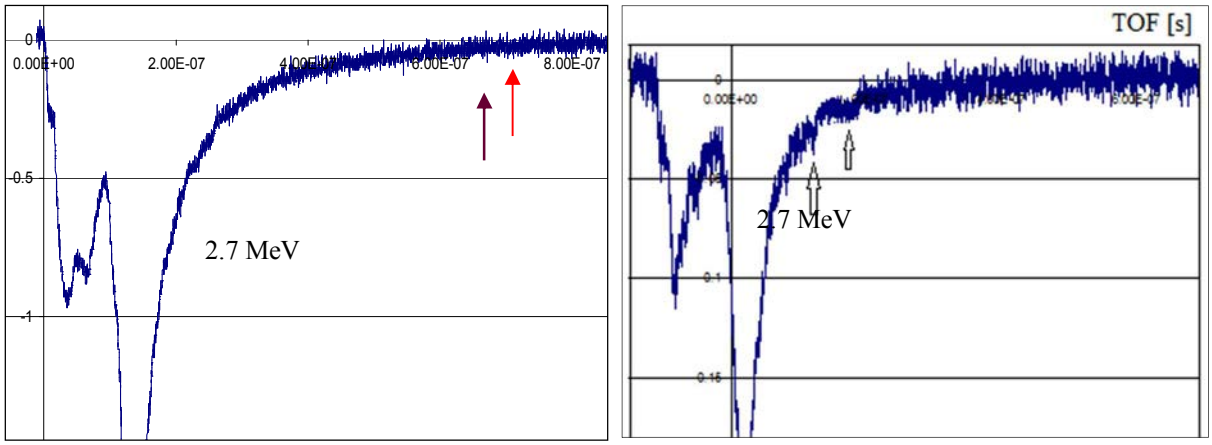

FIG. 42. Two shots produced in the same conditions as above.

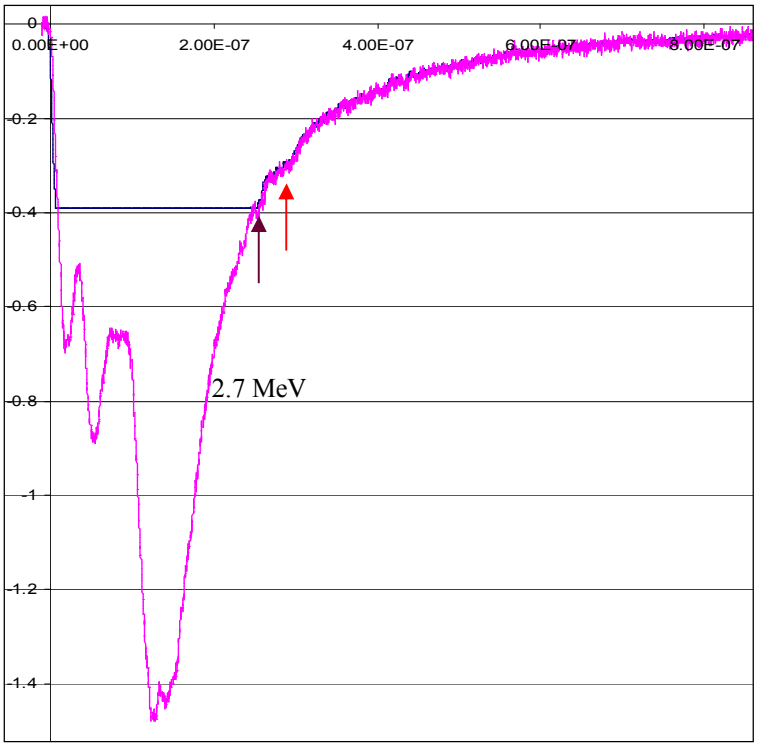

FIG. 43. The shot with the main paraffin screen placed along the direct neutron beam from DPF chamber to the PMT+Scintillator; higher neutron yield.

Then we install additionally to the main paraffin screen another paraffin block with dimensions 50 cm × 50 cm × 50 cm along the direct beam of neutrons thus suppressing the main neutron pulse in a higher extent. The result is shown in Fig. 44. Comparison of one of these experimental oscilloscope traces versus our preliminary MCNP calculations are presented in Fig. 45. One may see the coincidence of the two peaks in both simulation curve and oscilloscope trace. Two vertical lines show the moments of starts of pulses of neutrons scattered by the fuel element and peaks at 200 ns discussed above.

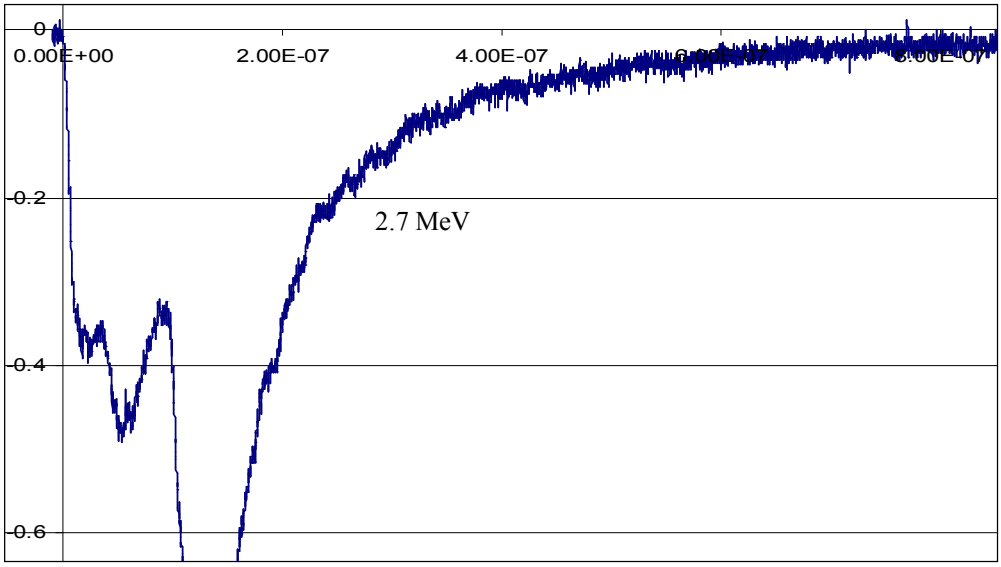

FIG. 44. Signals for the case with double screens.

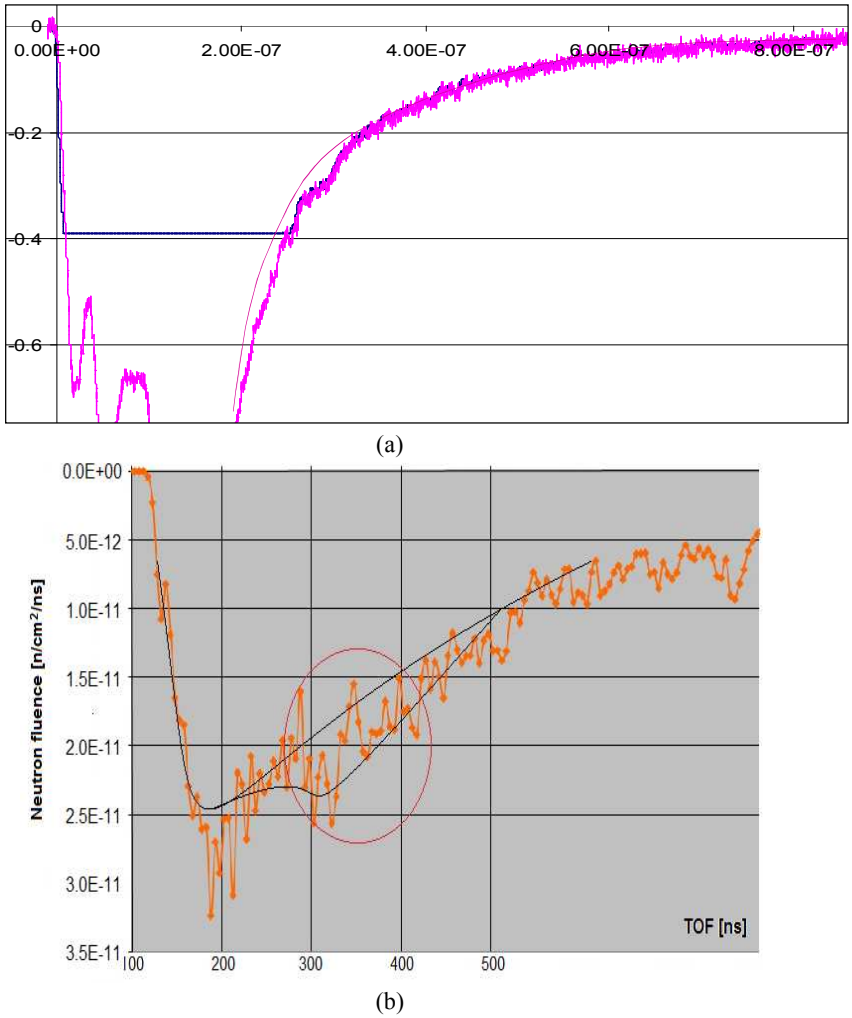

FIG. 45. (a) Experimental oscilloscope trace; (b) preliminary MCNP calculation curve.

Because one may see in our oscilloscope traces several other peaks inside the zone of interest we can try to confront them with the calculated (and estimated) peaks related to other materials composing our fuel element. For this purpose we have subtracted one oscilloscope trace taken without fuel element from the other, which was taken with the EK-10 in its position near the DPF chamber (Fig. 46).

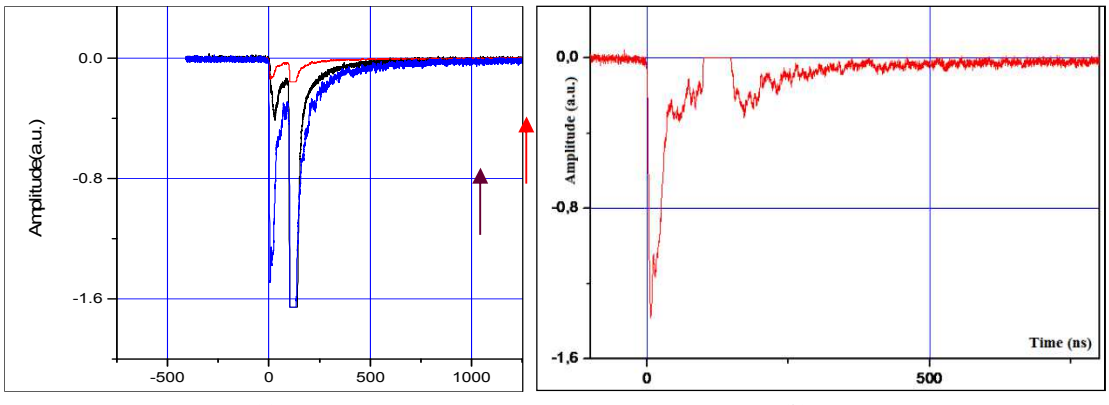

FIG. 46. (a) Two oscilloscope traces overlapping one another, one is taken without fuel element (the black one, smooth) and another one is taken with fuel element (the blue one with multiple peaks); (b) result of subtraction of the oscilloscope traces.

The same oscilloscope's traces subtraction with attempts of attribution of different peaks and comparison with results of MCNP modeling calculations are presented in Fig. 47. All other peaks without any indications on the picture are presumably connected with additional small current breakdowns, which produce low-amplitude flashes of hard X rays and neutrons. These subpulses can easily be confronted with each other in both pulses of hard X rays and neutrons using the same time delay as for the main hard X rays and neutrons pulses. It is easy to estimate how many neutrons N we have registered in the above pulses relating to fissile materials. According to MCNP calculations their intensity at the distance 6 m from the fuel element is $I = 2.5 \times 10^{-11}$ n · cm^{-2} · ns. Taking into consideration volume of our scintillators V (5 cm or 10 cm in lengths l and diameters d), efficiency of neutrons registration ($k \approx 1/2$) and pulse durations registered ($\tau \approx 40$ ns) one can find the figure for the worst case ($d = l = 5$ cm), then $N = I \times V \times k \times \tau = (2.5 \times 10^{-11}$ n · cm^{-2} · ns) × {(3.14 × 25)/(4 × 2) cm^2} × (40 ns) = 10^{-8} neutrons per pulse taken from the number of neutrons irradiating the fuel element.

In the previous paragraphs we showed that the signature of fissile material in the neutron TOF spectrum of a DPF can be observed by a single shot nanosecond neutron pulsed technique. It is quite evident that in future experiments with our PF-6 device we have to find better premises to eliminate parasitic scatterers (to diminish the long tail produced by them), to decrease distance between object and PMT+S probe to 1 m (what is acceptable due to our present experience) and to use 100 mm by 100 mm scintillator. In this case we can increase our signal by two orders of magnitude.

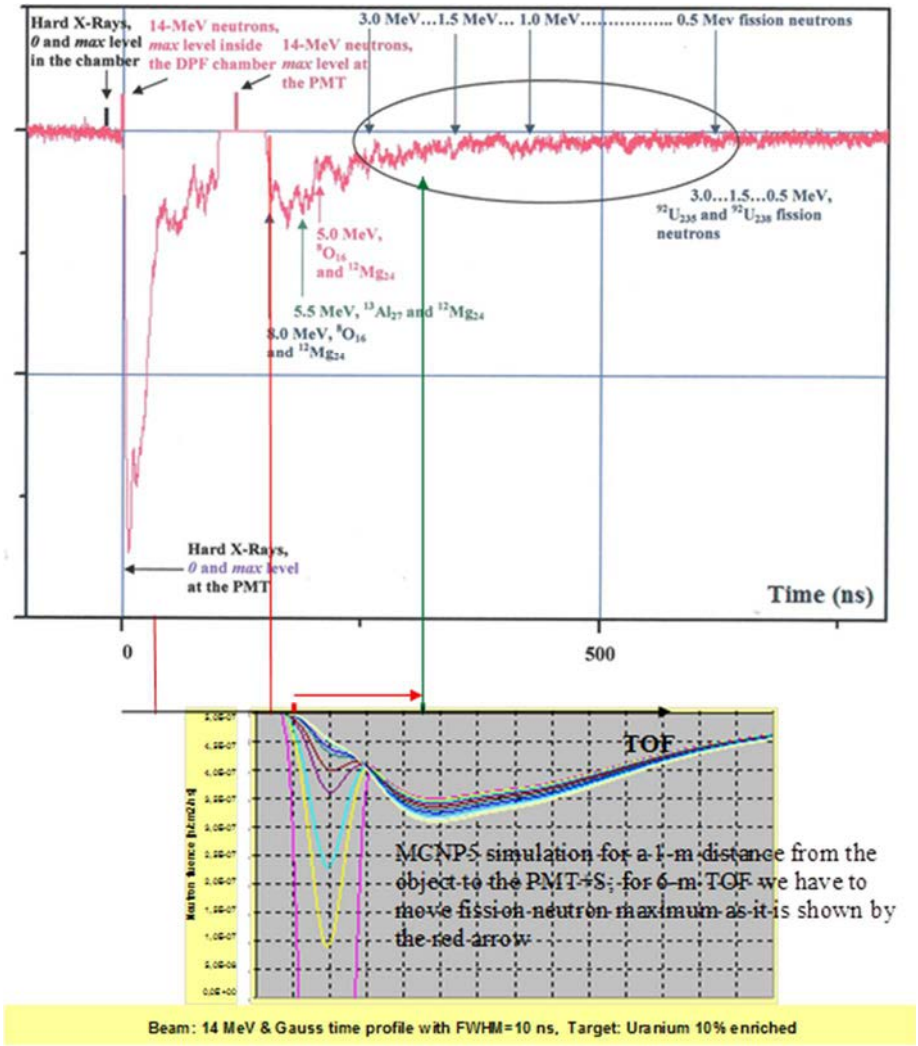

FIG. 47. The same as above subtraction of oscilloscope traces with attribution of different peaks and comparison with results of MCNP modeling calculations (stretched from 1 m distance as it was done in the MCNP modeling to fit the real 6 m distance from the fuel element to the PMT+S).

Geometry of irradiation decreases this figure in relation to the overall neutron yield of the device additionally by one order of magnitude. It gives for each pulse from 40 to 200 neutrons registered depending of our neutron yield of the device, Y = (0.4–2.0) × 10^{11} neutrons per pulse in full solid angle. This statistics is above the border of acceptability. Due to these proofs of principle experiments, which were supported by the wide range MCNP calculations, we are of the opinion now that the NINIS technique can probably find its niche among neutron based methods of disclosure of hidden objects containing fissile materials. In the case of success of these future works the main perspective of this method seems to be in unveiling of fissile materials at the express interrogation of fast moving vehicles (cars, wagons of a train).

6.2.6. **Dynamic quality control (stressedly deformed compounds car tires)**

Because DPF is able to generate flashes of hard/soft X rays and neutrons in nanosecond range, it seems attractive to use it for dynamic quality control of machines and mechanisms in a course of their operation. It would allow seeing some features of their details that are not observable in a static state, e.g. a turbine blade may have a crack that is invisible in a static position, but may be opened by a centrifugal force at the turbine rotation. Spatial resolution of an X ray image of a mechanism detail (turbine's blade, car tire, piston of a car engine) taken during its operation by a flash of the hard X ray radiation from DPF determined by:

- Pulse duration of X rays (ns) versus a speed of an object movement (rotation);
- Size of the source of X rays (<100 μ in a DPF);
- Diffraction (X ray wavelength, distance);
- Contrast degree of an object's detail to be visualized (spectrum of hard X rays).

Theoretically for DPF it could be ~ 1 μm in a 10 cm distance from the source to the detail. We have made tests of this possible usage of the PF-6 facility in relation to a car tire. Fig. 48 depicted the original images of the Pirelli tire in visible and hard X ray ranges whereas Fig. 49 presents these X ray pictures after a certain processing of them.

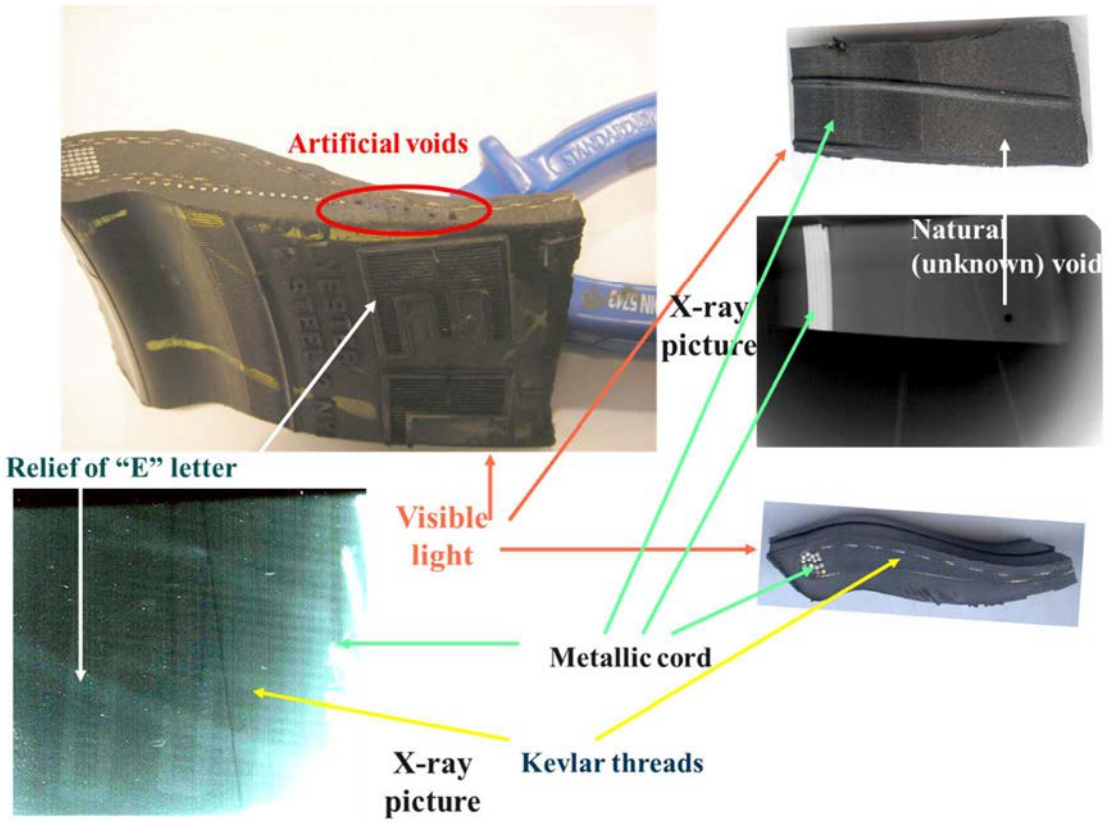

FIG. 48. Original pictures of a piece of a Pirelli tire taken in visible and hard X ray (>80 keV) ranges.

In these figures one may confront photographic images with X ray pictures (photons energy above 80 keV, pulse durations 10–15 ns) taken correspondingly by means of a common camera in visible light and with a single shot of the PF-6 device. As an object of control we used a piece of a Pirelli tire placed with an X ray film at a distance of 2 m from the X ray source. We found that artificial voids made by a drill (diameters 0.1–1.0 mm) are clearly seen in X ray images. Kevlar threads usually indistinguishable at its photographing with a conventional X ray tube on the background of the tire's rubber are very well visible. Unknown before the experiment a natural spherical void in the rubber having a diameter about 8 mm is resolvable. A letter 'E' (from 'PIRELLI') with a relief of about 1 mm above the ~ 50 mm thickness of the tire is observable.

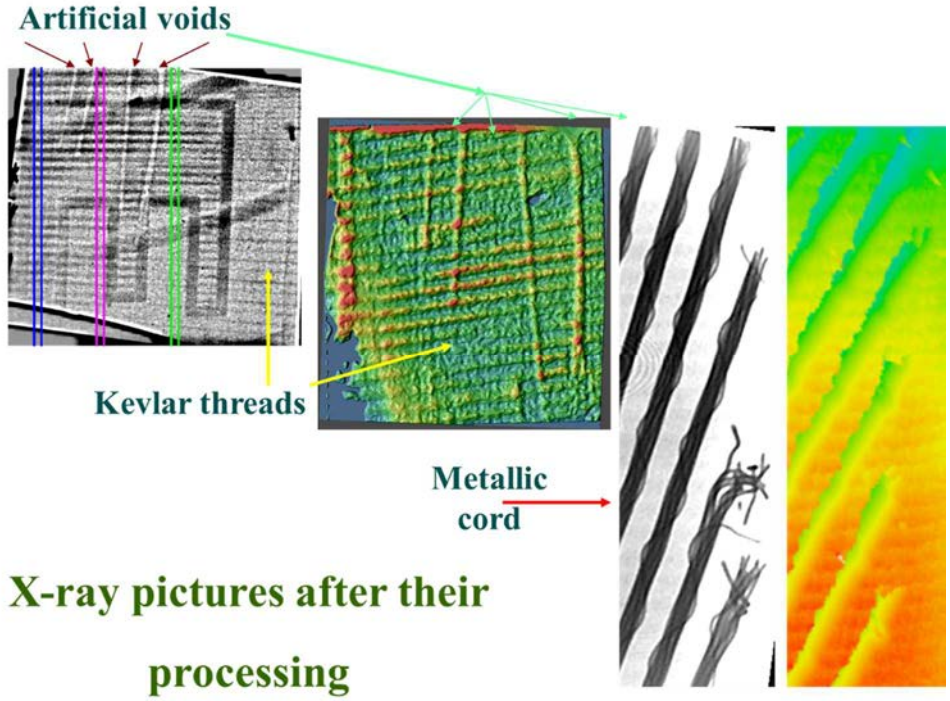

FIG. 49. The same X ray pictures of a piece of a Pirelli tire taken in a hard X ray (>80 keV) range shown after their processing.

ACKNOWLEDGEMENT

This research has been partially supported by the IAEA in the frame of the Contracts on the CRP "Investigations of Materials under High Repetition and Intense Fusion Pulses" Nos. RC-16931, RC-16932, RC-16954, RC-16955, RC-16956, RC-16960, and by the IAEA CRP Contract No. 17167 as well.

REFERENCES

[1] ITER, http://www.iter.org/
[2] SNIPES, J.A., "Plasma operation in ITER", paper presented at Joint ITER-IAEA-ICTP Advanced Workshop on Fusion and Plasma Physics, Trieste, Italy, 2011.
[3] FASOLI, A., "Physics of energetic ions in tokamaks", paper presented at Joint ITER-IAEA-ICTP Advanced Workshop on Fusion and Plasma Physics, Trieste, Italy, 2011.
[4] NIF, https://lasers.llnl.gov/
[5] HURRICANE, O.A., et al., Fuel gain exceeding unity in an inertially confined fusion implosion, Nature **506** (2014) 343.
[6] BERNARD, A., et al., Scientific status of plasma focus research, J. Moscow Phys. Soc. **8** (1998) 93.
[7] GRIBKOV, V.A., et al., New efficient low-energy dense plasma focus in IPPLM, Czechoslovak Journal of Physics **54** (2004) 191.
[8] GOMEZ, M.R., SLUTZ, S.A., SEFKOW, A.B., HAHN, K.D., et al., Demonstration of thermonuclear conditions in magnetized liner inertial fusion experiments, Phys. Plasmas **22** (2015) 056306.
[9] FUJITSUKA, M., et al., J. Nucl. Mater. **179** (1991) 189.

[10] LI, G., HU, L., CHEN, K., ZHANG, J., CHEN, Y., ZHOU, R., GAN, K., LIU, Y., Note: Tangential x-ray diagnosis for investigating fast MHD events in EAST tokamak, Rev. Sci. Instrum. **81** (2010) 106102.
[11] GRIBKOV, V.A., Physical processes taking place in dense plasma focus devices at the interaction of hot plasma and fast ion streams with materials under test, Plasma Phys. Control. Fusion **57** (2015).
[12] JAKHAR, S., RAO, C. V. S., SHYAM, A., DAS, B., Measurement of 14 MeV neutron flux from D-T neutron generator using activation analysis, IEEE Trans. Nucl. Sci. **NS-248** (2008) 2335.
[13] National Nuclear Data Center, Brookhaven National Laboratory, based on ENSDF and the Nuclear Wallet Cards, Decay radiation search (2014), http://www.nndc.bnl.gov/nudat2/indx_dec.jsp
[14] JEDNOROG, S., SCHOLZ, M., POPOVICHEV, S., MURARI, A., JET EFDA contributors, "Numerical optimization of activation samples for the application of the activation technique to measure neutrons in large fusion devices like JET and ITER", paper presented at 36th EPS Conference on Plasma Physics Sofia, Bulgaria, 2009.
[15] OECD, Java-Based Nuclear Data Information System (2014), http://www.oecd-nea.org/janisweb/index.html
[16] BRONSON, F.L., VENKATARAMAN, R., "Validation of the accuracy of the LabSOCS mathematical efficiency calibration for typical laboratory samples", paper presented at 46th Annual Conference on Bioassay, Analytical, and Environmental Radiochemistry, Seattle, Washington, DC, 2000.
[17] BRONSON, F. L., VENKATARAMAN, R., YOUNG, B., "Mass-symmetric efficiency calibrations of HPGe detectors for laboratory applications", paper presented at 44th Annual Conference on Bioassay, Analytical, and Environmental Radiochemistry, Albuquerque, NM, 1998.
[18] ZEL'DOVICH, YA.B., RAIZER, YU.P. Physics of Shock Waves and High-Temperature Hydrodynamic Phenomena, Dover Books on Physics, New York (2002).
[19] GRIBKOV, V.A., et al., Plasma dynamics in the PF-1000 device under the full-scale energy storage: II. Fast electrons and ions characteristics versus neutron emission parameters and gun optimization perspectives, J. Phys. D: Appl. Phys. **40** (2007) 3592.
[20] PINTSUK, G., Tungsten as a plasma-facing material, Ref. Mod. Mater. Sci. Mater. Eng., Compr. Nulc. Mater. **4** (2012) 551.
[21] GRIGORIEV I.S., MEILIKHOV E.Z., RADZIG A.A., Handbook of Physical Quantities, CRC Press LLC, Boca Raton, Florida (1997).
[22] NEKLJUDOV, I.M., TOLSTOLUTSKAYA, G.D., VANT, Problems of Atomic Science and Technology, Series Physics of Radiation Damages and Radiation Material Science **3** 83 (2003).
[23] DAW, M.S., BISSON, C.L., WILSON, W.D., Hydrogen binding to fixed interstitial impurities in metals, Solid State Communications **46** 10 (1983) 735.
[24] KODENTSOV, A.A., et al., Influence of dense deuterium plasma pulses on Fe and Fe-Mn alloy specimens in a plasma focus device, Proceedings of the Tallinn University of Social and Educational Sciences **B2** (2003) 51.
[25] ZWICKER, U., Titanium and Titanium Alloys, Springer-Verlag, Berlin (1974).
[26] BAI, L.S., LINER, D.I., SLESAREVA, E.N., TSYPIN, M.I., Oxidation of Titanium and Its Alloys, Metallurgiya, Moscow (1970).
[27] HALL, E., BRENNER, D., The dose-rate effect revisited: radiobiological considerations of importance in radiotherapy, Int. J. Radiat. Oncol. Biol. Phys. **21** (1991) 1403.
[28] ORLOVA, M.A., et al., Enzyme activation and inactivation induced by low doses of irradiation, Applied Biochemistry and Biotechnology **88** (2000) 243.
[29] GRIBKOV, V.A., DUBROVSKY, A.V., ORLOVA, M.A., SCHOLZ, M., Opportunities afforded by new generation of pulsed radiation sources in flash radiation physics and chemistry, Res. J. Chem. Environ. **9** (2005) 11.
[30] TSYB, A.F., et al., Neutrons in the Treatment of Cancer, Obninsk: BIST (2003).
[31] WAMBERSIE, A., MENZEL, H.G., Present status, trends and needs in fast netron therapy, Bull. Cancer Radiother. **83** (1996).
[32] GRIBKOV, V.A., "Pulsed radiobiology: possibilities and perspectives", Biological Physics 2000 (Proc. Int. Conf. Chulalongkorn University, Bangkok, Thailand, 2000), World Scientific, Singapore (2001).
[33] GRIBKOV, V.A., DUBROVSKY, A.V., et al., In-line and following-up tests of perspective fusion-reactor materials in plasma focus devices, Czech. J. Phys. **56** (2006) 1401.
[34] POHL-RULING, J., et al., Chromosomal damage induced in human lymphocytes by low-dose of D-T neutrons, Mutat. Res. **173** (1986) 267.
[35] LLOYD, D.C.., et al., Chromosome aberrations induced in human lymphocytes by D-T neutrons, Radiat. Res. **98** (1984) 561.
[36] BROOKS, F.D., et al., Determination of HCNO concentrations by fast neutron scattering analysis, Nucl. Instrum. Meth. Phys. Res. A **410** (1998) 319.
[37] NEBBIA, G., et al., "Use of neutron based technique in the control of illicit trafficking of fissile and explosive material", Countering Nuclear and Radiological Terrorism (APIKYAN, S., DIAMOND, D., Eds.), Springer, Dordrecht, Netehrlands, 2006.
[38] YANG, Y., LI, Y., HAIDONG,W., TIEZHU, L., BIN, W., Explosives detection using photoneutrons produced by X-rays, Nucl. Instrum. Meth. Phys. Res. A **579** (2007) 400.
[39] YOSHIKAWA, K., et al., Research and development of a compact discharge-driven D–D fusion neutron source for explosive detection, Nucl. Instrum. Meth. Phys. Res. B **261** (2007) 299.
[40] CLIFFORD, E.T.H., et al., A militarily fielded thermal neutron activation sensor for landmine detection, Nucl. Instrum. Meth. Phys. Res. A **579** (2007) 418.
[41] VOURVOPOULOS, G., WOMBLE, P. C., Pulsed fast/thermal neutron analysis: a technique for explosives detection, Talanta **54** (2001) 459.
[42] GIOS: Gerät zur Identifizierung Organischer Substanzen, Institut für Umwelttechnologien Gmbh, http://www.iut-berlin.de/

[43] GRIBKOV, V.A., MIKLASZEWSKI, R., On a possibility of the single-shot detection of hidden objects by using nanosecond impulse neutron inspection system, Acta Phys. Chim. Debr. **XXXVIII-XXXIX** (2005) 185.
[44] GRIBKOV, V.A., MIKLASZEWSKI, R.A., "Nanosecond radiation pulses for rapid detection of explosives", Combined Devices for Humanitarian Demining and Explosives Detection (Proc. IAEA Tech. Meet. Padova, Italy, 2006), http://www-pub.iaea.org/MTCD/publications/PDF/Pub1300_label.pdf
[45] GRIBKOV, V.A., et al., "Monte Carlo simulations of powerful neutron interaction with matter for the goals of disclosure of hidden explosives and fissile materials and for treatment of cancer diseases versus their experimental verifications", Applications of Monte Carlo Methods in Biology, Medicine and Other Fields of Science,(MODE, C.J., Ed.), ISBN: 978-953-307-427-6, InTech, Rijeka, Croatia, 2011, https://cdn.intechopen.com/pdfs-wm/13994.pdf
[46] GRIBKOV, V.A., et al., PF-6 – an effective plasma focus as a source of ionizing radiation and plasma streams for application in material technology, biology and medicine, Nucleonika **51** 1 (2006) 55.
[47] LEE, S., LEE, P., ZHANG, G., et al., High rep rate high performance plasma focus as a powerful radiation source, IEEE Trans. on Plasma Sci. **PS-26** 4 (1998) 1119.
[48] VERMA, R., et al., Realization of enhancement in time averaged neutron yield by using repetitive miniature plasma focus device as pulsed neutron source, J. Phys. D: Appl. Phys. **42** (2009) 235203
[49] MCNP – A General Monte Carlo N-Particle Transport Code, Version 5, X-5 Monte Carlo Team, Diagnostics Applications Group, Los Alamos National Laboratory, http://mcnp-green.lanl.gov/index.html
[50] MCNP5, http://mcnp-green.lanl.gov/about_mcnp5.html
[51] FLUKA, http://www.fluka.org/fluka.php

INVESTIGATION OF HOT PLASMA AND FAST ION/ELECTRON BEAMS IRRADIATION EFFECTS

E.V. DEMINA[*], V.A. GRIBKOV[*12], A.V. DUBROVSKI[*2], V.N. PIMENOV[*], S.V. MASLYAEV[*], M.D. PRUSAKOVA[*], A.S. DEMIN[*], E. ZIELINSKA[1], M. PADUCH[1]

Abstract

The results of irradiation of tungsten, prepared with the use of double forging for the reactor ITER, with pulsed flow of deuterium ions and high temperature deuterium plasma in three Plasma Focus devices have been presented. Irradiation was carried out in Bora, PF-1000 and PF-6 devices under power density of deuterium plasma flux on the target $q = 10^8$–10^{10} W/cm^2 and pulse duration $\tau \approx 100$ nanoseconds; power density of fast deuterons beam (~100 keV) $q = 10^{11}$–10^{12} W/cm^2 with a pulse duration $\tau \approx$ 10–20 ns. Damage properties and the erosion of the tungsten surface, elemental composition and structural state of the surface layer after extreme energy effects in the comparable exposure conditions have been investigated. Physical and chemical analysis of the behavior of tungsten-based mechanical alloy reinforced by oxides after the super powerful deuterium plasma/ion beam irradiation the investigations were provided as follows. Doping of oxides of the type La_2O_3 results in creation within the alloy of complex oxides of the type La-W-O that have their melting temperature lower compared with this value for La_2O_3. It leads to structural non-uniformities of the material in relation to its response to a high-temperature exposure. The results are discussed in terms of the intended application of tungsten in thermonuclear fusion devices. The nature of the failure rate, the structural characteristics, in particular the characteristics of the formation of surface defects and structural changes for the chromium–manganese low nickel austenitic steel of the type Cr12Mn14Ni4 (Al, Mo), modified by scandium under the influence of powerful pulses of fast deuterium ions (DI) and high-temperature deuterium plasma (DP), created in the installation of the type dense plasma focus PF-1000 were studied. These experiments were provided for a comparison these materials with the previously studied low activated austenitic (of the type of Cr12Mn14) and ferritic–martensitic (of the type Cr9WV) steels.

1. INTRODUCTION

The investigations provided in the framework of the current CRP of the IAEA on "Investigations of Materials under High Repetition and Intense Fusion Pulses" and were forced in three principal directions.

Testing of a number of materials, counted as perspective ones for the contemporary fusion reactors (FR) of both types with magnetic plasma confinement (MPC) and inertial plasma confinement (IPC) by irradiation of specimens with powerful streams of hot plasma and fast ion beams. We used two sorts of materials in particular intended:

a) For implementation in plasma facing components of the devices chambers (in the first wall and in the divertor elements, tungsten and some ceramics like CFC, alumina);
b) For construction systems (mainly different types of low activation stainless steels).

The last ones were tested in our works in the same regimes as it was applied for plasma facing components because of two motivations: for the reasons of accident risks when plasma facing elements will be broken thus uncovering the FR constructions and due to possible future usage of them as plasma facing elements in the next generation of FR chambers. Modification of surface layers of different materials with an aim to impart them improved characteristics like advanced corrosion and radiation resistance, higher hardness, and some others. Providing a comprehensive and precise analysis of the irradiated specimens aimed to understand character and mechanisms of damageability of specimens, their resulting properties and modifications, and to elaborate recommendations on the future use of them in FR.

Dense magnetized plasmas (DMP) produced by a number of different devices (various plasma accelerators, pinch facilities, high voltage/high current fast energy storage systems of the water-line type with wire loads, etc.) occupies a niche between the inertial plasma fusion devices (e.g. of the laser produced plasma types) and installations with the magnetic plasma confinement (for example, of the tokamak type) because of the characteristic times of their physical processes and their main plasma parameters.

[*] Institute of Metallurgy and Material Science, Moscow, Russian Federation.
[1] Institute of Plasma Physics and Laser Microfusion, Warsaw, Poland.
[2] Moscow Physical Society, Moscow, Russian Federation.

Besides its own intrinsic fusion perspectives discussed in 50's and now re-emerging due to new concepts put forward during the last few years, installations based on plasma of this type can serve as very powerful sources of various types of ionizing radiation for a number of important applications. In this CRP we used the subclass of DMP installations, the so called dense plasma focus (DPF) devices [1–2]. The DPF facility is a type of plasma accelerator that produces directed hot (T_{pl} ~ 1 keV) fast ($v_{pl} > 10^7$ cm/s) dense ($n_{pl} \approx 10^{16}$–10^{19} cm^{-3}) plasma streams, high energy ion ($E_i \approx 0.01$–100 MeV) and electron ($E_e \approx 0.01$–1.0 MeV) beams in addition to soft (E_{hv} ~ 0.1–10 keV) and hard (E_{hv} ~ 10–1000 keV) X rays and fusion neutrons (E_n ~ 2.45 and 14 MeV) [3]. These streams and beams have characteristic parameters that exist in present day accelerators and space vehicles, but in particular, in thermonuclear fusion devices employing inertial and magnetic plasma confinement, e.g. at plasma facing components of future fusion pilot reactors such as ITER and NIF facilities. They can also be used for a large number of applications where one needs short powerful pulses of radiation of the above mentioned types. Dense plasma focus devices, compared with other thermonuclear devices, have a number of important advantages:

- These devices provide an opportunity to expose different materials and objects to pulsed directed beams of various types: ion, electron, plasma, X ray, neutron and shock wave of high power flux density (up to 10^{13} W/cm^2 for fast electrons, 10^{12} W/cm^2 for fast ions, plasma streams and X ray photons and up to 10^9 n/cm^2 for neutrons) with pulse duration in the range 10^{-9}–10^{-6} s. Thermal loads in these devices produced by the above mentioned streams and a discharge current may reach magnitudes up to 10^{10} MW/m^2 with the characteristic time of their action up to about 10^{-4} s.
- Because all types of radiation generated by DPF are of penetrating nature these devices can produce important volumetric effects (in contrast to lasers).
- They enable the experimenter to choose the specific distribution of pulsed energy between all the above mentioned types of ionizing radiation: soft and hard X rays, neutrons, electron, ion and plasma beams. It is so because energy flux density may be significantly different for each type of radiation depending on the mode of a device operation.
- These streams in DPF devices can be separated in time due to different velocities of their (quasi)particles;
- These beams in DPF devices can also be separated in space due to different angular distributions and by application of a magnetic field as well as because of their dissimilar linear energy transfer (LET).
- Very high brightness of radiation of the above types gives important opportunities for new and sometimes unusual applications in pulsed radiation physics and chemistry in general, and in different branches of material sciences (radiation material science, nanotechnologies, dynamic quality control of machines and mechanisms during their operation, express neutron activation analysis) in particular.
- The physics of interaction of high power pulses of radiation generated in different fusion devices with materials is especially important for study of damage produced in elements of these installations including the discharge chamber of the DPF itself, but specifically the plasma facing walls of thermonuclear fusion installations with inertial (laser, wire array Z-pinches and heavy ion fusion) and magnetic (tokamak and stellarator) plasma confinement. In the latter case DPF devices can simulate radiation loads, which are typical ones for the stressed regimes of the reactor's operation (edge localized modes, VDEs, disruption instability).

2. IRRADIATION EQUIPMENT AND ANALYTICAL METHODS USED

2.1. Equipment used in the irradiation experiments

2.1.1. The PF-5M device and its metrology

This device PF-5M was elaborated by IMET during the fulfilment of the current IAEA CRP in cooperation with the MPS, and it is based at IMET. The works on this device was carried out by MPS and IMET in close collaboration with colleagues from other institutes participants of the CRP (IPPLM, ICDMP, TU). The PF-5M device now is in operational status. The main function of the device is connected with its use in radiation material science. The series of austenitic and ferrite samples, Al_2O_3, CFC, tungsten samples were irradiated by hot plasma jets (temperature T_{pl} ~ 300 eV, speed $v_{pl} \sim 2\times10^7$ cm/s) and fast ions (energy E_i ~ 100 keV) under different irradiative conditions (the number of irradiative pulses was changed from 1 to 50, distances between the anode and a specimen were in the range 3–15 cm). In process of the experiments the following diagnostics were used for registration of:

- Oscilloscope traces of the discharge current (by the Rogowski coil) and voltage (by the resistive divider);
- Oscilloscope traces of the time derivative of the discharge current dI/dt (by magnetic probes);
- Hard X ray doses (by the gas ionization chamber);
- Temporal behaviour of X ray and visible light pulses (by detectors of the type E.CCDI38 based on the photomultiplier tubes (PMT) of the type SNFT18 (time resolution $\tau \sim 2.5$ ns, linear output current $I_{linear} \sim 5$ A) equipped with plastic scintillators (S);
- Thermal loads (based on thermocouple calorimeter method with the copper washer of precisely weighted mass as calorimetric detector. Digital thermocouple thermometer of *K*-type was used to measure a temperature difference between measuring and ballast elements directly after each DPF shot).

The new demountable stainless steel DPF chamber was designed and has been realized. It is fitted for works of testing of various new constructions as well as different metals in order to optimize the chamber design.

2.1.2. Other irradiation facilities and corresponding diagnostics

Besides of using the PF-5M device IMET continued its participation in mutual experiments on PF-6 device (7 kJ, IPPLM, Poland), PF-1000 facility (1.0 MJ, ICDMP, Poland) and Bora set-up (5 kJ, ICTP, Trieste, Italy) with colleagues from other institutes-participants of the CRP (IPPLM, ICDMP, ICTP, TU and Ferrara University, Ferrara, Italy).

The above mentioned devices are equipped by some additional to the above mentioned diagnostics giving opportunities to investigate the process of interaction of radiation with targets (material specimens) in more details (laser interferometry, plasma self-luminescence, plasma spectroscopy) and with high temporal (~1 ns) and spatial (~10 μm).

2.1.3. Equipment used in the analysis of the irradiated specimens

For the instrumental analysis of the irradiated specimens we have used equipment as follows:

- Optical microscopes NU-2E and Neopot-32 with computerized image processing;
- Scanning multi-microscope VMM-2000;
- Scanning microscope LEO 430i;
- Focused beam microscope VEGA/SBU with a system of X ray energy dispersion microanalysis, Oxford Instruments;
- Atomic force/ tunnel microscope;
- High precision X ray Diffractometer, Rigaku Ultima IV (III Thin-film);
- Optical emission spectrometer based on a glow discharge Leco GDS-850A;
- Automated micro- and macro-hardness meters 401/402-MVD and Digi-Testor 930N;
- Universal test instrumentation MicroTester 5848 and Electropuls E3000, Instron;
- Unit for measuring of nano-hardness NanoTest, Micro-Materials Ltd.

3. THE EVOLUTION OF THE TUNGSTEN SURFACE STATE IN A PLASMA FOCUS DEVICES

3.1. Introduction

It is common knowledge that tungsten is considered as perspective material for its use in a working chamber of nuclear fusion reactors (NFR) in general and in a divertor assembly of NFR with MPC, ITER in particular [1–5]. This material has a number of useful characteristics (high melting temperature, good thermoconductivity, low sputtering coefficient, poor tritium capture and retention) that determined its usage expediency as the first wall material (FWM). However up to the present time it is not clear what would be the best form of this material to be implemented in the energy-loaded zones of NFR. Possible variants are discussed: recrystallized cold-shaped metal; material after smelting and hot rolling; in the form of a tungsten-based alloy containing particles of oxides (e.g. W 1% La_2O_3, W 0.3% Y_2O_3); as a tungsten coating (VPS-W) manufactured by plasma spraying in vacuum

[6]. Complexity of the choice is determined by the facts that inside a NFR (e.g. in ITER) this material is subjected by an impact of extreme energy streams (EES) producing a very high heat load. At the same time it must withstand to radiation influence of plasma, streams of fast electrons, ions, neutrons and alpha particles, and also to have low induced activity after a long term work in neutron fields and low sorption capacity in relation to isotopes of hydrogen and to helium [7–10].

In the light of the above mentioned demands the researches of radiation resistance and damageability specifics of tungsten and its alloys in the conditions of pulsed EES that are close to those realized in NFR with magnetic and IPC are topical ones. Such imitation experiments are provided at various types of devices that use plasma, electron, ion streams and neutron irradiation as well [11–16]. At that the most frequent investigations are related to a so called edge localized modes (ELMs) effects [14–18] sporadic contacts of tokamak plasma with a FWM. These effects have a duration ≤ 1 ms and repetition rate 1-100 Hz. They result in damage of material due to high heat load upon its ~ 10^6 J/m^2 at the power flux density $q \approx 10^5$ W/cm^2. In the work [18] it is shown that DPF devices [19–22] are quite perspective for modeling of ELMs effects. Their uniqueness is determined by the fact that imitation of radiation thermal impacts inside these devices are produced by the same carriers (hot plasma, fast ion and electron streams) and with parameters close to the ones expected on the FWM of NFR.

However each DPF device has its specificity connected with its bank energy, construction features, element base, configuration of construction and functional materials, volume of working chamber etc. All these factors influence upon conditions of irradiation tests and determine 'imitation' performance capability of each device. The main aim of the work is an investigation of evolution of a surface state of tungsten irradiated in dissimilar DPF devices in the regimes close to those obtained in tokamak reactors at ELMs effects as well as in harsher environment expected in NFR with IPC. The investigations are mostly devoted to a detection of damageability specificity and structure changes in surface layers (SL) of tungsten irradiated in comparing experiments as well as to estimations of influence of irradiation conditions realized in each DPF facility used. Besides a 'sensitivity' of the tungsten SL characteristics to the elemental content and configuration of construction and functional components of a DPF chamber as well as to energy of its bank are of a special interest.

3.2. Material, conditions of irradiation and analytical methods

For our experiments we use specimens supplied to us by the IAEA that were manufactured in Germany [23]. This material is intended for use in the divertor assembly of NFR ITER, and the technology includes melting of the material and double forging of samples. Size of all samples was 1.2 cm × 1.2 cm × 0.4 cm. The samples were irradiated in two small devices PF-6 (IPPLM) and Bora (ICTP) with banks charged up to 2 kJ each and in the PF-1000 facility at 19 kV that ensures the overall energy of the condenser bank on the level 235 kJ.

Compartments of the PF-6 and PF-1000 devices intended for radiation material science with specimens' holders were manufactured of stainless steel (SS) Cr16Ni10Ti whereas in the chamber of Bora device they were made of aluminum alloy. Anode and cathode in PF-6 and Bora devices and PF-1000 anode were made of oxygen less copper, but the cathode tubes in the PF-1000 chamber were manufactured from SS. During irradiation a tungsten sample target was placed in the cathode zone of a DPF chamber on its Z-axis, i.e. at normal incidence of the irradiating plasma and ion streams. Working gas was deuterium in all experiments. Distances from anodes to the samples were quite short: in Bora and PF-6 devices they were 3.4 cm from the anode's surface whereas in PF-1000 facility it was 7.0 cm.

At these distances irradiation parameters in all devices were about the same, yet the irradiated surface in the PF-1000 facility exceeds the ones in PF-6 and Bora by several times. Temperature of plasma was about T_{pl} ~ 1 keV, plasma density was $n_{pl} \sim 10^{18}$ cm^{-3}, velocity of the hot plasma stream was about $v_{pl} \sim 2 \times 10^7$ cm/s and pulse duration of the hot plasma action usually was $\tau_{pl} \sim 50$–100 ns. Energy of fast deuterons accelerated in vortex electric fields of DPF was about $E_i \sim 0.05$–1.0 MeV with maximum in the range of 100 keV. Pulse duration of the fast ion stream was 10–50 ns. Maximal power flux density of the hot plasma stream on the sample's surface was $q_{pl} \sim 10^9$–10^{10} W/cm^2 whereas for the fast ion stream it reached $q_i \sim 10^{11}$–10^{12} W/cm^2. A so called integral damage factor $F = q \times \tau^{0.5}$ [24] that characterizes a degree of approximation of the imitation regime of irradiation to the real conditions in NFR was $F_{pl} \sim 10^5$–10^6 W · cm^{-2} · s$^{0.5}$ for maximal value of the deuterium plasma (DP) q_{pl}, but for fast ion stream (FIS) it was correspondingly $F_i \sim 10^7$–10^8 W · cm^{-2} · s$^{0.5}$. For divertor plates in ITER during ELMs events this parameter is expected on the level $F \approx 10^4$–10^5 W · cm^{-2} · s$^{0.5}$ [25]. Thus irradiation conditions of tungsten in our researches at maximal power flux densities of hot plasma and fast ion streams were more severe compared with NFR with MPC and even with the ones expected in NFR with IPC [26].

The overall pulse duration of the individual ELM event is $\tau_{ELM} \leq 1$ ms, but it has a rise time shorter than 1 μs (not measured yet in a ns range). So with our pulses of EES in DPF we may simulate the initial (and most hard) phase of ELMs. To increase duration of action of hot plasma stream (supporting by a current flow) upon a target in a DPF and to approach the imitation regime to the real conditions in ITER we manufactured a special geometry of anode lids in PF-6 and PF-1000 devices. It allowed us to increase time of irradiation up to 30 μs in PF-6 device and up to 100 μs in the PF-1000 facility. This innovation together with a variation of a distance from the anode lid to the targets allowed to approach in a number of experiments the conditions very similar to a regime of EES irradiation of tungsten during ELMs effects in ITER. Irradiation conditions of the experiments produced are depicted in Table 1.

TABLE 1. CONDITIONS OF IRRADIATION OF TUNGSTEN SAMPLES IN THREE DPF DEVICES

Device's name	N. of irradiation pulses	Maximal discharge current (kA)	Volume of a discharge chamber, (cm^3)	Distance from an anode lid to a target (cm)	Power flux density of radiation on a target surface (W/cm^2)
PF-1000	2 4 8	2000	$\sim 2 \times 10^6$	7.0	10^9–10^{10} (plasma) 10^{11}–10^{12} (fast ions)
PF-6	4	360	300	3.4	10^8–10^9 (plasma) 10^{10}–10^{12} (ions)
Bora	4 32	160	300	3.4	10^7–10^8 (plasma) 10^9–10^{11} (ions)

Irradiated samples were investigated by methods of optical and scanning electron microscopy (SEM) with a help of optical microscope Neopot and scanning electron microscope EVO-40 manufactured by ZEISS company and equipped with energy dispersion X ray analyzer and X ray phase analyzer executed by diffractometer of the Rigaku company.

3.3. Results and discussions

3.3.1. Surface relief and cracks formation

In Fig. 1 photomicrographs of parts of W surfaces irradiated in the PF-1000 facility with various numbers of shots are presented. One may see that the samples have a typical for such irradiation regimes microscopic appearance, a wave like relief containing microcracks.

Such a character of a SL similar by its topographic structure was observed in a number of works [11–19, 27–30] where samples were irradiated by pulsed plasma and electron streams in the regimes simulating ELMs effects. At that a net of microcracks appeared on a surface of a tungsten specimen not only at its melting but also in more soft regimes without SL melting [28].

In our experiments one fact attracts a special attention: length and width of cracks lying in an irradiated plane of the samples are increased with an increase of irradiation dose (number of DPF pulses), and at the multiple impacts of powerful energy streams (PES) its extension reaches several hundred μm.

This fact shows that each subsequent impact of heat fields acting upon a SL of material in every shot increases a process of development of microcracks produced earlier. If one adopt that the main mechanism of cracks' "healing" after production on the surface of W target of liquid phase is a process of diffusion transport of atoms, it is possible to estimate a value of a characteristic diffusion length d_0 that atoms of W can be shifted during the time of the liquid phase existence t_0. According to the data of the work [27] this time $t_0 \approx 250$ ns at the power flux density of radiation $q = 10^8$–10^{10} W/cm^2.

Taking for the rough estimate of the diffusion coefficient in liquid tungsten the value $D \approx 5 \times 10^{-5}$ cm^2/s, we shall obtain for the parameter $d_0 \approx (2Dt_0)^{0.5} \approx 50$ nm. It means that microcracks having a width large compared with 50 nm do not disappear after a solidification of the W melt but they remain within a bulk of the hardened SL. Thermal stresses appeared within a SL at the stage of a high-speed crystallization of melt [27, 29] help to an increase of microcracks formed earlier whereas a new pulsed impact of energy results in a further growth of fracturing of material.

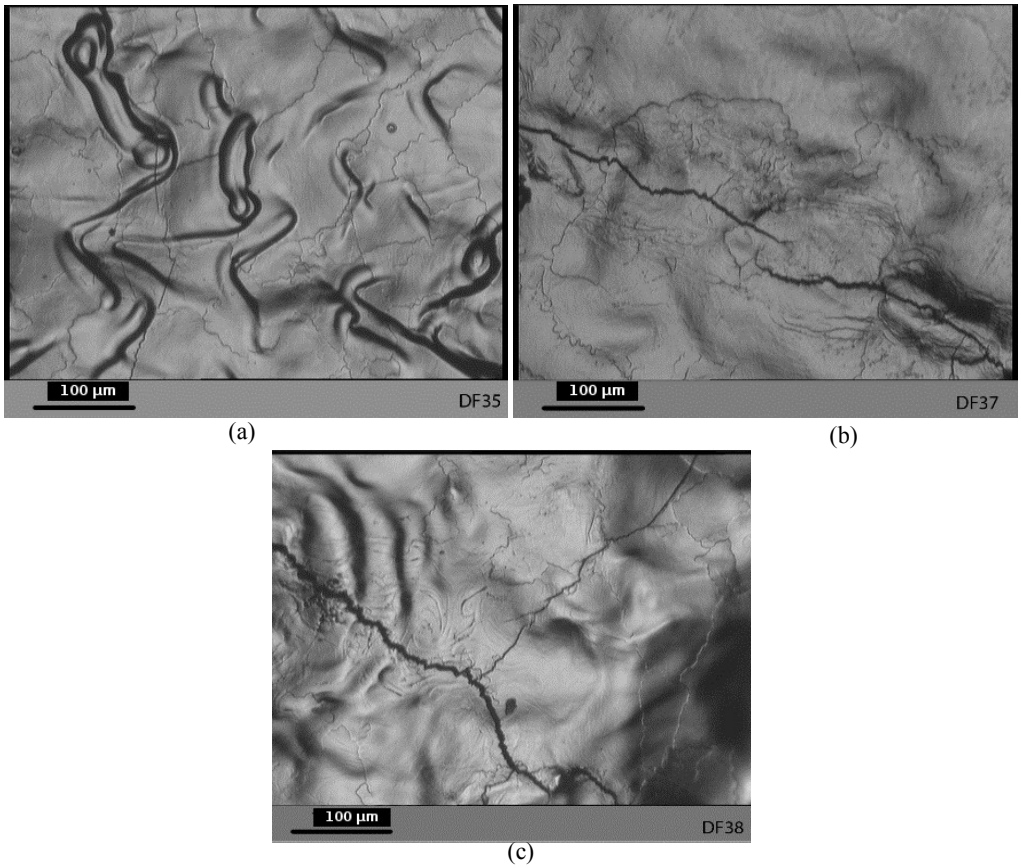

FIG. 1. (a) SEM photomicrographs of zones of surfaces of tungsten samples irradiated in PF-1000 facility, specimen DF35, 2 shots; (b) specimen DF37, 4 shots; (c) specimen DF38, 8 shots.

Analysis of cracks development in the plane of cross-section (into the bulk of material in the direction normal to the irradiated surface) has shown that the depth of cracks penetration was usually a few μm. A numerical evaluation has shown that this magnitude conforms approximately to a thickness of melted SL of tungsten produced in the regimes realized in PF-1000 facility and in PF-6 device.

Fig. 2 presents SEM photomicrographs of surfaces of tungsten specimens after their irradiation in PF-1000, PF-6 and Bora devices with an equal number 4 of impacts of streams of hot plasma (HPS) and fast ions (FIS). Analysis has shown that at Bora device a damageability of SL resulted from its melting and cracking is noticeably weaker compared with the same phenomena obtained in the experiments in PF-1000 and PF-6 devices This fact is stipulated by lower intensity of pulsed energy actions upon the W specimens surfaces in Bora device (see Table 1) that results from longer discharge current period and lower current amplitude of it compared with two other facilities. Because of this fact only intergranular cracks are observed in the samples irradiated in Bora device, see Fig. 2(b) whereas in the samples irradiated in PF-6 and in PF-1000 facilities one may see microcracks along the body of a grain, Figs 2(c) and (d) that indicates the transcrystalline mechanism of cracking.

Same character of crack formation is described in works [27, 30] at an irradiation of samples of a pure W and an alloy W–1%La_2O_3 provided in the PF-1000 facility with a power flux density $q \geq 10^{10}$ W/cm^2. In some zones of an irradiated surface of W specimens one may observe specific structure defects – droplets of their aggregates having a spherical shape, see Figs 2(c) and 3. However the analysis of irradiated samples has shown that their nature is different at dissimilar devices. At the surfaces of samples irradiated in PF-1000 and PF-6 installations these defects are fragments of a wave like surface of tungsten sample and look as a drop-like top of a wave, see Fig. 2(c), or represent individual droplets deposited upon a sample target, see Fig. 3(a). Among such fragments one may meet spool-like structures, see Fig. 3(a) that were observed previously in a work [30] at the action of pulsed HPS and FIS upon an alloy W–1%La.

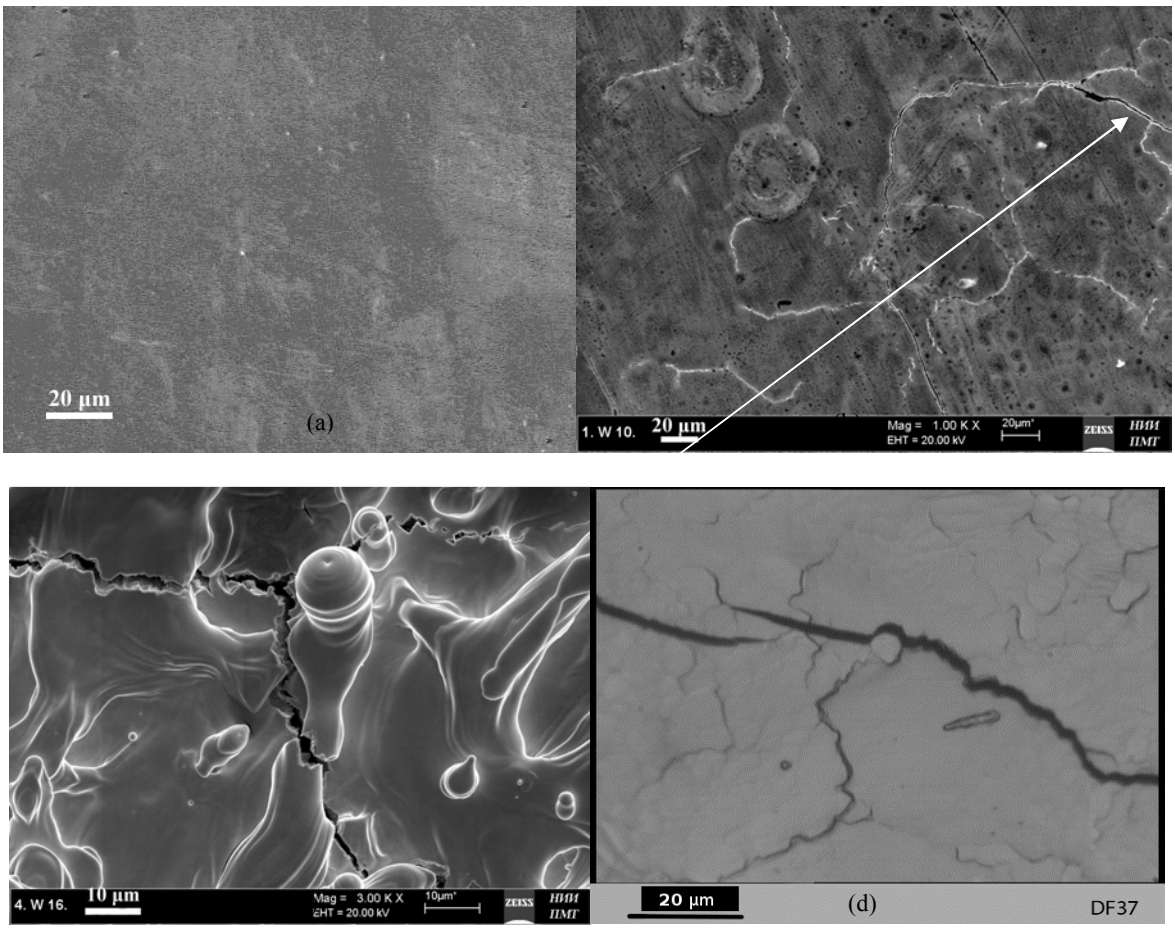

FIG. 2. (a) SEM photomicrographs of zones of surfaces of tungsten specimens virgin sample; (b) after irradiation with Bora device (specimen DF10); (c) after irradiation in PF-6 device (specimen DF16); (d) after irradiation in PF-1000 facility (specimen DF37).

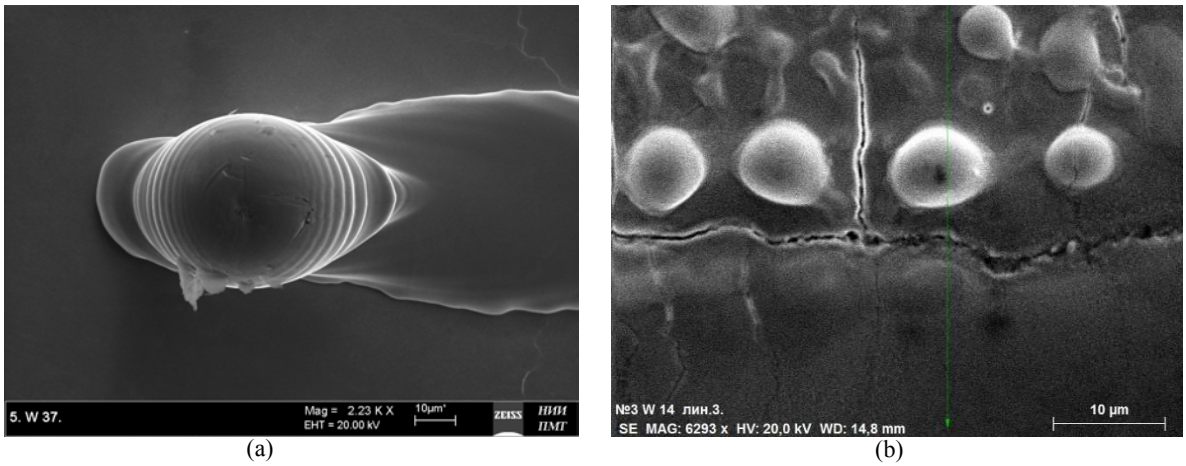

(a) (b)

FIG. 3. (a) SEM photomicrographs of zones of tungsten after 4 pulsed irradiations by HPS and FIS containing droplets of spheroidal shape, irradiation in PF-1000 facility; (b) irradiation in Bora device.

These structures remind spirals of growth appeared at solidification of liquid phase around screw dislocations. However in our case of a not steady-state fast quenching of melt a mechanism of production of these structures demands a special investigation. Just opposite to the above mentioned mechanism the droplets observed on tungsten surface after its irradiation in Bora device represent metal of its working chamber (Al) precipitated after its sputtering by HPS and FIS.

3.3.2. *Erosion of materials*

Weighing of tungsten samples before and after irradiation has shown that regimes of high energy radiation (HER) streams realized in all experiments with DPF were resulted in erosion due to evaporation and mass loss. Analysis has demonstrated that the lowest erosion of W took place in Bora device at the most soft regime of irradiation. In these cases thickness of a layer h evaporated at a single impact of HER streams upon a sample target was in the limits ~ 10–100 nm. In more harsh conditions of irradiation produced by PF-6 and PF-1000 installations the value of h was ~ 2 μm, and with an increase of a number of shots an intensity of the evaporation process slightly increases. In the conditions of a very hard mode of irradiation (at $q_i \sim 10^{11}$–10^{12} W/cm^2) the evaporation speed of the SL of tungsten increased even more reaching values ≥ 3 μm per pulse. It is very likely connected with realization of not only ion/atom but also cluster mechanism of evaporation. It is important to emphasize that the observed erosion of W resulted in production and collection of tungsten dust particles that were deposited at various elements placed inside a DPF chamber. The same phenomenon could take place at the use of W in divertor assembly of a tokamak ITER in the conditions of ELMs effects accompanied by possible and very undesirable capture of tritium atoms by these tungsten particles from deuterium–tritium plasma. It is important to note that the cluster mechanism of erosion observed in these experiments and accompanied by its precipitation by elements of a chamber in form of droplets very probably will take place in chambers of NFR with inertial plasma confinement at a use of tungsten for technological elements of the devices.

3.3.3. *Elemental analysis of surface layers*

Results of X ray spectral analysis of the elemental content of W specimens irradiated in comparable experiments at various DPF are presented in Fig. 4.

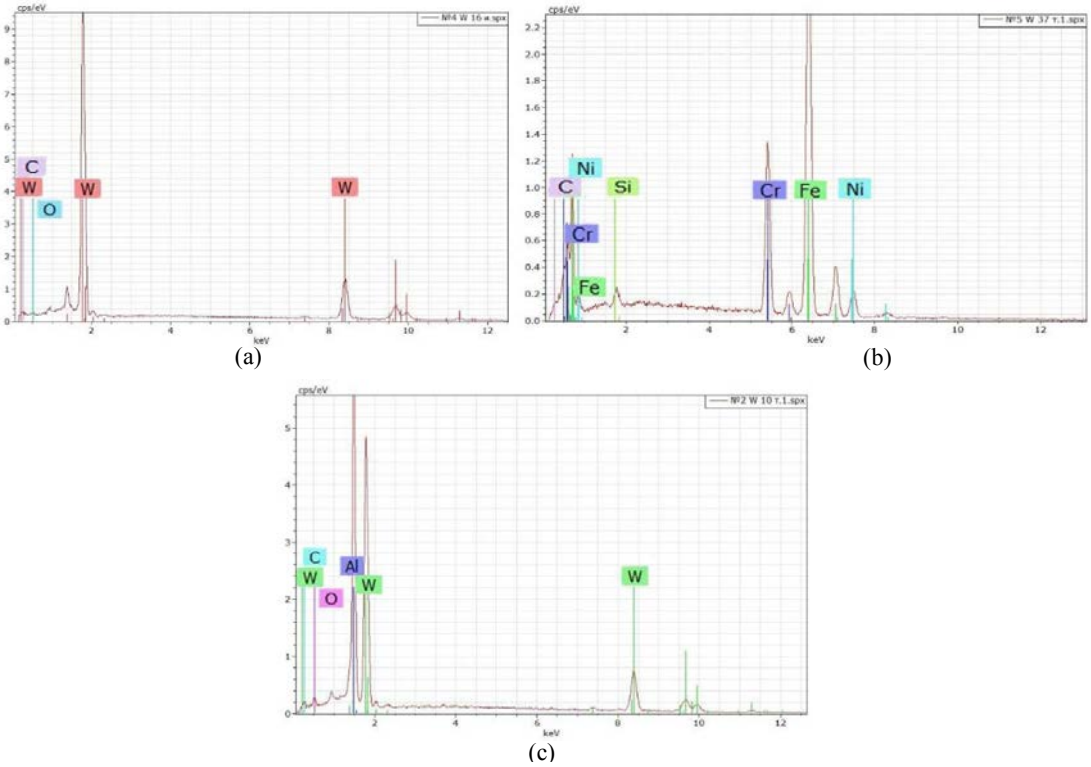

FIG. 4. (a) X ray spectra for various zones of the SL of tungsten irradiated in DPF device PF-6 ; (b) PF-1000; (c) Bora.

As it can be seen from the X ray spectra the elemental contents in the SL zones under investigations are different. So, an X ray spectrum of the W surface presented in Fig. 4(a) relates to a primordial content of W containing carbon and oxygen as impurities elements. Same spectrum is observed as a rule for all W specimens investigated after irradiation in each DPF device. This spectrum is typical for those zones of SL where initial content of tungsten has not been changed after an action of HPS and FIS. But certain zones contain copper, the anode and cathode materials of the device. This fact results from two reasons, small volume of the DPF chamber

(≈50 cm^3) in comparison with the chamber of PF-1000 (≈2×10^6 cm^3) and a very high power flux density released in this chamber in comparison with Bora set-up.

However for the majority of zones of SL of W specimens irradiated in PF-1000 and Bora X ray spectra contain also lines belonging to elements deposited to the target from components of their chambers: in PF-1000 these elements are Fe, Ni, Cr, Si, C, see Fig. 4(b), in Bora set-up mainly aluminum, Fig. 4(c), and also copper contained in the chamber electrodes. The observed elements (with exception of Al) are distributed rather uniformly across the areas of some zones. It is testified by results of scanning of irradiated surfaces of W specimens in characteristic X ray radiation of elements under analysis. It is an evidence in favor of ion-atom mechanism of their precipitation. As for aluminum, it was evaporated and deposited mainly by a cluster mechanism as it was observed on the surface of tungsten samples in forms of separate droplets, see Fig. 5.

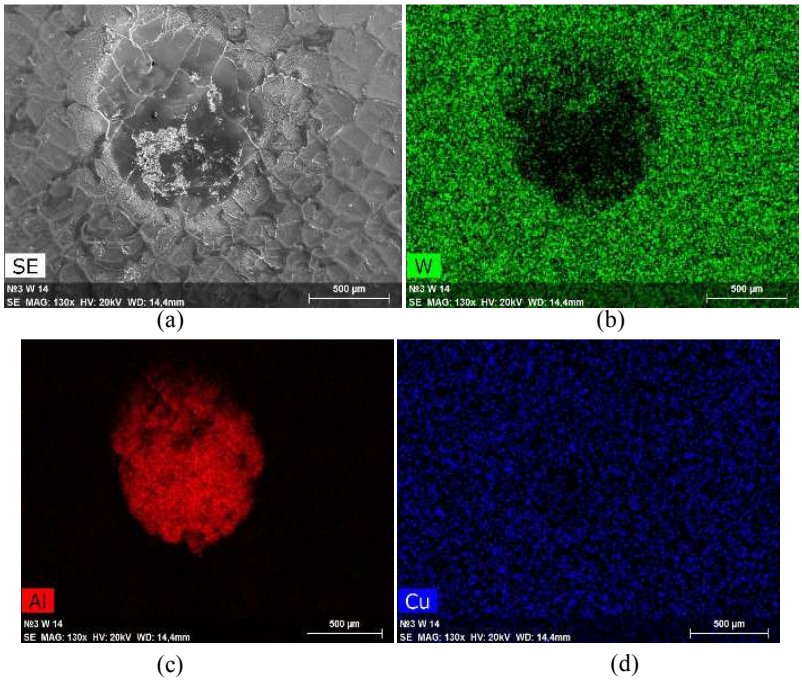

FIG. 5. (a) Scans of a zone of a tungsten SL irradiated in Bora device, specimen DF14, 32 pulses of HPS and FIS in secondary electrons; (b) characteristic luminescence of W; (c) Al; (d) Cu.

Distribution character of Al and Cu along the scanned surface area is presented in Fig. 5. It is seen that copper is distributed on the surface evenly whereas aluminum is deposited as a droplet having a size of more than 500 µm. Presence of foreign elements on the surfaces of W specimens after irradiation experiments in installations PF-1000, PF-6 and Bora indicates the facts that at the irradiation regimes realized these elements were evaporated from the surfaces of functional and construction materials placed inside the working chambers of DP foci. In the facility PF-1000 elements Fe, Ni, Cr, Si, C are parts of the stainless steel cathode tubes and the main chamber. However taking into consideration the very large volume of the chamber (see Table 1) and the remoteness of its wall from a target the role of cathode tubes must be admitted as the dominating one.

The main discharge part of the devices PF-6 and Bora was manufactured of copper. This material was evaporated by powerful streams of hot plasma and fast electrons as it is observed in DPF chambers having no a hole in the central part of the anode. This material was then deposited onto the surface of W sample. In DPF Bora the material science part of the discharge chamber was manufactured from aluminum alloy. So the presence of Al on the W target's surface testified the fact that at a relatively small volume of this part of the chamber (see Table 1) its influence as the main source of evaporated material (Al) has been the dominant one. It must be noted that the precipitation of elements from functional materials (cathode tubes and a sample holder manufactured from SS) by the W target surface during the process of its irradiation by HPS and FIS was also observed in a work [27] yet in a softer regime of irradiation ($q = 4 \times 10^8$ W/cm^2). In those cases a multiple pulsed irradiation by HER was resulted in diffusion penetration of deposited elements into a SL [27]. Just opposite to it in this very work a very hard regime of irradiation was realized in PF-1000 and PF-6 devices when a thickness of an evaporated layer was 2–3 µm. At these conditions a deposition of elements took place very likely after the end of each pulsed discharge and accompanied interaction of HPS and FIS with the target's material. Because of this the deposited elements penetrate the material to a small depth (less than 1 µm) during a cooling period of the SL

of tungsten heated to the high temperature. And at the subsequent pulsed impact they were removed off together with the evaporated layer. At the same time the SS elements (Fe, Ni, Cr, Si, C) observed in the experiments were deposited during the final period of pulsed action of HPS and FIS and they are concentrated within a thin SL of thickness ~ 100 nm as the analysis (both experimental and theoretical) has shown. These elements provide alloying and hardening of this layer.

3.3.4. Structure phase state of the surface layer

Fig. 6 presents X ray diffraction patterns of W specimens under investigation in their virgin state and after irradiation in DPF.

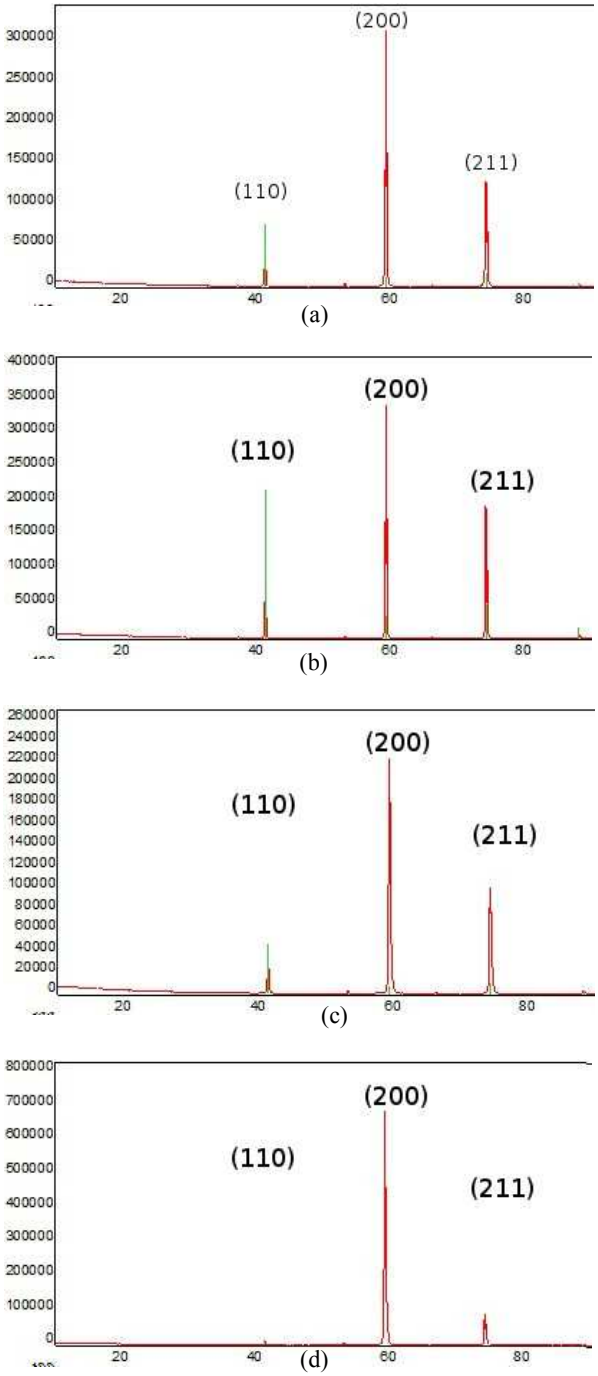

FIG. 6. (a) X ray diffraction patterns for W samples in its virgin state; (b) after irradiation by HPS and FIS in the facility PF-1000; (c) after irradiation by HPS and FIS in the facility PF-6; (d) after irradiation by HPS and FIS in the facility Bora.

One may see from this pictures that in the initial unexposed sample there is a texture in the direction (200). In our experiments this direction was parallel to the incoming streams of energy (the plane of irradiation (200) was perpendicular to the direction of HER). In the irradiated specimens of tungsten the maximal diffraction peak is also corresponded to the orientation (200), but the relationship of lines intensities I from planes (200), (110) and (211) in comparable specimens are dissimilar.

So, if before irradiations the ratio $[I_{(200)}/I_{(211)}] \sim 2.4$ and the ratio $[I_{(200)}/I_{(110)}] \sim 15$, these relationships after irradiations appeared to be ~ 1.8 and 8.2 for PF-1000 and ~ 2.2 and 11 for PF-6. For Bora device ~ 9 and 66 (line (110) at the diffraction pattern is very weak, see Fig. 8. Saying by other words these diffraction patterns have shown that if the irradiation conditions realized in the PF-6 device did not changed practically the initial ratio of the above-mentioned lines and the ones in PF-1000 preserved initial texture making it a bit less pronounced, but the most soft irradiation regime realized in Bora device brought the surface to the most remarkable structure changes. Indeed the diffraction pattern of Fig. 8(d) demonstrates an about double increase of the line (200), a noticeable (~ 1.5 times) decrease of the reflex of the line (211) and an almost complete absence of the line (100) observed in all comparable cases. Similar situation was observed in a work [27] at the irradiation in PF-1000 facility of the samples of sintered tungsten with the initial texture in the direction (100) (the irradiated plane was perpendicular to HER streams). After experiments provided at a relatively not very high power flux density $q \approx 10^8$ W/cm^2 the observed texture was more pronounced compared with the initial one. At the high power flux density $q \approx 10^{10}$ W/cm^2 the initial texture was preserved but appeared to be less pronounced than before irradiation. X ray phase analysis of tungsten has shown that a chemical interaction of precipitated elements with W and with each other is absent. But the liquid phase doping (alloying) of SL melt by the above mentioned elements took place with a small depth of subμm scale in the conditions of a superfast cooling of the liquid phase.

The results obtained in the present work show that the crystallization conditions of SL of tungsten in all experiments and at all three DPF devices had a common law-govern process: solidification of a liquid phase had a directional character and took place with a high speed in the direction of an increase of the temperature gradient from deep layers to the surface. At that the texture of the crystallization was formed that coincided with the initial texture (200), and the preferential grains orientation within samples ruled by technology of the initial samples of tungsten manufacturing was preserved after irradiation. Regimes of the W specimens' irradiations with a high power flux densities $q \geq 10^{10}$W/cm^2 realized in PF-6 and PF-1000 installations produced a weak effect upon the initial crystallographic grains orientation with the SL. The reason for this fact is connected with the intense explosion-like evaporation in the regime of irradiation known as an ablation (similar to that at the laser ablation [31, 32]). As a result a noticeable part of the irradiated SL of tungsten was removed at the action of HPS and FIS and it did not make any impact in the process of the texture formation at the stage of solidification of a liquid phase and cooling of SL. Our estimates has shown that the thickness of melt and depth of the adjacent heated solid layer of W at the power flux density of HER streams $q \sim 10^{11}$–10^{12} W/cm^2 and pulse duration 20–30 ns is much lower the ones for more soft regimes of irradiation (at $q = 10^8$–10^9 W/cm^2, $\tau \approx 20$ ns) realized at Bora device. Observed in the last case a noticeable increase of reflex for the line (200), a decrease of the line (211) and a practical disappearance of the line (100) (see Fig. 8(d)) show an additional reorientation of grains within the irradiated SL in the direction that coincides with the orientation (200). This process as it was mentioned above is connected with the directional solidification of the SL melt (thickness of which is much larger than in the conditions of experiments with PF-6 and PF-1000 devices) and formation of the crystallization texture in the direction (200). The process under examination took place in Bora device not only at the solidification of melt but partly at the recrystallization of more deep solid layers of W heated to high temperature. Thus regime of experiments realized in Bora device produced more profound influence on structure state of SL in W samples in comparison with more harsh regimes created in PF-6 and PF-1000 installations.

3.4. Conclusions

— It is found that irradiation in dissimilar DPF devices PF-1000, PF-6 and Bora of tungsten grades of the same type DF (double forged tungsten) by powerful pulsed streams of hot plasma and fast ions at the power flux density $q = 10^8$–10^{12} W/cm^2 in nano and microsecond ranges of pulse durations resulted in a damage, erosion and changes of a structure state of surface layers.
— In the above mentioned conditions processes of melting and partial evaporation of SL, formation of the wave-like relief and microcracks at the solidification a liquid phase take place.
— In more soft regime of irradiation (at $q = 10^8$–10^{10} W/cm^2, $\tau \approx 20$–30 ns, realized at Bora device) microcracks are produced mainly by a process of intergranular cracking whereas at higher power flux densities (at $q = 10^{10}$–10^{12} W/cm^2, $\tau \approx 30$–50 ns, realized at PF-6 and PF-1000 facilities) this mechanism is supplied by the other one transcrystalline cracking along the body of a grain.

— Cracks penetrate the bulk of the material to the depth of about of a thickness of the melt layer ~ 1 μm, and with an increase of a number of pulsed impacts cracking of the SL of a tungsten specimens is increased up to 50 μm.
— As it was shown in the previous report on the years 2013–2014 in the results of a shockwave action that produced by powerful ion stream shearing processes takes place that produce discontinuity flaws at much higher depths (up to 200–500 μm).
— It is found that regimes of pulsed irradiation realized in experiments with DPF result in erosion of material connected with its evaporation and mass loss.
— Erosion process depends on the particular irradiation regime power flux density and pulse duration of radiation pulses, as well as on the number of pulses of irradiation.
— In the regimes realized in Bora device erosion takes place mainly according to the ion, atom sputtering mechanism whereas in more harsh regimes realized in PF-6 and PF-1000 this evaporation follows to ablation mechanism including ion, atom and cluster evaporation.
— It is revealed that the structure changes in SL of irradiated tungsten is connected with the creation of microstructure defects of the types of microwaves, droplets and microcracks as well as with the formation of a texture determined by a high speed directional crystallization of melted layer and by a recrystallization of deeper layers of solid material heated up to high temperature.
— It is determined that on the irradiated surface of tungsten a number of elements belonging to constructional and functional parts of a DPF chamber of a device are presented.
— It shows that these parts were evaporated by powerful HPS and FIS at pulsed discharges with a subsequent deposition of them upon the tungsten specimens.
— This process does not resulted in a chemical interaction of these precipitated elements with tungsten and with each other, however it helps to liquid phase doping (alloying) of the surface layer to the depth of subμm scale.
— The results received are oriented to a possible use of tungsten in NFR with magnetic and inertial plasma confinement.
— A phenomenon of the tungsten dust particles production taking place at the evaporation of the specimens' surfaces observed in these experiments may take place in ELMs effects in tokamaks that can be accompanied by an undesirable subsequent capture and retention of tritium from tokamak plasma.
— Cluster mechanism of W evaporation may take place in fusion reactors with inertial plasma confinement.

4. PHYSICAL AND CHEMICAL ANALYSIS OF TUNGSTEN BASED MECHANICAL ALLOY

4.1. Introduction

Tungsten alloys manufactured by a powder metallurgical production process with addition of oxides of rare-earth metals, in particular oxides La_2O_3 aiming improvement of their physicomechanical properties, are counted at present time as perspective materials for usage in structures of the divertor assembly of thermonuclear reactors with magnetic plasma confinement. At present time practically the total output volume of tungsten is produced by a powder metallurgical production process [32, 33]. Due to a high melting point of tungsten its sintering takes place at high enough temperatures. After this a process of forming operation is provided to obtain high density of the material. This last process determines volumetric mechanical characteristics. However a long lasting curing of tungsten at high temperatures results in grain growth and decrease of mechanical properties due to weakening of grains borders.

In a number of works it was shown that the disperse particles of oxides (of the types La_2O_3, Y_2O_3, HfO_2, ZrO_2 and CeO_2) suppress recrystallization and grain growth, increase strength and creeping resistance due to slowing-down of the grain-border glide [34, 35]. In this work we have provided more detailed analysis of features of the structure phase changes within the surface layer of the W–1%La_2O_3 alloy produced under the action of high-temperature deuterium plasma and fast ions of deuterium in the regime simulating the disruptive instability in tokamak when material exposed by an extremely powerful thermal shock.

4.2. Material and investigation methods

Material for the investigations was sintered alloy W–1%La_2O_3 (the WL10 alloy – PLANSEE), prepared by a powder metallurgical production process. In the ready to use state we had a rolled bar of 4 mm thickness. Our samples were prepared from it with the sizes 20 mm × 20 mm. The samples were irradiated with hot deuterium plasma and fast deuterons in pulsed regime at the Dense Plasma Focus PF-1000 facility (IPPLM). Power flux density of deuterium plasma in a subμs range of pulse durations was $q \approx 10^9$ W/cm^2, whereas for the beam of fast ions (E_i ~ 100 keV) this quantity was up to 10^{12} W/cm^2 at the pulse duration $\tau \approx 100$ ns. Total number of

irradiation pulses was 2 produced with the interval of a few minutes. Scheme of irradiation and metallographic sections preparation are shown in Fig. 7.

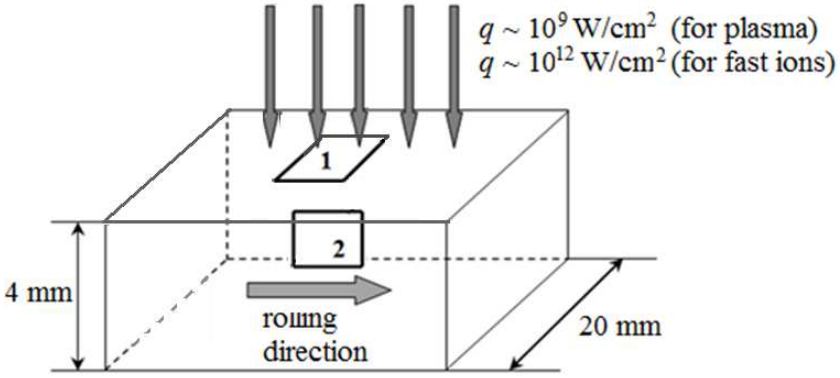

FIG. 7. Scheme of irradiation and preparation for investigations of metallographic sections of the alloy W–1%La_2O_3.

Surface microstructure of the irradiated samples of tungsten alloy was investigated by methods of optical and scanning electron microscopy (LEO430i, Japan), as well as by local X ray spectral analysis (attachment OXFORD Link). Metallographic sections were prepared by methods of mechanical polishing and finishing. X ray analysis was performed in Cu K_α-radiation at the Dron-3 device attached to a computer.

4.3. Results and discussion

Microstructure of the alloy W–1%La_2O_3 obtained at investigations with methods of optical and scanning electron microscopy at flat unetched metallographic sections is presented in Fig. 7. In the plane perpendicular to the irradiation stream (position 1 in Fig. 7) secondary phases having size 2–6 μm look as roundish figures of not regular shapes uniformly enough distributed in the plane (Fig. 8(a)). In the cross section of the sample (position 2 in Fig. 7) the secondary phases have a shape of strokes or lenses stretched along the direction of rolling (Fig. 8(b)). This circumstance indicates in favor of the fact that the phases initially having relatively equiaxial shape within the mechanically doped alloy change it in a process of plastic deformation of the sintered alloy. Microstructures of the samples surfaces of the alloy W–1%La_2O_3 obtained before and after irradiation by a method of scanning electron microscopy are presented in Figs 8(a) and 9(a)–(d). One may see that the microstructure of the surface of the rolled bar is a conglomeration of crystalline particles having inclusions of secondary phases inside of them (Fig. 8(a)). X ray spectrum of parts of the initial surface showing presence of elements W and La is shown in Fig. 9(b) whereas Fig. 9(c) shows impurity contents of it.

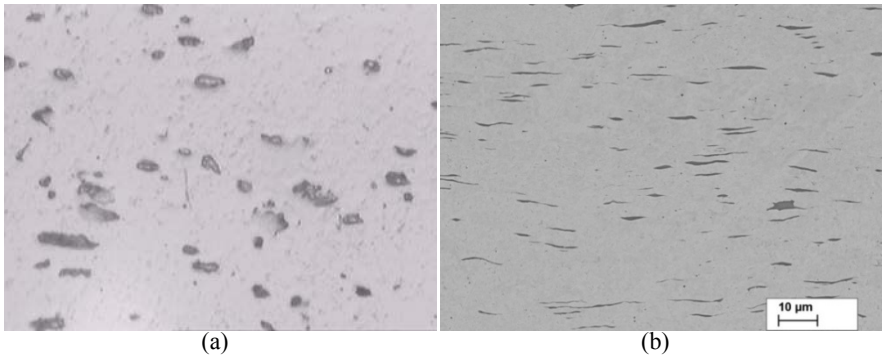

(a) (b)

FIG. 8. (a) Microstructure of the alloy W–1%La_2O_3 obtained at the unetched metallographic sections at the irradiation plane (position 1 in Fig. 7); (b) in the transverse direction (position 2 in Fig. 7), optical microscopy.

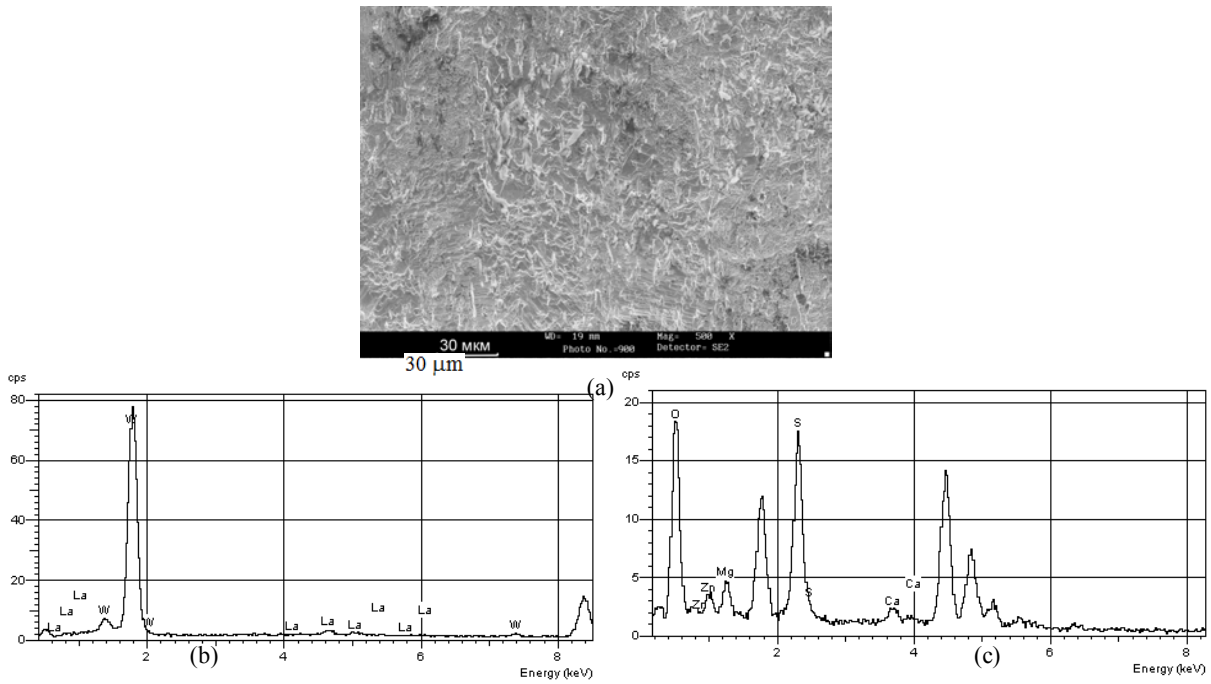

FIG. 9. (a) Microstructure of the surface of the alloy W–1%La_2O_3 before irradiation (scanning electron microscopy); (b) X ray spectra of the surface parts; (c) X ray spectra of the surface parts.

At the irradiation by high temperature plasma and beam of fast ions the surface layer is melted. It means that temperature of it exceeds the melting point of tungsten. Thickness of the melted layer in some parts of the surface does not exceed 1 μm. Microphotographic images of several parts of the melted layer are presented in Fig. 10.

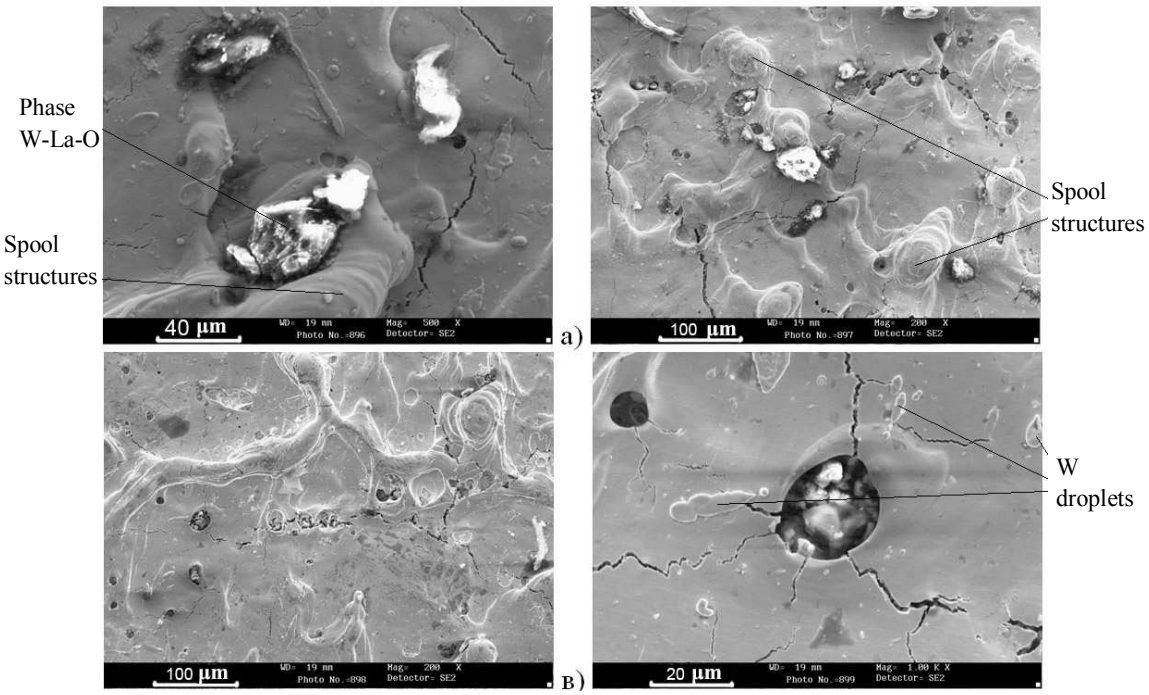

FIG. 10. Microstructure of parts of the alloy W–1%La2O3 surface after irradiation with deuterium plasma and deuterons in PF-1000 facility; power flux density of plasma stream q ~ 10^9 W/cm^2, for fast deuterons q ~ 10^{12} W/cm^2; scanning electron microscopy. One may see separations of secondary phases and microcracks at the irradiated surface.

Investigations have shown that an aerodynamic action of powerful streams of dense deuterium plasma and fast deuterons results in formation of the wave-like structure of the samples' surface. Besides in these pictures one may observe particles of secondary phases, droplets of solidified spit of liquid tungsten, as well as bubbles at various stages of their development. At the tops of the wave-like relief the spool-like structures appear. They are similar to the spiral growth patterns observed at solidification of alloys from liquid state around screw dislocations. These details of the structure are shown by arrows in Fig. 10 whereas the corresponding X ray spectra of elements are presented in Figs 11(a) and (b). Results of numerical calculations of temperature distribution by depth of the irradiated samples made following to the method described in [36] are presented in Fig. 12. Estimations has shown that the zone of thermal action is extended to the depth of about 6–8 μm. However the thickness of the layer melted during the irradiation process was changed by a quite complicated way (Fig. 12(b)). It results from the fact that during irradiation we have two competitive processes: movement of the border melt–solid phase inside the sample and a process of intense evaporation from the surface reducing to a decrease of the thickness of the melted layer. The melt on the surface is solidified completely after ~ 200 ns after the beginning of irradiation, and resulted thickness of the remelted layer after irradiation is about 0.5 μm. It coincides with the experimental data. Subsequent cooling of the crystallized and adjacent layers can takes place at a very high temperature gradient. Indeed at t = 250 ns after irradiation pulse (curve 3 in Fig. 12(a)) an average value of gradT ≈ 5×10^5 degree/cm. And this high magnitude of the gradT is preserved at a remarkable depth from the irradiated surface, 1 order of magnitude bigger compared with the thickness of the melted layer.

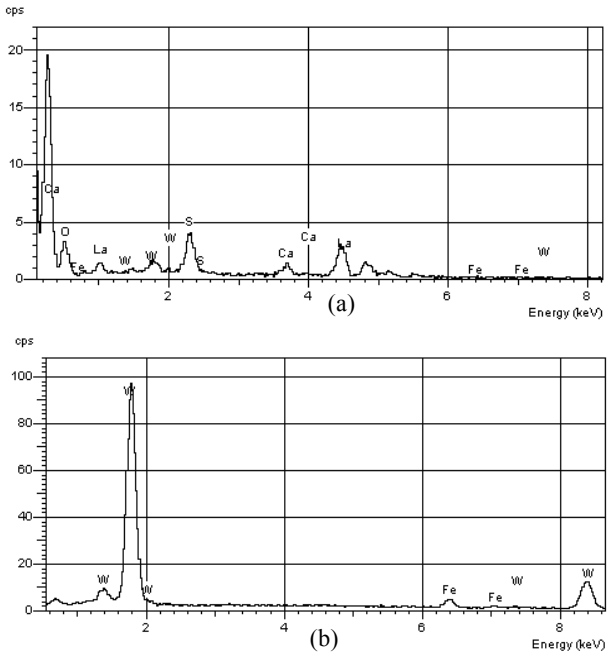

FIG. 11. (a) X ray spectra obtained at the particle of the secondary phase; (b) in a droplet.

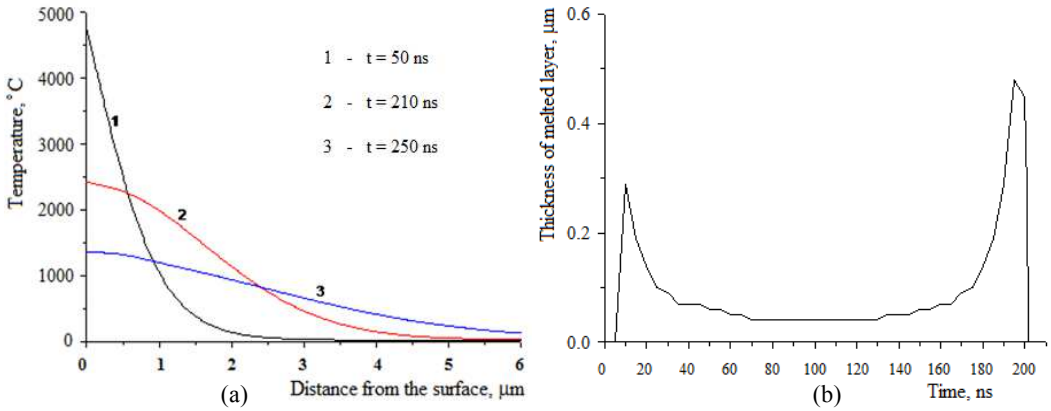

FIG. 12. (a) Distribution of temperature by the depth for different time moments; (b) changes of thickness of the liquid phase at its surface during the irradiation.

At the surface of the irradiated samples one may clearly see the branched network of cracks (see Fig. 10). This net appears after crystallization of the melted layer in the conditions of fast quench. During this stage thermal stresses appear due to sharp gradient of temperature pointed inward the sample volume. Magnitude of these stresses exceeds the strength limit of the material. This fact results in its cracking. With an increase of the number of shots the picture is repeated when the old cracks are healed whereas the new ones are created. As it well seen in Fig. 10 solidification of the droplets sputtered from the tungsten surface took place after formation of cracks on which this spit is settled. Same phenomenon was described by the authors of the work [37], which observed them at investigations of tungsten erosion during the simulation of the plasma disruption. It was also established [38] that the emission of drops starts at the heat loads higher compared with the melt limit of tungsten (Q_{melt} = 1.0 MJ/m^2) but lower in comparison with its boiling limit (Q_{boil} = 1.9 MJ/m^2). Meanwhile according to data obtained in [38] this emission of tungsten spit under the action of high-intensity plasma took place as during the discharge time having duration $\Delta t \sim 0.5$ ms, so during a certain subsequent period of time $\Delta t \sim 1.5$ ms. Structure fragments of the fritted surface layer of our samples presented in Fig. 10 show also that microparticles of the secondary phases play an important role in initiation and propagation of cracks. By means of diffraction X ray phase analysis we found small amount of different oxide phases within the surface layers of both virgin and irradiated samples.

Their contents are presented in the Table 2.

TABLE 2. PHASES PRESENTED IN THE COMPOSITE ALLOY W–1%LA_2O_3 BEFORE AND AFTER IRRADIATION ACCORDING TO DATA OF X RAY PHASE ANALYSIS

Alloy's state	Secondary phases
Before irradiation	La_2O_3, WO_3, W_3O, $La_2W_{1,25}O_{6,75}$, $La_2O_33WO_3$
After irradiation of samples with hot deuterium plasma ($q_{pl} \sim 10^9$ W/cm^2) and stream of fast deuterons (q_d = 10^{12} W/cm^2) at the number of pulses N = 2	La_2O_3, W_3O, $La_2O_33WO_3$, La_2WO_6

In virgin samples the nature of the secondary phases is caused by technology of manufacturing of the composite alloy W–1%La2O3. Namely the oxide La2O3 is the alloying addition specially introduced in the matrix in the form of a disperse powder; trioxide WO3 an impurity unreduced at the production of the initial powder of tungsten, as well as a suboxide of tungsten W3O that is referred by authors of a number of papers as beta-tungsten (β-W) stabilized by oxygen and another impurities dissolved in it [39]. Besides these samples contain multicomponent oxide phases La2W1,25O6,75 and La2O33WO3 that enclose La and W simultaneously. It points to the processes of diffusive interaction with participation of La2O3 and tungsten within the alloy W–1%La2O3 during the procedures of sintering and hot deformation. The total quantity of the secondary phases does not exceed 5%. One may suppose that creation of these multicomponent oxides in the initial alloy takes place on the borders of the oxides La2O3 microparticles with the surrounding tungsten matrix. Hardness of the investigated alloy W–1%La2O3 is Hv 100 g = 440. This fact points to the relatively high material density. It means that these phases are created during diffusive processes taking place at temperatures of hot pressing (T ~ 1400°C). One may suppose that the multicomponent oxides La-W-O envelope the initial oxide La2O3.

As it is seen from the Table 1 on page 167 after irradiation the surface layer contains practically the same phases as the initial one. The only exception is the oxide WO3 that has the lowest melting point (1473°C). It dissociates in the metal heated to higher temperatures. During heating of the surface layer under the action of hot plasma and fast ion streams the initial oxides can be spheroidizied. At the temperature close to the melting point of tungsten a certain part of oxides can be volatilized from the active surface of the alloy contacting with plasma and fast ion streams due to their lower melting points compared with that of tungsten. Another (main) part of the oxides being inside the microlayer of liquid tungsten and below it may probably confined in the form of melted complexes with their subsequent crystallization at the alloy's cooling. An important part in the consolidation of these complexes may be taken by surface active lanthanum.

Thus one may see that the initial state of the mechanically doped alloy under investigation contains a certain collection of microparticles of oxide phases having their own complexes of physicochemical and mechanical properties that may influence the behavior of the alloy in tote. First of all these oxides have dissimilar melting points that are lower compared with the temperature of melting of the main alloying oxide La2O3 and considerably lower of the melting point of pure tungsten (Fig. 13 [40]).

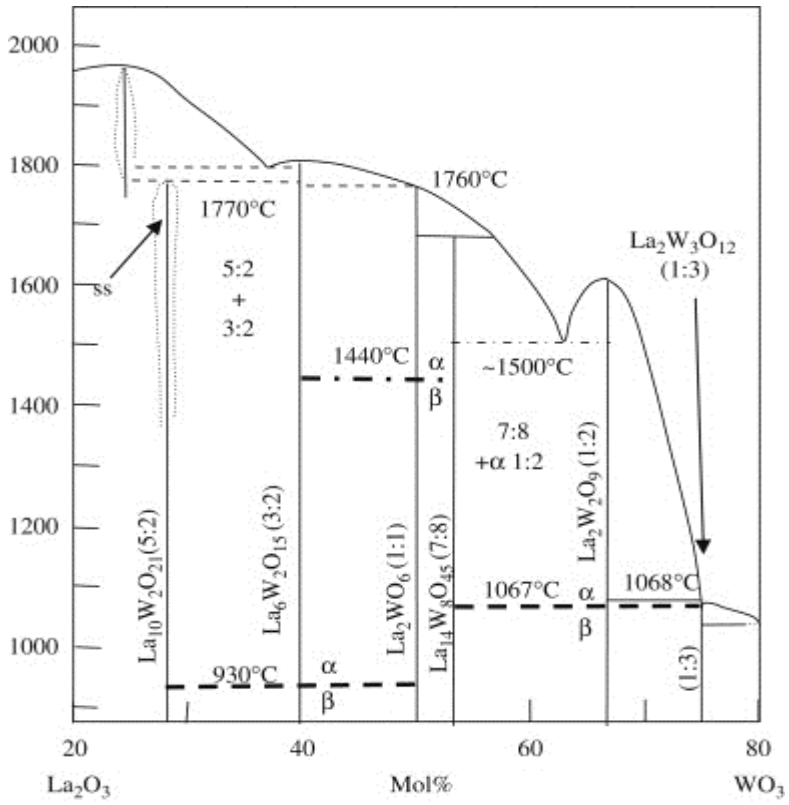

FIG. 13. Phase diagram of La_2O_3–WO_3 [38].

It has to be noted that as a rule different impurities like Ca, Mg, S, and Zn are presented in a close vicinity to the microparticles of secondary phases. X ray spectra of them are seen in Fig. 9(b) and 11(a). These inclusions produce also an influence upon physicochemical and mechanical characteristics of the alloy. There is a ground to believe that these impurities are attracted by the oxides presented in tungsten. The noted facts take an important part in estimation of exploitation properties of tungsten alloyed with oxide La_2O_3 particles. Data obtained by the X ray structure analysis have shown that the samples of the initial alloy display a texture of rolling along the plane (200) (Fig. 14(a)) that is absent in the structure of the surface of the irradiated samples (Fig. 14(b)). Comparison of the parameters of the bbc lattice of virgin and irradiated samples of tungsten (Table 3) shows a weak decrease of the W lattice parameter after irradiation. It is probably connected with a diminution of the unlinked atoms of impurities (O, H, and N). It is known that solubility of interstitial impurities (O, H, N, and C) in the crystalline lattice of tungsten is very low even at the melting temperatures of tungsten.

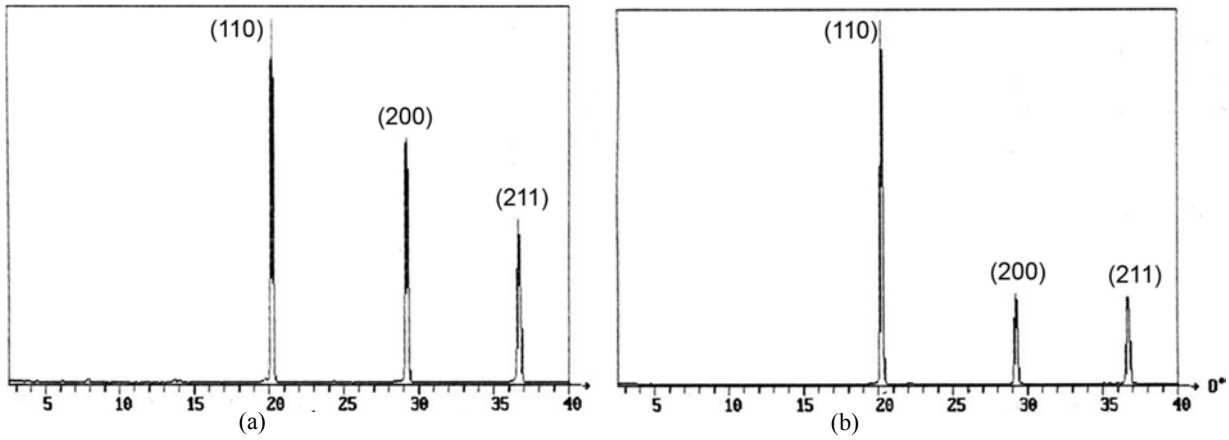

FIG. 14. (a) Diffraction patterns of the alloy W–1%La_2O_3 in the initial state; (b) after irradiation in the facility PF-1000: q_{pl} ~ 10^9 W/cm^2, q_d ~ 10^{12} W/cm^2.

From the other side the deuterium retention is quite possible within the pores of the sintered composite alloy. It supposedly results from data on specific densities of metallic and sintered tungsten (19.3 and 17.8 g/cm3

respectively). It is very likely that the conductors for the collected gases outlet from the surface of the alloy samples may be the oxides particles above which swelling and buckling of fritted metal may take place (Fig. 10(c)).

TABLE 3. W LATTICE PARAMETERS IN THE COMPOSITE ALLOY W–1%LA_2O_3 ACCORDING TO THE X RAY PHASE ANALYSIS

Alloy's state	Lattice parameter, a (Å)	Volume of elemental cell, V ($Å^3$)
Before irradiation	3,1638	31,67
After irradiation of samples with hot deuterium plasma ($q_{pl} \sim 10^9$ W/cm^2) and stream of fast deuterons ($q_d = 10^{12}$ W/cm^2) at the number of pulses $N = 2$	3,1613	31,59

4.4. Conclusions

— Irradiation of samples of the composite alloy W–1%La2O3 with powerful streams of high-temperature deuterium plasma of power flux density $q_{pl} \sim 10^9$ W/cm^2 and stream of fast deuterons of $q_d = 10^{12}$ W/cm^2 having pulse durations in the subμs range results in production on their surface of the wave-like fritted layer of thickness up to 1 μm.
— This layer has a number of specific defects: pores, bubbles, droplets of tungsten, spool-like structures as well as the microcracks network.
— Deformation texture observed in the virgin samples vanishes.
— Insertion of oxides La2O3 in tungsten brings to the production within the sintered alloy of multicomponent oxides La-W-O having melting temperature lower compared with that one for the oxide La2O3.
— It results in the structure no uniformity of the material in relation to the high temperature influence upon it;
— Presence of the dispersed phases of the lanthanum oxides as well as the multicomponent oxides La-W-O stimulate gas buckling of the material in places of their accumulation.
— The fact that the oxide phases observed in the initial alloy are preserved in its surface layer within the zone of thermal influence after irradiation permits an opportunity to suppose an existence of liquid complexes of the oxides La-W-O in tungsten in the conditions of the superfast heating of it to the temperatures in the range 1500°C T_{melt} of tungsten.
— Practicability of a use of the alloy W–1%La2O3 in construction elements of the divertor instead of pure tungsten will be determined on the base of further comparative investigations of properties of both materials, in particular including the analysis of the mass loss from the surface layer of samples at dissimilar radiation loads as well as by means of more detailed study of the features of the crack formation within surface layers produced at powerful energetic actions.

5. STRUCTURAL AND PHASE CHANGES IN AUSTENITIC STEEL PRODUCED BY HIGH ENERGY DEUTERIUM PLASMA IRRADIATION

5.1. Introduction

The high level of stability of mechanical and physical properties of structural materials used in nuclear devices (ND) and fusion devices (FD) during their long lifetime is one of the main requirements for the elements manufactured of them. Together with volumetric structural and phase changes that occur under the influence of neutron irradiation and lead to the reduction of mechanical, physical and other properties of the material, the effects arising within a surface layer of the first wall and divertor materials of thermonuclear fusion reactor due to the interaction of high temperature pulsed plasma (HTPP) streams play a major role in the behavior of the structural and the plasma-facing components.

Among the materials promising for use in the FD, as well as high power plasma accelerators, the stainless steels of austenitic and ferritic-martensitic classes occupy an important place [41, 42]. In particular, low activated ferritic-martensitic steels, including those obtained using new technologies and methods of alloying, are one of the most promising structural materials in fusion reactor (ITER Project), as well as in the construction of the fusion reactors of the next generation [43]. In addition, austenitic chromium–nickel steels are widely used in the working chambers of various plasma systems [44, 45]. Therefore, in recent years the relevant study of damage,

the phase structural changes of the SL of the above mentioned steels of different types irradiated by high power pulsed beams of fast ions and by HTPP streams, become very important. The austenitic steels, in which nickel replaced partially or completely by manganese, are of particular interest here. Such a replacement produces an effect of a so called low activated steel with accelerated decline of induced radioactivity after their prolonged use in neutron fields [46, 47]. However, studies have shown that these steels, in spite of generally favorable set of their physical, chemical and technological properties, have less stable austenite, in particular, during neutron irradiation, and the high rate of evaporation of manganese at high temperatures [48, 49].

Steel with low nickel content, such as the Cr12Mn14Ni4 (Al, Mo, Sc) type unlike Cr–Mn steel have a higher stability of austenite to the structural phase transitions and have a good combination of strength and plastic mechanical properties, as well as satisfactory welding characteristics [50]. Introduction of small amounts of aluminum, silicon and molybdenum contributes to the high temperature strength and resistance of steel. Micro-additives of scandium improve fracture toughness [51] and radiation resistance of austenitic steels [52]. However it should be noted that the presence of nickel, molybdenum and aluminum has an adverse effect on the residual radioactivity for a long term use of such steels at heavy neutron irradiation due to the formation of long lived radionuclides [53].

The aim of the present work was to study within the DPF the nature of the failure rate, the structural characteristics, in particular the characteristics of the formation of surface defects and structural changes for the chromium–manganese low nickel austenitic steel of the type Cr12Mn14Ni4 (Al, Mo, Sc) modified by scandium under the influence of powerful pulses of fast deuterium ions (DI) and high-temperature deuterium plasma (DP), created in the installation of the type DPF PF-1000. These experiments were provided for a comparison these materials with the previously studied low activated austenitic (of the type of Cr12Mn14) and ferritic-martensitic (of the type Cr9WV) steels.

5.2. Materials and methods

The chemical composition of the investigated steel is shown in Table 4. Sample subjected to pulsed plasma irradiation is a plate of the size 16 cm × 16 cm made of cold rolled sheet with a thickness of 1 mm. After high temperature annealing at 1100 °C and cooling in the water the sheet has 10% cold deformation.

TABLE 4. CHEMICAL COMPOSITION OF STEEL CR12MN14NI4(AL,MO,SC)

Elements (wt. %)								
C	Si	Mn	Cr	Ni	Mo	Al	Sc	Fe
0.05	0.47	12.9	12.9	4.55	0.30	1.30	0.02	Res.

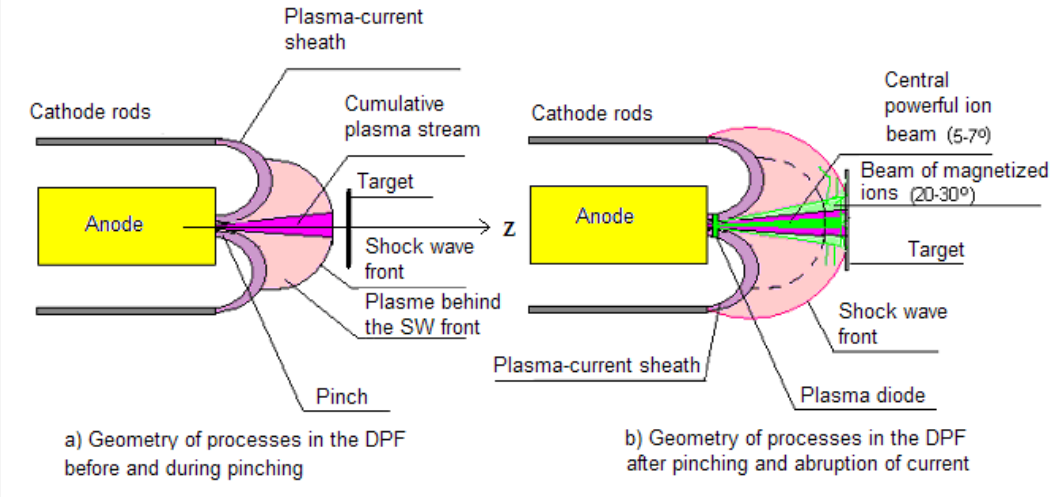

FIG. 17. The scheme of the experiment at the PF-1000 device with cumulative plasma streams and beams of head-on and magnetized fast ions.

Irradiation was carried out by use the PF-1000 facility operated with the energy supply of ~ 600 kJ at the IPPLM [54]. Experimental layout is shown in Fig. 15. The working gas used was pure deuterium at an initial pressure of ~ 470 Pa. The initial voltage applied to the electrodes, was U = 35 kV. In the process of operation the collapse of the plasma discharge current sheet (CS) on the axis of the chamber near the anode takes place, resulting in the generation of a powerful cumulative stream of HTPP directed to the target and moving at a speed of (2–5) × 10^7 cm/s. The density of the plasma in the cumulative jet moving along the Z-axis of the chamber and creating a front of a hemispherical shock wave is of the order of (3–5) × 10^{18} cm^{-3}. About 100 ns after the formation of the pinch in the DPF (i.e. of the region of maximum compression of the plasma) a plasma diode is created. This diode generates a beam of fast (high energy) deuterium ions (FIB) with energies in the range of 10–200 keV having a maximum at about 100 keV, that propagates in the direction of the sample target (cathode).

The distance between the anode and the plane located normal to the incident energy fluxes and coincides with the sample's surface was $L \approx 14$ cm, duration of the exposure pulse of HTPP on the irradiated surface of the sample was 0.5–1.0 μs, and the maximum power density was $q \approx 10^{10}$ W/cm^2 for HTPP. The area under irradiation by a pulse of HTPP, where its power decreases from the center to the periphery of the sample, covered almost the entire surface of the plate.

The duration of the impact of the pulse of FIB on the irradiated surface of the sample was about 0.2–0.4 μs, and there were two circular footprints of it with diameters approximately 8 and 2 cm respectively (as it is shown in Fig. 15). The power density of the FIB irradiation on the surface of the target in a large circle was $q \approx 10^9$–10^{11} W/cm^2, and in the small one it was 10^{11}–10^{12} W/cm^2. These characteristics of the impact of the beam of fast ions on the surface of the target resulted from the structure of the beam in the zone near the target surface were investigated by methods of plasma high-speed photography, by laser interferometry, by track-detector technique, and by a number of some other methods [55]. The total number of discharge pulses N was varied from 2 to 4. The neutron yield in pulsed discharges were within $Y_n = 10^9$–10^{11} neutrons per pulse.

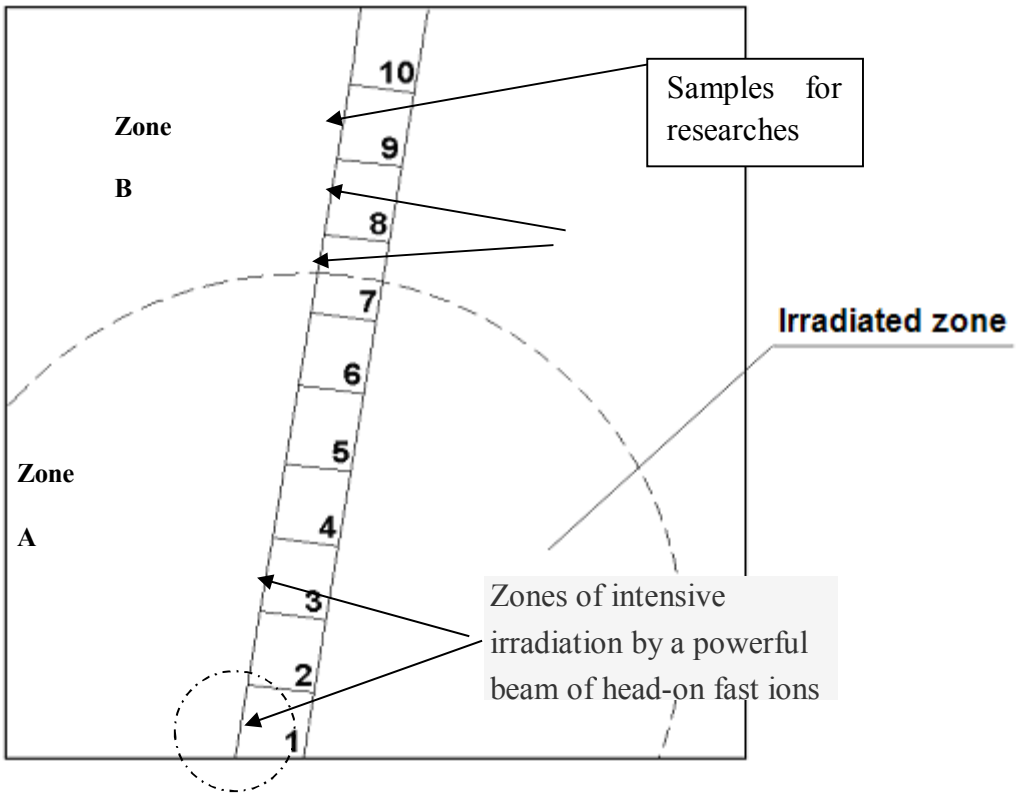

FIG. 16. Scheme of the fragments (samples taken for subsequent analytical investigations) of the plate of Cr12Mn14Ni4 (Al, Mo, Sc) steel irradiated by pulses of high temperature plasma streams and beams of fast ions (head-on and magnetized).

It should be noted that in this study we used as the targets various samples of the relatively large size. We placed them perpendicular to the axis Z of the chamber and at dissimilar distances from the anode of the device. Under these conditions it led to a variation during the experiment in the power flux density q on the surface of the

irradiated sample plates. The largest values of q, as it was discussed above, are related to the central area of the sample with a footprint diameter of ≈ 4–5 cm, as a result of action of both the plasma streams and the beams of head-on accelerated fast ions. Outside this zone, the material worked out mainly by a plasma stream (yet with some addition of magnetized ions). The value of q decreased with the distance from the center in the radial direction from 10^{11}–10^{12} W/cm^2 in the central part to the values of 10^{7}–10^{8} W/cm^2 at the periphery of the plate. Having in mind this fact, the samples for analytical researches were cut from different zones of the irradiated plate as it is shown in Figure 16. Each sample of the size 15 mm × 15 mm was investigated by optical and scanning electron microscopy, by X ray elemental, X ray structure and X ray phase analysis, and by atomic emission spectroscopy.

5.3. Experimental results and discussion

5.3.1. Damaging and surface defects

Analysis of the irradiated surface of the plates has shown that the surface has a multizone structure. In the central zone A (Fig. 17) the damage of a SL irradiated by a pulsed flow of energy has its maximum. There is a wave-like surface relief formed as ridges extended in the radial direction. This zone represents the area of the most intensive action of the beam of the head-on fast deuterons with the highest flux density (up to 10^{12} W/cm^2), irradiating the target together with streams of hot dense DP.

In Zone B a damage of the SL was markedly weaker, topography was smoother and it consisted mainly of a set of equiaxed ‘burls’. This area was mainly exposed to jets of HTPP (supported by relatively weak beams of magnetized fast ions) with a flux density ≤ 10^{10} W/cm^2. Morphology segments corresponding to zones A and B are shown in Fig. 18.

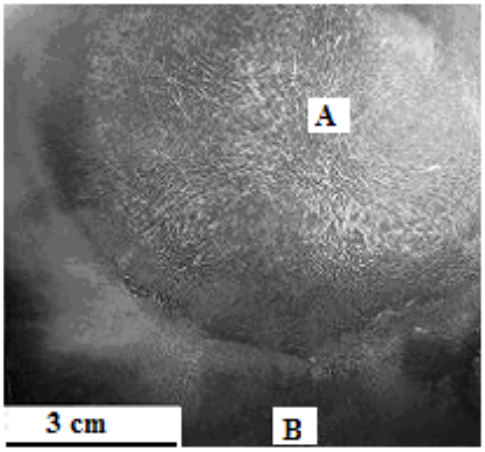

FIG. 17. Macrostructure of the surface of Cr12Mn14Ni4 (Al, Mo, Sc) steel plate irradiated at q ~ 10^{10} W/cm^2 with 2 pulses of DP and DI.

Note that the irradiated surface has practically no structural defects such as pores, craters, bubbles and microcracks observed previously in samples of chromium–manganese austenitic steels in similar experiments [56–58]. It seems that the main reason of this reduction of surface defects is the change of the investigated steel. The presence of nickel, working together with less content of manganese and with complex doping, including scandium, affect the processes of the surface defect formation.

A special role in this phenomenon is played by the presence in the steel of additions of scandium. Due to this doping a decrease of the probability of appearance of bubbles, pores, microcracks and craters at the stage of a high speed crystallization of the liquid phase takes place.

This issue, which is related to the influence of scandium upon a decrease of damage and erosion of steel and increase of its thermal radiation, deserves some further specific studies. However, one can assume that the refined action of scandium and the formation of the fine dispersed allocations of compounds of Sc with implantations elements suppress effects of defects formation within the SL of steel under investigation [59, 60].

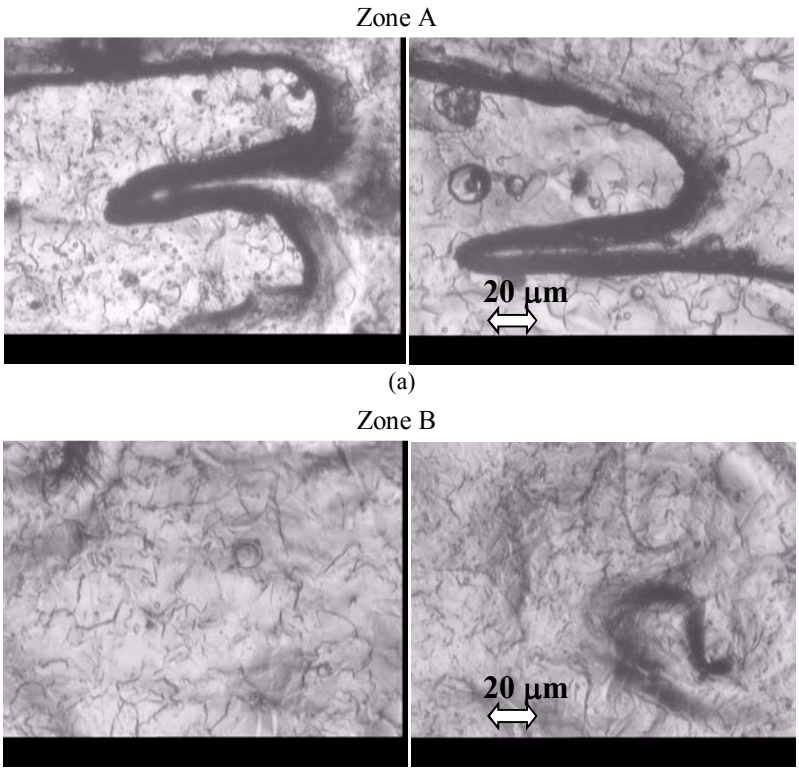

FIG. 18. (a) The surface morphology of Cr12Mn14Ni4 (Al, Mo, Sc) steel irradiated at the center; (b) irradiated at the peripheral areas of the plate.

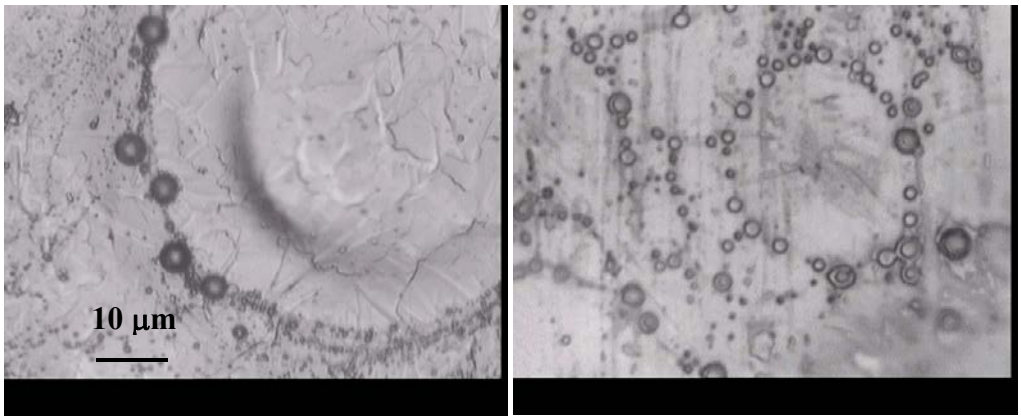

FIG. 19. (a) The surface microstructure of different austenitic steels after pulsed deuterium plasma irradiation, Cr12Mn14Ni4 (Al, Mo, Sc) steel , zone B, sample № 9 in Fig. 16; (b) low activation 25Cr12Mn20W steel, hexagonal tube, peripheral zone of the outer surface.

In the peripheral zone B at the edge of the plate (see Fig. 19) another kind of surface structural defects of a spherical shape are produced. They are located along the closed loops, similar in the shape to a circle. The characteristic sizes of the spherical defects are ranged from 1 to 1o μm whereas the diameters of their loops are tens of microns. The formation of these defects has been observed previously [61] on the external surface area of the hexagonal tube made of Cr12Mn20Wsteel and irradiated by pulsed deuterium plasma streams (Fig. 19(b)). It was suggested [59] that the mechanism responsible for the origin of the observed defects is the emergence of bubbles at the grain boundaries (in an area of high concentration of vacancies and micropores) near the interface melted SL solid phase. Subsequent growth of the bubbles was resulted from evaporation of manganese (as the most volatile component of steel Cr12Mn20W) and due to vapors of compounds of implanted deuterium and oxygen. It seems that similar mechanism of the formation of structural defects of a spherical shape on the surface is realized in experiments with steel Cr12Mn14Ni4 (Al, Mo, Sc) containing scandium doping.

Note that the size of the circular loops is significantly higher than the average grain size in the final structure of the investigated steel (Fig. 19(a)). Therefore it can be assumed that the alignment of bubbles in the contours occurred in the liquid phase and are frozen in the process of quenching the melt. The characteristic size of the observed contours (tens of μm) is close to the characteristic size of grains in the initial state of the samples, which makes the grain boundaries an effective source of gas production.

X ray spectral analysis has shown that the austenitic steel in the initial state contains a small amount (about 6–8%) of the deformation martensite (alpha and epsilon martensite). It can be transformed by a diffusionless way into the γ-phase.

Method of the atomic emission spectroscopy shows that during irradiation an evaporation of gamma-stabilizing elements (nickel, manganese) and other elements (Cr) inside a thin (3 μm) surface layer takes place. Concentration of Ni and Mn at the surface is decreased from 4.5% and 13% respectively down to 3.5% and 10%.

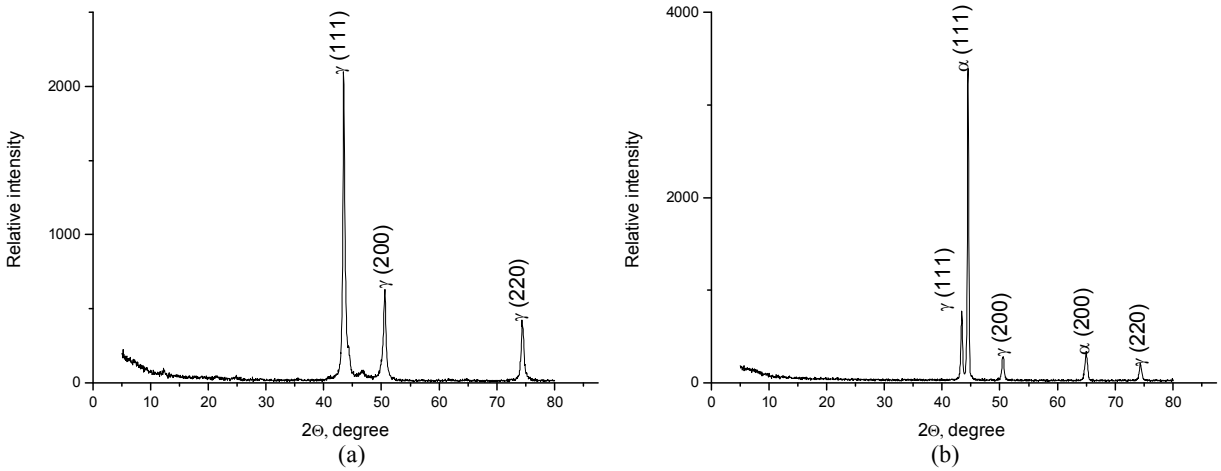

FIG. 20. (a) X ray diffraction patterns central part of the Cr12Mn14N4 (Al, Mo, Sc) steel plate № 1 before irradiation; (b) after irradiation.

As a result of this effect the austenite becomes unstable, and the subsequent rapid cooling of the sample is resulted in the transformation of the significant part of the austenite into the alpha–martensite (γ→ α).

This is shown by appearance of the α lines in the X ray diffraction patterns (Fig. 19). The content of α–martensite phase in zone A of the samples (Fig. 17) is about 85% vol., and in Zone B about 70%.

X ray analysis shows that the back side of the non-irradiated plates keeps the structure corresponding to the initial state of austenite containing a small amount of deformation alpha–martensite. It shows that during the irradiation process an average temperature at the non-irradiated back side of plates does not exceed a temperature of reverse martensitic transformation (i.e. <500 γ C). It should be noted that in the SL of the irradiated plates the iron hydride FeH is presented however in very small amounts (<1%). This indicates that part of the implanted deuterium reacts with iron forming the hydride (deuteride) compound with iron.

5.3.2. Surface effects on the non-irradiated side of the plates

Figs 21 and 22 are photographs of sections of a non-irradiated surface (‘back wall’) of the plates under research. On the periphery of the plate number 2 (Fig. 21) there are the clearly visible bright spots. They were formed very likely during the deposition on the surface of droplets captured by the current sheath rounding (enveloping) the target.

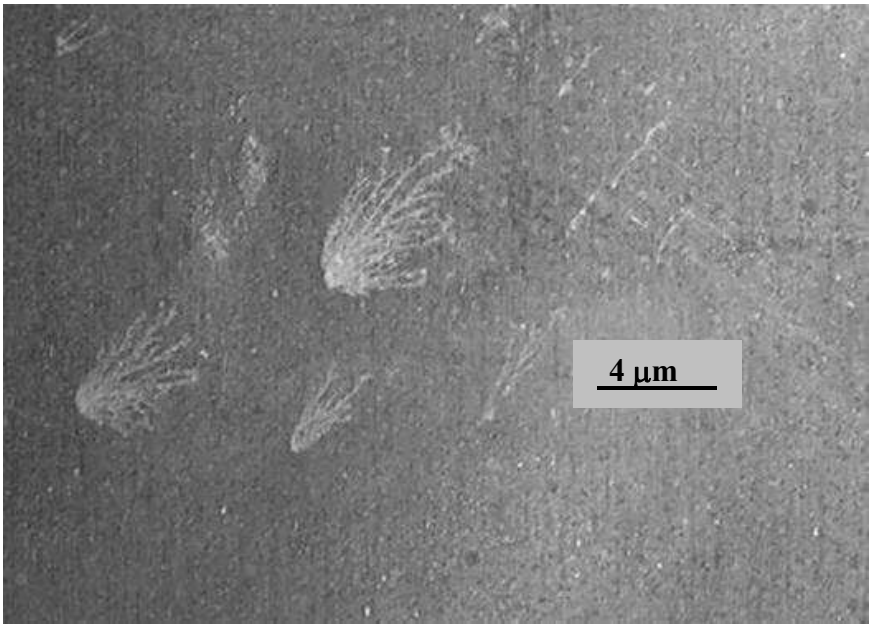

FIG. 21. Peripheral zone of the non-irradiated 'back wall' of the steel plate № 2 after 4 irradiation pulses. Precipitated visible droplets of complex shape are visible.

Point fragments observed in the central part of the plate number 1 (Fig. 22) have a rounded shape and they appeared to be the local melted parts of the surface layer of the plate itself. The topology of these sites is presented in micrographs in Fig. 22. The X ray spectral analysis showed that the concentrations of the main elements in these molten (flowed) fragments correspond to the elemental composition of the plates in the initial state. This result confirms the fact that here we have namely the melting of non-irradiated SL at the plate itself in the local micro-regions. The mechanism of this process may be associated with the following factors.

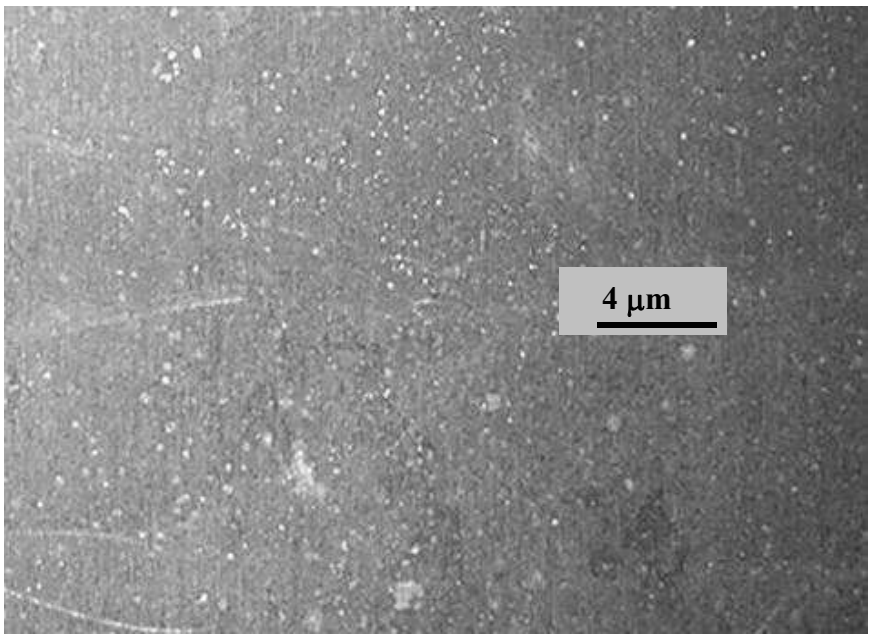

FIG. 22. Central zone of the non-irradiated 'back wall' of the plate №1 after 2 irradiation pulses.

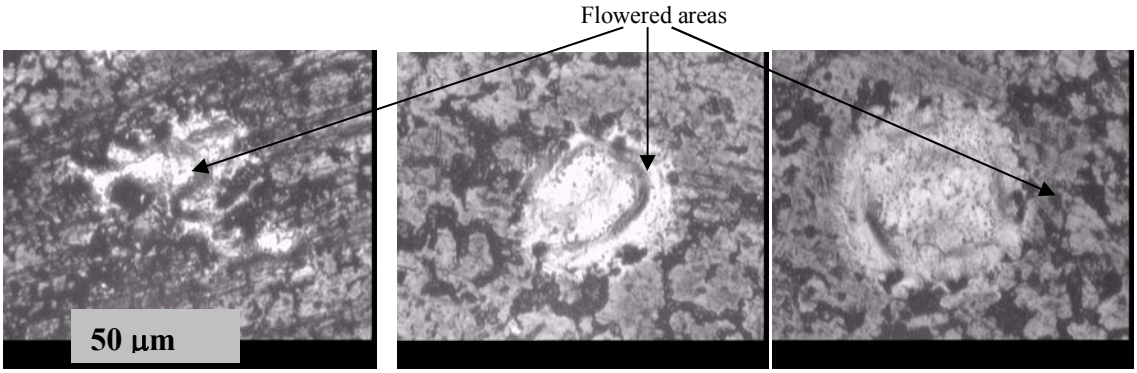

FIG. 23. Local melting zones on the non-irradiated surface of Cr12Mn14Ni4(Al, Mo, Sc) steel (plate № 1).

It has been shown [62, 63] that during the pulsed irradiation of materials with a power flux density $q \geq 10^{10}$–10^{12} W/cm^2 in the bulk of the material an acoustic wave spreads, which at a certain depth from the surface of the radiation is transformed into a shockwave (SW). In this case, at the front of SW there are a large tangential stress that is resulted in shear deformation and the generation of defects such as vacancies, Frenkel pairs, cascades of vacancies, and dislocations. In these conditions, in contrast to the conditions of stationary radiation (when the highest concentration of the bulk radiation defects is resulted in accelerated migration of them to different sinks grain boundaries, lattice distortions of the interface section), here in the non-stationary conditions the chemical bonds can be cut down, the crystal lattice can be damaged, and the accelerated phase transformations may take place in a solid material [64–67].

Estimations showed that in the experiments with the plates of the steel Cr12Mn14Ni4 (Al, Mo) containing Sc, the SW formation may occur in the central zone of the target volume (where the power flux density has its maximum) in the vicinity of the non-irradiated back surface at a distance of about several hundred μm from the interface solid phase gas. Based on the observed results on the emergence of the set of frozen melt spots in the central part of the surface (see Figs 22 and 23), we can conclude that in this region on the back surface of the plate we had melting of the material that has a local nature. It could be so because the presence of surface microdefects that might enhance the action of SW. In these local areas of the surface near the above microdefects, which were melted, the impact of the shock wave was manifested most strongly. In these microareas we had probably microexplosions, obtained loose of the material, reducing its density and decreasing of the melting temperature.

In other words, the possible synergistic effect of the mechanical stress produced by the shock wave upon the back side of the plate in conjunction with its thermal heating of it by the enveloping plasma flowing around this target could cause local melting of the SL and the appearance of the observed fragments of solidified melt, having a convex shape.

It is undoubtedly of interest to provide the detailed elucidation of the mechanism of this effect. But this issue requires special study and will be done later.

5.4. Conclusions

— As a result of the multiple pulse irradiation of the surface of the steel plate the multizone macro and microstructure is formed, which is caused by variation of intensity of the power flux density of the deuterium plasma stream and the beam of fast deuterium ions in the radial direction from the center of the action of the streams.

— Irradiation at a power flux density of the order of 10^9–10^{12} W/cm^2 in subμs pulse duration range produces a quite strong depletion of the material by dopant materials (Mn, Ni, Cr) within the steel plate surface, which leads to a change in the composition and formation in the surface layer during its rapid cooling of a significant (about 80%) amount of the α–martensite phase.

— It is found that the irradiation of the surface layer of the Cr12Mn14Ni4(Al, Mo, Sc) steel by high power pulsed plasma and fast ion beam does not contain structural defects such as pores, craters, bubbles and microcracks observed usually in Cr–Mn austenitic steels at similar conditions.

— This fact can be explained by an influence of complex alloying in general and by positive influence of Sc on the steel structure in particular.

— The presence of the flowed microvolumes within the SL of the non-irradiated back wall of the plate can be explained by the effect of the shock wave formed in the volume of the plate acting together with the thermal influence of the plasma streams enveloping the target.

REFERENCES

[1] ITER, http://www.iter.org/
[2] PHILIPPS, V., Tungsten as material for plasma-facing components in fusion devices, J. Nucl. Mater. **415** 1 (2011) 2–9.
[3] SHU, W.M., et al., Deuterium retention, blistering and local melting at tungsten exposed to high-fluence deuterium plasma, J. Nucl. Mater. **390–391** (2009) 1017–1021.
[4] NEU, R.L., et al., Operational conditions in a W-clad tokamak, J. Nucl. Mater. **367–370** (2007) 1497–1502.
[5] NEU, R.L., Experience with high-Z plasma-facing materials and extrapolation to future devices, IEEE Trans. Plasma Sci. **PS-38** (2010) 453–460.
[6] KRIVCHENKO, O.V., KURILO, YU.P., SHEPELEV, A.G. Optimum candidate material for future thermonuclear engineering, Problems of atomic science and technology (PAST), Vacuum, pure materials, superconductors **6** (2011) 62–70;
[7] BOLT, H., BARABASH, V., KRAUSS, W., LINKE, J., NEU, R.L, SUZUKI, S., YOSHIDA, N., Materials for the plasma-facing components of fusion reactors, J. Nucl. Mater. **329–333** (2004) 66–73.
[8] LINKE, J., High heat performance of plasma facing materials and components under service conditions in fusion reactors, Fusion Sci. Technol. **49** 2 (2006) 455–464.
[9] RIETH, M., et al., Tungsten as structural divertor material. Materials Challenges for Future Nuclear Fission and Fusion Technologies (VINCENZINI, P., LIN, H.T., FOX, K., Eds.), Trans. Tech. Publ., Ser.: Advances in science and technology **73** (2011) 11–21.
[10] DEMINA, E.V., et al., Influence of pulsed streams of high temperature deuterium plasma and fast ions on the structure of the surface layer of the alloy W-1%La_2O_3, Physics and Chemistry of material treatment **3** (2013) 18–25.
[11] BONDARENKO, G.G., UDRIS, YA.YA., YAKUSHIN, V.L., On behaviour of W-Cu composition as a candidate divertor material under irradiation by high intensive hydrogen plasma, Fusion Engineering and Design **51–52** (2000) 81–84.
[12] HIRAI, T., PINTSUK, G., LINKE, J., BATILLIOT, M., Cracking failure study of ITER-reference tungsten grade under single pulse thermal shock loads at elevated temperatures, J. Nucl. Mater. **390–391** (2009) 751–755.
[13] GARKUSHA, I.E., BURDAKOV, A.V., IVANOV, I.A., KRUGLYAKOV, E.P., et al., Plasma surface interaction during ITER transient events simulation with QSPA Kh–50 and Gold–3 facilities, Problems of atomic science and technology (PAST), Ser.: Plasma Physics **14** (2008) 58–60.
[14] ZHITLUKHIN, A., et al., Effects of ELMs on ITER divertor armour materials, J. Nucl. Mater. **363–365** (2007) 301.
[15] POZNYAK, I.M., KLIMOV, N.S., PODKOVYROV, V.L., SAFRONOV, V.M., ZHILTUKHIN, A.M., KOVALENKO, D.V., Erosion of metals under exposure of intensive plasma flux VANT, Thermonuclear synthesis **4** (2012) 23–33.
[16] HIRAI, T., EZATO, K., MAJERUS, P., ITER relevant high heat flux testing on plasma facing surfaces, Mater. Trans. **46** (2005) 412–436.
[17] KIRK, A., et al., Evolution of filament structures during Edge Localized Modes in the MAST Tokamak, Phys. Rev. Lett. **96** (2006) 185001.
[18] LOEWENHOFF, TH., HIRAI, T., KEUSEMANN, S., LINKE, J., PINTSUK, G., SCHMIDT, A., Experimental simulation of Edge Localised Modes using focused electron beams – features of a circular load pattern, J. Nucl. Mater. **415** (2011) 51–54.
[19] IVANOV, L.I., PIMENOV, V.N., GRIBKOV, V.A., Interaction of power pulsed energy streams with materials, Physics and Chemistry of material treatment **1** (2009) 23–37.
[20] SCHOLZ, M., MIKLASZEWSKI, R., GRIBKOV, V.A., MEZZETTI, F., PF-1000 device. Nukleonika **45** 3 (2000) 155.
[21] GRIBKOV, V.A., et al., New efficient low-energy dense plasma focus in IPPLM, Czechoslovak Journal of Physics **54** (2004) 191–197;
[22] http://mlab.ictp.it/uploads/C1/cK/C1cKba2XDKJNeoN26x5GmA/Dense-Plasma-Focus-BoraICTP.pdf
[23] PINTSUK, G., Tungsten as a plasma-facing material, Comprehensive Nuclear Materials, (KONINGS, R.J.M., Ed.), Elsevier, Amsterdam (2012) 551–581.
[24] FUJITSUKA, M., SHINNO, H., TANABE, T., SHIRAISHI, H., Thermal shock experiments for carbon materials by electron beams, J. Nucl. Mater. **179** A (1991) 189–195.
[25] PIMENOV, V.N., MASLYAEV, S.A., DEMINA, E.V., IVANOV, L.I., KOVTUN, A.V., GRIBKOV, B.A., DUBROVSKY, A.V., UGASTE, YU.E., The influence of pulsed energy streams on the surface of aluminum alloy tube in Plasma focus device, Advanced materials **4** (2006) 43–52.
[26] J. DUDERSTADT J.AMES, A. MOSES GREGORY. Inertial Confinement Fusion Moscow: Energoatomizdat, 1984, 301 p. (*In Russ.*); b) https://lasers.llnl.gov/
[27] PIMENOV, V.N., et al., Interaction of power pulsed energy streams with the tungsten surface in plasma focus device, Physics and Chemistry of material treatment **3** (2008) 5–14.
[28] GARKUSHA, I.E., et al., Performance of deformed tungsten under ELM-like plasma exposures in QSPA Kh-50, J. Nucl. Mater. **415** (2011) 65–69.
[29] BUDAEV, V.P., et al., Tungsten recrystalisation and cracking under ITER–relevant heat, Problems of atomic science and technology (PAST), Ser.: Nuclear Fusion **36** (2013) 53–60.
[30] BARMINA, E.V., STRATAKIS, E., FOTAKIS, K., SHAFEEV, G.A., Generation of nanostructures under laser ablation of the metals in liquids: New Results, Quantum electronics **40** 11 (2010) 1012–1020.

[31] PYACHIN, S.A., PUGACHEVSKY, M.A. New technologies for fabrication of functional nanomaterials, Laser ablation, Electrospark effect, Khabarovsk: TOGU [PNU] (2013) 38.
[32] ALYMOV, M.I., Powder metallurgy of nano-crystalline materials, Metallurgy, Scandium, Moscow (1985).
[33] LIBENSON, G.A., LOPATIN, V.YU., KOMARNITSKY, G.V., Processes of powder metallurgy, MISiS (2001) 367.
[34] MABUCHI, M., OKAMOTO, K., SAITO, N., Tensile properties at elevated temperature of W-1%La_2O_3, Materials Science and Engineering **A214** (1996) 174–176.
[35] RYU, H.J., HONG S.H., Fabrication and properties of mechanically alloyed oxide-dispersed tungsten heavy alloys, Materials Science and Engineering **A363** (2003) 179–184.
[36] MASLYAEV, S.A., Thermal effects at pulsed irradiation of materials in the Dense Plasma Focus device, Perspective materials **5** (2007) 47–55.
[37] GUSEVA, M.I., et al., Investigation of erosion of a surface of different tungsten grades and of the morphology of products of their erosion in simulation experiments on plasma disruption, J. Tech. Phys. **72** 7 (2002) 48.
[38] KLIMOV, N.S., PODKOVYROV, V.L., ZHITLUKHIN, A.M., Spitting of tungsten at the action of intense plasma stream, Problems of atomic science and technology, Ser. Thermonuclear fusion **2** (2009) 52.
[39] WOOD, E.A., et al., Beta-wolfram structure of compounds between transition elements and aluminum, gallium and antimony, Acta Crystallogr. **11** 89 (1958) 604.
[40] YOSHIMURA, M., ROUANET, A., High temperature phase relation in the system La_2O_3-WO_3, Mater. Res. Bull. **1** 2 (1976) 151–158.
[41] TAVASSOLI, A.A., Comparison of austenitic stainless steels and martensitic steels for fusion reactors, Plasma Devices and Operations **4** (1996) 163.
[42] LEE, E.Y., MANSUR, L.K., Fe-15Ni-13Cr austenitic stainless steels for fission and fusion reactor applications, J. Nucl. Mater. **278** (2000) 20.
[43] KOHYAMA, A., HISHINUMA, A., GELLES, D.S., KLUEH, R.L., DIETZ, W., EHRICH, K., Low-activation ferritic and martensitic steels for fusion application, J. Nucl. Mater. **233**–**237** (1996) 138.
[44] GRIBKOV, V.A., Influence of dense deuterium plasma pulses on materials in plasma focus device, Nukleonika **45** (3) (2000) 149.
[45] GRIBKOV, V.A., et al., PF-6 – an effective plasma focus as a source of ionizing radiation and plasma streams for application in material technology, biology and medicine, Nukleonika **51** 1 (2006) 55–62.
[46] IVANOV, L.I., PLATOV, Y.M., DEMINA, E.V., Application prospects of the Cr-Mn steels in fusion energy, Advanced Materials **2** (1995) 37.
[47] DEMINA, E.V., PRUSAKOVA, M.D., ROSHCHIN, V.V., VINOGRADOVA, N.A, ORLOVA, G.D., Low-activated austenitic Fe-Cr-Mn steel for nuclear power, Advanced materials **4** (2009) 43.
[48] DEMINA, E.V., et al., Radiation creep and phase instability of low-activated austenitic 12Cr-20Mn-W steel by neutron irradiation in a fast reactor FFTF, Advanced Materials **1** (2011) 20.
[49] SHAMARDIN, V.K., IVANOV, L.I., DEMINA, E.V., BULANOVA, T.M., NEUSTROEV, V.S., PRUSAKOVA, M.D., The impact of neutron flux in the reactor BOR-60 on hexagon covers material made of Cr-Mn steel, Physics and Chemistry of Materials Processing **6** (1989) 5.
[50] RUMYANTSEVA, L.E., ROSHCHIN, V.V., DEMINA, E.V., PRUSAKOVA, M.D., KURANOV, V.M., Weldability and properties of welded joints of austenitic Cr12Mn14Ni4 steel, Problems of Atomic Science and Technology, Series: Welding in nuclear technology **1** (1987) 3.
[51] GUREVICH, S.E., DEMINA, E.V., EDIDOVICH, L.D., PRUSAKOVA, M.D., The influence of doping on the characteristics of the cyclic crack resistance of Cr-Mn-Ni austenitic steel weld material used in a fusion reactor, Physics and Chemistry of material Treatment **4** (1991) 145.
[52] ZELENSKY, V.F., et al.., Simulation study of the effects of radiation swelling of nickel and its alloys, Reactor materials **2** (1978) 4.
[53] DEMINA, E.V., PRUSAKOVA, M.D., VINOGRADOVA, N.A., ORLOVA, G.D., Influence of purity of the initial charge materials for the maintenance of radiologically "dangerous" impurities in low-activated steels, Advanced Materials **5** (2008) 56.
[54] SCHOLZ, M., GRIBKOV, V.A., MIKLASZEWSKI, R., MEZZETTI, F., PF-1000 device, Nukleonika **45** 3 (2000) 55.
[55] GRIBKOV, V.A., et al.., Physical processes taking place at the interaction of pulsed ion and plasma streams with a target surface made in the forms of plates and pipes in the chamber of the Dense Plasma Focus device, Applied Physics **3** (2011) 43.
[56] PIMENOV, V.N., et al., On the new opportunities of plasma focus installations for modifying the surface layers of materials, Advanced Materials **1** (2003) 13.
[57] PIMENOV, V.N., et al., Interaction of the flows of deuterium ions and dense plasma with the low-activated austenitic steel material of a tube in Plasma Focus, Advanced Materials **2** (2007) 48.
[58] GRIBKOV, V.A., et al., The impact of the interaction of dense deuterium and hydrogen plasma with ferritic and austenitic steels in the Dense Plasma Focus device, Advanced Materials, **1** (2008) 16.
[59] SVISTUNOVA, T.V., BOBKOV, O.S., BELYASOV, B.D., Influence of scandium on the structure and properties of corrosion-resistant steels, Metallurgy and heat treatment of metals (MITOM) **5** (2008) 9.
[60] KORSHUNOV, B.G., REZNIK, A.M., SEMENOV, S.A., Metallurgy, Scandium, Moscow, (1987).
[61] PIMENOV, V.N., et al., Damage and modification of materials produced by pulsed ion and plasma streams in Dense Plasma Focus device, Nukleonika **53** 3 (2008) 111.
[62] BOROVITSKAYA, I.V., IVANOV, L.I., DEDYURIN, A.I., KROKHIN, O.N., NIKULIN, V.Y., TIKHOMIROV, A.A., The impact of high pulse deuterium plasma for vanadium, Advanced Materials **2** (2003) 24.
[63] VALYAEV, A.N., POGREBNYAK, A.D., LAVRENTIEV, V.I., VOLKOV, S.N., PLOTNIKOV, S.V., The influence onto α-Fe of the pressure gradient of the shock wave produced by high-power ion beam irradiated on the appearance of a maximum microhardness at great depths, Tech. Phys. Lett. **24** 3 (1998) 47–53.

[64] ZEL'DOVICH, YA.B., RAIZER, YU.P., Physics of Shock Waves and High-Temperature Hydrodynamic Phenomena, Nauka, Moscow (1966).
[65] ZABABAHIN, E.I., Phenomena Unlimited Accumulation, Nauka, Moscow (1988).
[66] LOBODYUK, V.A., The effect of shock waves produced on the martensitic transformations in metals and alloys, Metal Physics, Naukova Dumka **76** (1979) 3.
[67] TEPLOV, V.A., TALUTS, G.G., MASLOV, R.A., MURYSHEV, E.J., SINITSYN, A.V., Features of the microstructure of iron-nickel alloy during loading of a plane shock wave at pressure 30 GPa, FMM **66** 5 (1988) 920.

INVESTIGATION OF ITER-LIKE TUNGSTEN UNDER HIGH KINETIC ENERGY PLASMAS

A.V. VORONIN[*], B.YA. BER[*], A.A. BORMATOV[1], P.N. BRUNKOV[*], V.K. GUSEV[*], E.V. DYOMINA[2], A.N. NOVOKHATSKY[*], YU.V. SUD'ENKOV[3], G.YU. SOTNIKOVA[*]

Abstract

Experimental study of tungsten under high kinetic energy hydrogen and helium plasma jets as well deuterium plasma of the tokamak Globus-M was performed. The original plasma gun test bench was developed for investigation of material irradiation at high energy density plasma flow comparable to conditions in fusion reactor. Structure and morphology of single crystal, hot rolled; as well powder made V_MP and JSC POLEMA tungsten irradiated by the jet at different energy densities and several numbers of shots were tested. Irradiation with the energy densities 0.25–1 MJ/m^2 (heat flux factor 80–230 MJ · m^{-2} · s$^{-1/2}$) offered basic physical and mechanical degradation processes: melting surface, destruction of near-surface layer arising due to thermal stresses, plastic flow and dynamic recrystallization in bulk. The depth of the molten layer about 1–3 μm and the zone of active thermal effects about 15–20 μm was registered. Surface of monocrystal tungsten irradiated by jet obtained a regular crack structure probably in the direction of maximum shear. The V_MP and JSC POLEMA tungsten became a regular particle size of less than 1 μm. Hot rolled samples had not obtained such structure. JSC POLEMA tungsten proved to be the most resistant to damage. At low energy density and large amount of shots the surface layer of the V_MP tungsten got some healing effect. Long repetition irradiations with the energy equivalent to edge localized modes (ELMs) events changed the nature of the surface even more. After 100 shots the structure of JSC POLEMA and PLANSEE tungsten was similar to the pattern after 10–20 shots in general, but more pronounced large columnar assembly perpendicular to the plane surface was performed. After 1000 shots character of the surface layer changed dramatically. It was roughening recrystallized layer was formed. JSC POLEMA tungsten was cyclically irradiated by helium plasma jet at the test bench of the gun for the purpose of obtaining the nanostructure in the form expected in divertor of the ITER reactor. First experiments showed that the multiple helium plasma jet irradiations may create bubbles and pores when the temperature of tungsten didn't reach melting. The nanostructure was similar to which was formed by helium neutral beam injection. Tungsten specimens previously damaged with hydrogen plasma jet were placed in the divertor region of the tokamak. Non-uniform temperature field on damaged samples after discharge termination was registered. Surface temperature of previously irradiated tungsten at 1000 ELMs events by the jet exceeded the temperature of other samples. After tokamak shots PLANSEE tungsten surface layers were modified, the columnar and droplet shape structures were smoothed. X ray diffraction method showed that subsequent irradiation by plasma of the tokamak Globus-M gradually deleted this damaged area. In turn, irradiation only by the tokamak plasma also formed the damaged area with more considerable microstresses than obtained with plasma gun. In-depth distribution of D, H and other elements in PLANSEE tungsten showed that the characteristic depth of the layer accumulating impurities reached more than 0.5 μm. Samples irradiated by the gun and the tokamak had the greatest damaged depth and quantity of the impurity.

1. INTRODUCTION

Selection of the materials for the first wall is one of the most challenging problems for construction a thermonuclear tokamak reactor. In terms of power density the loads are the following: normal operation 1 MW/m^2; ELMs 30 GW/m^2; disruption phase 100 GW/m^2. Plasma-surface interaction is an important issue of creating protective materials for ITER divertor. Its main function is absorption of heat flow out of the edge plasma and extraction of helium which is a product of burning in the reaction of thermonuclear fusion. It is assumed that the walls of the divertor will be irradiated with a flow of helium ions 10^{22}–10^{24} He m^{-2} s^{-1} (<500 eV) as well thermal stresses as a result of ELM events will be occurred. Tungsten is one of the basic coatings for plasma facing components of fusion reactors due to its capability to survive in high temperature and high neutron irradiation environment [1]. However there is uncertainty in the behavior of the discharge during ignition and burning process in a tokamak with tungsten wall. Tungsten elements of protection can melt and have little ability to shaping plasma. As a result plasma heavy impurity contamination can be increased. In future reactor the remolten and modified surface layers may growth in thickness up to 100 μm or more [2]. These layers will lead to a sharp increase of the thermal loads on the divertor tiles. Degradation of tungsten surface has been extensively studied all over the world under conditions of irradiation both in tokamaks and using other plasma sources. For example, the elements of beryllium wall and tungsten diverter are studied on the Joint European Torus (JET), axially symmetric diverter experiment (ASDEX), and other installations [3–6]. However none of the existing tokamaks can generate heat fluxes necessary for the reactor under development. Therefore electron beams [7, 8], linearly plasma devices [9], plasma guns [10, 11], plasma focus machines [12, 13] are also applied

[*] Ioffe Institute, St. Petersburg, Russian Federation.
[1] Peter the Great Polytechnic University, Saint Petersburg, Russian Federation.
[2] Institute of Metallurgy and Material Science, Moscow, Russian Federation.
[3] St. Petersburg State University, St. Petersburg, Russian Federation.

to study the behavior of materials at thermal loads close to reactor condition. At present time the most adequate ITER like plasma wall interaction may be experimentally investigated in real existing tokamaks equipped with tungsten tiles preliminary irradiated (damaged) by alternative high heat flux sources. Such experiments must be concentrated on the study both tungsten layer properties, structure dynamics, flaking formation and tokamak plasma parameters. The present work is aimed at experimental study of action of high heat fluxes of hydrogen and helium plasma of jets, as well deuterium plasma of tokamak on tungsten elements that are currently designed for the ITER divertor. The work is based on two plasma sources, the original gun device and the spherical tokamak Globus-M. Comparable investigations of tungsten irradiation with plasma flows generated both by the gun and the Globus-M plasma were performed.

2. INVESTIGATION OF TUNGSTEN IRRADIATED BY PLASMA JET

2.1. Development of the plasma gun test bench facility for material irradiation

2.1.1. Plasma gun set-up

We use an approach based on plasma gun which is powerful enough for simulation of the thermal loads on tungsten close to the ITER conditions [14]. The plasma gun could generate pure highly ionized hydrogen plasma jet during ≥ 10 μs, with density 3×10^{22} m^{-3}, total number of the accelerated particles $(1–5) \times 10^{19}$ and jet flow velocity 100–200 km/s. Advantages of the gun are the high kinetic energy and clean hydrogen plasma jet. Stored energy of the gun capacitors is about 2 kJ. The plasma gun test bench was reconstructed for investigation of ITER-like first wall material irradiation at high energy density plasma flow [15]. Small vacuum chamber was developed and manufactured (Fig. 1(a)). This chamber was installed between plasma gun and main vacuum chamber. Over vacuum shutter the chambers were connected. Plasma gun may irradiate specimens with diameter up to 50 mm inside of the cross chamber. Many specimens may be irradiated per one day. Additionally the main vacuum chamber was equipped with shutter and feedthrough located at the opposite porter to the plasma gun. Thus the jet can irradiate specimens fixed on movable rod at different distances from gun (0.05–1.8 m). Scheme of experiment is presented in (Fig. 1(b)). Power density of the plasma jet could exceed 100 GW/m^2. Heat flux factor produced by the jet could be similar to the highest ELM event in ITER: $\varepsilon_{ELM} = 30$ GW/$m^2 \times (100$ μs$)^{-1/2} = \varepsilon_{gun} = 100$ GW/$m^2 \times (10$ μs$)^{-1/2} = 300$ MW $\cdot$ $m^{-2} \cdot s^{-1/2}$. This factor is higher that the melting parameter for tungsten which is ~ 50 MW $\cdot$ $m^{-2} \cdot s^{-1/2}$ [2].

a

b

FIG. 1. (a) Reconstructed plasma gun test bench for irradiation of specimens, view of plasma gun with main and small vacuum chambers; (b) scheme of experiment.

2.1.2. *Measurement of plasma jet pressure and power density*

The plasma jet pressure was determined by piezoelectric and interferometric methods simultaneously during each irradiation (Fig. 2). The piezodetector allows recording the time variation of relative pressure, and the interferometer recorded its absolute values. A test specimen was glued to the front end face of rod. The lateral surface of the rod was covered by a heat shrink tube, which cushioned the effect of the plasma flow passing around the lateral surface of the rod. The rod could move along the axis by a vacuum feedthrough, and its front end face with the test specimen could be at any distance from the plasma source. The diameter and length of the rod were 20 mm and 270 mm respectively. The disk of PZT_19 piezoceramic 0.5 mm in thickness and 20 mm in diameter was glued to the rear end of the rod. The end face of a similar rod 100 mm long with a free mirror surface at the end was glued to the rear side of the disk. Its motion was controlled by the laser Michelson interferometer with photoelectric fringe counting. The glued surfaces provided a good acoustic contact at the rod–sensor–rod interfaces. The interferometer recorded the induced motion of the rod's free surface with a high spatial resolution. Shift $\delta(t)$ of the free surface and phase difference $\varphi(t)$ between interfering waves are related as:

$$\delta(t) = \lambda/4\pi\, \varphi(t) \tag{1}$$

where λ is the wavelength of the laser source.

If an elastic approximation is adopted and the decay of the elastic wave is ignored, the pressure exerted by the plasma jet on the front surface of the rod can be calculated from the relationship:

$$P(t) = [\rho c v_s(t)]/2 = (\rho c)/2\ \partial/\partial t[\delta(t)] = (\rho c \lambda)/8\pi\ \partial/\partial t[\varphi(t)] \tag{2}$$

where ρ is the density of the rod, c is the sound velocity in the rod, and $v_s(t)$ is the velocity of the rod's free surface. The time variation of the hydrogen jet power density was calculated by the formula:

$$w(t) = P(t)v(t) = P(t)^{3/2}\sqrt{2/(m_p \bar{n}(t))} = 3.5 \times 10^{13} P(t)/\sqrt{\bar{n}(t)} \tag{3}$$

where $v(t)$ is the velocity of the jet, $\bar{n}(t)$ is the average plasma density, and m_p is the mass of proton.

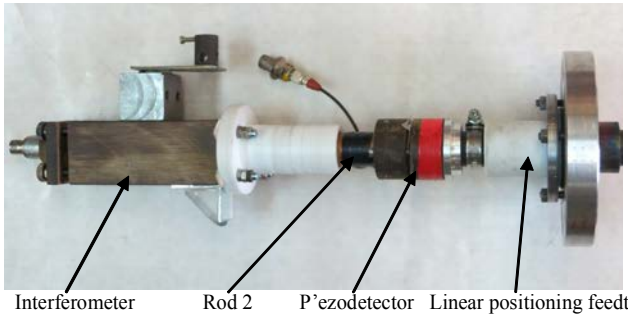

FIG. 2. External view of the piezoelectric and interferometric pressure sensors.

2.1.3. *Measurement of plasma jet density*

The electron density of the plasma was measured by interferometer. This method determined the phase shift of the wave having passed through the target. Phase shift $\varphi(t)$ and electron concentration $n(t)$ are related as:

$$\varphi(t) = \pi K\, (ln(t))/(\lambda n_c) \tag{4}$$

where l is the path the probing wave travels in the plasma, λ is the probing wavelength of a source, K is a coefficient taking into account the concentration distribution over the path, and n_c is the critical concentration of plasma electrons at which the laser radiation cannot pass through the plasma. The critical concentration was found by the formula:

$$n_c = m\omega^2/(4\pi l^2) = 1.12 \times 10^{21}/\lambda^2 \quad (5)$$

where m is the mass of an electron and ω is the plasma frequency.

For a plasma concentration on the order of 10^{22} m^{-3}, K = 1. Average density of plasma along the probing wave direction was calculated by the formula:

$$\bar{n}(t) = 3.57 \times 10^{12}\, \varphi(t)/(\lambda l) \quad (6)$$

We designed and fabricated an interferometer measuring the average density of the plasma along the diameter of the jet at different distances from the accelerator. A Michelson laser interferometer with photoelectric fringe counting was mounted on a through flange (Fig. 3(a)). We used second harmonic of 30 mW YAG : Nd laser at λ = 532 nm. Its output radiation was split into two coherent waves by a semitransparent mirror (Fig. 3(b)). One wave pass through the plasma jet twice in forward and backward directions, thereby producing a phase shift relative to the wave in the reference arm. The radiation resulting upon wave interference on the semitransparent mirror was transmitted through a fiber cable to a photomultiplier. The influence of the plasma radiation on the interference signal was suppressed by an aperture and a 532FS10_12.5 (Andover Corporation) interference filter with a pass band of 532.56 ± 5 nm. An ADC digitized the signal from the photomultiplier for computer processing and subsequent analysis. The plasma density near the test specimen was higher than 3×10^{22} m^{-3}.

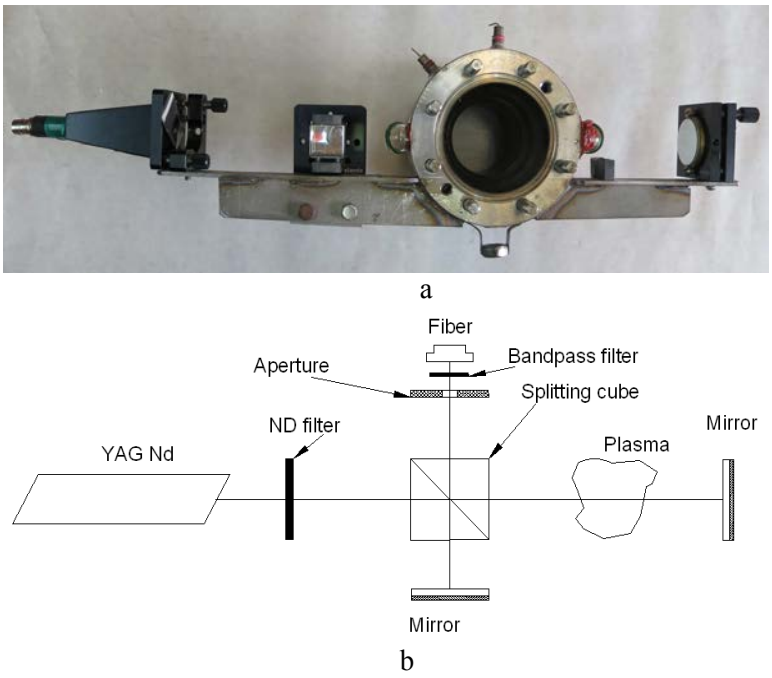

FIG. 3. (a) Laser interferometer mounted on a through flange; (b) scheme of the Michelson interferometer used to measure the plasma density.

2.1.4. Two color pyrometer

Two color high speed pyrometer developed at the Ioffe Institute allowed measurements of the surface temperature of tungsten during/after irradiation of jet or tokamak plasmas. (Fig. 4) [16].

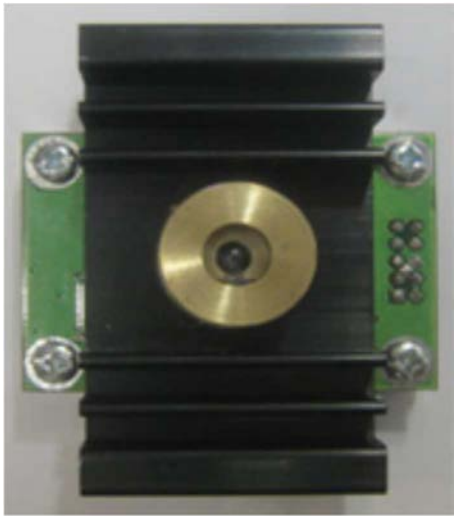

FIG. 4. Two color IR detectors in one box with temperature stabilization obtained by calibration; λ_1=3.3 μm, λ_2=4.7 μm.

Two infrared detectors placed one by one were mounted in a box with temperature stabilization, with time resolution of about 1 μs. Correlation between measured and calculated ratios of signals of two detectors was acquired by formula:

$$R(\lambda_1)/R(\lambda_2) = A(\lambda_2/\lambda_1)^5(e^{hc/(\lambda_2 kt)}-1)/(e^{hc/(\lambda_1 kt)}-1 \quad (7)$$

where A is obtained by calibration; λ_1 = 3.3 μm, λ_2 = 4.7 μm.

2.2. Influence of plasma jet on different types of tungsten

Several types of material were irradiated with few shots by the plasma gun [17,18] for preliminary analyzing and establishment of data base of erosion behavior of tungsten. Pictures of the irradiated surfaces (Fig. 5) show that JCS POLEMA had no sign of macrocracking of the surface.

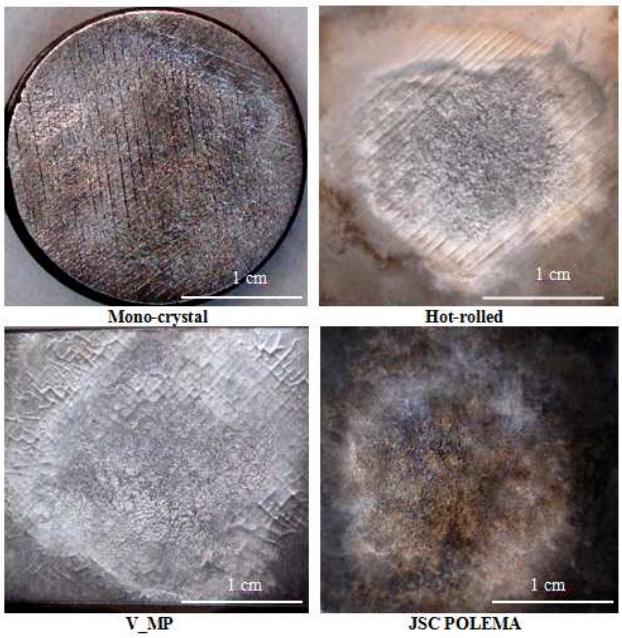

FIG. 5. Several types of material irradiated with plasma gun 0.78 MJ m^{-2} (ε = MJ · m^{-2} · $s^{-1/2}$), 5 shots.

But hot rolled, monocrystal and powder made V_MP are cracked. Traces of cracking are probably a consequence of technological rolling of the material. Atomic force microscopy (AFM) showed (Fig. 6) the depth of damaged layer which was for: monocrystal ~200 nm, hot rolled ~150 nm, V_MP ~ 50 nm, JCS POLEMA ~ 50 nm. The structure of the material had a regularity of the characteristic particle size of 100–200 nm. In the non-irradiated specimen such a structure was not found. JCS POLEMA and V_MP tungsten were powder made by Russian POLEMA JSC. The first tungsten had the grain structure orientated perpendicular to the irradiated surface but the second one had no orientation of the grain structure.

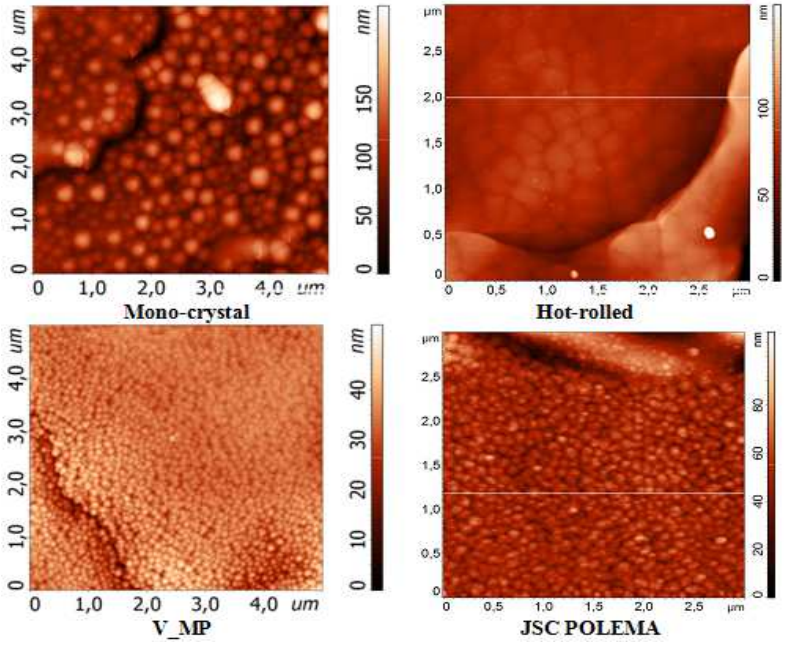

FIG. 6. AFM topographies of different materials irradiated with plasma gun 0.78 MJ m^{-2} (ε=200 MJ · m^{-2} · $s^{-1/2}$), 5 shots.

Surface of monocrystal tungsten after cyclic irradiation by plasma jet was investigated in [19]. In nature mono-crystal tungsten has a plastic viscous surface layer. Degradation of tungsten during the action of plasma jet with an energy density of 0.25–1 MJ/m^2 was accompanied by surface evaporation, melting and the fracture of surface layers on scales of 150–250 μm. After several shots we observed a regular crack structure probably in the direction of maximum shear (Fig. 7).

The results of numerical simulation of the thermomechanical processes occurred in tungsten during the action of plasma jet were performed. The degradation proceeded continuously from the action (evaporation, melting) to the times that were more than three orders of magnitude longer than the action time. Probably it was caused by the thermomechanical processes occurring in the tungsten target. Moreover the action of thermal stresses led to structural and morphological changes throughout the sample volume. These changes were accompanied by recrystallization in adiabatic shear bands.

FIG. 7. Surface of monocrystal tungsten after cyclic irradiation by plasma jet 1 MJ/m^2; ε =230 MJ · m^{-2} · s$^{-1/2}$.

Scanning electron microscope (SEM) observed the surface of the JSC POLEMA tungsten irradiated with plasma gun. Microstructure on a surface and polished cut of sample was registered (Fig. 8). The surface has structural defects such as craters and microcracks.

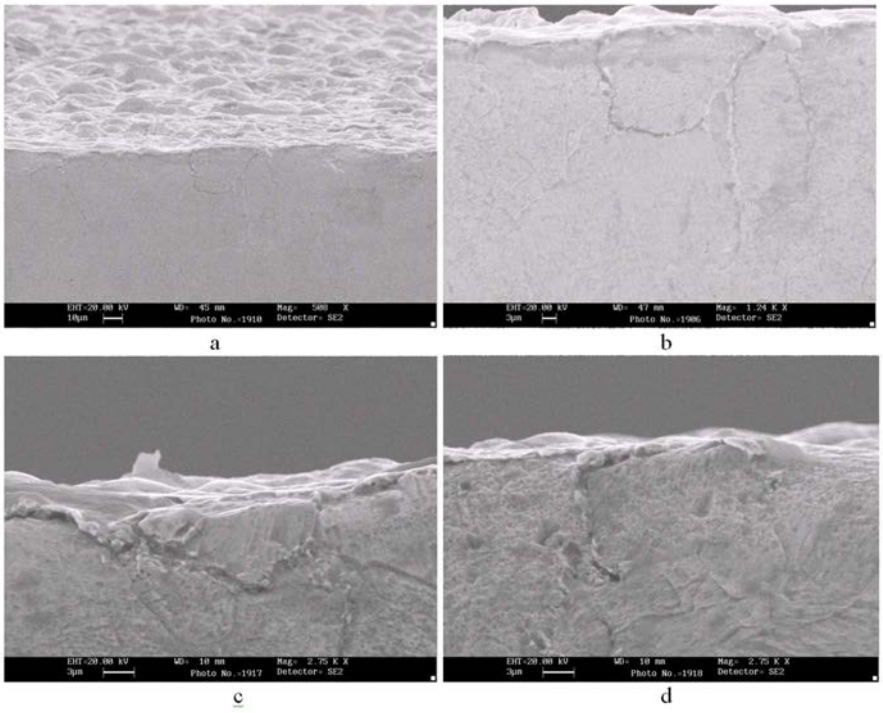

FIG. 8. Microstructure of JSC POLEMA tungsten on surface and polished cut of sample, ε =200 MJ · m^{-2} · s$^{-1/2}$; 5 shots.

Wave relief with depth of the molten layer about 1–3 μm was registered (Fig. 8(a)). Region of active thermos impact with depth of 15–20 μm and probably plastic displacements of the block structure was found (Figs 8(c)–(d)). The structure proved to be some resistant to damage.

Diffractograms of JCS POLEMA tungsten after and before irradiation showed very pronounced texture on a plane associated with the processes of melting and crystallization of the surface. Structural analysis do not showed any impurities imbedded into tungsten body. Any phases except tungsten with a cubic structure were not registered. After irradiation very pronounced texture on a plane (110) associated with the processes of melting and crystallization of the surface layer was found (Fig. 9(a)).

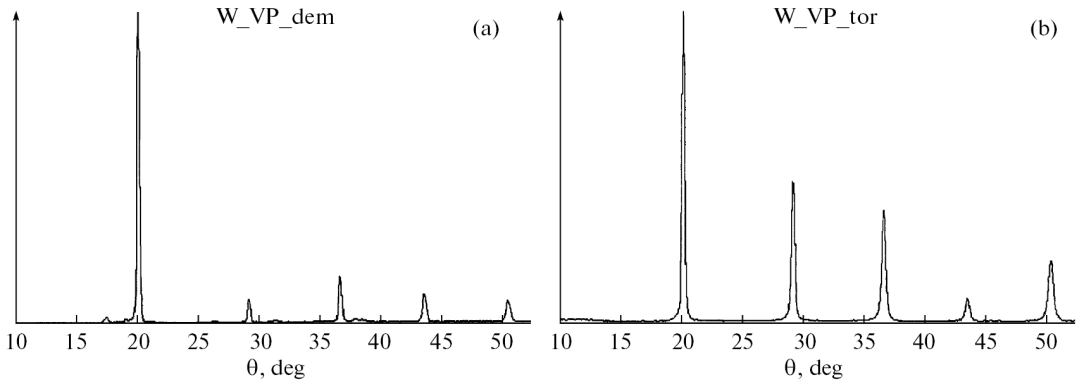

FIG. 9. Diffractograms taken of the JSC POLEMA tungsten (a) after and (b) before irradiation: the scattering angle is 20° for W(110), 29° for W(200), 36.5° for W(211), 43.5° for W(211), and 50.5° for W(211).

Diffractograms showed texture on a plane (200) in the original sample due to the process of preparation of material (hot pressing) (Fig. 9(b)). Table1 presents parameters of the crystal lattice of tungsten samples before and after irradiation by jet. After irradiation there was a weak reduction of parameter of a crystal lattice of tungsten (Δa = 0.0035 Å), explained probably to a decrease of untied atoms of impurity, first of all, C, O, H, N. It is known that solubility of impurity of introduction (O, H, N, C) in a crystal lattice of tungsten is extremely insignificant even at a temperature of melting of tungsten.

TABLE 1. TUNGSTEN LATTICE PARAMETERS BEFORE AND AFTER IRRADIATION BY PLASMA GUN (CuKa RADIATION)

Sample	Lattice parameters a (Å)	Elementary cell volume V (Å^3)
As prepared JSC POLEMA tungsten	3.1660	31.74
JSC POLEMA tungsten after irradiation, 5 shots, 0.7 MJ/m^2, ε =200 MJ · m^{-2} · s$^{-1/2}$	3.1625	31.63
Hot-rolled tungsten after irradiation, 5 shots, 0.7 MJ/m^2, ε =200 MJ · m^{-2} · s$^{-1/2}$	3.1639	31.67
Decrease in JSC POLEMA tungsten lattice parameters after irradiation	Δa = 0.0035	–

2.3. Irradiation of tungsten with different plasma jet conditions

The surface layer of the V_MP tungsten was tested after multiple irradiations by the plasma jet with different energies [17]. Fig. 10 demonstrates the surface microstructure of the irradiated samples. It is seen that the higher the energy density the greater the damage. At the lower energy density and a larger amount of shots the damage was small. It seems that such irradiation conditions favors healing of the defects.

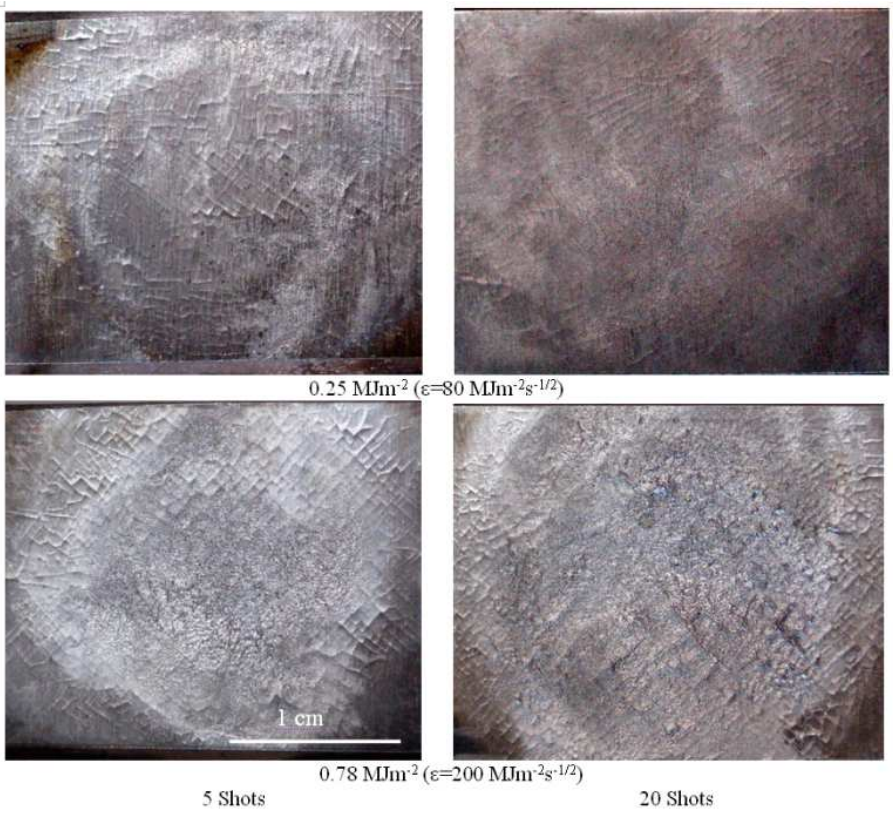

FIG. 10. Micrographs of the V_MP tungsten surface after cyclic irradiation with different energy densities.

AFM topograms of V_MP tungsten surface after cyclic irradiation by the plasma with different energy densities are shown in Fig. 11. At high energy density (0.78 J/m^2, ε_{gun} = 200 MJ · m^{-2} · s$^{-1/2}$) and any number of shots a regular structure of the material with a characteristic particle size of less than 1 μm appeared. At low energy density of 0.25 MJ/m^2 (ε_{gun} = 80 MJ · m^{-2} · s$^{-1/2}$) this effect was absent.

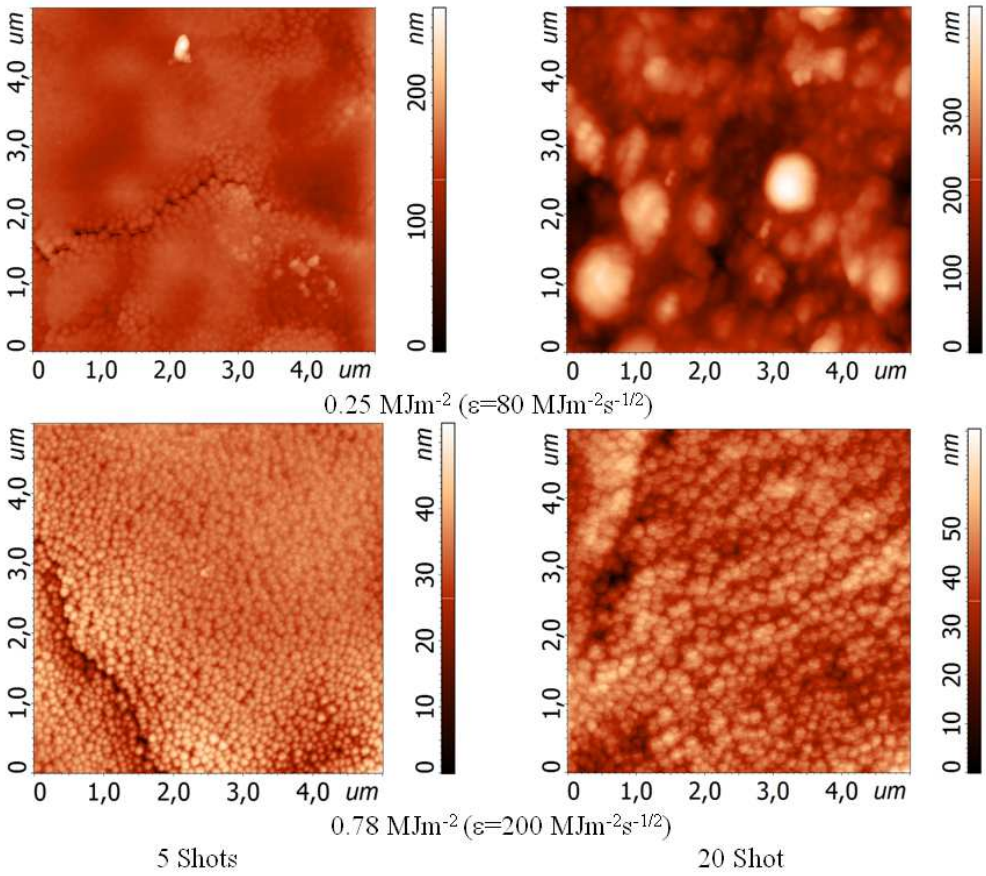

FIG. 11. AFM topograms of V_MP tungsten surface after cyclic irradiation by the plasma with different energy densities.

2.4. Study of tungsten at long repetition irradiation by hydrogen plasma jet

We studied the structure and morphology of multiply remelted (damaged) surface layers of tungsten irradiated by plasma gun at high kinetic energy [20]. Many cycle irradiations modified the nature of the irradiated surface even more. Experiments were performed with ITER like tungsten of two types: JSC POLEMA and PLANSEE double forged. The cyclic plasma jet irradiation ensured multiply repeated remelting of tungsten. The level of thermal load from the plasma jet in these experiments significantly exceeded values obtained in existing tokamaks. For ELM events in ITER the heat flux factor will be typically within ε_{ELM} = 77–123 MJ m^{-2} $s^{-1/2}$ [2]. In the case of a plasma gun the heat flux factor reached of $\varepsilon_{gun} \sim 230$ MJ $\cdot$ $m^{-2} \cdot s^{-1/2}$. The gun was capable of generating up to 200 pulses per day in an automated regime. The samples were irradiated with a number of pulses up to 1000. It allowed the material damage close to the ITER operation during 1 shot.

2.4.1. JSC POLEMA tungsten

As was shown previously irradiation at several gun shots significantly influenced the character of the surface layer of tungsten. Five irradiation cycles melted the metal to a depth of 3–6 μm and created a wavy surface relief, while the structure of separate regions at a distance of 20–30 μm from the irradiated zone clearly revealed a relative shift of blocks along their boundaries. Subsequent investigations showed that a heat affected region with traces of grain boundary shift could extend up to a depth of 100–200 μm or more from the irradiated surface. Multiply repeated cycles of plasma jet action changed the character of the irradiated tungsten surface to an even greater degree (Fig. 12).

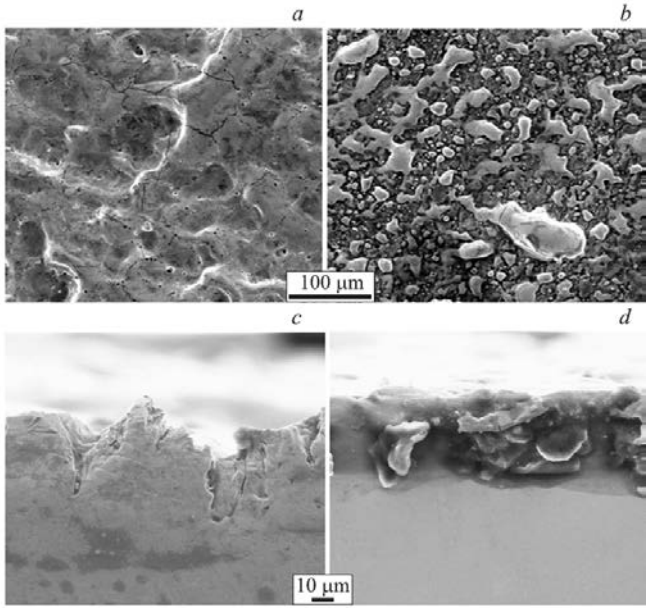

FIG. 12. (a) Microstructure of surface of JSC POLEMA tungsten after 150 irradiations by plasma jet; (b) microstructure of surface of JSC POLEMA tungsten after 1000 irradiations by plasma jet; (c) transverse section of JSC POLEMA tungsten after 150 irradiations by plasma jet; (d) transverse section of JSC POLEMA tungsten after 1000 irradiations by plasma jet.

After 150 shots a clearly pronounced hole to peak wavy surface relief was observed over the whole irradiated area (Fig. 12(a)). This character indicated that tungsten occurred in the melted state. The surface exhibited a developed network of microcracks that appeared as a result of thermal stresses during high rate cooling. After 1000 cycles, the surface showed a droplet dendritic morphology formed against the background of a relatively flat plateau, which was also covered by a network of microcracks (Fig. 12(b)). The depth of a damaged surface layer formed upon 100 and 1000 plasma jet pulses was clearly distinguished on transverse sections of irradiated samples. It shows the microstructure of the surface layer. In the former case (Fig. 12(c)) the micrograph revealed a defect, a loose hole to peak wavy relief with amplitude 60–70 μm. After 1000 shots (Fig. 12(d)), this structure vanished and a smoothed ('welded') relief appeared representing a mixed layer of fused and solidified metal agglomerates extending to a depth of up to 90 μm. Thus a tenfold increase in the number of cycles led to a change in the mechanism of degradation of the irradiated tungsten. The sharp loose 'ridges' were melted with the formation of a welded morphology with droplet structures. Under the action of plasma jet these droplet structures can detach from the surface while melted and then settle back when solidified. Additional estimation of a modified layer thickness of tungsten was made by the measurements of HV microhardness on the polished cross section samples (Fig. 13). One can see decreasing the microhardness with increasing number of plasma jet cycles at a depth up to hundreds μm. For comparison the microhardness of tungsten irradiated by electron beam was low.

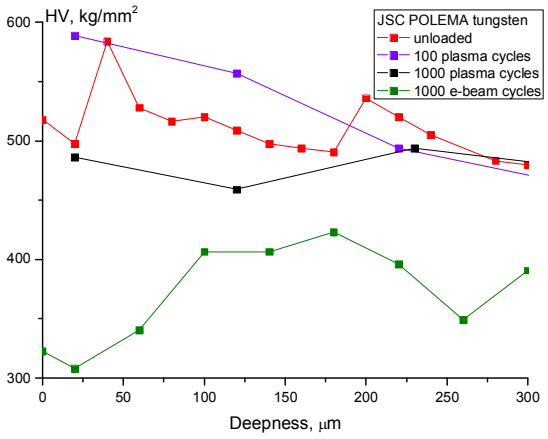

FIG. 13. HV microhardness of irradiated tungsten vs depth (indentation load 50 gf).

2.4.2. PLANSEE double forged tungsten

The surface structures of irradiated samples exposed to 100 and 1000 plasma jet pulses were also significantly different (Fig. 14). In the former case the series of pulses led to the formation of 'bobbin' structures oriented almost perpendicular to the irradiated surface (Fig. 14(a)). After 1000 plasma jet pulses the multiply remelted surface exhibited significant roughening and the spatial structural elements became wider (Fig. 14(b)). Similarly to in the case of JSC POLEMA tungsten the surface morphology of samples loaded by 1000 cycles corresponded to roughly remelted metal. The transverse sections of samples upon 100 plasma jet pulses revealed wedge shaped cracks propagating from the surface in-depth of material and showed a loose layer formed under the irradiated surface (Fig. 14(c)). The depth of cracks reached about 30 μm, and their localization was probably related to the boundaries of blocks emerging on the irradiated surface. In addition shear bands and regions of loose material were observed. Probably indication of a shockwave action upon the irradiated target was developed. An increase in the number of shots to 1000 led to expansion of the cracked region and formation of a loose material layer along the surface, the thickness of which reached 100–200 μm (Fig. 14(d)).

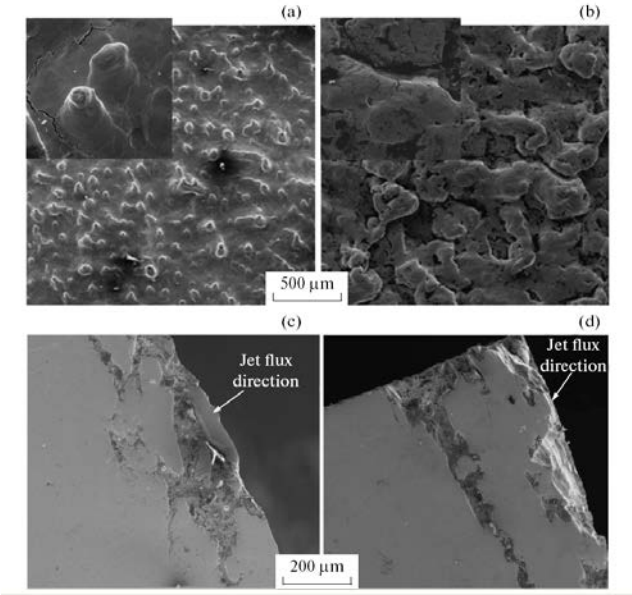

FIG. 14. (a) Microstructure of surface of PLANSEE tungsten after 100 irradiations by plasma jet; (b) microstructure of surface of PLANSEE tungsten after 1000 irradiations by plasma jet; (c) transverse section of PLANSEE tungsten after 100 irradiations by plasma jet; (d) transverse section of PLANSEE tungsten after 1000 irradiations by plasma jet.

Note that the results of our investigation of the resistance of tungsten to the action of hydrogen plasma pulses with high kinetic energy generated by a gun agree well with the reported data of some other studies with different plasma sources, in particular with deuterium plasma focus devices [21].

In-depth distribution of hydrogen in tungsten was determined by dynamical SIMS technique. Profiling was carried out using a magnetic sector instrument CAMECA IMS 7f. The primary beam of $^{133}Cs^{+}$ ions with 4 keV kinetic energy was restored over 200 μm × 200 μm area of the sample biased by 3 kV. $^{1}H_{2}^{-}$ secondary negative molecular ions and $^{184}W^{-}$ secondary ions were collected from a central 60 μm diameter area of the bottom of a sputtering crater. Quantification of the SIMS data was done using relative sensitivity factors determined by using implanted standards [22]. Crater depths were measured by an AMBIOS XP-1 surface stylus profilometer. The in-depth distributions of hydrogen in the tungsten samples non-irradiated and irradiated by 150, 1000 plasma pulses are presented on the Fig. 15.

One can see that hydrogen penetrated in tungsten up to depth ~1 μm and its quantity increased with rising of number irradiation. Thus our investigation of the irradiated tungsten by plasma gun showed that there were three main mechanisms of material degradation: melting of the surface layer to a depth of several microns, fracture of a 15–250 μm thick near surface layer, plastic deformation and dynamic recrystallization.

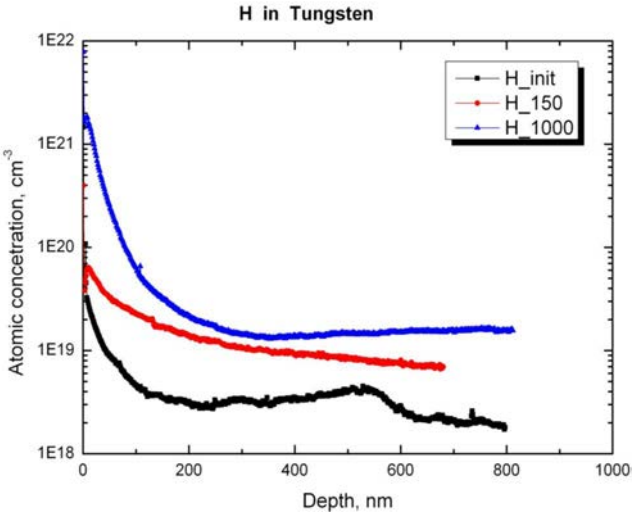

FIG. 15. In-depth distribution of H in JSC POLEMA tungsten after plasma gun treatment.

The JSC POLEMA tungsten proved to be more resistant to irradiation. Significant changes in the surface layer were observed upon multiply repeated exposure to plasma jet pulses. The surface became rough and a recrystallized layer was formed to a depth of ~ 100 μm. The transverse sections showed wedge shaped cracks propagating from the surface in-depth of material and confirmed a loose layer created under the irradiated surface.

2.5. Helium implantation experiments

2.5.1. Motivation

It is known that impacts of helium and hydrogen plasma on walls are differed. Helium, being inert gas, has low solubility in materials and deeply penetrates into them. It can assemble in form of bobbles of gas or complicate nano cluster associations (fuzz) with own and induced defects of material. Helium effects on structure modification, porosity development, processes of swelling and embrittlement of materials. For comparison of the achieved results a review of works on helium implantation was performed. Nanostructures in tungsten are obtained and studied. In total there are more than 2000 works. Summary of Japanese and US helium implantation experiments in support of ITER tungsten divertor development was presented in [23]. Particles of helium may be implanted at the energies from several eV to MeV, target temperature from 300 to 2600 K and fluence 10^{19}–10^{26} He/m^2. The surface morphology of tungsten changes to a nanotendril structure (fuzz, bubbles and pores) due to the presence of He in the right plasma conditions [24, 25]. In experiments at the divertor plasma simulator NAGDIS-II (NAGoya University Divertor Simulator-II) and other devices the fuzz was obtained [26]. Cross section of tungsten fuzz showing depth scale and growth conditions is presented in (Fig. 16). The data of diagram of fuzz and bubble formation was presented in [27] (Fig. 17). One can see an extensive area of the bubble formation.

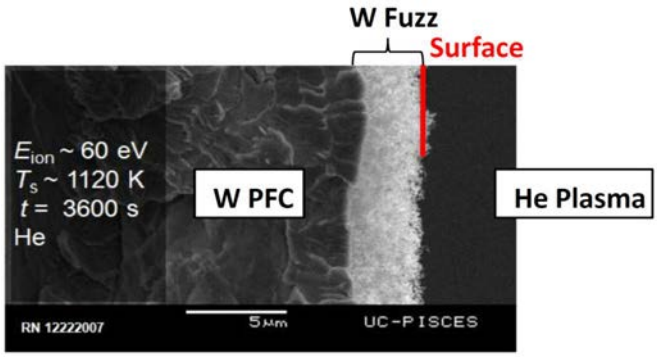

FIG. 16. Cross section of tungsten fuzz showing depth scale and growth conditions.

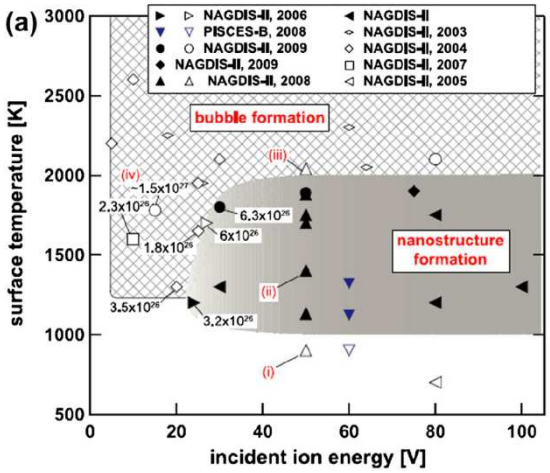

FIG. 17. Surface temperature plotted against the incident ion energy for helium irradiation experiments conducted in the divertor simulator NAGDIS-II and PISCES-B.

Tungsten fuzz can be grown on surfaces in a tokamak divertor. Nanotendril grew in the Alcator C-Mod lower divertor at conditions T_s = 1000–2000 K, E^{He+} > 20 eV [28]. After 14 consecutive helium L-mode discharges in Alcator C-Mod the tip of a tungsten Langmuir probe at the outer strike point was fully covered with a layer of nanotendrils (Fig. 18). The thickness of the individual nanotendrils (50–100 nm) and the depth of the layer (600±150 nm) were consistent with observations from experiments on linear plasma devices. These structures not only survived under the intense heat flux up to ~ 40 MW/m^2 and transient conditions, but grew up.

Helium beam of neutral atoms (NBI facility) implanted in tungsten was observed and offered in [29]. The tungsten got nanostructure in the form of bubbles.

Helium Implantation in tungsten by inertial confinement electrostatic device was performed and presented in [30]. Tungsten got nanostructure in the form of pores. Thus the nanotendrils are fragile and present a possible source of tungsten contamination for the core plasma. ITER fuzz layer depths could become large (>10 μm) over the life time of the tokamak.

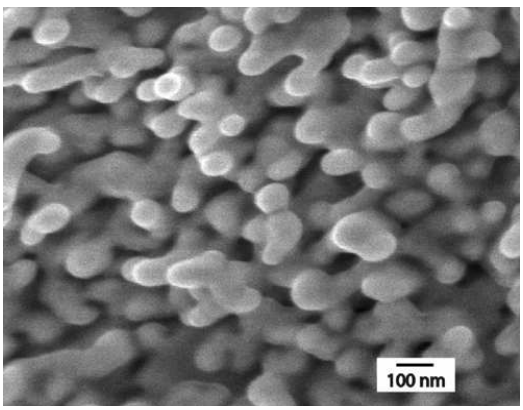

FIG. 18. SEM image of the W probe surface in the Alcator C-Mod divertor after helium plasma irradiation.

Eventually it can be the reason of reduction of operation period or even destruction of elements of reactor. The structure and growth mechanisms of this fuzz are not well understood. Further investigations are needed.

2.5.2. Modification of coaxial gun for helium implantation

For realization of helium implantation the laboratory model developed in Ioffe Institute was chosen as a prototype of plasma gun [31]. Adapting the accelerator for generation a jet of helium plasma was performed. The

high-speed gas valve of electrodynamic type was made and tested. The power supply and a control system of the valve were manufactured. During ~ 300 μs the valve filled the accelerator by gas with full quantity of particles of ~ 5×10^{19}. Parameters of helium plasma jet were investigated at the test bench equipped with a set of diagnostics. General view of the coaxial accelerator equipped with the high speed gas valve is presented in Fig. 19.

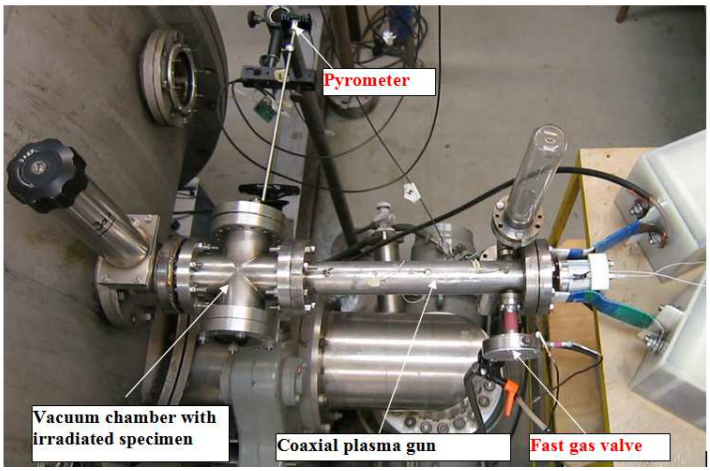

FIG. 19. Top view of the gun for tungsten irradiation with helium plasma jet.

The gun generated helium plasma during 15 μs, with density ~ 10^{22} m^{-3}, velocity up to 100 km/s, total number of particles, kinetic energy of ions up to 100 eV, fluence 10^{22} He $m^{-2} \cdot shot^{-1}$. The gun generated plasma jet in cyclic mode (up to 400 shots/day) providing multiple irradiation of tungsten. In few days the gun allowed getting material damage close to the condition in fusion reactor. Scanning electron microscopy (LEO 430, JEOL JSM-7001F) was used for investigation of irradiated surfaces.

2.5.3. Helium implantation by plasma jet

Samples of JSC POLEMA tungsten were cyclically irradiated by helium plasma jet at the test bench of the gun for the purpose of obtaining the nanostructure in the form of fuzz, bubbles, etc. expected in divertor of the ITER reactor [32]. The scheme of experiment is presented in (Fig. 20). Samples were placed at distance 240 mm from a source of plasma jet. The region without melting of tungsten was formed (heat flux factor ≤ 50 MJ $\cdot$ $m^{-2} \cdot s^{-1/2}$).

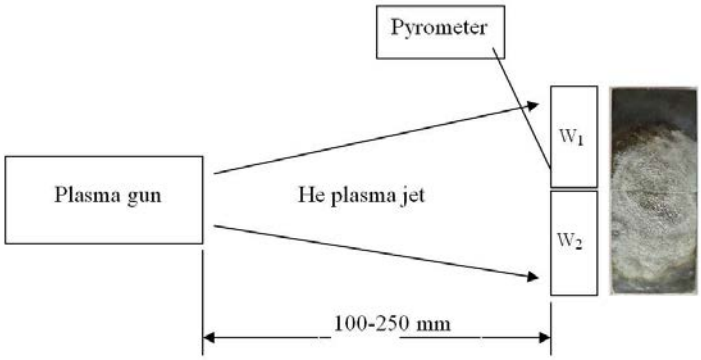

FIG. 20. Scheme of experiment on tungsten irradiation by helium plasma jet at the test bench of plasma gun.

SEM images of surface of JSC POLEMA tungsten after cyclic irradiation by helium plasma jet is presented in Fig. 21.

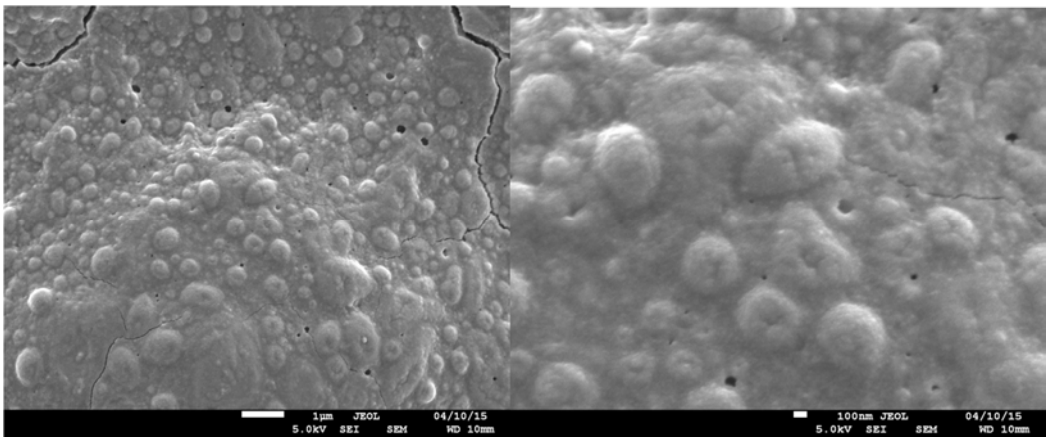

FIG. 21. SEM images of surface of JSC POLEMA tungsten after irradiation by helium plasma jet; number of pulses 1000; pulse duration 15 μs; distance between gun and sample 240 mm; fluence 10^{23}–10^{24} He/m^2; power density ≤ 0.2 MW/m^2; heat flux factor ≤ 50 MJ · m^{-2} · s$^{-1/2}$ (without melting).

Image showed that the tungsten surface has bubbles and pores. The nanostructure was similar to which was created after irradiation by helium neutral beam with energy 25 keV [29]. Further experiments with different jet parameters as higher fluence, lower incident energy are suggested.

3. STUDY OF TUNGSTEN AT LONG REPETITION IRRADIATION

Relatively compact spherical Globus-M tokamak has a high power density flow to the wall from plasma column: R = 0.36 m and r = 0.24 m, B = 0.4 T, I ~ 200 kA, pulse duration up to 100 ms, energy of the confined plasma 1–3 kJ/m^3 [33]. Preliminary experiments showed that in the diverter region, where separatrix contacts with tiles the deposited energy density of plasma flow could be high enough and can reach value of few MW/m^2. A scrape of layer (SOL) heat flux width at the upstream point (normally at outer middle plane) is a principal parameter which determines heat loads onto the divertor plates at the given geometry and magnetic configuration. This is specifically critical for spherical tokamaks because of their reduced major radius. A movable triple Langmuir probe provided measurements (from shot to shot) of both electron density and temperature profiles at the outer midplane SOL. Spatial distributions of ion saturation current I_{sat} and electron temperature T_e at the divertor plates were measured by means of a set of 10 flat embedded Langmuir probes with 8 mm diameter. Measurements were performed for three different plasma currents (I_{p1} =200 kA, I_{p2} =150 kA, I_{p3} =115 kA) in ohmically heated shots at lower single null (LSN) divertor configurations (Fig. 22). At the outer strike point region of the Globus-M lower divertor the deposited energy density reaches about 1–2 MW/m^2. Two color pyrometer with spatial resolution about 1 cm registered surface temperature of low divertor region (Fig. 23). One can see that the temperature of the tiles could reach the value ≥ 400°C. Radial displacement of the outer branch of the separatrix/ELMs could cause a variation of the temperature on time.

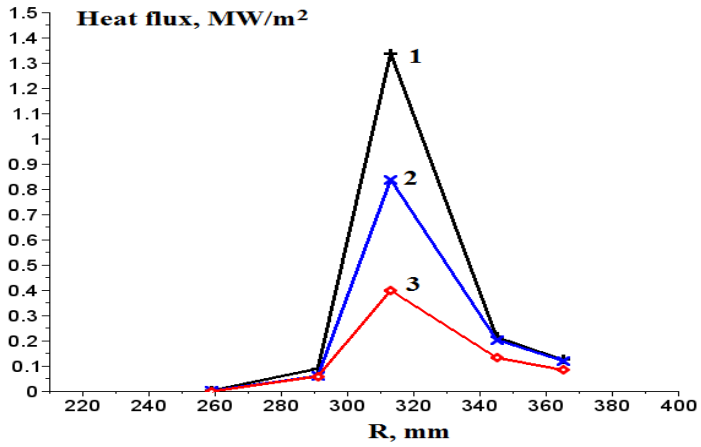

FIG. 22. Power density profiles near outer strike point in LSN OH discharges; 1: #34409, 200 kA; 2: #34354, 150 kA; 3: #34436, 115 kA.

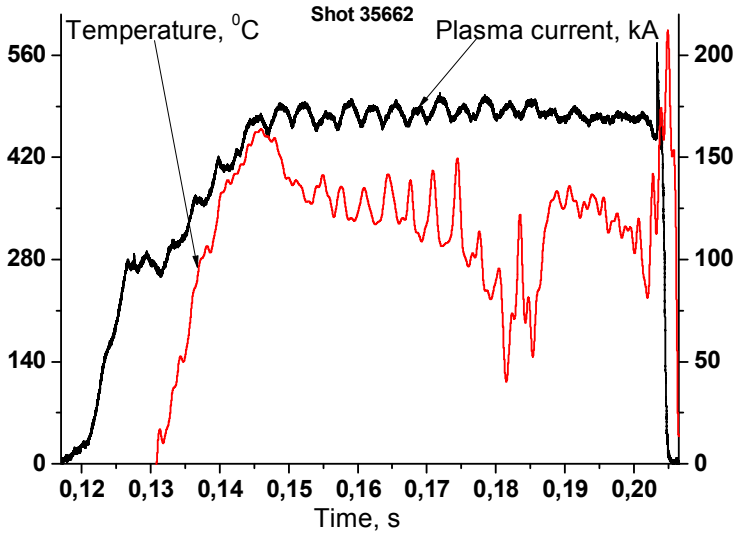

FIG. 23. Dependences of the Globus-M plasma current and the tile surface temperature on time; power density ≤ 2 MW/m^2; heat flux factor ≤ 1 MJ · m^{-2} · s$^{-1/2}$.

3.1. Tungsten poloidal limiters

The limiters were installed on outer cylindrical part of the Globus-M vacuum vessel. Study an interaction of the limiters with deuterium plasma was performed [34], see Fig. 24. The V_MP tungsten (powder metallurgy produced by JSC POLEMA, Russian Federation) limiters were made from 2.7 mm thick tungsten brazed onto copper substrates [35], see Fig. 25.

After 13770 pulses (total duration ~ 1400 s) the limiters were taken of for postmortem analysis. Limiter located nearby an RF antenna was chosen for analysis (Fig. 26(a)). A part of the tungsten plate surface was covered by films. This part was situated in the shadow of the RF antenna. Three samples (1, 2 and 3) were cut mechanically from the plate (Fig. 26(b)).

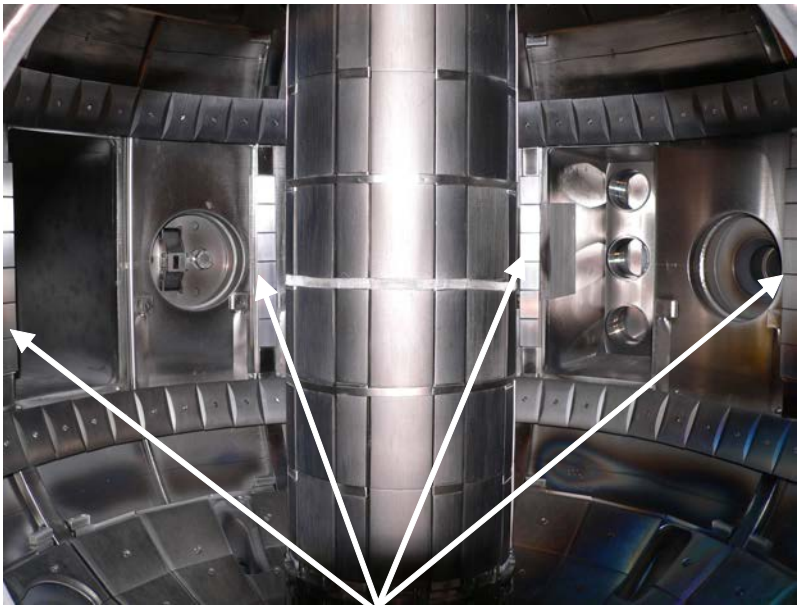

FIG. 24. Internal view of the Globus-M tokamak.

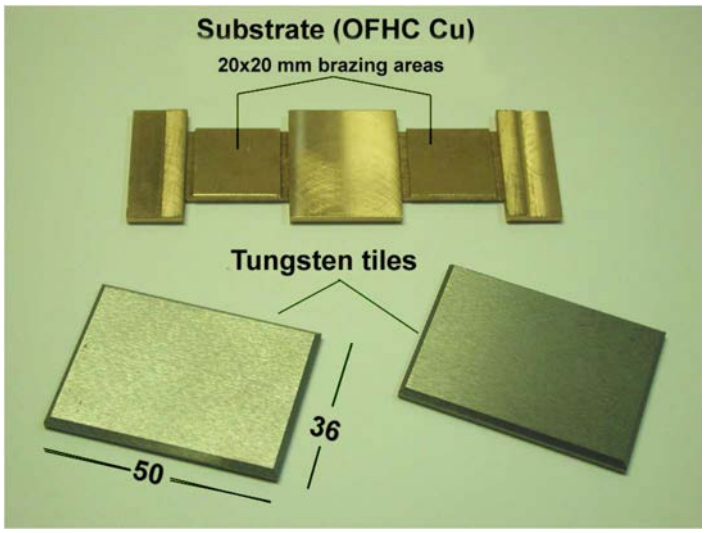

FIG. 25. Details of tungsten limiters.

Chemical composition of the limiters was studied by electron probe microanalysis (EPMA) on a microanalyzer Camebax (Cameca, France) equipped with a Si(Li) energy dispersive spectrometer. Characteristic X rays were generated by electron beam bombardment at 15 kV and 150 nA under residual vacuum of 10^{-6} Torr. The beam raster and the take-off angle (with respect to the sample surface) of the emitted X rays were 50 μm × 50 μm and 40°, respectively. Analysis time was 100 s. Areal densities of chemical elements in the near-surface layers were calculated by a code based on the Yakowitz–Newbury method [36]. Bulk diamond, SiO_2, Cr, Fe, and Ni were used as standards for the analysis of C, O, Cr, Fe, and Ni. Optical micrographs showed practically clean tungsten surface of the sample No 1 but there were black and light areas on sample 3. From EPMA data it follows that the black areas of the surface, situated in the shadow of the RF antenna, were covered with films containing carbon, oxygen and main elements of stainless steel.

Structure of the tungsten samples (1, 2 and 3) was investigated by means of X ray diffraction (XRD). The XRD analysis was fulfilled using a diffractometer DRON-3 with a copper tube (λ_{Cu} = 0.154 nm) and a graphite monochromator. The registration of diffracting beams was carried out in the range of angles 2θ from 5° to 90° with step 0.05° , exposition time in each point 3 s and depth of analysis ~ 1 μm [37]. Metallic tungsten with body-centered lattice (a = 0.317 nm) was observed on all XRD spectra of the samples.

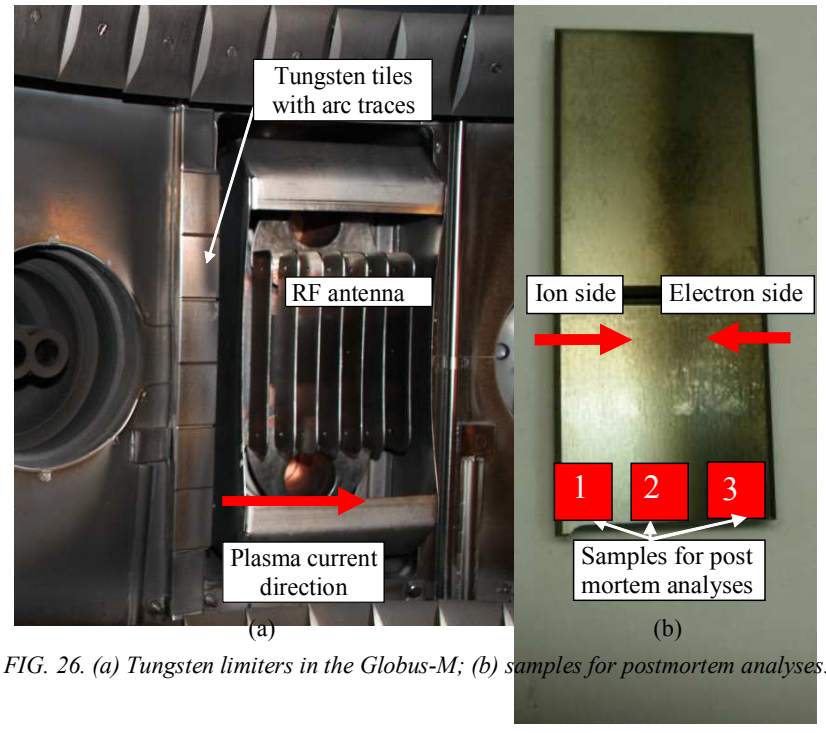

FIG. 26. (a) Tungsten limiters in the Globus-M; (b) samples for postmortem analyses.

However there were some weak peaks connected with graphite, iron and nickel on the XRD spectrum of the sample 3. Minimal imperfection was registered for the sample 3 because a splitting of W(211) reflection took place as opposed to W(211) reflection for the sample 1. This fact was confirmed by comparison of ratios of W(220) peak intensities to W(110) peak intensities (maximal intensity) for each sample: sample 1 of 6.8%, sample 2 of 7.0%, sample 3 of 7.6%. Lowering of W(220) peak intensity was connected with accumulation of various deformation defects in the analyzed layer. Probably this was caused by plasma flow directed to the samples 1 and 2, where the sample 3 was situated in the shadow of the RF antenna. Deuterium retention was evaluated by degassing the samples 1 and 3 in a thermal desorption spectroscopy (TDS) set-up. The samples were placed inside a quartz tube which was heated by an outer heater. The temperature was measured with Pt-Rh thermocouple, welded to the samples through a nickel intermediate plate. The released molecules HD, D_2 and some others were detected by a quadrupole mass spectrometer (Extorr XT200M). The quadrupole was calibrated by pumping a definite amount of the gas (H_2 or D_2).

Degassing curves of HD and D_2 molecules from the samples 1 and 3 are shown in Fig. 27. Integrating the curves gives total deuterium retention of 3×10^{20} D/m^2 in sample 1 and 1.5×10^{21} D/m^2 in sample 3. It should be noted that the samples exhibited similar degassing behavior. One explanation for higher retention in sample 3 was that deuterium was codeposited with carbon to form D rich layers. On the other hand the redeposited layers on the sample 3 might change the surface recombination coefficient that also gave raise the D retention. No significant changes in discharge behavior of the tokamak Globus-M equipped with tungsten limiters were observed.

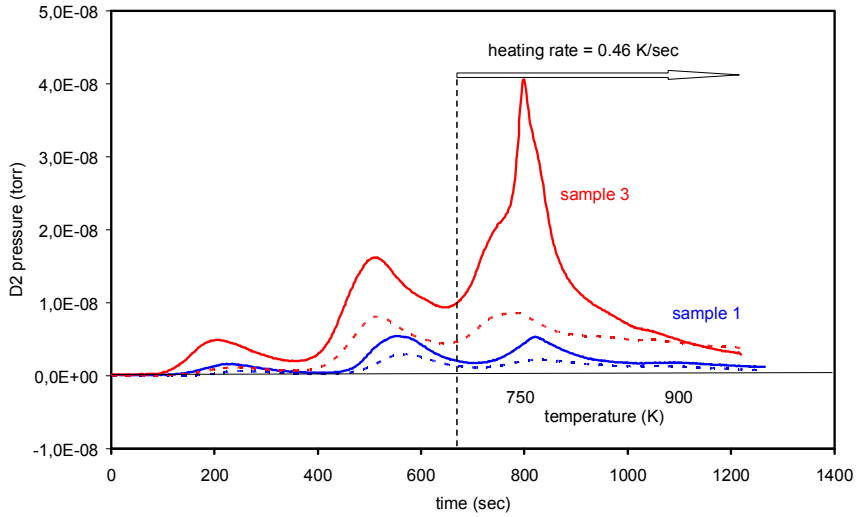

FIG. 27. Desorption spectra of D_2 (solid) and HD (dash) from samples 1 and 3.

3.2. Hot rolled tungsten

Hot rolled tungsten tiles were tested at the lower divertor region of the tokamak Globus-M for long repetition irradiation. Surface of the tiles was analyzed with video camera before (Fig. 28(a)) and after 3000 pulses (total duration 210 s) plasma irradiation (Fig. 28(b)). One can see that tungsten surfaces interacted with plasma. Discharge damaged the plates. Traces on the polished surface were probably following for magnetic field lines structure. No changes in discharge behavior of the tokamak Globus-M equipped with hot rolled tungsten tiles were observed.

3.3. JSC POLEMA and PLANSEE Double Forged tungsten

A sector of the lower divertor region was equipped with priory damaged two types of ITER-like tungsten JSC POLEMA and PLANSEE double forged (Fig. 28(c)). The tiles were placed at the region of outer strike point along poloidal direction. Two JSC POLEMA tiles were priory damaged by an electron beam at 1000 and 2000 ELM-events accordingly. The electron beam heat loads were performed by Tsefey-M facility (at the Efremov Institute) [38] with 195 kW beam power and 18 μs pulse duration. It was enough to provide the local tungsten melting. One JSC POLEMA tile and two PLANSEE specimens were priory damaged by hydrogen plasma jet with heat flux factor 200 MJ · m^{-2} · s$^{-1/2}$ at 100 and 1000 ELM-events.

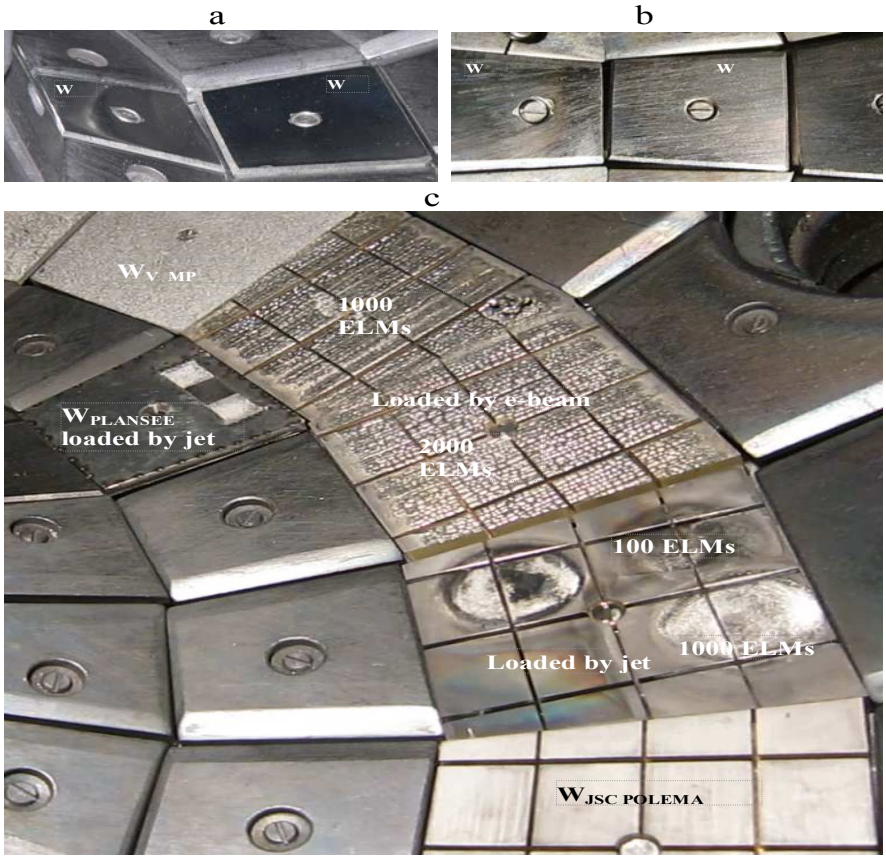

FIG. 28. (a) $W_{Hot\text{-}rolled}$ tiles before irradiation; (b) traces on $W_{Hot\text{-}rolled}$ tiles after 3000 shots; (c) arranging the divertor of the tokamak Globus-M with different types of tungsten for long repetition irradiation.

The tiles were observed during and shortly after discharge termination by infrared (Flir SC 7300M MWR MCT) and visible (Optronis CR Series) cameras at lower X-point divertor configuration. The infrared camera was sensitive in the spectral range of 3–5 μm. Video camera showed that during and right after discharge termination the visible radiation on a surface of the tiles was observed independently on material treatment (Fig. 29); perhaps dust luminescence was registered.

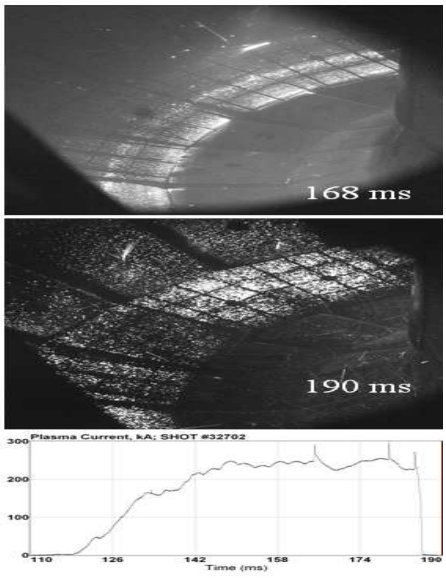

FIG.29. Video frames of the Globus-M divertor, shot 32702.

However, infrared camera showed non-uniform temperature field at the tiles (Fig. 30), for instance the temperature of PLANSEE tungsten pre irradiated by plasma jet with 100 and 1000 ELM events was higher in comparison with temperature of the non-irradiated tungsten and graphite tiles. The highest temperature of JSC POLEMA tungsten pre-irradiated with 1000 jet cycles was registered. Possibly the loose layer created by jet interfered with heat removal from surface to tile depth. Temperature of the surface damaged with electron beam was low. It is likely that surface remelted by electron beam did not lead to formation of loose coating under irradiated surface. No changes in discharge behavior of the tokamak Globus-M equipped with different tungsten tiles were observed.

After 2370 shots (total duration ~ 200 s) the PLANSEE double forged tungsten samples were taken out for analysis.

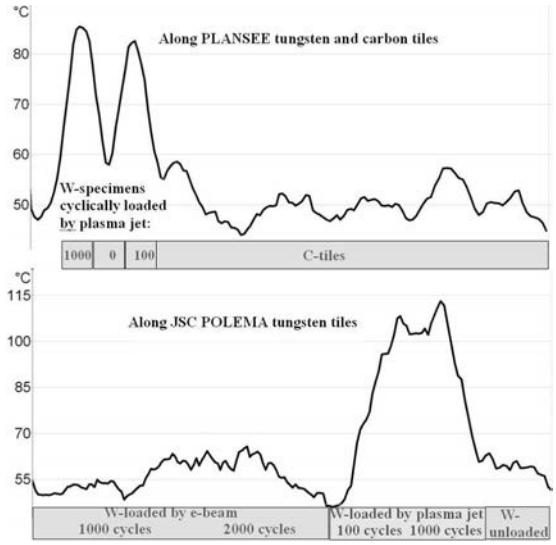

FIG. 30. Temperature distributions along tile surfaces after current termination. Shot 32702.

View of the tile before and after plasma interaction near outer strike point is presented in Fig. 31. One can see remarkable macrochanges on tungsten surfaces. Influence only of tokamak plasma created the damaged area differed of the plasma gun.

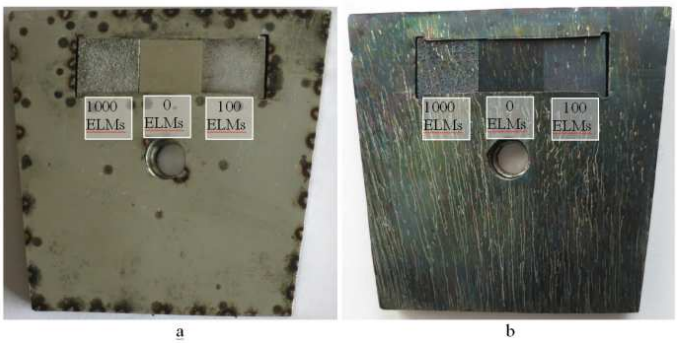

FIG. 31. (a) View of the tile arranging with PLANSEE tungsten specimens before Globus-M plasma interaction; (b) after 200 seconds Globus-M plasma interaction.

Structure of tungsten surface layers irradiated by the hydrogen plasma jet and their subsequent exposure in deuterium plasma of the tokamak Globus-M was investigated with microscopy [39, 40]. SEM images of the surfaces of damaged PLANSEE tungsten samples are presented in Fig. 32. One can see that tokamak plasma

smoothed the columnar and droplet shape structures created by plasma jet. It is possible to assume that subsequent irradiation of tokamak plasma gradually deleted the damaged layer created by plasma gun.

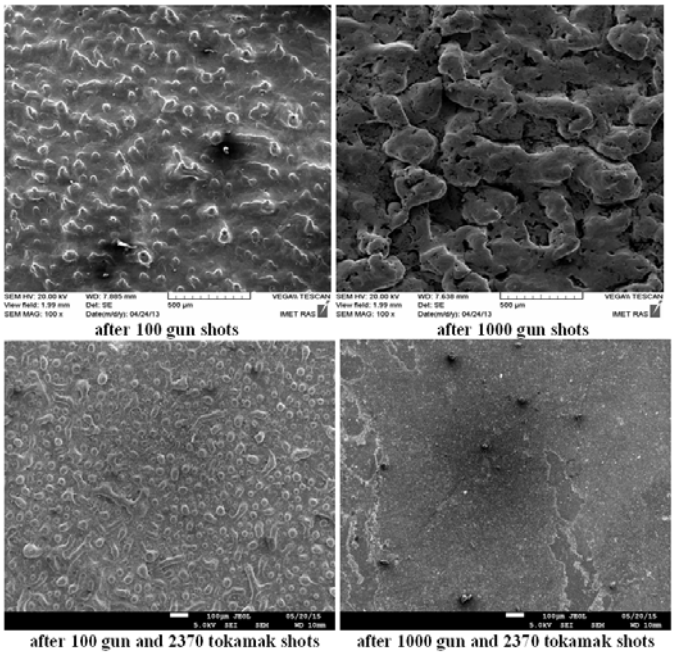

FIG. 32. SEM images of surfaces of PLANSEE tungsten after cyclic irradiation by the hydrogen plasma jet and deuterium plasma of the Globus-M.

The microstructure of near-surface area of samples of PLANSEE tungsten was investigated by X ray diffraction method on the D2Phaser diffractometer of Bruker AXS firm with use of the Topas and EVA programs for processing of diffractograms, and also on the DRON-6 diffractometer in CuK_{α} radiation. The obtained results are given in Table 2.

TABLE 2. MICROSTRUCTURE OF SAMPLES OF TUNGSTEN ACCORDING TO X-RAY DIFFRACTOMETRY

Sample name	N. irradiations by hydrogen plasma gun	N. irradiations by deuterium plasma of tokamak Globus-M	(Texture) ACD (nm) 1) avg. sizes ACD, (nm); 2) parameter of the lattice, Angstrom	Damaged area: 1) avg. sizes ACD (nm); 2) microstress	Supplement
Initial	0	0	(100), 330; (111), 120; 1) 150; 2) a = 3,1746	no	
100 gun shots	100	0	Texture wasn't found 2) a = 3,1658	1) 50; 2) 0.5	Damaged area ~50% of area of the analysis
1000 gun shots	1000	0	Texture wasn't found 2) a = 3,1592	1) 45; 2) 0.35	Damaged area ~93% of area of the analysis
2370 tokamak shots	0	2370	Texture wasn't found	1) 40; 2) 0.75	Damaged area ~80% of area of the analysis

100 gun+2370 tokamak shots	100	2370	Texture wasn't found	1) 50; 2) 0.5	Damaged area ~72% of area of the analysis
1000 gun+2370 tokamak shots	1000	2370	(100), 140; (111), 70; 1) 100;	Damaged area wasn't registered 2) 0.07	Damaged area wasn't registered

Samples of the studied tungsten represented identical rectangular parallelepipeds of 12 mm × 12 mm × 5 mm in size. Initial (non-irradiated) tungsten represented the polycrystalline sample textured on the planes (100) and (111) with an average size of the area of coherent dispersion (ACD) of equal 150 nm and the allocated size of ACD (equal 120 nm) of the crystallites located the crystallographic planes (111) parallel to a sample surface. The samples irradiated by gun showed existence of the damaged area (tungsten recrystallization area) which was characterized by reduction of ACD in comparison with an initial sample and some reduction of parameters of an elementary cell that was shown on diffraction curves by intensity 'inhaling' in area of big angles 2θ, see Figs 33(b) and (c). Peaks got a little triangular form.

The maximum shift in area of smaller angles had reflection from the damaged area in the sample which irradiated with 1000 gun shots. The similar picture was shown by the sample irradiated only with plasma of the tokamak (Fig. 33(d)). Diffraction curves are slightly displaced relative to peaks of non-irradiated tungsten. However, the obtained violations led not so much to reduction of ACD, but to increase of microstresses.

In the sample irradiated with 1000 gun and 2370 tokamak shots the damaged area wasn't registered, and the texture of tungsten repeated texture of initial sample (Figs 33(a) and (f)). The similar phenomenon can be connected with elimination by the plasma gun of damaged area in the course of irradiation. All other analyzed samples showed diffractograms with the ratio of intensities of various reflections similar to the given ICDD (No. 00-004-0806). Possibly it was connected with recrystallization of tungsten after melting as a result of irradiation.

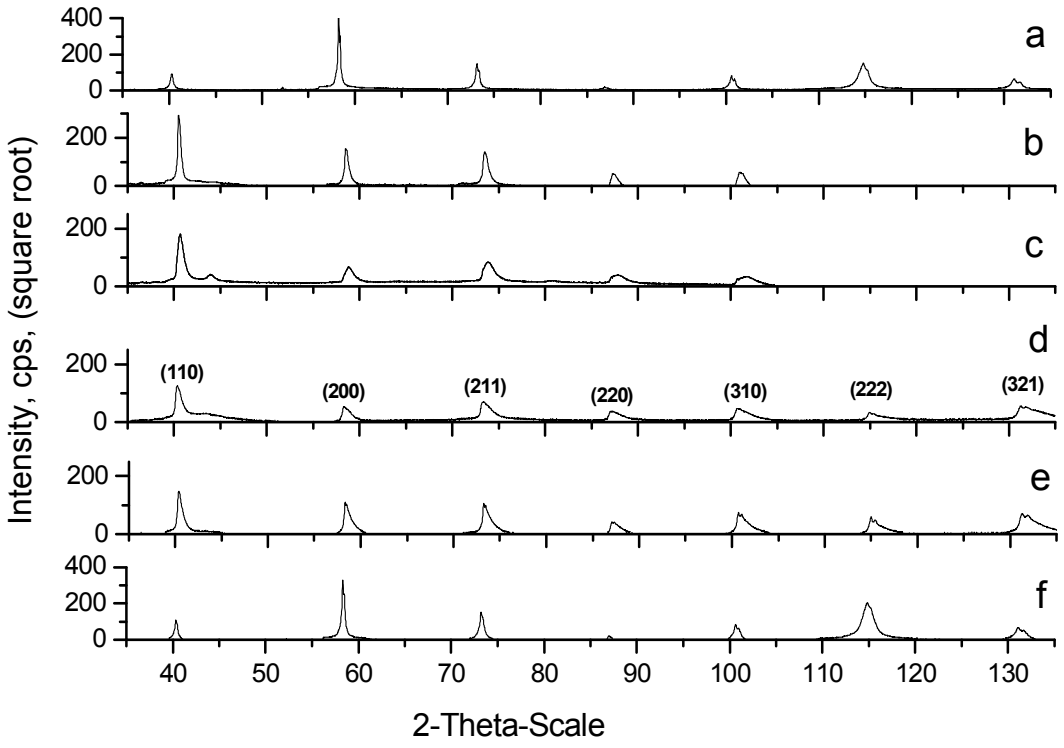

FIG. 33. (a) Initial diffractograms of intensities of different reflections of PLANSEE tungsten; (b) 100 gun shots; (c) 1000 gun shots; (d) 2370 tokamak shots; (e) 100 gun + 2370 tokamak shots; (f) 1000 gun + 2370 tokamak shots.

In sample with 100 gun and 2370 tokamak shots the damaged area occupied smaller volume than in the sample irradiated with plasma gun. It can testify that process of elimination of the damaged area just begun (Fig. 33(e)).

Phase structure all samples represented polycrystalline tungsten with the displaced center of gravity of peaks in area of big angles. Distinction in parameters of a lattice of metal tungsten and the damaged area was about 0.0178 Å. In samples with 2370 tokamak shots and 1000 gun shots presence of additional phases was noted. In sample with 2370 tokamak shots it was boron carbide, and in sample with 1000 gun shots, tungsten nitride W_2N or WN. Thus irradiation by hydrogen plasma jet of PLANSEE tungsten led to formation of the damaged area which was characterized by the reduced value of ACD and considerable microstresses. The subsequent irradiation by tokamak Globus-M plasma gradually deleted this damaged area. In turn, influence only plasma of the tokamak Globus-M also formed the damaged area differing from the plasma gun obtained as a result of influence in more considerable microstresses. An in-depth distribution of D, H and other elements in PLANSEE tungsten was determined by SIMS CAMECA IMS 7f. Fig. 34 shows in-depth profiles of elements in PLANSEE tungsten. One can see that characteristic depth of the layer accumulating impurities was more than 0.5 μm. The sample irradiated with 1000 gun and 2370 tokamak shots had the greatest depth and quantity of the impurity (Fig. 34(c)). Mainly the layer accumulated impurity of boron (boronization of the tokamak chamber was conducted regularly in order to improve the discharge reproducibility). The amount of other elements in the layer was not more than a few percent.

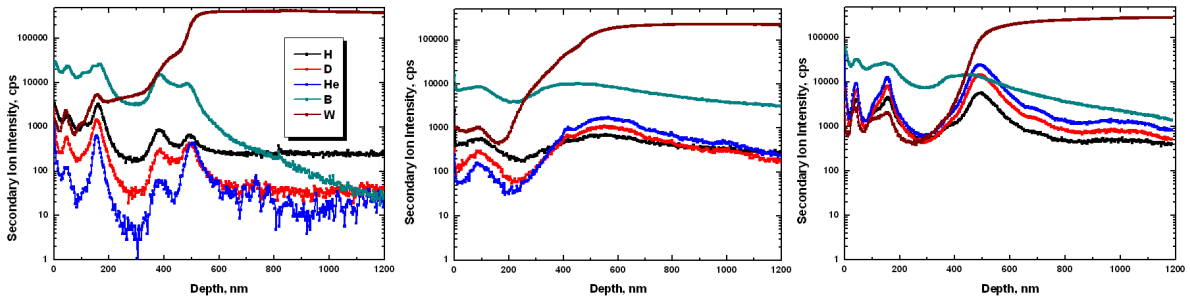

FIG. 34. (a) SIMS in-depth profiles of elements in PLANSE tungsten after irradiation by 2370 tokamak shots; (b) 100 gun + 2370 tokamak shots; (c) 1000 gun+2370 tokamak shots. $\varepsilon_{gun} \leq 200\ MJ \cdot m^{-2} \cdot s^{-1/2}$; $\varepsilon_{Globus\text{-}M} \leq 1\ MJ \cdot m^{-2} \cdot s^{-1/2}$.

Similar postmortem analysis will be completed after extraction the JSC POLEMA tiles from the tokamak during its reconstruction.

4. SUMMARY

Experimental study of tungsten under high kinetic energy plasmas was performed. Comparable investigations of tungsten irradiated with hydrogen and helium plasma jets as well deuterium plasma of the tokamak Globus-M were achieved.

The original plasma gun test bench was developed for investigation of material irradiation at high energy density plasma flow comparable to ELM event conditions of designed fusion reactor. The hydride titanium gun generated hydrogen plasma jet during ≥ 10 μs, with density ~ 10^{22} m^{-3}, velocity up to 200 km/s, total number of particles (1–5) × 10^{19}, kinetic energy of protons up to 300 eV. Providing multiple irradiation of tungsten in cyclic mode the jet allowed getting ITER-like material damage in few days. Diagnostic technique, laser interferometer, jet pressure detectors and two color pyrometer was developed and manufactured.

Preliminary analyzing and establishment of a data base of erosion behavior of different types of tungsten irradiated by the plasma jet was performed. The structure and morphology of single crystal, hot rolled, as well powder made V_MP and JSC POLEMA tungsten were tested. Irradiation with the energy densities 0.25–1 MJ/m^2 offered basic physical and mechanical degradation processes: melting surface, destruction of near surface layer arising due to thermal stresses, plastic flow and dynamic recrystallization in bulk. The depth of the molten layer about 1–3 μm and the zone of active thermal effects about 15–20 μm was registered.

The structures of the V_MP and JSC POLEMA tungsten become distinctly regular with a typical particle size of less than 1 μm. In hot rolled samples, such a structure was not observed. JSC POLEMA tungsten proved to be the most resistant to damage. Diffractograms showed very pronounced texture on a plane associated with the processes of melting and crystallization of the surface.

Surface of monocrystal tungsten irradiated by the jet obtained a regular crack structure probably in the direction of maximum shear. Numerical simulation of the thermomechanical processes occurred in tungsten showed that the degradation proceeded continuously to the times that were more than three orders of magnitude longer than the action time. The thermal stresses led to structural and morphological changes throughout the sample volume accompanied by recrystallization in adiabatic shear bands.

The surface layer of the V_MP tungsten was tested at multiple irradiations and different energies. At higher energy density the greater the damage was observed. At the lower energy density and a larger amount of shots, the damage was small. Probably such irradiation conditions favor healing of the defects.

Long repetition irradiations with the energy equivalent to ELM events changed the nature of the surface even more. Experiments with ITER like tungsten of two types, JSC POLEMA tungsten and PLANSEE were performed. After 100 shots of JSC POLEMA tungsten the 'hole–peak' structure of the loosened metal was created. 1000 shots changed character of topography considerably. The distinguished ridges were melted with formation of drop structures. The surface became rough.

Significant changes of the surface layer of PLANSEE - tungsten under multiple irradiations were observed. After 100 shots the structure in general is similar to the pattern after 10–20 shots, but more pronounced large columnar structure perpendicular to the plane surface was performed. After 1000 shots character of the surface layer changed dramatically. It was roughening recrystallized layer was formed. The wedge shaped cracks going from the irradiated surface deep into material was observed. The loose coating under irradiated surface was formed. The recrystallized layer up to depth ~ 100 μm was obtained. Review of works on helium implantation was done. Particles of helium may be implanted at the energies from several eV to MeV, target temperature 300–2600 K and fluence 10^{19}–10^{26} He/m^2. Modification of coaxial gun for generation of helium plasma was performed. The high speed gas valve of electrodynamic type was developed and manufactured. The gun generated helium plasma during 15 μs, with density ~10^{22} m^{-3}, velocity up to 100 km/s, total number of particles ~ 5×10^{19}, kinetic energy of ions up to 100 eV. Plasma jet generated in cyclic mode up to 400 shots/day providing multiple helium implantations in tungsten. In several days the gun allowed getting material damage close to the condition of fusion reactor.

Samples of JSC POLEMA tungsten were cyclically irradiated by helium plasma jet at the test bench of the gun for the purpose of obtaining the nanostructure in the form expected in divertor of the ITER reactor. Conducted experiments showed that the multiple helium plasma jet irradiations may create bubbles and pores when the temperature of tungsten didn't reach melting. Further investigations are suggested. Tungsten limiters were irradiated in equatorial plane of the tokamak Globus-M. Optical, X ray and TDS microanalysis of the samples showed minor structural damage in the surface layer thickness of about 1 μm. Graphite and stainless steel dust covered sample that placed in shadow of the RF antenna. This sample had the highest deuterium retention. Hot-rolled tungsten tiles were irradiated in the divertor region of the tokamak. Enough intensive ablation process of tungsten surface under Globus-M plasma conditions was registered. Traces on the polished hot rolled tungsten surfaces were observed after 3000 shots.

PLANSE double forged and JSC POLEMA tungsten specimens previously damaged with hydrogen plasma jet or e-beam were irradiated in the divertor region of the tokamak. Non-uniform temperature field on damaged samples after discharge termination was registered. Surface temperature of previously irradiated PLANSEE tungsten at 100 and 1000 ELM events exceeded the temperature of non-irradiated sample. Surface temperature of preliminary irradiated JSC POLEMA tungsten at 1000 ELM events exceeded the temperatures registered in other tiles. Two color pyrometer registered surface temperature of low divertor region up to 400°C. No changes in discharge behavior of the tokamak Globus-M equipped with different tungsten tiles were observed.

After tokamak shots the PLANSEE tungsten surface layers was modified, the columnar and droplet shape structures were smoothed. Probably subsequent irradiation by tokamak plasma gradually deleted this damaged layer by gun. X ray diffraction method showed that microstructure of near surface area of samples of PLANSEE tungsten irradiated by gun led to formation of damaged area, which was characterized by considerable microstresses. The subsequent irradiation by plasma of the tokamak Globus-M gradually deleted this damaged area. In turn, irradiation only by the tokamak plasma also created the damaged area with more considerable microstresses than obtained by plasma gun.

An in-depth distribution of D, H and other elements in PLANSEE tungsten showed that the characteristic depth of the layer accumulating impurities reached more than 0.5 μm. The samples irradiated both by the gun and the

tokamak had the greatest damaged depth and quantity of the impurity. Mainly the layer accumulated the boron impurity. The amount of other elements in the layer was not exceeded few percent.

ACKNOWLEDGEMENT

This work was supported by the IAEA research contracts 16939, 16960 and MINOBRNAUKA agreements 14.621.21.0007 (ID RFMEFI62114X0007), 14.619.21.0001 (ID RFMEFI61914X0001).

REFERENCES

[1] NEU, R., Preparing the scientific basis for an all metal ITER, Plasma Phys. Control. Fusion **53** (2011) 124040.
[2] PITTS, R.A., et al., A full tungsten divertor for ITER: Physics issues and design status, J. Nucl. Mater. **438** (2013) S48.
[3] MATTHEWS, G.F., et al., Current status of the JET ITER-like Wall Project, Phys. Scr. **T138** (2009) 014030.
[4] MATTHEWS, G.F., et al., Development of divertor tungsten coatings for the JET ITER-like wall, Nucl. Mater. **390–391** (2009) 934.
[5] GRUBER, O., et al., Compatibility of ITER scenarios with full tungsten wall in ASDEX Upgrade, Nucl. Fusion **49** (2009) 115014.
[6] SUGIYAMA, K., et al., Deuterium inventory in the full tungsten divertor of ASDEX Upgrade, Nucl. Fusion **50** (2010) 035001.
[7] SHOSHIN, A., et al., Plasma-surface interaction during ITER type 1 ELMs : Comparison of simulation with QSPA Kh-50 and the GOL-3 Facilities, Fusion Sci. Tech. **59** (2011) 57.
[8] HIRAI, T., ITER Organization, Cadarache, France, unpublished data.
[9] DE TEMMERMAN, G., et al., ELM simulation experiments on Pilot-PSI using simultaneous high flux plasma and transient heat/particle source, Nucl. Fusion **51** (2011) 073008.
[10] GARKUSHA, I.E., et al., Performance of deformed tungsten under ELM-like plasma exposures in QSPA Kh-50, J. Nucl. Mater. **415** (2011) S65.
[11] SAFRONOV, V.M., et al., Probl. At. Sci. Technol., Ser.: Plasma Phys. **16** 6 (2010) 51.
[12] SCHOLZ, M., KARPINSKI, L., KUBEŠ, P., PADUCH, M., SADOWSKI, M.J., Progress in MJ plasma focus research at IPPLM, Nukleonika **57** 2 (2012) 183−188.
[13] PIMENOV, V.N., et al., Damage and modification of materials produced by pulsed ion and plasma streams in Dense Plasma Focus device, Nukleonika **53** 3 (2008) 111−121.
[14] VORONIN, A.V., GUSEV, V.K., GERASIMENKO, YA.A., Investigation of discharge behavior in coaxial accelerator of plasma jet, Technical Physics, **58** 3 (2013) 462.
[15] VORONIN, A.V., GUSEV, V.K., GERASIMENKO, YA.A., SUD'ENKOV, YU.V., Parameter measurement of plasma jet in material irradiation, Technical Physics, **58** 8 (2013) 1122.
[16] VORONIN, A.V., http://www.ioffeled.com/index.php?option=com_content&view=article&id=31&Itemid=80.
[17] ANKUDINOV, A.V., et al., Irradiation of different type of tungsten by plasma jet, Technical Physics **59** 3 (2014) 346.
[18] VORONIN, A.V., et al., "Investigation of tungsten interaction with high kinetic energy plasmas", P4.080, paper presented at 39th European Physical Society Conference on Plasma Physics, Stockholm, Sweden, 2012.
[19] VORONIN, A.V., SUD'ENKOV, YU.V., SEMENOV, B.N., ATROSHENKO, S.A., N.S., NAUMOVA, Degradation of tungsten under the action of a plasma jet, Technical Physics **59** 7 (2014) 981–988.
[20] VORONIN, A.V., GUSEV, V.K., DEMINA, E.V., NOVOKHATSKY, A.N., PRUSAKOVA, M.D., Study of tungsten at cyclic interaction with jet of plasma gun, Technical Physics Letters **40** 24 (2014).
[21] SHIROKOVA, V., et al., Armor materials' behavior under repetitive dense plasma shots, Phys. Scr. **T161** (2014) 014045.
[22] WILSON, R.G., STEVIE, F.A., MAGEE, C.W., Secondary Ion Mass Spectrometry: A Practical Handbook for Depth Profiling and Bulk Impurity Analysis, Wiley, New York (1989).
[23] SHARAFAT, S., TAKAHASHI, A., NAGASAWA, K., GHONIEM, N., A description of stress driven bubble growth of helium implanted tungsten, J. Nucl. Mater. **389** (2009) 203–212.
[24] WOLLER, K., WHYTE, D., WRIGHT, G., Depth profiles of Helium and Deuterium in tungsten "fuzz" using Elastic Recoil Detection, UP9.00018, Bulletin of the American Physical Society 52nd Annual Meeting of the APS Division of Plasma Physics **55** 15, Chicago, Illinois 2010.
[25] BALDWIN, M.J., DOERNER, R.P., Formation of helium induced nanostructure 'fuzz' on various tungsten grains, J. Nucl. Mater. **404** (2010) 165.
[26] SAKAGUCHI, W., KAJITA, S., OHNO, N., TAKAGI, M., KURISHITA, H., Formation condition of fiberform nanostructured tungsten by helium plasma exposure, Plasma and Fusion Research **5** (2010) S1023.
[27] OHNO, N., et al., Influence of crystal orientation on damages of tungsten exposed to helium plasma, J. Nucl. Mater. **438** (2013) S879.
[28] WRIGHT, G.M., et al., Tungsten nano-tendril growth in the Alcator C-Mod divertor, Nucl. Fusion **52** (2012) 042003.
[29] TOKITANI, M., et al., Microscopic deformation of tungsten surfaces by high energy and high flux helium/hydrogen particle bombardment with short pulses, Plasma and Fusion Research **5** (2010) 012.
[30] RADEL, R.F., KULCINSKI, G.L., Implantation of He^+ in candidate fusion first wall materials, J. Nucl. Mater. **367−370** (2007) 434.
[31] VORONIN, A.V., Dense plasma source development and jet injection in Globus-M, Nukleonika **53** 3 (2008) 103.
[32] VORONIN, A.V., et al., "Experimental studies of cyclical plasma effects on tungsten", P5.175, paper presented at 42nd EPS Conference on Plasma Physics, Lisbon, Portugal, 2015.

[33] GUSEV, V.K., et al., Globus-M results as the basis for a compact spherical tokamak with enhanced parameters Globus-M2, Nucl. Fusion **53** (2013) 093013.
[34] NOVOKHATSKY, A.N., et al., "Composition and morphology of tungsten limiter surface after interaction with deuterium plasma in Globus-M tokamak", P2.074, paper presented at 39th European Physical Society Conference on Plasma Physics, Stockholm, Sweden, 2012.
[35] MEROLA, M., AKIBA, M., BARABASH, V., MAZUL, I., J. Nucl. Mater. **307–311** 2 (2002) 1524.
[36] GOLDSTEIN, J., et al., Scanning Electron Microscopy and X ray Microanalysis, Plenum, New York (1981).
[37] JAMES, R.W., The Optical Principles of the Diffraction of X rays, Bell, London (1950).
[38] GAGEN-TORN, V.K. , et al., "Experimental complex for high heat flux materials interaction research", 18th Symposium on Fusion Technology (SOFT) (Proc. Int. Conf. Karlsrue, Germany, 1994).
[39] VORONIN, A.V., et al., Experimental investigation of cyclical plasma impact on tungsten, Tech. Phys. **61** 3 (2016).
[40] UMANSKY, YA.C., SKAKOV, YU.A., IVANOV, A.N., RASTORGUEV, L.N., Crystallography, rentgenolography and electron microscopy, Metallurgy, Scandium, Moscow (1982).

TUNGSTEN IRRADIATION STUDIES IN NX3 AND UNU-ICTP PLASMA FOCUS DEVICES

R.S. RAWAT, P. LEE, S.V. SPRINGHAM, T.L. TAN, A. TALEDITAHER, U. ILYAS, Y. WANG, H. SHARIF, K.S. TAN, A. HUSNAIN, S. JAVADI
National Institute of Education,
Nanyang Institute of Technology

Z. ZHENG
Institute of Materials Research and Engineering

Singapore, Singapore

Abstract

The paper reports several sets of experiments that were conducted towards the IAEA CRP entitled "Investigations of Materials under High Repetition and Intense Fusion Pulses". Experiments were planned to irradiate the PLANSEE double forged W samples in NX3 and United Nation University (UNU)-ICTP plasma focus devices. Since NX3 was used for the first time, the neutron emission characteristics of NX3 were evaluated to optimize its neutron yield. While neutron optimization studies in NX3 were being conducted and we were waiting for PLANSEE tungsten samples from Julich, the locally procured tungsten were irradiated in UNU-ICPT plasma focus device using different number of shots to gain initial experience. PLANSEE double forged tungsten samples, once obtained, were irradiated at different distances (5, 10, 15 and 20 cm) from the anode top for fixed 50 focus shot using 10 kJ NX3 plasma focus (PF) device with deuterium as the filling gas. The NX3 PF device, driven by a 100 μF, 20 kJ modular capacitor bank, consisted of a 140 mm long anode with 110 mm deep cavity to minimize the ablation of anode material. An aluminum double aperture with 1 cm aperture size was used to reduce the anode material from reaching the irradiated PLANSEE double forged W sample surface. The virgin and irradiated samples were analyzed in detail using SEM, EDX, XPS and XRD. The impurity material ablated from anode (Fe and Cr) and aperture (Al) were found to be deposited on W substrate surface. This was a serious problem for material irradiation studies as it led to impurity material deposition on irradiated substrate which should be avoided or minimized. In order to evaluate the major source of impurity deposition on irradiated substrate another systematic experiment was performed in 3 kJ UNU-ICTP PF facility. Silicon substrates were irradiated using different number of PF shots (1, 5, 10 and 20 shot) at fixed irradiation distance of 6 cm with and without double aperture assembly of bronze (as bronze has greater ablation threshold compared to aluminum). The investigation confirms that the impurities mostly being contributed by contributed by aperture, but only for higher number of irradiation PF shots. After determining the major factors of impurity formation, final set of experiments were conducted using next batch of 8 new PLANSEE double forged tungsten sample to irradiate them in UNU-ICPT plasma focus device and irradiated samples are again characterized extensively using SEM, XRD, XPS and nano-indentor.

1. INTRODUCTION

The most important aspect in iterating out the most suitable plasma facing candidate material for the future fusion reactor is the evaluation of the effects of extreme radiations, which include fusion neutrons and complex energetic plasma wind, on their microstructures and hence various other physical properties. Though there are several plasma facing candidate materials such as beryllium, CFC, tungsten, SiC, it was however decided, in December 2011 meeting in Vienna that under the scope of the current CRP we will concentrate on irradiation of PLANSEE double forged tungsten (PDF-W) samples which will be provided by the group in Julich.

Several experiments were conducted during the course of this four year CRP duration which can be broadly classified as follows:

a) The neutron yield optimization of 10 kJ NX3 plasma focus device which is to be used for irradiation of PDF-W samples;
b) Irradiation experiments on locally procured commercial tungsten (C-W) samples using 3 kJ UNU-ICTP plasma focus facility (while waiting for PDF-W from FZJ, Julich) for different (5, 10 and 15) number of plasma focus shots at a given distance from the top of the focus anode;
c) Irradiation of PDF-W samples from FZJ at different distances (5, 10, 15 and 20 cm) from the anode top for fixed 50 focus shot using 10 kJ NX3 plasma focus device;
d) Developing strategies for removal or minimization of impurity deposition on irradiated samples using silicon as substrate;
e) Irradiation of PDF-W samples from FZJ at different distances using different number of focus shots using 3 kJ UNU-ICTP plasma focus device.

2. IRRADIATION EQUIPMENT AND ANALYTICAL METHODS

2.1. Plasma focus devices used in the irradiation experiments

2.1.1. The 10 kJ NX3 plasma focus device

The NX3 plasma focus device is driven by a 100 μF, 20 kJ modular capacitor bank. It comprises of eight 2.5 kJ (12.5 μF, 20 kV) low inductance (<40 nH) metal can capacitors (#SM203YW012H procured from Aerovox Corp., USA) connected in parallel and arranged in modular fashion. Each capacitor is rated for 80% reversal and has peak current delivering capacity of ~ 150 kA. Simultaneous discharge from eight modules, cumulatively delivers peak current in the range of 200–600 kA depending upon charging voltage. The quarter cycle of discharge is ~ 3 μs. The main parameters of NX3 plasma focus device are summarized in Table 1 and the assembly is shown in Fig. 1. For rapidly transferring the energy stored in capacitors to the dense plasma focus (DPF) load, a 150 kA / 20 kV hold off pseudo spark switch (model #TDI1-150k/25 procured from M/s Pulsed Technologies Ltd., Russian Federation) has been installed on each of the capacitors.

TABLE 1. PARAMETERS OF NX3 PLASMA FOCUS DEVICE

Maximum stored energy / charging voltage	20 kJ / 20 kV
Total capacitance	100 μF
No. of capacitors	8 Nos. (× 12.5 μF)
No. of switches/ type	8 Nos./ Pseudospark
Working voltage range (typical)	12–16 kV
External inductance/ resistance (with PF as load)	~ 54 nH / 7.5 mΩ
Quarter time period of discharge	~ 3 μs
Insulator sleeve length	30 mm
Insulator sleeve material	Pyrex
Operating gas	Deuterium (D_2)
Average neutron yield (DD)	$\geq 1 \times 10^9$ neutrons/pulse

For obtaining initial anode dimensions, electrical parameter of short circuit discharge current trace was investigated to measure the system inductance L_0, system impedance Z_0, peak discharge current I_0 and the quarter time of period T/4 of the discharge current.

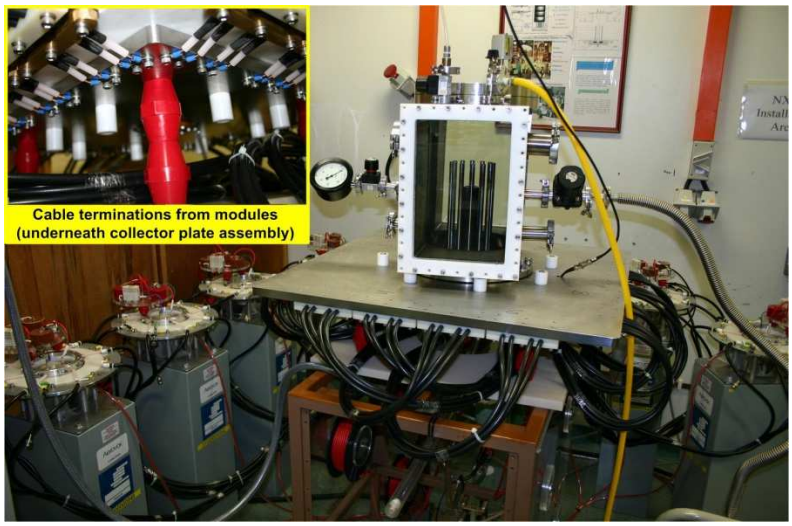

FIG. 1. NX3 plasma focus device.

According to Lee and Serban [1] most of the neutron optimized plasma focus devices have the typical speed factor, i.e. $(I_0/a)/\sqrt{p}$ (here, I_0 is the peak discharge current in kA, a is the anode radius in cm and p is the filling

gas pressure in Torr) of about 89 ± 8 kA · cm^{-1} · $Torr^{-1/2}$. Hence by using the short circuit peak discharge current measured by current probe and by approximating a deuterium operating pressure (in the range of 5–10 mbar), the preliminary value of anode radius was obtained. The criteria for deciding optimum anode length (Z_a) is that the time required for the discharge current to reach the maximum value must match with the quarter time period of the discharge current. This infers the relation $Z_a = v_a (T/4 - a/v_r)$, where v_a and v_r represent the typical axial and radial speeds of current sheath in axial and radial phases having typical values of about 10 and 25 cm/μs, respectively.

On the basis of aforementioned estimations and experimental iterations, the coaxial electrode assembly of the NX3 plasma focus head consisting of a 160 mm long, cylindrical anode of stainless steel (SS) having diameter of 40 mm and a squirrel cage cathode, consisting of twelve, 12 mm diameter brass rods, uniformly spaced on a coaxial circle of 90 mm diameter was designed. Since, hollow anode structures have been reported to produce higher neutron yields with better stability of the pinched plasma, in comparison with solid anodes [2] therefore a 60 mm deep cavity of 32 mm diameter was bored at the center of anode. An insulator sleeve of Pyrex glass with a breakdown length of 30 mm was placed between the anode and cathode. The rotary vane pump was used to create the base pressure of about 3×10^{-2} mbar and then a turbo molecular pump was used to get a vacuum better than 4 10^{-2} mbar. Turbo molecular pump was used to reduce the residual impurity gas in plasma focus chamber.

The employed diagnostics includes:

a) Rogowski Coil, a high bandwidth Rogowski coil has been used as an electrical diagnostic tool for probing discharge current waveform signals.
b) ^{3}He proportional counter for neutron yield measurement, a high sensitivity ^{3}He proportional counter has been used for the measurement of neutron output in 4πsr. In the customized arrangement, moderator (i.e. Polyethylene cylinder; ϕ 230 mm × 600 mm) having cavity of ϕ 65 mm × 550 mm at the center (i.e. ~ 8 cm of wall thickness) was used to maximize the counting efficiency of the high sensitivity ^{3}He neutron detector tube #2533 from LND Inc., USA (having nominal sensitivity length of 495 mm with 51 mm diameter). The thickness of moderator was estimated using MCNP simulation for D–D neutrons. ORTEC 556 was used as NIM high voltage module (0 to ± 3000 V). For providing power to various transistorized modules viz. amplifiers, high voltage supplies etc. standard NIM bin module 4001C from ORTEC was used.
c) Beryllium activation counter for measuring anisotropy in neutron yield. A calibrated pair of identical size Beryllium activation counters has been used for measuring anisotropy in neutron yield [3, 4].
d) Scintillator photomultiplier detectors (Plastic and CsI) for time resolved measurements. For the time resolved measurements of neutrons and hard X rays emission, combination of two different scintillators NE-102A (diameter of 52 mm, thickness of 40 mm) and CsI (diameter of 50 mm, thickness of 50 mm) have been used along with 14 stage high gain photomultiplier tube EMI 9813BK. A high voltage power supply, model PM28B from Thorn EMI electron tubes, was used to provide -1800V bias to the photomultiplier tubes. The data acquisition system consists of two Yokogawa oscilloscopes (DL9140, 5GS/s, 1 GHz) and a computer.

2.1.2. The 3 kJ UNU-ICTP Plasma Focus Device

Another plasma focus device at NIE/NTU that is used for irradiation experiments is a 3.3 kJ, Mather type plasma focus device that is popularly known as UNU-ICTP plasma focus facility (PFF). It is powered by a single 15 kV, 30 μF Maxwell capacitor and is switched by a parallel plate swinging cascade spark gap. A step up transformer is used to trigger the spark gap. The main parameters of UNU-ICTP plasma focus device are listed in Table 2 on the following page.

The UNU-ICTP PFF has the following subsystems:

a) Driver (high voltage charger, capacitor and high voltage cables);
b) Switch (swinging cascade spark gap);
c) Focus tube (discharge chamber, input flanges and electrode system);
d) Vacuum system (vacuum pump, nano valves, working gas, vacuum chamber);
e) Triggering system and control electronics (master pulse trigger generator, high voltage SCR unit, high voltage transformer, and delay units);
f) Data acquisition system.

TABLE 2. PARAMETERS OF UNU-ICPT PLASMA FOCUS DEVICE

Maximum stored energy / charging voltage	3.3 kJ / 15 kV
Total capacitance	30 μF
No. of switches/ type	1 Nos./ Swinging Cascade Spark Gap Switch
Working voltage range (typical)	12–15 kV
External inductance/ resistance (with PF as load)	~ 110 nH / 7.5 mΩ
Quarter time period of discharge	~ 3 μs
Insulator sleeve length	25 mm
Insulator sleeve material	Pyrex
Operating gas	Deuterium (D_2)
Average neutron yield (DD)	$\geq 7 \times 10^7$ neutrons/pulse

The fast discharging oil filled Maxwell capacitor (30 μF / 15kV with 27 nH internal inductance) is connected to the high voltage charger and to the input flanges of coaxial electrode assembly of focus chamber by UR-67 high voltage coaxial cables. A swinging cascade spark gap is used as a low inductance high current switch with the gap ratio as 3:2 (4.5:3 mm). The electrodes of the spark gap are made of copper plates of 12 mm thickness and the gap is triggered via an isolating capacitor from a -560 V silicon controlled rectifier (SCR) unit of 50 ns rise time via a step up transformer (ratio 1:50, 1 μs rise time). The focus tube consists of input flanges, electrode system and the discharge chamber. The electrode assembly in the focus tube consists of a hollow copper anode fitted firmly to the positive flange. The outer diameter of the anode is 19 mm and its effective length is 160 mm. Coaxial to the anode are outer electrodes (cathode rods) of six equally spaced copper rods attached to the back wall plate. These rods have a dimension of 10 mm in diameter and 157 mm in length. The plasma chamber is a stainless steel tubing of diameter 165 mm and is 300 mm in length which is further extended in length with another chamber with axially moveable substrate holder. The vacuum of the chamber is provided by a double stage rotary pump, reaching base pressure of ~ 2×10^{-2} mbar, and a turbo molecular for achieving the base pressure of 10^{-4} mbar. A low voltage SCR unit was used as the master pulse trigger generator. It is used to send out pulse to high voltage SCR unit, which sends an -560 V (2 μs rise time) to the triggering pin of the spark gap via a step-up transformer to transfer the electrical energy stored in capacitor to focus tube. The schematic of the device is shown in Fig. 2.

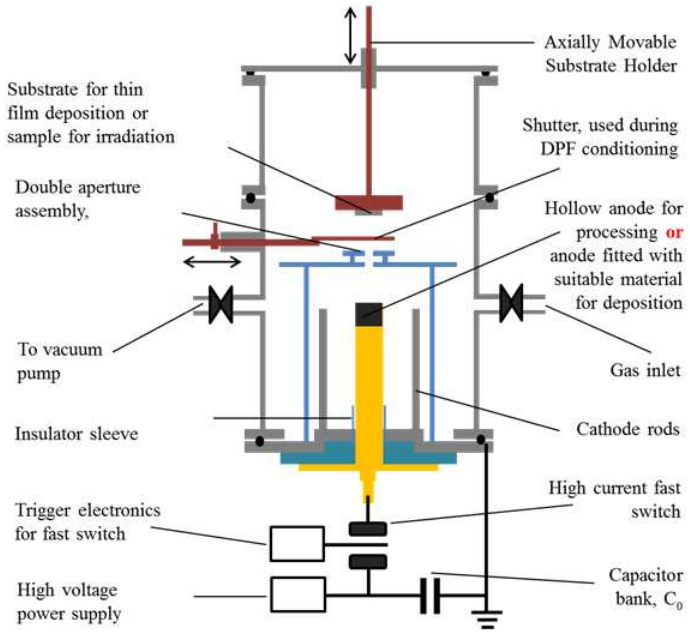

FIG. 2. Schematic of UNU/ICPT plasma focus device

2.2. Equipment used in the analysis of the irradiated specimens

Analysis of irradiated samples was done using following characterization facilities:

- Field emission scanning electron microscopy (FESEM) analysis was conducted using JEOL JSM-6700F;
- Energy dispersive X ray (EDX) spectroscopy was conducted using Oxford Instrument device attached to JEOL JSM-6700F FESEM;
- X ray diffraction (XRD) was conducted using SIEMENS D5005;
- X ray photoelectron spectroscopy (XPS) analysis was conducted using VG ESCALAB 220i-XL XPS with a monochromatic Al Kα (1486.7 eV) X ray source;
- Hardness measurements were done using Nano-indentor.

3. VARIOUS EXPERIMENTS USING NX3 AND UNU-ICTP PLASMA FOCUS FACILITIES

3.1. Experiment 1: neutron yield optimization from NX3 plasma focus device

The NX3 plasma focus device was designed, developed and assembled just about a year before the award of this CRP to our team. NX3 plasma focus device, with its maximum storage energy of 20 kJ at maximum allowable charging voltage of 20 kV for the capacitor bank used, is the most powerful plasma focus devices available at our Plasma Radiation Sources Lab at NIE/NTU in Singapore. Since we were planning to use this for irradiation of PDF-W samples, the first aim was to optimize this device by maximizing its neutron yield.

3.1.1. Diagnostics used on NX3 Plasma Focus Device

In order to optimize the NX3 plasma focus device electrical and neutron measurement diagnostics were employed. The employed diagnostics includes Rogowski Coil for electrical measurement and ^{3}He proportional counter and Beryllium activation counter for neutron measurements.

The data acquisition system consists of:

a) Two Yokogawa oscilloscopes (DL9140, 5 GS/s, 1 GHz);
b) A computer;
c) Rogowski Coil: a high bandwidth Rogowski coil has been used as an electrical diagnostic tool for probing discharge current waveform signals;
d) ^{3}He proportional counter for neutron yield measurement: a high sensitivity ^{3}He proportional counter has been used for the measurement of neutron output in 4πsr. In the customized arrangement, moderator (i.e. Polyethylene cylinder; ϕ 230 mm × 600 mm) having cavity of ϕ 65 mm × 550 mm at the center (i.e. ~ 8 cm of wall thickness) was used to maximize the counting efficiency of the high sensitivity ^{3}He neutron detector tube #2533 from LND Inc., USA (having nominal sensitivity length of 495 mm with 51 mm diameter). The thickness of moderator was estimated using MCNP simulation for D–D neutrons. ORTEC 556 was used as NIM high voltage module (0 to ± 3000 V). For providing power to various transistorized modules viz. amplifiers, high voltage supplies etc. standard NIM bin module 4001C from ORTEC was used.
e) Beryllium activation counter for measuring anisotropy in neutron yield: a calibrated pair of identical size Beryllium activation counters has been used for measuring anisotropy in neutron yield [3, 4].
f) Scintillator photomultiplier detectors (Plastic and CsI) for time resolved measurements: For the time resolved measurements of neutrons and hard X rays emission, combination of two different scintillators NE-102A (diameter of 52 mm, thickness of 40 mm) and CsI (diameter of 50mm, thickness of 50mm) have been used along with 14 stage high gain photomultiplier tube EMI 9813BK. A high voltage power supply, model PM28B from Thorn EMI electron tubes, was used to provide -1800V bias to the photomultiplier tubes.

3.1.2. Optimization configurations used on NX3 device

The initial coaxial electrode assembly of the NX3 plasma focus head consists of a cylindrical anode of stainless steel (SS) having length (z) of 160 mm, radius (a) of 20 mm and a squirrel cage cathode, consisting of twelve, 12 mm diameter brass rods, uniformly spaced on a coaxial circle of radius (c) of 51 mm. This electrode assembly is named as A20Z160 (where A and Z symbolize anode radius and length in mm). While the experiments were

being conducted and analyzed using initial electrode assembly configuration A20Z160, the further optimization of NX3 neutron yield and an investigation of finding the correlation between the speed factor and the neutron yield were planned. The dimensional details of all electrode assembly configurations (A20Z160, A26Z160, A55Z160, A20Z140, A26Z140 and A55Z70) are given in Table 2. The cathode radius, *b*, was increased to 81 mm for A55Z160 and A55Z70 configurations to accommodate the 55 mm radius anode.

TABLE 3. DIFFERENT ELECTRODE ASSEMBLY CONFIGURATIONS

Anode Design	Anode radius (a)	Anode Length (z_0)	Cathode Radius (b)
A20Z160	20 mm	160 mm	51 mm
A26Z160	26 mm	160 mm	51 mm
A55Z160	55 mm	160 mm	81 mm
A20Z140	20 mm	140 mm	51 mm
A26Z140	26 mm	140 mm	51 mm
A55Z70	55 mm	70 mm	81 mm

3.1.3. Results and Discussion for A20Z160, the Initial Electrode Assembly Configuration

The measurement of neutron output from NX3 device was performed to investigate optimum Deuterium (D_2) filling gas pressure for operation of device at charging voltages in the range of 12kV to 15kV. The measured average neutron yield for different D_2 gas pressures for initial electrode assembly configuration A20Z160 are shown in Fig. 3.

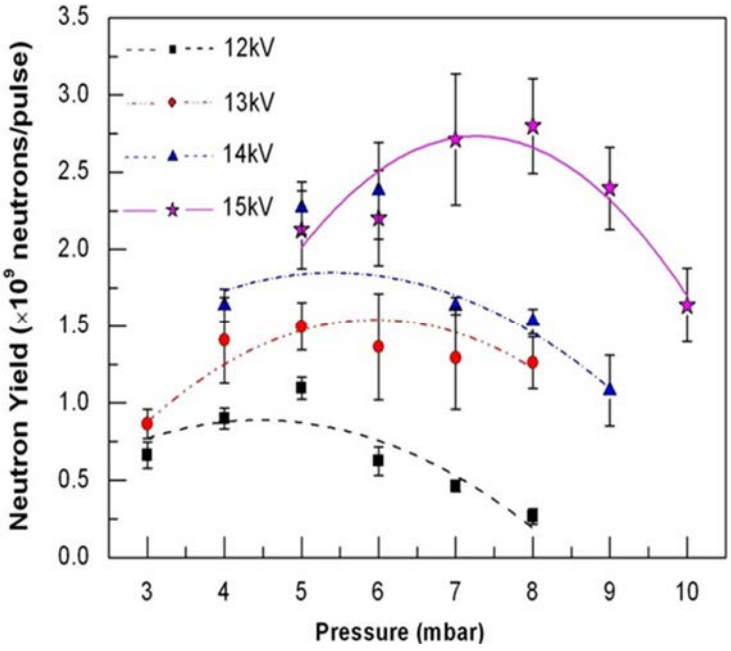

FIG. 3. Average neutron yield at different charging voltages and D_2 gas filling pressures for initial A20Z160 electrode assembly.

It may be noted that the neutron yield continue to increase with the increase in charging voltage which basically result is higher storage energy as well as high discharge current and was maximized at 15 kV, ~ 8 mbar D_2 filling gas pressure producing average maximum neutron yield of about $(2.8 \pm 0.3) \times 10^9$ neutrons/shot.

The typical signals (Ch2 and Ch3) from the scintillator photomultiplier detectors SPMT1 (having NE102A plastic scintillator) and SPMT2 (having CsI inorganic scintillator) and the corresponding current derivative signal (Ch1) measured by the Rogowski coil, for a typical shot at 15 kV / 8 mbar D_2 filling gas pressure are collectively shown in Fig. 4.

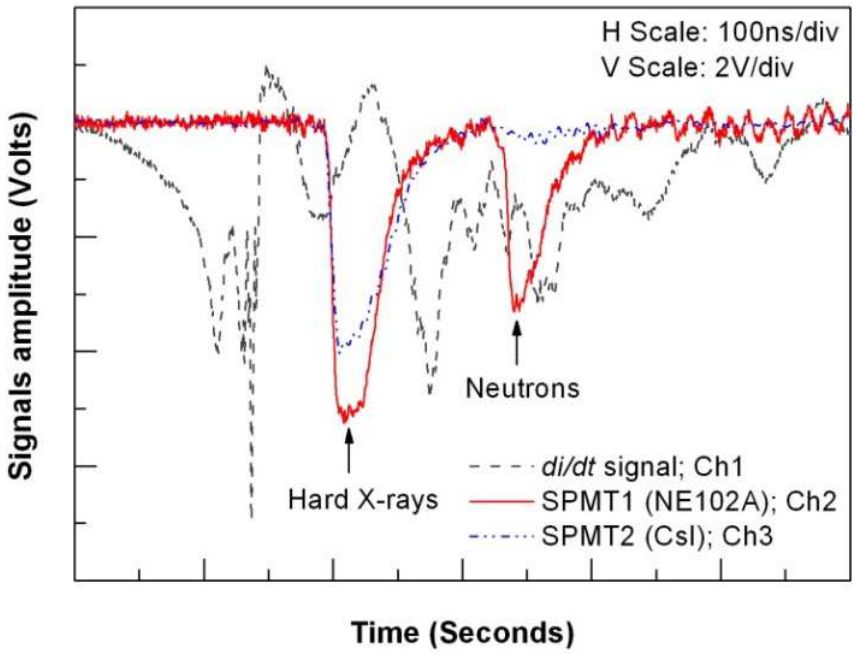

FIG. 4. Current derivative signal trace (Ch1) with hard X ray and neutron signal recorded from end-on positioned scintillator photomultiplier detectors SPMT1 (Ch2) and SPMT2 (Ch3) respectively.

Both the scintillator photomultiplier detectors were placed in the side-on direction at a common distance of 3 m from central/anode axis of the NX3 plasma focus. For avoiding saturation in the time resolved signals, lead sheets of 8 mm common thickness was used at the front end of SPMT's for attenuated screening. The two distinct peaks observed in the SPMT signals (Ch2 and Ch3) were confirmed to be of hard X rays and neutrons on the basis of time of flight separation in the peaks of SPMT1 (Ch1) trace. The observed time difference of ~ 140 ns between the two peaks complements the expected difference in time of flight (TOF) for hard X ray and 2.45 MeV neutrons. The first peak is of non-thermal, hard X rays produced by the interaction of instability generated energetic electrons with the stainless steel anode, whereas the second peak was confirmed to be due to neutrons on the basis of time of flight separation. The coincident and overlapping trace of SPMT2 detector (on trace of SPMT1 detector) also confirmed the identity of hard X ray and neutron peak. The relatively lower cross section of CsI scintillator for neutrons is explicitly evident in the obtained trace. The typical durations of hard X ray and neutron pulses, estimated from full width at half maximum (FWHM) were observed as 50 ± 7 ns and 40 ± 5 ns in the radial direction. The delay of ~ 50 ns in hard X ray peak with respect to the steep minimum of the current derivative signal is due to the inherent delay of ~ 30 ns in the photomultiplier tube signal and the excess length of cable used for transport of d*i*/d*t* signal. Neutron anisotropy measurement is important to identify the prevailing dominant mechanism of neutron production in PF device. The anisotropy Y_{0°/Y_{90° (*i.e.* neutron flux ratios in the axial and radial direction) was measured using Beryllium detectors placed at the identical distance of 28 cm in the end-on and side-on direction outside the chamber. During the anisotropy investigation charging voltage was kept fixed at ~ 14 kV and D_2 filling gas pressure was varied in the range 4–8 mbar. The relative variation of average neutron anisotropy as a function of pressure is shown in Fig. 5.

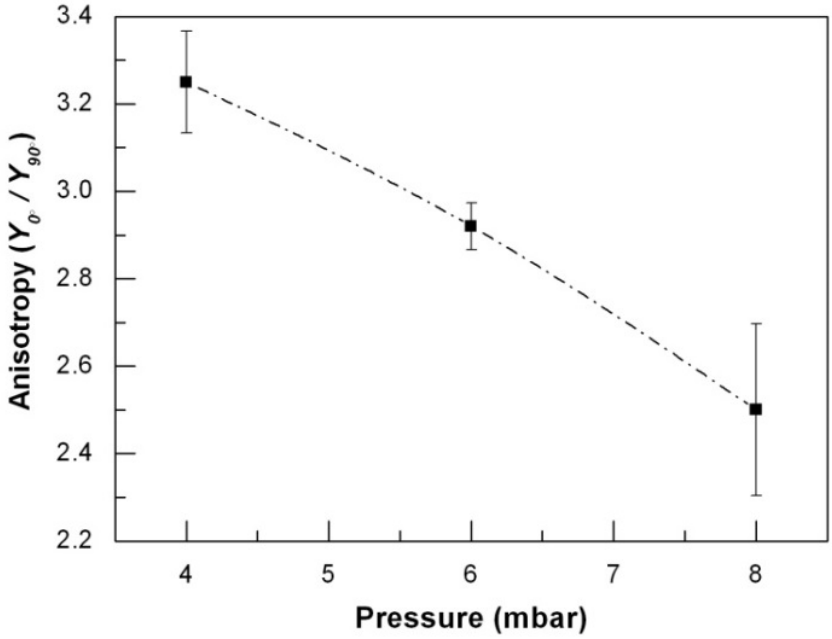

FIG. 5. Variation in neutron anisotropy as a function of D_2 gas filling pressure.

Each data point shown in the graph is an average of 5 shots. The average neutron anisotropy of ~ 3.2 at 4 mbar, ~ 2.9 at 6 mbar and ~ 2.5 at 8 mbar indicates that the neutron production mechanism at play depends upon the operating gas pressure, a result which was also described by Zakaullah et al. [5]. The presence of anisotropy, under neutron optimized conditions, indicates a deuteron velocity distribution with a peak along the axis and rules out the possibility of purely thermal emission [6].

3.1.4. Results and discussion for other electrode assembly configurations

The average neutron yield in the deuterium pressure range of 0.25 to 9 mbar at 14 kV (~10 kJ) for different electrode assembly configurations (A20Z160, A26Z160, A55Z160, A20Z140, A26Z140 and A55Z70) was measured and is shown in Fig. 6. The peak average neutron yield was ~ (2.38 ± 0.31) × 10^9 n/shot for initial A20Z160 configuration which increased marginally to ~ (2.54 ± 0.24) × 10^9 n/shot for A26Z160 but increased significantly by about 1.4 times to ~ (3.40 ± 0.43) × 10^9 n/shot for A26Z140. The increase in anode radius from 20 to 26 mm while keeping the anode length same at 160 mm increased the yield marginally; but the increase in anode radius with simultaneously decrease in anode length to 140 mm increased the yield significantly.

The other three anode configurations (A20Z140, A55Z70 and A55Z160), however, resulted in lower average neutron yield. One of these electrode configurations, A55Z70 has a further increase in anode radius and reduction in anode length as compared to initial A20Z160 and new A26Z140 configurations but the average neutron yield has rather decreased. The average neutron yield dropped significantly by almost about two orders of magnitude to 10^7 neutrons/shot for electrode assembly configuration A55Z160 i.e. when only the anode radius was increased significantly to 55 mm from initial 20 mm or optimized 26 mm anode while keeping the anode length same at 160 mm. The reduction in anode length to 70 mm for the anode of radius 55 mm in A55Z70 increased the average neutron yield back to the level of high 10^8 to low 10^9 neutrons/shot.

The comparison of plots in Figs 6 and 7 indicates that for most of the electrode configurations (A20Z160, A26Z160 and A26Z140) higher average neutron yield was obtained when the time to pinch was about 3.2–3.6 μs; which is close to the quarter time period of the NX3 PF device.

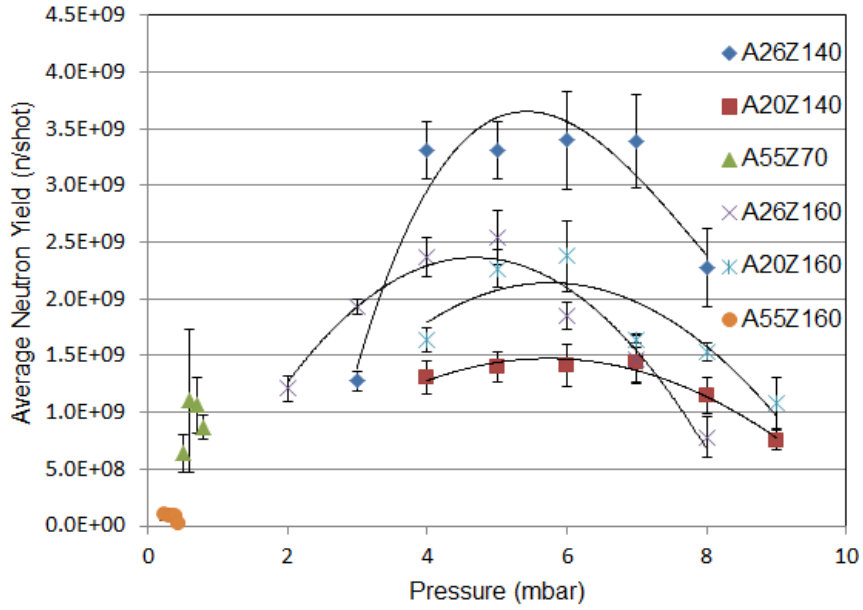

FIG. 6. Average neutron yield for different electrode assembly configurations at 14 kV charging for different D_2 gas filling pressures.

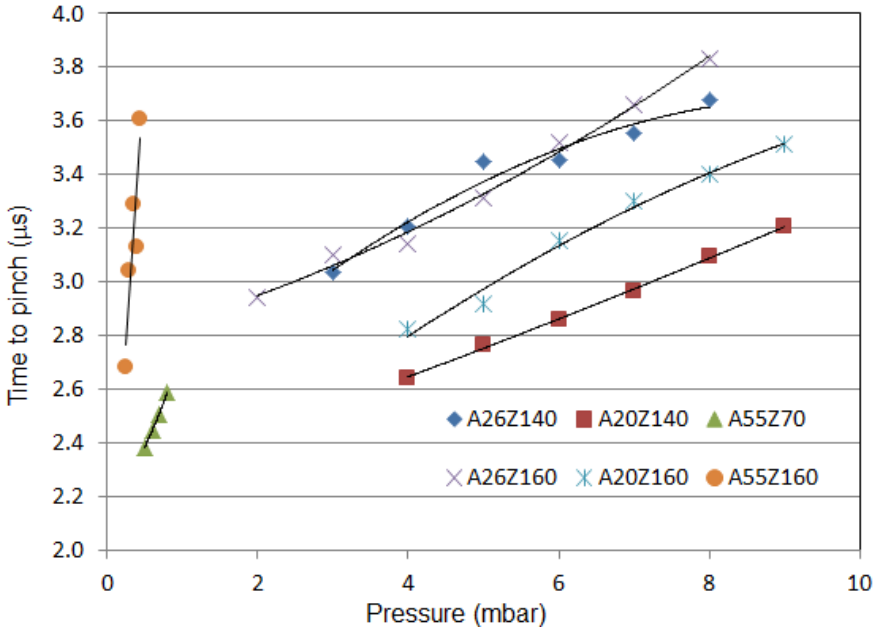

FIG. 7. Average time to pinch for different electrode assembly configurations at 14 kV charging for different D_2 gas filling.

However, for the electrode configuration A55Z160 even though the time to pinch in the similar range was obtained for some of the operating pressures, refer Fig. 7, but the neutron yield was relatively low whereas A55Z70 had relatively low time to pinch between 2.4–2.6 µs but the average neutron yield was significantly better. This further emphasizes that the rule for neutron yield optimization is not unique or simple but it is rather a complex mix of few interdepending variables such as the one in speed factor [1]. To gain the better understanding of the trends of neutron yields for different electrode assembly configurations the corresponding speed factors, *s*, were investigated. The average neutron yield is plotted as a function of speed factor in Fig. 8.

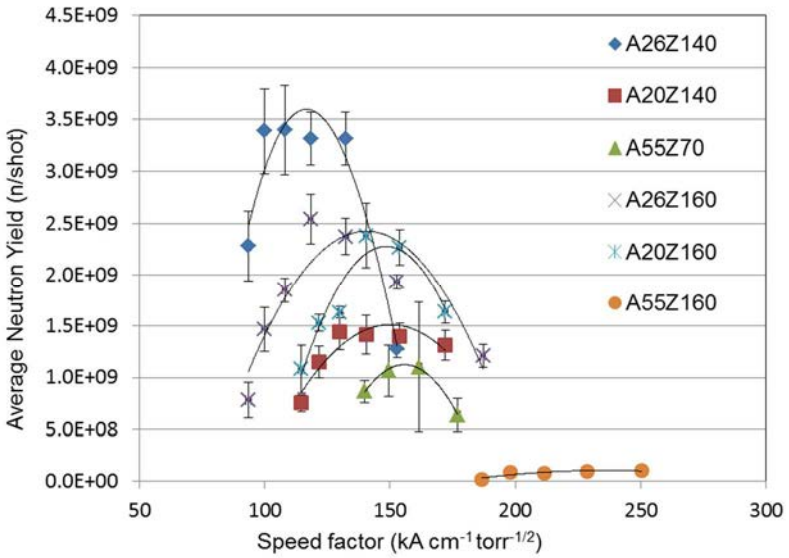

FIG. 8. Average neutron yield as function of speed factor for different electrode assembly configurations at 14 kV. The band shows the range of typical values of speed factor for neutron optimized devices [1].

The speed factor, $s = (I_0/a)/\sqrt{p}$, is calculated using $I_0 = 600$ kA (the peak discharge current at 14 kV charging voltage), the anode radius, *a,* of the given electrode assembly configuration, and the pressure *P* as the experimentally measured filling gas pressure of deuterium (converted in Torr). According to Lee and Serban [1], most of the neutron optimized plasma focus devices have the typical speed factor value of about 89 ± 8 kA · cm^{-1} · Torr$^{-1/2}$, depicted by a band in Fig. 8. This figure shows that for all electrode assembly configurations the values of speed factor was mostly higher than the typical value for neutron optimized devices. The configuration A26Z140 with highest neutron yield had speed factor ranging from about 94 to 153 kA · cm^{-1} · Torr$^{-1/2}$ while the configuration A55Z160 with lowest neutron yield had very high speed factors in the range from 187 to 250 kA · cm^{-1} · Torr$^{-1/2}$. It is remarkable to note that lower is the deviation in value of the speed factor from the reported typical value for neutron optimized focus devices the higher is the average neutron yield from the NX3 device. This highlights the reliability of the speed factor as the guiding rule for neutron yield optimization in plasma focus device.

3.2. Experiment 2: irradiation of locally procured commercial tungsten (C-W) samples using UNU-ICTP plasma focus device

Since NX3 was used for the first time, the neutron emission characteristics of NX3 were evaluated to maximize its neutron yield by doing optimization studies discussed above. While neutron optimization studies in NX3 were being conducted and also as we were waiting for PLANSEE double forget tungsten (PDF-W) samples to be delivered to us from Julich via the IAEA, the locally procured tungsten were irradiated in UNU-ICPT PFF [7] using different number of shots to gain initial experience. In this section we will discuss the experiments and results related to that.

3.2.1. Irradiation experiment details and ion emission characteristics of UNU-ICTP PFF

The locally procured commercial tungsten (C-W) samples of 10 mm × 8 mm × 5 mm dimensions were mechanically polished and later cleaned with acetone, alcohol and deionized water, in that order for 10 minutes each, in ultrasonic water bath. The samples are then placed above the anode top at 5 cm axial position with the help of an axially moveable holder and are irradiated for multiple numbers of (5, 10, and 15) focus shots. The plasma focus device was operated at 14 kV with hydrogen as the filling gas. Earlier, Jiaji et al [8] have used Faraday cup to investigate the hydrogen ions emitted from plasma focus device. The pulsed duration of highly energetic H^+ ions from plasma focus device was estimated to be in the order of few hundred ns. The ion energy of H^+ ions in plasma focus device was found to be in the range from 35 keV to 1.5 MeV range. Following the method reported by Sanchez et al. [9], the total number of ions passing through a 0.5 mm diameter pinhole placed at 10 cm above the anode, with energy in the range from 35 keV to 1.5 MeV, was estimated to be about 1.29×10^{11} with a mean energy of 124 keV per ion. The ion flux at 5 cm was therefore estimated to be 2.63 ×

10^{14} ions/cm^2. The irradiated and virgin samples so far have been analyzed by X ray diffractometer (XRD) for their structure and field emission scanning electron microscope (FESEM) for their surface morphology.

3.2.2. Results and discussion of irradiation of C-W samples in UNU-ICTP PFF

The FESEM images of the virgin and irradiated samples are shown in Fig. 9. The virgin mechanically polished sample in Fig. 9(a) shows the rough surface but as such does not show any nanostructure formation. The surface shows mechanical polishing marks along a particular orientation and has other irregular features. The 5 shot irradiation of tungsten sample, in Fig. 9(b), shows the smoothening of the surface which is due to surface reconstruction because of the transient processing in plasma focus device. The intense transient phenomena which include pulsed energetic ion beams, pulsed hot and dense decaying plasma, fast strong shock and ionization wave-front impart a very complex and high energy density plasma wind on the exposed sample surface. This results in strong thermal effect on the exposed material surface due to extremely high temperature rise rate followed by rapid quenching which rapidly process the exposed material to bring out the changes in their several physical properties and compositional characteristics. The careful look at the background in Fig. 9(b) shows that there are already nanoparticles that are formed in the background. This can clearly be seen in samples processed with 10 and 15 focus shots and are shown in Figs 9(c) and (d). Fig. 9(c) shows the formation of nanoparticles on the irradiated surface with particle size of about 1520 nm. The nanoparticles are also seen to agglomerate resulting in the formation of particle agglomerates with size varying from 100 to 300 nm. The sample irradiated with 15 shots, refer Fig. 9(d), shows mostly particle agglomerates with the further increase in their size to about 200–800 nm. It may however be noted that these big size particle agglomerates are made up of nanoparticles with nanoparticles size varying from about 40 to 60 nm. The increase in nanoparticle and particle agglomerate size with greater number of irradiation shots can be attributed enhanced transient thermal treatment of the sample surface.

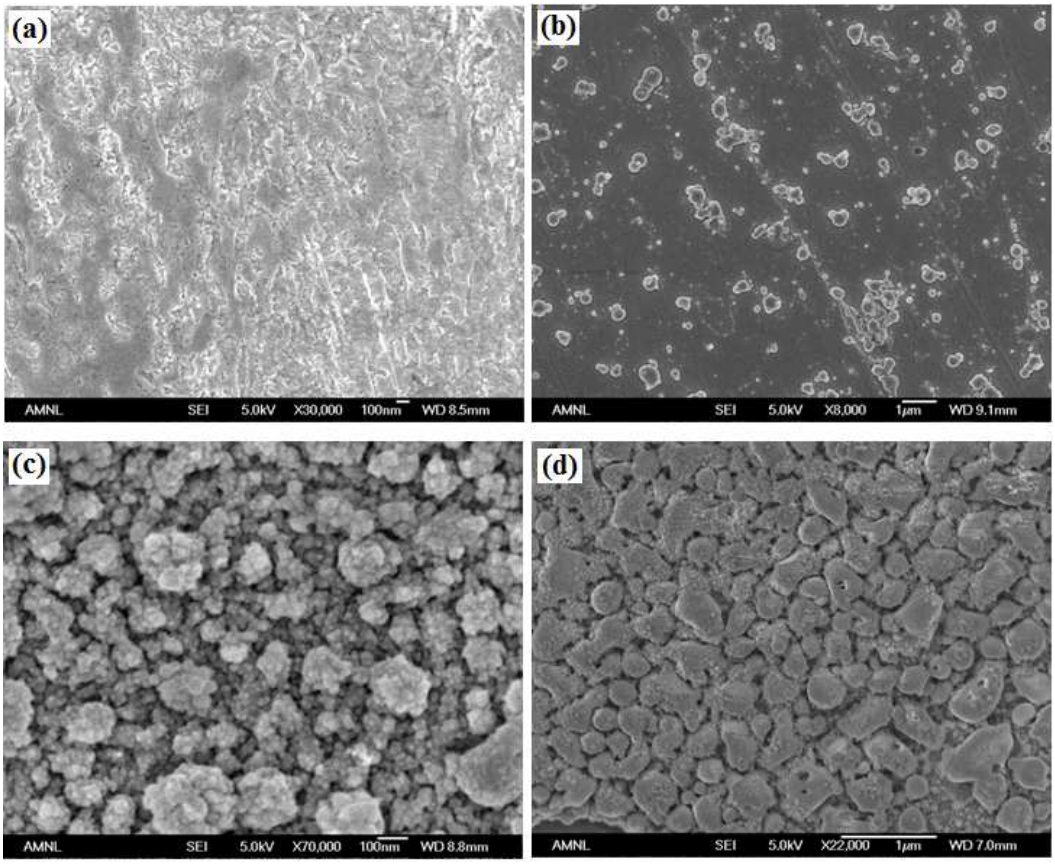

FIG. 9. (a) FESEM images of virgin C-W sample; (b) C-W samples irradiated using 5 shots in UNU-ICTP PFF; (c) C-W samples irradiated using 10 shots in UNU-ICTP PFF; (d) C-W samples irradiated using 15 shots in UNU-ICTP PFF.

The XRD patterns of the virgin and irradiated sample are shown in Fig. 10. The XRD pattern of virgin (unexposed) sample shows the diffraction peaks corresponding to tungsten at 2θ values of 40.47°, 58.45° and 73.29° corresponding (110), (200) and (211) planes.

All these peaks correspond to body centered cubic phase of pure tungsten. No impurity, tungsten oxide, phase is seen to occur on this sample which indicated that mechanical polishing might have efficiently removed any oxide layer that might have been formed on the sample surface after prolonged exposure. The samples irradiated using 5, 10 and 15 focus shots show the same above-mentioned tungsten peaks, however they also exhibit an additional peak at $2\theta = 43.45°$. This additional peak matches with the diffraction peak of tungsten oxide as well as copper. We hypothesize that since the irradiation of the samples has resulted in the nanostructurization of the surface resulting in significant enhancement in the total surface area and hence greatly increasing the surface oxidation of the sample upon its exposure to atmosphere. However, as we note that the nanoparticle and nanoparticle agglomerate size increases with the increase in the number of irradiation shots then in that case we would expect the decrease in the surface oxidation as the available surface area would have decreased. The XRD results, however, shows the continuous increase in the diffraction peak at 43.45°. This indicates that there should be a strong contribution from copper impurities. The copper impurities are contributed by the ablation of hollow copper anode rim by hot dense plasma and energetic electron beam. The increase in number of irradiation shots will result in greater accumulation of copper impurities and hence may result in increase in diffraction peak intensity

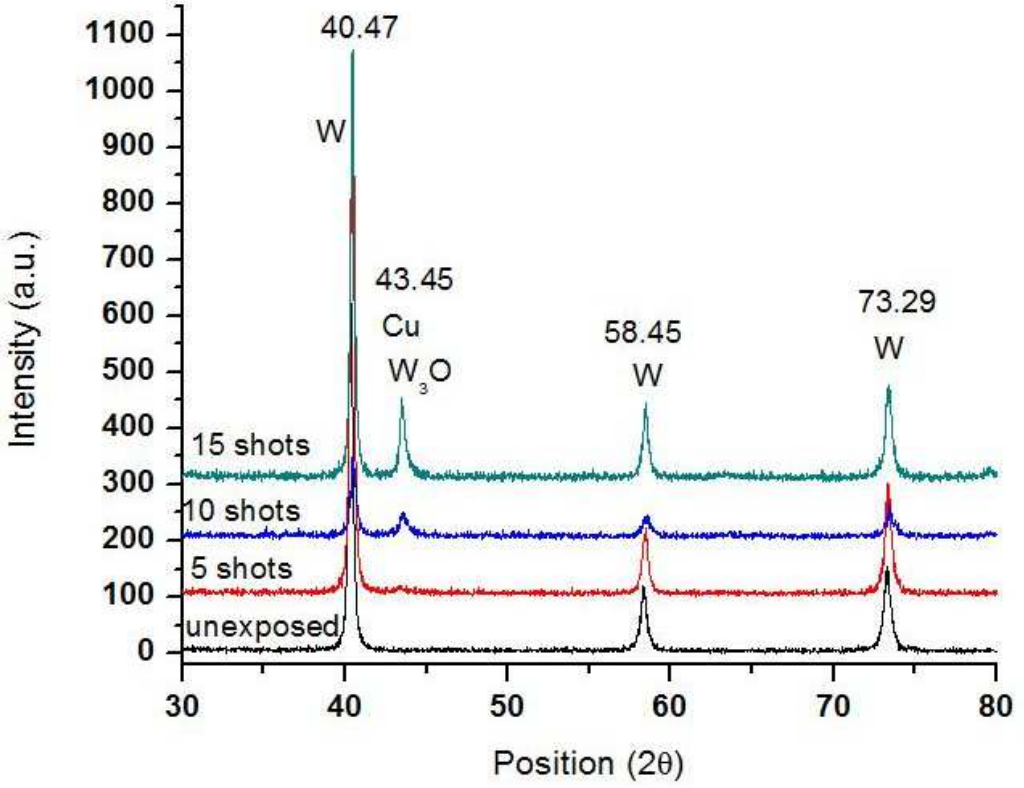

FIG. 10. The XRD patterns of unexposed and irradiated samples.

Moreover, the hardness measurements using nano-indentenor for different load for unexposed and irradiated samples are shown in Fig. 11. It shows that that unexposed sample has highest surface hardness of 10–40 GPa for different load and the hardness drops and stabilizes between 6–8 GPa at the depth of about 600 nm and above. For 5 shot irradiation the surface hardness was found to decrease to 2–10 GPa (mostly < 4 GPa) and then the hardness mostly increases as indentation depth increases which point a very thin copper impurity layer on surface of the irradiated sample. The hardness initially increases as indent penetrates from surface copper layer at the sample surface to tungsten and then stabilizes. For 15 shot irradiation the copper layer might be thicker and that is why the hardness initially decreases before it starts to increase again.

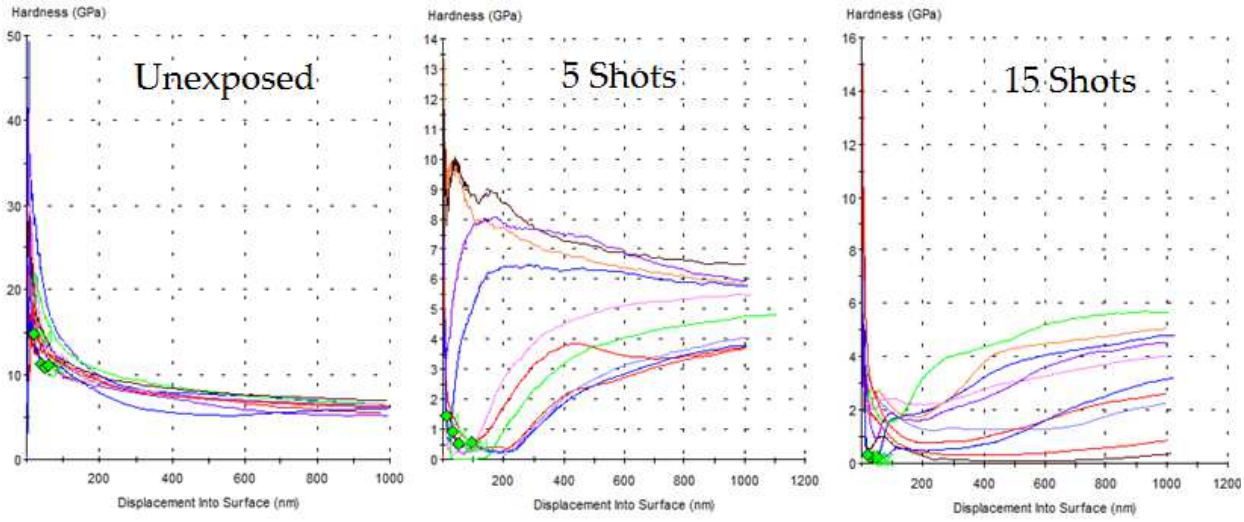

FIG. 11. Hardness measurements on unexposed and irradiated sample surface.

In conclusion, initial experiments on irradiation of locally procured tungsten sample do exhibit the remarkable change in the morphological properties in terms of the sample surface being reconstructed with nanoscale feature appearing on processed sample. The structural property analysis using XRD indicate the formation of additional impurity phase on the irradiated samples.

3.3. Experiment 3: irradiation of PLANSEE double forged tungsten (PDF-W) samples using NX3 plasma focus device

Five PDF-W samples, received from Julich via the IAEA, were having numbers 17, 21, 44, 46 and 92 written on them; so these samples are hence forth referred as W-17, W-21, W-44, W-46 and W-92. These samples were about 12 mm × 12 mm × 5 mm in size. These samples were extensively analyzed before and after exposure to NX3 plasma focus device.

3.3.1. Characterization of virgin (unexposed) PDF-W samples

The virgin PDF-W samples were analyzed using SEM, EDX, XRD and XPS. The SEM images of all 5 virgin/unexposed samples at two different magnifications of × 250 and × 10000 are shown in Fig. 12. At lower magnifications, the surfaces seems to be smooth however at higher magnification one can easily observed crisscross marks of mechanical polishing. The other two samples, not shown here, also have similar surface morphologies with only polishing marks and no other interesting features.

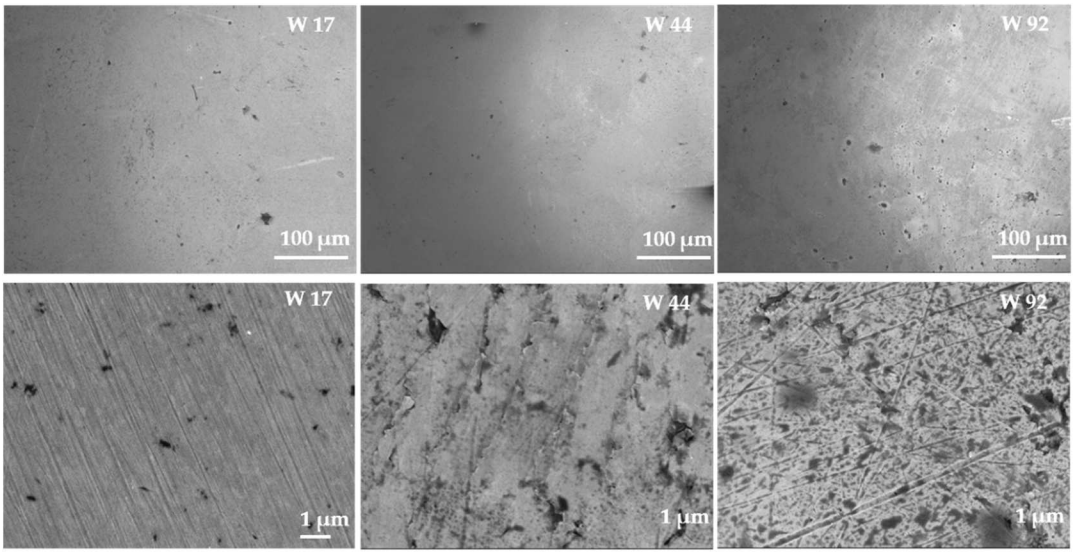

FIG. 12. SEM image three (W-17, W-44 and W-92) virgin samples at two different magnifications. Upper row is at × 250 magnification while the lower one is at × 10000.

Fig. 13 shows the sample surface along with corresponding EDX spectrum for two of the samples (W-17 and W-44). In order to obtain the gross chemical composition of these sample surface EDX was performed at low magnification. The pink color box rectangle on the SEM images demarcates the area over which the broad area EDX scan was performed to get the overall composition of the sample surface. Both samples exhibit identical chemical composition of the sample surface with atomic percentage of W being 100% on both of them. Thus the EDX did not show any oxide layer formation or any other impurity on sample surfaces. Similar results were obtained for all other samples whose EDX spectra are not included in Fig. 13.

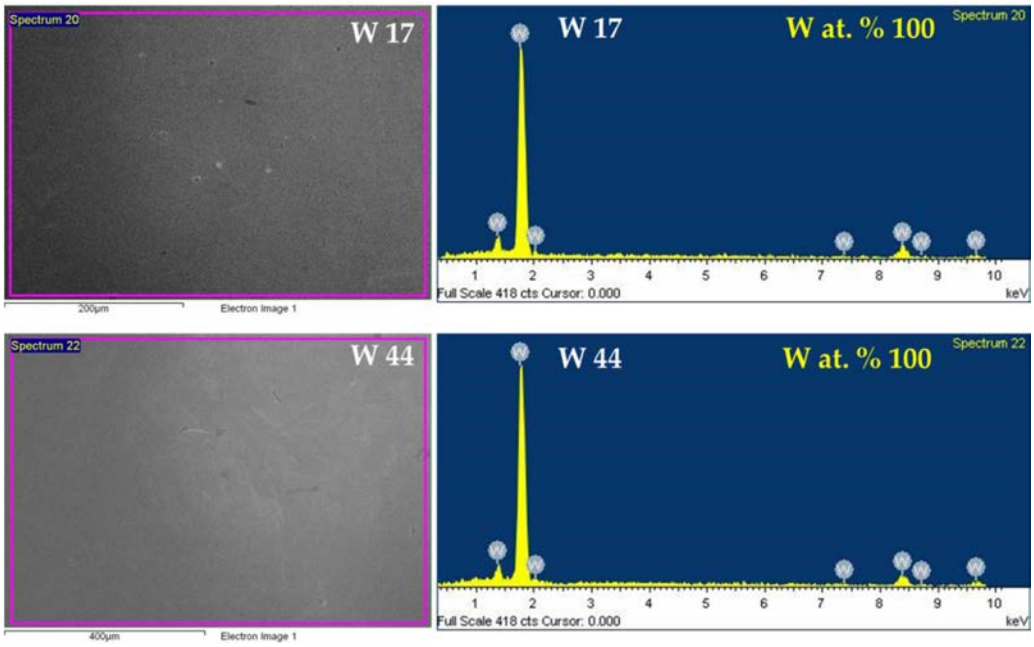

FIG. 13. Broad area EDX scan for two of the unexposed samples, sample W-17 and W-44.

It is expected that oxide layer, if any, on virgin PDF-W samples should be quite thin with relatively smaller amount of oxygen and that is why it is not observed in EDX analysis whose sensitivity is rather limited. In order to find the composition and the elemental oxidation states on sample surface, we performed the XPS analysis of W-17 and W-44 samples whose EDX was shown in Fig. 13. The W 4f core level XPS spectra of W-17 and W-44 are shown in Fig. 14 which reveals the presence of tungsten in its different oxidation states.

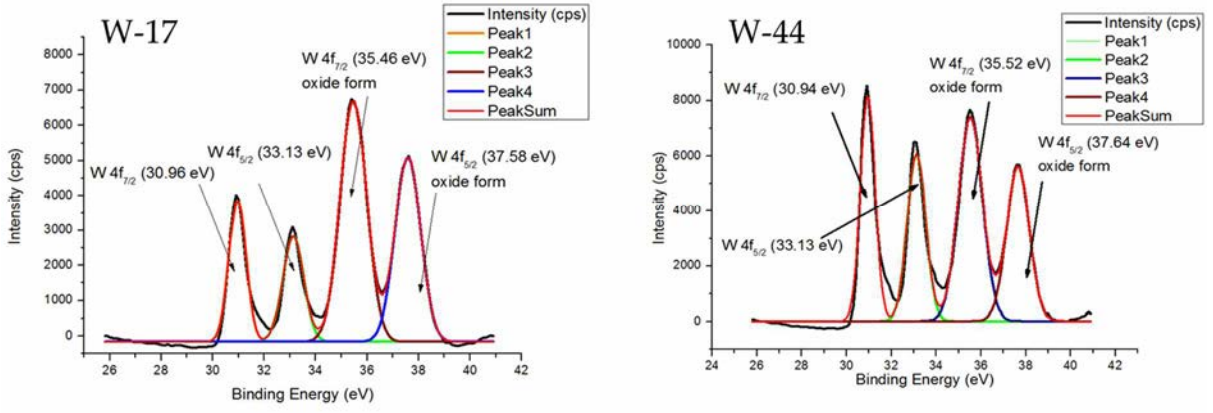

FIG. 14. W 4f core level XPS spectra of W-17 and W-44.

The relative concentration of oxide form of tungsten was estimated using the relative area under the curves of different peaks. For sample W-17, most of the tungsten was found in the oxide form with the relative concentration of 40.6% and 29.9 % for $W_{7/2}$ and $W_{5/2}$ core level peaks respectively which correspond to oxide forms. The contribution from the core level XPS peaks of elemental $W_{7/2}$ and $W_{5/2}$ was only 15.3 and 14.0 % respectively. Therefore for this sample about 70% of tungsten on surface is in oxide form. Similarly, for sample W-44 tungsten in the oxide form was found with the relative concentration of 33.23% and 23.68 % for $W_{7/2}$ and $W_{5/2}$ core level peaks respectively; whereas the contribution from elemental core level peaks of $W_{7/2}$ and $W_{5/2}$ was slighter higher at 22.33 and 20.74 % respectively. But still the tungsten in oxide form dominated over the elemental tungsten even for this sample. Hence it can be concluded from XPS analysis that most of the sample surfaces were heavily oxidized.

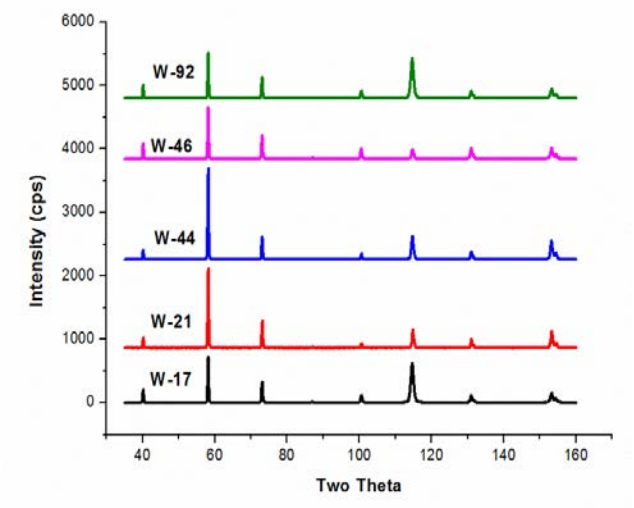

FIG. 15. XRD patterns of all five virgin/unexposed PDF-W samples.

Crystalline quality of the tungsten samples was studied using X ray diffraction analysis. From Fig. 15 it is evident that the different samples have different diffraction peak intensities and accordingly different crystalline qualities. We specifically study the crystalline behavior of the samples W-17 and W-44 for which we have done the XPS analysis. W-44 sample reveals the maximum diffraction peak intensity among all the samples under investigation. We have done the XPS analysis for W-17 which has the similar diffraction peak intensities with W-46 and W-92. The reduced concentration of diffraction peak intensity for W-17 can be attributed to the presence of oxide form of tungsten (~70%), as is estimated through our XPS results which might have affected the crystalline quality of tungsten. It may be noted that all peaks correspond to bcc-phase of metallic tungsten and no peak corresponding to tungsten oxide is observed.

3.3.2. Irradiation of PDF-W samples in NX3 plasma focus device: results and discussion

The NX3 plasma focus device, driven by a 100 μF, 20 kJ modular capacitor bank, delivers peak current in the range from 200 to 600 kA depending upon charging voltage. The quarter cycle of discharge is ~ 3 μs. On the basis of Lee Code estimations and experimental iterations, the finally optimized coaxial electrode assembly, A26Z140, of the NX3 plasma focus head consisting of a 140 mm long, cylindrical anode of SS having diameter of 52 mm and a squirrel cage cathode, consisting of twelve, 12 mm diameter brass rods, uniformly spaced on a coaxial circle of 90 mm diameter was used for irradiation experiment. Since, hollow anode structures have been reported to produce higher neutron yields with better stability of the pinched plasma, in comparison with solid anodes, and also to reduce the ablation of anode material by backward hot dense plasma and relativistic electron beam the 30 mm deep anode cavity was extended to 110 mm at the center of anode; as shown in Fig. 16. An aluminum double aperture with 1 cm aperture size is used to reduce the anode material from reaching the irradiated PDF-W sample surface. The PDF-W samples were irradiated at 10 kJ energy storage and different irradiation distances of 5, 10, 15 and 20 cm using 50 NX3 focus shots with deuterium as the filling gas. So the PDF-W samples were not only irradiated to hot-dense decaying plasma and instability acceleration ion beams but also to 2.45 MeV fusion neutrons.

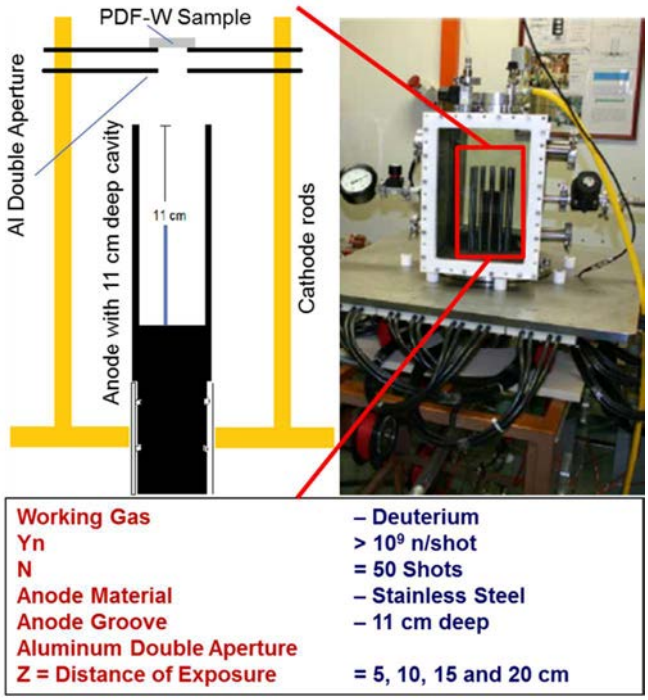

FIG. 16. Irradiation set-up and experimental parameters in NX3 plasma focus device.

Table 4 provide the sample identification and its irradiation distance while keeping all other irradiation parameters such as charging voltage, operating gas, gas pressure and number of focus irradiation shot (at 50 shots) fixed.

TABLE. 4. SAMPLE IDENTIFICATION NUMBER AND IRRADIATION DISTANCE FROM ANODE TOP

Sample Identification Number	Irradiation Distance from Anode Top
Wx-46	20 cm
Wx-92	15 cm
Wx-21	10 cm
Wx-44	5 cm

The sample surface size of each PDF-W sample was about 12 mm × 12 mm and the exposed/irradiated area (limited by double aperture assembly) was about 10 mm; shown by circle in Fig. 16. The SEM and EDX analysis was performed at 4 different locations on each of the samples; which are firstly at about the center of the circular irradiated zone and then at three more locations at the distance of approximately 2, 4 and 6 mm from the center in radially outward direction as shown in Fig. 17; the light blue circle in the center represent the irradiated part.

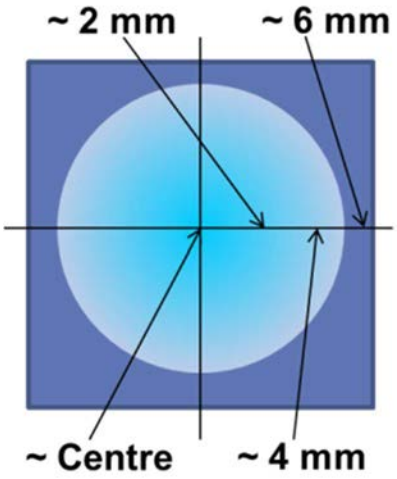

FIG. 17. Locations of positions on irradiated samples where SEM and EDX analysis were perfomed.

The SEM images, EDX spectra and EDX micro-analysis for Wx-47 sample exposed to 50 NX3 plasma focus shots at irradiation distance of 20 cm anode top and taken at four different locations (approximately at center and at about 2, 4 and 6 mm from center) of irradiated circular zone of are shown in Fig. 18. For detailed morphological studies the SEM images were taken at many different magnifications, however we only show the images at the magnifications of × 20000 (for images taken at center and 2 and 4 mm from center) and × 7500 for outermost location of 6 mm from center. The SEM images at lower magnifications (not included here) show varied features ranging from cracks, droplets, craters etc. on the irradiated surface at different locations. The extent of variation in surface features is highest in SEM images taken at central position and then it decreases as the observation location is moved radially outwards with almost negligible changes at location of 6 mm from center. The stronger variation in surface features is due to the higher deposition of anode and aperture ablated material at central location rather than due to the degradation of the irradiated surface by fast energetic ions and hot decaying plasma stream.

The EDX analysis shows the presence of Al, Fe, Cr, and O at the central position. No W was observed in EDX spectrum at this central position (Fig. 18). This means that W substrate surface is covered by material ablated from the anode (Fe and Cr from SS anode) and double aperture assembly (Al). Moreover, Fe and Al can be easily oxidized by atmospheric oxygen when the sample is removed from the chamber which is confirmed by presence of large amount of oxygen in EDX microanalysis.

The situation remain similar at 2 mm from center as only impurities contributed from anode, aperture and double sided tape (used for mounting sample) were observed. It is only at 4 mm position some W can be seen which is due to the fact that with increasing angular position the flux of ablated material will decrease. The outer most position of 6 mm (very close to the edge of the substrate) shows only W, as it was probably covered by the aperture. Also the surface features at 6 mm from center were very similar to unexposed sample, as one can observe the polishing scratch marks, indicating there by that this part was probably covered by the aperture not allowing it to be processed by energetic ions and energetic hot decaying plasma keeping its surface feature mostly intact.

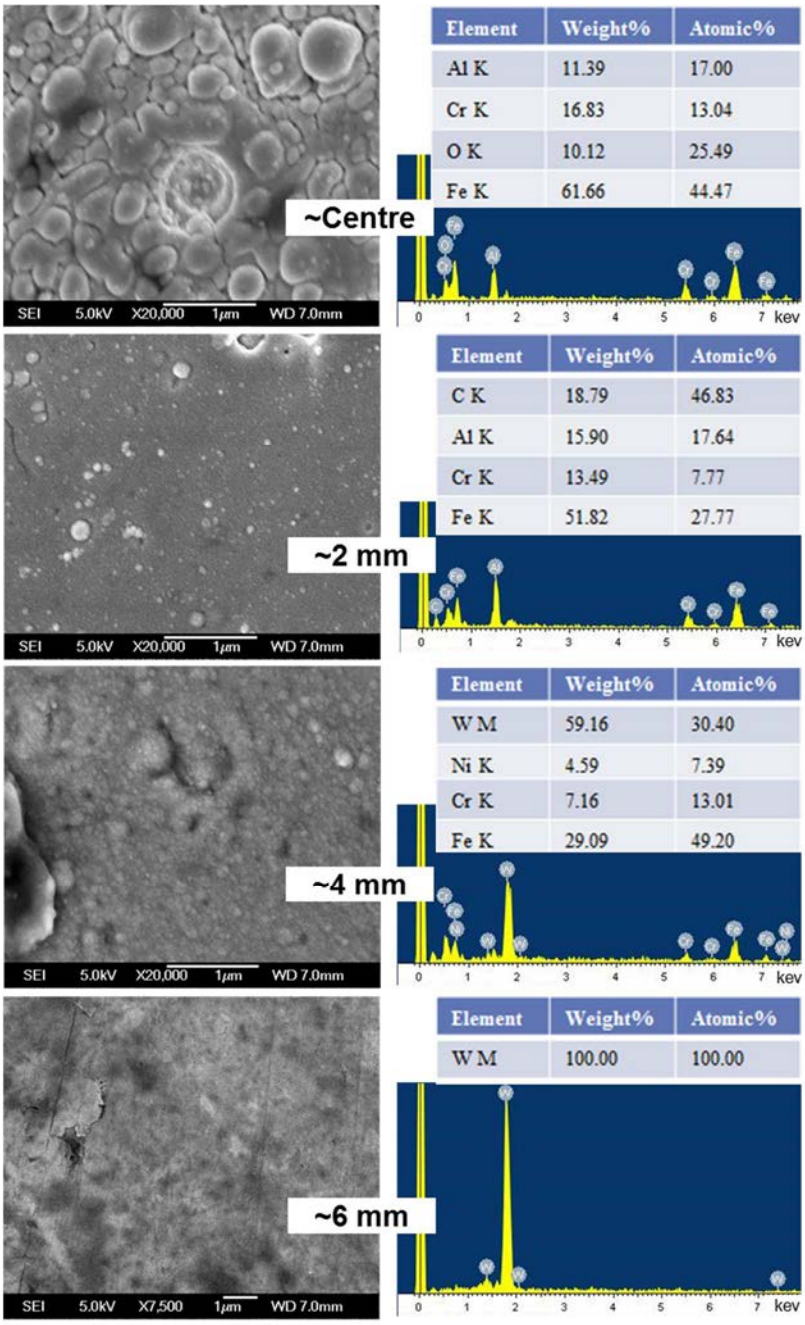

FIG. 18. The SEM images, EDX spectra and EDX microanalysis for Wx-47 sample, exposed at irradiation distance of 20 cm from anode top, at four different locations of approximately centre and about 2, 4 and 6 mm from centre of irradiated circular zone as shown in Fig. 17.

The SEM images and EDX micro-analysis results for samples Wx-92 and Wx-21 exposed to 50 NX3 plasma focus shots at irradiation distance of 15 and 10 cm from anode top respectively and taken at four different locations (approximately at center and about 2, 4 and 6 mm from center) of irradiated circular zone of are shown in Figs 19 and 20, respectively.

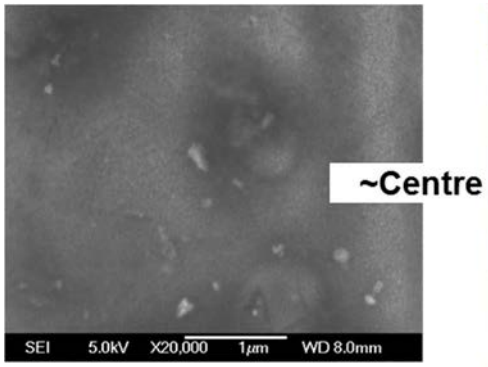

Element	Weight%	Atomic%
Al K	18.44	12.20
C K	41.26	61.30
Si K	2.62	1.66
O K	15.94	17.78
Fe K	16.81	5.37
Cr K	4.93	1.69

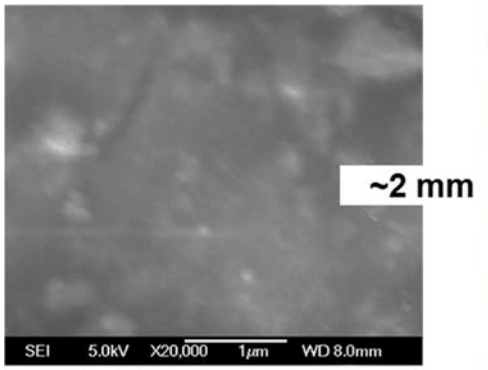

Element	Weight%	Atomic%
Al K	19.51	12.35
C K	45.33	64.44
Si K	3.12	1.90
O K	15.02	16.03
Fe K	13.43	4.10
Cr K	3.59	1.18

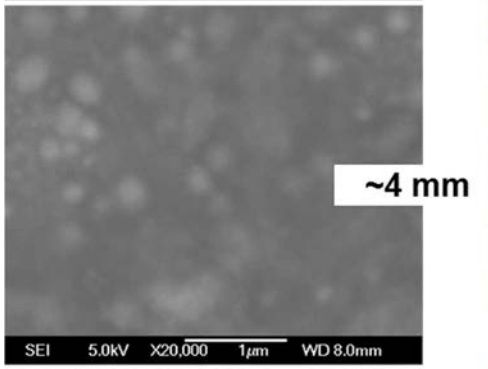

Element	Weight%	Atomic%
Al K	14.85	9.85
C K	42.88	63.93
Si K	3.05	1.94
O K	14.48	16.21
Fe K	18.83	6.04
Cr K	5.91	2.04

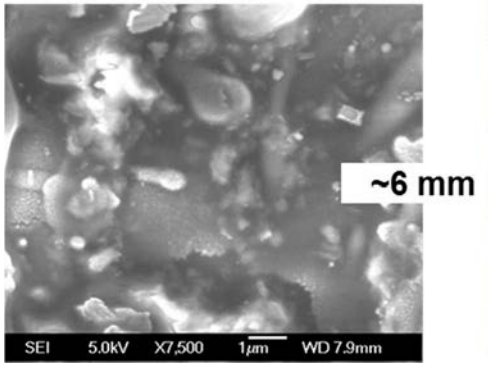

Element	Weight%	Atomic%
Al K	14.02	12.42
C K	29.50	58.71
Si K	3.05	1.94
O K	12.05	18.00
Fe K	13.14	5.62
Cr K	3.57	1.64
W M	27.71	3.60

FIG. 19. The SEM images and EDX microanalysis for Wx-92 sample, exposed at irradiation distance of 15 cm from anode top, at four different locations of approximately centre and about 2, 4 and 6 mm from centre of irradiated circular zone as shown in Fig. 17.

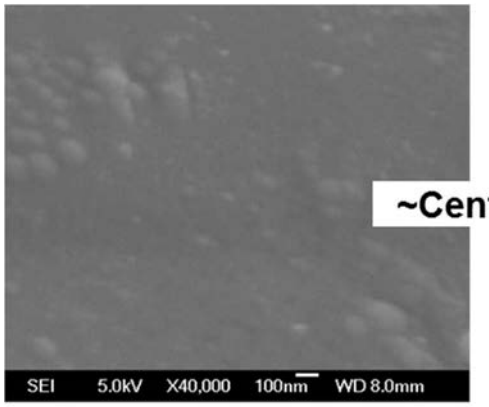

Element	Weight%	Atomic%
Al K	66.16	69.50
O K	10.54	18.68
Fe K	23.29	11.82

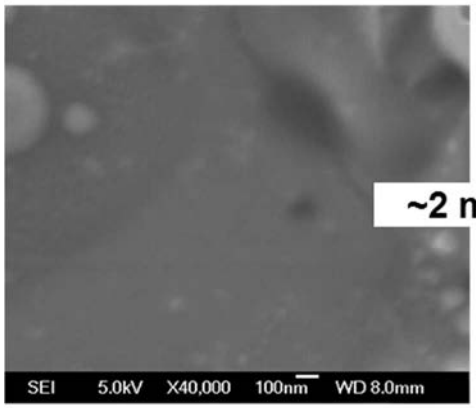

Element	Weight%	Atomic%
Al K	50.91	64.87
O K	10.04	21.58
W M	24.48	4.58
Fe K	14.57	8.97

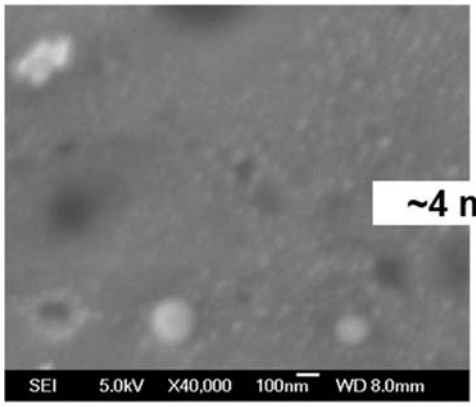

Element	Weight%	Atomic%
Al K	25.32	19.89
C K	34.85	61.49
O K	7.20	9.54
W M	13.02	1.50
Fe K	15.00	5.69
Cr K	4.61	1.88

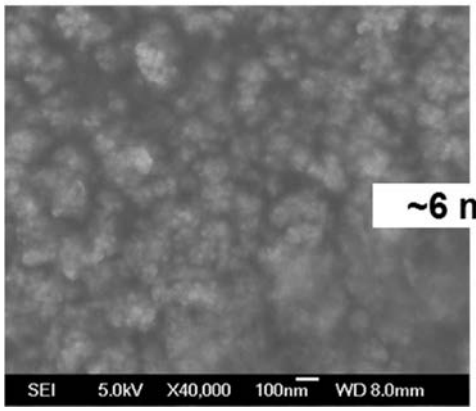

Element	Weight%	Atomic%
Al K	1.25	1.47
C K	21.16	56.18
O K	15.87	31.63
W M	61.73	10.71

FIG. 20. The SEM images and EDX microanalysis for Wx-21 sample, exposed at irradiation distance of 10 cm from anode top, at four different locations of approximately centre and about 2, 4 and 6 mm from centre of irradiated circular zone as shown in Fig. 17.

The SEM images in both Figs 19 and 20 show that the trend has reversed and the surface features are smoother at the central position and get coarser as one move radially outward from the center. The lowering of irradiation distance leads to higher energy flux being delivered at the substrate surface which may lead to higher mobility of the deposited surface atoms leading to smoother surface. However, as the energy flux is expected to decrease in radial direction (as energetic ions are highly forward directed) resulting in lesser mobility of surface atoms and hence surface will become coarse, as observed. The EDX microanalysis once again shows the strong presence of Al and Fe and also Cr pointing to deposition of material being ablated from SS anode and aluminium double aperture. Oxygen presence once again point to oxidation of Al, Fe and Cr metal nanoparticles by air. Another important feature to note is the very large atomic % of carbon at all locations on irradiated Wx-92 sample and outer positions on sample Wx-21. The decrease in irradiation distance and use of large number of focus shots (50) might have resulted in significant increase in temperature of irradiated sample as well as that of double aperture assembly leading much higher carbon being contributed from double sided tape that was used to stick the PDF-W sample to the double aperture assembly. Once again no W was observed in at center, 2 mm and 4 mm position for Wx-92 sample surface indicating that PDF-W samples gets covered by material ablated from the anode, double aperture assembly and double sided tape.

For sample Wx-21, which is irradiated at smaller distance of 10 cm, the W is observed at most locations except at center, see Fig. 20. This is quite puzzling as with the decrease in irradiation distance there should be higher deposition of anode and aperture ablated material and hence the sample should rather be covered with more of ablated material and the chances of W being observed should be lesser. This observation however can be explained on the basis of ablation of W material itself by energetic ion beam. It is well known that ablation resistance of W is much better compared to that of SS and aluminium and hence as higher irradiation distance (20 and 15 cm in present case) it is very difficult to ablate the W from the irradiated PDF-W substrate as the ion energy flux as well as the hot dense decaying plasma flux at higher distance of exposure is low. However, at low distance of irradiation the enhanced energy flux of instability accelerated ions as well as hot dense decaying plasma is much higher and probably leads to ablation of W from PDF-W sample which gets re-deposited on sample along with the material ablated or vaporized from SS anode, aluminium double aperture and double sided tape leading to observation of W along with other materials for most locations on the surface of sample Wx-21. The relative abundance of Al, Fe, Cr, C (which are basically undesirable impurity elements here) as compared to that of W depends on relative ablation and deposition of impurity elements as compared to that of W which depend on the distance of irradiation.

On the next page, Fig. 21 presents the EDX spectra and microanalysis of sample Wx-44 irradiated at the distance of 5 cm from anode top for 50 NX3 focus shots. This time only the Al and C impurities contributed from aluminium double aperture and double sided tape are observed. For this sample the Fe/Cr from SS anode is not observed. The main reason for this is that double sided tape and aluminium are relatively softer materials compared to that of SS and W and hence due to reduced distance of irradiation their comparative ablation/vaporization was much higher which completely over shadowed other materials in the irradiated sample surface. This was also visible and apparent from almost very significant destructions of lower aluminium plate of double aperture assembly and melting of double sided tape.

The XRD spectra of samples Wx-46, Wx-21 and Wx-44 irradiated to 50 NX3 plasma focus shots at distances of 20, 10 and 5 cm, respectively, are shown in Fig. 22 along the XRD spectra of their corresponding virgin/unexposed samples. The impurity peaks (marked by triangle and arrow) can be seen on all irradiated samples. The non-marked peaks are that of W. The XRD spectra at most/higher distances of irradiation match well with that of bcc-phase tungsten while having additional peaks correspond to complex unidentified phases of impurities.

The amount of impurities contributed from ablated anode, aperture and mounting tape material continue to increase with the decrease in irradiation distance. The irradiation at lower distances also resulted in greater processing of deposited impurity material which caused additional impurity peak phases to appear in XRD results. The sample irradiated at 5 cm had relatively thicker coating of ablated impurity material which is indicated by the fact that the W peaks either disappeared or diminished.

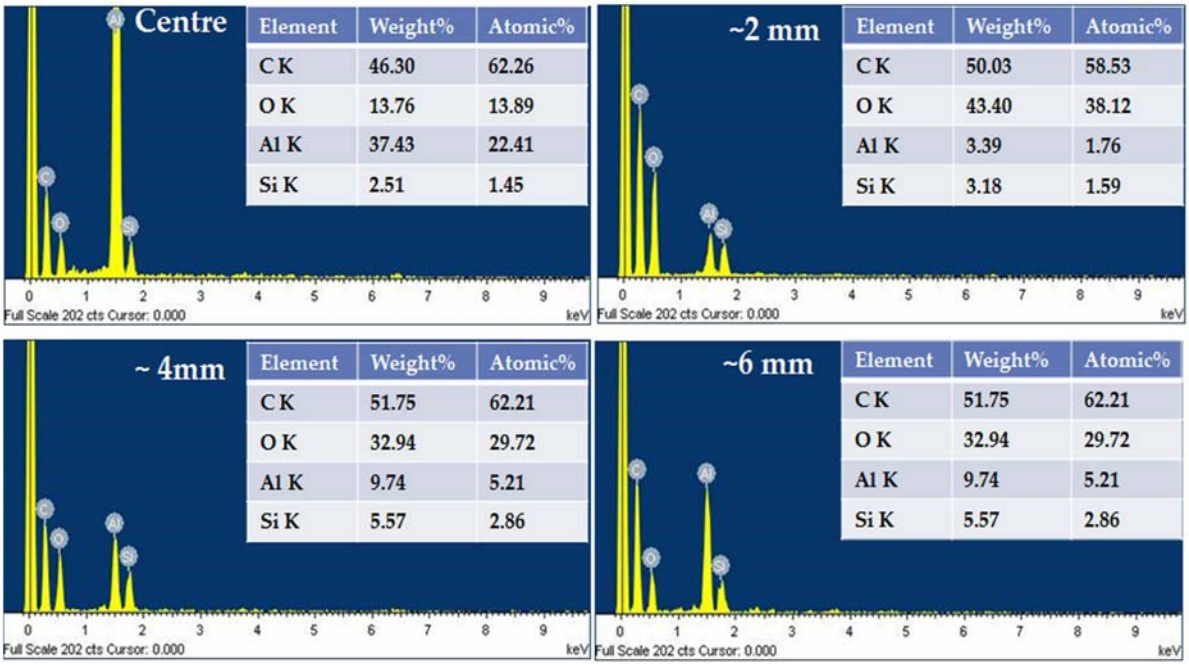

FIG. 21. The EDX spectra and EDX micro-analysis for Wx-44 sample, exposed at irradiation distance of 5 cm from anode top, at four different locations of approximately centre and about 2, 4 and 6 mm from centre of irradiated circular zone as shown in Fig. 17.

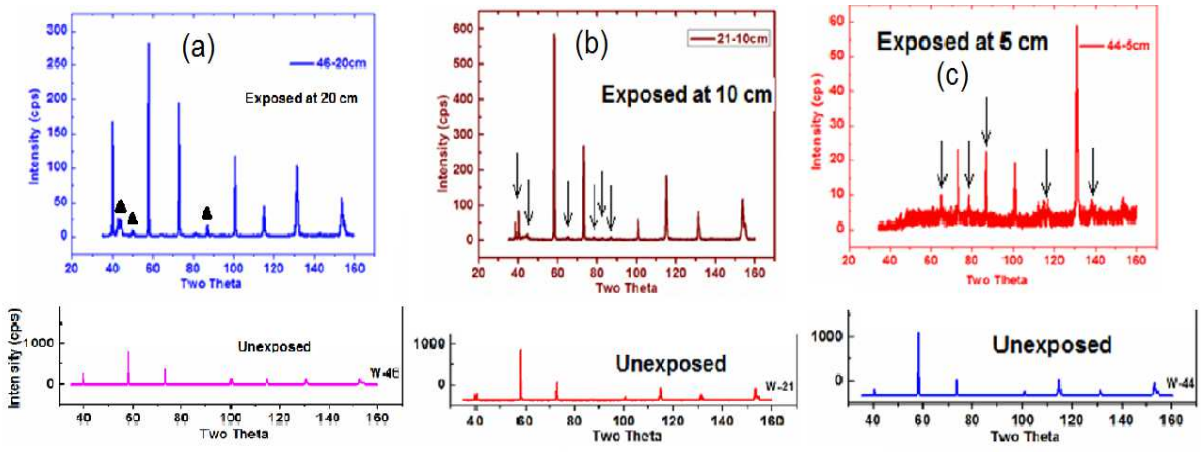

FIG. 22. XRD spectra of samples (a) Wx-46, (b) Wx-21 and (c) Wx-44 irradiated to 50 NX3 plasma focus shots at distances of 20, 10 and 5 cm, along with XRD spectra of their corresponding virgin/unexposed samples. The peaks marked with triangle and arrows are impurity peaks while other non-marked peaks are that of W.

3.4. Experiment 4: developing strategies for removal or minimization of impurity deposition on irradiated samples using silicon as substrate

The results of experiment 3 using 50 NX3 plasma focus shots on PDF-W samples showed the large amount of deposition of impurities from ablation or vaporization of SS anode, aluminum double aperture assembly and double sided tape on the irradiated samples. In order to develop strategies for removal or minimization of impurities next set of experiment was done using Si samples/substrate. Following steps were taken to remove/minimize impurities:

a) The use of double sided tape was removed for sample/substrate mounting.
b) UNU-ICTP plasma focus device was used with hollow copper anode and much thinner anode wall. The anode in UNU-ICTP device uses anode with much deeper groove (about 20 cm) which along with thinner anode wall is expected to reduce anode material impurities (Cu in this case) significantly.
c) Two sets of experiments were performed, irradiation experiment using double aperture assembly made up of bronze which is has much higher ablation threshold compared to aluminum and hence is expected to have lower amount of impurity ablation, and direct irradiation of sample/substrate without any use of aperture assembly.

The irradiation experiments were conducted at fixed charging voltage of 14.1 ± 0.1 kV of mid energy range UNU-ICTP plasma focus facility using 1, 5, 10 and 50 focus shots. The device was operated with hydrogen at filling gas pressure of 4 mbar and for multiple shot irradiation experiments the device was operated at 2 minute shot interval with gas being refreshed after every 5 shots. All irradiation were conducted anode to sample/substrate distance of 5 cm. As mentioned earlier, since the major aim of this activity was minimize or reduce the impurities on the sample being irradiated and hence the substrate used was easily available Si rather than expansive W. Each Si sample was cut to about 10 mm × 10 mm size and were cleaned sequentially in acetone, ethanol and de-ionized water for 10 minutes each in ultrasonic bath.

3.4.1. Irradiation of Si samples with bronze double aperture assembly

The SEM images of Si samples irradiated at fixed distance of 5 cm using 1, 5, 10 and 50 shots of UNU-ICTP plasma focus shots in the presence of bronze double aperture assembly are shown in Figs 23(a)–(d).

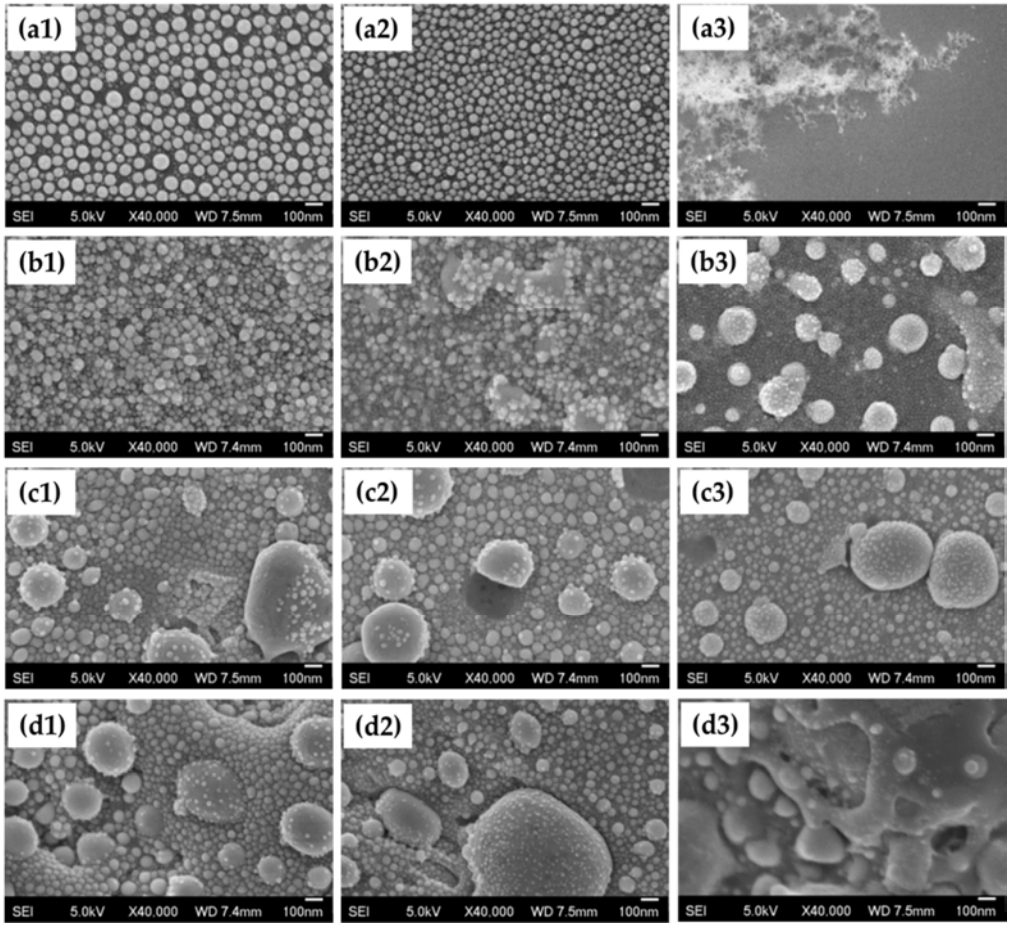

FIG. 23. (a) SEM images of Si samples irradiated at the distance of 5 cm from anode top using 1 UNU-ICTP focus shots in the presence of bronze double aperture assembly; (b) 5 focus shots; (c) 10 focus shots; (d) 50 focus shots.

The images shown in Fig. 23 represent the images taken as center, intermediate and corner position of the samples irradiated using different number of shots. The typical EDX spectra of irradiated Si samples are shown in Figs 23(a3) and 24, taken at corner position of sample irradiated with one shot, shows most part of the Si sample is similar to unexposed sample with most of the sample being clean with some scattered splash of nanoparticles at one side.

The images taken at central and intermediate (between center and corner) positions, shown in Fig. 23(a1) and (a2) respectively, show presence of well rounded nanoparticles which were bigger in size (from 40 to 90 nm) at center and slightly smaller (about 2050 nm) at intermediate positon. It may however be pointed that the presence of nanoparticles was not even distributed throughout the surface of irradiated sample rather they were in several scattered pockets but almost everywhere. The EDX area scan on a1 to a3, with typical one shown in Fig. 24(a), exhibit mainly the Si peak with negligible or very peak corresponding to Cu and/or Zn indicating that for one focus shot irradiation the amount of material ablated from bronze double aperture is less; but it may also be related to sensitivity of EDX. The presence of well defined nanoparticles on irradiated Si sample surface confirms that significant amount of material is ablated from bronze double aperture even in single shot exposure.

The EDX spectra shown if Figs 24(b)–(d) show that the amount of Cu and Zn increase while that of Si decreases with the increase in number of UNU-ICTP irradiation shots. The increase in Cu and Zn peaks intensity in EDX spectra with the increase in number of irradiation shots confirms the increasing amount of impurities ablated from bronze double aperture.

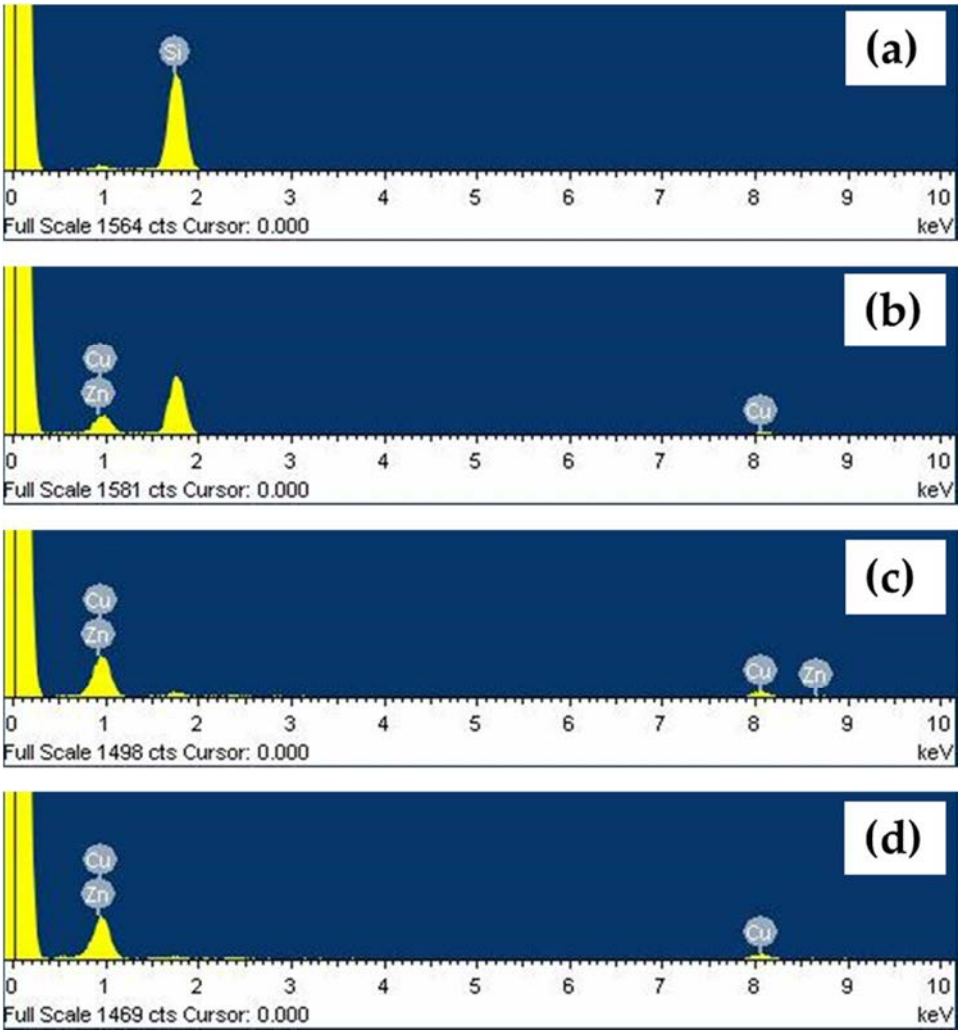

FIG. 24. (a) Typical EDX spectra of Si samples irradiated at the distance of 5 cm from the anode top using 1 UNU-ICTP focus shots in the presence of bronze double aperture assembly; (b) 5 focus shots; (c) 10 focus shots; (d) 50 focus shots.

Since all irradiation experiments were conducted at irradiation distance of 5 cm from anode top hence the bronze double aperture assembly was placed at about 2 cm from anode top. It is well known that if any obstruction is placed at the distance greater than the anode radius then it does not affect the pinching efficiency of the plasma focus device [10] and hence 2 cm distance was appropriate. However, as the distance of apertures assembly was small it was irradiated by very high energy flux from instability accelerated energetic ions and hot dense decaying plasma leading to ablation of aperture material. For 10 shot irradiation the amount of impurities, Cu and Zn from aperture, increased significantly leading to thicker coating of ablated impurity material on irradiated sample surface and hence the EDX peak corresponding to Si diminished substantially. No Si peak was observed on Fig. 24(d) indicating very thick coating of ablated impurity material for 50 shot irradiation. All this is also evident from SEM images as more and more ablated material can be seen to deposit on irradiated Si sample surface. Another noticeable feature on multiple shot irradiation, 10 and 50 shots, is the agglomeration of nanoparticles to form bigger sized agglomerate which can be attributed to the greater amount of energy being imparted to the material deposited on sample surface with increasing number of irradiation shots.

3.4.2. Irradiation of Si samples without any aperture assembly in between

The experiment performed with bronze double aperture assembly confirmed that the energy flux delivered by energetic ions and hot dense decaying plasma in plasma focus device was too strong to be handled by bronze and most impurities on irradiated sample surface were coming from the aperture which was initially placed to reduce the impurities from ablation of anode material. Hence, as the natural consequence we decided to do irradiation experiments in UNU-ICTP plasma focus device without any aperture assembly with a goal to determine how severe/significant is the impurity contribution from the anode material ablation which was the major concern at first place. The SEM images of Si samples irradiated at fixed distance of 5 cm using 1, 5, 10 and 50 shots of UNU-ICTP plasma focus shots, without using any aperture assembly, are shown in Fig. 25(a)–(d). The images shown in Fig. 25 represent the images taken as center, intermediate and corner positions of irradiated Si samples.

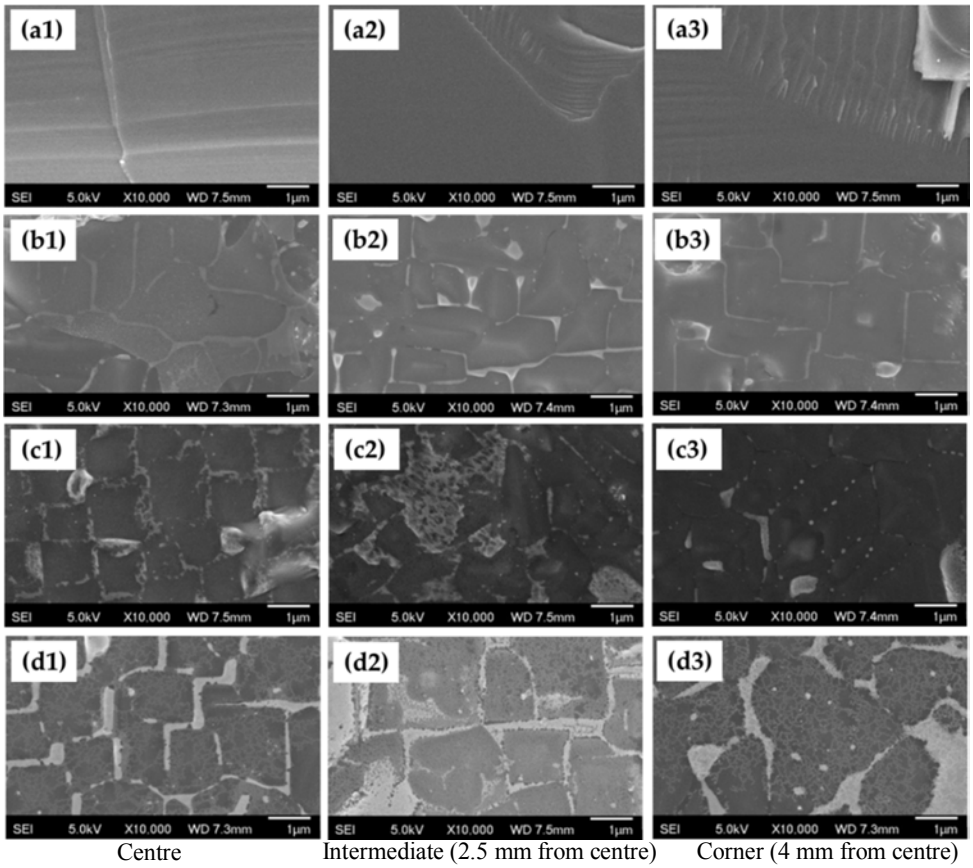

FIG. 25. (a) SEM images of Si samples irradiated at the distance of 5 cm from anode top using 1 UNU-ICTP focus shots with no aperature assembly being used; (b) 5 foucs shots; (c) 10 focus shots; (d) 50 focus shots.

The SEM images in Fig. 25 show entirely different morphology as compared to that of those shown in Fig. 23. No nanoparticles were seen to deposit on Si samples irradiated with 1 and 5 shots as can be seen in Fig. 25(a1) and (a2). The long linear structures seen on these surface are simple the cracks on Si surface caused by intense energy flux delivered by instability acceleration ions of filling gas (hydrogen in present case), hot dense decaying plasma and the shockwave due to shorter distance of exposure and non-usage of any aperture assembly. The number and density of cracks were found to increase with the increasing number of shots from 1 to 10; whereas for 50 shots some of the cracks appear to be covered by material ablated from anode. It can be noticed from Figs 25(c2) and 25(d1)–(d3) that these 4 SEM images are covered with circular shape nanoparticles, similar to that one seen in Figs 23(a) and (b). The nanoparticles are seen to form linear network chain like structure i.e. the particles are isolated (non-agglomerated) with background Si surface still being visible. Hence, the SEM images shown in Fig. 25 reveal that there is no sign of ablated impurity material on samples irradiated with 1 and 5 shots; there is very small amount of anode ablated material on sample irradiated with 10 shots as low density, isolated and scattered nanoparticles are found only at intermediated position; and increasing number of irradiation shots to 50 increases the density of nanoparticles but no particle agglomerates were observed indicating that amount of ablated impurity material is much less.

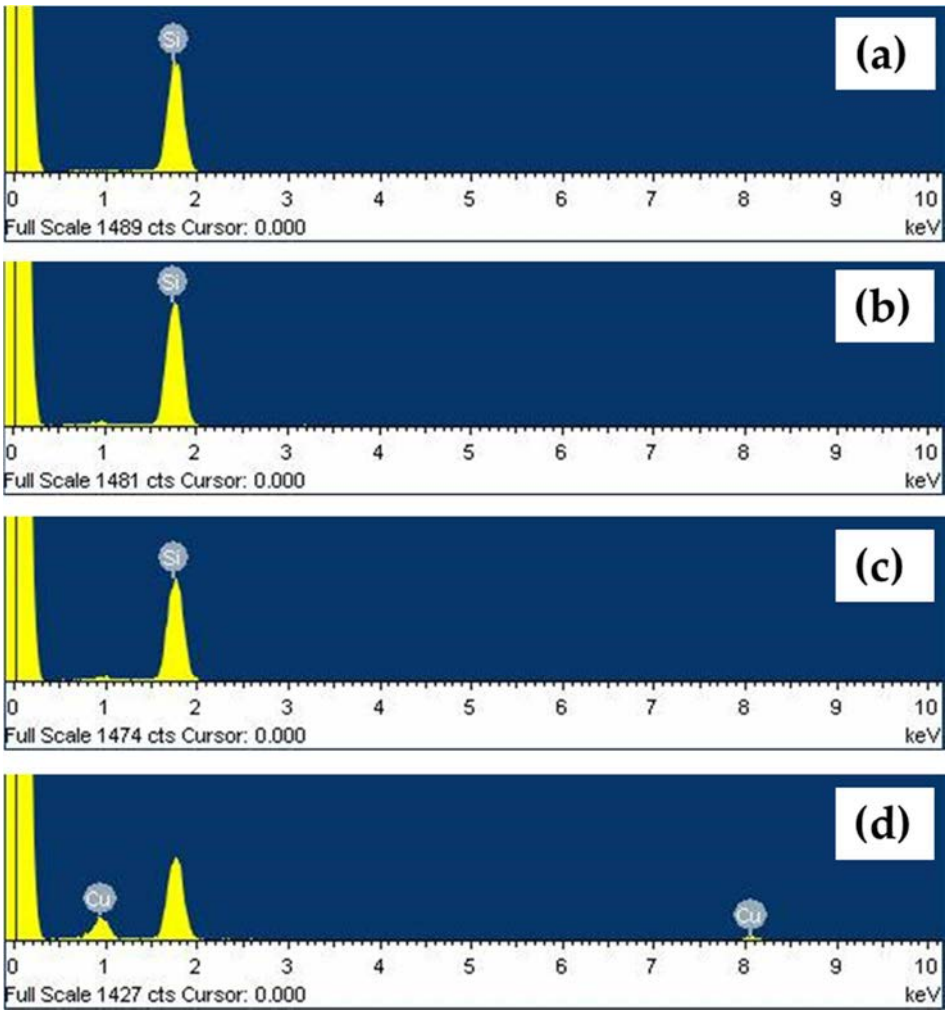

FIG. 26. (a) Typical EDX spectra of Si samples irradiated at the distance of 5 cm from the anode top using 1 UNU-ICTP focus shots without any aperture assembly between anode and the sample; (b) 5 focus shots; (c) 10 focus shots; (d) 50 focus shots.

3.5. Experiment 5: irradiation of PDF-W samples from FZJ at different distances using different number of focus shots using 3 kJ UNU-ICTP plasma focus device

Another set of 8 PDF-W samples were provided by FZJ Julich via the IAEA in January 2014. Based on the experimental results discussed above, it was very much evident that the ablation of double aperture assembly placed in between the anode top and the sample under irradiation (for reduction of material debris from anode to sample) was the major impurity material observed on the irradiated sample. It was also proved beyond doubt that further reduction in amount of impurity material on irradiated sample surface can be obtained by using hollow anode with deep groove and with very thin anode wall. Moreover, number of focus shots should be limited to maximum of 10 otherwise for larger number of shots the amount of impurity material deposited on surface will start to modify/manipulate the surface features of irradiated sample surface and it would be difficult to identify that whether the change in surface properties is due to energy ion pulse and hot dense plasma exposure or due to the deposited material. It is for this reason we decided to continue to use UNU-ICTP plasma focus device for this final irradiation experiments as it uses hollow anode with deep groove and with very thin anode wall. In this experiment, all eight 12 mm × 12 mm × 5 mm PDF-W samples were ultrasonically cleaned with acetone, methanol and deionized water for 10 min each, respectively. The PDF-W samples were then mounted on a sample holder at an axial distance of 5 cm above the anode tip to irradiate them with different number of focus shots (1, 5 and 10). Moreover, the irradiation of PDF-W samples was also carried out at different axial distances from the top of the anode (5, 7, 9 and 11 cm) by using fixed 5 focus shots.

The UNU-ICTP plasma focus device was operated with deuterium at fixed filling gas pressure of 3 mbar. To monitor the focusing efficiency, a Rogowski coil and a high voltage probe (HV) are applied. A shutter is placed between the anode and the sample holder until the strong focusing is confirmed by an intense voltage spike in the probe signal and a steep dip in the current signal which is monitored on a digital oscilloscope.

Table 5 presents the experimental conditions for irradiation for different PDF-W samples.

TABLE 5. SAMPLES, IRRADIATION DISTANCES AND NUMBER OF FOCUS SHOTS

Sample #	Distance of irradiation (cm)	N. of focus shots
W-131	5	1
W-132	5	5
W-133	5	10
W-134	7	5
W-135	9	5
W-136	11	5
W-137	5	5
W-138	–	–

Fig. 27 shows the typical wave forms of *V*, dI/dt and I for deuterium gas at the optimum pressure of 3 mbar. The UNU-ICTP plasma focus was operated as fixed charging voltage of 14 kV.

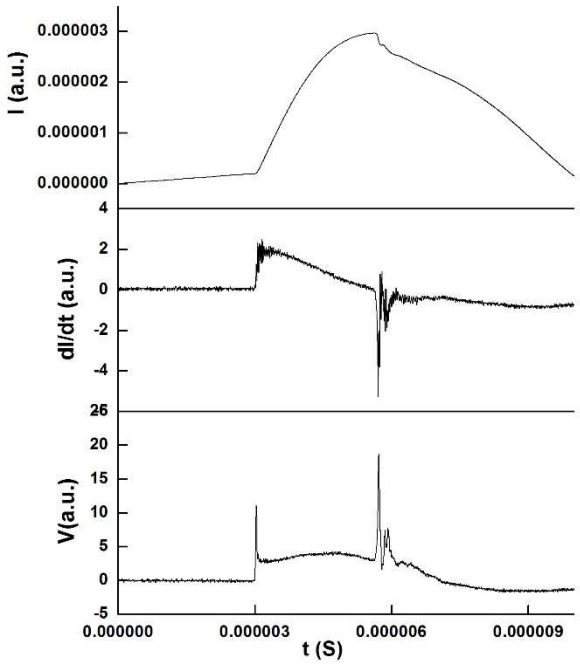

FIG. 27. Typical oscillographic traces of current, current derivative and voltage signal of UNU-ICTP plasma focus device at 3 mbar deuterium.

The XRD patterns of the reference and irradiated tungsten samples exposed to various number of shots (1, 5 and 10) at a fixed distance of 5 cm and 5 focus shots at different axial distances from the anode tip (5, 7, 9 and 11 cm) are shown in Figs. 28 and 29, respectively.

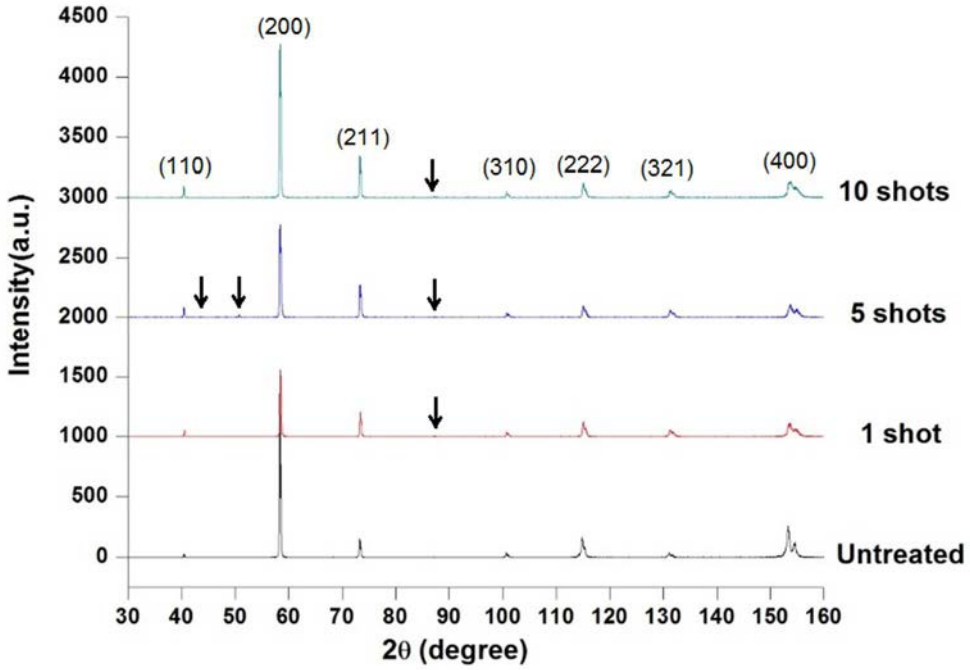

FIG. 28. XRD spectra of PDF-W unexposed sample and samples irradiated with different number of focus shots at fixed irradiation distance of 5 cm from the anode top.

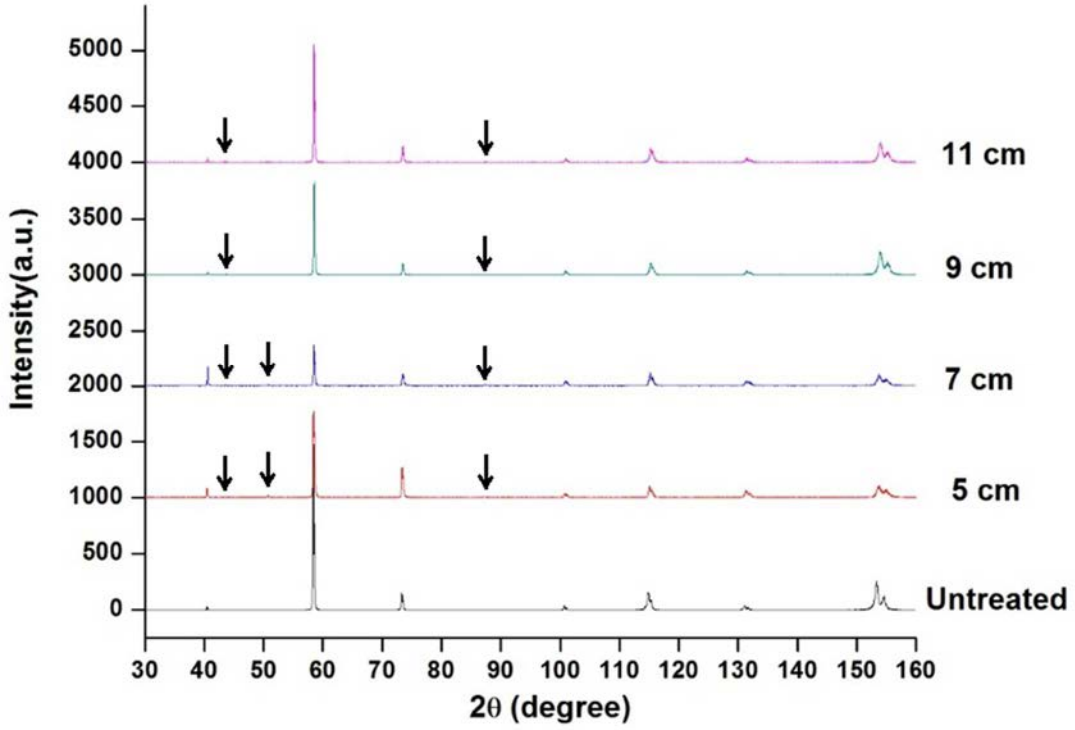

FIG. 29. XRD spectra of PDF-W unexposed sample and samples irradiated with different number of focus shots at fixed irradiation distance of 5 cm from the anode top.

The diffraction spectra were recorded using locked coupled scanning mode from 2θ of 30° to 160° at a scan rate of 0.02. As you can see from the XRD spectrum of the reference sample, the diffraction peaks related to bcc-tungsten crystalline planes are recognized showing that the untreated sample has bcc-structure, same as in earlier batch of samples. All bcc-tungsten peaks are labelled in Fig. 28. In all the exposed samples, both in Figs 28 and 29, besides the crystalline planes of bcc-tungsten, the new diffraction peaks (though very week and hardly visible in Fig. 28 and marked by arrow) are observed. These additional diffraction peaks are found to be consistent with the most intense peak of face centered cubic (fcc) structure. It is reported in literature that fcc-tungsten (also referred as γ-tungsten) is formed normally in thin films of tungsten. Hence it can be concluded that even with single shot exposure the top layer of bcc-tungsten sample has probably been melted by intense energy flux of incident ion beam and hot dense plasma and gets re solidified in thin layer of fcc-tungsten at the top. The increase in number of shots to 5 increased the number of fcc-tungsten peak indicating greater processing of top layer of fcc-tungsten layer. However, with further increase in number of shots to 10, the number of additional peaks related to fcc-tungsten reduces again which might be either due to the processing to fcc-tungsten to bcc-tungsten as the layer gets thicker or due to additional impurity atoms from anode material getting deposited at the irradiated sample surface. Similarly for samples irradiated at different distances, shown in Fig. 29, using fixed 5 focus shots show that at smaller distance of exposure the number of fcc-tungsten peaks were three which reduced to two peaks at higher distance due to decrease in ion energy densities.

XRD patterns of irradiated samples, confirm the structural transformation in tungsten samples due to deuterium ion irradiation. On the other hand, a comparison of XRD patterns of reference and exposed samples indicates that there is a small shifting of diffraction peaks towards the higher angular positions (Bragg angles). This phenomenon can be explained based on the compressive internal stress developed in the irradiated samples due to the thermal load exposed on the surface by the intense deuterium beam. Indeed, the internal stress that emanates from the thermal stress can be due to the quenching and volume change at the sample's surface. In addition, local melting of the irradiation surface may be result in the further thermal stress. The surface micrographs of the reference ad exposed tungsten samples for different number of shots (1, 5 and 10) at a 5 cm distance from the anode top and various distances from the top of the anode (5, 7, 9 and 11 cm) each irradiated with 5 shots are presented in Figs 30 and 31, respectively. The SEM image of the sample exposed to 1 shot (Fig. 30(a) shows a non-uniform surface with a heterogeneous granular structure showing the modification of polish marked sample surface. With regard to the sample treated with 5 focus shots, the SEM image shows a uniform

and homogenous surface modification with the presence of nanosized grains with bi-modal distribution; one having very small size of about 20–30 nm and other one in bigger size of about 60–100 nm. It can be explained based on the sufficient energy flux of ions and hot dense decaying plasma that treats the top surface of irradiated sample to such features. The surface of the sample exposed to 10 focus shots presents a significant surface damage including microcracks and blisters formation due to multiple heat loads on sample surface by deuterons ion pulses and also delivering an excessive energy to the sample surface that causes damage to the surface of the tungsten sample.

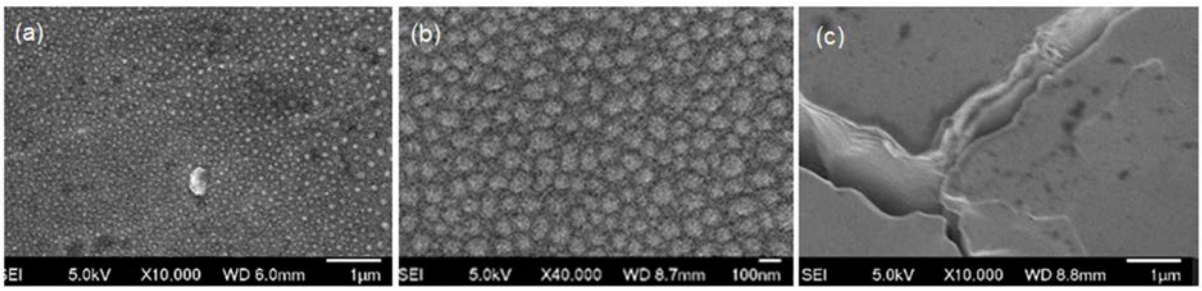

FIG.30. (a) SEM micrographs of PDF-W samples irradiated at the distance of 5 cm from the anode top using 1 UNU-ICTP plasma focus shots; (b) 5 focus shots; (c) 10 focus shots.

Fig. 31 shows SEM micrographs of PDF-W samples irradiated at various axial distances from the anode top to 5 focus shots.

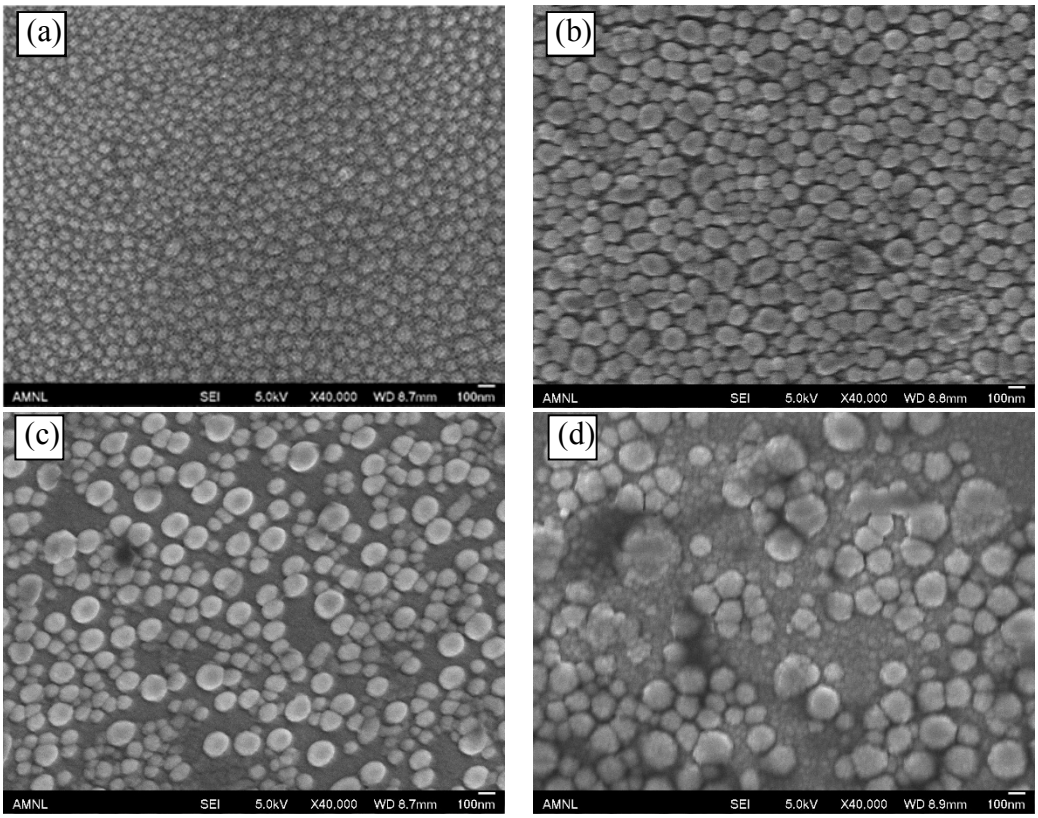

FIG. 31. (a) SEM micrographs of W exposed samples at various axial distances from the anode tip exposed to 5 shots at distances of 5 cm from top of the anode; (b) 7 cm from top of the anode; (c) 9 cm from top of the anode; (d) 11 cm from top of the anode.

The distances of exposures are 5, 7, 9 and 11 cm from top of the anode. As it can be seen from Figs 31(a)–(d), an increase in the distance from 5 to 11 cm makes the size of the grains on the sample surface increases due to the agglomeration of tungsten particles and leads to the reduction in the uniformity of the surface and the number density of the grains due to the exposure of the surface to ions with lower energy and number density. The chemical composition of the reference and irradiated tungsten samples are performed by X ray photoelectron spectroscopy (XPS).

Fig. 32 shows XPS spectra of reference/unexposed PDF-W sample and samples irradiated using 1, 5, and 10 focus shots at the fixed distance of 5 cm from the anode top.

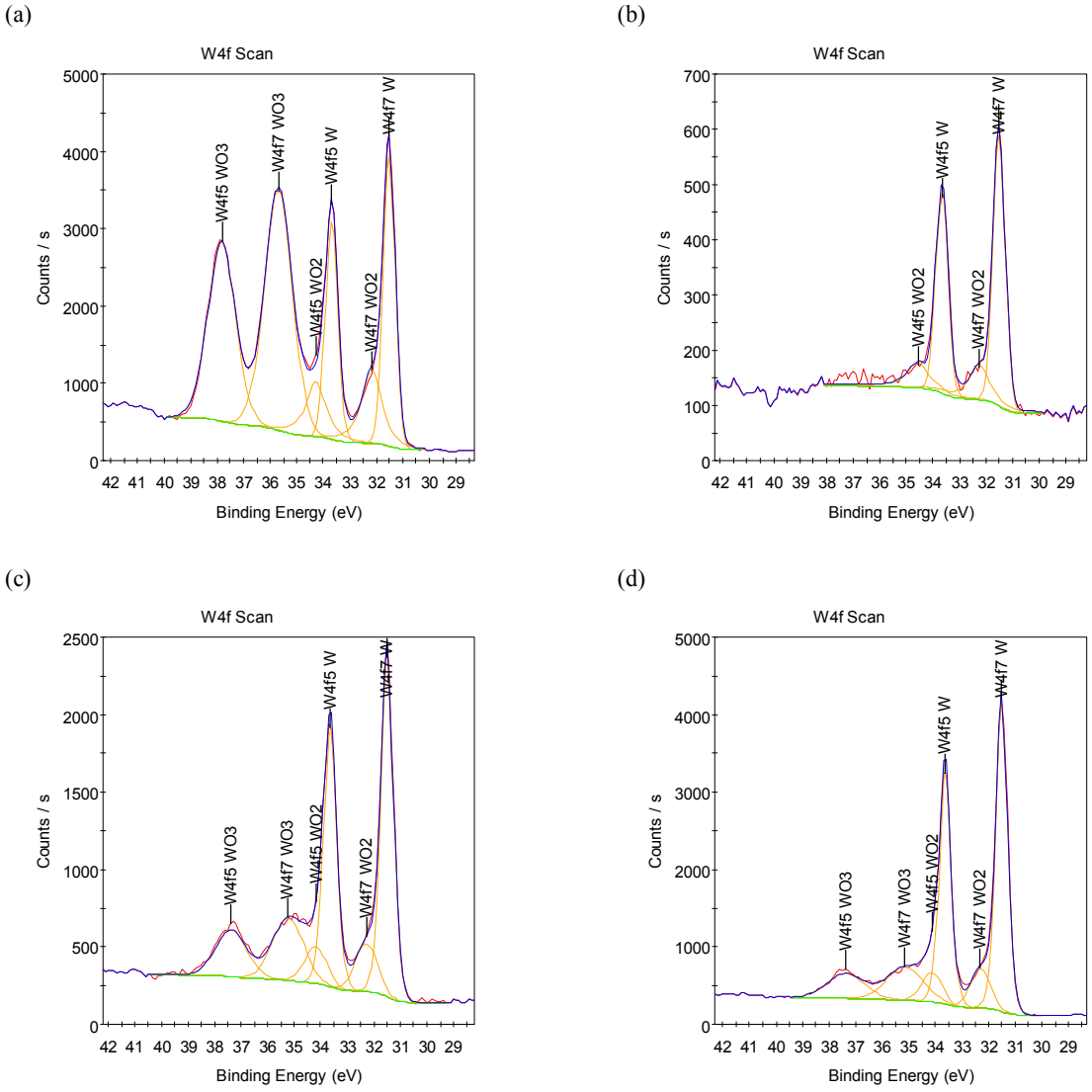

FIG. 32. (a) XPS spectra of PDF-W reference/unexposed samples; (b) samples irradiated using 1 focus shots at the fixed distance of 5 cm from the anode top; (c) 5 focus shots; (d) 10 focus shots.

All samples (unexposed and irradiated) exhibit the presence of metallic and oxide form of tungsten. The relative amount of metallic and oxide form of tungsten was estimated these XPS peaks. For unexposed sample the oxide form of tungsten was found to be dominating chemical state on sample surface with about 72% of tungsten in oxide form (note stronger and wider oxide peaks in Fig. 32(a)). The exposure of sample to 1 plasma focus shot at 5 cm lead to significant decrease in oxide form to about 23% while for 5 and 10 shots the oxide form of tungsten was estimated to be 40% and 34% respectively. The decrease in oxide form of tungsten can be attributed to

breaking of bonding between tungsten and oxygen by the energetic ions and hot dense decaying plasma. The XPS analysis also shows the presence of Cu, O and N on all samples (unexposed and irradiated ones) and that analysis is not completed yet and will be included in the research papers which will be communicated later.

4. CONCLUSIONS

The key conclusions for each of the five experiments that were performed under the purview of the IAEA CRP on "Investigation on materials under high repetition and intense fusion pulses" are as follows:

a) NX3 Plasma Focus was optimized using different electrode assembly and the best electrode assembly that yielded maximum neutron yield of about 3.34×10^9 n/s was the one with anode radius of 26 mm and length 140 mm. It was found that the electrode configuration with highest average neutron yield was operating at speed factor values closer the one reported them of optimized neutron production. The higher the deviation in speed factor from this optimized value, the lower was the yield. This highlights the reliability of the speed factor as the guiding rule for neutron yield optimization in plasma focus device.
b) Irradiation experiments on locally procured commercial tungsten samples (C-W) using hydrogen operated UNU-ICTP plasma focus device at the fixed axial distance of 5 cm using 5, 10 and 15 plasma focus exhibited:
   (i) Nanostructurization of irradiated sample surfaces.
   (ii) Emergence of additional peak on XRD which matched with indicated copper or tungsten oxide on irradiated samples.
   (iii) Decrease in hardness of the irradiated samples as well as decrease the hardness with indentation first and increase to stable bulk hardness value of tungsten, implying thereby there is coating of softer copper on the irradiated sample surface.
c) Irradiation of PDF-W (Plansee double forged tungsten) samples using 50 NX3 shots with aluminum double aperture assembly showed major issues related to impurity material accumulation on irradiated samples from anode material ablation, ablation of the aperture material and vaporization of carbon from double sided tape. The conclusions that were derived from this experiment were:
   (i) Aluminum is very soft as aperture material and should not be used.
   (ii) Double sided tape should not be used as larger number of focus shots is able to heat the irradiated surface resulting in melting and vaporization of tape material leading to significant presence of carbon on irradiated sample surface.
   (iii) Anode should have as deep groove as possible and it is advisable to make anode wall as thin as possible.
   (iv) NX3 plasma focus has very strong focusing efficiency and can cause the ablation of aperture assembly material even at large distance (approximately at 18–20 cm) of exposure.
   (v) Using large number of NX3 focus shots is not useful as the irradiated sample gets heavily covered with impurity material ablated from anode and aperture so when one wants to investigate the effects of energetic ions and hot dense on tungsten sample surface actually ends up looking on at the impurity layer deposited on the irradiated tungsten sample.
   (vi) Irradiation experiments should be conducted in stage-wise irradiations of 1, 5, 10, 20, 40 and finally 50 shots.
d) Irradiation experiments were conducted on Si substrates using 1, 5, 10 and 50 UNU-ICTP plasma focus shots with and without bronze double aperture to understand the role of double aperture assembly. The conclusions derived were as follows:
   (i) Using bronze double aperture (with bronze know to have much higher ablation threshold compared to previously used aluminum in Experiment 3) did not help as the copper and zinc impurities were observed for 5, 10 and 50 shots irradiation indicating that energy flux delivered to the aperture assembly by energetic ions and hot dense decaying plasma is too strong for bronze to handle.
   (ii) For 50 shots irradiation in the presence of bronze double aperture assembly, the amount of impurity material present on the irradiated sample surface was so big that Si EDX peak could not be seen implying thereby that irradiated sample surface does not show sample surface feature but shows only that of deposited impurity material features; certainly not the investigation that we wanted to perform at the first place, and hence once again confirm the need to carefully plan the number of irradiation shots that one should plan for irradiation experiments.
   (iii) For experiments conducted without the double aperture assembly, no impurity deposition was seen until 10 focus shots, but for 50 shots copper impurity can be seen but with significantly less compared to the one when aperture assembly was used.

(iv) Hence, it was concluded that it is better not to use aperture assembly particularly at smaller distance of exposure and also limit the number of irradiation shots to smaller values (probably maximum of 10 irradiation shots).

e) Final irradiation experiment on next batch of eight PDF-W samples was performed using UNU-ICTP PF with deuterium without any aperture assembly. The PDF-W samples were irradiated to 1, 5 and 10 focus shots at fixed distance of 5 cm and also at different distances (5, 7, 9 and 11 cm) using fixed 5 focus shots. The study revealed:
   (i) Virgin sample has bcc structure with preferred (002) orientation and with over 55 to 80% of sample surface in oxide form.
   (ii) Irradiation by UNU-ICTP plasma focus lead to the creation of fcc phase tungsten at the surface (while bulk of the sample still strongly retains bcc phase) and as it is well known that fcc phase normally appears in tungsten thin films indicating thereby that top layer of PDF-W sample was significantly transformed/processed by energetic ions and hot dense decaying plasma.
   (iii) The XPS analysis shows that the oxide form of tungsten on irradiated sample is reduced significantly, with metallic tungsten soaring to about 60% to 77%, which once again points to significant processing of irradiated sample surface by energetic ions and hot dense decaying plasma.
   (iv) Surface nanostructurization of all irradiated PDF-W has taken place and sample surface shows other features like that of cracks, blisters and holes.

As final conclusion, several investigations performed over last four year under the purview of the IAEA CRP on irradiation of tungsten material were highly successful as it helped in highlighting the very important issue of ablated impurity material deposition on the irradiated material surface and making us develop strategies in term of modification of irradiation assembly and procedure to minimize or eliminating these impurities on irradiated sample surface so that the actual effects of irradiation on tungsten surface can be studied.

ACKNOWLEDGEMENT

This research has been supported by the IAEA Research Contract No. 16961 on “Investigation on Materials under High Repetition and Intense Fusion Pulses”, and NTU Tier 1 research grant No RP 1/11 RSR “Physics and Technology of High Repetition Rate Plasma Focus Neutron Source and Its Applications”. We sincerely acknowledge the support of the IAEA and FZJ, Julich for providing 13 samples of highly polished PLANSEE double forged tungsten samples for irradiation.

REFERENCES

[1] LEE, S., SERBAN, A., Dimensions and lifetime of the plasma focus pinch, IEEE Trans. Plasma Sci. **PS-24** (1996) 1101.
[2] LU, M.F., Plasma motion and neutron emission in a 18-kJ plasma focus, Nucl. Instrum. Meth. Phys. Res. B **117** (1996) 452.
[3] MAHMOOD, S., et al., Novel fast-neutron activation counter for high repetition rate measurements, Rev. Sci. Instrum. **77** (2006) 10E713.
[4] ROSHAN, M.V., PhD thesis, Nanyang Technological University, Singapore (2010), unpublished data.
[5] ZAKAULLAH, M., AKHTAR, I., MURTAZA, G., WAHEED, A., Imaging of fusion reaction zone in plasma focus, Phys. Plasmas **6** (1999) 3188.
[6] VERMA, R., RAWAT, R. S., LEE, P., KRISHNAN, M., SPRINGHAM, S.V. , TAN, T.L., Experimental study of neutron emission characteristics in a compact sub-kilojoule range miniature plasma focus device, Plasma Phys. Control. Fusion **51** (2009) 075008.
[7] LEE, S., et al., A simple facility for the teaching of plasma dynamics and plasma nuclear fusion, American J. Phys. **56** (1988) 62.
[8] LIN, J.J., et al., FePt nanoparticle formation with lower phase transition temperature by single shot plasma focus ion irradiation, J. Phys. D: Appl. Phys. **41** (2008) 135213.
[9] SANCHEZ, G., FEUGEAS, J., The thermal evolution of targets under plasma focus pulsed ion implantation, J. Phys. D: Appl. Phys. **30** (1997) 927.
[10] LEE, S., et al., Effects of targets on plasma focus dynamics, IEEE Trans. Plasma Sci. **PS-18** (1990) 1028.

PLASMA FACING MATERIALS RESPONSE TO REPETITIVE PULSES SIMULATING FUSION REACTOR CONDITIONS

I.E. GARKUSHA, V.A. MAKHLAJ, S.V. MALYKHIN , V.V. CHEBOTAREV, M.S. LADYGINA,
A.K. MARCHENKO, O.V. BYRKA, V.V. STALTSOV, N.V. KULIK, YU.V. PETROV, N.N. AKSENOV,
S.S. HERASHCHENKO, D.G. SOLYAKOV, T.N. CHEREDNICHENKO, P.B. SHEVCHUK, S.I. LEBEDEV
Institute of Plasma Physics,
National Science Center Kharkov Institute of Physics and Technology,
Kharkov, Ukraine

Abstract

The performed simulation experiments in quasi-stationary plasma accelerators (QSPA) Kh-50 plasma accelerator were concentrated on studies of plasma surface interaction features under irradiation of different candidate materials for the divertor of fusion reactor with high power plasma loads of variable parameters. Dynamics of erosion products, both in form of droplets and solid dust, from exposed tungsten and carbon surfaces under QSPA plasma exposures have been investigated. Analysis of particles velocity distribution and angular dependencies, as well as their start times from the surface has been performed. Different sources of dust: bifurcation of major cracks, fine cracks along the grains, resolidified microbridges through the cracks, material modification have been recognized and investigated in simulation experiments with QSPA Kh-50. It is shown that modification of W after the repetitive pulses with development of ordered subμm cellular structures may contribute significantly to the nm droplets and dust that remain on the material surface. Macroscopic erosion of castellated targets has been studied to investigate key plasma surface interactions (PSI) effects in 3D geometry. Edge effects became dominating in target erosion. Emission of the droplets has threshold character and cyclical nature. New erosion mechanism introduced by edge effects, results in extremely growing droplet size and even submillimetre particles. The investigations were aimed to support mainstream fusion research in part of testing of plasma facing materials perspective for large thermonuclear devices of both types (with magnetic and inertial plasma confinement) and for plasma technologies.

1. INTRODUCTION

The anticipated regime of the tokamak ITER is the edge localized mode (ELM) H-mode. The ELMs, intrinsic for this regime, produce short periodic pulses of heat flux to the divertor armor, being the most heat loaded part of the tokamak. The disruptions can also occur, despite of mitigation schemes such as the massive gas injection and others. The expected transient events determine the erosion rate and the lifetime of PFCs, being one of the most important issues that influence on the tokamak performance.

The energy range of ITER disruptions and ELMs will be clearly higher than in the existing tokamaks. Taking into account the laboriousness of the experiments on PSI in these devices, experimental investigations have to be performed with other powerful plasma sources able to reproduce the energy and particles loads during the transients and to provide examinations of plasma facing materials under the repetitive plasma pulses. Impacts of the ITER relevant energy loads to the material surfaces are simulated now with powerful pulsed plasma guns, QSPA, PSI devices and e-beam facilities. Plasma surface interaction during transient events in ITER is comprehensively analyzed also applying the predictive numerical codes validated against experimental results in different simulators.

For ITER disruptions, the displacement of melt layer is considered to be dominating mechanism of macroscopic erosion and material splashing. Melt motion effects driven by external forces such as gradients of both plasma pressure and recoil pressure of evaporating material, surface tension and Lorentz force have been investigated in previous studies with QSPA Kh-50 in conditions similar to the expected at ITER disruption. It should be mentioned that QSPA application for studies of the melt layer behavior is quite suitable due to much longer pulse duration than in pulsed plasma guns [1–15], possibility to form different plasma pressure gradients along the surface, ability to simulate the vapor shield effect and some other plasma features that could not be reproducible e.g. with e-beams. For instance, increasing pressure of impacting plasma stream allowed to make clear the influence of plasma pressure gradient on the melt motion even for QSPA plasma pulse of 0.25 ms duration and to approach the melt velocities to those expected for ITER disruptions. It was demonstrated that melt-layer motion produces significant macroscopic erosion of metals and, in the case of tungsten, it may prevail e.g. the cracking destruction. Influence of $J \times B$ force on the melt resulting in erosion crater formation with the mountains of the resolidified material at the crater edge was also measured.

In contrast to disruptions that are relatively rare events, type I ELMs are foreseen to occur with a frequency of the order of 1 Hz (i.e. few hundred ELMs per ITER pulse). Plasma loads at the W surface for type I ELMs are expected to be of Q = 0.2–2 MJm^{-2} and the ELM duration of t = 0.1–0.5 ms. Thus, the melting of tungsten in

ITER divertor may also occur in the course of ELMs. In spite of much lower external forces expected, the plasma friction under inclined impacts to the surface and melt layer intrinsic instabilities of Kelvin-Helmholtz or Rayleigh-Taylor type may contribute to the melt losses during the ITER ELMs.

The droplets splashing from the tungsten surfaces in ELM simulation experiments is accompanied by ejection of solid dust that generated due to various processes [16]. The relative contribution of droplets and dust particles to the material erosion is difficult to estimate from the material surface analysis and even from CCD imaging of emitted erosion products traces and particles collection [14–23]. Therefore, further comprehensive studies aimed at investigations of tungsten performance under high transient loads, determination of erosion mechanisms in ITER relevant conditions, as well as analysis of erosion products dynamics in the plasma are required.

Now, so called castellated geometry is considered as reference design for the divertor plate's surfaces. Such sectioning of the surface of PFCs is supposed to reduce the influence of electric currents induced on the metallic surfaces during the reactor operation as well as to minimize the thermal stresses and resulting tungsten erosion caused by the formation of macro crack meshes on the surface. At the same time, presence of sharp edges in castellated structure may lead to their enhanced erosion. Also, one needs to expect that available edges will influence on energy load distribution, they would provoke the melting effects on the exposed divertor targets. Appearance of a liquid layer of molten material could be further accompanied by splashing of droplets under the influence of different external forces and melt instabilities. It is known that various instabilities could be developed at the interfaces having different physical properties. For example, it is intrinsic for the following interfaces:

- The liquid (molten) layer on the irradiated surface that contacted with incident plasma. In this case plasma can be considered either as light liquid or as plasma wind along the surface;
- The liquid metal and a shielding plasma layer (when the thermal load results in the vaporization of the target material);
- Between the moving molten layer and the solid bulk, different perturbations could be developed depending on surface geometry and possibility of the lost contact of the melt and bulk in the vicinity of slits, that will lead to significant macroscopic erosion.

Depending on the impacting energy load, plasma stream density and velocity a variety of mechanisms may be responsible for the development of those instabilities. Under the exposures with heat loads above the melting threshold, plasma flow along the surface (plasma wind) would trigger the Kelvin-Helmholtz instability. When high heat load results in vaporization of the target material, a dense plasma layer consisting of both the evaporated material of the target and the stopped head part of plasma flow is formed. Small initial perturbations on the surface together with the fast movement of the vapor along the molten surface of the target can lead to the development of both the Kelvin-Helmholtz and Rayleigh-Taylor instability. Recoil pressure of the vapor will also influence significantly on the melt layer motion and droplet splashing.

All mentioned above indicates necessity to perform comprehensive studies of erosion features for the surfaces of sectioned targets. It is considered as important direction of simulation experiments aiming a validation of the MEMOS code developed in KIT and adopted to 3-D geometry.

This report presents the results of simulation experiments with powerful plasma impacts to the different tungsten grades as ITER relevant PFMs, analysis of residual stresses in tungsten and cracking development as well as erosion mechanisms resulting in droplets and solid dust particles ejection from the exposed surfaces. Evaluation of melt losses under the QSPA Kh-50 plasma exposures simulating ITER disruption and ELMs are performed, liquid and solid particles generation in ELM conditions are distinguished. The experiments in the frame of the current CRP were also aimed at comparative and complementary studies of plasma-surface interaction features under irradiation of different candidate materials of fusion reactor with high power plasma loads of variable parameters [24–53].

2. EXPERIMENTAL SET-UP AND DIAGNOSTICS

The simulation experiments were carried out with QSPA Kh-50 [24–29] and pulsed plasma gun (PPA) [3, 7, 14] in Ukraine and multi-rod plasma injector (RPI)-IBIS facility in Poland [18].

The full block powerful quasi-steady state plasma accelerator QSPA Kh-50 consists of two stages. The first one is used for plasma production and pre-acceleration. The second stage (main accelerating channel) is a coaxial

system of shaped active electrodes transformers with magnetically screened elements (those elements are current supplied either from independent power sources or branching partly the discharge current in self-consistent regime of operation).

The plasma stream generated by QSPA is injected into vacuum chamber of 10 m in length and 1.5 m in diameter. The total energy content of the main discharge condenser battery is 2.2 MJ (at U_c = 25 kV). The amplitude and time duration of discharge current is up to 700 kA and 300 ms respectively. The main characteristics of plasma streams depending on operations regime and distance from accelerator output can be varied in the wide range: density of plasma from 10^{15} to 8×10^{16} cm^{-3}, velocity up to 4.2×10^7 cm/s, energy density of plasma stream from 5 J/cm^2 to 2 kJ/cm^2, total energy containment in plasma stream up to 600 kJ. Average plasma stream diameter (in the absence of magnetic system of longitudinal B field) is 0.5 m at the distance of 1 m and it is up to 1 m at the distance > 3 m from accelerator output. This provides possibility of plasma tests even of full-scale prototypes of divertor cassette.

In disruption simulation experiments QSPA generated the plasma streams with energy density up to 20 MJ/m^2, the mean proton energy ~ 0.9 keV, and maximum plasma pressure achieving 1.6 MPa. The plasma pulse duration was 0.25 ms and the temporal shape of the pulse was approximately triangular. The particle loads to exposed surfaces were varied in the range of 10^{23}–10^{27} ion/m^2 s.

For ELM simulations, the main parameters of the plasma stream were as follows: ion impact energy 0.4–0.6 keV, maximum plasma pressure ~ 0.32 MPa and the plasma stream diameter 0.18 m. It allows achievement of very small pressure gradient values in the target region, where plasma pressure is practically constant. Experiments were performed with several fixed surface energy loads chosen in the range of 0.45–1.1 MJ/m^2 (measured precisely with calorimetry) i.e. either below the melting threshold, or resulted in strong melting of exposed surface.

PPA device consists of coaxial plasma gun (with outer cylindrical anode of 14 cm in diameter, and inner cylindrical cathode of 4 cm in diameter; electrodes length is 60 cm) and vacuum chamber of 120 cm in length and 100 cm in diameter. The power supply system is condenser bank with stored energy of 60 kJ under the voltage of 35 kV. The current of discharge is 400 kA, the time duration of a plasma generation is (3–6) ms. The PPA generates plasma streams with parameters as follows: energy of plasma ions is up to 3 keV, plasma density from 2×10^{15} to 10^{16} cm^{-3}, specific plasma power 10 MW/cm^2, plasma energy density varied in the range of 5–55 J/cm^2. Either helium or hydrogen was used as working gases. The tasks for PPA device include investigation of effects due to helium ions impact to the surfaces (blistering, physical sputtering) in conditions of simultaneous action of corpuscular bombardment and heat loads, and also study of the influence of pulse duration on the tungsten damage induced by plasma pulses.

Deuterium plasma streams with a power density of 1–5 MW/cm^2 and pulse duration of 1–5 μs, generated by RPI-IBIS were used for comparative studies and determination of an initial stage of evaporated impurities dynamics during plasma surface interaction as well as features of surface damage under varied plasma parameters.

Observations of plasma interactions with exposed surfaces, the dust particles dynamics and the droplets monitoring were performed with high speed 10 bit CMOS pco.1200 s digital camera PCO AG (exposure time from 1 μs to 1 s, spectral range 290–1100 nm). Information from consecutive camera frames with traces of particles flying from the tungsten surface after plasma shot allowed calculation of velocities of emitted particles and the time moments of their startup from the target surface. The observed region in front of the target was 8 cm due to design features of the vacuum chamber of QSPA Kh-50. Thus, the particles with velocity higher than 35 m/s were able to fly away the observation region during ~ 2.2 ms. Therefore pulsed system of synchronization was used for improvement of temporal resolution for applied registration system in comparison with our previous studies. The frame exposure time was not exceeded 1.5 ms. It was proved that, the particles with sizes more than 10 μm can be clearly detected with CCD registration system. Temporal distributions of quantity and velocity of emitted particles were obtained for varied heat loads to the tungsten surfaces.

In order to determinate the main plasma parameters (electron density and temperature) and to investigate the impurities behavior during the time of discharge, optical methods of diagnostics were used. The spectroscopic measurements were performed by means of a two different spectrometers that provide with good space and time resolution. Particularly, Mechelle®900 spectrometer equipped with a CCD camera and operated in the wavelength range (300–1100 nm) with different exposition times was in use [13, 17, 18, and 23].

Surface heat load was measured with thermocouple calorimeters. Temperature of irradiated targets was measured in situ by special thermocouple attached to different sides of the target. Surface analysis was carried out with an optical microscope MMR-4, equipped with CCD camera and with scanning electron microscopy (SEM). Measurements of weight losses and microhardness of the surface were performed also. XRD method was applied for structure analysis and measurements of stresses in thin surface layer by $\sin^2 \psi$ method (X ray tonometry).

3. EXPERIMENTAL RESULTS

Figure1 shows a high speed imaging of QSPA Kh-50 plasma interaction with the inclined tungsten target. First frame corresponds to the plasma pulse time and the next images show dynamics of the tungsten droplets and solid W dust in front of the target surface.

Information from several frames with detected traces of particles flying from the W surface after the plasma shot was used for calculation of the particles velocity and the time moment when they started from the target surface. Tungsten particles registered in the experiment have velocity up to 20 m/s for earlier instants. For latter moments the velocity decreased to several m/s. Analysis of obtained experimental results and comparison with the numerical simulation allows conclusion that W particles generation in the form of droplets may occur only during the plasma pulse and (as latest) few tens microseconds after the pulse end. Thus, in spite of the energy load to be sufficient for melting, only first traces are attributed to the fast W droplets. Others are formed by the ejected solid dust. Generation of a dust is registered also for exposures the graphite targets (Fig. 1).

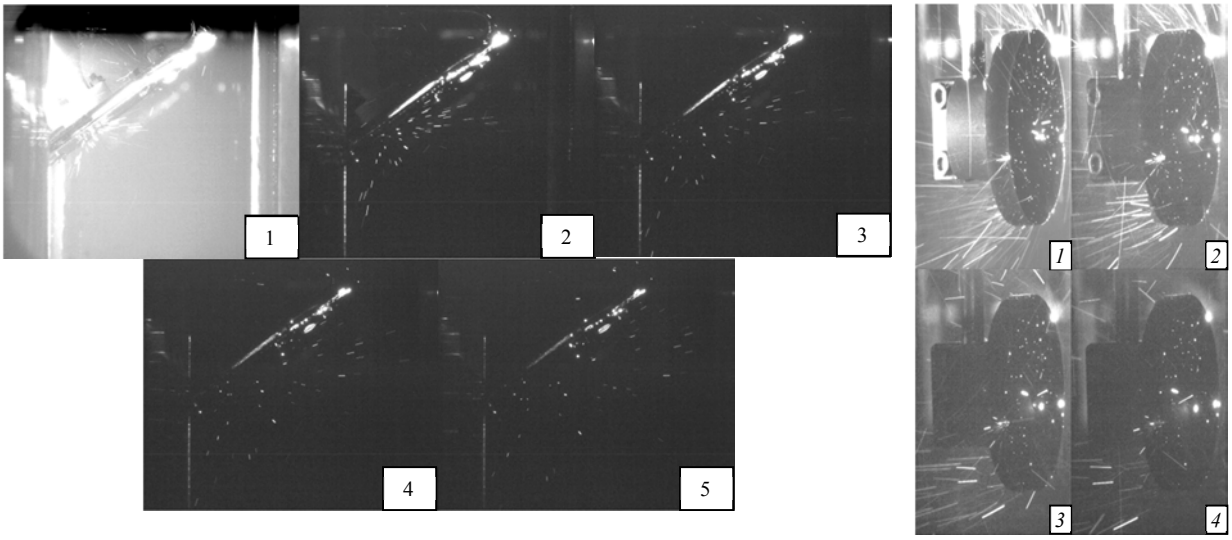

FIG. 1. High speed imaging of QSPA Kh-50 plasma interaction with inclined tungsten target (left), (t_{exp} = 0.25 ms): (1) 0 ms (plasma impact); (2) 1.16 ms; (3) 2.32 ms: (4) 3.48 ms; (5) 4.64 ms. Q = 0.75 MJ/m^2. Exposures of graphite target (right), inclined at 45^0 in vertical plane (t_{exp} = 1 ms): t_1= 1 ms; t_2= 2 ms; t_3= 3 ms; t_4= 4 ms after pulse, Q_{surf} = 0.5 MJ/m^2.

Dust generation mechanisms for tungsten are associated with W cracking. Fig. 2(a) shows a cross cut of the target and also the exposed W surface with major cracks and intergranular microcrack meshes. Major cracks are attributed to ductile to brittle transition effects while microcracks are due to resolidification of the surface layer. Solid particles may split from the crack edges during its rupture. Elastic energy stored in stressed tungsten surface layer is the motive force for the cracking process [4].

Results of residual stresses measurements are presented in Fig. 2(b). Similar level of residual stresses is obtained also for short pulse hydrogen exposures in PPA and for helium plasma pulses. The main part of the elastic energy is spent for the cracking itself and the rest of the elastic energy remain after splitting the particle is transformed to the particle acceleration. Such mechanism is obviously important for microparticles formation, e.g. in the course of crack bifurcation, as it is demonstrated in Fig. 3(b). Brittleness effects result in a dust arisen from major cracks. However, in addition, dust particles are able to be formed from the resolidified melt bridges across micro-cracks. The bridges caused by melt motion, capillary effects and significant viscosity of W melt. This mechanism is illustrated by Fig. 3(a). It could not be responsible for a μm size dust due to very small crack thickness. But a lot of nano size particles can be originated from the bridges.

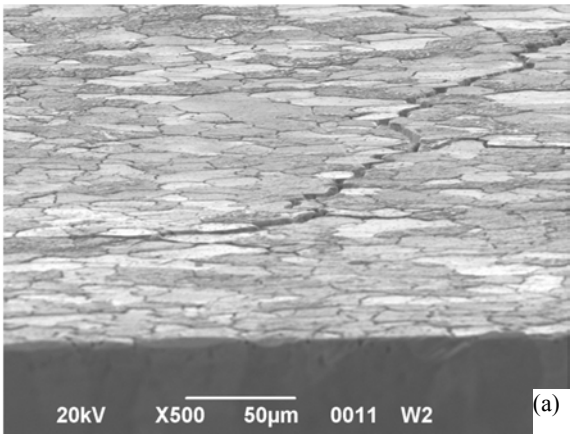

(a)

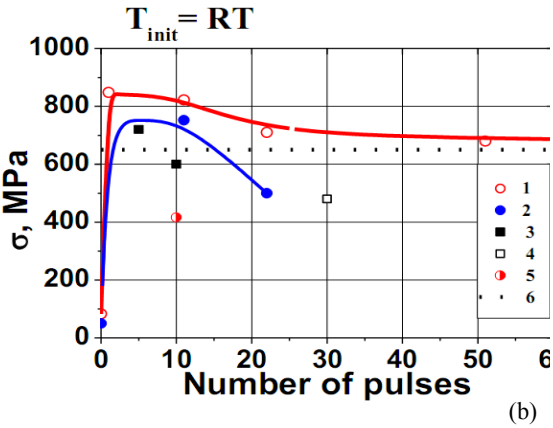

(b)

FIG. 2. (a) Exposed W surface with major and microcracks after QSPA plasma impacts; (b) residual stresses in tungsten targets versus the number of plasma pulses of QSPA (hydrogen: 1, 0.45 MJ/m^2; 2, 0.75 MJ/m^2) and PPA (helium: 3, 0.4 MJ/m^2; 4, 0.2 MJ/m^2; and 5 hydrogen 0.4 MJ/m^2), dashed line shows stress magnitude after 270 QSPA hydrogen plasma pulses of 0.45 MJ/m^2.

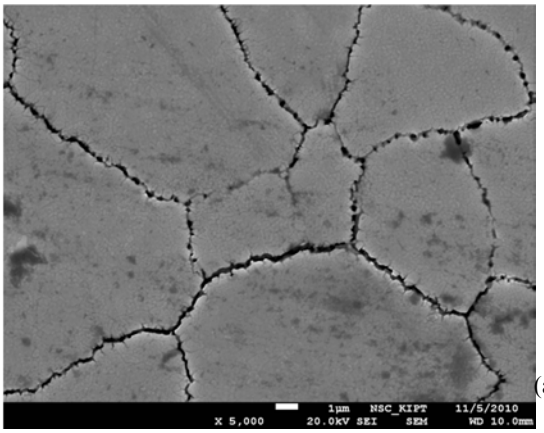

(a)

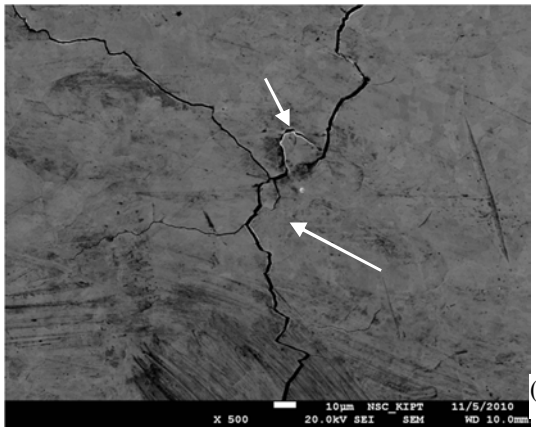

(b)

FIG. 3. (a) W surface after QSPA exposures, possible source of nano sized dust particles; (b) µm sized dust particles.

Examples of nano size dust particles that have been recognized on exposed W surface after multiple plasma exposures are presented in Fig. 4.

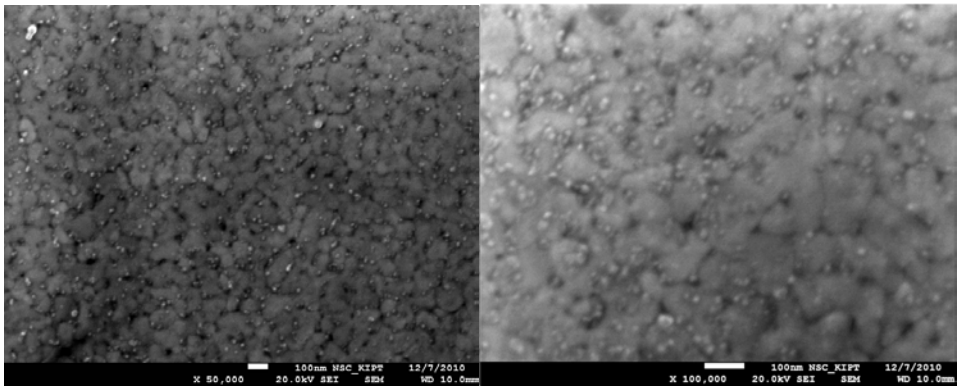

FIG. 4. Dust of nanometre size collected on W surface.

These images illustrate one more possible mechanism of dust production, which is due to the material modification with formation of fine cellular structure of the surface layer (typical size of the cellular structures is 100–500 nm.). Origination of voids between fine cells can also be accompanied by a dust ejection. Then edges of the ejected nm particles are able to be melted even for rather small heat loads below the surface melting threshold. It can be reason for a ball shape of nm particles on a solid surface of the target. Such solid dust particles are deposited back to the target surface by plasma pressure in the pulse tail stage. Larger particles (tens μm), in principle, have more chances to fly away irreversibly from the surface. Nevertheless, tungsten balls of nm and μm size were detected earlier inside the major crack voids in the regimes with pronounced melting. Therefore in those experiments the contribution of resolidified droplets to W balls population inside cracks was quite significant. Size distributions of W nano particles and collected W balls in crack voids are presented in Fig. 5.

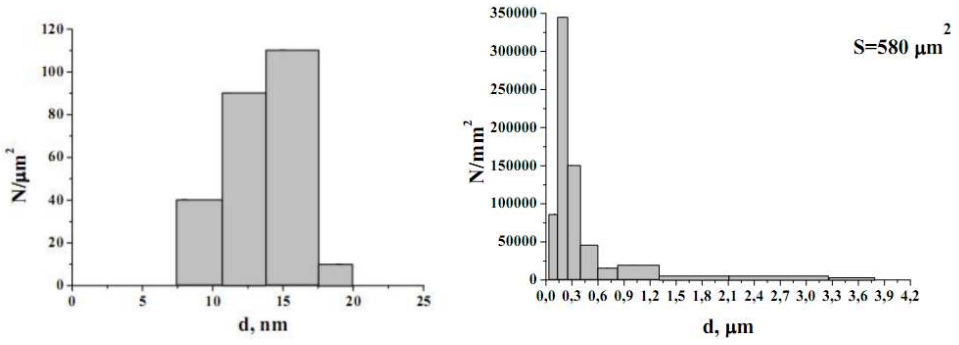

FIG. 5. (a) Size distributions of W nanoparticles; (b) collected W balls in crack voids.

In IBIS experiments, spectroscopy studies of appeared WI and WII spectral lines of eroded tungsten in plasma provided possibility for monitoring of tungsten spectral lines and accurate measurement of W plasma density in front of the target. Information about dynamics of the W ions production (mainly from the dust particles evaporation in front of the surface) was obtained. On the basis of the space and time resolved spectroscopic measurements of the D_α line in RPI-IBIS, it was estimated that the highest electron density of the plasma layer in front of the target surface amounted to about 3.4×10^{16} cm^{-3}. Thus plasma pressure is quite sufficient to bring a small-size fraction of the ejected dust back to the exposed surface.

3.1. ELM simulation experiments

Fig. 6 shows comparison of camera frames registered with the same exposures for different plasma heat loads. The particles emission from the surface starts for heat loads exceeding the melting threshold under the QSPA Kh-50 plasma pulse (0.6 MJ/m^2).

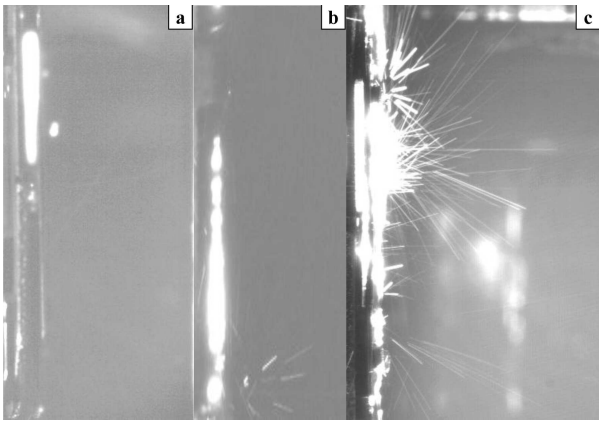

FIG. 6. (a) High speed imaging of plasma interaction with tungsten target: t = 1.2 ms after the start of plasma surface interaction, t_{exp} = 1.2 ms, Q = 0.45 MJ/m^2; (b) Q = 0.6 MJ/m^2; (c) Q = 0.75 MJ/m^2.

The number of ejected particles grows significantly with further increase of the surface heat load. For instance, twice increase of the number of emitted particles is observed with of heat load elevation from 0.65 to 0.75 MJ/m^2. Fig. 7 shows velocity distributions and the number of particles versus time of their startup from the exposed surface, obtained for Q = 0.75 MJ/m^2.

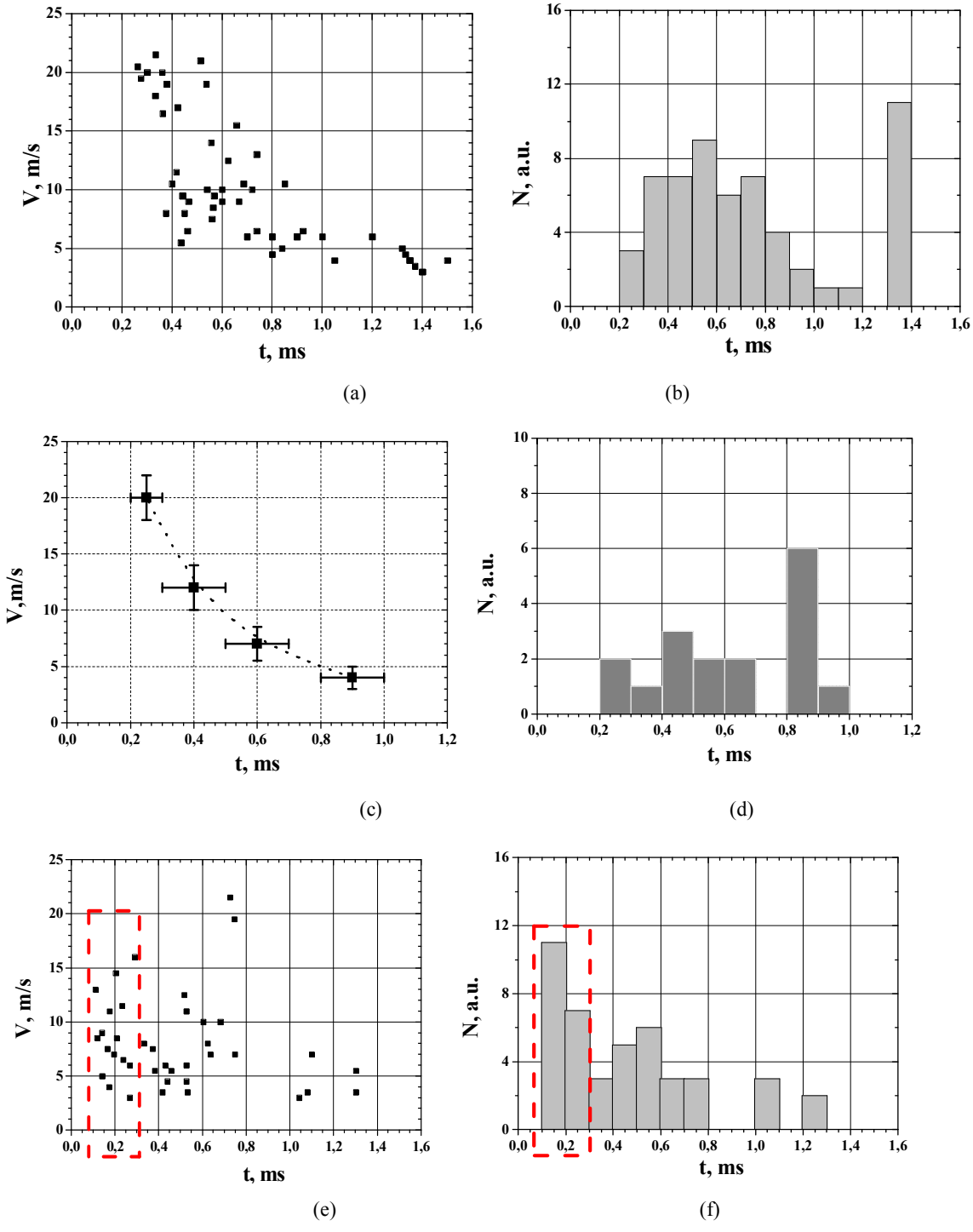

FIG. 7. (a) Velocity distribution versus particle startup time from the exposed surface, Q = 0.75 MJ/m^2; (b) number of ejected particles versus particle startup time from the exposed surface, Q = 0.75 MJ/m^2; (c) velocity distribution versus particle startup time from the exposed surface, Q = 0.6 MJ/m^2; (d) number of ejected particles versus particle startup time from the exposed surface, Q = 0.6 MJ/m^2; (e) velocity distribution versus particle startup time from the exposed surface, Q = 0.9 MJ/m^2; (f) number of ejected particles versus particle startup time from the exposed surface, Q = 0.9 MJ/m^2. t=0 corresponds to the beginning of plasma target interaction. Emitted drops are marked with rectangle.

Analysis of the obtained experimental results and comparison with numerical simulation, shows that even for heat loads of 0.75 MJ/m^2 (that is far above the melting threshold) the generation of W particles in the form of droplets may occur only during the plasma pulse and (as latest) few tens microseconds after the pulse end. Thus, only first bar(s) in Fig. 7(b) definitely correspond to the detected droplets. Other traces could probably be attributed to the solid dust. Velocity of registered tungsten particles achieves 25 m/s for earlier instants. For the later moments, velocity decreases to several m/s.

To distinguish experimentally the liquid droplets and the solid particles from the recorded traces in the CCD imaging the observations of emitted particles were performed for varied surface heat loads, both decreased and increased in magnitude. The obtained distributions of emitted particles for Q = 0.6 MJ/m^2 and Q = 0.9 MJ/m^2 are presented in Figs 7(c)–(f). As follows from the obtained results for Q = 0.6 MJ/m^2 (Fig. 7(c)), in spite of smaller number of particles, all the traces registered are attributed to solid dust, with velocities distribution, that is quite similar to Fig. 7(a). They start from the surface after the pulse end (t = 250 μs).

For increased heat load up to 0.9 MJ/m^2 the start time of particles ejection shifts to earlier instants (100–200 μs), when the surface of target is in the molten state (Figs 7(d) and (f)). With increasing heat load, the velocity of ejected droplets, corresponding to earlier time moments in $v(t)$ dependence, is falling down. As far as, mass loss measurements demonstrate growing erosion with increase of energy load, the obtained result can be explained by increasing size of ejected particles as a sequence of the growing thickness of the melt layer. Appeared droplets with larger mass a probably have smaller velocities, that is in agreement with results obtained in Troitsk QSPA-T device.

Detailed imaging of dynamics of the emitted particles, corresponding to Figs 7 (e) and (f) plots is shown in Fig. 8. Generally, the brightness of the particle trace is decreased with time due to the particle cooling. However, it is important to mention a sharp increase of the luminosity of some droplets traces, that is well seen on many tracks for time instants of t = 3–7 ms from the plasma impact. Examples are shown by arrows in Fig. 8. Sharply increasing luminosity of traces is resulted from the liquid to solid transition.

Thus the solidification moments could be successfully recorded from CCD imaging in this case. It should be noticed that the droplets are solidified much latter than the melt surface they emitted from. The resolidification of molten pool on the surface is influenced by cold bulk. Therefore target surface resolidification occurred just after the pulse end while droplets cooling are hampered.

However, obtained results show, that even for relatively high energy loads in ELM simulation experiments the droplets are still not dominate the material erosion. The erosion rate estimated from the target mass loss is on the level of 5–12 μg/cm^2 pulse. Most of the droplets are ejected with relatively small angles in respect to the normal to the surface.

From such angular distribution of emitted droplets in predominantly upstream direction, one possible to expect, that droplets generation mechanism is Kelvin-Helmholtz instability, which is due to the plasma wind propagating along the surface. Performed estimations of the instability increment γ and typical wavelength λ for tungsten exposure conditions in QSPA Kh-50 give as follows: $\gamma \approx 10^6$ c^{-1}, λ = 50–90 μm, $\omega \approx 3 \times 10^3$ c^{-1}.

This estimate of the wavelength is supported by the profilometry measurements (Fig. 9). Pronounced wavy structures relevant to Kelvin-Helmholtz instability have been observed for Cu, Ti and other metals with smaller melt viscosity that were also exposed to check the typical wavelengths ($\lambda_{Cu} \sim$ 150 μm, $\lambda_{Ti} \sim$ 450 μm). One need to point out again, that experimental set-up in QSPA Kh-50 allows eliminate the pressure gradient influence on melt motion. Absence of melt motion and any crater formation from macroscopic erosion have been proved with profilometry.

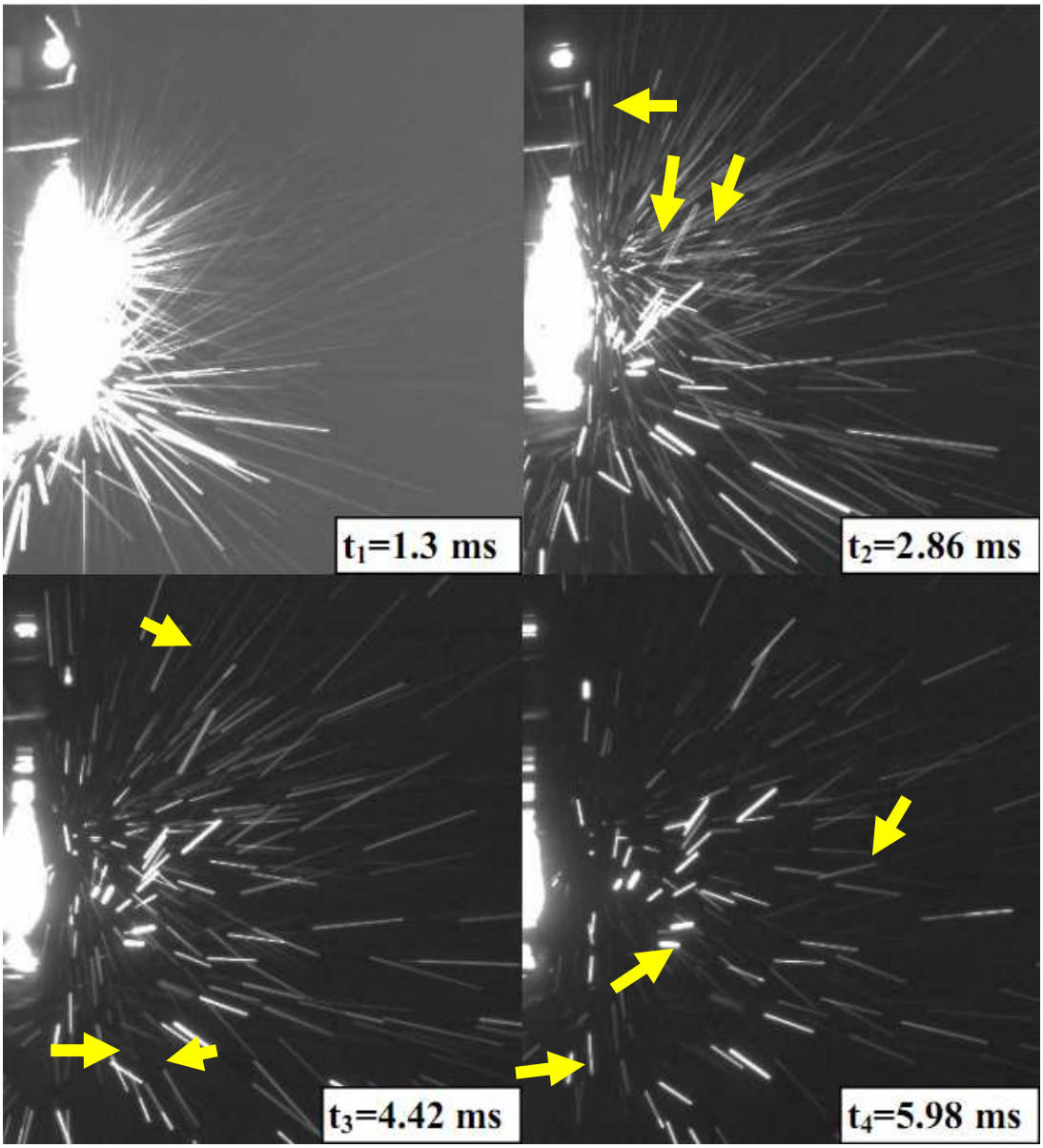

FIG.8. CCD imaging of emitted particles. Q = 0.9 MJ/m^2, Frames correspond to the indicated time instants from the beginning of plasma-surface interaction. Arrows mark some examples of droplets traces with sharply increased luminosity, attributed to the solidification.

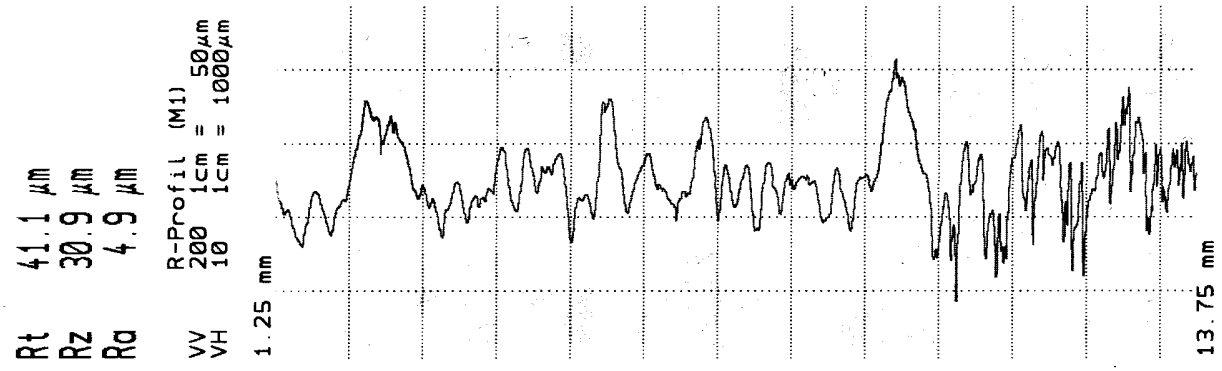

FIG. 9. Profile of tungsten surface after QSPA exposures.

Quantitative characterization of the tungsten melt layer losses and resulting contribution of the splashing process to the target mass loss in chosen conditions of ELM simulation experiments is quite difficult. Nevertheless experiments are shown that the droplets splashing does not prevail the dust ejection from resolidified surface. Only small fraction of the melt layer mass is splashed in the form of the droplets. Analysis of the cross cut of W target exposed with Q = 0.75 MJ/m^2 shows resolidified layer thickness of 7 μm. Thus, most of the melt remained on the surface and resolidified.

The obtained results show that after the plasma pulse the dust particles ejection is occurred in the course of the target resolidification. Elastic energy stored in stressed tungsten surface layer after high-speed resolidification in conditions of strong temperature gradient should be considered as the motive force for the cracking process with following acceleration of separated solid particles in this case.

In result of large number of the plasma pulses, both networks of major and of secondary cracks are developed on the exposed surface as well as blisters and bubbles of 100–300 μm in size. A lot of spherically shaped particles balls of 0.01–1 μm size are collected inside the cracks (Fig. 10). Majority of the balls have size less than 0.2 μm.

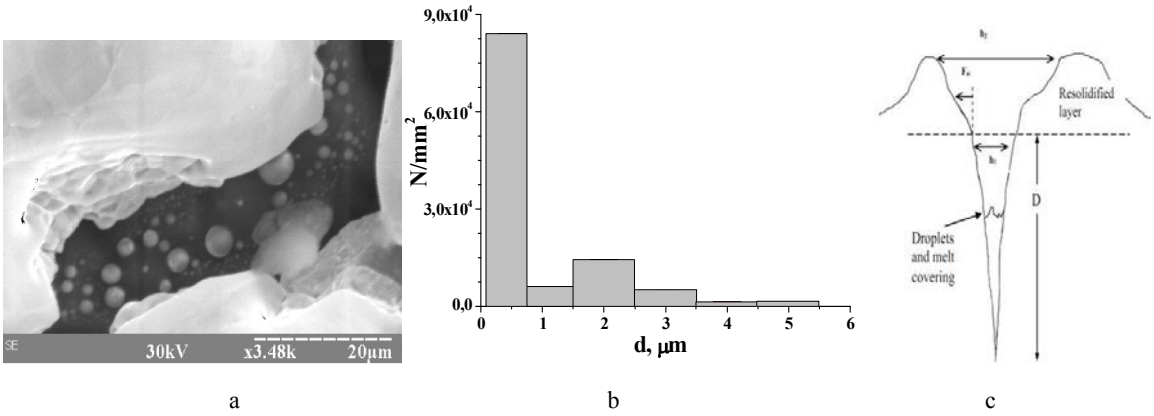

FIG. 10. (a) SEM image of tungsten surface; (b) size distributions of resolidified particles inside the crack void after 350 pulses of 0.75 MJ/m^2; (c) scheme of cracks cover by melt.

4. DISRUPTION SIMULATION EXPERIMENTS

The disruption simulation experiments showed that the melt motion dominates in tungsten macroscopic erosion, resulting in formation of the craters with rather large edge ridges of displaced material. The melt motion is accompanied by splashing of the metal droplets of the sizes up to 100 μm, mainly onto unexposed target surface. Because of strong vapor shield formed in the front of exposed surface, the CCD imaging became quite complicated in this case. Shielding layer is characterized by high luminosity and the plasma density in the shield is one order of magnitude exceeds the plasma stream density. Melt motion along the surface and vapor shield pressure contribute to the tangential projective of droplet velocity. As result, overwhelming majority of ejected droplets remains on the sample surface (Fig. 11).

The droplets size is varied from 1 to 100 μm. The droplet velocity was evaluated on the basis of the droplet size, the distance of their displacement and the duration of the incident plasma stream exposure. The estimated velocity value depends on the particle size and, as a rule, it is more than 5–10 m/s. Analysis of tungsten droplet tracks have shown that the droplets registered far from the melt edges were ejected with at least several tens m/s velocities.

The erosion in disruption simulation experiments is caused by both evaporation and melt splashing and performed measurements for different W targets show erosion rate of ~ 0.1–0.4 μm/pulse.

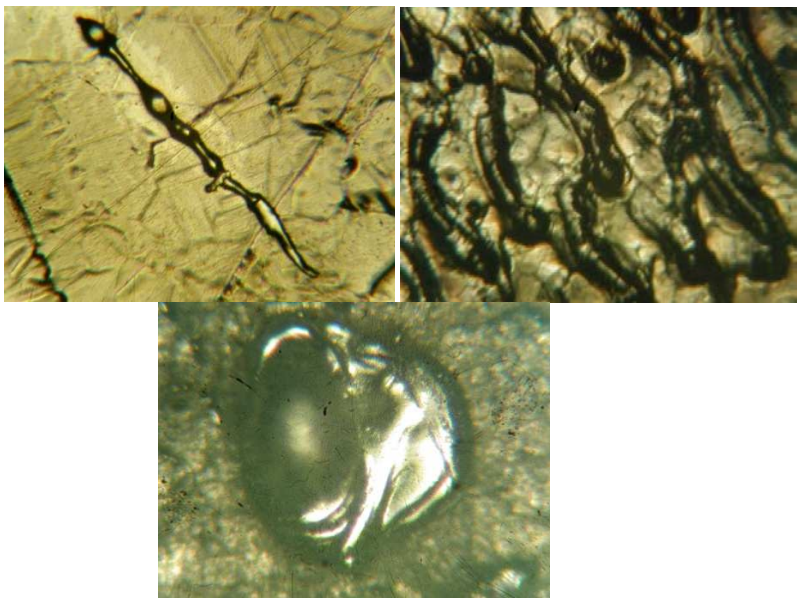

FIG. 11. Optical microscopy images showing examples of splashed W droplets in disruption simulation experiments.

4.1. Damage features for castellated targets

Because of tungsten melt is quite viscous, heavy and also due to the necessity of larger loads to achieve W melting in some appropriate surface layer, other material could be used for simulation of key dynamical effects on the castellated targets. Titanium material with well-known physical properties has been chosen to enhance the dynamics of the melt and to achieve the recognizable and measurable effects for smaller number of plasma pulses as well as to make clear the analysis of different possible mechanisms of the surface relief development. The target design is shown in Fig. 12. It represents the castellated structure, consisting of nine cubes of titanium with dimensions 1 cm × 1 cm× 1 cm. Each cube is attached to a copper plate. The gaps between the cubes were approximately 1 mm. All cubic blocks were placed at the same height. After the initial pulses impacts the sharp edges of cubes became locally overheated. It is observed a cleaning of fixing elements of cubes substrate resulting in expansion of the particles from the rear surface. These are impurity particles from the surface films, loosely coupled fragments. With a further increase in the number of irradiating pulses the effect of overheating of exposed surfaces recorded of all the cubes and intensive ejection of particles from the front surface of the target occurs (Fig. 13). For irradiation dose exceeding 25 pulses, quantity of the particles ejected from the surface varies periodically with further exposures. Average scale for such fluctuations of the ejected particles number is approximately 10–20 pulses. Maximum number of particles (ejected droplets) is registered for the range of shots from 35 to 40 pulses. Such character of the dependence of erosion products on the impacting plasma pulses is caused, apparently, by the destruction of mountains of the resolidified displaced material on the outer face of the cube, which arose after the previous irradiating pulses (Fig. 12(b)).

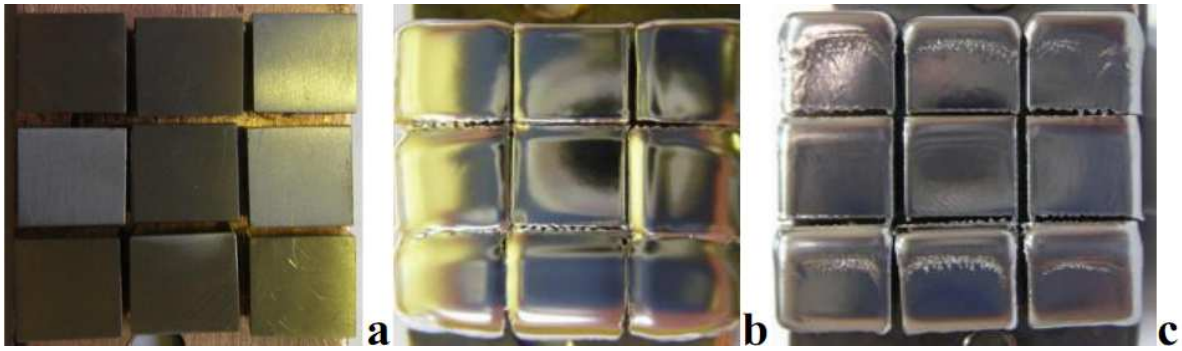

FIG. 12. (a) *General view of the target surface, initial plasma exposure with 30 plasma pulses of 0.75 MJ/m^2; (b) normal plasma exposure; (c) inclined plasma exposure .*

The dependencies of number of emitted droplets and their velocity on the start time of the plasma-surface are plotted on the base analyze of continuity registered by high-speed camera. The particles begin to be emitted from the surface almost immediately after the start of the interaction (Fig. 13). The average delay time is 10–40 μs which is in reasonable consistent with estimates of the time of formation of the molten layer.

Particles are emitted toward the incident plasma flow, which may indicate the development of Kelvin-Helmholtz instability at the interface between the molten layer and moved plasma. There are two different groups of particles that could be distinguished. Particles with the small velocities, i.e. below 5 m/s, are displayed on the frames as short tracks with a higher intensity of luminescence.

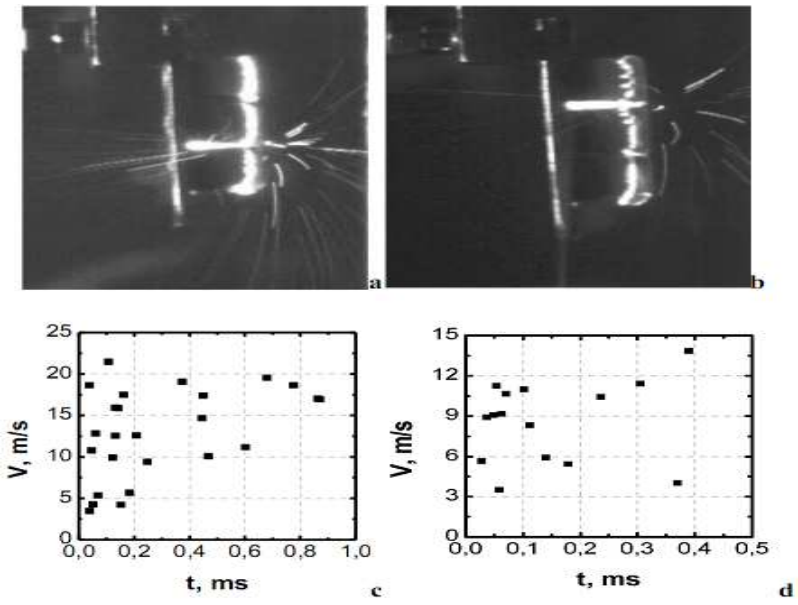

FIG. 13. (a) Frame of the digital camera and with the traces of erosion products corresponding to 1.12–2.32 ms after the start of plasma surface interaction (t_{exp} = 1.2 ms) from the exposed surface for after 30 plasma exposures of 0.75 MJ/m^2; (b) Frame of the digital camera and with the traces of erosion products corresponding to 1.12–2.32 ms after the start of plasma surface interaction (t_{exp} = 1.2 ms) from the exposed surface for after 75 plasma exposures of 0.75 MJ/m^2; (c) distributions of velocities of ejected particles versus particle startup time from the exposed surface for after 30 plasma exposures of 0.75 MJ/m^2; (d) distributions of velocities of ejected particles versus particle startup time from the exposed surface for after 75 plasma exposures of 0.75 MJ/m^2. Normal plasma irradiation.

Particles that emitted with velocities in the range of 15–20 m/s, are displayed on the frames by longer tracks and thus with lower light intensity (Fig. 13(c)). A decrease of the droplet velocity with increasing number of irradiation pulses is observed (Fig. 13(d)). This decrease could be attributed to the growing size of the droplets ejected from mountains of the re-solidified material on the edge of target and bridges between elements of castellated stricture. (Fig. 12(b)).

To approach the simulation experiment to the expected conditions in ITER target, the plasma exposures were performed also for the target inclined at the angle of 30° to the direction of the plasma flow. After few initial plasma pulses the overheating of some cubes and expansion fastening material particles is occurred similar to the case of a normal irradiation of the target.

Dependence of the emitted particles number on the pulse number has a clear periodic character. The number of particles increases with growing number of irradiating pulses. This is due to the increasing height of the mountains of re-solidified material on the faces of cubes, formation and destruction of bridges of solidified material between adjacent cubes.

With increasing amount of irradiating pulses up to 30, the number of ejected droplets increases. Intense overheating of the upper upstream part of the target is observed with the formation of an excrescence of shifted material to the neighborhood areas, This resolidified material mountain is the predominant region from which most of the particles are emitted (Fig. 14) observed. Droplets are flying toward the flow of plasma. Drops with the highest velocities start at earlier time instances in the range of 0.2–0.4 ms from the beginning of plasma surface interaction. After 40 pulses an intense emission of particles is recorded from the shifted material

excrescence at the front of the castellated structure (Fig. 14). The velocity for majority of the particles is in the range of 10–15 m/s. Almost all the drops are flying along the flow direction of the impacting plasma.

Under the powerful plasma irradiation significant mountains of displaced material (excrescences) are formed due to the plasma pressure action on the faces of castellated elements. It is seen an intense formation of two excrescences, the first has height of 35 μm, height of the second one is 70 μm (Fig. 15). On the base of performed measurements the dependences of the height of the mountains are obtained as it is shown in Fig. 16. It can be noted that the size of the mountains oat the outer perimeter of the macro-brush increases linearly with the amount of plasma pulses. At the same time on the upper side of the macrobrush structure the mountains height first increases abruptly, and then after 56 pulses rite aches some saturation. Such behavior is connected with the peculiarities of the target fixing to the holder.

Mountains from the displaced material are formed not only on the outer perimeter, but also at the internal borders of the cubes. By increasing the number of irradiating pulses such excrescences became to be transformed into jumpers (bridges) between the individual blocks of the castellated target (Fig. 12(b)). Erosion products are flying away both from sides of castellated structure and from the bridges between the cubic elements, which were destroyed during the subsequent plasma pulses. This process occurs until the gaps between the individual elements of the castellated structure are completely filled with resolidified melt.

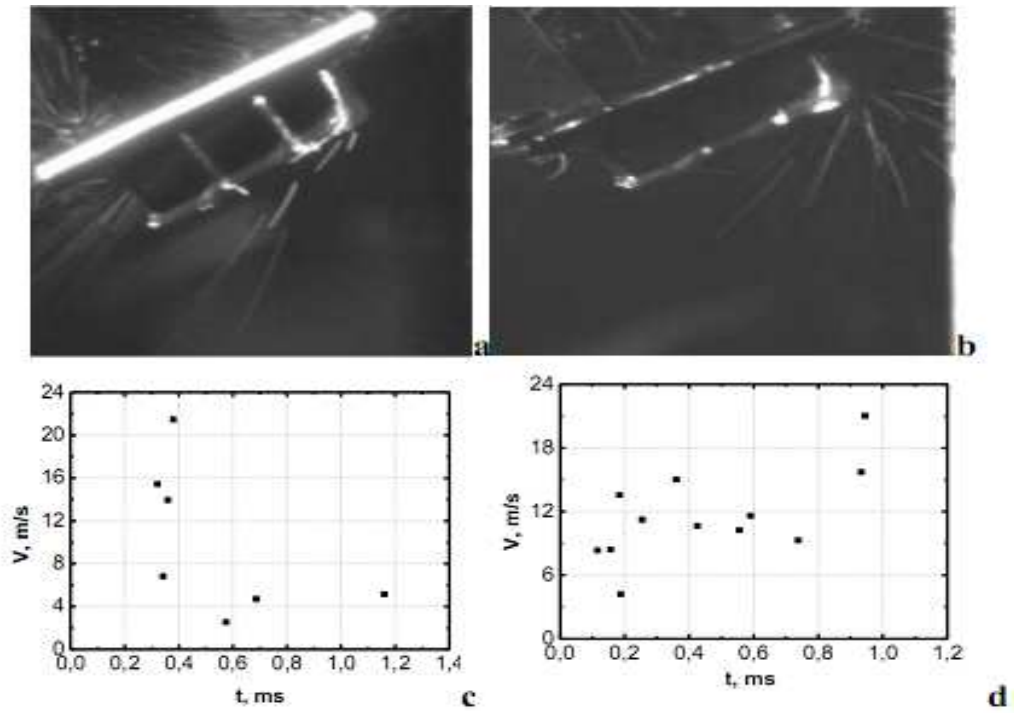

FIG. 14. (a) Frame of the digital camera and with the traces of erosion products corresponding to 1.12–2.32 ms after the start of plasma surface interaction (t_{exp} = 1.2 ms) from the exposed surface for after 30 plasma exposures of 0.75 MJ/m^2; (b) Frame of the digital camera and with the traces of erosion products corresponding to 1.12–2.32 ms after the start of plasma surface interaction (t_{exp} = 1.2 ms) from the exposed surface for after 40 plasma exposures of 0.75 MJ/m^2; (c) distributions of velocities of ejected particles versus particle startup time from the exposed surface for after 30 plasma exposures of 0.75 MJ/m^2; (d) distributions of velocities of ejected particles versus particle startup time from the exposed surface for after 40 plasma exposures of 0.75 MJ/m^2. Inclined plasma irradiation.

The target irradiation with inclined orientation in respect of the direction of plasma stream also leads to the formation of an excrescence consisting of the re-solidified material (Fig. 12(c)). These knurls are formed primarily in the area of maximum impact i.e. on the top part of the castellated structure.

FIG. 15. Image of target lateral face after 2 pulses (left) and profile of surface marked in image (right). Normal irradiation.

At the center of the target and at the lower part an intensive splashing of the molten material is observed. This observation can be explained by following way: under the inclined exposures the protecting plasma layer, which is essentially no uniform along the surface, is formed and it shielded the mentioned surface areas of the target.

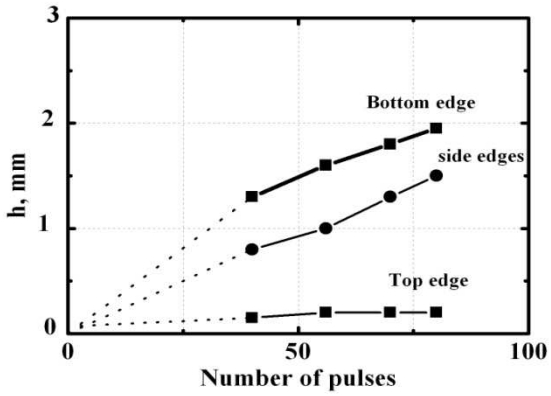

FIG. 16. Size of mountains of resolidified material on different parts of target.

For accurate measurements of the energy density delivered to different areas of the composite target surface a special target has been prepared, which is a set of coaxial cylinders of different diameters. Scheme of the target is presented in Fig. 17. The smallest diameter of 4 cm had the cylinder 1. Diameter of the cylinder 2 was 5.5 cm, height all these cylinders was equal 1 cm. Cylinder 3 with diameter of 7.1 cm and a height of 3 cm was used as the basis for the entire target structure.

To measure the energy density delivered to the surface of the target three calorimeters were used in different places of the target. The first calorimeter was located in the center of the front surface of the first cylinder. The second was installed into a lateral surface of the cylinder 1, as it is shown in Fig. 17. The distance from the front surface to this calorimeter was 6 mm. The third calorimeter was placed in the extended front surface area of the second cylinder at the distance of 2.4 cm from the center of the target. The measurements have been performed under 90° and 30° to incident plasma stream. Those targets were also exposed to perpendicular and inclined plasma irradiation.

For the front calorimeter (number 1) the vapor shielding of the surface begins to appear at an energy density in the incident flow above 1.5 MJ/m^2 under perpendicular irradiation (Fig. 18(a)). It corresponds to the saturation of the dependence curve and indicates the evaporation influence on the energy transfer processes.

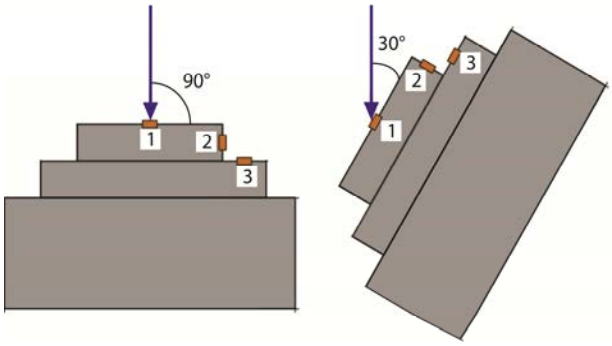

FIG. 17. Scheme of the target with installed calorimeters and direction of plasma impact.

With increasing energy of the incident plasma stream above 1 MJ/m^2 the energy value, which recorded by calorimeter installed to the lateral surface (calorimeter 2) saturates and it does not exceed 0.1 MJ/m^2. This value is at least 7.5 times less than the energy coming to the frontal surface at the maximal specific energy in the impacting plasma stream. The behavior of value of heat load registered by calorimeter 3 is same as for calorimeter 1. The difference between the values of heat load reaching the different parts of the combined target is due to the formation of the plasma shielding layer.

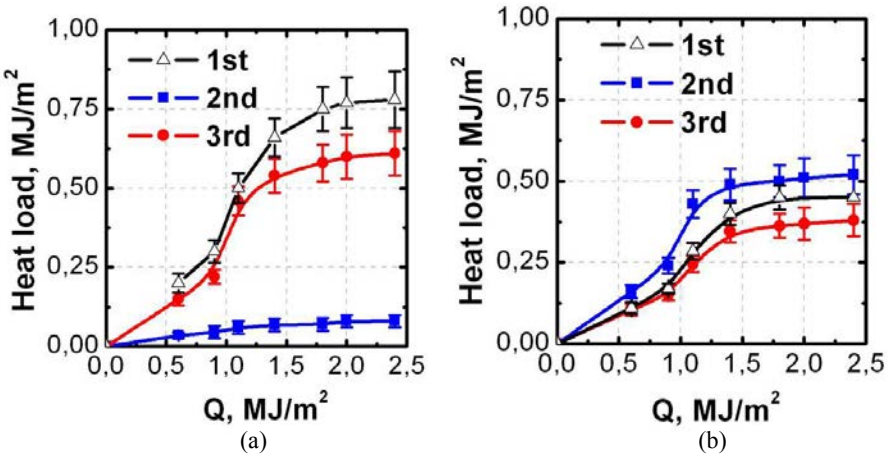

FIG. 18. (a) Heat load to different parts of the target surface versus energy density in plasma stream for perpendicular target; (b) for inclined target.

For inclined irradiation, thickness of the shielding layer is smallest at the upper edge of the sample. This layer of cold plasma is responsible for decreasing part of incident plasma energy which is delivered to the surface (Fig. 18(b)). First of all, it is concern of value of heat load received with calorimeter 1 and 3. The value of heat load measured by calorimeter 2 is at least 5 times larger than the energy measured for perpendicular target. In such case calorimeter is situated closer to incoming plasma than under perpendicular irradiation.

For inclined target, the main part of energy density of incident plasma stream delivers to the top of target. The edges of cubes are melted and molten material displaces under by the action of pressure gradient of incident plasma stream with heat load of 0.75 MJ/m^2. As result, the mountains of resolidified material appear. The melt motion leads to the formation of the bridges between the edges of the structure units. The bridges may break away with the next plasma pulses. Droplet ejection is observed mainly from top region of target. Development of instabilities in the molten layer causes droplets splashing. The droplets fly towards the plasma stream. It may indicate the predominance of Kelvin-Helmholtz instability. At the same time, other instabilities develop in the melt layer on the external edges of the target. It should be mention, that the melt losses due to such instabilities are negligible.

The more intensive melt motion on the surface target is observed under plasma irradiation with the energy density up to 0.9 MJ/m^2. The melt motion leads to filling of the gaps between the units of target by molten metal and appearance of the ripple structure in the affected surface layer. The main mechanisms of particle ejection are separation of the liquid metal from the solid surface (the Taylor criterion) and the Rayleigh-Taylor instability.

Under inclined irradiation the particle startup time from the exposed surface is in range of (0.1–1) ms from the beginning of the plasma surface interaction. The difference between the particle startup times from the exposed surfaces for perpendicularly and inclined can be explained by formation of non-uniform vapor shield.

Second series of experiments has been performed with tungsten brush surfaces. The tungsten macrobrash castellated target consists of nine cylinders with diameter of 5 mm, height of 2 cm and minimal gap between the cylinders of 1 mm (Fig. 19).

FIG. 19. General view of tungsten castellated structures.

Targets were exposed to perpendicular and inclined (inclination angle from parallel to surface incidence is 30º) plasma irradiation with various numbers of pulses.

For normal exposures, castellated tungsten target was irradiated with energy density of 0.9 MJ/m^2. The maximum number of plasma impacts was 100 pulses. The plasma pulses of such energy density caused pronounced melting of target surface. The ripple structures and cracks developed on resolidified tungsten surface (Fig. 20). The microcrack network is attributed to melting and following resolidification. Under the action of next pulses the major cracks are partly filled by molten metal. The edges of cylinders are melted and the mountains of displaced material are formed by the action of pressure gradient with increasing of number of plasma pulses.

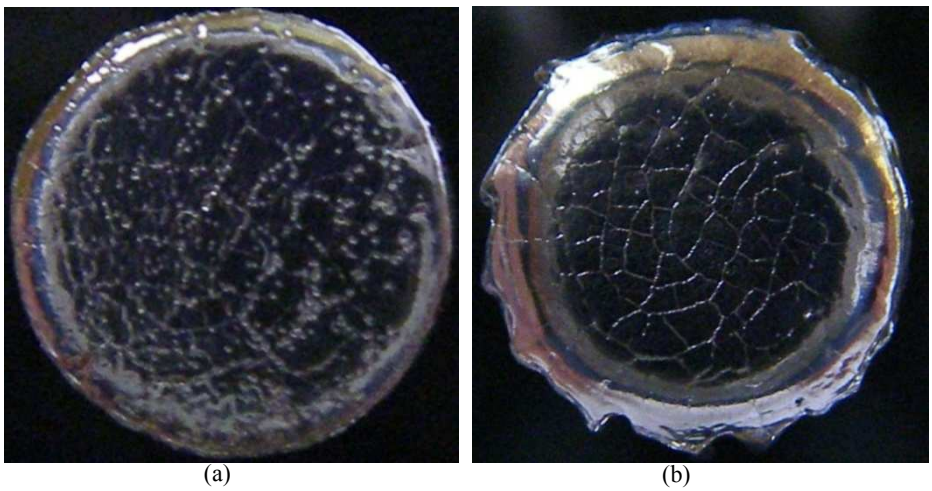

(a) (b)

FIG. 20. (a) Exposed surface of tungsten cylinder after 20 plasma impacts; (b) after100 plasma impacts.

The large number of ejected particles flies away the target surface after 0.2 ms from the beginning of plasma surface interaction (Fig. 21). Therefore, considerable number of particles is ejected in solid state. They may break off from the crack edges during plasma impact.

The major cracks with average network size of 0.8 mm are formed due to the ductile to brittle transition effects. In additional, there are particles which ejected from liquid surface. They have smaller velocities and startup time. It indicates the growing of instabilities on the edges of construction units. Velocity of tungsten particles was up to 20 m/s (Fig. 21).

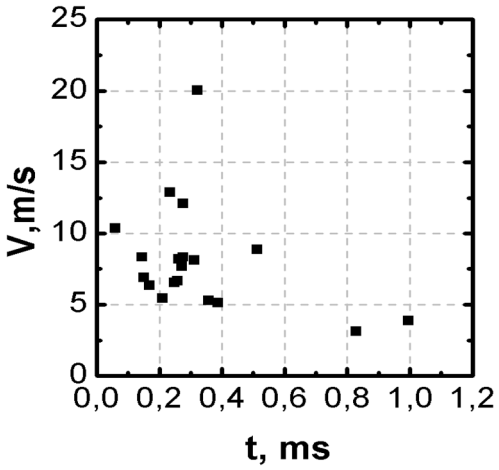

FIG. 21. Velocity distribution of ejected particles versus particle startup time from the exposed tungsten surface after 20 pulses. t=0 corresponds to beginning of plasma-surface interaction.

Both for normal irradiation and for inclined exposures, the dependence of the emitted particles number relative to the pulse number has a clear periodic character (Fig. 22). This is due to the increasing height of the mountains of resolidified material on the faces of cubes, formation and destruction of bridges of resolidified material between adjacent cubes. With increasing amount of irradiating pulses up to 30, the number of ejected droplets increases. Intense overheating of the upper upstream part of the target is observed with the formation of an excrescence of shifted material to the neighborhood areas.

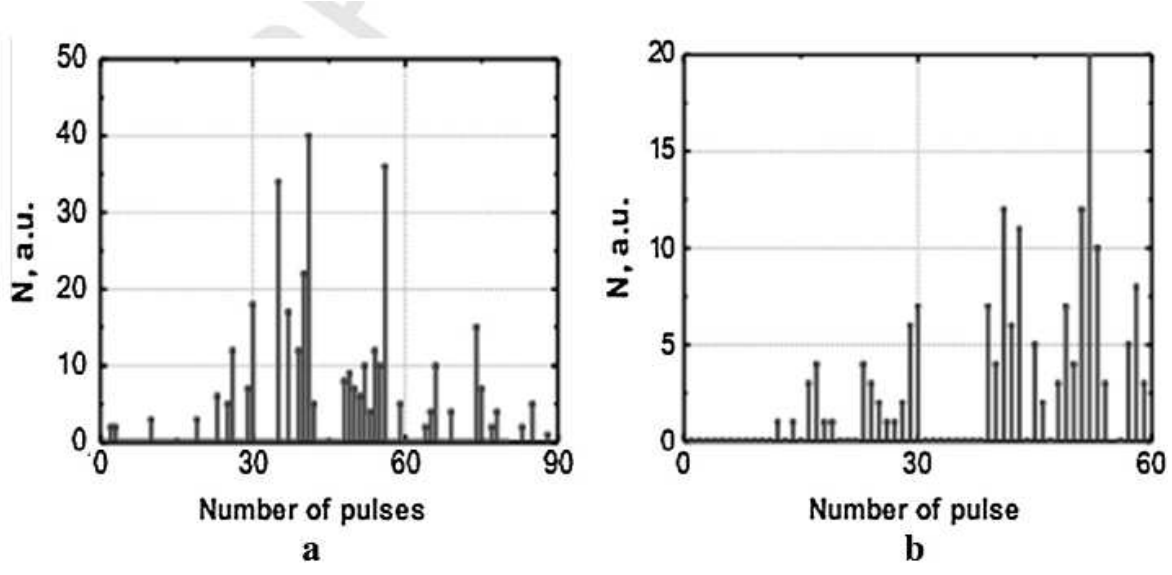

FIG. 22. (a) Number of ejected Ti particles versus number of plasma pulses, normal irradiation; (b) inclined irradiation. Plasma heat load of 0.75 MJ/m^2.

Thus emission of the droplets has a threshold character and the cyclical nature, i.e. it begins only after a certain number of irradiating pulses when the mountain of shifted molten material is developed on the edges of castellated structure. The same conclusion can be done for W brush target damage features (Fig. 23).

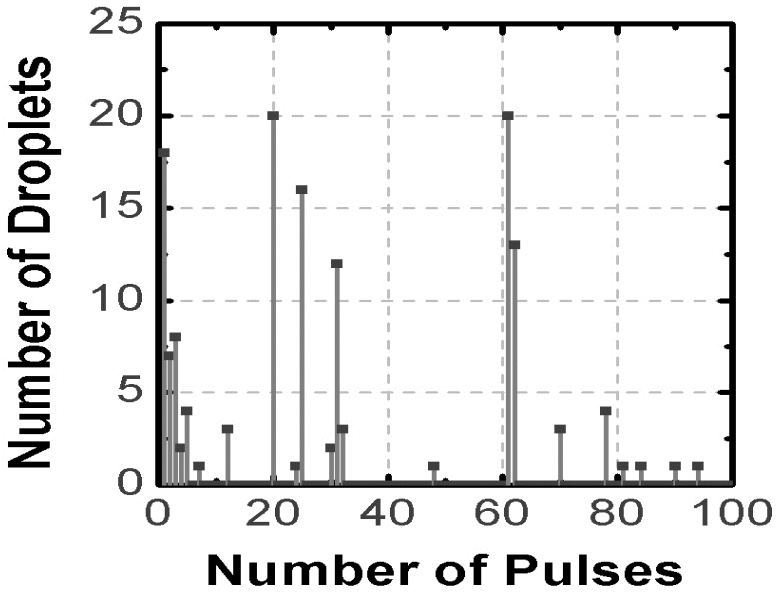

FIG. 23. Number of ejected W particles versus number of plasma pulses.

4.2. Characterization of material surface damage in round robin tests in qspa kh-50 device.

Eight CRP samples have been received from the IAEA. Seven samples have been exposed. One CRP sample remains unexposed. The exposure regimes were as follows:

TABLE 1. TREATMENT CONDITIONS FOR CRP SAMPLES

Target	Heat load (MJ/m^2) pulse duration 0.25 ms	N. of pulses
CRP75	0.45	100
CRP76	0.45	100
CRP73	0.45	10
CRP74	0.45	10
CRP18	0.45	10
CRP19	0.75	10
CRP21	0.75	10

Also, two FZJ samples were exposed for comparative investigations of e-beam and plasma impacts. Surface roughness development in the course of plasma exposures is summarized in the table below:

TABLE 2. ROUGHNESS OF EXPOSED SAMPLES

Target	Heat load (MJ/m^2)	N. of pulses	Roughness		
			Rmax (μm)	Rz (μm)	Ra (μm)
CRP75	0.45	100	1.3	0.9	0.1
CRP76	0.45	100	1.6	1.4	0.2
CRP73	0.45	10	1.0	0.6	0.1
CRP74	0.45	10	0.9	0.8	0.1
CRP18	0.45	10	1.0	0.8	0.1
CRP19	0.75	10	3.1	1.2	0.1
CRP21	0.75	10	2.1	1.2	0.2
CRP20	–	–	1.0	0.7	0.1

XRD analysis of stresses that induced in surface layer by plasma pulses has been performed also.

It was revealed that the lattice parameter does not changed significantly.
For 0.45 MJ/m^2 heat load the maximum stress is ~ 400 MPa and it does not depend on the initial state (see DF 73 and 74). With increased number of pulses up to 100, stresses relaxed to 270−284 MPa. The line width (B) decreases i.e. changing dislocation density in the irradiated layer.

Asymmetry δS (the difference between left and right side of the line profile) become negative, i.e. increasing the right hand side.

TABLE 3. XRD ANALYSIS OF EXPOSED SAMPLES

Target	Heat load	N. of pulses	a_0 (å)	σ (MPa)	B(degree)	δS (%)
DF73	0 (initial)	0	3.1640	-33	0.56	+8
	0.45 MJ/m^2	10	3.1649	440	0.52	-3
DF74	0 (initial)	0	3.1640	-360	0.55	+7
	0.45 MJ/m^2	10	3.1645	390	0.53	-12
DF75	0 (initial)	0	3.1641	-380	0.56	+6
	0.45 MJ/m^2	100	3.1644	270	0.44	-7
DF76	0 (initial)	0	3.1640	-365	0.58	+7
	0.45 MJ/m^2	100	3.1646	284	0.48	-13
DF21	0 (initial)	0	3.1642	-47	0.5	+2
	0.75 MJ/m^2	10	3.1647	301	0.47	-1.5

This may be explained by increase in the number of interstitial complexes, which is consistent with a slight increase in the lattice parameter. For heat load of 0.75 MJ/m^2 trends are the same as for energy density of 0.45 MJ/m^2.

5. CONCLUSIONS

The performed experiments were concentrated on comparative studies of plasma surface interaction features under irradiation of different candidate materials of fusion reactor with high power plasma loads of variable parameters. The investigations were aimed to support mainstream fusion research in part of testing of radiation-resistant materials perspective for large thermonuclear devices of both types (with magnetic and inertial plasma confinement) and for plasma technologies. The performed activity included:

- Adjustment of operational regimes of QSPA Kh-50 and PPA devices to achieve adequate variation of energy and particles loads to the exposed candidate materials. Measurements of plasma parameters in different operational regimes of simulation experiments.
- Investigations of particles ejection, both in form of droplets and solid dust, from exposed tungsten and carbon surfaces under QSPA plasma exposures. Analysis of particles velocity distribution and angular dependencies, as well as their start times from the surface. Systematization of the experimental results obtained for different regimes of tungsten exposures.
- Evaluation of resulting contribution of the droplet splashing to the mass loss of tungsten in different experimental conditions (pressure, its gradient, heat load, duration).
- Comparison of the experimental results with prediction of numerical modeling (MEMOS code). Extrapolation of the obtained results to ITER impacts.
- Investigations of damage features of targets edges in castellated geometry. Experimental study of damage thresholds and melt splashing mechanisms for different parts of castellated targets in applied experimental conditions (pressure, its gradient, impact energy, pulse duration).
- Characterization of the melt motion in edge areas, droplets splashing and melt bridges through the brush slits. Estimations of possible contribution of plasma pressure, surface tension, Kelvin-Helmholtz melt instability, friction force and other factors to the erosion process for brush geometry.
- Systematization of the experimental results obtained for different regimes of inclined brush targets exposures.
- Round robin tests of the IAEA distributed W targets in QSPA Kh-50 device.
- Characterization of material surface damage in Round Robin tests. Participation in development of joint database on material erosion in the course of plasma exposures in differen devices from CRP participating teams.
- Participation in joint experiments with dense plasma devices in Poland, taking part in workshops, schools.

In performed simulation experiments with QSPA Kh-50 several mechanisms of a dust generation under the transient energy loads to the tungsten surfaces have been recognized and identified. Dust particles with sizes up to ten μm could be ejected from the surface due to the cracking development and major cracks bifurcation. This mechanism would be important for first transient impacts when crack mesh is formed. The energy loads can be moderate and even could not result in melting. However, it has to be above the cracking threshold. Taking into account that for many repetitive pulses the cracking threshold shifts to smaller energy loads, this mechanism can only be enfeebled by tungsten preheating above the ductile to brittle transition temperature. Fatigue cracks are still able to be developed after a large number of transient impacts to the preheated W surface.

Melting of a surface and development of fine meshes of cracks along the grain boundaries are accompanied by resolidified bridges formation through the fine cracks in the course of melt motion and capillary effects. With next heat pulses (even without melting) such bridges produce nanosize dust. For this mechanism the mass taken away by any single particle is much smaller, but the number of dust particles is considerable.

Furthermore, even if mitigated cracking, the effects of surface modification of tungsten material after the repetitive plasma pulses with development of ordered subμm cellular structures are able to contribute significantly to the dust generation. However the obtained experimental results show that majority of generated dust particles are deposited back to the surface by a plasma pressure. This result is confirmed by plasma parameters measurements in front of the surface (both in IBIS and in QSPA Kh-50). As a sequence, spectral lines of W atoms and ions in plasma are observed during the pulse in very thin near surface layer only.

In experimental studies of tungsten response to the ELM-like plasma exposures, the erosion products emitted from the exposed W surfaces in the form of droplets and solid dust have been clearly distinguished by variation

of impacting heat load with performed analysis of the particles ejection start time, their velocities and jump changes of brightness of the particle traces recorded with CCD technique in front of the target surface.

Droplets are emitted during the plasma exposure and the dust generation dominates after the end of plasma pulse, at the time of the following material cooling. Droplets are emitted predominantly in upstream direction, possible mechanism of droplets splashing in ELM simulation experiments is considered to be from Kelvin-Helmholtz instability. Decrease of the droplets velocity with increasing surface heat load is observed. It could be attributed to the growing size of the droplets for higher energy load.

Obtained results demonstrate that only small fraction of the melt mass is lost by splashing in ELM-like exposures. Following resolidification of the target surface is accompanied by dust ejection in the course of the cracking process.

In disruption simulation experiments the droplets with size up to 100 μm were splashed away from the exposed surface due to the tungsten melt motion mechanism. The estimated velocity of the droplets depends on the particle size and it typically achieves 10 m/s and more. The obtained experimental results on dynamics of splashing and droplets velocity distributions are going to be used for further validation of the MEMOS numerical code.

Comprehensive experimental studies of the macroscopic erosion of castellated targets with a fragmented structure and macrobrush have been performed with a quasi-stationary plasma accelerator QSPA Kh-50. On the basis of the performed analysis, the following key features could be stressed: With increasing the heat load value the startup moment of droplet ejection from the surface became shifted to earlier moments of the plasma - surface interaction. Emission of the droplets has a threshold character and the cyclical nature, i.e. it begins only after a certain number of irradiating pulses when the mountain of shifted molten material is developed on the edges of castellated structure. For a relatively small number of irradiating pulses the excrescences accumulation from the displaced melt material is occurred at the edges of the combine macrobrush structure. Maximal erosion with pronounced splashing of the material attributed mainly to these areas of excrescences. With further increasing the amount of irradiating pulses the bridges between individual cubic elements are formed, which are then destroyed by subsequent pulses. Such destruction of the bridges together with mountain of the displaced material became the main sources ejected droplets. For relatively large number of pulses (more than 80 pulses was applied in our recent studies), the gaps between the elements of the castellated structure are filled completely with the resolidified melt. Accordingly to that effect, the behavior of the target, which had segmented structure initially, is practically become similar to that of the monolithic sample, because of the melt covering the target gaps.

Thus, it is shown that melt dynamics on the structure edges, droplet splashing and molten bridges through the slits are determining processes in macroscopic erosion of castellated surface structures. Both for normal irradiation and for inclined exposures, the dependence of the emitted particles number relative to the pulse number has a clear cyclic character, i.e. it begins only after a certain number of irradiating pulses when the mountain of shifted molten material is developed on the edges of castellated structure

Plasma exposures of the IAEA distributed tungsten targets have been carried out with QSPA Kh-50 in the frame of round robin tests. First analysis of exposed samples has been performed. After this first step, some of QSPA exposed samples were subjected to irradiation with other simulators. Database on material surface characterization after exposures with different devices has been created (roughness values, crack distance, crack depth and width).

ACKNOWLEDGEMENT

This research has been supported by the targeted research program of NAS of Ukraine “Plasma Physics and Plasma Technologies”, STCU project 6057 and the IAEA CRP F1.30.13.

REFERENCES

[1] SHOSHIN, A.A., BURDAKOV, A.V., CHEBOTAREV, V.V., GARKUSHA, I.E., IVANOV, I.A., KUKLIN, K.N., MAKHLAJ, V.A., MARCHENKO, A.K., POLOSATKIN, S.V., TERESHIN, V.I., Plasma-surface interaction during ITER Type 1 ELMs: Comparison of simulation with QSPA Kh-50 and the GOL-3 Facilities, Fusion Science and Technology **59** (2011) 57.

[2] SKLADNIK-SADOWSKA, E., MALINOWSKI, K., SADOWSKI, M.J., KUBKOWSKA, M., JAKUBOWSKA, K., PADUCH, M., SCHOLZ, M., GARKUSHA, I.E., LADYGINA, M., TERESHIN, V.I., Optical spectroscopy of free-propagating plasma and its nteraction with tungsten targets in PF-1000 facility, Contrib. Plasma Phys. **51** (2011) 288.
[3] BANDURA, A.N., BYRKA, O.V., CHEBOTAREV, V.V., GARKUSHA, I.E., MAKHLAY, V.A., TERESHIN, V.I., SKOBLO, T.S., PUGACH, S.G., Alloying and modification of structural materials under pulsed plasma treatment, International J. Plasma Environmental Sci. and Technology **5** (2011) 2.
[4] PESTCHANYI, S., GARKUSHA, I., LANDMAN, I., Simulation of residual thermostress in tungsten after repetitive ELM-like heat loads, Fusion Eng. Des. **86** (2011) 1681.
[5] MAKHLAJ, V.A., GARKUSHA, I.E., BYRKA, O.V., CHREBOTAREV, V.V., LANDMAN, I.S., LEBEDEV, S.I., MALYKHIN, S.V., PUGACHEV, A.T., SHEVCHUK, P.B., TERESHIN, V.I., Influence of hydrogen and helium plasma streams exposures on modification of tungsten structure under powerful transient loads, Problems of Atomic Science and Technology, Series: Plasma Physics **1** (2011) 71.
[6] BANDURA, A.N., BYRKA, O.V., GARKUSHA, I.E., LADYGINA, M.S., MARCHENKO, A.K., PETROV, YU.V., SOLYAKOV, D.G., CHEBOTAREV, V.V., CHUVILO, A.A., Characteristics of plasma streams and optimization of operational regimes for magnetoplasma compressor, Problems of Atomic Science and Technology, Series: Plasma Physics **1** (2011) 68.
[7] BYRKA, O.V., BANDURA, A.N., CHEBOTAREV, V.V., GARKUSHA, I.E., GARKUSHA, V.V., MAKHLAJ, V.A., TERESHIN, V.I., Influence of plasma stream parameters in pulsed Plasma gun on modification processes in exposed structural materials, Problems of Atomic Science and Technology, Series: Plasma Physics **1** (2011) 158.
[8] LADYGINA, M.S., GARKUSHA I.E., MARCHENKO, A.K., MAKHLAI, V.A., SADOWSKI, M.J., SKLADNIK-SADOWSKA, E., AKSENOV, N.N., TERESHIN, V.I., Spectroscopy of plasma surface interaction in experiments simulating ITER transient events., Fusion Science and Technology **60** (2011) 27.
[9] GARKUSHA, I.E., et al, Discharge characteristics and dynamics of compressive plasma streams generated by a compact magnetoplasma compressor, Plasma Phys. Rep. **37** 11 (2011) 948.
[10] GARKUSHA, I.E., et al., Performance of deformed tungsten under ELM-like plasma exposures in QSPA Kh-50, J. Nucl. Mater. **415** (2011) S65–S69.
[11] PETROV, YU.V., GARKUSHA, I.E., HASSANEIN, A., SOLYAKOV, D.G., MARCHENKO, A.K., CHEBOTAREV, V.V., LADYGINA, M.S., STALTSOV, V.V., YELISYEYEV, D.V., Diagnostic system for EUV radiation measurements from dense xenon plasma generated by MPC, Problems of atomic science and technology, Series: Plasma Physics **1** (2011) 185.
[12] KWIATKOWSKI, R., SKLADNIK-SADOWSKA, E., MALINOWSKI, K., SADOWSKI, M.J., CZAUS, K., ZEBROWSKI, J., KARPINSKI, L., PADUCH, M., SCHOLZ, M., GARKUSHA, I.E., KUBEŠ, P., Measurements of electron and ion beams emitted from the PF-1000 device in the upstream and downstream direction, Nukleonika **56** 2 (2011) 119−123.
[13] MARCHENKO, A.K., GARKUSHA, I. E., CHEBOTAREV, V.V., LADYGINA, M.S., PETROV, YU.V., SOLYAKOV, D.G., TERESHIN, V.I., AKSENOV, N.N., STALTSOV, V.V., HASSANEIN, A., SKLADNIK-SADOWSKA, E., Features of plasma focus formation in different operation modes of gas-discharge magnetoplasma compressor, ActaTechnica **56** (2011) T113.
[14] BYRKA, O.V., BANDURA, A.N., GARKUSHA, I.E., MAKHLAI, V.A., TARAN, V.S., TERESHIN, V.I., Application of pulsed plasma streams for surface modification of constructional materials, Acta Technica **56** (2011) T362.
[15] MAKHLAJ, V.A., GARKUSHA, I.E., AKSENOV, N.N., et al., Simulation of ITER edge localized modes' impacts on the divertor surfaces within plasma accelerators, Physica Scripta **T145** (2011) 014061.
[16] PESTCHANYI, S., GARKUSHA, I., MAKHLAJ, V., LANDMAN, I., Estimation of dust production rate from tungsten armour after repetitive ELM-like heat loads, Physica Scripta **T145** (2011) 014062.
[17] KWIATKOWSKI, R, SADOWSKI, M.J., SKLADNIK-SADOWSKA, E., ZEBROWSKI, J., MALINOWSKI, K., CZAUS, K., GARKUSHA, I.E., Time- and space-resolved measurements of high-energy ion beams emitted from PF-type discharges, Nukleonika **57** 2 (2012) 211.
[18] SKLADNIK-SADOWSKA, E., CZAUS, K., MALINOWSKI, K., SADOWSKI, M.J., NOWAKOWSKA-LANGIER, K., LADYGINA, M.S., GARKUSHA, I.E., Optical emission spectroscopy of plasma produced from tungsten target irradiated within RPI-IBIS facility, Nukleonika **57** 2 (2012) 193.
[19] MAKHLAJ, V.A., CHEBOTAREV, V.V., GARKUSHA, I.E., ELISEEV, D.V., LADYGINA, M.S., MARCHENKO, A.K., PETROV, YU.V., SOLYAKOV, D.G., Characterization of dense plasma streams generated by MPC and their interaction with surfaces, Nukleonika **57** 2 (2012) 197-200.
[20] GARKUSHA, I.E., CHEBOTAREV, V.V., SOLYAKOV, D.G., PETROV, YU.V., LADYGINA, M.S., MARCHENKO, A.K., STALTSOV, V.V., YELISEYEV, D.V., Compression zone of a magnetoplasma compressor as a source of extreme UV radiation, Plasma Phys. Rep. **38** 2 (2012) 110.
[21] GARKUSHA, I.E., AKSENOV, N.N., CHUVILO, A.A., LANDMAN, I.S., MAKHLAJ, V.A., MALYKHIN, S.V., PUGACHEV, A.T., SADOWSKI, M.J., SKLADNIK-SADOWSKA, E., Transient plasma loads to the ITER divertor surfaces: simulation experiments with QSPA Kh-50, Nukleonika **57** 2 (2012) 167.
[22] CHUVILO, A.A., GARKUSHA, I.E., MAKHLAJ, V.A., PETROV, YU.V., Calorimetric studies of the energy deposition on a material surface by plasma jets generated with QSPA and MPC devices, Nukleonika **57** 1 (2012) 49−53.
[23] KWIATKOWSKI, R., SKLADNIK-SADOWSKA, E., MALINOWSKI, K., SADOWSKI, M.J., CZAUS, K., ZEBROWSKI, J., GARKUSHA, I.E., Research on spatial and energetic characteristics of the ion beams emitted in the PF-360 discharges, Nukleonika **57** 1 (2012) 67−74.
[24] MAKHLAJ, V.A., GARKUSHA, I.E., AKSENOV, N.N., BYRKA, O.V., LANDMAN, I., LEBEDEV, S.I., SHEVCHUK, P.B., Plasma-surface interaction and mechanisms of dust production in ITER ELM simulation experiments with Qspa Kh-50, Problems of Atomic Science and Technology, Series: Plasma Physics **6** 18 (2012) 55.

[25] MAKHLAJ, V.A, Characterization of QSPA plasma streams in plasma-surface interaction experiments: Simulation of ITER disruption, Problems of Atomic Science and Technology, Series: Plasma Physics **6** (2012) 126.
[26] BAZDYREVA, S.V., GARKUSHA, I.E., MAKHLAJ, V.A., MALYKHIN, S.V., PUGACHOV, A.T., The influence of irradiation by hydrogen plasma on the structure and phase composition Ti-Zr-Ni alloys containing quasicrystalline phase, Problems of Atomic Science and Technology, Series: Plasma Physics **6** (2012) 226.
[27] CHEBOTAREV, V.V., CHEREDNYCHENKO, T.N., ELISEEV, D.V., GARKUSHA, I.E., KOZLOV, A.N., KULIK, N.V., LADYGINA, M.S., MARCHENKO, A.K., MORGAL, YA.I., PETROV, YU.V., SOLYAKOV, D.G., STALTSOV, V.V., MHD Characteristics of compression zone in plasma stream generated by MPC, Problems of Atomic Science and Technology, Series: Plasma Physics **6** (2012) 123.
[28] MAKHLAJ, V.A., GARKUSHA, I.E., AKSENOV, N.N., CHUVILO, A.A., LANDMAN, I.S., High-speed monitoring of dust particles in ITER ELMs simulation experiments with QSPA Kh-50, Acta Polytechnica **53** 2 (2013) 193–196.
[29] MAKHLAJ, V.A., AKSENOV, N.N., BYRKA, O.V., GARKUSHA, I.E., BIZYUKOV, A.A., BIZYUKOV, I.A., GIRKA, O.I., SEREDA, K.N., BAZDYREVA, S.V., MALYKHIN, S.V., PUGACHOV, A.T., Combined exposures of tungsten by stationary and transient hydrogen plasmas heat loads: Preliminary results, Problems of Atomic Science and Technology **1** 83 (2013) 70.
[30] CHEREDNYCHENKO, T.N., GARKUSHA, I.E., CHEBOTAREV, V.V., SOLYAKOV, D.G., PETROV, Y.V., LADYGINA, M.S., ELISEEV, D.V., CHUVILO, A.A., Local magnetohydrodynamic characteristics of the plasma stream generated by MPC, Acta Polytechnica **53** 2 (2013) 131–133.
[31] MAKHLAJ, V.A., Characterization of QSPA plasma streams in plasma-surface interaction experiments: Simulation of ITER ELMs, Problems of Atomic Science and Technology, Series: Plasma Physics **1** (2013) 73.
[32] ASTASHYNSKI, V.M., ANANIN, S.I., CHEBOTAREV, V.V., CHEREDNYCHENKO, T.N., ELISEEV, D.V., GARKUSHA, I.E., KULIK, N.V., LADYGINA, M.S., MARCHENKO, A.K., MORGAL, YA.I., PETROV, YU.V., SOLYAKOV, D.G., STALTSOV V.V., Energy characteristics of plasma streams, generated by MPC, Problems of Atomic Science and Technology, Series: Plasma Physics **1** (2013) 122.
[33] KOZLOV, A.N., GARKUSHA, I.E., KONOVALOV, V.S., NOVIKOV, V.G., The radiation intensity of the lyman alpha line at the ionization front in the quasi-steady plasma accelerator, Problems of Atomic Science and Technology, Series: Plasma Physics **1** (2013) 128.
[34] SADOWSKI, M.J., CZAUS, K., KWIATKOWSKI, R., MALINOWSKI, K., SKŁADNIK-SADOWSKA, E., ŻEBROWSKI, J., PADUCH, M., SCHOLZ, M., GARKUSHA, I.E., MAKHLAY, V.A., Passive corpuscular diagnostics of charged particles emission from high-temperature plasma experiments, Problems of Atomic Science and Technology, Series: Plasma Physics **1** (2013) 252.
[35] SKŁADNIK-SADOWSKA, E., KWIATKOWSKI, R., MALINOWSKI, K., SADOWSKI, M.J., ŻEBROWSKI, J., KUBKOWSKA, M., PADUCH, M., SCHOLZ, M., GRIBKOV, V.A., GARKUSHA, I.E., LADYGINA, M.S., MARCHENKO, A.K., Optical emission spectroscopy of free-propagating plasma streams and plasma produced during their interactions with solid targets, Problems of Atomic Science and Technology, Series: Plasma Physics **1** (2013) 279.
[36] MAKHLAJ, V.A., GARKUSHA, I.E., AKSENOV, N.N., CHUVILO, A.A., CHEBOTAREV, V.V., LANDMAN, I., MALYKHIN, S.V., PESTCHANYI, S., PUGACHOV, A.T., Dust generation mechanisms under powerful plasma impacts to the tungsten surfaces in ITER ELM simulation experiments, J. Nucl. Mater. **438** (2013) S233–S236.
[37] GARKUSHA, I.E., CHEREDNYCHENKO, T.N., LADYGINA, M.S., MAKHLAY, V.A., PETROV, YU.V., SOLYAKOV, D.G., STALTSOV, V.V., YELISYEYEV, D.V., HASSANEIN, A., EUV radiation from pinching discharges of magnetoplasma compressor type and its dependence on the dynamics of compression zone formation, Phys. Scr. **T161** (2014) 014037.
[38] MAKHLAJ, V.A., GARKUSHA, I.E., AKSENOV, N.N., BAZYLEV, B., LANDMAN, I., LINKE, J., MALYKHIN, S.V., PUGACHOV, A.T., SADOWSKI, M.J., SKLADNIK-SADOWSKA, E., WIRTZ, M., Tungsten damage and melt losses under plasma accelerator exposure with ITER ELM relevant conditions, Physica Scripta **T159** (2014) 014024.
[39] GARKUSHA, I.E., MAKHLAI, V.A., AKSENOV, N.N., BAZYLEV, B., LANDMAN, I., SADOWSKI, M., SKLADNIK-SADOWSKA, E., Tungsten melt losses under the QSPA Kh-50 plasma exposures simulating ITER ELMs and disruptions, Fusion Science and Technology **65** (2014) 186.
[40] MAKHLAJ, V.A., GARKUSHA, I.E., AKSENOV, N.N., BAZYLEV, B., BYRKA, O.V., LANDMAN, I., LINKE, J., MALYKHIN, S.V., PUGACHOV, A.T., SADOWSKI, M.J., SKLADNIK-SADOWSKA, E., WIRTZ, M., Plasma exposure of different tungsten grades with plasma accelerators under ITER-relevant conditions, Phys. Scr. **T161** (2014) 014040.
[41] SKLADNIK-SADOWSKA, E., KWIATKOWSKI, R., MALINOWSKI, K., SADOWSKI, M.J., CZAUS, K., ZALOGA, D., ŻEBROWSKI, J., NOWAKOWSKA-LANGIER, K., KUBKOWSKA, M., PADUCH, M., SCHOLZ, M., ZIELINSKA, E., LADYGINA, M.S., GARKUSHA, I.E., GRIBKOV, V.A., DEMINA, E.V., MASLYAEV, S.A., PIMENOV, V.N., Research on interactions of intense deuterium plasma streams with SiC TARGETS in plasma-focus experiments, Problems of Atomic Science and Technology **6** (2014) 72.
[42] MARCHENKO, A.K., LADYGINA, M.S., GARKUSHA, I.E., PETROV, YU.V., SOLYAKOV, D.G., CHEREDNICHENKO, T.N., MAKHLAJ, V.A., CHEBOTAREV, V.V., STALTSOV, V.V., YELISYEYEV, D.V., KRAUZ, V.I., Compression zone formation in the plasma streams generated by MPC facility operating the gasses with sufficiently different mass, Problems of Atomic Science and Technology, Series: Plasma Physics **6** (2014) 83.
[43] GARKUSHA, I.E., MALYKHIN, S.V., MAKHLAJ, V.A., PUGACHOV, A.T., Changes in the structure and substructure of tungsten during irradiation by hydrogen plasma flows at the specific energy close to the heat loads on the ITER surface, Technical Physics **59** 11 (2014) 1620.
[44] STALTSOV, V.V., Pulsed injector of the working substance for magnetoplasma compressor, Problems of Atomic Science and Technology **4** 98 (2015) 140.
[45] LADYGINA, M.S., SKLADNIK-SADOWSKA, E., ZALOGA, D.R., MALINOWSKI, K., SADOWSKI, M.J., KUBKOWSKA, M., KOWALSKA-STRZECIWILK, B., PADUCH, M., ZIELINSKA, E., MIKLASZEWSKI, R.,

GARKUSHA, I.E., GRIBKOV, V.A., Study of tungsten surface interaction with plasma streams at DPF-1000U, Nukleonika **60** 2 (2015) 293.
[46] MAKHLAJ, V.A., GARKUSHA, I.E., AKSENOV, N.N., BAZYLEV, B., BYRKA, O.V., CHEBOTAREV, V.V., LANDMAN, I., HERASHCHENKO, S.S., STALTSOV, V.V., Damage of target edges in brush-like geometry in the course of ELM-like plasma pulses in QSPA Kh-50, J. Nucl. Mater. **463** (2015) 210–214.
[47] GARKUSHA, I.E., MAKHLAJ, V.A., AKSENOV, N.N., BYRKA, O.V., MALYKHIN, S.V., PUGACHOV, A.T., BAZYLEV, B., LANDMAN, I., PINSUK, G., LINKE, J., WIRTZ, M., SADOWSKI, M.J., SKLADNIK-SADOWSKA, E., High power plasma interaction with tungsten grades in ITER relevant conditions, J. Phys., Conferences series **591** (2015) 012030.
[48] MAKHLAI, V.A., GARKUSHA, I.E., AKSENOV, N.N., BAZYLEV, B., BYRKA, O.V., CHEBOTAREV, V.V., LANDMAN, I., HERASHCHENKO, S.S., STALTSOV, V.V., Damage of target edges in brush-like geometry in the course of ELM-like plasma pulses in QSPA Kh-50, J. Nucl. Mater. **463** (2015) 210–214.
[49] LADYGINA, M.S., SKLADNIK-SADOWSKA, E., KWIATKOWSK, R., MALINOWSKI, K., SADOWSKI, M.J., ZALOGA, D., ŻEBROWSKI, J., KUBKOWSKA, M., PADUCH, M., SCHOLZ, M., ZIELINSKA, E., MAKHLAJ, V.A., Spectroscopic studies of plasma streams generated in a 1-MJ plasma-focus facility with and without gas-puffing, Problems Atomic Science Technology, Series: Plasma Physics **21** (2015) 114.
[50] STALTSOV, V.V., CHEBOTAREV, V.V., MAKHLAJ, V.A., High-speed gas injector for powerful plasmadynamic systems, Problems Atomic Science Technology, Ser. Plasma Physics **21** (2015) 118.
[51] BAZDYRIEVA, S.V., GARKUSHA, I.E., MAKHLAJ, V.A., MALYKHIN, S.V., PETROV, YU.V., PUGACHOV, A.T., Modification of Ti-Zr-Ni alloys by powerful plasma stream of different gases, Problems of Atomic Science and Technology, Series: Plasma Physics **21** (2015) 166.
[52] GARKUSHA, I.E., MAKHLAJ, V.A., AKSENOV, N.N., BYRKA, O.V., MALYKHIN, S.V., PUGACHOV, A.T., BAZYLEV, B., LANDMAN, I., PINSUK, G., LINKE, J., WIRTZ, M., SADOWSKI, M.J., SKLADNIK-SADOWSKA, E., High power plasma interaction with tungsten grades in ITER relevant conditions, J. Phys. : Conference Series **591** (2015) 012030.
[53] ZALOGA, D.R., SKLADNIK-SADOWSKA, E., KUBKOWSKA, M., LADYGINA, M.S., MALINOWSKI, K., KWIATKOWSKI, R., SADOWSKI, M.J., PADUCH, M., ZIELINSKA, E., MAKHLAJ, V.A., Comparison of optical spectra recorded during DPF-1000U plasma experiments with gas-puffing, Nukleonika **60** 2 (2015) 309

Annex

Database of surface damage, structural and compositional changes of tungsten materials irradiated under well defined heat and particle load conditions in plasma and particle accelerators. In the following tables, R_m is the maximum roughness, R_z is the average distance between highest peak and lowest valley, R_a is the average roughness, XRD is the X ray diffraction, EDX is the energy dispersive X ray, SEM stands for scanning electron microscopy, XPS stands for X ray photoelectron microscopy, and TEM stands for transmission electron microscopy.

TABLE A–1. IRRADIATION CONDITIONS QSPA Kh-50

<table>
<tr><td rowspan="3">Irradiation Conditions

QSPA Kh-50
UKRAINE</td><td colspan="5">Material (initial state, specimens irradiated)
PLANSEE double forged tungsten</td></tr>
<tr><td colspan="4">Damage of the Surface Layer (after irradiation)</td><td rowspan="2">Change of structure, phase state, chemical composition and properties
(initial state, specimens irradiated)</td></tr>
<tr><td>Surface State</td><td>Defects</td><td>Crack Formation</td><td>Erosion Rate (μm/pulse)</td></tr>
<tr><td>Power Flux Density (W/cm^2):
up to 4×10^5

Pulse Duration (μs):
250

Heat Flux Factor ($W \cdot s^{0.5} \cdot cm^{-2}$):
$(3–6) \times 10^3$

N. of Pulses:
10–400

Working Gas:
Hydrogen

Target Orientation:
Normal</td><td>No melt:
R_m = 1.6 μm,
R_z = 1.2 μm,
R_a = 0.2 μm.

Melt:
R_m = 2.2 μm,
R_z = 1.6 μm,
R_a = 0.2 μm.</td><td>Complexes of point defects;

Interstitial atoms.</td><td>Major crack mesh with ~ 0.5 mm cell size;

Fine inter-granular cracks for resolidified layer of ~ 20–50 μm depth.</td><td>For ELM-like loads
(i) No melt: 0.01;
(ii) Melt: 0.05.

For disruption like loads 0.4.</td><td>XRD analysis:
a) Lattice parameter ‘a’ does not change significantly;
b) Types of defects created: interstitial atoms;
c) Measurement of residual stresses in irradiated samples: maximum stress is ~ 400 MPa; and stress is relieved for repetitive pulses with melting.

EDX analysis:
a) Change in elemental composition: NO;
b) Any oxidation as background gas pressure may be high: NO;
c) Presence of elements from the anode rim ablation: NO.
Microhardness measurements: hardness of exposed sample surfaces decreased by 10–15% from the initial values.</td></tr>
</table>

TABLE A–2. IRRADIATION CONDITIONS PLASMA GUN

Irradiation Conditions PLASMA GUN RUSSIAN FEDERATION	Material (initial state, specimens irradiated) PLANSEE double forged tungsten				
	Damage of the Surface Layer (after irradiation)				Change of structure, phase state, chemical composition and properties (initial state, specimens irradiated)
	Surface State	Defects	Crack Formation	Erosion Rate (μm/pulse)	
Power Flux Density (W/cm^2): $(2.5–10) \times 10^6$ Pulse Duration (μs): 10–15 Heat Flux Fact. ($W \cdot s^{0.5} \cdot cm^{-2}$): $(8–32) \times 10^3$ N. of Pulses: 100–1000 Working Gas: Hydrogen Target Orientation: Normal	After 100 shots columnar assembly perpendicular to the surface plane. After 1000 shots multiple surface melting and its restructuring with increased roughness.	Pores and delamination.	Wedge shaped cracks going from the irradiated surface.	Not measured.	XRD analysis: initial tungsten showed polycrystalline nature with (100) and (111) planes and with an average size of the area of coherent dispersion (ACD) equal 150 nm; irradiated samples showed reduction in ACD; the lattice parameter changed by 0.0178 Å upon irradiation. Estimation of lattice parameter 'a': initial 'a' = 3.1746 Å; after 100 shots 3.1658 Å; after 1000 shots 3.1592 Å. EDX analysis: after 1000 pulses tungsten nitride W_2N or WN was observed.

TABLE A–3. IRRADIATION CONDITIONS TOKAMAK GLOBUS-M

Irradiation Conditions TOKAMAK GLOBUS-M RUSSIAN FEDERATION	Material (initial state, specimens irradiated) PLANSEE double forged tungsten				
	Damage of the Surface Layer (after irradiation)				Change of structure, phase state, chemical composition and properties (initial state, specimens irradiated)
	Surface State	Defects	Crack Formation	Erosion Rate (μm/pulse)	
Power Flux Density (W/cm^2): 10^2	About 1 μm surface was etched and smoothened.	No new defects.	No noticeable changes.	Not measured.	XRD analysis: after 1000 pulses of plasma gun and 2370 tokamak pulses the XRD pattern remains the same; after 100 gun shots and 2370 tokamak pulses the grain size was reduced compared to the sample irradiated only with plasma gun. EDX analysis: after 2370 tokamak pulses boron carbide was detected.
Pulse Duration (μs): ≤ 100					
Heat Flux Factor ($W \cdot s^{0.5} \cdot cm^{-2}$): ≤ 1					
N. of pulses: 2370					
Working Gas: Deuterium					
Target Orientation: Normal					

TABLE A–4. IRRADIATION CONDITIONS PF-1000U, PF-6, PF-5M, BORA

Irradiation Conditions PF-1000U, POLAND PF-6, POLAND PF-5M, RUSSIAN FEDERATION, BORA, ITALY	Material (initial state, specimens irradiated) PLANSEE double forged tungsten				
	Damage of the Surface Layer (after irradiation)				Change of structure, phase state, chemical composition and properties (initial state, specimens irradiated)
	Surface State	Defects	Crack Formation	Erosion Rate (μm/pulse)	
Power Flux Density (W/cm^2): 10^{10}–10^{12} (theoretical estimate)	Wave-like structure, pores, craters, blisters (open and closed), spool-like structures, nanostructure formations, cracks, W-droplets.	Discontinuity flaws (~200 μm), blocks' displacement, defect formation with a decrease of micro-conductivity in the layer up to 500 μm, splashing of material.	A net and a subnet of micro-cracks along grain boundaries and of inter-crystalline type as well inside a re-melted layer.	5×10^{-2}–5.0	XRD analysis: a) Estimation of lattice parameter 'a': on the average 1% (~0.01 Å); b) Change in cell volume: see point a); c) Types of defects created : interstitial; d) Measurement of residual stresses in irradiated samples: residual stresses were increased at the immersion of a sample inside the pinch plasma. EDX analysis: a) Change in elemental compositions: impurities from construction elements of the DPF chambers were on the level of ~ 1 w% (weight%) for W; b) Presence of elements from the anode rim ablation: Cu. SEM analysis: observation of a) Gas bubbles; b) Droplets formation; c) Melt depth of a few μm; d) Damage depth up to 500 μm. Other properties using suitable techniques: a) X ray portable diffractometer combining X ray single photon detection with high spectroscopic and angular resolutions for surface investigations; b) Interplanar distances, d, in W after irradiation increased by 0.01–0.07 Å; c) Impurity lines, Fe (weak) and Ni (strong) were observed after irradiation (DPF chamber's materials).
Pulse Duration (μs): 0.1–0.05					
Heat Flux Factor ($W\cdot s^{0.5}\cdot cm^{-2}$): 3×10^{6}–2×10^{8} (theoretical estimate)					
N. of Pulses: 1–32					
Working Gas: Deuterium					
Target Orientation: Normal; outside of the pinch and immersed into the pinch plasma					

TABLE A–5. IRRADIATION CONDITIONS UNU-ICTP

Irradiation Conditions UNU-ICTP Plasma Focus SINGAPORE	Material (initial state, specimens irradiated) Commercial tungsten grade and PLANSEE double forged tungsten				
	Damage of the Surface Layer (after irradiation)				Change of structure, phase state, chemical composition and properties (initial state, specimens irradiated)
	Surface State	Defects	Crack Formation	Erosion Rate (μm/pul.)	
Power Flux Density (W/cm^2): ~ (1–4) × 10^6 Pulse Duration (μs): ~ 1.0 Heat Flux Factor ($W \cdot s^{0.5} \cdot cm^{-2}$): (1–4) × 10^3 N. of Pulses: 1, 5, 10, 15 and 50 Working gas: Hydrogen, Deuterium Target Orientation: Normal to the ion/plasma stream	For expt. done with aperture assembly on other W grade in H_2: initial mechanical polish marks disappeared, surface reconstruction was observed, and nanostructure formation was noticed. For expt. done without aperture assembly on Plansee double forged W in D_2: initial mechanical polishing marks disappeared, surface reconstruction was observed, and nanostructure formation was noticed.	For expt. done with aperture assembly on other W grade in H_2: vacancy defects and compressive internal stress. For expt. done without aperture assembly on Plansee double forged W in D_2: vacancy defects and compressive internal stress.	For expt. done with aperture assembly on other W grade in H_2: formation of microcracks on reconstructed surface. For expt. done without aperture assembly on Plansee double forged W in D_2: Formation of microcracks on reconstructed surface.	For expt. done with aperture assembly on other W grade in H_2: not measured. For expt. done without aperture assembly on Plansee double forged W in D_2: not measured.	XRD analysis: for expt. done with aperture assembly on other W grade in H_2, the XRD pattern of virgin (unexposed) sample shows reflection peaks corresponding to body centered cubic phase of pure tungsten; the samples irradiated using 5, 10 and 15 focus shots show bcc-tungsten peaks, and an additional peak at $2\Theta = 43.45°$ (which increases with increasing number of shots) indicating the presence of copper. For expt. done without aperture assembly on Plansee double forged W in D_2, the reference unexposed sample exhibits diffraction peaks corresponding to bcc-tungsten with preferred orientation along (002) plane; for all irradiated samples showed the formation of new additional diffraction peaks corresponding to fcc-tungsten appear; the increase in number of shots increased number of fcc-tungsten peaks. XPS analysis: for expt. done with aperture assembly on other W grade W in H_2, not performed. For expt. done without aperture assembly on Plansee double forged W in D_2, all samples (unexposed and irradiated) exhibit the presence of metallic and oxide form of tungsten; for unexposed sample, the oxide form of tungsten was about 72%. The exposure of sample to 1 plasma focus shot at 5 cm leads to significant decrease in oxide form to about 23% while for 5 and 10 shots the oxide form of tungsten was estimated to be 40% and 34%, respectively. Microhardness measurements: for expt. done with aperture assembly on other W grade in H_2, unexposed sample has highest surface hardness of 10–40 GPa at surface which drops and stabilizes between 6–8 GPa at the depth of about 600 nm; for 5 shot irradiation the surface hardness was found to decrease to 2–10 GPa (mostly <4 GPa) and then the hardness mostly increases pointing to a very thin copper impurity layer on surface. For expt. done without aperture assembly on Plansee double forged W in D_2: not performed.

TABLE A–6. IRRADIATION CONDITIONS NX3

Irradiation Conditions NX3 Plasma Focus SINGAPORE	Material (initial state, specimens irradiated) PLANSEE double forged tungsten				
	Damage of the Surface Layer (after irradiation)				Change of structure, phase state, chemical composition and properties (initial state, specimens irradiated)
	Surface State	Defects	Crack Formation	Erosion Rate (μm/pulse)	
Power Flux Density (W/cm^2): ~ 6×10^6–9×10^7	Initial mechanical polish marks disappeared; surface reconstruction observed; droplets, craters, and particles (dust) along with over layer formation; nanostructure formation was also noticed.	Vacancy defects were observed.	Microcracks formation were observed at larger distance but their density decreases at lower distance due to impurity layer formation.	Not measured.	XRD analysis: unexposed sample showed bcc-tungsten phase with (002) preferred orientation; additional XRD peaks corresponding to complex unidentified phases of impurities were observed; for irradiation at 5 cm the W peaks disappeared or diminished significantly. EDX analysis: the presence of Fe, Cr, and O along with W was observed for sample irradiated at 20 cm; for 15 and 10 cm irradiation, EDX peak of impurity elements (Fe, Cr, Al, O and C) increased and that of W decreased; the sample irradiated at 5 cm did not show any EDX peak related to W. XPS analysis: unexposed sample exhibited metallic and oxide form of tungsten; the oxide form was about 72%; the exposure to 1, 5 and 10 shots decreased the oxide form to about 23, 40 and 34% respectively; the presence of Cu, O and N was shown on all samples (unexposed and irradiated ones).
Pulse Duration (μs): ~ 1.0					
Heat Flux Factor (W·s$^{0.5}$·cm^{-2}): ~ 6×10^3–9×10^4					
N. of Pulses: 50					
Working Gas: Deuterium					
Target Orientation: Normal to the ion/plasma stream					

TABLE A–7. IRRADIATION CONDITIONS PF-400J

<table>
<tr><td rowspan="3">Irradiation Conditions

PF-400J
CHILE</td><td colspan="5">Material (initial state, specimens irradiated)
PLANSEE double forged tungsten</td></tr>
<tr><td colspan="4">Damage of the Surface Layer (after irradiation)</td><td rowspan="2">Change of structure, phase state, chemical composition and properties
(initial state, specimens irradiated)</td></tr>
<tr><td>Surface State</td><td>Defects</td><td>Crack Formation</td><td>Erosion Rate (μm/pulse)</td></tr>
<tr><td>Power Flux Density (W/cm^2):
2.6×10^3–9.2×10^6</td><td rowspan="6">Surface roughness is found to increase with increasing power flux density; holes formation and melted zones observed.</td><td rowspan="6">Formation of grain boundaries observed at higher power flux density.</td><td rowspan="6">Microcracks formation is observed.</td><td rowspan="6">Not measured.</td><td rowspan="6">XRD analysis: X ray analyses show compressive stress on tungsten; after irradiation, W is melted and recrystallized to the (011) preferred orientation.

SEM analysis: microcracks, holes, and surface melting were observed.</td></tr>
<tr><td>Pulse Duration (μs):
0.075–0.533</td></tr>
<tr><td>Heat Flux Factor (W·s$^{0.5}$·cm^{-2}):
$(1.9–2.5) \times 10^3$</td></tr>
<tr><td>N. of Pulses:
50</td></tr>
<tr><td>Working Gas:
Deuterium</td></tr>
<tr><td>Target Orientation:
Normal</td></tr>
</table>

TABLE A–8. IRRADIATION CONDITIONS INTI PF

Irradiation Conditions INTI PF MALAYSIA	Material (initial state, specimens irradiated) PLANSEE double forged tungsten				
	Damage of the Surface Layer (after irradiation)				Change of structure, phase state, chemical composition and properties (initial state, specimens irradiated)
	Surface State	Defects	Crack Formation	Erosion Rate (μm/pulse)	
Power Flux Density (W/cm^2): 3.4×10^{10} (theoretical estimate at pinch exit point)	Roughness increase with average surface roughness of 12 μm for 50 shots; for lower number of shots melting and holes formation (~500 nm to 5 μm) were observed.	Not analyzed.	Cracks of width of ~ 300–500 nm.	Not measured.	EDX analysis: high percentage of Cu (~60%) and Zn (~10%) impurities observed for 50 shot; for lower number of shot about ~ 92% tungsten and 8% carbon and some iron (sputtered from shutter material) and oxygen on irradiated surface were observed. SEM analysis: melts, microcracks, and holes observed
Pulse Duration (μs): 0.0076					
Heat Flux Factor ($W \cdot s^{0.5} \cdot cm^{-2}$): 2.9×10^6 (theoretical estimate at pinch exit point)					
N. of Pulses: 1, 5, 10 and 50					
Working Gas: Deuterium					
Target Orientation: Normal					

TABLE A–9. IRRADIATION CONDITIONS PF-12

Irradiation Conditions PF-12 ESTONIA	Material (initial state, specimens irradiated) Commercial tungsten and tungsten with 1% La_2O_3 (WL10) and PLANSEE double forged tungsten				
	Damage of the Surface Layer (after irradiation)				Change of structure, phase state, chemical composition and properties (initial state, specimens irradiated)
	Surface State	Defects	Crack Formation	Erosion Rate (μm/pulse)	
Power Flux Density (W/cm^2): 5×10^7–5×10^8 Pulse Duration (μs): 0.05–0.15 Heat Flux Factor ($W\cdot s^{0.5}\cdot cm^{-2}$): 1.15×10^4–1.2×10^5 N. of Pulses: 25, 100 Working Gas: Deuterium	Wave-like structure, pores, craters, blisters (open and closed), spool-like structures, nanostructure formations, cracks, W droplets. Roughness: R_a = 1.1–5.6 μm, R_z= 20–120 μm.	Bubbles, grooves, droplets.	Mesh of macro and microcracks; the cell size for macrocracks varied 120–500 μm, and for microcracks 25–150 μm.	Not measured.	SEM analysis: wave-like structure, pores, craters, blisters (open and closed), spool-like structures, nanostructure formations, cracks were observed. EDX analysis: copper traces in samples irradiated with 5×10^7 W/cm^2 power flux density for 100 pulses were observed. Measurement of conductivity showing depth of influences material; depth of diminished conductivity is up to 0.5 mm.

TABLE A–10. IRRADIATION CONDITIONS PLASMA FOCUS

Irradiation Conditions Plasma Focus Sofia University BULGARIA	Material (initial state, specimens irradiated) PLANSEE double forged tungsten, sintered tungsten				
	Damage of the Surface Layer (after irradiation)				Change of structure, phase state, chemical composition and properties (initial state, specimens irradiated)
	Surface State	Defects	Crack Formation	Erosion Rate (μm/pulse)	
Power Flux Density (W/cm^2): 2×10^6–2×10^7	Surface became rough from melting and resolidification. Formation of bubbles, grooves and droplets observed.	Not measured.	Well developed mesh of micro and macro cracks.	Not measured.	XRD analysis: not performed. Optical microscope and SEM analysis: at 6 cm distance from the anode evaporation, small blisters, mesh of big and small crack and re-solidification were observed; at 10 cm distance from the anode partially melted regions and cracks formation were observed.
Pulse Duration (μs): 0.05–0.2					
Heat Flux Factor ($W\cdot s^{0.5}\cdot cm^{-2}$): 4.5×10^2–9×10^3					
N. of Pulses: 25, 30, 35					
Working Gas: Deuterium					
Target Orientation: Normal					

TABLE A–11. IRRADIATION CONDITIONS DC 60

<table>
<tr><td rowspan="2">Irradiation Conditions

DC60
Cyclotron
KAZAKHSTAN</td><td colspan="4">Material (initial state, specimens irradiated)
PLANSEE double forged tungsten</td></tr>
<tr><td colspan="4">Damage of the Surface Layer (after irradiation)</td><td rowspan="2">Change of structure, phase state, chemical composition and properties (initial state, specimens irradiated)</td></tr>
<tr><td>Surface State</td><td>Defects</td><td>Crack Formation</td><td>Erosion Rate (μm/pulse)</td></tr>
<tr><td>Energy
45 keV

Irradiation Fluence
1.5×10^{18} cm^{-2}

Particles
$^{4}He^{+2}$</td><td>Appearance of spherical porous spots with diameter up to 10 μm reaching depth of about 100 nm; their density is about several 100 per mm^2.</td><td>Not measured.</td><td>Not found.</td><td>Not measured.</td><td>EDX analysis: no change in elemental composition was observed.

SEM and AFM analysis: formation of bubbles in the straggling area, i.e. in the alpha particles deceleration area; for alpha particles with energy of 45 keV straggling area is located in the near-surface layers of tungsten; bubbles were observed to move to the surface, causing blistering and flaking of the surface; spherical porous spots with diameter up to 10 μm reaching depth of about 100 nm were also and their density is estimated to be about several 100 per mm^2.

Microhardness measurements: the measured values of microhardness $N\mu$ = 570 MPa showed that irradiation with low-energy alpha particles resulted in the surface softening.</td></tr>
</table>

CONTRIBUTORS TO DRAFTING AND REVIEW

Blagoev, A.B.	Sofia University St. Kliment Ohridski, Bulgaria
De Temmerman, G.	Institute for Plasma Physics Rynhuizen, Netherlands
Demina, E.	Russian Academy of Sciences, Russian Federation
Dubrovsky, A.	Moscow Physical Society, Russian Federation
Garkusha, I.	National Science Center, Ukraine
Gribkov, V.	Institute of Plasma Physics and Laser Microfusion, Poland
Gupta, S.C.	Bhabha Atomic Research Centre, India
Jednorog, S.	Institute of Plasma Physics and Laser Microfusion, Poland
Kubes, P.	Czech Technical University, Czech Republic
Laas, T.	Tallinn University, Estonia
Linke, J.	Forschungszentrum Jülich, Germany
Paduch, M.	Institute of Plasma Physics and Laser Microfusion, Poland
Rawat, R.	Nanyang Technological University, Singapore
Saw, S.H.	INTI International University, Malaysia
Soto, L.A.	Comisión Chilena de Energía Nuclear, Chile
Tazhibayeva, I.	Institute of Atomic Energy, Kazakhstan
Tuniz, C.	International Centre for Theoretical Physics, Italy
Voronin, A.	Ioffe Institute, Russian Federation
Yousefi, H.R.	Islamic Azad University, Iran

Research Coordination Meetings

Vienna, Austria: 6–9 December 2011, 12–15 January 2016
Singapore, Singapore: 10–13 June 2013

IAEA
International Atomic Energy Agency

No. 25

ORDERING LOCALLY

In the following countries, IAEA priced publications may be purchased from the sources listed below or from major local booksellers.

Orders for unpriced publications should be made directly to the IAEA. The contact details are given at the end of this list.

CANADA

Renouf Publishing Co. Ltd

22-1010 Polytek Street, Ottawa, ON K1J 9J1, CANADA
Telephone: +1 613 745 2665 • Fax: +1 643 745 7660
Email: order@renoufbooks.com • Web site: www.renoufbooks.com

Bernan / Rowman & Littlefield

15200 NBN Way, Blue Ridge Summit, PA 17214, USA
Tel: +1 800 462 6420 • Fax: +1 800 338 4550
Email: orders@rowman.com Web site: www.rowman.com/bernan

CZECH REPUBLIC

Suweco CZ, s.r.o.

Sestupná 153/11, 162 00 Prague 6, CZECH REPUBLIC
Telephone: +420 242 459 205 • Fax: +420 284 821 646
Email: nakup@suweco.cz • Web site: www.suweco.cz

FRANCE

Form-Edit

5 rue Janssen, PO Box 25, 75921 Paris CEDEX, FRANCE
Telephone: +33 1 42 01 49 49 • Fax: +33 1 42 01 90 90
Email: formedit@formedit.fr • Web site: www.form-edit.com

GERMANY

Goethe Buchhandlung Teubig GmbH

Schweitzer Fachinformationen
Willstätterstrasse 15, 40549 Düsseldorf, GERMANY
Telephone: +49 (0) 211 49 874 015 • Fax: +49 (0) 211 49 874 28
Email: kundenbetreuung.goethe@schweitzer-online.de • Web site: www.goethebuch.de

INDIA

Allied Publishers

1st Floor, Dubash House, 15, J.N. Heredi Marg, Ballard Estate, Mumbai 400001, INDIA
Telephone: +91 22 4212 6930/31/69 • Fax: +91 22 2261 7928
Email: alliedpl@vsnl.com • Web site: www.alliedpublishers.com

Bookwell

3/79 Nirankari, Delhi 110009, INDIA
Telephone: +91 11 2760 1283/4536
Email: bkwell@nde.vsnl.net.in • Web site: www.bookwellindia.com

ITALY

Libreria Scientifica "AEIOU"

Via Vincenzo Maria Coronelli 6, 20146 Milan, ITALY
Telephone: +39 02 48 95 45 52 • Fax: +39 02 48 95 45 48
Email: info@libreriaaeiou.eu • Web site: www.libreriaaeiou.eu

JAPAN

Maruzen-Yushodo Co., Ltd

10-10 Yotsuyasakamachi, Shinjuku-ku, Tokyo 160-0002, JAPAN
Telephone: +81 3 4335 9312 • Fax: +81 3 4335 9364
Email: bookimport@maruzen.co.jp • Web site: www.maruzen.co.jp

RUSSIAN FEDERATION

Scientific and Engineering Centre for Nuclear and Radiation Safety

107140, Moscow, Malaya Krasnoselskaya st. 2/8, bld. 5, RUSSIAN FEDERATION
Telephone: +7 499 264 00 03 • Fax: +7 499 264 28 59
Email: secnrs@secnrs.ru • Web site: www.secnrs.ru

UNITED STATES OF AMERICA

Bernan / Rowman & Littlefield

15200 NBN Way, Blue Ridge Summit, PA 17214, USA
Tel: +1 800 462 6420 • Fax: +1 800 338 4550
Email: orders@rowman.com • Web site: www.rowman.com/bernan

Renouf Publishing Co. Ltd

812 Proctor Avenue, Ogdensburg, NY 13669-2205, USA
Telephone: +1 888 551 7470 • Fax: +1 888 551 7471
Email: orders@renoufbooks.com • Web site: www.renoufbooks.com

Orders for both priced and unpriced publications may be addressed directly to:

Marketing and Sales Unit
International Atomic Energy Agency
Vienna International Centre, PO Box 100, 1400 Vienna, Austria
Telephone: +43 1 2600 22529 or 22530 • Fax: +43 1 2600 29302 or +43 1 26007 22529
Email: sales.publications@iaea.org • Web site: www.iaea.org/books

International Atomic Energy Agency
Vienna
ISBN 978–92–0–108217–6
ISSN 1011–4289